UNIWERSYTET IM. ADAMA MICKIEWICZA W POZNANIU

Wydział Chemii

mgr Daria Anna Nowicka (Brykczyńska)

Rozprawa doktorska

Wielordzeniowe architektury supramolekularne jako układy wielozadaniowe

Multicore supramolecular architectures as multitasking systems

Promotor

Prof. dr hab. Violetta Patroniak

Promotor pomocniczy

dr Adam Paweł Gorczyński

Poznań 2026

UNIWERSYTET IM. ADAMA MICKIEWICZA W POZNANIU

Wydział Chemii

Mojemu Mężowi Jakubowi i Synowi Antoniemu

za nieocenione wsparcie, miłość i wspólnie spędzone chwile

Dziękuję

Rodzicom

za motywację i nieustającą wiarę we mnie

Dziękuję

Prof. dr hab. Violetcie Patroniak

za opiekę, wyrozumiałość oraz możliwości rozwoju

Dziękuję

Dr Adamowi Pawłowi Gorczyńskiemu

za ofiarowany czas i cenne rady

Dziękuję

Koleżankom i Kolegom z Zakładu Syntezy Nanostruktur Funkcjonalnych

za pomoc i niezapomnianą atmosferę w pracy

Prof. UAM dr hab. Teresie Łuczak

Prof. UAM dr hab. Izabeli Pospiesznej-Markiewicz

Prof. dr hab. Maciejowi Kubickiemu

Prof. Arturowi Ciesielskiemu

Dr Nahir Vadra

Dr Dawidowi Pakulskiemu

Panu Grzegorzowi Dutkiewiczowi

za współpracę i możliwość zdobywania doświadczenia

SPIS TREŚCI

WYKAZ SKRÓTÓW 9

STRESZCZENIE W JĘZYKU POLSKIM 11

STRESZCZENIE W JĘZYKU ANGIELSKIM 15

ANKIETA DOROBKU NAUKOWEGO 19

PRZEWODNIK PO PUBLIKACJACH STANOWIĄCYCH ROZPRAWĘ DOKTORSKĄ 27

1. WSTĘP TEORETYCZNY 27
2. CEL PRACY 34
3. OMÓWIENIE WYNIKÓW BADAŃ 36

3.1. Publikacja nr 1 (P1): „Biomimetic O-Demethylation at a copper(II) center with imine ligand: a structural and computational study" – New Journal of Chemistry, 2026, DOI: 10.1039/D5NJ04478B 36

3.2. Publikacja nr 2 (P2): „ Self-assembly of simple Schiff base ligand into unique saddle-type [4x4] tetranuclear architecture and its application as selective voltammetric dopamine sensor in aqueous conditions" – Electrochimica Acta, 2024, 476, 143754. 47

3.3. Publikacja nr 3 (P3): "Application of a simple copper(II) complex compound as an epinephrine selective voltammetric sensor in the presence of uric acid under aqueous conditions " – Dalton Transactions, 2025, 54, 1000-1012. 59

3.4. Publikacja nr 4 (P4): "The effect of ionic versus covalent functionalization of Polyoxometalate hybrid materials with coordinating subunits on their stability and interaction with DNA" – Dalton Transactions, 2024, 53, 11678-11688. 70

3.5. Publikacja nr 5 (P5): "Overview of Wells-Dawson Polyoxometalates: from structure and functionalization to application" – Coordination Chemistry Reviews, 2024, 519, 216091. 77

4. WNIOSKI 86
5. LITERATURA 88

KOPIE PUBLIKACJI NAUKOWYCH WCHODZĄCYCH W ZAKRES ROZPRAWY DOKTORSKIEJ 97

New Journal of Chemistry, 2026, DOI: 10.1039/D5NJ04478B

Electrochimica Acta, 2024, 476, 143754

Dalton Transactions, 2025, 54, 1000-1012

Dalton Transactions, 2024, 53, 11678-11688

Coordination Chemistry Reviews, 2024, 519, 216091

OŚWIADCZENIA WSPÓŁAUTORÓW 258

WYKAZ SKRÓTÓW

^{1}H NMR (*proton Nuclear Magnetic Resonance*) – spektroskopia magnetycznego rezonansu jądrowego protonów

^{13}C NMR (*carbon-13 Nuclear Magnetic Resonance*) – spektroskopia magnetycznego rezonansu jądrowego węgla

^{31}P NMR (*phosphorus-31 Nuclear Magnetic Resonance*) – spektroskopia magnetycznego rezonansu jądrowego fosforu

AA *(Ascorbic Acid)* – kwas askorbinowy

ATR-IR *(Attenuated Total Reflectance Infrared Spectroscopy)* – spektroskopia w podczerwieni ze wzmocnionym całkowitym odbiciem światła

COF *(Covalent Organic Framework)* – organiczna sieć kowalencyjna

CPE (*Carbon Paste Electrode*) – pastowa elektroda węglowa

CV *(Cyclic Voltammetry)* – woltamperometria cykliczna

DA *(Dopamine)* – dopamina

DFT *(Density Functional Theory)* – teoria funkcjonału gęstości

DMSO *(Dimethyl Sulfoxide)* – dimetylosulfotlenek

DPV *(Differential Pulse Voltammetry)* – różnicowa woltamperometria pulsowa

EDAX *(Energy Dispersive X-ray Analysis)* – analiza rentgenowska z dyspersją energii

EP *(Epinephrine)* – epinefryna

EtOH *(Ethanol)* – etanol

ESI-MS *(Electrospray Ionisation Mass Spectrometry)* – spektrometria masowa z elektrorozpylaniem

FT-IR (*Fourier-Transform Infrared Spectroscopy*) – spektroskopia w podczerwieni z transformacją Fouriera

HRMS *(High-Resolution Mass Spectrometry)* – spektrometria masowa wysokiej rozdzielczości

LOD *(Limit Of Detection)* – granica wykrywalności

LOQ *(Limit Of Quantification)* – granica oznaczalności

MeCN *(Acetonitrile)* – acetonitryl

MeOH *(Methanol)* – metanol

PBS *(Phosphate-buffered solution)* – roztwór buforowany fosforanami

PGE (*Pencil Graphite Electrode*) – ołówkowa elektroda grafitowa

POM *(Polyoxometalate)* – polioksometalan

RSD *(Relative Standard Deviation)* – względne odchylenie standardowe

SCE *(Saturated Calomel Electrode)* – nasycona elektroda kalomelowa

SEM *(Scanning Electron Microscpe)* – skaningowy mikroskop elektronowy

SPE (*Screen Printing Electrode*) – elektroda sitodrukowana

TBA (*TetraButylammonium Anions*) – aniony tetrabutyloamoniowe

TGA (*Thermogravimetric Analysis*) – analiza termograwimetryczną

TRIZMA (*Tris(hydroxymethyl)aminomethane*) – tris(hydroksymetylo)aminometan

UA *(Uric Acid)* – kwas moczowy

UV-Vis *(Ultraviolet-Visible Spectroscopy)* – spektroskopia w świetle ultrafioletowym oraz widzialnym

STRESZCZENIE W JĘZYKU POLSKIM

Celem naukowym niniejszej rozprawy doktorskiej pt. "**Wielordzeniowe architektury supramolekularne jako układy wielozadaniowe**" jest:

1. Projektowanie, synteza oraz charakterystyka strukturalno-spektroskopowa architektur supramolekularnych jonów metali *d*-elektronowych, polioksometalanów oraz materiałów hybrydowych.
2. Zbadanie właściwości biomimetycznych oraz elektrochemicznych otrzymanych związków z uwzględnieniem wpływu szkieletu organicznego liganda, aldehydu, jonu metalu, przeciwjonu, rozpuszczalnika, temperatury oraz stosunku molowego substratów na multifunkcjonalność otrzymanych architektur supramolekularnych.

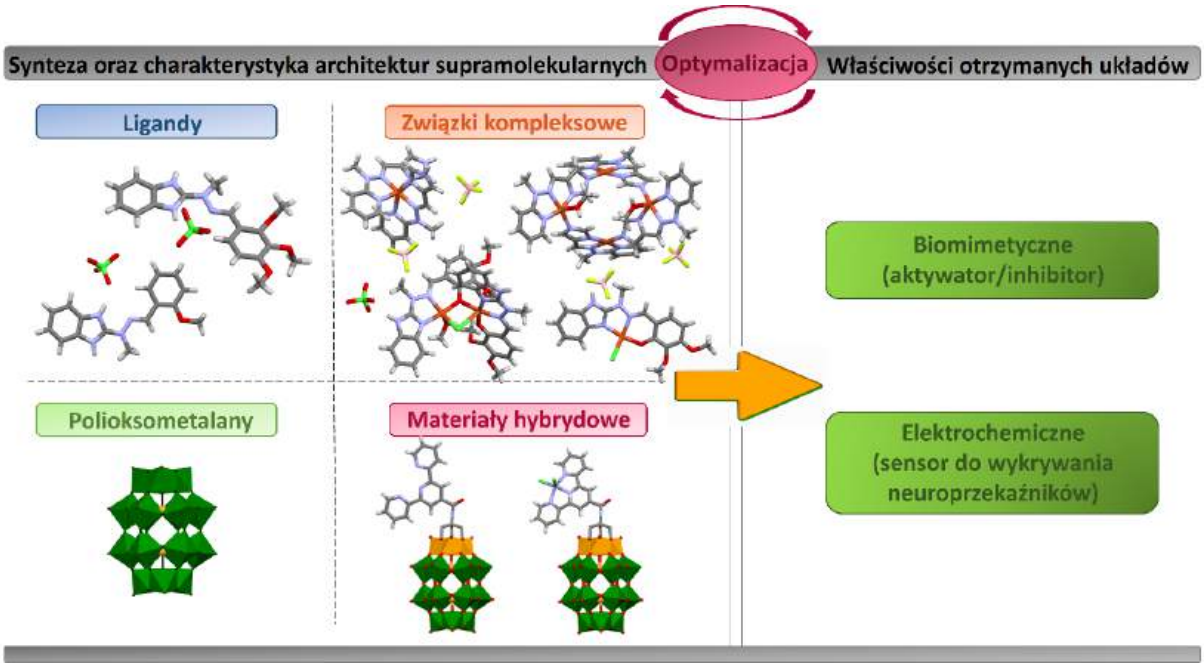

Praca doktorska obejmuje pięć publikacji naukowych, które opisują syntezę oraz charakterystykę strukturalno-spektroskopową układów supramolekularnych w postaci związków kompleksowych metali *d*-elektronowych, polioksometalanów oraz materiałów hybrydowych. Opracowanie strategii syntetycznych poprzez odpowiednie zaprojektowanie struktur architektur supramolekularnych jest kluczowe dla efektywnego wykazywania właściwości biomimetycznych oraz elektrochemicznych przez otrzymane układy.

Pierwsza publikacja z cyklu opisuje pierwszy w literaturze przykład oksydacyjnej *O*-demetylacji zachodzącej przy udziale centrum Cu(II) opartego na ligandzie iminowym, bez dodatku silnych utleniaczy, takich jak nadtlenki. W pracy przedstawiono procesy samoorganizacji trzech ligandów N,N,O-donorowych typu zasady Schiffa **L1** [$C_{18}H_{20}N_4O_3$], **L2** [$C_{16}H_{16}N_4O$] oraz **L3** [$C_{18}H_{20}N_4O_2$] wobec jonów Cu^{2+} w obecności wybranych kationów: Mn^{2+}, Na^+ oraz anionów: Cl^-, ClO_4^-, mających pełnić rolę biomimetyków enzymu jakim jest demetylaza oksydacyjna.

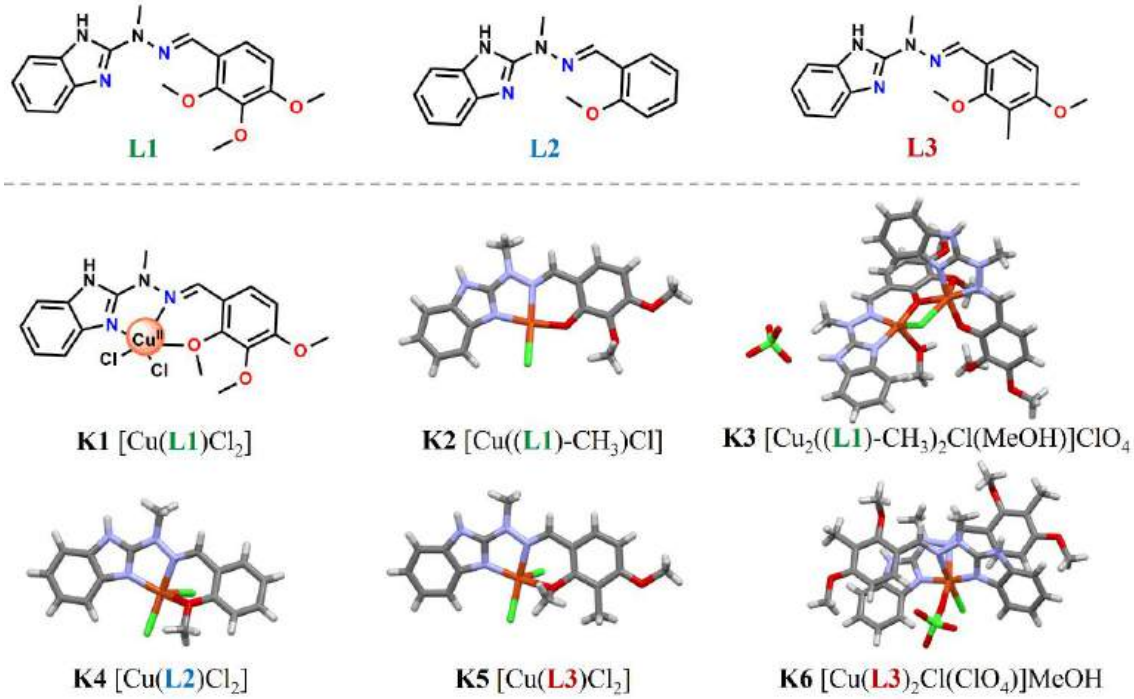

Szczególnie istotna jest obecność wiązania C-O-C w strukturze szkieletu liganda, na bazie którego została badana reakcja oksydacyjnej *O*-demetylacji polegająca na usunięciu grupy metylowej przyłączonej do atomu tlenu, prowadząc do powstania grupy hydroksylowej. Optymalizacja reakcji pozwoliła określić wpływ różnych czynników na otrzymane produkty, co z kolei umożliwiło opracowanie strategii prowadzącej do uzyskania demetylowanego produktu w łagodnych warunkach reakcji. W publikacji przedstawiono sześć związków kompleksowych: **K1** [Cu(L1)Cl_2], **K2** [Cu((L1)-CH_3)Cl], **K3** [Cu_2((L1)-CH_3)$_2$Cl(MeOH)]ClO_4, **K4** [Cu(L2)Cl_2], **K5** [Cu(L3)Cl_2] oraz **K6** [Cu(L3)$_2$Cl(ClO_4)]MeOH. *O*-demetylację oksydacyjną obserwowano tylko dla związków bazujących na ligandzie **L1** przy zastosowaniu odpowiednich warunków reakcji. Po dodaniu anionu chloranowego(VII) do

kompleksu **K1**, ligand **L1** ulega demetylacji w centrum metalu, co powoduje utworzenie kompleksów **K2** i **K3** z demetylowanym ligandem.

Druga oraz trzecia publikacja przedstawiają samoorganizację liganda N,N,N-donorowego typu zasady Schiffa **L4** [$C_{10}H_{11}N_5$] w obecności soli $Cu(CH_3CN)_4BF_4$ oraz $Cu(BF_4)_2 \cdot xH_2O$ tworząc kolejno wielordzeniowy związek kompleksowy **K7** [$Cu_4((L4)\text{-}H)_4(BF_4)_2(MeOH)_2](BF_4)_2$ oraz monometaliczny kompleks **K8** [$Cu(L4)_2](BF_4)_2$.

L4

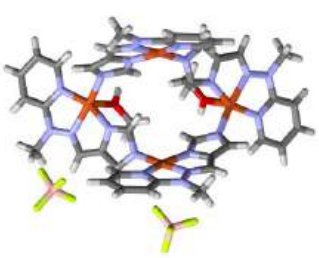

K7 [Cu_4((**L4**)-H)$_4(BF_4)_2(MeOH)_2](BF_4)_2$

K8 [Cu(**L4**)$_2](BF_4)_2$

Otrzymane układy supramolekularne zastosowano do modyfikacji powierzchni elektrody złotej i sprawdzono czy tak zmodyfikowana elektroda może posłużyć jako element przewodzący w elektrochemicznym sensorze do wykrywania neuroprzekaźników obecnych w żywych organizmach (dopamina oraz epinefryna). Budowa badanych układów supramolekularnych pozwoliła na ich adsorpcję na powierzchni złota bez konieczności wykorzystania ugrupowań tiolowych, które pomimo swoich licznych i dobrze znanych wad, takich jak podatność na zmiany pH, utleniacze i rozpuszczalniki organiczne, są szeroko stosowane w modyfikacji powierzchni złota ze względu na łatwość wiązania S-Au. Kolejnym atutem jest fakt, że tak zmodyfikowane elektrody złote mogą być stosowane do niezależnej detekcji dopaminy oraz epinefryny, a także do ich wykrywania w obecności czynników zakłócających (kwas askorbinowy oraz kwas moczowy) w warunkach wodnych, czyli zbliżonych do fizjologicznych. Wykorzystanie zaproponowanych czujników woltamperometrycznych może przyczynić się do kontrolowania zawartości neuroprzekaźników w organizmach żywych zwiększając szansę na szybsze wykrycie chorób neurodegeneracyjnych.

Czwarta publikacja dotyczy materiałów hybrydowych **H1** – **H3** otrzymanych w wyniku reakcji pomiędzy ligandem pirydynowym **L5** [$C_{20}H_{19}N_3O_2$] z ugrupowaniem R^1-C(=O)-O-R^2, gdzie R^1 – $C_{17}H_{14}N_3$, R^2 – C_2H_5, bądź jego kompleksami **K9** [$Zn(L5)Cl_2$] lub **K10** [$Zn(L5)_2](ClO_4)_2$ oraz zmodyfikowanym polioksometalanem typu Wellsa-Dawsona **WD-POM** $(TBA)_4H_2$ [$H_2NC(CH_2O)_3P_2V_3W_{15}O_{59}] \cdot 3C_3H_7NO$ zawierającym ugrupowanie R^3-NH_2.

Publikacja koncentruje się na dobraniu odpowiedniej drogi syntezy pożądanych produktów, badaniu stabilności oraz interakcji z kwasami nukleinowymi.

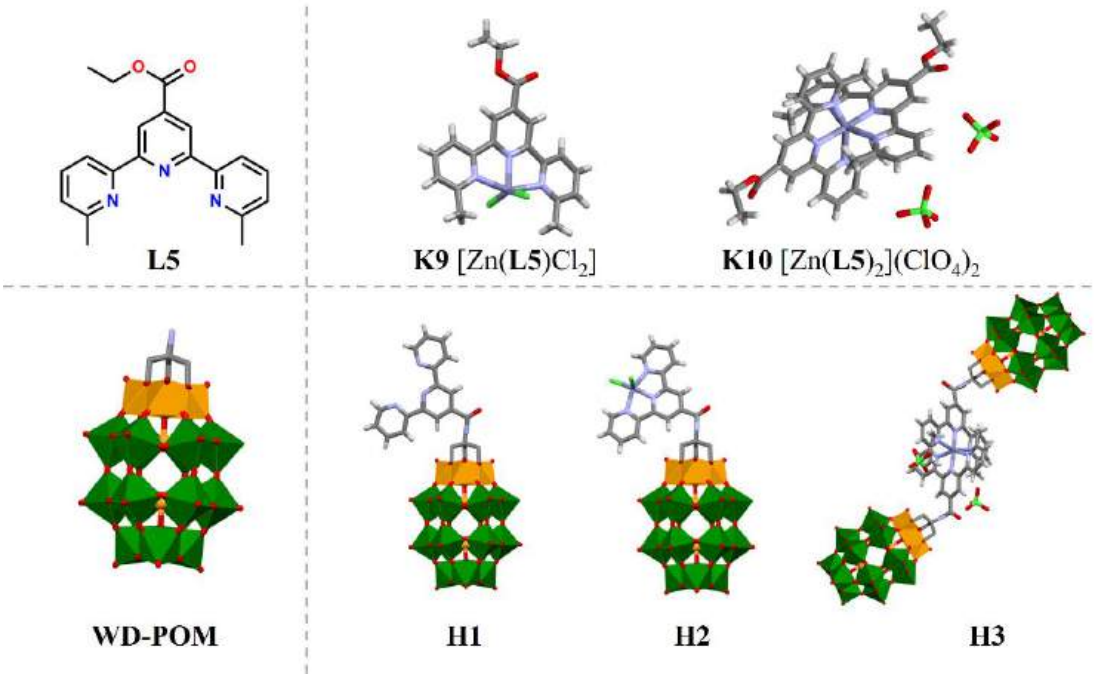

Ostatnia publikacja z cyklu jest publikacją przeglądową obejmującą obszerny temat polioksometalanów typu Wellsa-Dawsona, ich strukturę, typy modyfikacji, możliwości funkcjonalizacji wykorzystujące wprowadzenie podstawników organicznych, w tym ligandów bądź ich kompleksów, specjacje w środowiskach o różnych wartościach pH, a także możliwości aplikacyjne w dziedzinach takich jak: kataliza, magnetyzm, medycyna oraz jako inne materiały funkcjonalne.

STRESZCZENIE W JĘZYKU ANGIELSKIM

The scientific objective of this dissertation, entitled "**Multicore supramolecular architectures as multitasking systems**" is:

1) Design, synthesis and structural-spectroscopic characterization of supramolecular architectures of *d*-electron metal ions, polyoxometalates and hybrid materials
2) Study of the biomimetic and electrochemical properties of the obtained compounds, taking into account the influence of the organic backbone of the ligand, aldehyde, metal ion, counter ion, solvent, temperature and molar ratio of the substrates on the multifunctionality of the obtained supramolecular architectures.

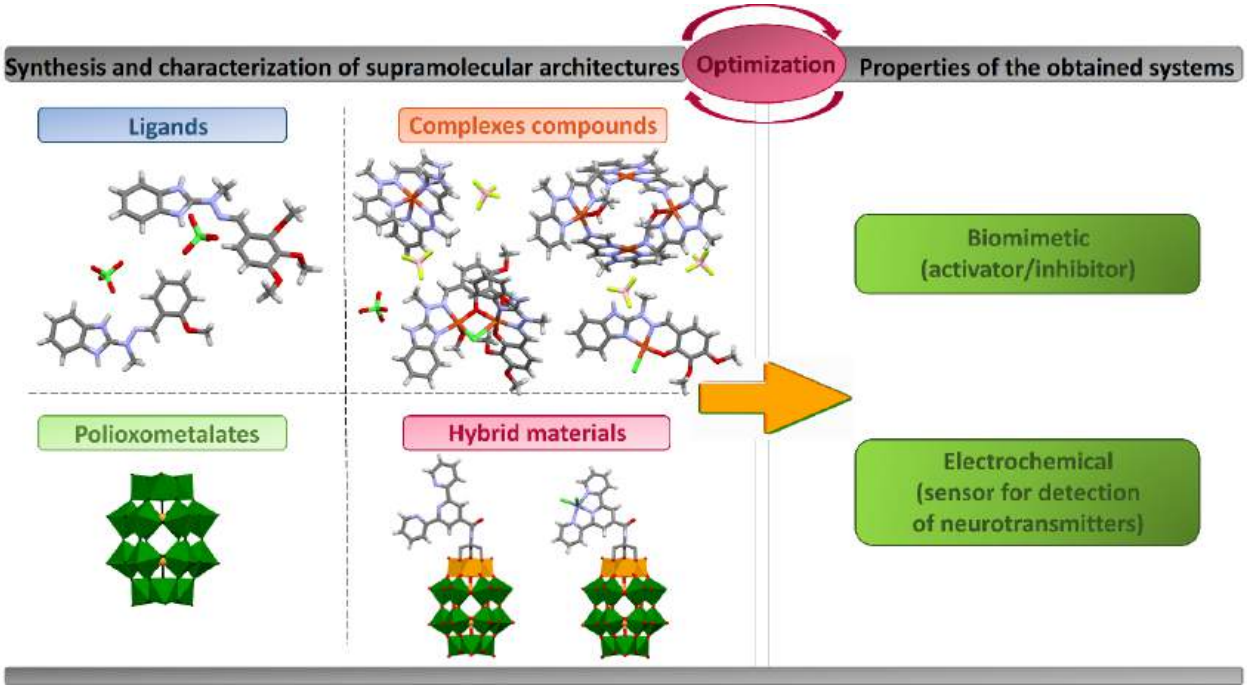

The dissertation includes five scientific publications that describe the synthesis and structural-spectroscopic characterization of supramolecular systems in the form of *d*-electron metal complex compounds, polyoxometalates and hybrid materials. Developing synthetic strategies by properly designing the structures of supramolecular architectures is crucial for the resulting systems to effectively exhibit biomimetic and electrochemical properties.

The first publication in the series describes the first example in the literature of oxidative *O*-demethylation occurring with the participation of a Cu(II) center based on an imine ligand

without the addition of strong oxidants such as peroxides. The paper presents the self-organization processes of three N,N,O-donor ligands of the Schiff base type **L1** [$C_{18}H_{20}N_4O_3$], **L2** [$C_{16}H_{16}N_4O$] and **L3** [$C_{18}H_{20}N_4O_2$] with respect to Cu^{2+} ions in the presence of selected cations: Mn^{2+}, Na^+ and anions: Cl^-, ClO_4^-, which are to act as biomimetics of the enzyme oxidative demethylase.

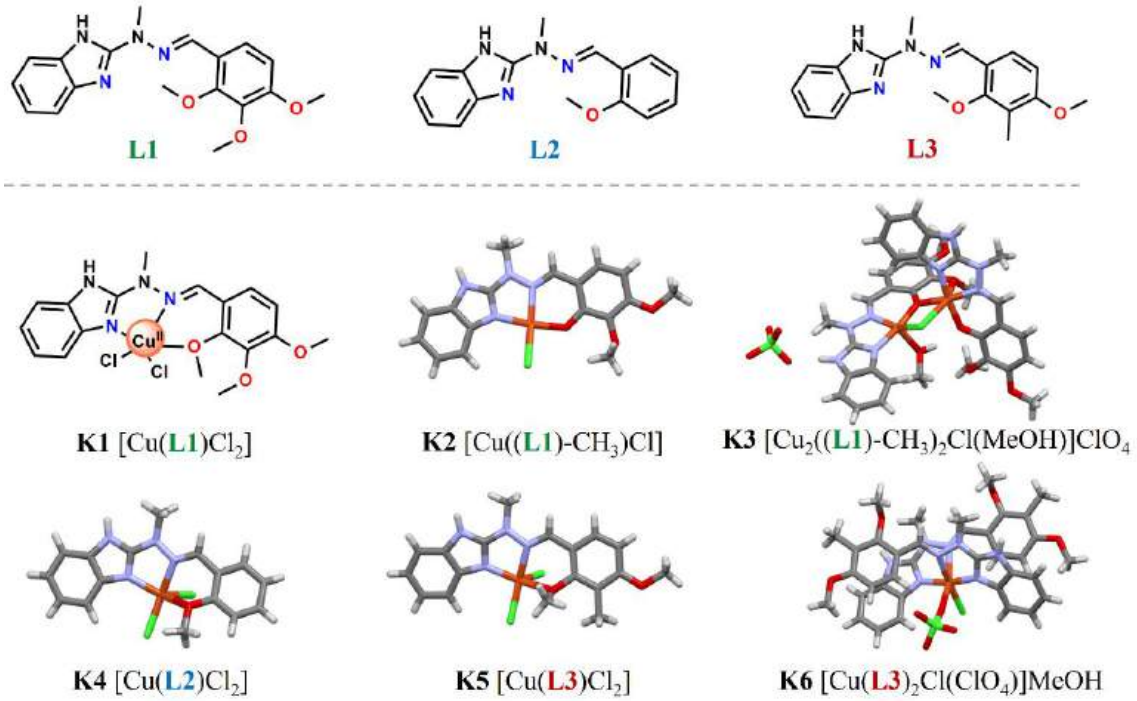

The presence of a C-O-C bond in the ligand skeleton structure is particularly important. Based on this, the reaction of oxidative *O*-demethylation was studied, which involves the removal of a methyl group attached to an oxygen atom, leading to the formation of a hydroxyl group. Optimization of the reaction allowed the influence of various factors on the obtained products to be determined, which in turn enabled the development of a strategy leading to the obtaining of a demethylated product under mild reaction conditions. In this publication, six complex compounds is presented: **K1** [Cu(L1)Cl_2], **K2** [Cu((L1)-CH_3)Cl], **K3** [Cu_2((L1)-CH_3)$_2$Cl(MeOH)]ClO_4, **K4** [Cu(L2)Cl_2], **K5** [Cu(L3)Cl_2] and **K6** [Cu(L3)$_2$Cl(ClO_4)]MeOH. Oxidative *O*-demethylation was observed only for compounds based on the **L1** ligand using appropriate reaction conditions. When a chlorate(VII) anion is added to the **K1** complex, the **L1** ligand is demethylated at the metal center, resulting in the formation of **K2** and **K3** complexes with the demethylated ligand.

The second and third publications show the self-assembly of the N,N,N-donor ligand of the Schiff base type **L4** [$C_{10}H_{11}N_5$] in the presence of $Cu(CH_3CN)_4BF_4$ and $Cu(BF_4)_2 \cdot xH_2O$ salts to form the multicore complex compound **K7** $[Cu_4((L4)\text{-}H)_4(BF_4)_2(MeOH)_2](BF_4)_2$ and the monometallic complex **K8** $[Cu(L4)_2](BF_4)_2$, respectively.

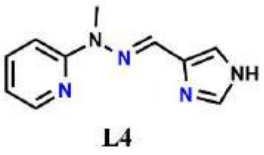

L4

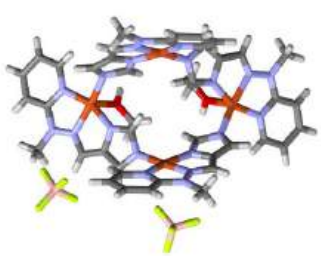

K7 $[Cu_4((\mathbf{L4})\text{-}H)_4(BF_4)_2(MeOH)_2](BF_4)_2$

K8 $[Cu(\mathbf{L4})_2](BF_4)_2$

The resulting supramolecular systems were used to modify the surface of the gold electrode, and it was verified whether the electrode so modified could serve as a conducting element in an electrochemical sensor for detecting neurotransmitters present in living organisms (dopamine and epinephrine). The structure of the studied supramolecular systems allowed their adsorption on the gold surface without the use of thiol moieties, which, despite their numerous and well-known disadvantages, such as susceptibility to pH changes, oxidants and organic solvents, are widely used in gold surface modification due to the ease of S-Au binding. Another advantage is that gold electrodes modified in this way can be used for independent detection of dopamine and epinephrine, as well as for their detection in the presence of interfering agents (ascorbic acid and uric acid) under aqueous, i.e. near physiological conditions. The use of the proposed voltammetric sensors can help control the content of neurotransmitters in living organisms increasing the chance of faster detection of neurodegenerative diseases.

The fourth publication deals with hybrid materials **H1** – **H3** obtained by a reaction between the pyridine ligand **L5** [$C_{20}H_{19}N_3O_2$] with the R^1-C(=O)-O-R^2 grouping, where R^1 – $C_{17}H_{14}N_3$, R^2 – C_2H_5, or its complexes **K9** $[Zn(L5)Cl_2]$ or **K10** $[Zn(L5)_2](ClO_4)_2$ and a modified Wells-Dawson-type polyoxometalate **WD-POM** $(TBA)_4H_2[H_2NC(CH_2O)_3P_2V_3W_{15}O_{59}] \cdot 3C_3H_7NO$ containing the R^3-NH_2 grouping. This publication focuses on selecting an appropriate route to synthesize the desired products, studying stability and interactions with nucleic acids.

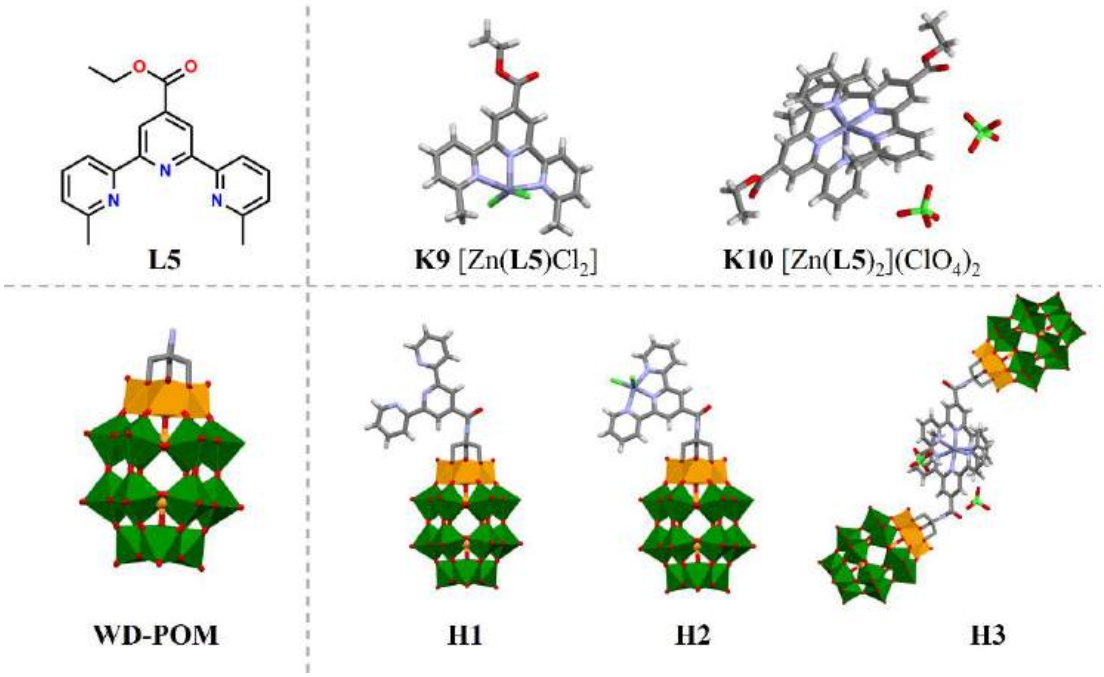

The last publication in the series is a review publication covering the broad topic of Wells-Dawson-type polyoxometalates, their structure, types of modifications, functionalization possibilities using the introduction of organic substituents, including ligands or their complexes, species in environments with different pH values, and application possibilities in fields such as catalysis, magnetism, medicine and as other functional materials.

ANKIETA DOROBKU NAUKOWEGO

mgr Daria Anna Nowicka

Wykaz opublikowanych prac naukowych lub twórczych prac zawodowych oraz informacja o osiągnięciach dydaktycznych, współpracy naukowej i popularyzacji nauki.

A. Publikacje wchodzące w skład rozprawy doktorskiej

1. **Daria Nowicka***, Karol Garbaczewski, Giuseppe Consiglio, Giuseppe Forte, Maciej Kubicki, Teresa Łuczak, Violetta Patroniak, Adam Gorczyński, *„Biomimetic O-demethylation at a copper(II) center with imine ligand: a structural and computational study”,* **New Journal of Chemistry,** 2026, DOI: 10.1039/D5NJ04478B. **IF = 2,5**.

Wkład doktorantki obejmował powtórzenie pierwszego etapu, przeprowadzenie drugiego etapu syntezy trzech nowych ligandów typu zasady Schiffa **L1** [$C_{18}H_{20}N_4O_3$], **L2** [$C_{16}H_{16}N_4O$] oraz **L3** [$C_{18}H_{20}N_4O_2$], syntezę ich kompleksów z jonami metali: **C1** [$Cu(L1)Cl_2$], **C2** [$Cu((L1)\text{-}CH_3)Cl$], **C3** [$Cu_2((L1)\text{-}CH_3)_2Cl(MeO)$], **C4** [$Cu(L2)Cl_2$], **C5** [$Cu(L3)Cl_2$] oraz **C6** [$Cu(L3)_2Cl(ClO_4)$]MeOH, ich charakterystykę strukturalno-spektroskopową (HRMS ESI, FT-IR, ^{1}H NMR, ^{13}C NMR), w tym otrzymanie monokryształów odpowiednich do pomiarów rentgenostrukturalnych, wykonanie badań metodą spektroskopii UV-Vis, przeprowadzenie badań elektrochemicznych pod kierunkiem prof. UAM dr hab. Teresy Łuczak, przygotowanie części graficznej pracy, napisanie pierwszej wersji publikacji z wyłączeniem opisu struktur krystalicznych oraz obliczeń DFT, omówienie wyników w ujęciu całościowym, udział w edycji manuskryptu oraz naniesieniu poprawek edytorskich, w tym przygotowaniu odpowiedzi do recenzentów.

2. **Daria Nowicka***, Maciej Kubicki, Violetta Patroniak, Teresa Łuczak, Adam Gorczyński, *„Self-assembly of simple Schiff base ligand into unique saddle-type [4x4] tetranuclear architecture and its application as selective voltammetric dopamine sensor in aqueous conditions”*, **Electrochimica Acta**, 2024, 476, 143754. **IF = 5,6**.

Wkład doktorantki obejmował powtórzenie syntezy liganda typu zasady Schiffa **HL** [$C_{10}H_{11}N_5$], syntezę jego czterordzeniowego kompleksu z jonami Cu(II) **Cu_4L_4** [Cu_4(L-

$H)_4(BF_4)_2(MeOH)_2](BF_4)_2$, charakterystykę strukturalno-spektroskopową (ESI-MS, FT-IR), w tym otrzymanie monokryształu odpowiedniego do pomiarów rentgenostrukturalnych, modyfikacja powierzchni elektrody złotej, jej charakterystyka (SEM, EDAX, X-ray energy dispersion, ATR-IR) oraz przeprowadzenie badań elektrochemicznych pod kierunkiem prof. UAM dr hab. Teresy Łuczak z wykorzystaniem zmodyfikowanej elektrody wobec detekcji dopaminy, przygotowanie części graficznej pracy, wspólne napisanie publikacji, udział w edycji manuskryptu oraz naniesieniu poprawek edytorskich, w tym przygotowaniu odpowiedzi do recenzentów.

3. **Daria Nowicka***, Karol Garbaczewski, Teresa Łuczak, Giuseppe Forte, Giuseppe Consiglio, Maciej Kubicki, Violetta Patroniak, Adam Gorczyński, *„Application of a simple copper(II) complex compound as an epinephrine selective voltammetric sensor in the presence of uric acid under aqueous conditions”*, **Dalton Transactions**, 2025, 54, 1000 - 1012. **IF = 3,3**.

Wkład doktorantki obejmował powtórzenie syntezy liganda typu zasady Schiffa **L** $[C_{10}H_{11}N_5]$, syntezę jego kompleksu z jonem Cu(II) **CuL_2** $[CuL_2](BF_4)_2$, charakterystykę strukturalno-spektroskopową (HRMS ESI, FT-IR), w tym otrzymanie monokryształu odpowiedniego do pomiarów rentgenostrukturalnych, modyfikacja powierzchni elektrody złotej poprzez utworzenie samoorganizującej się monowarstwy na powierzchni elektrody, jej charakterystyka (SEM, EDAX, X-ray energy dispersion, ATR-IR) oraz przeprowadzenie badań elektrochemicznych pod kierunkiem prof. UAM dr hab. Teresy Łuczak z wykorzystaniem zmodyfikowanej elektrody wobec detekcji epinefryny, przygotowanie części graficznej pracy, wspólne napisanie publikacji, udział w edycji manuskryptu oraz naniesieniu poprawek edytorskich, w tym przygotowaniu odpowiedzi do recenzentów.

4. **Daria Nowicka**[#], Dawid Marcinkowski[#], Nahir Vadra, Martyna Szymańska, Maciej Kubicki, Giuseppe Consiglio, Wojciech Drożdż, Artur R. Stefankiewicz, Violetta Patroniak, Marta Fik-Jaskółka, Adam Gorczyński, *„The effect of ionic versus covalent functionalization of polyoxometalate hybrid materials with coordinating subunits on their stability and interaction with DNA”*, **Dalton Transactions**, 2024, 53, 11678-11688. **IF = 3,3**. (pierwszeństwo współautorów)[#]

Wkład doktorantki obejmował syntezę nowych materiałów hybrydowych: H1^{cov} (POM + L^{tpy}) [V_3POM+TRIZMA+L^{tpy}]TBA$_6$; H2^{cov} (POM+K1) [Zn(V_3POM+TRIZMA+L^{tpy})Cl$_2$]TBA$_6$; H3^{cov} (POM+K2) [Zn(V_3POM+TRIZMA+L^{tpy})$_2$(ClO$_4$)$_2$]TBA$_{(12-x)}$H$_x$; x = 11.5; H4^{cov} (H1^{cov}+ZnCl$_2$) [Zn(V_3POM+TRIZMA+L^{tpy})Cl$_2$]H$_2$TBA$_4$; H5^{cov} (H1^{cov}+Zn(ClO$_4$)$_2$) [Zn(V_3POM+TRIZMA+L^{tpy})$_2$(ClO$_4$)$_2$]H$_{12}$; H6^{cov} (POM+L^{tpy}+ZnCl$_2$) [Zn(V_3POM+TRIZMA+L^{tpy})Cl$_2$]TBA$_{(6-x)}$H$_x$; x = 5.75; H7^{cov} (POM+L^{tpy}+Zn(ClO$_4$)$_2$) [Zn(V_3POM+TRIZMA+L^{tpy})$_2$(ClO$_4$)$_2$]TBA$_{(12-x)}$H$_x$; x = 11.5 oraz ich charakterystykę strukturalno-spektroskopową (ESI-MS, FT-IR, ^{1}H NMR, ^{31}P NMR), napisanie części publikacji dotyczącej syntezy oraz charakterystyki strukturalno-spektroskopowej, udział w przygotowaniu części graficznej pracy oraz wewnętrznej okładki czasopisma (*Inside Front Cover*), udział w edycji manuskryptu oraz naniesieniu poprawek edytorskich, w tym przygotowaniu odpowiedzi do recenzentów.

5. **Daria Nowicka**, Nahir Vadra, Ewelina Wieczorek-Szweda, Violetta Patroniak, Adam Gorczyński, *„Overview of Wells-Dawson Polyoxometalates: from structure and functionalization to application”,* **Coordination Chemistry Reviews,** 2024, 519, 216091. **IF = 23,5**.

Wkład doktorantki obejmował dogłębny przegląd literatury naukowej z zakresu polioksometalanów typu Wellsa-Dawsona, wyselekcjonowanie i zebranie pozycji literaturowych, podział artykułu na odpowiednie sekcje tematyczne, napisanie publikacji z wyłączeniem części aplikacyjnej, udział w przygotowaniu części graficznej pracy, zebranie copyright, udział w edycji manuskryptu oraz naniesieniu poprawek edytorskich, w tym przygotowaniu odpowiedzi do recenzentów.

B. Pozostałe publikacje:

1. **Daria Nowicka**, Verónica Montes-García, Aleksandra Sikora, Violetta Patroniak, Adam Gorczyński, Dawid Pakulski, Artur Ciesielski, *„Polyoxometalate imide-linked molecules, covalent organic polymers and frameworks: dimensionality effects on supercapacitors performance”*, **Advanced Sustainable Systems**, 2025, e00356.

2. Dawid Pakulski, Adam Gorczyński, **Daria Brykczyńska**, Verónica Montes-García, Włodzimierz Czepa, Iwona Janica, Michał Bielejewski, Maciej Kubicki, Violetta Patroniak, Paolo Samorì, Artur Ciesielski, *„New Anderson-Based Polyoxometalate Covalent Organic*

Frameworks as Electrodes for Energy Storage Boosted Through Keto-Enol Tautomerization", **Angewandte Chemie International Edition**, 2023, 62, e202305239.

3. Łukasz Banach, **Daria Brykczyńska**, Adam Gorczyński, Bożena Wyrzykiewicz, Maciej Skrodzki, Piotr Pawluć, *„Markovnikov-selective double hydrosilylation of challenging terminal aryl alkynes under cobalt and iron catalysis"*, **Chemical Communications**, 2022, 58, 13763 – 13766.

4. Paul Chatelain, Cyprien Muller, Abhijit Sau, **Daria Brykczyńska**, Maryam Bahadori, Christopher N. Rowley, Joseph Moran, *„Desulfonative Suzuki–Miyaura Coupling of Sulfonyl Fluorides"*, **Angewandte Chemie International Edition**, 2021, 60, 25307 – 25312.

5. Aleksandra Bocian, Martyna Szymańska, **Daria Brykczyńska**, Maciej Kubicki, Monika Wałęsa-Chorab, Giovanni N. Roviello, Marta A. Fik-Jaskółka, Adam Gorczyński, Violetta Patroniak, *„New artificial biomimetic enzyme analogues based on Iron (II/III) schiff base complexes: an effect of (Benz) imidazole organic moieties on phenoxazinone synthase and DNA recognition",* **Molecules**, 2019, 24, 3173.

6. Aleksandra Bocian, **Daria Brykczyńska**, Maciej Kubicki, Zbigniew Hnatejko, Monika Wałęsa-Chorab, Adam Gorczyński, Violetta Patroniak, *„Complexation behavior of 6, 6 "-dimethyl-2, 2': 6', 2 "-terpyridine ligand with Co (II), Au (III), Ag (I), Zn (II) and Cd (II) ions: Synthesis, spectroscopic characterization and unusual structural motifs"* **Polyhedron**, 2019, 157, 249-261.

C. Sumaryczny impact factor wszystkich publikacji doktoranta według listy Journal Citation Reports (JCR) na rok wydania publikacji wynosi: **88,267**.

D. Łączna liczba cytowań wszystkich publikacji doktoranta według bazy Web of Science (02.02.2026): **147**.

E. Indeks Hirscha dla wszystkich publikacji doktoranta według bazy Web of Science (02.02.2026): **7**.

F. Zgłoszenie patentowe:

Nazwa wynalazku: Sposób otrzymywania nanowłókien hybrydowych lignina-POM-COF lub lignosulfonian-POM-COF z wykorzystaniem techniki elektroprzędzenia

Opis wynalazku: Przedmiotem wynalazku jest sposób otrzymywania nanowłókien hybrydowych lignina-POM-COF lub lignosulfonian-POM-COF za pomocą techniki elektroprzędzenia z wykorzystaniem rozpuszczalników głęboko eutektycznych. Stosując metodę elektroprzędzenia, poli(alkohol winylowy) oraz ligninę typu kraft rozpuszczono w mieszaninie głęboko eutektycznej składającej się z mocznika i kwasu mlekowego w stosunku molowym 1:2 uzyskując roztwory o stężeniu 1% (poli(alkoholu winylowego)) i 2,5% (lignina). Kolejno, do otrzymanego roztworu dodano 100 mg hybrydy POM-COF i rozpoczęto proces elektroprzędzenia w temperaturze pokojowej w zakresie objętościowego natężenia przepływu roztworu równego 0,02 ml/min przy odległości dyszy przędzalniczej (igła w rozmiarze 25 G (0,5 × 2,5 mm)) od kolektora (stalowa płytka owinięta folią aluminiową umieszczona w kąpieli wodnej) równej 10 cm i napięciu wynoszącym 22,6 kV. Ostatecznie, otrzymane nanowłókna lignina-POM-COF są przenoszone z kolektora na folię PTFE i suszone w temperaturze pokojowej.

Numer zgłoszenia patentowego: P.448971

Data i miejsce rejestracji: 2024-06-25; Urząd Patentowy Rzeczpospolitej Polskiej,

Zasięg rejestracji: krajowy

Autorstwo: Marcin Wysokowski, Adam Gorczyński, Aleksandra Sikora, Daria Nowicka, Dawid Marcinkowski, Patrycja Frąckowiak, Filip Kaspryszyn, Eryk Jędrzejczak, Michał Niemczak, Dawid Pakulski, Violetta Patroniak, Artur Ciesielski, Teofil Jesionowski

G. Staże międzynarodowe:

1. 19.09.2022 – 30.09.2022 – Staż naukowy w grupie prof. Paolo Samorì, Institut de Science et d'Ingénierie Supramoléculaires, Univerité de Strasbourg, Francja (współautorstwo publikacji: **Advanced Sustainable Systems,** 2025, e00356).

2. 01.03.2020 – 31.05.2020 – Staż naukowy w grupie prof. Joseph Moran, Institut de Science et d'Ingénierie Supramoléculaires, Univerité de Strasbourg, Francja (współautorstwo publikacji: **Angewandte Chemie International Edition** 2021, 60, 25307 – 25312).

H. Udział w projektach badawczych:

1. Grant Narodowego Centrum Nauki PRELUDIUM **2022/45/N/ST4/00632** *„Nowe kompleksy metali przejściowych zdolne do modyfikacji elektrody złotej jako układy do selektywnego wykrywania neuroprzekaźników"* – kierownik projektu
2. Grant Inicjatywa Doskonałości – Uczelnia Badawcza „Minigranty Doktoranckie" **054/13/SNŚ/0019** *„O-demetylacja oksydacyjna wybranych ligandów iminowych w obecności jonów metali bloku d"* – kierownik projektu
3. Grant Ministerstwa Nauki i Szkolnictwa Wyższego „Najlepsi z Najlepszych 3.0." **MNISW/2019/10/DIR/NN3** *„Badanie właściwości biologicznych i katalitycznych związków kompleksowych Cu(II), Ni(II), Zn(II), Co(II/III), Fe(II/III) z ligandami zawierającymi ugrupowanie sulfonoamidowe"* – wykonawca projektu i współautor wniosku
4. Grant Narodowego Centrum Nauki SONATA **22020/45/N/ST4/01182** *„Wielofunkcyjny charakter makrocyklicznych kompleksów miedzi(II) – wgląd w polimeryzację rodnikową z przeniesieniem atomu (ATRP) oraz nanomagnetyzm molekularny (NMM)"* – wykonawca projektu
5. Grant Narodowego Centrum Nauki OPUS **2016/21/B/ST5/00175** *„Oddziaływania supramolekularne w układach opartych na heteropolianionach skondensowanych"* – wykonawca projektu

I. Udział w konferencjach:

a) Wystąpienia ustne:

1. 1st Polish-Italian Conference on Chemistry, Materials and Biomedicine (CMB), 17-19/09/2025, Rzym, Włochy *„The multifunctionality of self-assembling copper(II) supramolecular systems based on imine ligands"* – konferencja międzynarodowa, autor prezentujący

2. 30th Colloquy on Organometallic Chemistry for Catalysis, 5-6/10/2022, Poznań, Polska *„Catalytic properties of hydrazone metal complexes”* – konferencja międzynarodowa, autor prezentujący
3. French-Polish Symposium on Chemistry, 23-25/05/2022, Paryż, Francja „*The multifunctionality of complexes based on hydrazone-type ligands”* – konferencja międzynarodowa, autor prezentujący
4. The Fifth International Scientific Conference „Advances in Synthesis and Complexing”, 22-26/04/2019, Moskwa, Rosja *„The impact of asymmetrical binding subunits on the richness of (metallo)supramolecular architectures”* – konferencja międzynarodowa, autor prezentujący
5. III Ogólnopolskie Sympozjum Chemii Bioorganicznej, Organicznej i Biomateriałów, 7/12/2019, Poznań, Polska *„Architektury supramolekularne o właściwościach biomimetycznych”* – konferencja krajowa, autor prezentujący

b) Wystąpienia posterowe:

1. 17th International Symposium on Macrocyclic and Supramolecular Chemistry (ISMSC–2023), 25-29/06/2023, Reykjavik, Islandia *„Diversity of multinuclear structures of imine-based supramolecular complexes and their electrochemical properties”* – konferencja międzynarodowa, autor prezentujący
2. Zjazd Zimowy SMPTChem 2021**,** 31/01/2022, Poznań, Polska *„Self-assembly of the imine-type coordination systems in the context of the multifunctionality”* – konferencja krajowa, autor prezentujący
3. Sixth International Conference on Multifunctional, Hybrid and Nanomaterials, 11-15/03/2019, Sitges, Hiszpania *„Iron (II/III) complexes of 25oltam-base ligands as novel biomimetic oxidation models”* – konferencja międzynarodowa, autor prezentujący
4. Chemistry Beyond Nature, 21-22/06/2018, Poznań, Polska *„New complexes of transition metal ions with Schiff base ligands”* – konferencja międzynarodowa, autor prezentujący

J. Nagrody:

1. Laureatka Stypendium START Fundacji na rzecz Nauki Polskiej, 2025 r.
2. Laureatka Stypendium Fundacji UAM dla najlepszych doktorantów 2023/2024 r.
3. Laureatka grantu Narodowego Centrum Nauki: PRELUDIUM, 2022 r.
4. Laureatka Stypendium Rektora I-go stopnia dla najlepszych studentów 2019/2020 r.
5. Laureatka Stypendium Ministra Nauki i Szkolnictwa Wyższego 2018/2019 r.
6. Laureatka Stypendium Rektora I-go stopnia dla najlepszych studentów 2018/2019 r.
7. Laureatka grantu Ministerstwa Nauki i Szkolnictwa Wyższego „Najlepsi z Najlepszych 3.0.”, 2018 r.

PRZEWODNIK PO PUBLIKACJACH STANOWIĄCYCH ROZPRAWĘ DOKTORSKĄ

„Wielordzeniowe architektury supramolekularne jako układy wielozadaniowe”

1. Wstęp teoretyczny

Chemia supramolekularna stanowi jedną z dziedzin chemii, zwaną również jako „chemią poza cząsteczką” (ang. *chemistry beyond the molecule*), skupiającą się na układach molekularnych złożonych z odrębnych indywiduów chemicznych połączonych ze sobą za pomocą oddziaływań niekowalencyjnych[1]. Swój początek zawdzięcza trzem naukowcom: Jean-Marie Lehnowi, Charlesowi J. Pedersenowi oraz Donaldowi J. Cramowi, którzy w roku 1987 otrzymali Nagrodę Nobla za badania dotyczące rozpoznania molekularnego (ang. *molecular recognition*), które obejmuje wiązanie w sposób niekowalencyjny mniejszego układu z innym o większej strukturze. W celu poznania zaproponowanej idei chemię supramolekularną należy podzielić na: koncepcję typu gość – gospodarz oraz samoorganizację (ang. *self – organization*)[2, 3] (Rys. 1). Pierwsza z nich, powstała dzięki nobliście Donaldowi Cramowi i koncentrowała się na utworzeniu supramolekuły z „gospodarza” – większej cząsteczki i „gościa” – mniejszej cząsteczki. Przykładem układów spełniających tę koncepcję pod względem biologicznym są enzymy, zaś pod względem chemicznym związki kompleksowe, gdzie ligand pełni rolę „gospodarza”, a jon metalu „gościa”. W przypadku drugiej koncepcji, różnica wielkości między komponentami nie jest znacząca, a sam proces ich wiązania jest spontaniczny przy jednoczesnym zachowaniu równowagi pomiędzy nimi, co prowadzi do utworzenia samoorganizującej się architektury supramolekularnej. Przykładem układu powstałego na skutek procesu samoorganizacji jest kwas deoksyrybonukleinowy (DNA), który tworzy się wskutek połączenia dwóch nici[4, 5].

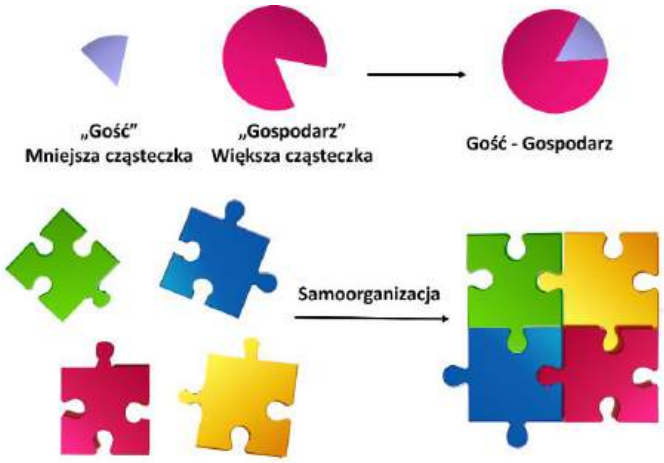

Rysunek 1. Schemat tworzenia supramolekuły według koncepcji typu gość – gospodarz oraz poprzez samoorganizację.

Chemia supramolekularna jest dziedziną interdyscyplinarną z powodu powiązania elementów chemii, biologii i fizyki[6, 7]. Otrzymywanie architektur supramolekularnych składających się z bloków budulcowych o ściśle określonej budowie jest kluczowe dla efektywnego wykazania aktywności między innymi: biomimetycznej[8-11], elektrochemicznej[12-20], katalitycznej[21-28] oraz biologicznej[29-40], co przekłada się na ogromną ilość dostępnych prac literaturowych, które dodatkowo potwierdzają szybki rozwój omawianej dziedziny nauki. Kontrolowana samoorganizacja małych cząsteczek prowadząca do utworzenie układów supramolekularnych spełniających odpowiednie kryteria do dalszych zastosowań nie należy do łatwych zadań. Ponadto, istnieje wiele rodzajów architektur supramolekularnych, wśród których obszerną grupę stanowią: związki kompleksowe[41-45], polioksometalany (POMy) [46, 47] oraz materiały hybrydowe[48-50].

Związki kompleksowe powstają w wyniku procesu koordynacji jonów metali do liganda organicznego. Należą do niezwykle istotnych układów supramolekularnych, głównie poprzez wzgląd na łatwą i przyjazną środowisku syntezę oraz szeroką gamę wykazywanych właściwości. Proces kontrolowanej syntezy związków kompleksowych jest determinowany w szczególności strukturą szkieletu liganda organicznego, a dokładniej ilością, rodzajem i rozmieszczeniem podstawników. Wpływ na otrzymanie układu o pożądanej strukturze ma również wybór odpowiedniego atomu centralnego pod względem jego rozmiaru, preferencji odnośnie liczby koordynacyjnej oraz stopnia utleniania. Przy tworzeniu się układów

nieorganiczno-organicznych dużą rolę odgrywa rodzaj zastosowanego przeciwjonu oraz warunki, w których prowadzona jest reakcja syntezy[5, 51].

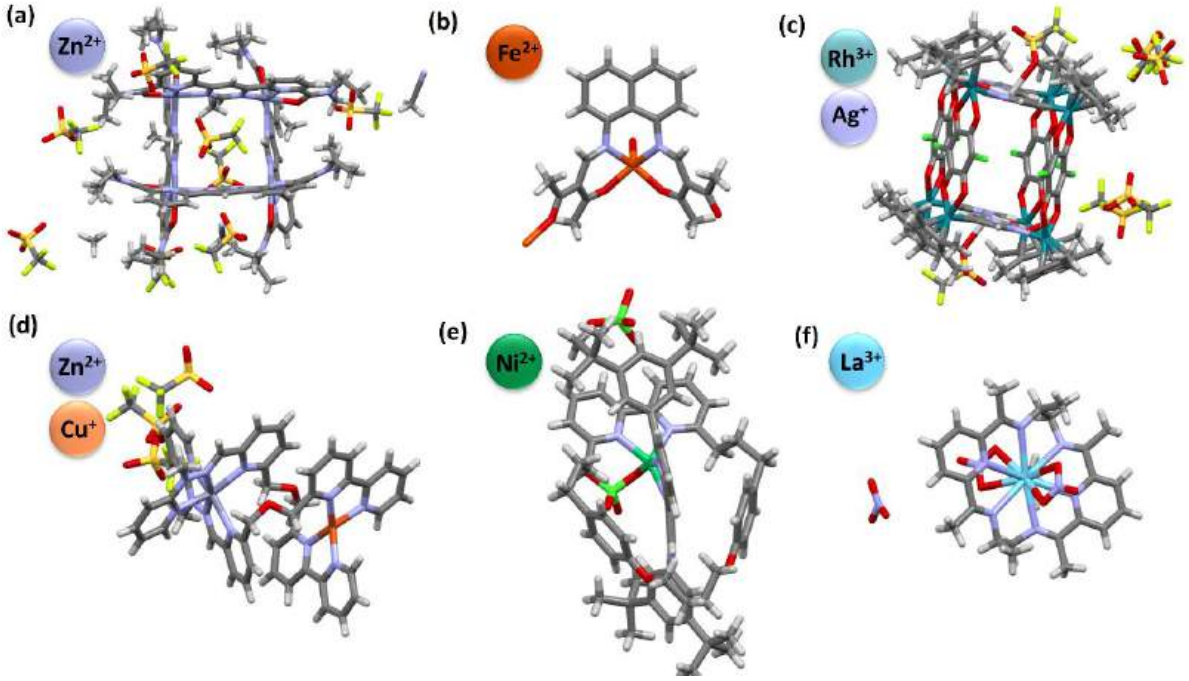

Rysunek 2. Przykładowe związki kompleksowe o zróżnicowanej strukturze: (a) kompleksy kratkowe[52], (b) kompleksy siodłowe[53], (c) kompleksy klatkowe[54], (d) helikaty[55], (e) rotaksany[56] oraz (f) kompleksy makrocykliczne[57].

Kolejna grupa układów supramolekularnych to należące do klasy związków nieorganicznych polioksometalany (POM; ang. *polyoxometalates*), które tworzą się wskutek kondensacji jonów metali przejściowych i atomów tlenu. POMy można zapisać wzorem ogólnym: $[X_xM_mO_o]^{n-}$, gdzie X = heteroatom a M = jon metalu przejściowego na najwyższym stopniu utlenienia (W^{6+}, Mo^{6+}, V^{5+})[58-66]. Formowanie się nieorganicznych bloków budulcowych z pojedynczych podjednostek jest kontrolowane głównie efektami sterycznymi generowanymi strukturą komponentów. Jednakże, na typ otrzymanej struktury ma wpływ również: wartość pH, rodzaj heteroatomów, temperatura, środki redukujące, szybkość jak i kolejność dodawania kolejnych składników[67-70]. Znanych jest kilka typów polioksometalanów, z których najważniejsze to: Lindqvist $[M_6O_{19}]^{n-}$ [71], Anderson-Evans $[XM_6O_{24}]^{n-}$ [72, 73], Keggin $[XM_{12}O_{40}]^{n-}$ [74], Silverton $[XM_{12}O_{42}]^{n-}$ [75], Wells-Dawson $[XM_{18}O_{62}]^{n-}$ [76] oraz Preyssler $[X^{n+}P_5W_{30}O_{110}]^{(15-n)-}$ [77] (Rys. 3). Możliwość samoorganizacji

w poszczególnych archetypach geometrycznych oraz rozmiarach tworzących się układów przejawia się w ich różnorodności strukturalnej, a co za tym idzie w wykazywanych właściwościach, gdzie szczególnie cenione są ich niezwykłe właściwości redoks[78-85].

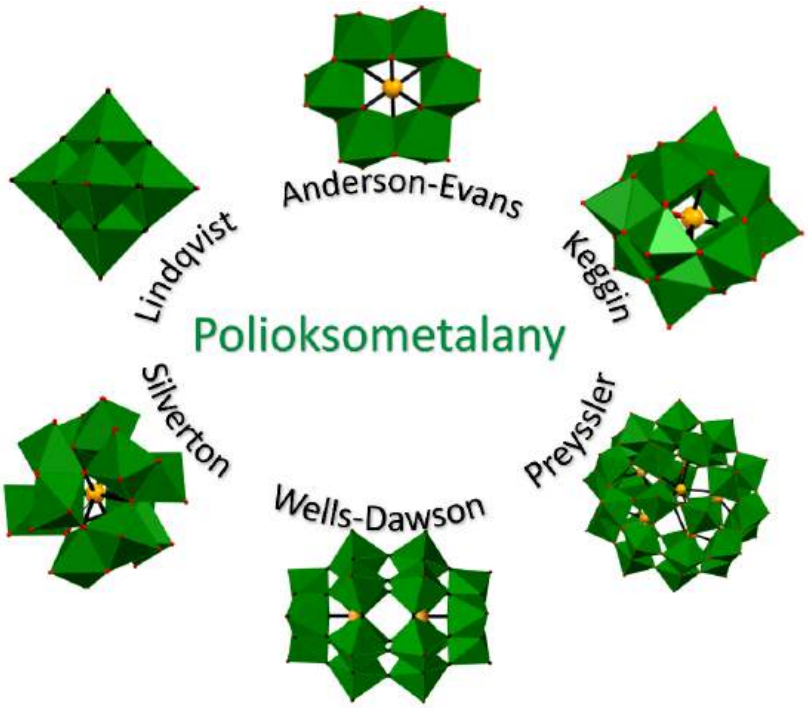

Rysunek 3. Przedstawienie najpopularniejszych struktur polioksometalanów: Lindqvist, Anderson-Evans, Keggin, Silverton, Wells-Dawson oraz Preyssler.

Zarówno związki nieorganiczne jak i organiczne o pożądanej strukturze stanowią podstawę do samoorganizacji złożonych układów jakimi są materiały hybrydowe, których kontrolowane tworzenie polega na doborze substratów z wybranymi grupami funkcyjnymi i przeprowadzeniu reakcji w odpowiednio dobranych warunkach[59, 86]. Materiały hybrydowe mogą stanowić połączenie obu opisanych wyżej grup związków, a więc polioksometalanów ze związkami kompleksowymi bądź z samymi ligandami (Rys. 4), prowadząc do opracowania materiałów o ulepszonej funkcjonalności. Ważnym aspektem, który cechuje hybrydy jest możliwość odwracalnego budowania sieci kowalencyjnych w postaci jedno-, dwu- oraz trójwymiarowych struktur[49].

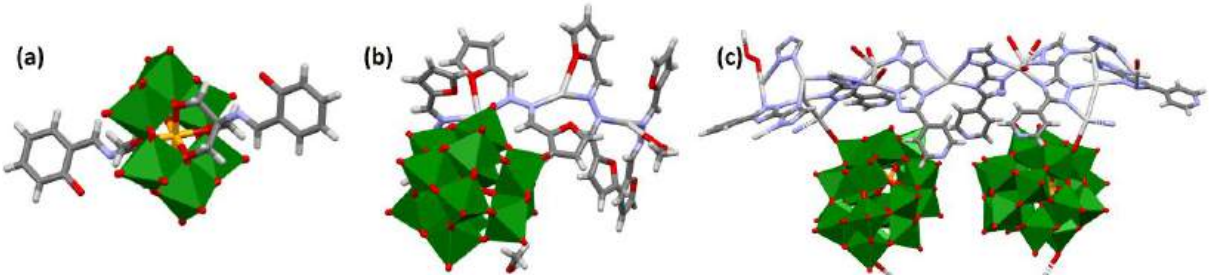

Rysunek 4. Przykłady materiałów hybrydowych bazujących na polioksometalanach typu (a) Andersona-Evansa[87], (b) Keggina oraz (c) Wellsa-Dawsona[88].

Najbardziej pożądanymi związkami są samoorganizujące się układy supramolekularne charakteryzujące się multifunkcjonalnością objawiającą się przede wszystkim aktywnością biomimetyczną oraz elektrochemiczną (Rys. 5). Kontrolowane tworzenie układów wielozadaniowych wymaga spełnienia odpowiednich kryteriów strukturalnych przez badane architektury supramolekularne.

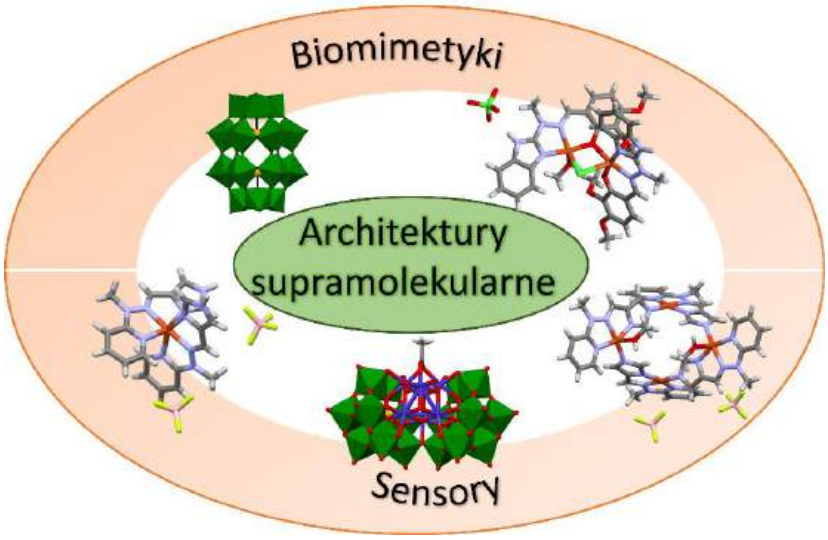

Rysunek 5. Schematyczne przedstawienie architektur supramolekularnych o przykładowych właściwościach.

Biorąc pod uwagę tworzenie biomimetyków, czyli układów mających za zadanie naśladowanie związków występujących w naturze, głównie enzymów, szczególnie ważne jest podobieństwo syntetycznego układu do występującego w środowisku naturalnym. Czerpanie inspiracji ze świata przyrody pozwala na szczegółowe poznanie badanego procesu oraz

pogłębianie wiedzy na temat budowy oraz działania naturalnie występujących enzymów, powodując możliwość inicjowania tego typu procesu na syntezowanych związkach chemicznych[89-91]. Duże znaczenie w chemii biomimetycznej mają układy z atomami tlenu, odgrywającymi rolę utleniacza w procesach utleniania i stanowiące wspólną cechę syntetycznego i naturalnego układu[92]. Istotną rolę odgrywają także związki zawierające w swojej strukturze jony miedzi, gdyż to właśnie te kationy znajdują się w wielu naturalnie występujących enzymach[93-96] (Rys. 6).

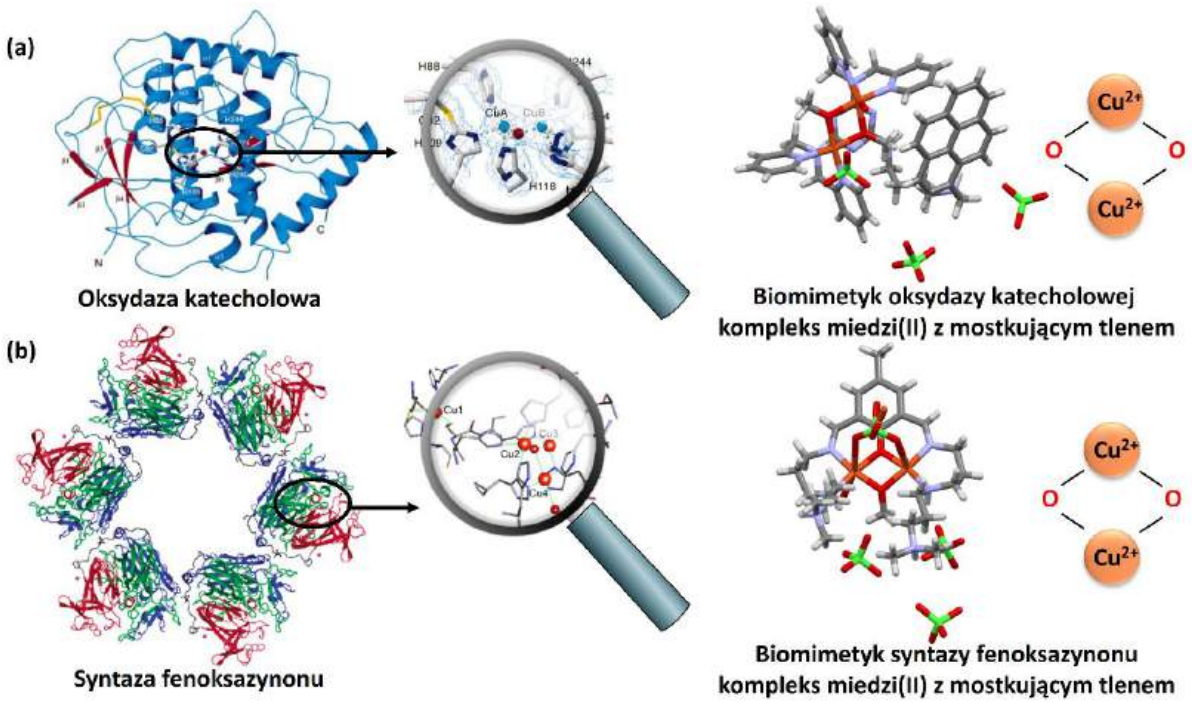

Rysunek 6. (a) Wstęgi oksydazy katecholowej wraz z przybliżeniem wybranego fragmentu[97] (po lewej) oraz przykładowy biomimetyk tego enzymu[98] (po prawej), (b) heksameryczna struktura syntazy fenoksazynonu wraz z przybliżeniem wybranego fragmentu[93, 99] (po lewej) oraz przykładowy biomimetyk tego enzymu (po prawej).

Problemem natury globalnej są choroby neurodegeneracyjne (np. choroba Alzheimera, Parkinsona, schizofrenia, zespół Touretta), których wczesne wykrycie umożliwia wcześniejsze rozpoczęcie leczenia i spowolnienie bądź nawet zahamowanie rozwoju choroby. Układy supramolekularne o odpowiednio dopasowanej budowie mogą pomóc w kontrolowaniu nie tylko poziomu jednego neuroprzekaźnika w organizmie człowieka, ale kilku (dopamina,

serotonina i epinefryna), gdyż ich odpowiednia proporcja warunkuje prawidłowe funkcjonowanie ludzkiego mózgu, którego zaburzenia powodują wspomniane wyżej choroby[100, 101]. Do najpopularniejszych metod detekcji neuroprzekaźników należą metody elektrochemiczne, ze względu na łatwość utleniania poszczególnych neuroprzekaźników, wysoką selektywność, czułość, dokładność, precyzję oraz stosunkowo niski koszt oprzyrządowania[102]. Jednakże te metody mają ograniczenia w postaci występujących wraz z neuroprzekaźnikami innych biocząsteczek, takich jak kwas askorbinowy czy też moczowy, które utleniają się na elektrodach niemodyfikowanych w prawie tym samym obszarze potencjału[103]. Konieczne jest zatem oddzielenie potencjałów utleniania tych związków, aby umożliwić dokładne oznaczenie neuroprzekaźnika. Z pomocą przychodzą układy supramolekularne, które umożliwiają modyfikację elektrod, stwarzając możliwość selektywnego oznaczania współistniejących molekuł[103-106] (Rys. 7).

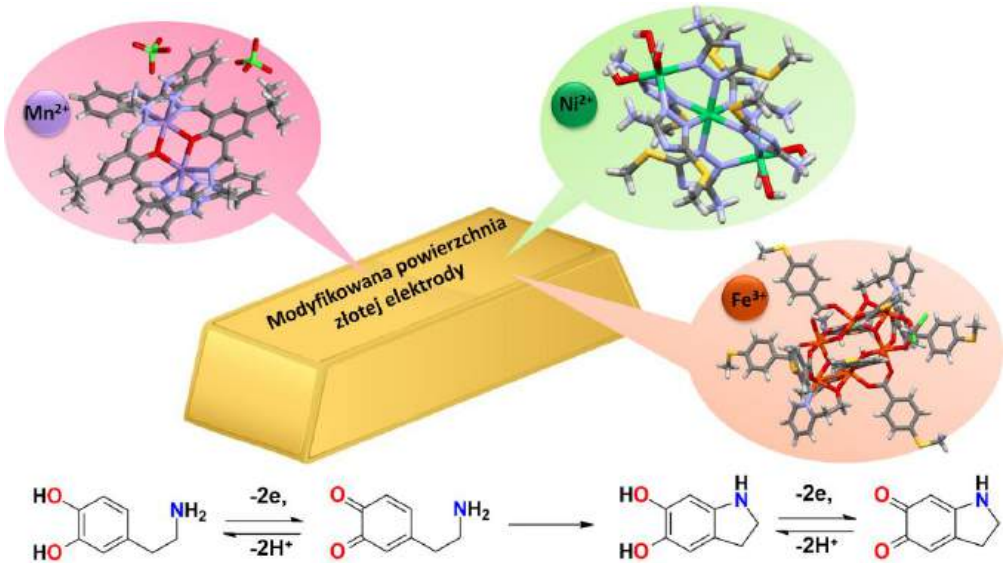

Rysunek 7. Trzy przykłady architektur supramolekularnych[104, 107, 108] stosowanych do modyfikacji powierzchni złotych elektrod używanych do selektywnej detekcji dopaminy.

W nieustannie szybko rozwijającym się świecie nauki, wielozadaniowość układów jest jednym z głównych trendów chemii supramolekularnej. Zapotrzebowania, a zarazem wymagania współczesnego świata skłaniają do pogłębienia wiedzy i przeprowadzenia badań w tej dziedzinie chemii w ramach prezentowanej rozprawy doktorskiej ze szczególnym naciskiem na właściwości biomimetyczne oraz elektrochemiczne.

2. Cel pracy

Celem naukowym niniejszej rozprawy doktorskiej pt. „**Wielordzeniowe architektury supramolekularne jako układy wielozadaniowe**” było opracowanie strategii syntetycznych obejmujących zaprojektowanie, zsyntezowanie oraz scharakteryzowanie strukturalne i spektroskopowe architektur supramolekularnych oraz zbadanie ich właściwości biomimetycznych (aktywujących bądź inhibitujących) oraz elektrochemicznych (jako sensorów do wykrywania neuroprzekaźników) (Rys. 8).

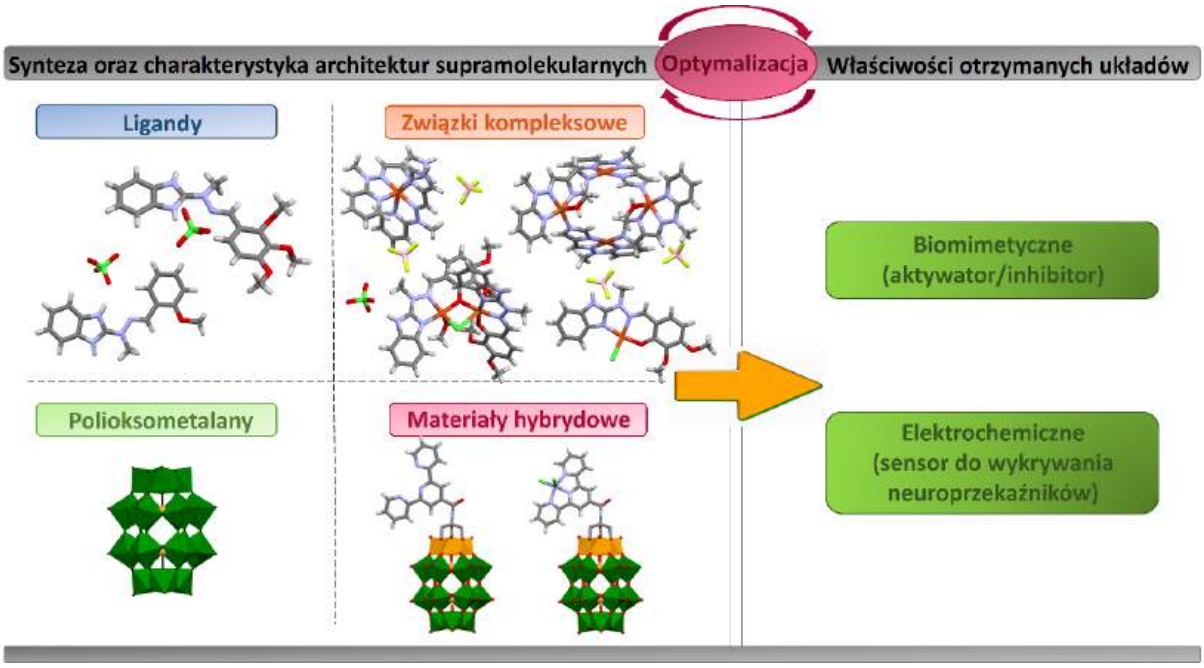

Rysunek 8. Schematyczne przedstawienie etapów pracy doktorskiej.

W pracy doktorskiej otrzymano pięć ligandów o zróżnicowanej strukturze szkieletu organicznego, które następnie poddano reakcjom kompleksowania z jonami metali *d*-elektronowych prowadząc do otrzymania związków kompleksowych o rozmaitych strukturach. Ponadto, zsyntezowany polioksometalan typu Wellsa-Dawsona poddano procesom funkcjonalizacji z wykorzystaniem wcześniej uzyskanego liganda bądź kompleksów, prowadząc do otrzymania materiałów hybrydowych. Otrzymane architektury supramolekularne zidentyfikowano wykorzystując analizę rentgenograficzną oraz następujące

metody i techniki: ^{1}H NMR, ^{13}C NMR, ATR-IR, FT-IR, ESI-MS, HRMS, CV, DPV, SEM, EDAX oraz UV-Vis.

Właściwości otrzymanych układów zbadano pod kątem aktywności biomimetycznej oraz elektrochemicznej z uwzględnieniem wpływu szkieletu organicznego liganda, aldehydu, bezwodnika, jonu metalu, przeciwjonu, rozpuszczalnika, temperatury oraz stosunku molowego substratów na multifunkcjonalność badanych architektur supramolekularnych.

Rozprawa doktorska obejmuje cztery publikacje dotyczące syntezy, charakterystyki oraz badania właściwości architektur supramolekularnych oraz jedną pracę przeglądową dotyczącą polioksometalanów typu Wellsa-Dawsona, na którą składa się obszerny opis struktur, różnorodnych modyfikacji, możliwości funkcjonalizacji, a także zastosowania ich w wielu dziedzinach nauki.

3. Omówienie wyników badań

3.1. Publikacja nr 1 (P1): „Biomimetic *O*-Demethylation at a copper(II) center with imine ligand: a structural and computational study" – New Journal of Chemistry, 2026, DOI: 10.1039/D5NJ04478B.

W publikacji P1 opisano syntezę i charakterystykę trzech ligandów iminowych **L1** – **L3** różniących się ilością grup metoksylowych, następnie przeprowadzono reakcje syntezy ich kompleksów miedzi(II) **K1** – **K6** różnymi metodami w celu określenia jak rodzaj metody oraz szkielet liganda wpływa na otrzymanie produktu *O*-demetylacji oksydacyjnej. Badany proces, polegał na przerwaniu wiązania C-O-C, za które w środowisku naturalnym odpowiadają enzymy demetylazy[109-111]. Ponadto, sprawdzono czy otrzymane układy supramolekularne mogą pełnić rolę analogów enzymu i wykazywać właściwości biomimetyczne.

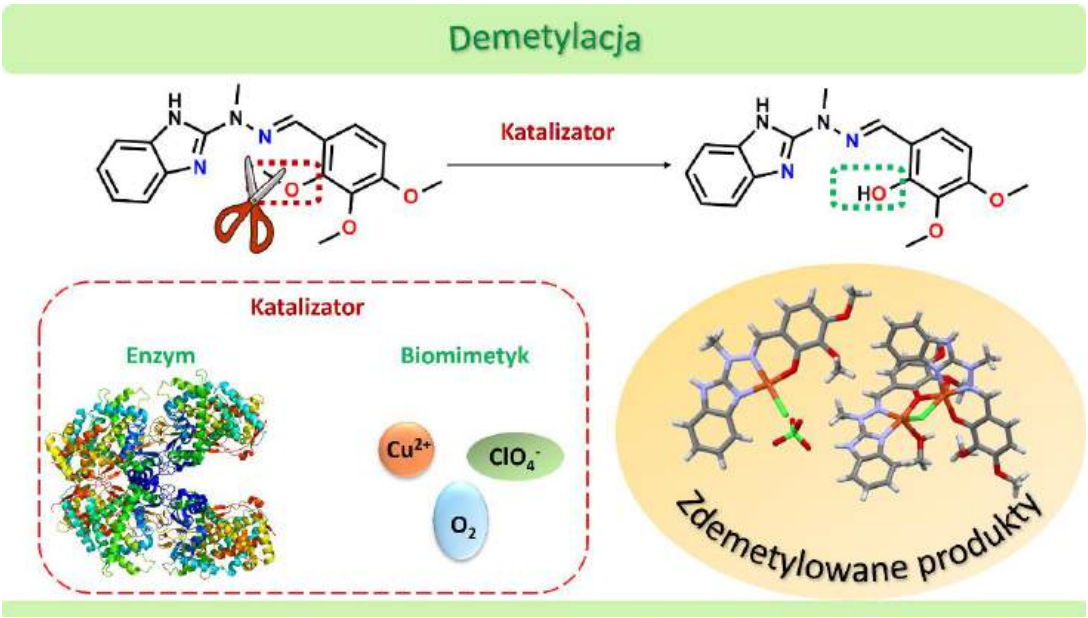

Rysunek 9. Schematyczne przedstawienie najważniejszych aspektów publikacji nr 1.

Trzy ligandy iminowe **L1** – **L3** zsyntezowano według dwuetapowej reakcji chemicznej przy użyciu linii próżniowo-gazowej. Pierwszy etap dla wszystkich trzech ligandów przebiegał jednakowo, zgodnie z wcześniej opublikowaną procedurą syntetyczną[112], według której, 2-chlorobenzimidazol poddano reakcji substytucji nukleofilowej z pięciokrotnym nadmiarem

metylohydrazyny. Drugi etap polegał na reakcji kondensacji otrzymanej pierwszorzędowej aminy: 2-(1-metylohydrazynylo)-1H-benzo[d]imidazolu z trzema różnymi aldehydami: 2,3,4-trimetoksybenzaldehydem, 2-metoksybenzaldehydem oraz 2,4-dimetoksy-3-metylobenzaldehydem, otrzymując odpowiednio ligand **L1** [$C_{18}H_{20}N_4O_3$], **L2** [$C_{16}H_{16}N_4O$] oraz **L3** [$C_{18}H_{20}N_4O_2$] (Rys. 10). Reakcje prowadzono w tych samych warunkach syntetycznych, gdzie stosunek substratów był równomolowy, a mieszaniny reakcyjne mieszano przez 3 godziny w bezwodnym etanolu (EtOH) w temperaturze 80°C.

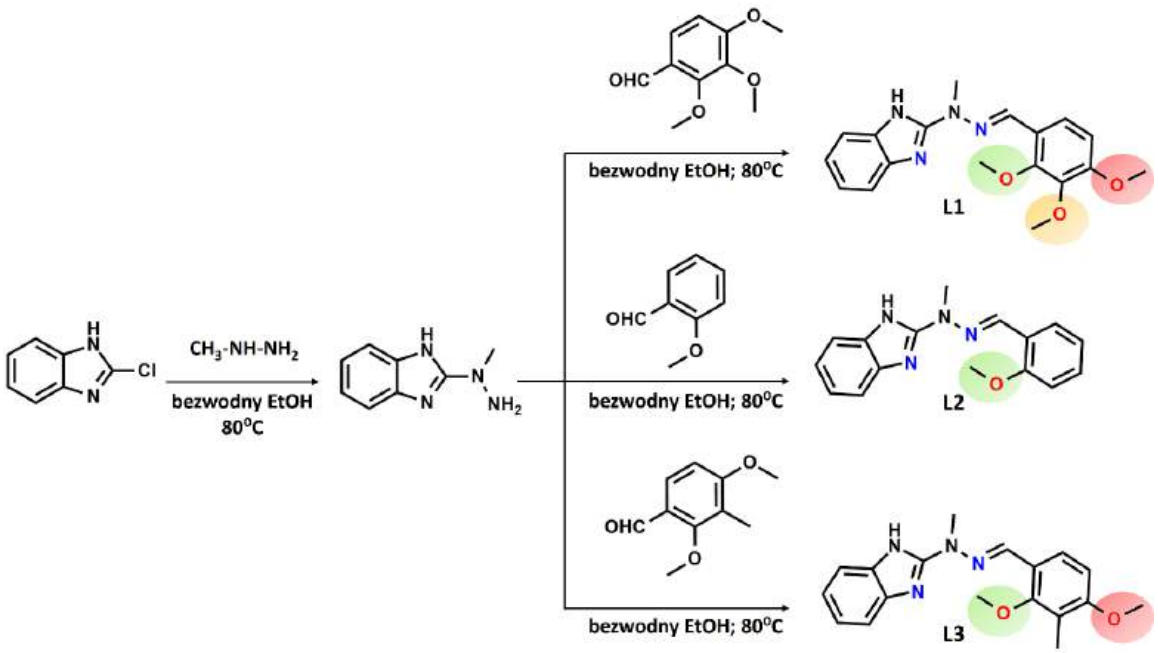

Rysunek 10. Schematyczne przedstawienie dwuetapowej syntezy ligandów **L1** – **L3**[113].

Zsyntezowane ligandy w postaci białych oraz krystalicznych proszków otrzymano z wydajnością równą 76,0% (**L1**), 86,0 % (**L2**) oraz 78,0 % (**L3**). Iminy **L1** – **L3** różniły się ilością ugrupowań metoksylowych, a ich strukturę oraz czystość sprawdzono przy wykorzystaniu dostępnych metod analitycznych: ^{1}H NMR (Rys. 11), ^{13}C NMR, HRMS/ESI-MS oraz FT-IR. Dodatkową weryfikację otrzymanych układów stanowiła identyfikacja techniką dyfrakcji rentgenowskiej, której poddano kryształy uzyskane dla wszystkich ligandów w postaci sprotonowanej metodą powolnej dyfuzji w niskiej temperaturze (4°C) eteru diizopropylowego do roztworów ligandów.

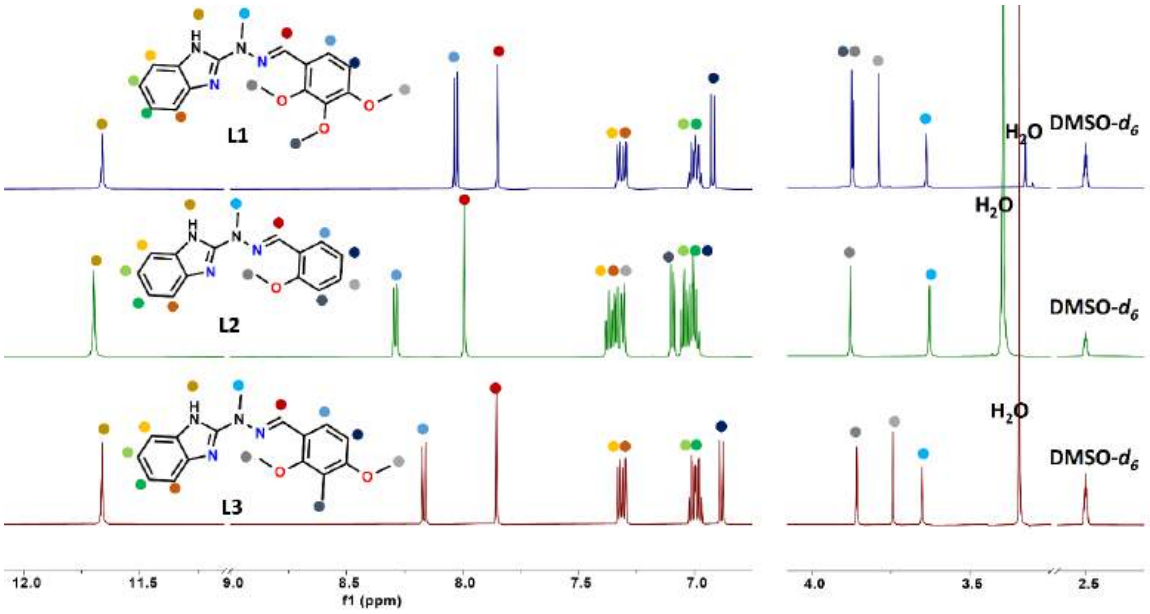

Rysunek 11. Widma ^{1}H NMR ligandów **L1** – **L3** zarejestrowane w DMSO-d_6[113].

W celu optymalizacji procesu *O*-demetylacji oksydacyjnej oraz głębszego zrozumienia czynników określających ten proces, otrzymane ligandy iminowe różniące się ilością i rozmieszczeniem podjednostek R-O-CH_3 poddano reakcjom kompleksowania z solami miedzi(II) różnymi metodami.

W pierwszej kolejności, sprawdzono różne drogi syntezy bazując na ligandzie **L1** (Rys. 12).

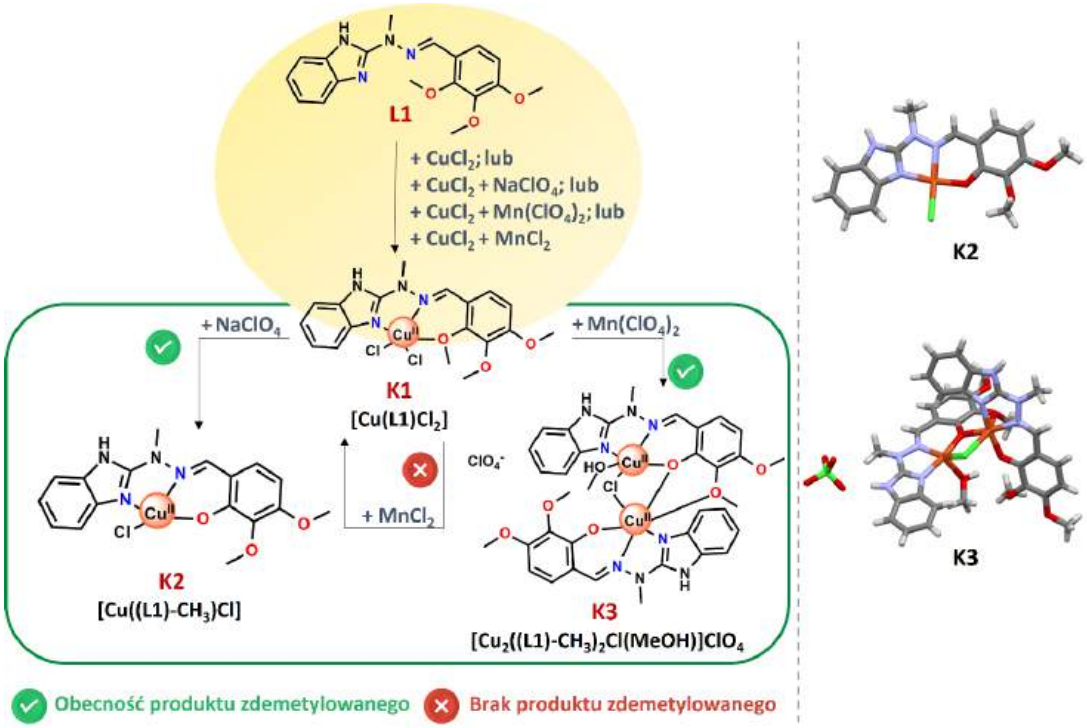

Rysunek 12. Schematyczne przedstawienie procedury syntezy kompleksów Cu(II) **K1**, **K2** oraz **K3**; wraz z uzyskanymi strukturami krystalicznymi kompleksów[113].

Stosując metodę „krok po kroku" ligand **L1** mieszano z solą $CuCl_2 \cdot 2H_2O$ w stosunku równomolowym w acetonitrylu (MeCN) w temperaturze pokojowej przez 48 godzin, prowadząc do izolacji monometalicznego kompleksu **K1** $[Cu(L1)Cl_2]$ z wydajnością 93,3%. Kolejno otrzymany kompleks potraktowano jako materiał wyjściowy i poddano dalszym trzem reakcjom różniącym się dodawaną solą, celem określenia wpływu przeciwjonu oraz jonu metalu na otrzymany produkt. Interesujący okazał się fakt, że dodanie soli zawierającej aniony chloranowe(VII): $NaClO_4 \cdot H_2O$ lub $Mn(ClO_4)_2 \cdot 6H_2O$ prowadzi do demetylacji jednej grupy R-O-CH_3 (w pozycji *orto*), przy czym dwie pozostałe pozostają niezmienione. Natomiast, gdy do reakcji dodano $MnCl_2$, demetylacja nie zachodzi, a struktura produktu jest identyczna ze strukturą substratu **K1**. Można zatem wnioskować, że do pomyślnego przebiegu reakcji demetylacji niezbędne jest użycie anionów chloranowych(VII), natomiast rodzaj kationu metalu nie jest czynnikiem determinującym badany proces. W konsekwencji, w przypadku użycia następujących soli: $NaClO_4 \cdot H_2O$ oraz $Mn(ClO_4)_2 \cdot 6H_2O$ otrzymano kolejno kompleksy: **K2** $[Cu((L1)\text{-}CH_3)Cl]$ oraz **K3** $[Cu_2((L1)\text{-}CH_3)_2Cl(MeOH)]ClO_4$. Dodatkowo zbadano, że

reakcje prowadzące do otrzymania **K2** i **K3** nie przebiegają w warunkach beztlenowych oraz bezwodnych, co potwierdza, że kluczowa jest także obecność tlenu cząsteczkowego oraz wody (wraz z uwzględnieniem obecności kationu wodorowego oraz anionu wodorotlenkowego). Co ciekawe, przeprowadzenie reakcji metodą templatową z użyciem tych samych substratów i tych samych warunków syntetycznych jak w przypadku metody „krok po kroku" nie powoduje demetylacji, a jedynie prowadzi do otrzymania kompleksu **K1**. Wszystkie otrzymane produkty **K1** – **K3** scharakteryzowano przy użyciu metod: HRMS oraz FT-IR. Ponadto, kryształy dla kompleksów **K2** i **K3**, odpowiednie do pomiarów krystalograficznych otrzymano poprzez powolną dyfuzję w niskiej temperaturze (4ºC) eteru diizopropylowego do fiolek z metanolowymi roztworami kompleksów.

Po określeniu jak rodzaj jonu metalu i przeciwjonu oraz typ metody („krok po kroku" oraz templatowa) wpływa na reakcję *O*-demetylacji, postanowiono sprawdzić czy ilość i rozmieszczenie ugrupowań metoksylowych również ma znaczenie na powodzenie badanej reakcji. W związku z tym, ligandy **L2** oraz **L3** poddano takim samym reakcjom jak w przypadku liganda **L1**. Ligand **L2** zawierający tylko jedną podjednostkę metoksylową w pozycji *orto*, poddany kompleksowaniu różnymi solami nie uległ procesowi *O*-demetylacji, a wszystkie przeprowadzone reakcje prowadziły do otrzymania monometalicznego kompleksu **K4** $[Cu(L2)Cl_2]$ (Rys. 13).

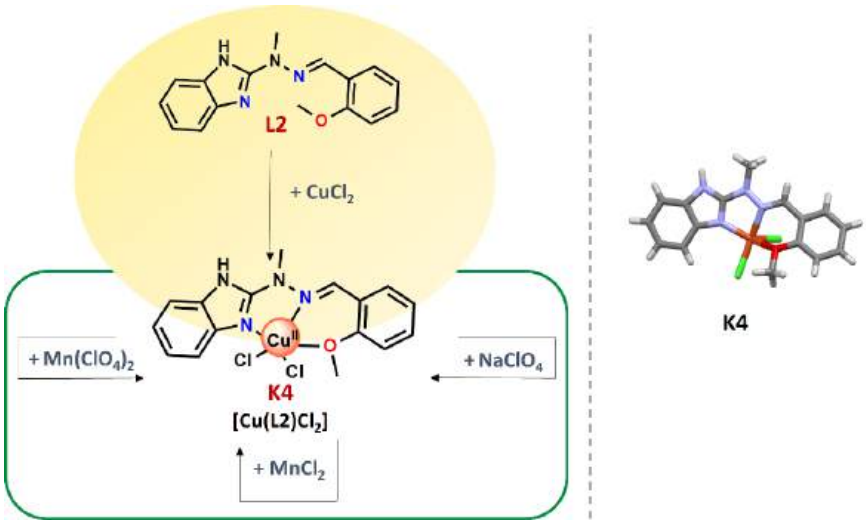

Rysunek 13. Schematyczne przedstawienie procedury syntezy kompleksu Cu(II) **K4**; wraz z uzyskaną strukturą krystaliczną kompleksu[113].

Natomiast, w przypadku liganda **L3** zawierającego dwie grupy metoksylowe, jedną również w pozycji *orto*, a drugą w pozycji *para*, kompleksowanie różnymi solami doprowadziło do otrzymania dwóch kompleksów **K5** $[Cu(L3)Cl_2]$ oraz **K6** $[Cu(L3)_2Cl(ClO_4)]MeOH$, jednakże sam proces *O*-demetylacji był również zakończony niepowodzeniem (Rys. 14).

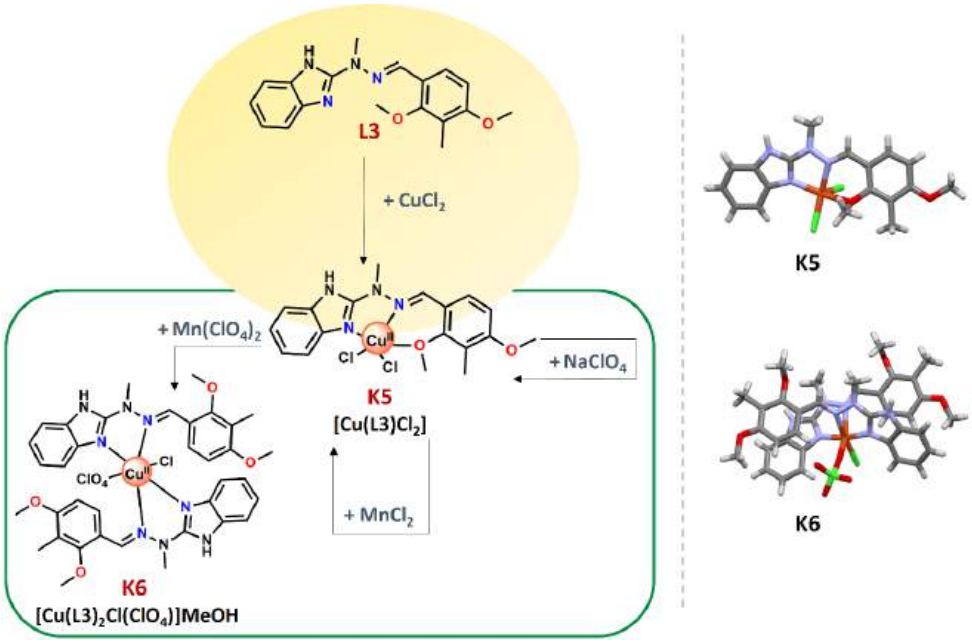

Rysunek 14. Schematyczne przedstawienie procedury syntezy kompleksów Cu(II) **K5** oraz **K6**; wraz z uzyskanymi strukturami krystalicznymi kompleksów[113].

Struktury wszystkich otrzymanych kompleksów potwierdzono za pomocą metod spektrometrycznych (ESI-MS) oraz spektroskopowych (FT-IR). Dodatkowo analizę rentgenograficzną wykonano dla otrzymanych kryształów kompleksów **K4**, **K5** oraz **K6** w wyniku powolnej dyfuzji eteru diizopropylowego do metanolowych roztworów kompleksów w niskiej temperaturze (4ºC).

Przeprowadzono badania metodą spektroskopii UV-Vis dla ligandów **L1** – **L3** oraz ich kompleksów **K1** – **K6** (wszystkie zarejestrowano w acetonitrylu w temperaturze pokojowej, a stężenie związków było równe 0,02 mM), które potwierdziły stabilność otrzymanych związków kompleksowych w roztworze, wskazując na brak dekoordynacji ligandów. Zaobserwowano pasma charakterystyczne dla kompleksów Cu(II) bazujących na ligandach iminowych[114, 115], które pojawiły się w zakresie 295 nm – 400 nm. Dodatkowo tylko dla

zdemetylowanych kompleksów **K2** i **K3** zauważono dodatkowe pasmo z maksimum przy ~400 nm świadczące o zmianach strukturalnych w szkielecie liganda[116, 117], co jest kolejnym potwierdzeniem zachodzącej reakcji *O*-demetylacji.

Dotychczas zbadano tylko roztwory acetonitrylowe (rozpuszczalnik aprotyczny), dlatego postanowiono sprawdzić czy rodzaj użytego rozpuszczalnika ma także znaczenie dla powodzenia procesu będącego tematem publikacji. W tym celu, zarejestrowano widma wybranego kompleksu **K2** w rozpuszczalnikach protycznych, takich jak metanol (MeOH) oraz etanol (Rys. 15a). Dodatkowe pasmo przy ~400 nm zaobserwowano tylko w przypadku użycia acetonitrylu, co może nasunąć wnioski, że wraz ze wzrostem polarności rozpuszczalnika proces *O*-demetylacji nie zachodzi. Przeprowadzone miareczkowanie spektrofotometryczne acetonitrylowego roztworu kompleksu **K1** o stężeniu 0,02 mM wzrastającą ilością soli (od 0,3 do 5,0 ekwiwalenta) $NaClO_4 \cdot H_2O$ zapewniło monitorowanie zachodzenia procesu *O*-demetylacji prowadzącego do otrzymania kompleksu **K2** (Rys. 15b). Po dodaniu 1,0 ekwiwalenta soli nie zaobserwowano dalszych zmian na widmie, co jest zgodne z opisaną procedurą syntetyczną.

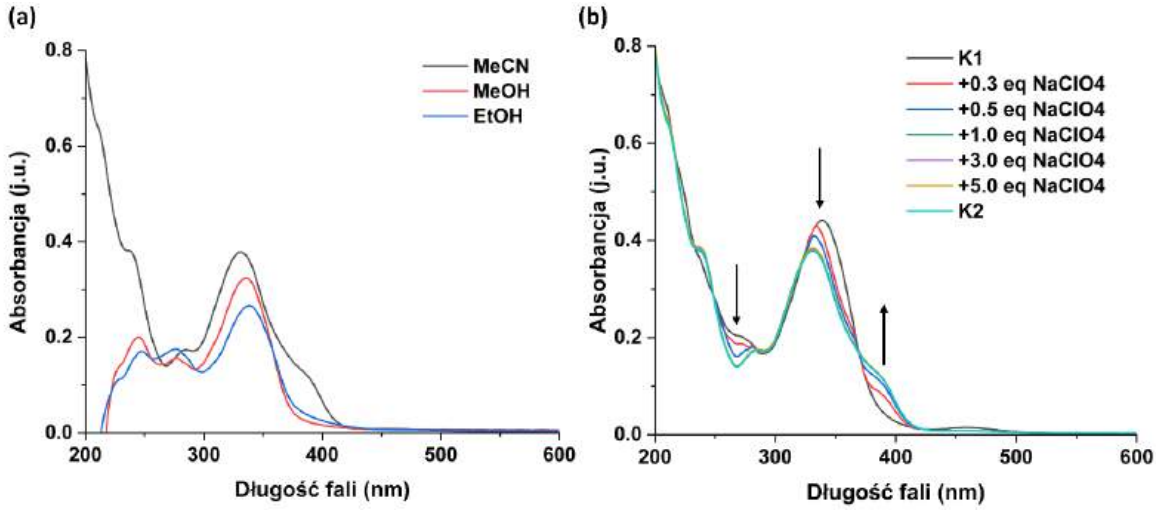

Rysunek 15. (a) Widma UV-Vis dla kompleksu **K2** o stężeniu równym c = 0,02 mM zarejestrowane w MeCN, MeOH i EtOH. (b) Miareczkowanie spektrofotometryczne kompleksu **K1** o stężeniu 0,02 mM w MeCN wzrastającą ilością soli $NaClO_4$ (od 0,3 do 5,0 ekwiwalenta) i widmo UV-Vis kompleksu **K2** o stężeniu 0,02 mM w MeCN[113].

Dzięki pomiarom elektrochemicznym dla wybranych układów: liganda **L1**, kompleksów **K1** oraz **K2** uzyskano wgląd we właściwości redoks badanych związków i związanych z nimi zachodzących zmian strukturalnych. Wszystkie woltamperogramy cykliczne (CV) zarejestrowano w odtlenionym acetonitrylu zawierającym 0,1 M $TBAClO_4$ (temperatura pokojowa, atmosfera gazu obojętnego) w zakresie potencjałów od -1,30 V do 1,45 V (Rys. 16) w układzie trójelektrodowym z elektrodą złotą (elektroda pracująca), platynową (elektroda pomocnicza)
i nasyconą elektrodą kalomelową (elektroda odniesienia). Dla liganda iminowego **L1** zaobserwowano trzy nieodwracalne piki anodowe zlokalizowane przy potencjałach: 0,25 V, 0,85 V oraz 1,15 V (Rys. 16a). Pierwszy z nich przypisano utlenianiu wiązania iminowego[118, 119], a pozostałe dwa piki związano z procesem utlenienia w grupach R-O-CH_3[120]. Z kolei, dla obu kompleksów można zauważyć wyraźne zmiany w kształcie zarejestrowanych woltamperogramów cyklicznych (Rys. 16b i 16c). Zarówno na jednym jak i na drugim pojawia się para quasi-odwracalnych pików świadczących o utlenianiu jonów Cu^{+} przy E = 1,40 V dla **K1** i przy E = 1,32 V dla **K2** i kolejno redukcji jonów Cu^{2+} przy E = 1,08 V dla **K1** oraz przy E = 1,05 V dla **K2**. Lokalizacja trzech pozostałych, nieodwracalnych pików anodowych w przypadku kompleksu **K1** oraz dwóch w przypadku kompleksu **K2** jest zbliżona do tych zaobserwowanych dla liganda **L1**, co świadczy o tych samych procesach utleniania. Dodatkowo brak jednego piku anodowego w CV zarejestrowanym dla kompleksu **K2** może być rezultatem procesu *O*-demetylacji zachodzącym w szkielecie liganda.

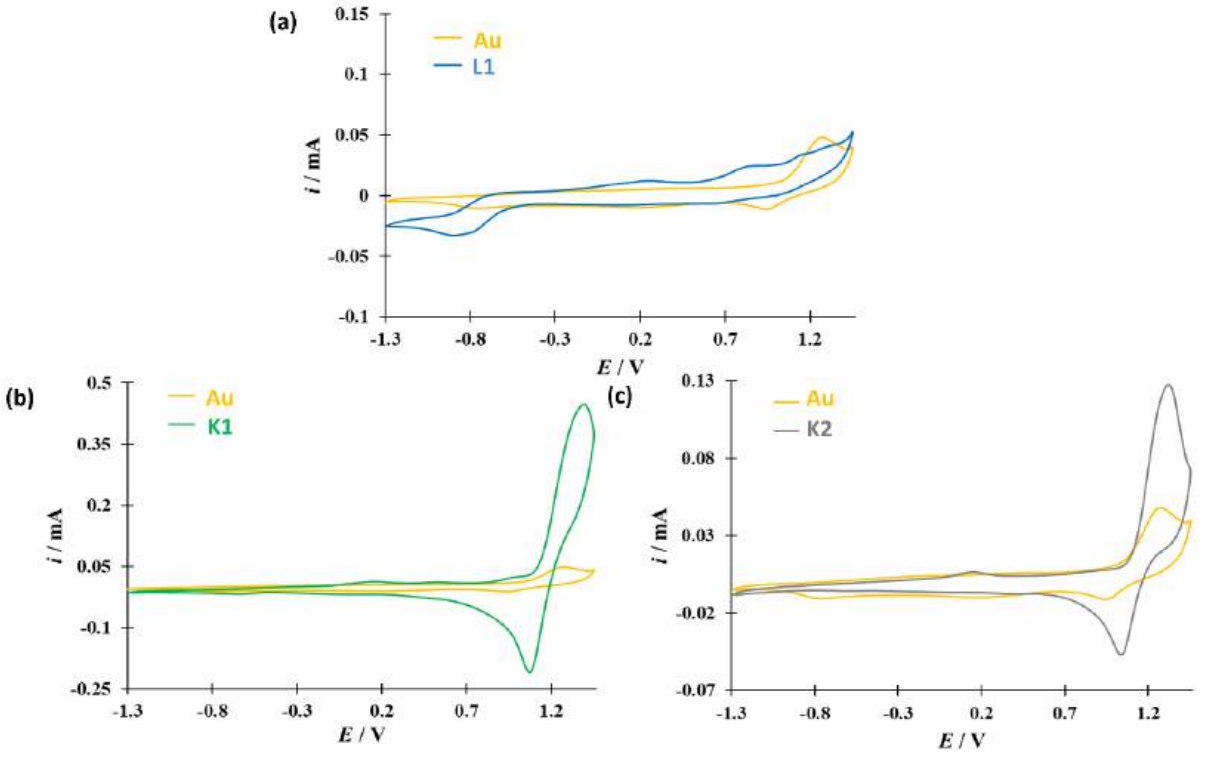

Rysunek 16. Cykliczne woltamperogramy elektrody złotej (żółty) w MeCN z 0,1 M $TBAClO_4$ i w obecności (a) 0,1 mM **L1** b) 0,1 mM **K1** oraz (c) 0,1 mM **K2**; d*E*/d*t* = 0,1 Vs^{-1} [113].

Dla kompleksu **K2** prześledzono wpływ szybkości nakładania potencjału na elektrodę w zakresie od 0,02 Vs^{-1} do 0,50 Vs^{-1} (Rys. 17a). Jak się można było spodziewać, wraz ze wzrostem szybkości skanowania potencjały pików utleniania przesuwają się w kierunku wyższych wartości, podczas gdy potencjały pików redukcji w kierunku niższych wartości. Tym zmianom towarzyszy również stopniowy wzrost natężenia prądu w pikach. Ponadto, przy wyższych szybkościach na rejestrowanych cyklicznych woltamperogramach pojawia się nowy pik katodowy, który może być wynikiem odwracalnych procesów redoks w grupie iminowej zachodzących w czasie[118, 119, 121]. Analizując zależności między logarytmem natężenia prądu utleniania jonu Cu^{+} do Cu^{2+} i logarytmem szybkości skanowania uzyskano prostoliniową zależność z kątem nachylenia d log i_p/d log v niższym od 0,5. Wynik ten łącznie z prostoliniową zależnością natężenia prądu w funkcji pierwiastka kwadratowego szybkości skanowania (Rys. 17b) świadczy o mieszanych dyfuzyjno-adsorpcyjnych ograniczeniach szybkości badanego procesu. W przypadku czystych dyfuzyjnych bądź adsorpcyjnych ograniczeń kinetyki

rozważanego procesu należałoby oczekiwać, że kąt d log i_p/d log v przyjmie graniczną wartość odpowiednio 0,5 lub 1.

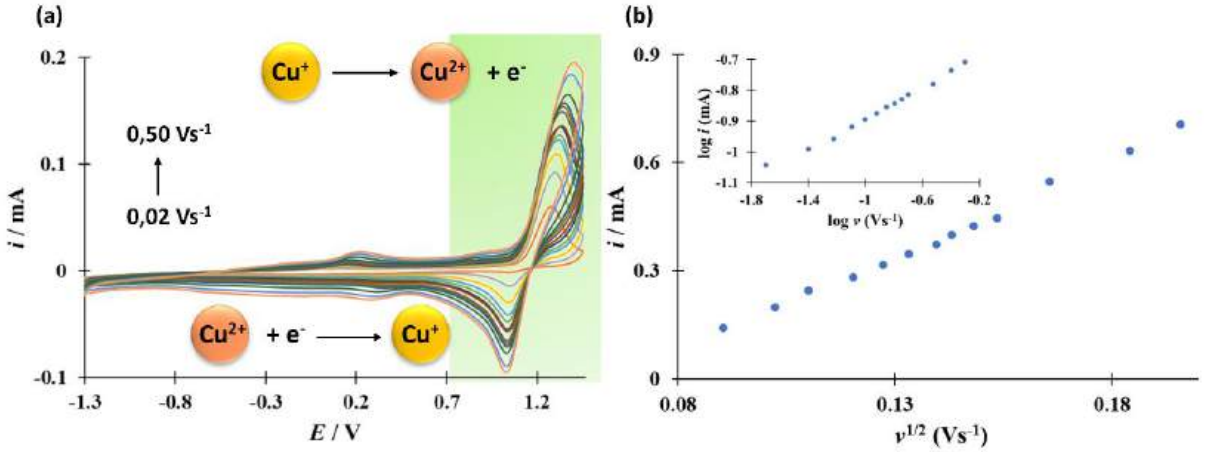

Rysunek 17. (a) Cykliczne woltamperogramy dla kompleksu **K2** zarejestrowane na złotej elektrodzie w MeCN z 0,1 M $TBAClO_4$ dla szybkości skanowania od 0,02 Vs^{-1} do 0,50 Vs^{-1}. (b) Zależności i_p - $v^{1/2}$. Panel wewnętrzny: log i_p - log v [113].

W celu dokładniejszego zbadania procesu *O*-demetylacji przeprowadzono obliczenia w oparciu o teorię funkcjonału gęstości (DFT), które wykonał prof. Giuseppe Forte z Uniwersytetu w Katanii. Wykazano, że sam anion chloranowy(VII) nie jest wystarczającym czynnikiem determinującym proces *O*-demetylacji. Z tego względu zbadano również wpływ wody oraz jonów H_3O^+ i OH^- (w warunkach bezwodnych badany proces nie zachodzi), wskazując, że anion wodorotlenkowy jest głównym czynnikiem odpowiedzialnym za pomyślność procesu *O*-demetylacji. Anion wodorotlenkowy powstaje w wyniku reakcji redoks iminowego kompleksu miedzi(II) **K1** w obecności światła widzialnego, tlenu i wody. W tej reakcji tlen działa jako utleniacz oraz odpowiada za regenerację katalizatora, którym są jony miedzi w kompleksie. Dodatkowo, obecność anionu chloranowego(VII) jako anionu słabo koordynującego zwiększa nukleofilowość anionu wodorotlenkowego w środowisku aprotycznym, prowadząc do wzrostu jego reaktywności jednocześnie umożliwiając przeprowadzenia reakcji *O*-demetylacji.

Powyższe badania stanowią pierwszy przykład *O*-demetylacji z udziałem iminowych kompleksów miedzi(II) przeprowadzonej w łagodnych warunkach, bez dodatku silnych

utleniaczy. Wykonana optymalizacja warunków reakcji pozwoliła na określenie najważniejszych czynników (szkielet liganda, metoda syntezy, rodzaj soli, typ rozpuszczalnika, obecność wody i tlenu) wpływających na pomyślność przeprowadzenia badanej reakcji. Opracowane wyniki wskazują, że koordynacja jonów miedzi(II) z ligandem osłabia wiązanie R-O-CH_3, a obecność dodatkowych grup metoksylowych w najbliższym sąsiedztwie przyczynia się do wzmocnienia tego efektu jednocześnie aktywując *O*-demetylację. Wykonane obliczenia DFT pozwoliły na określenie kluczowych czynników odpowiedzialnych za oksydacyjną *O*-demetylację, wskazując anion wodorotlenkowy jako główny nukleofil badanego procesu, przy jednoczesnym podkreśleniu, że aniony chloranowe(VII), tlen cząsteczkowy oraz woda również przyczyniają się do otrzymania zdemetylowanych produktów. Uzyskane wyniki otwierają drzwi do kolejnych badań i zastosowań iminowych kompleksów miedzi(II) w chemii biomimetycznej czy waloryzacji ligniny.

3.2. Publikacja nr 2 (P2): „ Self-assembly of simple Schiff base ligand into unique saddle-type [4x4] tetranuclear architecture and its application as selective voltammetric dopamine sensor in aqueous conditions" – Electrochimica Acta, 2024, 476, 143754.

W publikacji P2 opisano syntezę nowego, wielordzeniowego związku kompleksowego **K7** $[Cu_4((L4)\text{-}H)_4(BF_4)_2(MeOH)_2](BF_4)_2$ typu „siodłowego" otrzymanego w wyniku samoorganizacji liganda N,N,N-donorowego typu zasady Schiffa **L4** $[C_{10}H_{11}N_5]$ w obecności soli $Cu(CH_3CN)_4BF_4$, jego charakterystykę strukturalno-spektroskopową oraz właściwości elektrochemiczne i następcze zastosowanie otrzymanego układu do modyfikacji elektrody złotej w celu opracowania sensora do detekcji dopaminy samej i w obecności czynników interferujących w warunkach wodnych.

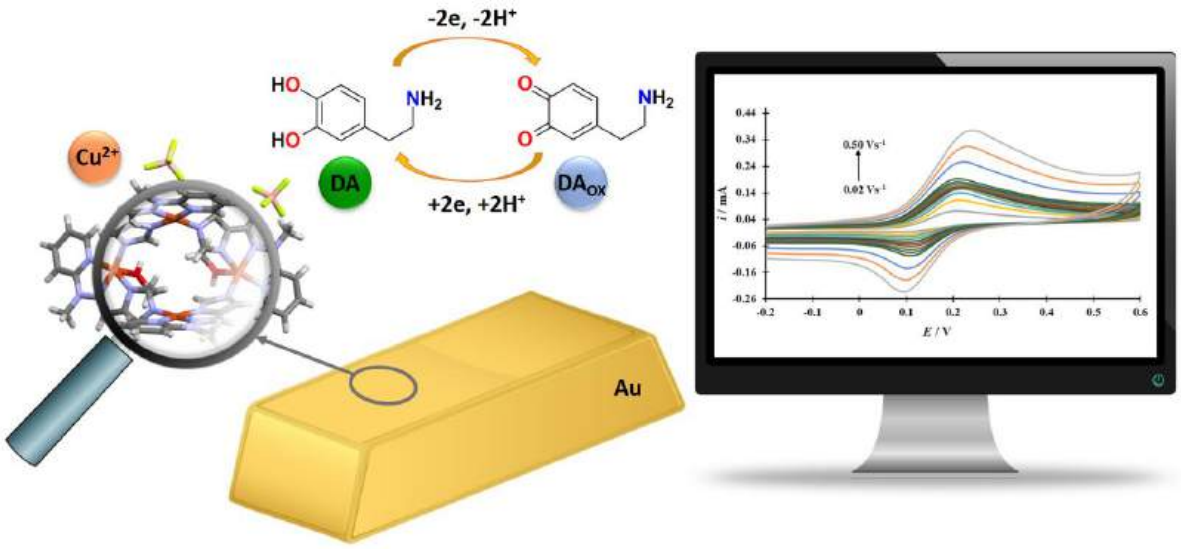

Rysunek 18. Schematyczne przedstawienie najważniejszych aspektów publikacji nr 2.

Ligand **L4** otrzymano według opisanej procedury syntetycznej[112], a charakterystyka (^{1}H NMR, ^{13}C NMR, FT-IR, ESI-MS) potwierdziła otrzymanie pożądanego produktu. Związek kompleksowy miedzi(II) **K7** powstał w wyniku syntezy między ligandem **L4**, a solą miedzi(I) $Cu(CH_3CN)_4BF_4$ w stosunku równomolowym w metanolu prowadzonej przez 24 godziny w temperaturze pokojowej (Rys. 19). Krystalizacja metodą powolnej dyfuzji w niskiej temperaturze (4ºC) eteru diizopropylowego do roztworu metanolowego kompleksu pozwoliła na uzyskanie kryształów odpowiednich do identyfikacji techniką dyfrakcji rentgenowskiej.

Dodatkowo otrzymany kompleks z wydajnością równą 85,3% scharakteryzowano metodami spektroskopowymi (FT-IR, ATR-IR) oraz spektrometrycznymi (ESI-MS).

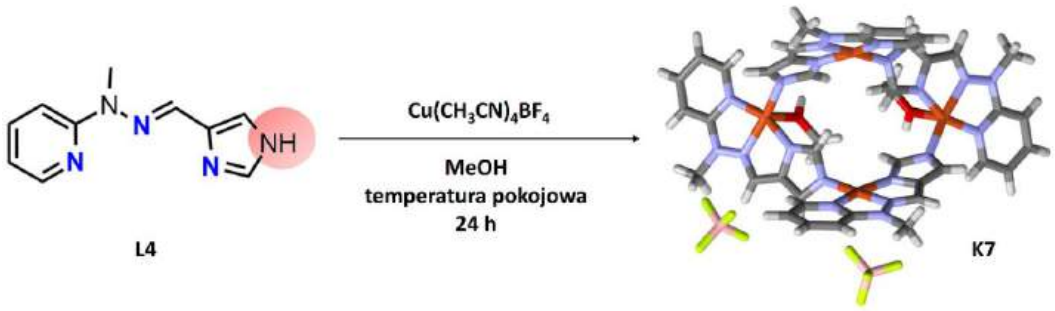

Rysunek 19. Samoorganizacja liganda **L4** z jednoczesną spontaniczną deprotonacją grupy NH w obecności soli miedzi(I) $Cu(CH_3CN)_4BF_4$ prowadząca do otrzymania związku kompleksowego miedzi(II) **K7** $[Cu_4((L4)\text{-}H)_4(BF_4)_2(MeOH)_2](BF_4)_2$.

Związek kompleksowy **K7**, dzięki swojej wielordzeniowej budowie, obecności jonów miedzi(II), możliwościom redoks oraz strukturze szkieletu liganda posiada łatwość akumulacji na powierzchni elektrody złotej pomimo braku w swojej strukturze ugrupowań tiolowych, co czyni go atrakcyjnym w aspekcie wykorzystania do modyfikacji powierzchni złota. Należy podkreślić, że związki z ugrupowaniami tiolowymi, mimo wad takich jak podatność na zmiany pH, utleniacze i rozpuszczalniki organiczne są nadal często stosowane do modyfikacji elektrod złotych z powodu łatwości tworzenia wiązań Au-S[122].

Przed przystąpieniem do modyfikacji powierzchni, elektrodę złotą poddawano elektrochemicznej aktywacji metodą cyklicznej woltamperometrii (CV) w 0,5 M roztworze NaOH w zakresie potencjału od E = -0,80 V do E = 0,6 V vs SCE z dE/dt = 0,1 Vs^{-1} aż do momentu uzyskania stabilnego cyklicznego woltamperogramu. Tak zaktywowaną elektrodę złotą poddawano modyfikacji kompleksem **K7** w warunkach *in situ* osadzając na jej powierzchni kompleks **K7** z jego 0,01 mM roztworu w PBS w zakresie potencjału od E = -0,80 V do E = 1,15 V vs SCE z dE/dt = 0,1 Vs^{-1} aż do momentu uzyskania stabilnego cyklicznego woltamperogramu (15 cykli). Zmodyfikowaną elektrodę złotą (Au/K7) poddano badaniom w celu scharakteryzowania jej powierzchni, a następnie wykorzystano w pomiarach elektrochemicznych z udziałem dopaminy.

Na cyklicznym woltamperogramie zarejestrowanym dla niezmodyfikowanej elektrody złotej w zakresie potencjałów od E = -0,80 V do E = 1,15 V vs SCE w dE/dt = 0,1 Vs^{-1}

w roztworze PBS. Na cyklicznym woltamperogramie nie zaobserwowano żadnych pików świadczących o reakcjach elektrochemicznych, a widoczny pik anodowy przy potencjale 0,93 V vs SCE i pik katodowy przy 0,45 V vs SCE odpowiada tworzeniu się tlenku złota i kolejno jego redukcji[123]. W tym samym zakresie potencjału zastosowany w syntezie ligand **L4** jest nieaktywny elektrochemicznie, natomiast para odwracalnych pików przy E = 0,25 V oraz E = 0,17 V widoczna na cyklicznych woltamperogramach rejestrowanych w obecności kompleksu **K7** odpowiada procesowi elektrochemicznego utleniania Cu^{+} do Cu^{2+} i redukcji Cu^{2+} do Cu^{+} (Rys. 20a)[124].

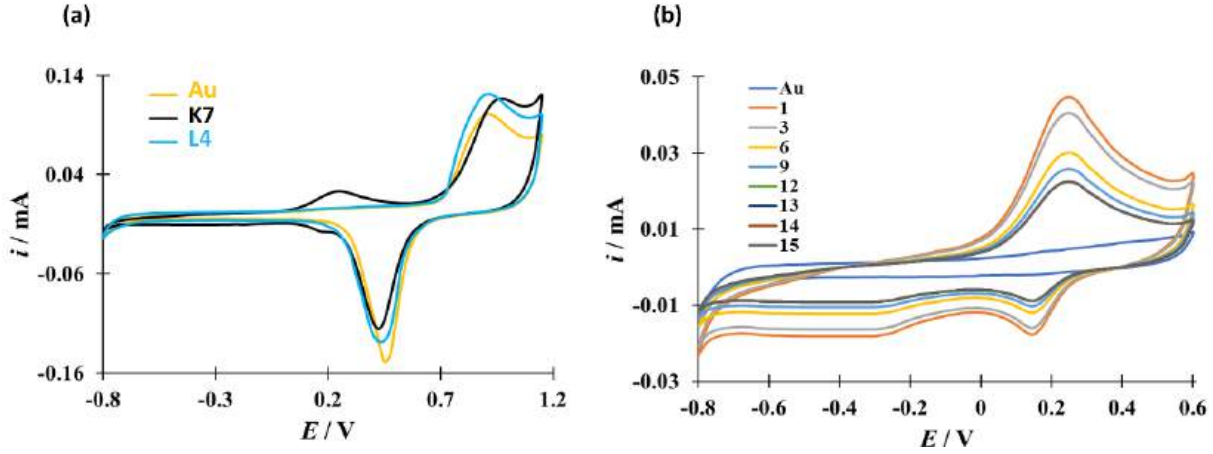

Rysunek 20. (a) Cykliczne woltamperogramy zarejestrowane dla niezmodyfikowanej elektrody złotej w PBS (żółty) w obecności 0,01 mM kompleksu **K7** (czarny) lub 0,01 mM liganda **L4** (niebieski). (b) Zestaw kolejnych cykli cyklicznych woltamperogramów zarejestrowanych dla elektrody złotej w PBS z kompleksem **K7**, dE/dt = 0,1 Vs^{-1} [125].

Proces osadzania kompleksu **K7** na elektrodzie Au prowadzono metodą cyklicznej woltamperometrii z 0,01 mM roztworu kompleksu w PBS w zakresie potencjału elektrody złotej od E = -0,80 V do E = 0,6 V vs SCE szybkością zmiany potencjału dE/dt = 0,1 Vs^{-1} (Rys. 20b). Wraz z kolejnymi cyklami (aż do 12 cyklu) obserwowano zmniejszanie się natężenia prądu w pikach co związano z tworzeniem zaadsorbowanej warstwy kompleksu **K7** na powierzchni elektrody złotej. O adsorpcji kompleksu na modyfikowanym podłożu świadczy liniowa zależność natężenia prądu w piku w funkcji szybkości skanowania (v) z wysoką wartością współczynnika korelacji (R^2 = 0,9996) (Rys. 21b). Adsorpcja cząsteczek kompleksu **K7** na powierzchni złota potwierdzona jest także zbliżoną do 1 wartością kąta nachylenia zależności we współrzędnych log i_p – log v.

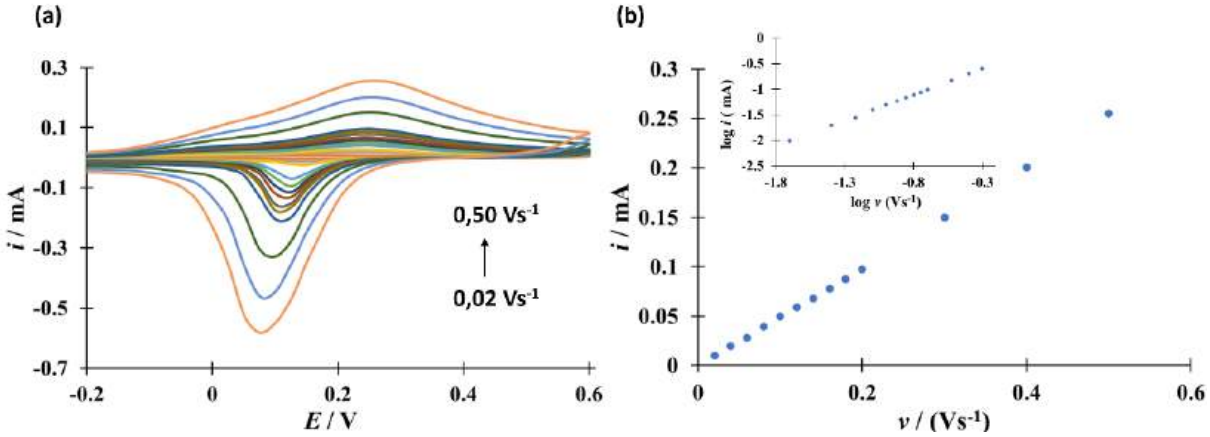

Rysunek 21. (a) Cykliczne woltamperogramy zarejestrowane dla zmodyfikowanej elektrody Au/K7 w PBS przy szybkościach skanowania od 0,02 do 0,50 Vs^{-1}. (b) Zależności: i_p - v; panel wewnętrzny: log i_p - log v [125].

Adsorpcja kompleksu **K7** na powierzchni złota niesie za sobą wiele korzyści jak np. ochrona powierzchni elektrody przed adsorpcją pośrednich i/lub końcowych produktów reakcji, które mogą być szkodliwe bądź nawet trujące dla powierzchni samej elektrody złotej. Kolejnym atutem jest obecność jonów miedzi(II), gdyż to właśnie jony tego metalu są najczęściej stosowane do koordynacji z białkami w kompleksach wielordzeniowych, które z kolei przyczyniają się do generowania miejsc aktywnych białek, takich jak: monooksygenaza dopaminy[126]. Ponadto, obecność wielu jonów metali wzmacnia centra redoks[124]. Co więcej, otrzymany kompleks **K7**, dzięki swojej „siodłowej" konformacji posiada dwa aktywne obszary, z których jeden wykazuje powinowactwo do elektrody złotej dzięki obecności N-heterocyklicznych ugrupowań aromatycznych, a drugi stanowi wnękę otoczoną czterema jonami miedzi(II) tworząc miejsce aktywne do katalitycznego utleniania dopaminy (Rys. 22).

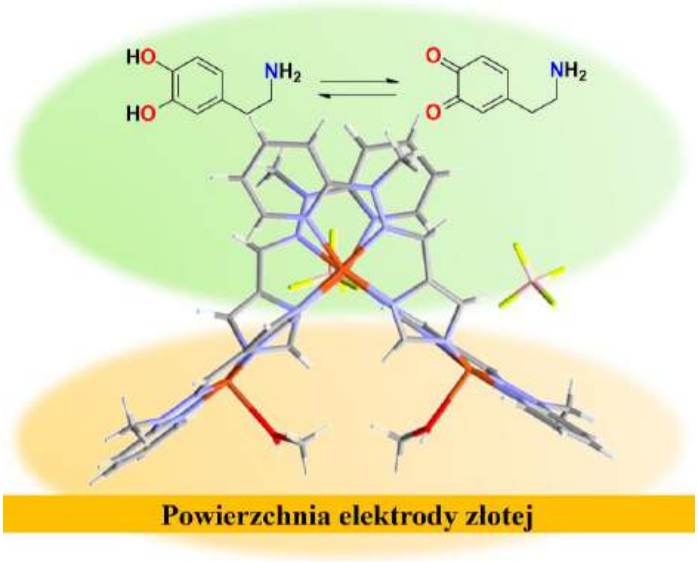

Rysunek 22. Schematyczne zobrazowanie rozmieszczenia kompleksu **K7** podczas pomiarów elektrochemicznych podkreślające dwa obszary, jeden związany z powierzchnią elektrody złotej, a drugi zapewniający aktywne miejsca utleniania dopaminy.

Związek **K7** adsorbując się na elektrodzie złotej zwiększa jej elektroaktywną powierzchnię i ułatwia przemieszczanie się elektronów między utlenianym analitem, a powierzchniowymi atomami złota. W celu dalszego potwierdzenia adsorpcji kompleksu **K7** na powierzchni elektrody złotej oraz określenia morfologii i składu powierzchni po modyfikacji przeprowadzono badania z wykorzystaniem spektroskopii w podczerwieni z tłumieniem całkowitego odbicia (ATR-IR) oraz skaningowej mikroskopii elektronowej (SEM) z analizą rentgenowską z dyspersją energii (EDAX). Zaobserwowane przesunięcia pasm C=N/C-N w zakresie 1500 - 1200 cm^{-1} świadczą o wysokim powinowactwie aromatycznych N-heterocykli do powierzchni złota. Ponadto, jak można zauważyć na poniżej przedstawionych zdjęciach (Rys. 23), występują znaczące zmiany pomiędzy powierzchnią elektrody złotej przed i po modyfikacji. Proces akumulacji cząsteczek kompleksu powoduje zmiany w morfologii powierzchni z jednoczesnym formowaniem nieregularnego układu mającym tendencję do agregacji. Przeprowadzona analiza EDAX stanowi dodatkowy dowód zaistniałej modyfikacji dzięki obecności jednorodnego rozkładu pierwiastków stanowiących skład kompleksu.

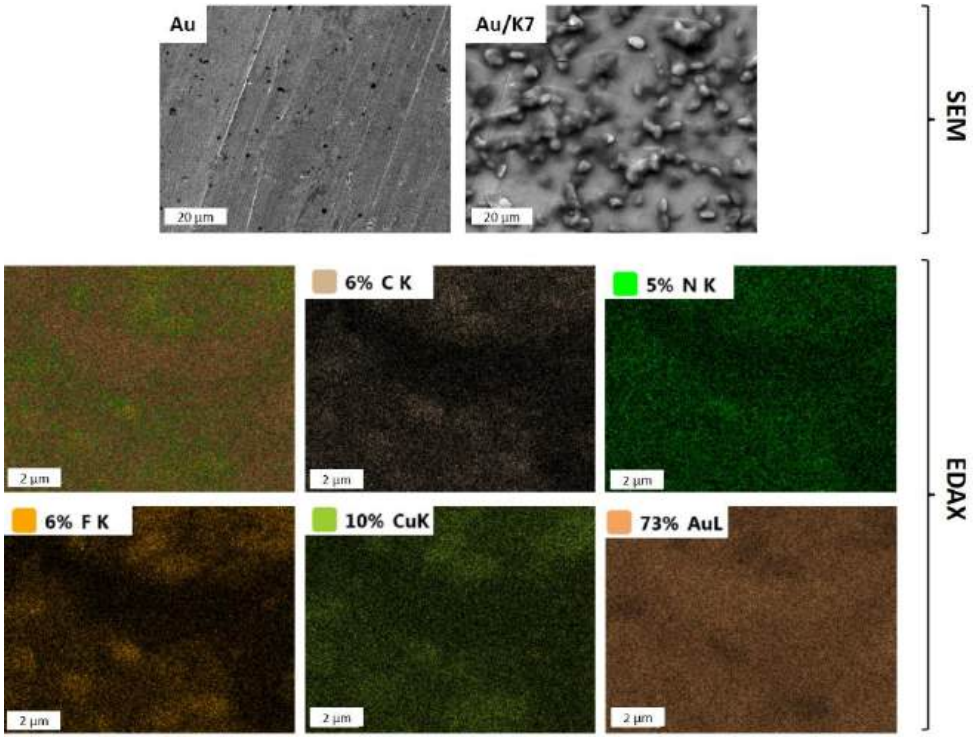

Rysunek 23. Analiza powierzchni SEM niezmodyfikowanej i zmodyfikowanej powierzchni elektrody złotej oraz analiza EDAX elektrody Au/K7[125].

Kolejny etap badań miał na celu sprawdzenie, czy opracowana modyfikowana elektroda Au/K7 może służyć jako element przewodzący w elektrochemicznym sensorze do detekcji dopaminy samej i w obecności czynników zakłócających. Badania woltamperometryczne wykonano w układzie trójelektrodowym ze zmodyfikowaną elektrodą złotą jako elektrodą pracującą oraz platynową elektrodą pomocniczą i nasyconą elektrodą kalomelową jako elektrodą odniesienia. Przebieg kolejnych skanów cyklicznych woltamperogramów zarejestrowanych na elektrodzie Au/K7 w roztworze wodnym PBS, pH = 7 z 0,5 mM DA w zakresie potencjału od E = -0,80 V do E = 1,15 V vs SCE z szybkością zmiany potencjału dE/dt = 0,1 Vs^{-1} odzwierciedla poszczególne etapy utleniania dopaminy w warunkach elektrochemicznych i jest w zgodzie z powszechnie akceptowanym w literaturze mechanizmem ECE, w którym E oznacza etap elektrochemiczny, natomiast C jest etapem chemicznym[102] (Rys. 24).

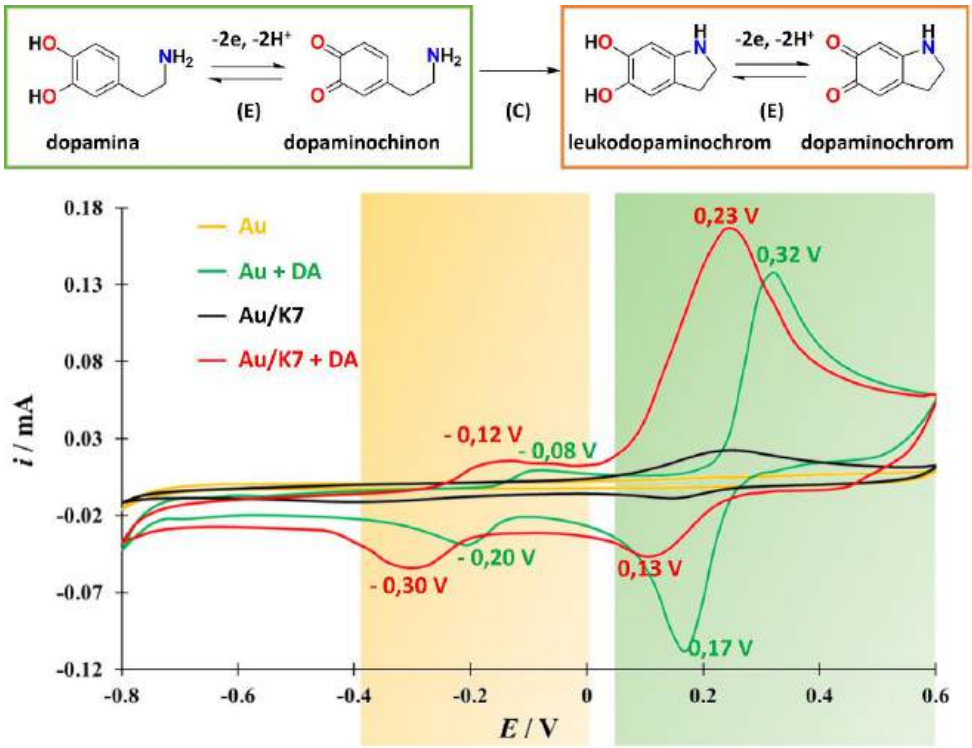

Rysunek 24. Cykliczne woltamperogramy (drugie skany) zarejestrowane dla niezmodyfikowanej elektrody Au (żółty) w PBS i w obecności 0,5 mM dopaminy (zielony), Cykliczne woltamperogramy (drugie skany) zarejestrowane dla zmodyfikowanej elektrody Au/K7 w PBS (czarny) i w obecności 0,5 mM dopaminy (czerwony), dE/dt = 0,1 Vs^{-1} [125].

Jak tego należało oczekiwać, zgodnie z przyjętym mechanizmem ECE, w pierwszym etapie elektrochemicznym (E) po wymianie 2 elektronów i 2 protonów ma miejsce proces quasi-odwracalnego utleniania i redukcji dopaminy do dopaminochinonu, o czym świadczy widoczna na cyklicznym woltamperogramie para pików z maksimum prądu odpowiednio przy E = 0,23 V (elektroutlenianie dopaminy do dopaminochinonu) i przy E = 0,13 V (redukcja dopaminochinonu do dopaminy). W drugim etapie – chemicznym (C) – chinon ulega przekształceniu do leukodopaminochromu, z którego w trzecim etapie – elektrochemicznym – po wymianie 2 kolejnych elektronów i odczepieniu kolejnych 2 protonów powstaje dopaminochrom, co przypisuje się parze pików obserwowanych odpowiednio przy E = -0,12 V (utlenianie leukodopaminochromu do dopaminochromu) i E = -0,30 V (redukcja dopaminochromu do leukodopaminochromu). Należy wspomnieć, że dopaminochrom posiada zdolność polimeryzacji[127]. Zwraca uwagę fakt, że wymienione pary pików prądowych pojawiają się przy znacznie niższych potencjałach, gdy utlenianie dopaminy ma miejsce na

modyfikowanej elektrodzie Au/K7 (Rys. 24). Niższa też jest potencjałowa separacja anodowych i katodowych pików prądowych (ΔE). Poza tym zastąpienie niemodyfikowanej elektrody Au elektrodą Au/K7 skutkuje wzrostem intensywności sygnałów prądowych. Te obserwacje świadczą o katalitycznym wpływie kompleksu **K7** zgromadzonego na powierzchni elektrody na proces utleniania/redukcji z udziałem dopaminy. Ponadto należy podkreślić, że zakres potencjału, w którym na cyklicznym woltamperogramie widoczna jest para pików przypisana elektroutlenianiu/elektroredukcji dopaminy do dopaminochinonu pokrywa się z zakresem potencjału utleniania/redukcji samego kompleksu **K7**, podczas gdy w tym samym czasie odpowiedź prądowa dopaminy na zmodyfikowanej elektrodzie Au/K7 jest około 7,5 razy wyższa od tej obserwowanej dla **K7**. Fakt ten silnie dowodzi, że zaadsorbowany na powierzchni elektrody kompleks jest mediatorem procesu redoks z udziałem badanego neurotransmitera.

Wykazano silny wpływ pH roztworu elektrolitu podstawowego (zakres pH od 3 do 11) na położenie w skali potencjału i intensywność sygnału utleniania dopaminy na elektrodzie Au/K7. Ze wzrostem pH obserwowano przesunięcie rozważanego procesu w kierunku mniej dodatnich wartości potencjału. W zakresie pH od 3 do 11 spełniona jest liniowa zależność E_p - pH ($R^2 = 0{,}9996$) z kątem nachylenia $dE_p/dpH = 0{,}060$. Wartość kąta zbliżona do teoretycznej wartości 0,059 wynikającej z równania Nernsta dowodzi, że podczas utleniania dopaminy na elektrodzie Au/K7 liczba wymienianych elektronów jest równa liczbie uwalnianych protonów[128]. Tym samym potwierdzona została słuszność wyżej przyjętego mechanizmu elektroutleniania dopaminy. Zwrócono też uwagę na fakt, że maksymalny wzrost sygnałów prądowych obserwowano dla układów w zakresie pH od 6 do 8 i w związku z tym dalsze badania z udziałem dopaminy prowadzono w roztworze elektrolitu podstawowego o pH = 7, a więc zbliżonym do pH płynów ustrojowych człowieka.

Wgląd w mechanizm elektroutleniania dopaminy na modyfikowanej elektrodzie Au/K7 uzyskano na podstawie woltamperogramów otrzymanych dla różnych szybkości (v) nakładania potencjału na elektrodę. Analizując intensywności prądowe w maksimum piku (i_p) przy zmianie szybkości we współrzędnych $\log i_p$ – $\log v$ obserwowano prostoliniową zależność z kątem nachylenia $d\log i_p/d\log v \approx 0{,}5$[129]. Wartość tego kąta oraz dodatkowo liniowa zależność natężenia prądu w funkcji pierwiastka kwadratowego szybkości skanowania potencjału nakładanego na elektrodę jednoznacznie świadczą o dyfuzyjnych ograniczeniach ogólnej

szybkości badanego procesu przy potencjale maksimum piku w zastosowanych warunkach eksperymentalnych. Oznacza to, że dyfuzja cząsteczek dopaminy do powierzchni elektrody jest wolniejsza zarówno od ich adsorpcji na granicy faz elektroda/roztwór elektrolitu jak i od następującego po niej przeniesienia ładunku. Należy podkreślić, że zależność taka jest korzystna dla ilościowych oznaczeń analitów w roztworach elektrolitów.

Biorąc powyższe pod uwagę, w kolejnym etapie badań elektrochemicznych przystąpiono do określenia czułości analitycznej modyfikowanej elektrody złotej Au/K7 dla ilościowego oznaczania dopaminy. Analizując woltamperogramy uzyskane techniką różnicowej woltamperometrii pulsowej (krzywe DPV) stwierdzono, że ze wzrostem stężenia dopaminy w roztworze wzrasta natężenie rejestrowanego prądu w maksimum piku (Rys. 25).

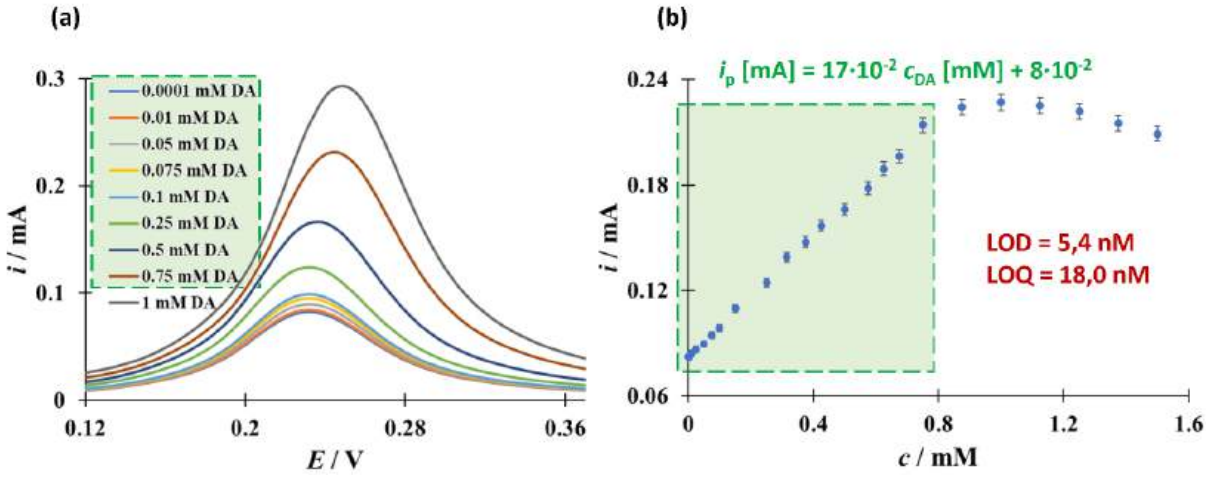

Rysunek 25. (a) Wybrane krzywe DPV zarejestrowane dla zmodyfikowanej elektrody Au/K7 po dodaniu różnych ilości dopaminy w PBS, dE/dt = 0,1 Vs^{-1}. (b) zależność i_p – c_{DA} w zakresie stężeń dopaminy od 0,0001 do 1,5 mM. Słupki błędów odpowiadają odchyleniom standardowym pomiarów (n = 3). Zielone kwadraty określają zakres liniowy[125].

Wykazano, że w zakresie stężenia analitu – dopaminy (c_{DA}) od 0,0001 do 0,75 mM (liniowy zakres dynamiczny) punkty doświadczalne analizowane we współrzędnych i_p – c_{DA} układają się wzdłuż linii prostej opisanej następującym równaniem regresji liniowej: i_p [mA] = 17·10^{-2} c_{DA} [mM] + 8·10^{-2} (n = 15, R^2 =0,998) ustalonym metodą najmniejszych kwadratów. Przy stężeniu dopaminy wyższym niż 0,875 mM wartość prądu anodowego zaczyna maleć najprawdopodobniej na skutek adsorpcji cząsteczek analitu na zmodyfikowanej powierzchni elektrody. Oszacowano wartość granicy wykrywalności, LOD = 5,4 nM oraz granicy

oznaczalności, LOQ = 18,0 nM oraz określono czułość detekcji (i_p/c_{DA}) dopaminy w roztworze PBS, pH = 7, na modyfikowanej elektrodzie Au/K7 przy dE/dt = 0,1 Vs^{-1} wynoszącą 0,17 A M^{-1}.

Otrzymane wartości granicy wykrywalności i oznaczalności oraz liniowy zakres dynamiczny jednoznacznie świadczą, że zaproponowana elektroda Au/K7 może z powodzeniem konkurować z innymi modyfikowanymi elektrodami (Tabela 1) przytaczanymi w literaturze dla oznaczeń dopaminy i może być obiecującym, praktycznym narzędziem do detekcji tego analitu w próbkach rzeczywistych. Potwierdzają to wyniki oznaczeń dopaminy w dostępnym na rynku jej roztworze do infuzji, gdzie otrzymane wartości odzysku wahały się w granicach 98,9 – 100,7%, co stanowiło potwierdzenie, że sensor jest niezawodny i skuteczny w oznaczaniu dopaminy w próbkach komercyjnych.

Tabela 1. Reprezentatywne wyniki oznaczania dopaminy przy użyciu różnych zmodyfikowanych elektrod[125].

elektroda	zakres liniowości [μM]	granica wykrywalności [nM]	literatura
elektroda złota modyfikowana czterordzeniowym kompleksem Cu(II) **Au/K7**	0,1 – 750	5,4	[125]
elektroda złota modyfikowana dwurdzeniowym kompleksem Cu(II)	0,2 – 30	80	[124]
elektroda złota modyfikowana kompleksem Mn(II)	0,0001 – 850	6,8	[104]
film polimerowy z dopaminą	1 – 600	200	[130]
elektroda grafitowa modyfikowana kompleksem Cu(II)	-	500	[131]
PGE[a] modyfikowana Cu-Ag	0,1 – 200	26	[132]
PGE[a] modyfikowana perylenodiimidem zintegrowanym z tlenkiem miedzi	5 – 500	6	[133]

Skróty: [a] PGE (ang. *pencil graphite electrode*) – ołówkowa elektroda grafitowa

Elektrochemiczne oznaczanie dopaminy w próbkach rzeczywistych na niemodyfikowanych elektrodach jest utrudnione ze względu na blokowanie powierzchni tych elektrod przez

produkty pośrednie i/lub końcowe oraz ze względu na współistnienie analitu w środowisku naturalnym z innymi związkami o znaczeniu biologicznym, które bardzo często ulegają utlenieniu/redukcji w zakresie potencjałów pokrywających się z zakresem charakterystycznym dla reakcji redoks z udziałem dopaminy[134]. W pracy podjęto badania mające na celu oznaczania dopaminy przy użyciu opracowanego sensora Au/K7 w obecności kwasu askorbinowego (AA) jako związku zakłócającego. Rezultaty przeprowadzonych badań przedstawione na rysunku 26 wyraźnie wskazują, że zastosowanie opracowanego sensora znacząco wpływa na zwiększenie separacji potencjałowej sygnałów prądowych odpowiadających procesom utleniania dopaminy oraz kwasu askorbinowego z 56 mV na elektrodzie Au do 267 mV w przypadku elektrody Au/K7.

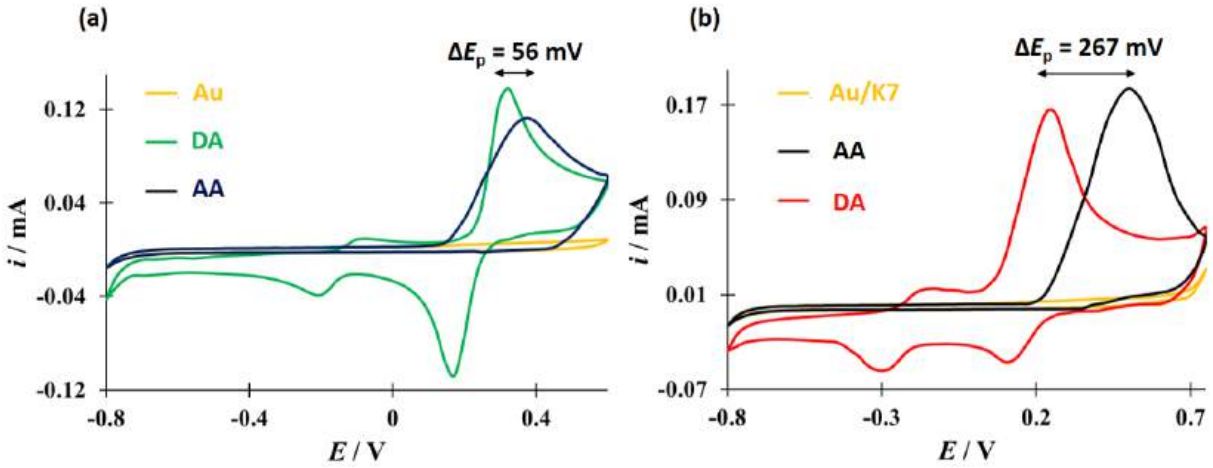

Rysunek 26. (a) Cykliczne woltamperogramy zarejestrowane dla niezmodyfikowanej elektrody Au w PBS (żółty) w obecności 0,5 mM dopaminy (zielony) oraz w obecności 0,5 mM kwasu askorbinowego (granatowy) w PBS, dE/dt = 0,1 Vs^{-1}. (b) Cykliczne woltamperogramy zarejestrowane dla zmodyfikowanej elektrody Au/K7 w PBS (żółty) w obecności 0,5 mM dopaminy (czerwony) oraz w obecności 0,5 mM kwasu askorbinowego (czarny) w PBS, dE/dt = 0,1 Vs^{-1} [125].

Wielkość zaobserwowanej różnicy ΔE nie pozostawia wątpliwości, że opracowany sensor może być z powodzeniem używany do jednoczesnego selektywnego wykrywania i analitycznego ilościowego oznaczania dopaminy w obecności kwasu askorbinowego, a zatem również do oznaczania tego kwasu w obecności dopaminy współistniejącej w mieszaninie dwuskładnikowej. Na podkreślenie zasługuje fakt, że uzyskane wartości granicy wykrywalności i oznaczalności podczas oznaczania dopaminy w mieszaninie z kwasem

askorbinowym są niemal identyczne z tymi uzyskanymi dla oznaczeń dopaminy w układzie bez obecności związku interferującego.

W pracy, oprócz określenia wpływu kwasu askorbinowego na ilościowe oznaczanie dopaminy, doświadczalnie przeanalizowano także wpływ innych interferentów, takich jak: Na^{+}, K^{+}, Mg^{2+}, Ca^{2+}, Zn^{2+}, NO_3^{-}, SO_4^{2-}, a wyniki przeprowadzonych badań potwierdzają, że opracowany sensor wykazuje dobrą zdolność do specyficznego wykrywania dopaminy bez żadnych zakłóceń ze strony wymienionych czynników interferujących.

W rezultacie otrzymano oraz scharakteryzowano wielordzeniowy kompleks miedzi(II) **K7**, który kolejno wykorzystano do modyfikacji powierzchni elektrody złotej otrzymując zmodyfikowaną elektrodę Au/K7. Związek kompleksowy **K7** wykazuje z jednej strony powinowactwo do powierzchni złota, a z drugiej stanowi centrum aktywne utleniania dopaminy. Ta nietypowa właściwość pozwoliła na jego adsorpcję na powierzchni elektrody złotej tworząc czujnik elektrochemiczny do ilościowego oznaczania dopaminy w warunkach zbliżonych do fizjologicznych. Zaproponowany w niniejszej pracy sposób modyfikacji elektrody Au kompleksem **K7** jest bardzo korzystny dla zastosowań analitycznych. Udowodniono, że zmodyfikowaną elektrodę Au/K7 można z powodzeniem wykorzystać jako materiał przewodzący w czujniku elektrochemicznym przeznaczonym do jakościowych i ilościowych oznaczeń dopaminy bez interferencji związków zakłócających przy niskiej wartości granicy wykrywalności oraz oznaczalności. Wyniki te otwierają drogę do dalszych badań nad wykorzystaniem kompleksów do modyfikacji elektrod z przeznaczeniem do wykorzystania jako czujników neuroprzekaźników lub innych substancji biologicznie czynnych. Układ taki może znaleźć zastosowanie jako medyczna sonda diagnostyczna w badaniach *in vitro*.

3.3. Publikacja nr 3 (P3): "Application of a simple copper(II) complex compound as an epinephrine selective voltammetric sensor in the presence of uric acid under aqueous conditions " – Dalton Transactions, 2025, 54, 1000-1012.

Publikacja P3 dotyczy monometalicznego kompleksu miedzi(II) **K8** $[Cu(L4)_2](BF_4)_2$ z ligandem N,N,N-donorowym **L4** $[C_{10}H_{11}N_5]$, jego właściwości elektrochemicznych oraz możliwości zastosowania otrzymanej zmodyfikowanej elektrody złotej jako elementu przewodzącego w czujniku elektrochemicznym do wykrywania epinefryny, zarówno w przypadku gdy występuje w roztworze sama jak i w obecności związków zakłócających.

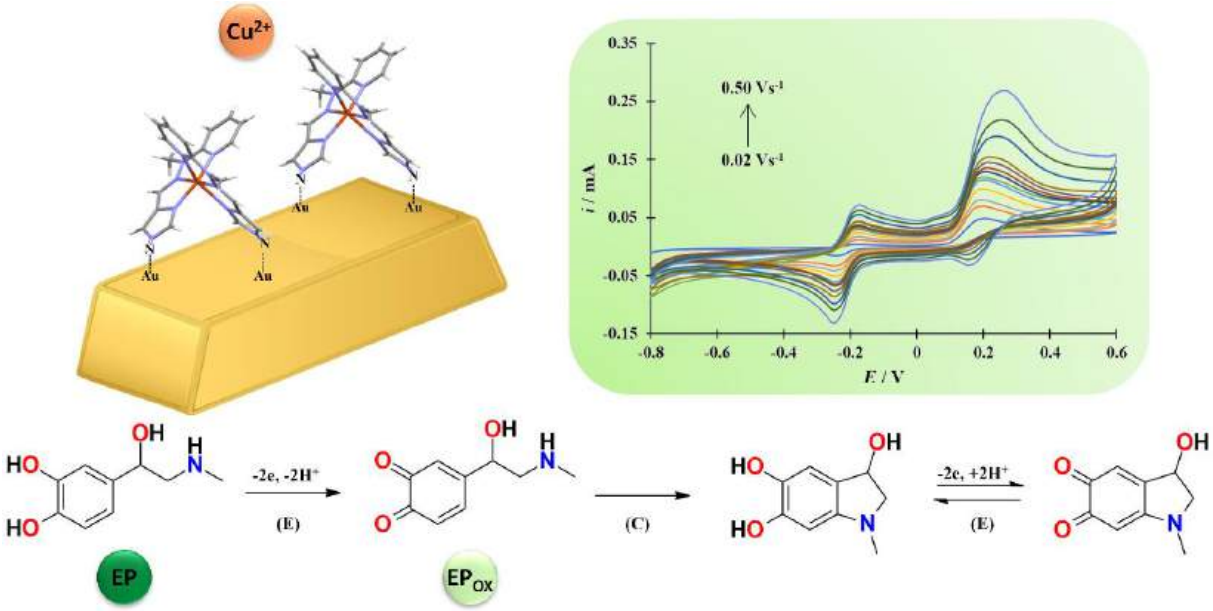

Rysunek 27. Schematyczne przedstawienie najważniejszych aspektów publikacji nr 3.

Związek kompleksowy **K8** otrzymano w wyniku reakcji liganda **L4** i soli miedzi(II) $Cu(BF_4)_2 \cdot xH_2O$ zmieszanych w stosunku molowym 2:1 w metanolu (Rys. 28). Syntezę prowadzono 24 godziny w temperaturze pokojowej prowadząc do izolacji zielonego proszku z wydajnością 88,7%. Kryształy kompleksu odpowiednie do pomiarów techniką dyfrakcji rentgenowskiej uzyskano metodą powolnej dyfuzji eteru diizopropylowego do metanolowego roztworu kompleksu **K8** w temperaturze ~ 4ºC. Ponadto, otrzymany związek kompleksowy scharakteryzowano za pomocą metod: HRMS, TGA, FT-IR oraz ATR-IR.

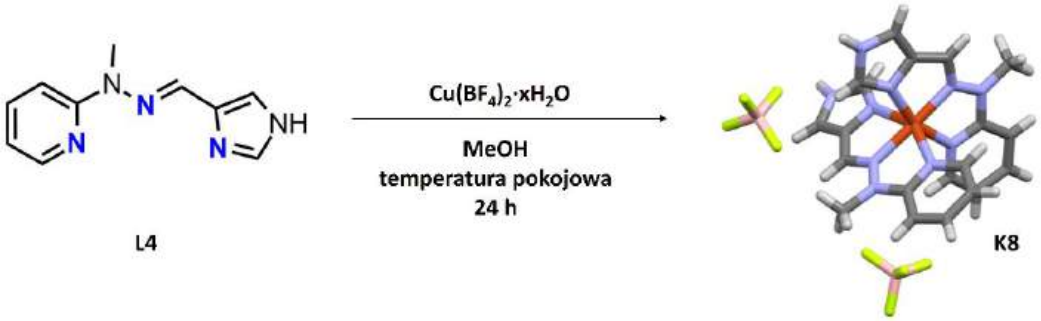

Rysunek 28. Samoorganizacja liganda **L4** w obecności soli miedzi(II) $Cu(BF_4)_2 \cdot xH_2O$ prowadząca do otrzymania monometalicznego związku kompleksowego miedzi(II) **K8** $[Cu(L4)_2](BF_4)_2$.

W kompleksie **K8** dodatni jon kompleksowy jest neutralizowany jonami tetrafluoroboranowymi z zewnętrznej sfery koordynacyjnej, a jon centralny jest skoordynowany z sześcioma atomami donorowymi azotu pochodzącymi od dwóch cząsteczek liganda **L4**. Ponadto, kompleks przyjmuje postać izomeru *mer*, który jest stabilny w roztworze i nie ulega przekształceniu w izomer *fac*, co zostało zweryfikowane obliczeniami przy użyciu teorii funkcjonału gęstości. Kompleks **K8** bazujący na zasadzie Schiffa posiada łatwość adsorbowania się na powierzchni elektrody złotej przez co może być stosowany do modyfikacji elektrod wykorzystywanych do badań elektrochemicznych.

Sam proces modyfikacji powierzchni elektrody złotej poprzedzono jej elektrochemiczną aktywacją w zakresie potencjału od E = -0,80 V do E = 0,6 V vs SCE z dE/dt = 0,1 Vs^{-1} w 0,5 M roztworze NaOH aż do uzyskania stabilnego woltamperogramu. Następnie, zaktywowaną elektrodę złotą zanurzono, w warunkach *ex situ*, w 0,01 mM roztworze kompleksu **K8** w PBS (0,06 M przy pH = 7) w temperaturze pokojowej na okres 16 godzin. Dla tak przygotowanej elektrody zarejestrowano cykliczny woltamperogram i porównano go z uzyskanym dla elektrody złotej przed modyfikacją w celu potwierdzenia adsorpcji kompleksu **K8** na powierzchni elektrody. Dodatkowo powierzchnię elektrody zobrazowano techniką SEM w połączeniu z analizą EDAX.

Na cyklicznym woltamperogramie zarejestrowanym dla niezmodyfikowanej elektrody złotej w zakresie potencjału od E = -0,80 V do E = 1,15 V vs SCE z dE/dt = 0,1 Vs^{-1} w roztworze PBS zaobserwowano parę odwracalnych pików zlokalizowanych odpowiednio przy E = 0,83 V i E = 0,48 V vs SCE i związanych z powstawaniem tlenku złota i jego redukcją[123]. Biorąc

pod uwagę fakt, że żadne reakcje elektrochemiczne nie zachodzą na elektrodzie złotej w zakresie od E= -0,8 V do E = 0,6 V, dalsze pomiary wykonano w tym zakresie potencjału (również ligand **L4** jest nieaktywny elektrochemicznie w tym zakresie[125]). Po modyfikacji, na cyklicznym woltamperogramie pojawiają się piki: anodowy i katodowy zlokalizowane odpowiednio przy E = 0,25 V i przy E = 0,18 V, które zgodnie z literaturą[124, 135] odpowiadają kolejno procesowi utleniania Cu^{+} do Cu^{2+} oraz redukcji Cu^{2+} do Cu^{+}. Dla elektrody złotej zmodyfikowanej kompleksem **K8** (Au/K8) stwierdzono prostoliniową zależność między intensywnościami natężenia prądu w wymienionych pikach (i_p) i szybkością nakładania potencjału na elektrodę (v) w zakresie od 0,02 Vs^{-1} do 0,50 Vs^{-1} (Rys. 29). Obserwacja ta łącznie z wartością kąta nachylenia dlog i_p/dlog $v \approx 1$ jest dowodem na to, że modyfikujący kompleks **K8** znajduje się na powierzchni elektrody w stanie zaadsorbowanym.

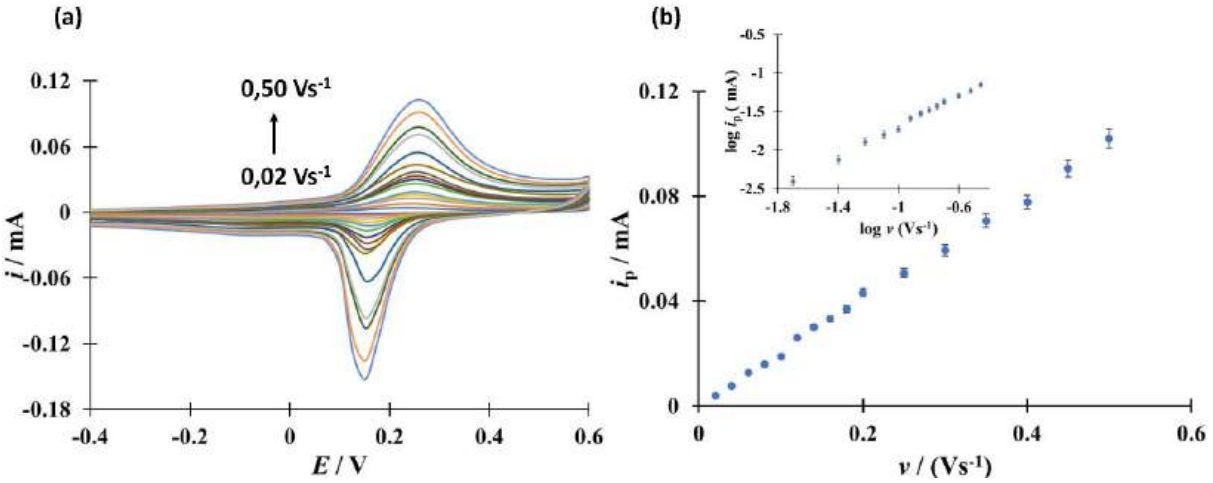

Rysunek 29. (a) Cykliczne woltamperogramy zarejestrowane dla zmodyfikowanej elektrody Au/K8 w PBS przy szybkościach skanowania od 0,02 do 0,50 Vs^{-1}. (b) Zależności: i_p - v; panel wewnętrzny: log i_p - log v [136].

Utworzenie samoorganizującej się monowarstwy na powierzchni elektrody złotej ma wiele zalet, między innymi ułatwia zachodzenie procesów utleniania i redukcji na granicy faz między elektrodą a roztworem, jak i również skutecznie chroni powierzchnię elektrody przed zatruwaniem powierzchni[137, 138]. Powierzchnia elektrody złotej wykazuje powinowactwo do atomów azotu obecnych w cząsteczkach w postaci grup NH oraz N-heterocyli[139, 140], w związku z czym można wnioskować, że elementem struktury kompleksu, odpowiedzialnym za jego adsorpcję na powierzchni elektrody złotej jest obecność dodatkowych atomów azotu nie

biorących udziału w koordynacji jonu metalu. Proces samoorganizacji monowarstwy kompleksu **K8** na powierzchni złota odbywa się poprzez utworzenie wiązania kowalencyjnego Au-N pomiędzy atomami azotu pochodzącymi z dwóch grup aminowych szkieletu liganda, a powierzchniowymi atomami złota (Rys. 30).

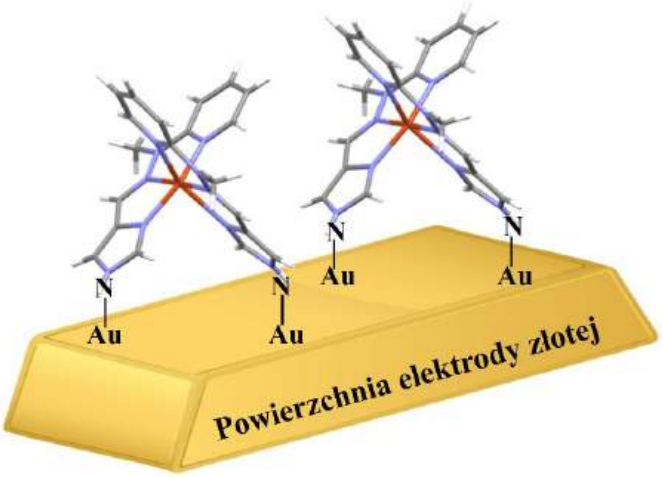

Rysunek 30. Schemat wiązania między atomami azotu ze struktury kompleksu **K8** i powierzchniowymi atomami złota[136].

Adsorpcję kompleksu **K8** oraz utworzenie monowarstwy na elektrodzie złotej potwierdzono dodatkowo obrazami SEM wraz z analizą EDAX. Na rysunku 31 wyraźnie można zauważyć różnicę w morfologii powierzchni przed i po modyfikacji elektrody złotej. Niezmodyfikowana powierzchnia charakteryzuje się równomiernym układem, jest gładka i pozbawiona wszelkich nierówności. Natomiast, ta zmodyfikowana ukazuje regularność ułożenia zaadsorbowanego materiału potwierdzając jednocześnie adsorpcję kompleksu na jej powierzchni. Ponadto, kolejny dowód stanowi równomierny rozkład pierwiastków: złota oraz miedzi na powierzchni zmodyfikowanej. Dodatkową weryfikację stanowi widmo ATR-IR, w którym zanik pasma charakterystycznego dla grupy N-H w zakresie 4000 – 3000 cm^{-1} świadczy o utworzeniu wiązania Au-N.

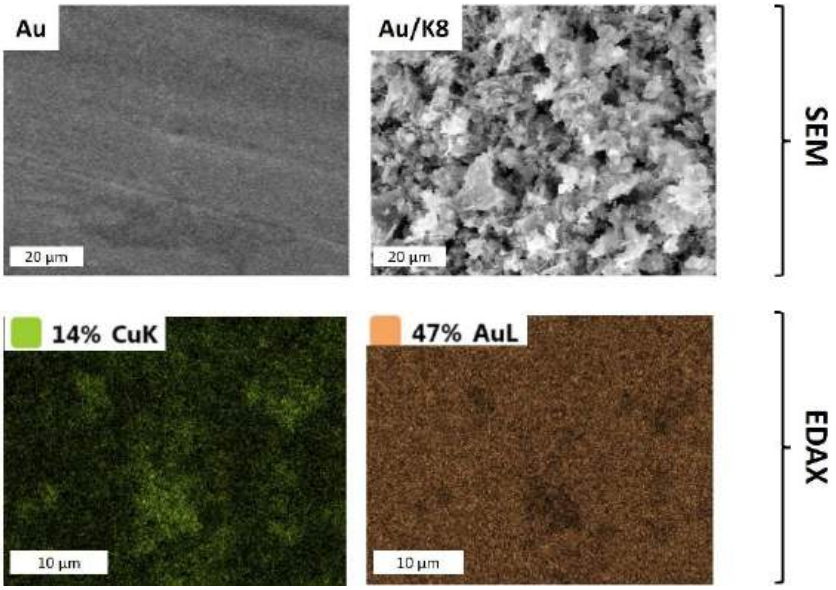

Rysunek 31. Analiza powierzchni SEM niezmodyfikowanej oraz zmodyfikowanej elektrody złotej oraz analiza EDAX powierzchni elektrody Au/K8[136].

Tak zmodyfikowaną elektrodę (Au/K8) wykorzystano do przeprowadzenia dalszych badań elektrochemicznych celem określenia jej przydatności jako elementu przewodzącego w sensorze elektrochemicznym do wykrywania samej epinefryny oraz w obecności interferentów. Pomiary metodą woltamperometrii cyklicznej wykonano w odtlenionym roztworze wodnym PBS stosując trójelektrodowy układ złożony z elektrody złotej (niezmodyfikowanej oraz zmodyfikowanej), elektrody platynowej oraz nasyconej elektrody kalomelowej w zakresie potencjału od E = -0,80 V do E = 0,6 V vs SCE, dE/dt = 0,1 Vs^{-1}. Cykliczne woltamperogramy zarejestrowane na niezmodyfikowanej i zmodyfikowanej elektrodzie złotej w obecności epinefryny w zakresie stężeń od 0,0001 mM do 1 mM przedstawiono na rysunku 32. Zgodnie z literaturą, utlenianie epinefryny podobnie jak dopaminy, przebiega według mechanizmu ECE[102].

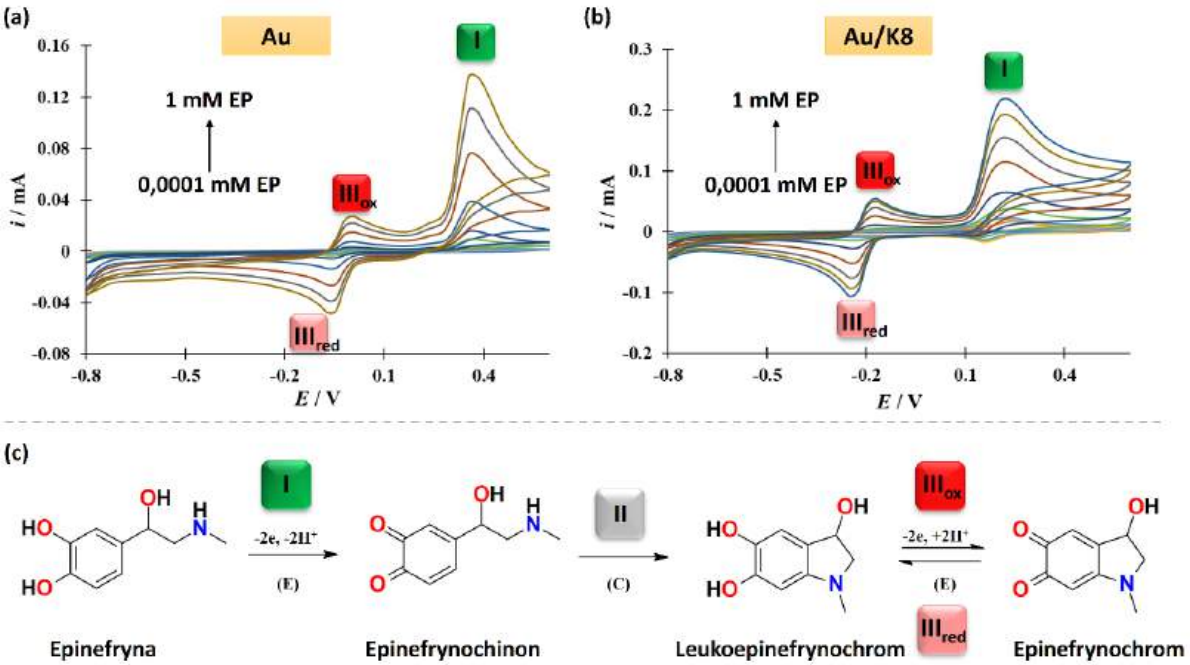

Rysunek 32. Cykliczne woltamperogramy (drugie skany) zarejestrowane w obecności epinefryny o różnych stężeniach od 0,0001 mM do 1 mM dla (a) niezmodyfikowanej elektrody Au oraz dla (b) zmodyfikowanej elektrody Au/K8 w PBS, dE/dt = 0,1 Vs^{-1}. (c) Mechanizm utleniania/redukcji epinefryny[136].

Na cyklicznych woltamperogramach zarejestrowanych podczas utleniania epinefryny dla niezmodyfikowanej elektrody złotej obserwuje się jeden szeroki, nieodwracalny pik anodowy z maksimum piku przy E = 0,36 V oraz parę odwracalnych pików o małej intensywności przy E = 0,01 V oraz E = 0,07 V (ΔE_p = 80 mV) (dane dla 0,5 mM roztworu epinefryny). Pierwszy z wymienionych pików odpowiada nieodwracalnemu przekształcaniu epinefryny w epinefrynochinon, a wymieniona para pików związana jest z odwracalnym utlenianiem leukoepinefrynochromu do epinefrynochromu. Zastąpienie elektrody Au zmodyfikowaną elektrodą Au/K8 skutkuje przesunięciem wymienionych pików prądowych w kierunku niższych wartości potencjału. Przy takim samym stężeniu analitu w roztworze nieodwracalny pik anodowy pojawia się przy E = 0,23 V, para odwracalnych pików jest zlokalizowana przy E = -0,18 V oraz E = -0,24 V (ΔE_p = 60 mV). W przypadku zmodyfikowanej elektrody, przesunięciu obu rozważanych procesów w kierunku niższych potencjałów towarzyszy wzrost intensywności prądowych oraz mniejsza separacja potencjału pików, co świadczy

o katalitycznym wpływie zaadsorbowanego kompleksu **K8** na powierzchni elektrody na rozpatrywane procesy redoks z udziałem epinefryny.

Wykazano, że szybkość procesu utleniania epinefryny jest kontrolowana dyfuzją cząsteczek substratu do powierzchni elektrod. Świadczy o tym prostoliniowa zależność pomiędzy wartościami prądu (i_p) w maksimum piku, a pierwiastkiem kwadratowym szybkości skanowania ($v^{1/2}$) w zakresie od 0,02 Vs^{-1} do 0,50 Vs^{-1} oraz równe wartości 0,51 nachylenie d log i_p/d log v (Rys. 33). Należy podkreślić, że dyfuzyjne ograniczenie szybkości procesu jest korzystne dla ilościowego oznaczania stężenia badanego analitu w roztworze elektrolitu[129]. Analizując wyniki uzyskane w roztworach elektrolitów o różnym pH (3 – 11) stwierdzono, że kąt nachylenia d E_p/d pH prostoliniowej zależności we współrzędnych E_p – pH przyjmuje wartość 0,0596, która zgodnie z teorią kinetyki elektrochemicznej[128] dowodzi, że podczas utleniania epinefryny na zmodyfikowanej elektrodzie wymianie ulega taka sama liczba elektronów co protonów. Wynik ten pozostaje w zgodzie z przyjętym powyżej mechanizmem elektroutleniania badanego analitu. Warto podkreślić, że w zakresie pH od 6 do 8 zanotowano maksymalne wartości sygnałów prądowych, dlatego kolejne eksperymenty elektrochemiczne prowadzono w roztworze o pH = 7, który jest zbliżony do wartości pH płynów ustrojowych.

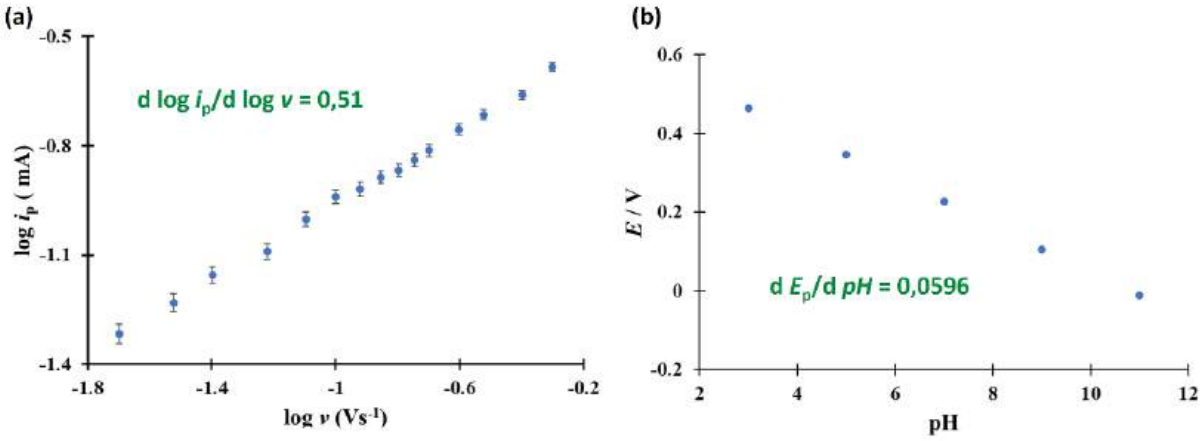

Rysunek 33. Wykresy zależności: (a) log i_p - log v oraz (b) E - pH[136].

Badania elektrochemiczne omówione w publikacji obejmowały również określenie czułości elektrody złotej po modyfikacji w odniesieniu do ilościowego oznaczania epinefryny. Do tego badania zastosowano technikę różnicowej woltamperometrii pulsowej, a pomiary wykonano dla stężeń epinefryny (c_{EP}) w zakresie: 0,0001 mM – 1,375 mM (Rys. 34).

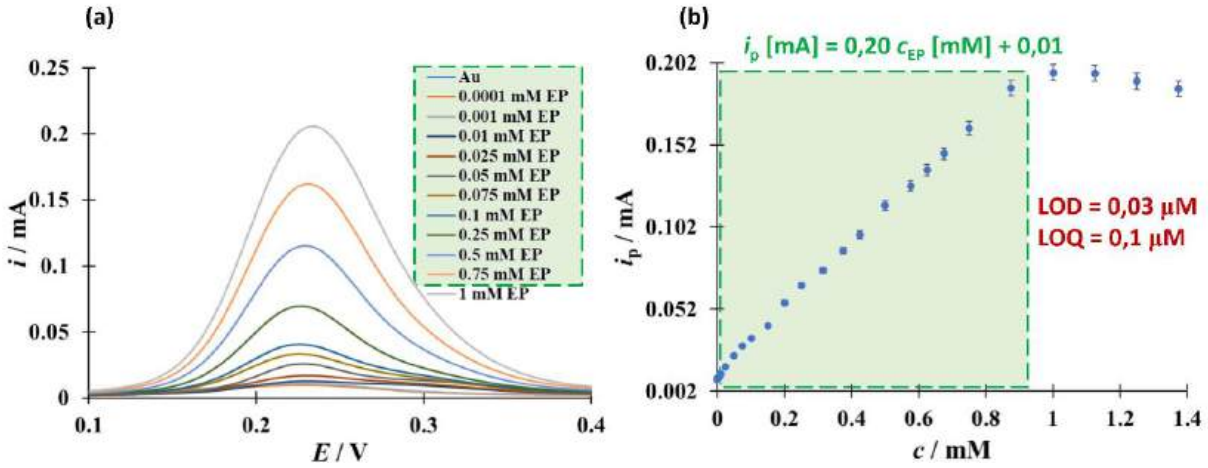

Rysunek 34. (a) Wybrane krzywe DPV zarejestrowane dla zmodyfikowanej elektrody Au/K8 po dodaniu różnych ilości epinefryny w PBS, dE/dt = 0,1 Vs^{-1}. (b) zależność i_p – c_{EP} w zakresie stężeń epinefryny od 0,0001 do 1,375 mM. Słupki błędów odpowiadają odchyleniom standardowym pomiarów (n = 3). Zielone kwadraty określają zakres liniowy[136].

Liniowość korelacji między natężeniem prądu w piku, a stężeniem epinefryny w głębi roztworu, osiągnięto w szerokim zakresie stężeń (0,0001 mM – 0,875 mM) i opisano następującym równaniem regresji liniowej: i_p [mA] = 0,20 c_{EP} [mM] + 0,01 (R^2 =0,9988) przy wartościach granicy wykrywalności i oznaczalności równych 0,03 µM oraz 0,1 µM, co w porównaniu z wartościami innych czujników opisanych w literaturze[141-146] (Tabela 2), bez wątpienia dowodzi skuteczności elektrody Au/K8 do elektrochemicznego oznaczania epinefryny w roztworach wodnych. Ponadto, wyniki oznaczeń epinefryny w próbkach komercyjnych cechowały zadawalające poziomy odzysku (98,6% – 101,7%) i niskie wartości RSD (1,8% - 2,7%) wskazując na skuteczność opracowanej metody oznaczania epinefryny przy zastosowaniu zmodyfikowanej elektrody Au/K8.

Tabela 2. Reprezentatywne wyniki detekcji epinefryny przy użyciu różnych zmodyfikowanych elektrod[136].

elektroda	zakres liniowości [μM]	granica wykrywalności [μM]	literatura
elektroda złota modyfikowana kompleksem Cu(II) **Au/K8**	0,1 - 875	0,03	136
elektroda złota modyfikowana kompleksem Fe(III)	0,01 - 900	0,0074	105
SPE[a] modyfikowana nanokompleksem Cu(II)	10 - 600	2,5	142
CPE[b] modyfikowana grafenowymi kropkami kwantowymi	0,36 - 380	0,0003	147
CPE[b] modyfikowana ftalocyjaniną Fe(II)	1 - 300	0,5	143
elektroda z węgla szklistego modyfikowana nanokompozytem SnO_2/grafen	0,5 - 200	0,017	148

Skróty: [a] SPE (ang. s*creen printing electrode*) – elektroda sitodrukowana; [b] CPE (ang. *carbon paste electrode*) – pastowa elektroda węglowa

Oznaczanie epinefryny metodami elektrochemicznymi na niemodyfikowanych elektrodach jest praktycznie niemożliwe w próbkach rzeczywistych zawierających inne biocząsteczki (np. kwas moczowy) ze względu na nakładanie się potencjałów ich utleniania i/lub redukcji, dlatego modyfikacja elektrod jest tak kluczowa. Analogiczne badania do tych przeprowadzonych dla roztworu zawierającego samą epinefrynę, wykonano dla mieszaniny epinefryny oraz kwasu moczowego (UA) (Rys. 35). Jak można się było spodziewać, zastosowanie zmodyfikowanej elektrody Au/K8 powoduje zwiększenie separacji sygnałów odpowiadającym potencjałom dla epinefryny i kwasu moczowego (ΔE_p = 220 mV), umożliwiając ich jednoczesne oznaczanie, co nie jest wykonalne przy użyciu niezmodyfikowanej elektrody złotej (ΔE_p = 20 mV). W tym ostatnim przypadku cykliczne woltamperogramy praktycznie się pokrywają.

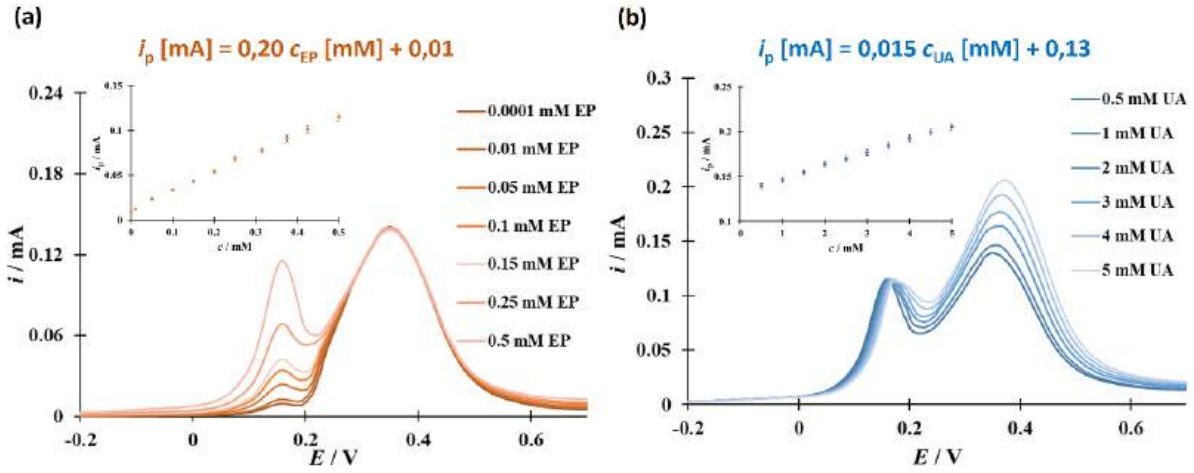

Rysunek 35. (a) Krzywe DPV zarejestrowane dla elektrody Au/K8 w PBS z 0,5 mM UA i rosnącymi ilościami epinefryny (od 0,0001 mM do 0,5 mM), dE/dt = 0,1 Vs^{-1}. Panel wewnetrzny: zależność i_p - c_{EP}. (b) Krzywe DPV zarejestrowane dla elektrody Au/K8 w PBS z 0,5 mM EP i rosnącymi ilościami kwasu moczowego (od 0,5 mM do 5 mM), dE/dt = 0,1 Vs^{-1}. Panel wewnętrzny: zależność i_p - c_{UA}[136].

Rozdzieleniu pików odpowiadających utlenianiu epinefryny oraz kwasu moczowego sprzyjają oddziaływania elektrostatyczne między ujemnie naładowaną zmodyfikowaną powierzchnią elekrody złotej Au/K8, a jonowymi formami badanych związków. Parametry analityczne uzyskane dla epinefryny w obecności stałej ilości kwasu moczowego są identyczne jak w przypadku oznaczania samej epinefryny, natomiast analiza ilościowa kwasu moczowego przy niezmiennej ilości epinefryny wykazała liniową zależność w przedziale stężeń od 0,5 mM do 5,0 mM opisaną równaniem: i_p [mA] = 0,015 c_{UA} [mM] + 0,13 (R^2 =0,9988) z wartościami granicy wykrywalności i oznaczalności równymi 40 µM i 133 µM. Obecność innych interferentów, takich jak: Na^+, K^+, Ca^{2+}, NH_4^+, Mg^{2+}, SO_4^{2-}, $C_2O_4^{2-}$, również nie powodowała zakłóceń w oznaczaniu epinefryny.

Biorąc pod uwagę powyżej przedstawione wyniki można wnioskować, że zmodyfikowana elektroda Au/K8 otrzymana w wyniku adsorpcji kompleksu **K8** na powierzchni złota, może być wykorzystana jako materiał przewodzący w czujniku elektrochemicznym podczas oznaczania samej epinefryny oraz w obecności czynników zakłócających, przy niskiej wartości granicy wykrywalności, wysokiej odtwarzalności i dobrej stabilności. Te rezultaty torują drogę do kolejnych badań poświęconych możliwościom modyfikacji elektrod kompleksami

otrzymanymi z udziałem zasad Schiffa w kontekście ich późniejszego zastosowania w czujnikach do ilościowej i jakościowej analizy neuroprzekaźników.

3.4. Publikacja nr 4 (P4): "The effect of ionic versus covalent functionalization of Polyoxometalate hybrid materials with coordinating subunits on their stability and interaction with DNA" – Dalton Transactions, 2024, 53, 11678-11688.

Publikacja P4 opisuje syntezę i charakterystykę strukturalno-spektroskopową nowych nieorganiczno-organicznych materiałów hybrydowych **H1** – **H3** otrzymanych na drodze reakcji między ligandem zawierającym rdzeń terpirydynowy z grupą estrową **L5** [$C_{20}H_{19}N_3O_2$] w obecności soli cynku bądź jego związkami kompleksowymi **K9** [$Zn(L5)Cl_2$] lub **K10** [$Zn(L5)_2](ClO_4)$, a polioksometalanem typu Wellsa-Dawsona **WD-POM** sfunkcjonalizowanym podjednostką organiczną R^3-NH_2. W pracy zaproponowano trzy różne metody syntezy materiałów hybrydowych, z których tylko jedna prowadziła do otrzymania pożądanych produktów (Rys. 36). Dla hybryd **H1** – **H3** przeprowadzono badania stabilności oraz zbadano ich oddziaływania z kwasem nukleinowym. Ponadto, w publikacji zbadano również jak typ funkcjonalizacji polioksometalanu, jonowy oraz kowalencyjny, wpływa na aktywność biologiczną. W tym celu przeprowadzono badania nie tylko dla opisanych w pracy materiałów hybrydowych **H1** – **H3**, ale również dla otrzymanych i opublikowanych wcześniej przez naszą grupę badawczą materiałów hybrydowych sfunkcjonalizowanych w sposób jonowy[149].

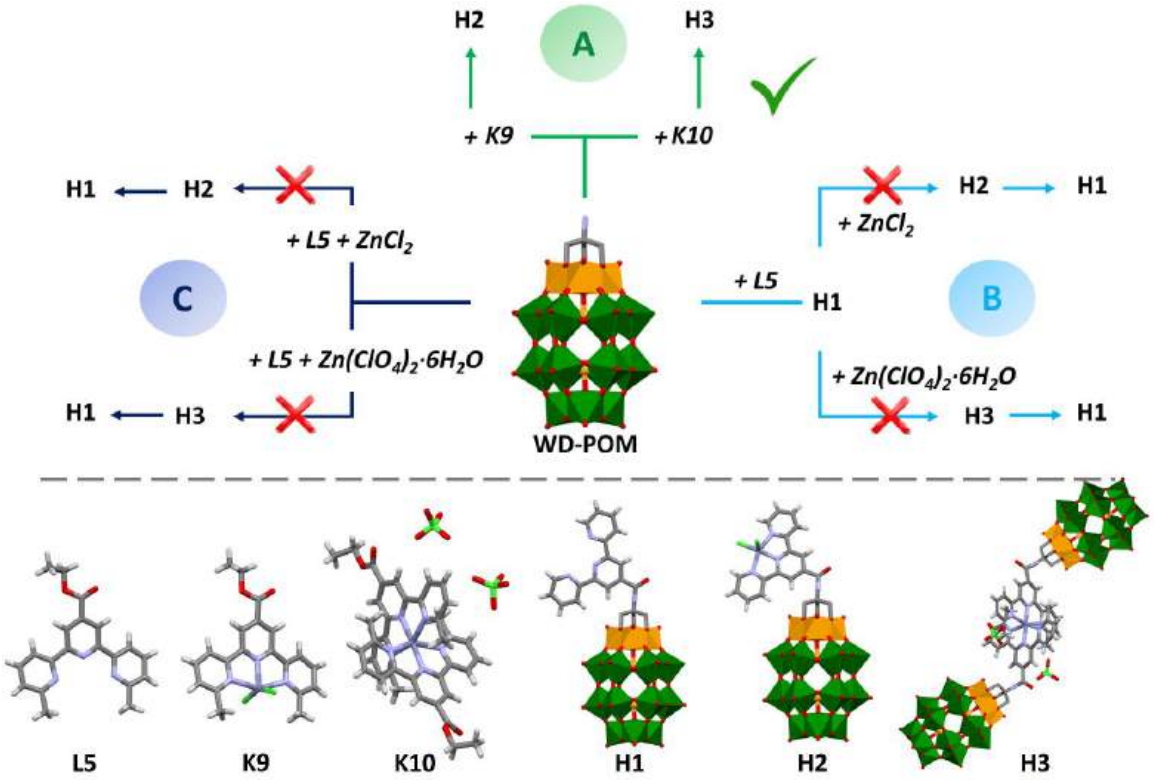

Rysunek 36. Graficzne zobrazowanie reakcji syntezy materiałów hybrydowych **H1** – **H3** trzema metodami A – C zachodzących między sfunkcjonalizowanym polioksometalanem Wellsa-Dawsona **WD-POM**, ligandem terpirydynowym **L5**, jego kompleksami **K9**, **K10** oraz solami Zn(II).

W ramach realizacji rozprawy doktorskiej połączono trzema różnymi drogami (A – C) ligand N,N,N-donorowy: 6,6''-dimetylo-[2,2':6',2''-terpirydyno]-4'-karboksylan etylu **L5** w obecności soli cynku $ZnCl_2$ lub $Zn(ClO_4)_2 \cdot 6H_2O$ bądź jego kompleksy z jonami Zn(II): **K9** oraz **K10** oraz polioksometalan typu Wellsa-Dawsona sfunkcjonalizowany za pomocą tris(hydroksymetylo)aminometanu **WD-POM** $(TBA)_4H_2[H_2NC(CH_2O)_3P_2V_3W_{15}O_{59}] \cdot 3C_3H_7NO$ w rezultacie otrzymując materiały hybrydowe **H1** – **H3**.

Ligand **L5**[150] oraz wszystkie etapy syntezy polioksometalanu **WD-POM**[151-153] zsyntezowano zgodnie z wcześniej opracowaną procedurą syntetyczną. Prekursory: ligand **L5**, kompleksy: **K9** i **K10**, sole cynku: $ZnCl_2$ i $Zn(ClO_4)_2 \cdot 6H_2O$ oraz **WD-POM** wykorzystano do syntezy materiałów hybrydowych różnymi metodami A – C, otrzymując trzy odrębne rodziny hybryd.

Do pierwszej z nich – A – wlicza się związki **H1**, **H2** oraz **H3**, które otrzymano w wyniku bezpośredniej reakcji **WD-POM** z ligandem **L5** lub jego kompleksami **K9** i **K10**, tworząc kolejno materiały hybrydowe **H1**, **H2** i **H3**. Każdą z reakcji prowadzono w acetonitrylu pod refluksem przez 72 (w przypadku **H1**) lub 24 godziny (w przypadku **H2** oraz **H3**) w stosunku molowym WD-POM : ligand/kompleks dla **H1** i **H2** równym 1:1, a dla **H3** wynoszącym 2:1. Wydajności otrzymanych produktów były równe: 78,0 % (**H1**), 87,6% (**H2**), 71,7% (**H3**). Wizualnym potwierdzeniem pomyślnego zajścia reakcji i otrzymania hybrydy **H1** była zmiana zabarwienia z brązowo-pomarańczowego na żółto-zielony. W przypadku pozostałych dwóch związków, barwa nie uległa zmianie, a dokładny skład każdej otrzymanej hybrydy, gdzie ujemny ładunek post-funkcjonalizowanego polioksometalanu był równoważony anionami tetrabutyloamoniowymi (TBA), określono z wykorzystaniem następujących metod: ESI-MS, analizy elementarnej, FT-IR, ^{1}H NMR oraz ^{31}P NMR. Na poniższym rysunku 37 przedstawiono porównanie charakterystyki hybryd **H1**, **H2** oraz **H3** na przykładzie wybranych analiz identyfikujących powstałe struktury.

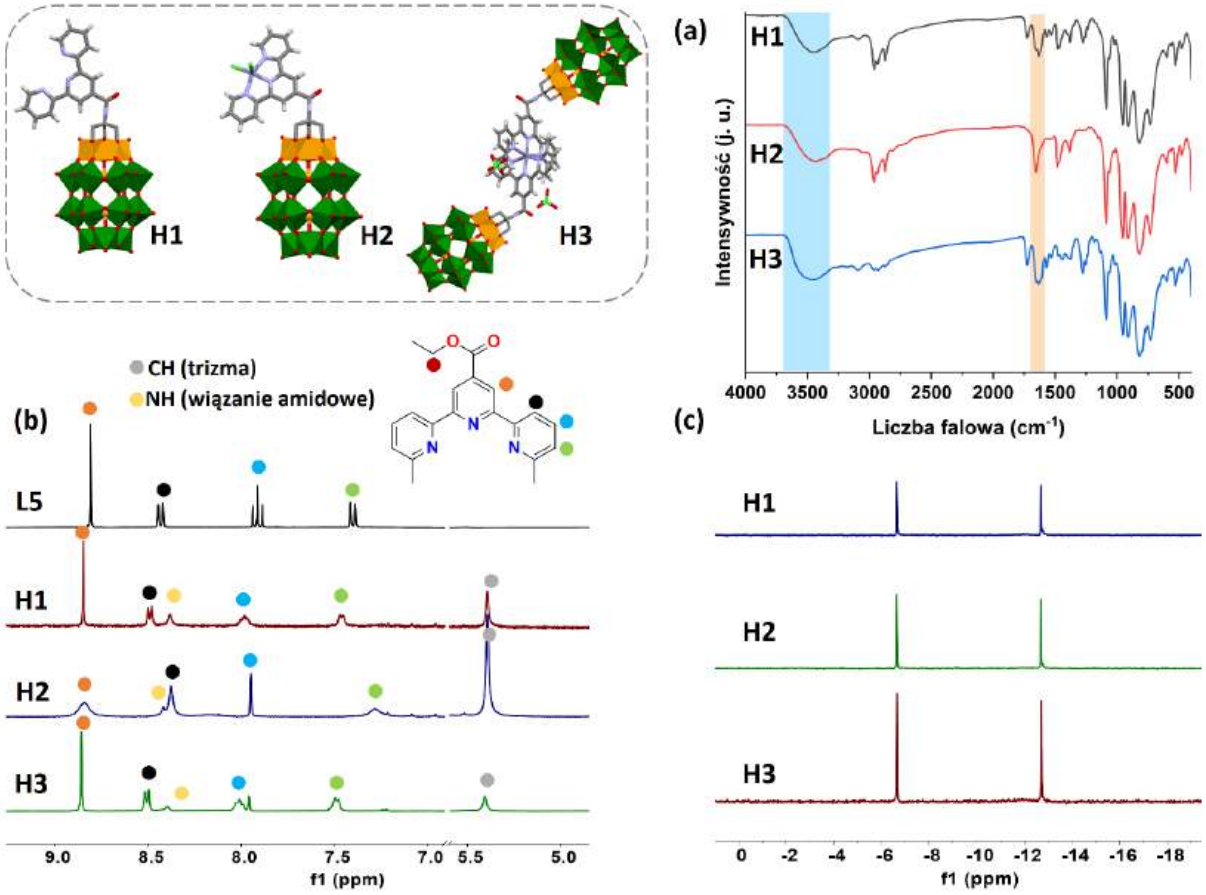

Rysunek 37. Porównanie widm (a) FT-IR, (b) ^{1}H NMR oraz (c) ^{31}P NMR otrzymanych materiałów hybrydowych **H1**, **H2** i **H3**.

Spektroskopia FT-IR (Rys. 37a) potwierdza tworzenie nowych materiałów hybrydowych **H4**, **H5**, **H6** wykazując przesunięcia pasm odpowiadające następującym grupom funkcyjnym: N-H w zakresie 3465-3430 cm^{-1} oraz C=O w zakresie 1645-1625 cm^{-1}. Kolejno, na przedstawionym widmie ^{1}H NMR (Rys. 37b) otrzymanie hybryd identyfikują przesunięcia sygnałów w zakresie aromatycznym wynikające z powstawania wiązania amidowego pomiędzy dwoma substratami **WD-POM** z grupą aminową jako kotwicą do dalszej funkcjonalizacji oraz ligandem bądź jego kompleksami zawierającymi w swojej strukturze grupą estrową. Dodatkowo na widmach produktów (zakres alifatyczny) zaobserwowano zanik sygnału od protonów grupy estrowej z szkieletu liganda, co również dowodzi utworzenia hybryd. Ponadto, potwierdzeniem zachowania integralności strukturalnej podjednostki polioksometalanu są widma ^{31}P NMR (Rys. 37c), o czym świadczy obecność dwóch sygnałów przy -6.65 ppm oraz -12.70 ppm. Po zanalizowaniu wszystkich wyników można przedstawić

wzory sumaryczne otrzymanych hybryd: **H1** – [WD-POM+L5]TBA_6, **H2** – [Zn(WD-POM+L5)Cl_2]TBA_6 oraz **H3** – [Zn(WD-POM+L5)$_2$(ClO_4)$_2$]$TBA_{(12-x)}H_x$; X=11.5.

W kolejnym etapie sprawdzono czy synteza prowadzona metodą B również pozwoli na otrzymanie pożądanych produktów reakcji. W celu weryfikacji przeprowadzono dwie reakcje polegające na zmieszaniu dwóch odczynników: otrzymanej wcześniej hybrydy **H1** z solą $ZnCl_2$ (stosunek molowy: 1:1) lub z solą $Zn(ClO_4)_2 \cdot 6H_2O$ (stosunek molowy: 2:1). W przypadku obu reakcji, odpowiednie ilości substratów umieszczono w kolbie okrągłodennej, dodano acetonitryl, mieszano przez 24 godziny pod refluksem. Po wytrąceniu osadów i ich wysuszeniu określono wydajności powstałych produktów, dla reakcji z $ZnCl_2$ równą 43,9 %, a dla reakcji z $Zn(ClO_4)_2 \cdot 6H_2O$ 98,7%. Planując te dwie reakcje oczekiwano, że efektem końcowym będą odpowiednio analogi materiałów hybrydowych **H2** oraz **H3**. Jednakże, po scharakteryzowaniu obu hybryd (ESI-MS, analiza elementarna, FT-IR, ^{1}H NMR oraz ^{31}P NMR), analizy wskazały na zajście niespodziewanych przemian w strukturze związków, wskazując na brak koordynacji jonów Zn(II) w kieszeni trójdonorowej liganda terpirydynowego, w zamian prowadząc do częściowej (w przypadku reakcji z $ZnCl_2$) lub całkowitej (w przypadku reakcji z $Zn(ClO_4)_2 \cdot 6H_2O$) wymiany jonów tetrabutyloamoniowych na rzecz protonów. Co ciekawe, anionowa składowa hybrydy **H1**, czyli sfunkcjonalizowany polioksometalan związany kowalencyjnie z ligandem, pozostała nienaruszona, świadcząc o stabilności tego układu.

Ostatnia droga otrzymania hybryd – metoda C – polegała na zmieszaniu trzech komponentów jednocześnie. W celu otrzymania kolejnych dwóch hybryd, w dwóch kolbach okrągłodennych umieszczono **WD-POM**, ligand **L5** oraz sól cynku: $ZnCl_2$ lub $Zn(ClO_4)_2 \cdot 6H_2O$. Stosunek molowy poszczególnych substratów (WD-POM:ligand:sól Zn(II)) był równy 1:1:1 oraz 2:2:1, odpowiednio dla reakcji z $ZnCl_2$ oraz reakcji z $Zn(ClO_4)_2 \cdot 6H_2O$. Obie mieszaniny reakcyjne mieszano w acetonitrylu przez 24 godziny pod refluksem, a otrzymane wydajności wynosiły odpowiednio 36,4% (w przypadku reakcji z $ZnCl_2$) oraz 62,7% (w przypadku reakcji z $Zn(ClO_4)_2 \cdot 6H_2O$). Tak samo jak w przypadku metody B, spodziewano się otrzymać analogi hybryd **H2** oraz **H3**, jednak po przeanalizowaniu otrzymanych wyników analiz (ESI-MS, analiza elementarna, FT-IR, ^{1}H NMR oraz ^{31}P NMR) okazało się, że identycznie jak w przypadku metody B, jony cynku nie koordynują się z N,N,N-donorową kieszenią koordynacyjną liganda, a jony tetrabutyloamoniowe uległy w większości wymianie na protony. Co interesujące, w wyniku obu przeprowadzonych reakcji doszło do

post-funkcjonalizacji polioksometalanu cząsteczką liganda i powstania hybrydy **H1**, co stanowi kolejne potwierdzenie, że ten układ cechuje wysoka stabilność.

Przeprowadzone reakcje metodami B oraz C dowodzą, że do utworzenia hybryd zawierających skoordynowane jony Zn(II) konieczne jest zastosowanie wcześniej utworzonych kompleksów (jak w przypadku metody A). Ponadto, niezależnie od zastosowanej metody syntezy, potwierdzono stabilność układu stanowiącego ujemną składową hybrydy **H1**, zarówno trwałość utworzonego wiązania amidowego między komponentami, jak i integralność samej podjednostki polioksometalanu, czego dowodem są przedstawione poniżej wybrane widma ^{1}H NMR oraz ^{31}P NMR (Rys. 38).

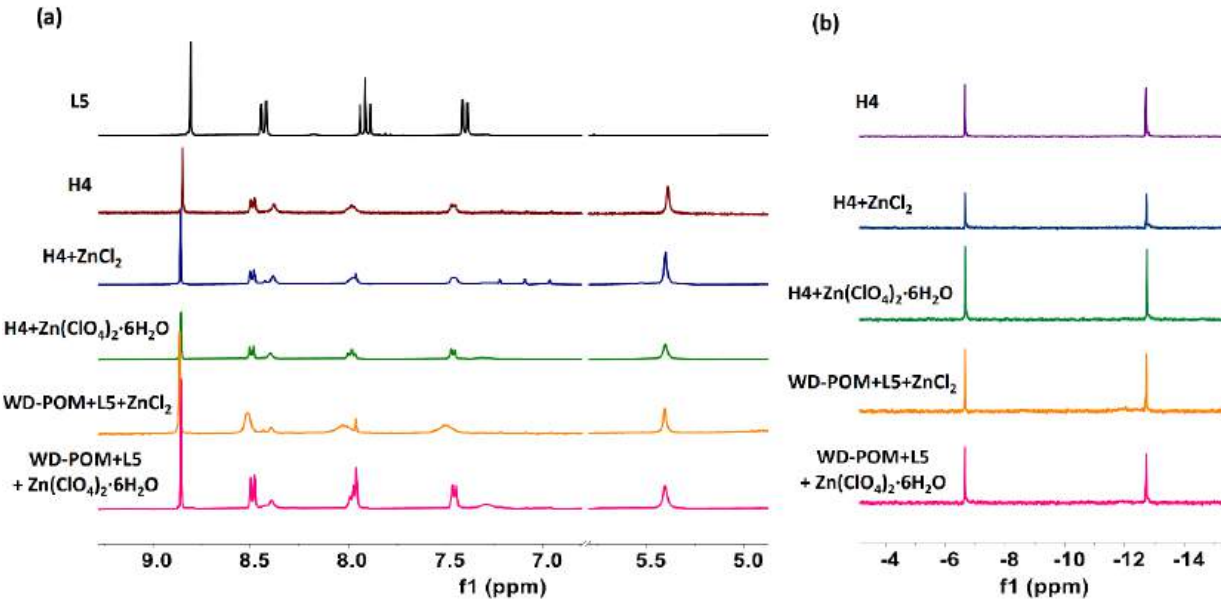

Rysunek 38. Porównanie widm (a) ^{1}H NMR oraz (b) ^{31}P NMR, liganda **L5** i hybrydy **H1** wraz z materiałami hybrydowymi otrzymanymi metodami B-C.

Dla wybranych materiałów hybrydowych **H1** – **H3** przeprowadzono badania stabilności oraz aktywności biologicznej, które kolejno porównano z badania przeprowadzonymi dla hybryd sfunkcjonalizowanych w sposób jonowy. Wyniki badań biologicznych przeprowadzonych przez dr Martę Fik-Jaskółkę wykazały, że hybrydy kowalencyjne w środowisku zasadowym ulegają hydrolizie prowadząc do uwolnienia liganda bądź kompleksu, a także do powolnego rozkładu jednostki polioksometalanowej. W przypadku jonowych hybryd również zaobserwowano częściową reorganizację materiałów w obecności DNA, jednak tym razem prowadzącą do uwolnienia liganda bądź kompleksów, ale przy jednoczesnym zachowaniu

integralności podjednostki polioksometalanu, świadcząc o jej stabilności. Co ciekawe, w badaniach biologicznych, ligand **L5** oraz jego kompleks **K10** wykazują wysoką stałą wiązania z DNA.

3.5. Publikacja nr 5 (P5): "Overview of Wells-Dawson Polyoxometalates: from structure and functionalization to application" – Coordination Chemistry Reviews, 2024, 519, 216091.

W publikacji P5 przedstawiono przegląd literatury obejmującej tematykę polioksometalanów typu Wellsa-Dawsona. W publikacji skupiono się na wykazaniu możliwości modyfikacji podstawowej podjednostki polioksometalanowej mogącej zachodzić w każdej jej części konstrukcyjnej poczynając od zmiany wewnętrznych dwóch atomów (heteroatomy), po zmiany podjednostek stanowiących zewnętrzną strukturę. W pracy również nie pominięto niekonwencjonalnych metod modyfikacji prowadzących do polioksometalanów Wellsa-Dawsona typu ang. *open* oraz *sandwich*. Ponadto, przedstawiono analizę specjacji polioksometalanów w roztworze w zależności od pH oraz oddziaływania jonowego pomiędzy ujemnie naładowanymi podjednostkami polioksometalanowymi a dodatnio naładowanymi przeciwjonami. Opisano również różne drogi funkcjonalizacji i post-funkcjonalizacji zmodyfikowanych podjednostek, które w konsekwencji przyczyniają się do ulepszenia ich właściwości fizykochemicznych mając ogromny wpływ na rozwój zastosowań w dziedzinach nauki związanych z energią, katalizą (foto- i elektrokataliza), medycyną (właściwości przeciwnowotworowe i przeciwbakteryjne) oraz jako inne materiały funkcjonalne, czujniki, materiały magnetyczne, elektrochromowe czy też optyczne.

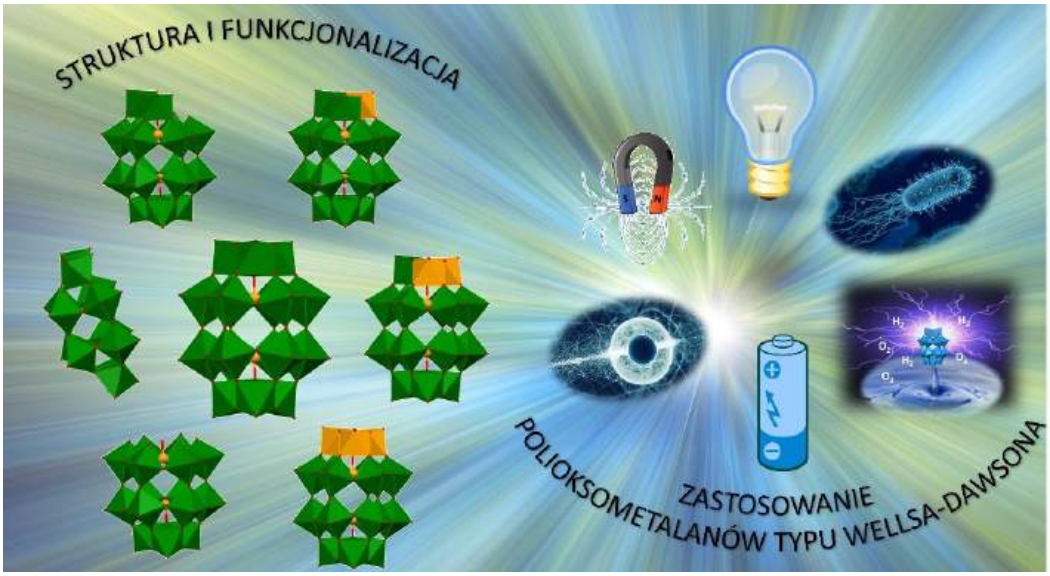

Rysunek 39. Graficzne streszczenie obrazujące najważniejsze aspekty publikacji nr 5.

Polioksometalany typu Wellsa-Dawsona są jednymi z najbardziej powszechnych typów polioksometalanów, które charakteryzują się wzorem ogólnym: $[X_2M_{18-n}Y_nO_{62}]^{n-}$, X = heteroatom (np. P, Si, S, As), M = metal przejściowy z początku bloku d (Mo, W, V), Y = inny metal (np. V, Cr, Sn, Co), n = 1, 2 lub 3[154-157]. Strukturę zewnętrzną polioksometalanów typu Wellsa-Dawsona można klasyfikować na dwie pozycje: górna i dolna część struktury to pokrywa (ang. *cap*), a środkowa to pas (ang. *belt*) (Rys. 40). Modyfikacja oryginalnej struktury poprzez włączenie innego jonu metalu w pozycji *cap* przyczynia się do tworzenia różnorodnych struktur oraz ułatwia funkcjonalizację[158-160]. Niemniej jednak modyfikacja pozycji *belt* jest również ważna, ponieważ prowadzi do powstania nieklasycznych struktur poliokosometalanów, takich jak struktura kanapkowa (ang. *sandwich*) oraz otwarta struktura kanapkowa (ang. *open*) polioksometalanu typu Wellsa-Dawsona[161-164].

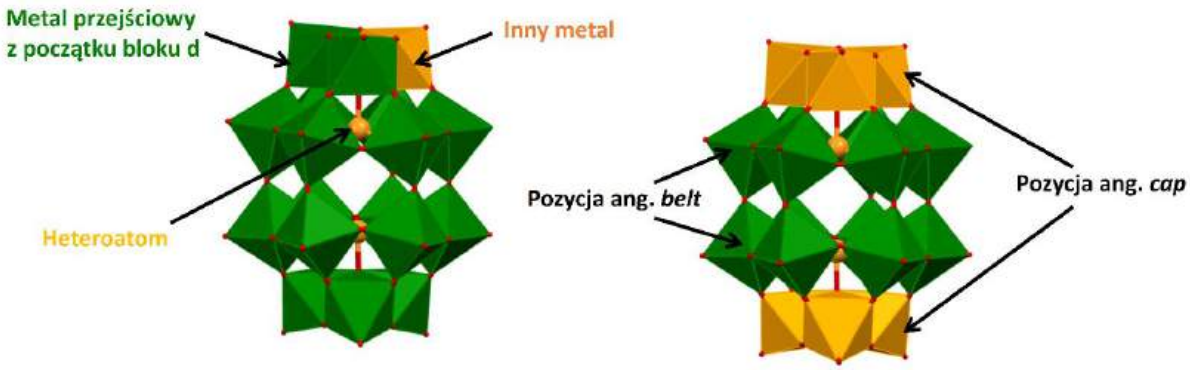

Rysunek 40. Schematyczne przedstawienie struktury polioksometalanu typu Wellsa-Dawsona z zaznaczonymi modyfikowalnymi grupami oraz pozycjami *cap* i *belt*.

Struktura polioksometalanu typu Wellsa-Dawsona w większości przypadków składa się z dwóch grup heteroatomów o wzorze ogólnym: $[XO_4]^{n-}$, np. $[PO_4]^{3-}$ [165, 166], $[AsO_4]^{3-}$ [167], $[SO_4]^{2-}$ [168], jednakże znane są także nieklasyczne typy nietetraedrycznych grup, takie jak: piramidalne $[XO_3]^{n-}$ ($[SO_3]^{2-}$ [169, 170], $[AsO_3]^{3-}$ [171], $[SbO_3]^{3-}$ [172], $[BiO_3]^{3-}$ [173], $[TeO_3]^{2-}$ [174], $[SeO_3]^{2-}$ [175]), ditetraedryczne $[P_2O_7]^{4-}$ [176], trygonalny-heksafluorosodan $[NaF_6]^{5-}$ [177, 178], trygonalny-pryzmatyczny $[WO_6]^{6-}$ [179] lub inne oktaedryczne $[XO_6]^{n-}$ ($[TeO_6]^{6-}$ [179], $[IO_6]^{5-}$ [180], $[SbO_6]^{7-}$ [181]). Wprowadzenie różnorodnych heteroatomów do wnętrza struktury zmienia właściwości fizykochemiczne[182] takie jak: rozpuszczalność, przewodnictwo, elastyczność funkcjonalizacji,

powierzchnia właściwa, degradacja i agregacja, dzięki czemu możliwe jest dostosowanie odpowiednich cech związków do ich dalszych zastosowań.

Kolejnym ważnym elementem strukturalnym są metale przejściowe z początku bloku d: Mo, W, V, Nb i Ta, które mają duże znaczenie dla reaktywności i rodzaju zastosowania[154, 183]. Szczególną cechą pierwszej grupy, polioksomolibdenianów, jest rozmiar i kształt. Ze względu na obecność bloków budulcowych złożonych z podjednostek $[Mo_2O_4]$ oraz $[(Mo)Mo_5]$ z centralnymi pięciokątnymi dwupiramidalnymi grupami $[MoO_7]$ w warunkach redukujących stanowią gigantyczne skupiska w kształcie kul[184]. Druga grupa, polioksowolframiany, występują jako prekursory lakunarne, które są stabilne i działają jako nieorganiczne ligandy, dzięki czemu mogą koordynować różne aktywne indywidua, co prowadzi do tworzenia różnorodnych struktur polioksometalanów[185]. Trzecia grupa, polioksowanadany, gwarantuje bogatą chemię redoks, a dzięki ich strukturze mogą powstawać szkielety metaliczno-organiczne[186]. Dwie ostatnie grupy to polioksoniobany i polioksotantalany, których chemia jest skomplikowana, charakteryzują się one neutralną naturą redoks, mają wysoką gęstość ładunku ujemnego, a ich zachowanie w warunkach wodnych dopiero zaczyna być badane[187].

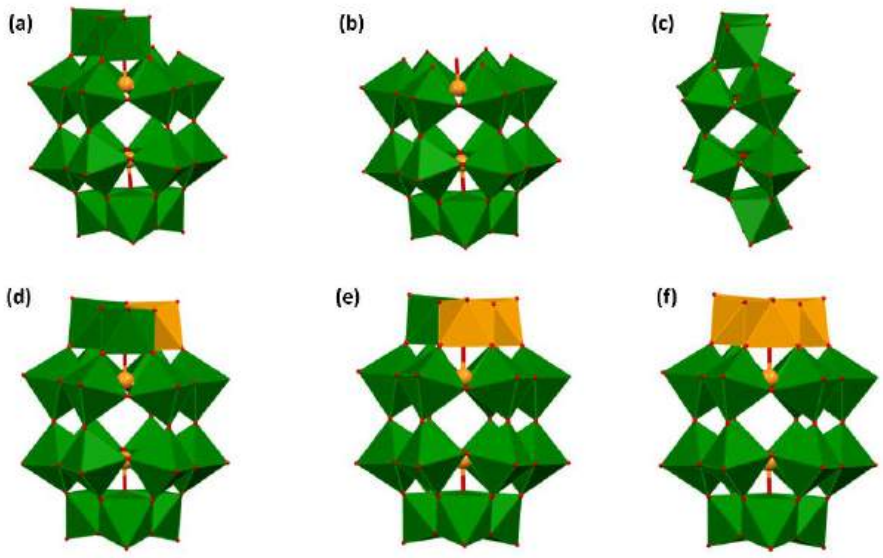

Rysunek 41. Rodzaje zmodyfikowanych struktur polioksometalanu typu Wellsa-Dawsona w sposób: (a) monolakunarny, (b) trilakunarny, (c) heksalakunarny, (d) jednopodstawiony, (e) dwupodstawiony, (f) trójpodstawiony.

Ostatni element strukturalny, wprowadzenie innego metalu, jest ściśle związany z modyfikacjami pozycji *cap* oraz *belt*, które są niezwykle ważne, gdyż umożliwiają proces dalszych funkcjonalizacji pozwalając na uzyskanie materiałów o określonych właściwościach. Należy podkreślić, że niezmodyfikowana podjednostka polioksometalanowa ma liczne ograniczenia, spośród których szczególnie istotna jest słaba stabilność chemiczna. Istnieje kilka możliwości modyfikacji struktur polioksometalanów typu Wellsa-Dawsona, w wyniku których można otrzymać: monolakunarny, trilakunarny, heksalakunarny, monopodstawiony, dwupodstawiony lub trójpodstawiony polioksometalan typu Wellsa-Dawsona (Rys. 41).

Jednym z najczęściej występujących typów modyfikacji jest zmiana w pozycji *cap*, w której struktura $[M_3P_2W_{15}O_{62}]^{n-}$, składa się z prekursora $[\alpha\text{-}P_2W_{15}O_{56}]^{12-}$ i trzech jonów metali przejściowych (M = V^V, Ta^V, Nb^V itd.)[188, 189]. Spośród wymienionych metali najpopularniejsza jest modyfikacja *cap* jonami wanadu, ponieważ poprawia właściwości fotochemiczne i elektrochemiczne, ale co najważniejsze, umożliwia selektywną modyfikację w pozycji *cap* za pomocą łączników, np. przy użyciu organicznych pochodnych tris-alkoholu lub innych grup organicznych[190-192]. Ponadto, obecność trzech jonów wanadu w strukturze polioksometalanu przyczynia się do wrażliwości na czynniki zewnętrzne, np. czynniki redukujące, pH i nukleofile[158] oraz sprawia, że zmodyfikowany w ten sposób polioksometalan staje się utleniaczem i zyskuje właściwości katalityczne[193, 194]. Oprócz dużego zainteresowania trójpodstawionymi polioksometalanami Wellsa-Dawsona wynikającego z możliwości manipulowania blokami budulcowymi, kontrolowania wielkości struktury i modulowania procesu funkcjonalizacji[195], znane są także jednopodstawione polioksometalany utworzone przez przyłączenie jonów metali o wysokiej sile kwasu Lewisa, np. Mn^{III}, Ni^{II}, Co^{II} [68, 157, 196] lub o wysokiej liczbie koordynacyjnej, np. Zr^{IV}, Sn^{IV}, Hf^{IV}, Ln^{III} [67, 68, 197, 198], z czego te ostatnie mogą występować w postaci monomerów lub dimerów, a także wpływać na wykazywane właściwości biologiczne modyfikowanych polioksometalanów[157, 197, 199].

Kolejny rodzaj modyfikacji jest związany z pozycją *belt*, która wzbudza mniejsze zainteresowanie wśród naukowców niż wspomniana powyżej modyfikacja pozycji *cap*, a polega na zastąpieniu metali Mo^{VI} i/lub W^{VI} najczęściej przez Cu^{II} [182], a rzadziej przez Mn^{III} sprawiając, że zmodyfikowany polioksometalan wykazuje lepsze właściwości fotokatalityczne[200]. W literaturze można zauważyć, że możliwe są również połączone

modyfikacje pozycji *cap* i *belt* w postaci heksalakunarnego polioksometalanu, którego połączenie z jonami metali przejściowych i metali alkalicznych zwykle prowadzi do utworzenia makrocyklicznego tetrameru[201], a rzadziej do dimeru[202], trimeru w kształcie litery U[203] bądź cyklicznego trimeru[204].

Jak wspomniano wyżej, modyfikacja pozycji *belt* prowadzi także do powstania niekonwencjonalnych struktur polioksometalanów typu Wellsa-Dawsona takich jak *open* lub *sandwich* (Rys. 42). Tworzenie tych pierwszych jest związane z integracją dwóch podjednostek polioksoanionowych typu Keggina $[\alpha\text{-}SiW_9O_{34}]^{10-}$ połączonych wiązaniami W-O-W[161]. W związkach zmodyfikowanych w ten sposób, powszechnie wprowadza się pięć atomów metali, które są paramagnetykami[162-164, 205], np. Mn^{II}, Fe^{III}, Co^{II}, Ni^{II}, Cu^{II}, Zn^{II}, Al^{III}, Ho^{III}, Gd^{III}, Ga^{III}, ale znane są modyfikacje, w których ich liczba jest równa dwa[206], trzy[161], cztery[207] lub więcej niż pięć[162]. Natomiast druga grupa, *sandwich*, może powstawać na pięć sposobów, z czego pierwsze cztery stanowią połączenia dwóch typów podjednostek: $[MW_9O_{34}]^{n-}$ lub $[MW_9O_{33}]^{n-}$ (M = Fe^{III}, Cu^{II}, Co^{II}, Zn^{II}, P^{V}, As^{III}, As^{V}, Si^{IV},Sb^{III}, Bi^{III}, Se^{IV} lub Te^{IV}), natomiast piąta modyfikacja polega na połączeniu dwóch podjednostek $[\alpha\text{-}X_2W_{15}O_{56}]^{12-}$ (X = As^{V} lub P^{V}) z potencjalną inkorporacją kationów metali przejściowych pomiędzy dwie podjednostki (M = Mn^{II}, Fe^{III}, Co^{II}, Ni^{II}, Cu^{II}, Zn^{II} i Cd^{II}), tworząc związki o wzorze $[M_4(H_2O)_2(P_2W_{15}O_{56})_2]^{n-}$ [208-212].

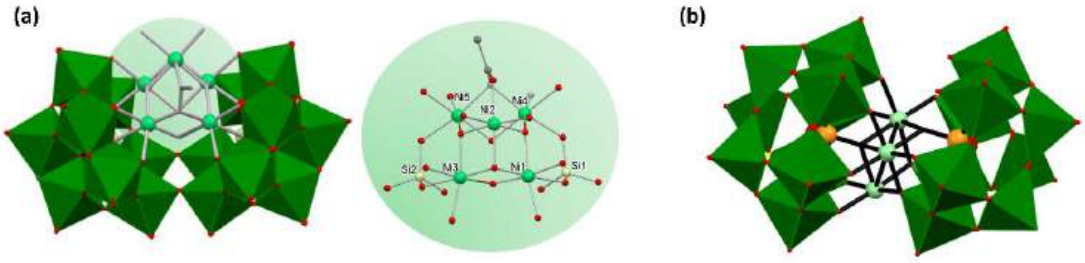

Rysunek 42. Przykłady niekonwencjonalnych struktur polioksometalanów Wellsa-Dawsona typu (a) *open* oraz (b) *sandwich*[63].

Publikacja P5 zawiera także zestawienie zachowania struktury polioksometalanu typu Wellsa-Dawsona w roztworach wodnych w zależności od pH (Rys. 43). Konwencjonalna podjednostka polioksometalanowa $[P^{V}_2W^{VI}_{18}O_{62}]^{6-}$ jest stabilna w środowisku kwaśnym przy pH niższym niż 6 i ulega degradacji przy wyższym pH tworząc monolakunarne

$[P^{V}_{2}W^{VI}_{17}O_{61}]^{10-}$, trilakunarne $[P^{V}_{2}W^{VI}_{15}O_{56}]^{12-}$ bądź heksalakunarne $[H_2P^{V}_{2}W^{VI}_{12}O_{48}]^{12-}$ podjednostki polioksometalanowe[213, 214]. Ponadto, wartość pH wpływa również na tworzenie się struktur funkcjonalizowanych i jest związana z częściowym lub całkowitym przekształceniem α-$[P_2W_{15}O_{56}]^{12-}$ w rzadko występujące α-$[P_2W_{16}O_{57}]^{8-}$ [215, 216]. Co ciekawe, utworzony przez polioksometalany heksalakunarne, makrocykliczny tetramer $[P_8W_{48}O_{184}]^{40-}$ jest stabilny przy niższym pH w zakresie od 1 do 8 [213, 214].

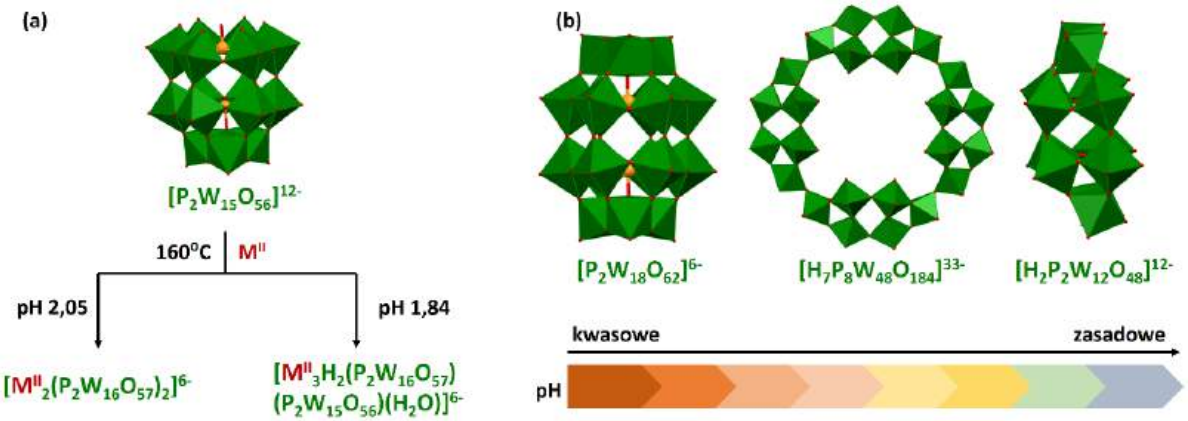

Rysunek 43. Schemat (a) przekształcenia *in situ* podjednostki α-$[P_2W_{15}O_{56}]^{12-}$ w rzadko występujące podjednostki α-$[P_2W_{16}O_{57}]^{8-}$ (M^{II} = jon metalu przejściowego); (b) hydrolitycznego przekształcenia $[P^{V}_{2}W^{VI}_{18}O_{62}]^{6-}$ wraz ze wzrostem wartości pH[63].

Polioksometalany typu Wellsa-Dawsona za pośrednictwem wiązań kowalencyjnych, jonowych, wodorowych lub koordynacyjnych mogą łączyć się ze związkami organicznymi i/lub ligandami tworząc materiały hybrydowe[59, 217-222]. Kolejno, takie układy mogą być poddane dalszej funkcjonalizacji prowadzącej do utworzenia bardziej złożonych materiałów. Niekończące się możliwości funkcjonalizacji skłoniły do otrzymania hybryd przy użyciu kolejnych grup organicznych takich jak: grupy amidowe, sulfonamidowe, estrowe i tioestrowe, oraz stosując następujące reakcje: sprzęganie Huisgena, Sonogashiry, Suzuki czy polimeryzację[59]. Funkcjonalizację można podzielić na dwie główne grupy: pojedynczą oraz podwójną. Spośród pierwszej z nich, można wyróżnić modyfikacje typu: monolakunarnego oraz trilakunarnego (Rys. 44).

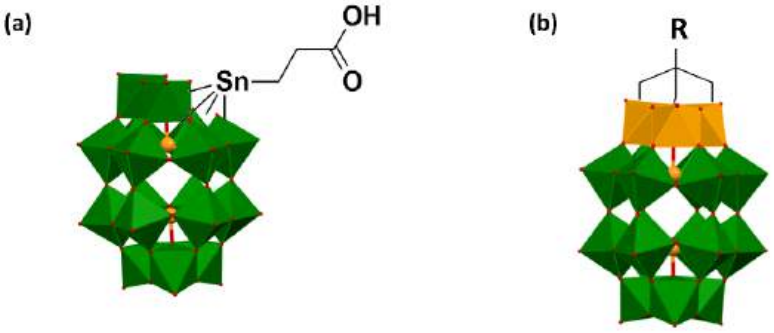

Rysunek 44. Przykłady materiałów hybrydowych bazujących na polioksometalanach typu Wellsa-Dawsona otrzymane w wyniku pojedynczej funkcjonalizacji w sposób (a) monolakunarny oraz (b) trilakunarny.

Pojedyncza modyfikacja w sposób monolakunarny umożliwia funkcjonalizację podjednostki polioksometalanowej grupą organocynową, krzemoorganiczną czy też fosforoorganiczną[61, 219, 220]. Co ciekawe, w literaturze potwierdzono przypadki tworzenia w ten sposób polimerów zawierających podjednostki polioksometalanowe[223]. Najbardziej rozpowszechniona jest jednak pojedyncza modyfikacja typu trilakunarnego. Jak już wspomniano wyżej, największym zainteresowaniem cieszą się podstawienia trzech jonów wanadu w pozycji *cap* ze względu na łatwą modulację struktury i rozszerzone właściwości[193, 224]. Obecność tego podstawnika poprawia właściwości utleniające, zapewniając w ten sposób więcej możliwości w zastosowaniach biologicznych[219] i katalitycznych[193]. Trójpodstawiony polioksometalan może być funkcjonalizowany wieloma grupami organicznymi, z których najbardziej powszechna jest grupa tris(hydroksymetylowa), tworząc materiały, które mogą być stosowane jako bloki budulcowe prowadzące do tworzenia bardziej złożonych hybryd w wyniku dalszej funkcjonalizacji [219, 220, 225-228].

Podwójna modyfikacja polioksometalanów wiąże się z wprowadzeniem grup organicznych w dwóch różnych miejscach w trzy możliwe sposoby: zgięty, liniowy lub asymetryczny (Rys. 45).

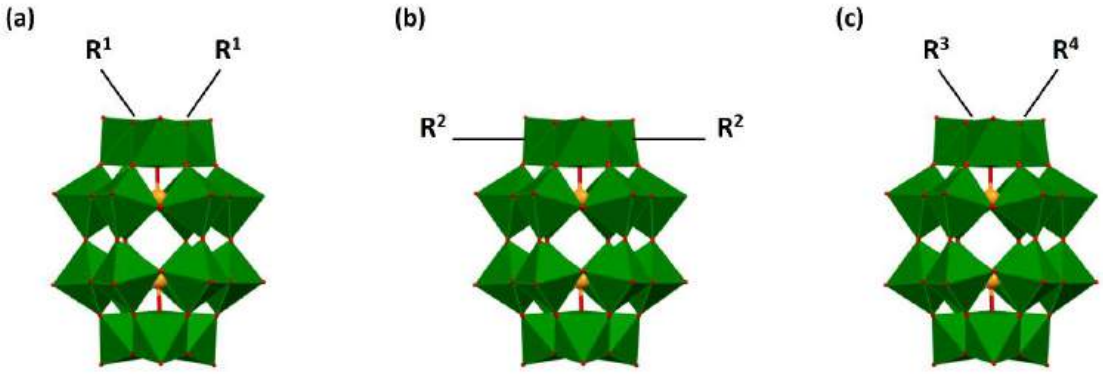

Rysunek 45. Schematyczne przedstawienie przykładowych materiałów hybrydowych bazujących na polioksometalanach typu Wellsa-Dawsona otrzymanych w wyniku podwójnej funkcjonalizacji w sposób (a) zgięty (b) liniowy oraz (c) asymetryczny.

Otrzymanie podwójnie zmodyfikowanego układu w sposób zgięty (Rys. 45a) jest możliwe np. poprzez reakcję sprzęgania Sonagashira, najczęściej stosowaną w post-funkcjonalizacji tego typu, ponieważ zapewnia sztywne połączenie między polioksometalanem a grupą organiczną z centrami fotoaktywnymi[229, 230]. Badania przedstawione w literaturze potwierdzają zwiększoną fotoaktywność układów dzięki sfunkcjonalizowaniu fotoaktywnych związków organicznych polioksometalanami przedstawioną metodą[231]. Modyfikacja w sposób liniowy (Rys. 45b) jest osiągalna także z udziałem reakcji sprzęgania z grupami organicznymi[232] natomiast większe trudności napotyka się w przypadku modyfikacji asymetrycznej (Rys. 45c), która stanowi wyzwanie syntetyczne. Uzyskanie sfunkcjonalizowanych asymetrycznych materiałów hybrydowych jest możliwe poprzez otrzymanie najpierw mieszaniny produktów symetrycznych i asymetrycznych, a następnie oczyszczanie w wyniku wielokrotnego dodania innego rozpuszczalnika, wirowanie i filtrację w celu oddzielenia składników mieszaniny. Mimo trudności, ten rodzaj funkcjonalizacji jest pożądany, ponieważ oferuje większe możliwości kontroli funkcji i aktywności fizykochemicznej układów, co prowadzi do specyficznych i ściśle zdefiniowanych zastosowań[79].

Biorąc pod uwagę dotychczasowe badania przedstawione w przeglądzie składającym się z 421 pozycji literaturowych, wskazano i zebrano razem główne ścieżki rozwoju i zainteresowania naukowców w postaci map bibliometrycznych oraz wymieniono możliwe trudności i ograniczenia, które mogą się pojawić przy pracy z tymi układami. Przygotowane

nowe zestawienie (poprzednie w roku 2003) kompleksowo opisujące polioksometalany typu Wellsa-Dawsona oraz prestiż czasopisma, w których zostało opublikowane, ze znacznym prawdopodobieństwem może mieć obiecujący wpływ na wzrost zainteresowania tymi wielozadaniowymi układami.

Ostatnia publikacja z cyklu stanowi powiązanie ze sobą układów supramolekularnych będących tematem rozprawy doktorskiej, gdzie polioksometalany, dzięki możliwości funkcjonalizacji za pomocą ligandów bądź też kompleksów mogą spełniać rolę układów wielozadaniowych mających zastosowania w wielu dziedzinach nauki.

4. Wnioski

Celem naukowym niniejszej rozprawy doktorskiej było zaprojektowanie, synteza oraz charakterystyka strukturalno-spektroskopowa nowych architektur supramolekularnych jonów metali *d*-elektronowych, polioksometalanów i materiałów hybrydowych oraz zbadanie ich właściwości biomimetycznych i elektrochemicznych z uwzględnieniem wpływu szkieletu organicznego liganda, aldehydu, jonu metalu, przeciwjonu, rozpuszczalnika, temperatury oraz stosunku molowego na multifunkcjonalność układów.

Najważniejsze osiągnięcia oraz wnioski wynikające z przeprowadzonych badań naukowych w ramach niniejszej rozprawy doktorskiej są następujące:

- Przeprowadzono po raz pierwszy reakcję oksydacyjnej *O*-demetylacji w łagodnych warunkach na związkach kompleksowych Cu(II) opartych na organicznym szkielecie liganda iminowego w obecności anionów chloranowych(VII), tlenu cząsteczkowego i wody. Dzięki przeprowadzonej optymalizacji reakcji oksydacyjnej *O*-demetylacji, określono wpływ czynników (rodzaj szkieletu liganda, metody syntezy, typu dodanej soli oraz wybór rozpuszczalnika) na powodzenie przeprowadzenia tego procesu, umożliwiając dobór najlepszych parametrów procedury syntetycznej. Obecność dodatkowych podstawników metoksylowych w najbliższym sąsiedztwie grupy demetylowanej, okazała się kluczowa dla *O*-demetylacji. Rezultaty tych badań otwierają drogę do łatwiejszego oraz przyjaźniejszego środowisku syntezowania biomimetyków pełniących rolę demetylaz.
- Za pomocą kompleksów Cu(II) z wykorzystaniem metody woltamperometrii cyklicznej oraz w wyniku utworzenia samoorganizującej się monowarstwy zmodyfikowano powierzchnię elektrod złotych. Przeprowadzone badania wykazały, że otrzymane układy można z powodzeniem wykorzystać jako materiały przewodzące w czujnikach elektrochemicznych do jakościowych i ilościowych oznaczeń neuroprzekaźników (dopaminy i epinefryny) bez interferencji związków zakłócających w warunkach zbliżonych do fizjologicznych przy niskich granicach wykrywalności i oznaczalności, a zarazem wysokiej stabilności i odtwarzalności. Otrzymane układy mogą zostać potencjalnie zastosowane jako medyczne sondy diagnostyczne w badaniach *in vitro*.

- Przeprowadzono proces optymalizacji mający na celu określenie wpływu trzech różnych metod syntetycznych na otrzymanie materiałów hybrydowych opartych na polioksometalanie typu Wellsa-Dawsona o określonej strukturze. Przy zastosowaniu każdej z metod otrzymano sfunkcjonalizowany związek, jednak tylko w przypadku jednej z nich otrzymano przykłady sfunkcjonalizowanych polioksometalanów ligandem organicznym dodatkowo koordynujących jony cynku(II). Sfunkcjonalizowane układy powstały w wyniku utworzenia wiązania kowalencyjnego miedzy grupą estrową liganda a grupą aminową polioksometalanu. Efekty przeprowadzonych badań wskazują na potencjalne zastosowanie polioksometalanów typu Wellsa-Dawsona jako układów służących do wprowadzania cząsteczek.
- Opracowano przegląd literatury dotyczący polioksometalanów typu Wellsa-Dawsona, opisu ich struktury, możliwości modyfikacji podstawowej podjednostki, funkcjonalizacji oraz zastosowania w wielu dziedzinach nauki między innymi w: medycynie, katalizie, elektrochemii oraz wielu innych gałęziach chemii. Mimo, iż to osiągnięcie nie jest wynikiem pracy eksperymentalnej jest bardzo ważne, gdyż stanowi ważny punkt wyjścia do dalszego racjonalnego projektowania struktur oraz syntezy układów hybrydowych z przeznaczeniem do określonych zastosowań.

5. Literatura

1. J.-M. Lehn, *Angew. Chem., Int. Ed. Engl.*, 1990, **29**, 1304-1319.
2. F. Huang and E. V. Anslyn, *Chem. Rev.*, 2015, **115**, 6999-7000.
3. B. Weber, in *Coordination Chemistry: Basics and Current Trends*, Springer, 2023, pp. 121-138.
4. J. W. Steed, D. R. Turner and K. J. Wallace, *Core concepts in supramolecular chemistry and nanochemistry*, John Wiley & Sons, 2007.
5. J. W. Steed and J. L. Atwood, *Supramolecular chemistry*, John Wiley & Sons, 2022.
6. V. Balzani and L. De Cola, *Supramolecular chemistry*, Springer Science & Business Media, 2012.
7. P. Beer, P. D. Beer, T. A. Barendt and J. Y. Lim, *Supramolecular Chemistry: Fundamentals and Applications*, Oxford university press, 2022.
8. J. Li, *Supramolecular chemistry of biomimetic systems*, Springer, 2017.
9. S. Aggarwal and S. Ikram, *Biotechnol. Bioeng.*, 2023, **120**, 352-398.
10. C. Wu, J. Chen, W. Nam and B. Wang, *Coord. Chem. Rev.*, 2025, **528**, 216429.
11. Y. Liu and Z.-G. Wang, *ACS nano*, 2023, **17**, 13000-13016.
12. R. Hein, P. D. Beer and J. J. Davis, *Chem. Rev.*, 2020, **120**, 1888-1935.
13. A. N. Davis, K. Parui, M. M. Butala and A. M. Evans, *Nanoscale*, 2024, **16**, 10142-10154.
14. M. M. Hasan, T. Islam, S. S. Shah, A. Awal, M. A. Aziz and A. S. Ahammad, *Chem. Rec.*, 2022, **22**, e202200041.
15. S. Halder and C. Chakraborty, *Nano Energy*, 2024, 110243.
16. W. Xu and A. Chen, *Aggregate*, 2024, **5**, e581.
17. N. Karmakar, P. Saha, R. A. Shital, S. A. Nayem, A. Awal, M. D. Hossain and A. S. Ahammad, *J. Electrochem. Soc.*, 2025.
18. R. Li, J. Li, Q. Liu, T. Li, D. Lan and Y. Ma, *ACHM*, 2025, **8**, 86.
19. P. Dubey, V. Shrivastav, T. Boruah, G. Zoppellaro, R. Zbořil, A. Bakandritsos and S. Sundriyal, *Adv. Energy Mater.*, 2024, **14**, 2400521.
20. M. F. Iqbal, F. Nasir, F. Shabbir, Z. U. D. Babar, M. F. Saleem, K. Ullah, N. Sun and F. Ali, *Adv. Energ. Sust. Res.*, 2025, 2400412.
21. P. W. van Leeuwen and M. Raynal, *Supramolecular catalysis: new directions and developments*, John Wiley & Sons, 2022.
22. P. Verma, J. Van Maarseveen and R. N. Shiju, *Chem. Commun.*, 2025.
23. G. Olivo, G. Capocasa, D. Del Giudice, O. Lanzalunga and S. Di Stefano, *Chem. Soc. Rev.*, 2021, **50**, 7681-7724.
24. D. Bokotial, K. Acharyya, A. Chowdhury and P. S. Mukherjee, *Angew. Chem. Int. Ed.*, 2024, **63**, e202401136.
25. J. Ning, W. Chen, Q. Niu, L. Li and Y. Yu, *ChemSusChem*, 2024, **17**, e202301963.
26. M. Komiyama, *Research*, 2024, **7**, 0466.
27. N. P. Dharmarajan, D. Vidyasagar, J. H. Yang, S. N. Talapaneni, J. Lee, K. Ramadass, G. Singh, M. Fawaz, P. Kumar and A. Vinu, *Adv. Mater.*, 2024, **36**, 2306895.
28. J. G. O'Connell-Danes, B. T. Ngwenya, C. A. Morrison and J. B. Love, *Angew. Chem. Int. Ed.*, 2024, **63**, e202409834.
29. A. Barba-Bon, M. Nilam and A. Hennig, *ChemBioChem*, 2020, **21**, 886-910.
30. Y. Li, C. Shao, Z. Pei and Y. Pei, *Green Chem.*, 2025.

31. S. Maity, V. K. Deb, S. Mondal, A. Chakraborty, K. Pramanick and S. Adhikari, *BioFactors*, 2025, **51**, e70005.
32. P. L. Scognamiglio, C. Platella, E. Napolitano, D. Musumeci and G. N. Roviello, *Molecules*, 2021, **26**, 3558.
33. B. Z. Momeni and A. S. Abd-El-Aziz, *Coord. Chem. Rev.*, 2023, **486**, 215113.
34. Y. Liu, L. Wang, L. Zhao, Y. Zhang, Z.-T. Li and F. Huang, *Chem. Soc. Rev.*, 2024, **53**, 1592-1623.
35. S. Datta, H. Itabashi, T. Saito and S. Yagai, *Nat. Chem.*, 2025, 1-16.
36. Y. Fu, L. Zhang, X. Yan and K. Liu, *ChemSystemsChem*, 2025, **7**, e202400068.
37. M. Shabbir, A. Atiq, J. Wang, M. Atiq, N. Saeed, I. Yildiz, X. Yan, R. Xing and M. Abbas, *Aggregate*, 2025, **6**, e672.
38. M. Yan, S. Wu, Y. Wang, M. Liang, M. Wang, W. Hu, G. Yu, Z. Mao, F. Huang and J. Zhou, *Adv. Mater.*, 2024, **36**, 2304249.
39. J. Zhou, L. Rao, G. Yu, T. R. Cook, X. Chen and F. Huang, *Chem. Soc. Rev.*, 2021, **50**, 2839-2891.
40. S. Shukla, B. Sagar, A. K. Sood, A. Gaur, S. Batra and S. Gulati, *ACS Appl. Bio Mater.*, 2023, **6**, 2089-2101.
41. M. Kumar, A. K. Singh, A. K. Singh, R. K. Yadav, S. Singh, A. P. Singh and A. Chauhan, *Coord. Chem. Rev.*, 2023, **488**, 215176.
42. S. Talreja and S. Tiwari, *J. Pharm. Pharmacol. Res*, 2023, **7**, 133-139.
43. C. Boulechfar, H. Ferkous, A. Delimi, A. Djedouani, A. Kahlouche, A. Boublia, A. S. Darwish, T. Lemaoui, R. Verma and Y. Benguerba, *Inorg. Chem. Commun.*, 2023, **150**, 110451.
44. A. Podolski-Renić, A. Č. Gašparović, A. Valente, O. Lopez, J. H. B. Nunes, C. R. Kowol, P. Heffeter and N. R. Filipović, *Eur. J. Inorg. Chem.*, 2024, 116363.
45. K. Debsharma, S. Dey, S. Dey and C. Sinha, *Inorg. Chem. Front.*, 2026, DOI: 10.1039/D5QI02060C.
46. M. Stuckart and K. Y. Monakhov, *Chem. Sci.*, 2019, **10**, 4364-4376.
47. Y. Gao, M. Choudhari, G. K. Such and C. Ritchie, *Chem. Sci.*, 2022, **13**, 2510-2527.
48. K. Rurack and R. Martínez-Máñez, *The supramolecular chemistry of organic-inorganic hybrid materials*, John Wiley & Sons, 2010.
49. A. B. Descalzo, R. Martínez-Máñez, F. Sancenón, K. Hoffmann and K. Rurack, *Angew. Chem. Int. Ed.*, 2006, **45**, 5924-5948.
50. A. Ebrahimi, L. Krivosudský, S. Khodabakhshi, M. Khaleghiabbasabadi, M. Sadeghi and M. Motola, *Coord. Chem. Rev.*, 2026, **548**, 217201.
51. J. L. Algar and D. Preston, *Chem. Commun.*, 2022, **58**, 11637-11648.
52. V. Patroniak, Paul N. W. Baxter, J.-M. Lehn, M. Kubicki, M. Nissinen and K. Rissanen, *Eur. J. Inorg. Chem.*, 2003, **2003**, 4001-4009.
53. S. Schlamp, P. Thoma, T. Bauer, R. Kempe and B. Weber, *ZAAC*, 2013, **639**, 1763-1767.
54. W.-Y. Zhang, Y.-J. Lin, Y.-F. Han and G.-X. Jin, *J. Am. Chem. Soc.*, 2016, **138**, 10700-10707.
55. A. Santoro, J. Holub, M. A. Fik-Jaskółka, G. Vantomme and J.-M. Lehn, *Chem. Eur. J.*, 2020, **26**, 15664-15671.
56. M. Cirulli, A. Kaur, J. E. M. Lewis, Z. Zhang, J. A. Kitchen, S. M. Goldup and M. M. Roessler, *J. Am. Chem. Soc.*, 2019, **141**, 879-889.

57. M. A. Fik-Jaskółka, I. Pospieszna-Markiewicz, G. N. Roviello, M. Kubicki, W. Radecka-Paryzek and V. Patroniak, *Inorg. Chem.*, 2021, **60**, 2122-2126.
58. N. I. Gumerova and A. Rompel, *Nat. Rev. Chem.*, 2018, **2**, 0112.
59. A. V. Anyushin, A. Kondinski and T. N. Parac-Vogt, *Chem. Soc. Rev.*, 2020, **49**, 382-432.
60. M. Aureliano, N. I. Gumerova, G. Sciortino, E. Garribba, C. C. McLauchlan, A. Rompel and D. C. Crans, *Coord. Chem. Rev.*, 2022, **454**, 214344.
61. J. M. Cameron, G. Guillemot, T. Galambos, S. S. Amin, E. Hampson, K. Mall Haidaraly, G. N. Newton and G. Izzet, *Chem. Soc. Rev.*, 2022, **51**, 293-328.
62. X.-K. Lian, H.-B. Chen, Y.-D. Lin, X.-X. Li and S.-T. Zheng, *Coord. Chem. Rev.*, 2023, **497**, 215440.
63. D. Nowicka, N. Vadra, E. Wieczorek-Szweda, V. Patroniak and A. Gorczyński, *Coord. Chem. Rev.*, 2024, **519**, 216091.
64. X. Xu, Y. Guo, B. Li, Y. Lv, Z. Wu, S. Liang, L. He and Y.-F. Song, *Coord. Chem. Rev.*, 2025, **522**, 216210.
65. G. Yang, Y. Liu and Y. Wei, *Coord. Chem. Rev.*, 2024, **521**, 216172.
66. I. Christodoulou, A. Vallée, L. Blayac, B. Malemo, M. Jeleff, S. Boujday, P. Mialane and A. Dolbecq, *Coord. Chem. Rev.*, 2026, **548**, 217226.
67. J. Rieger, T. Antoun, S.-H. Lee, M. Chenal, G. Pembouong, J. Lesage de la Haye, I. Azcarate, B. Hasenknopf and E. Lacôte, *Chem. Eur. J.*, 2012, **18**, 3355-3361.
68. L. Vandebroek, Y. Mampaey, S. Antonyuk, L. Van Meervelt and T. N. Parac-Vogt, *Eur. J. Inorg. Chem.*, 2019, **2019**, 506-511.
69. N. I. Gumerova and A. Rompel, *Sci. Adv.*, 2023, **9**, eadi0814.
70. Z. Tang, M. Tang, D. Wang, L. Chen and J. Zhao, *Coord. Chem. Rev.*, 2026, **548**, 217156.
71. I. Lindqvist, *Acta Crystallogr.*, 1952, **5**, 667-670.
72. H. T. Evans Jr, *J. Am. Chem. Soc.*, 1948, **70**, 1291-1292.
73. J. S. Anderson, *Nature*, 1937, **140**, 850-850.
74. J. F. Keggin, *Nature*, 1933, **132**, 351-351.
75. D. D. Dexter and J. Silverton, *J. Am. Chem. Soc.*, 1968, **90**, 3589-3590.
76. B. Dawson, *Acta Crystallogr.*, 1953, **6**, 113-126.
77. J. A. Fernández, X. López, C. Bo, C. de Graaf, E. J. Baerends and J. M. Poblet, *J. Am. Chem. Soc.*, 2007, **129**, 12244-12253.
78. C. Martin, K. Kastner, J. M. Cameron, E. Hampson, J. Alves Fernandes, E. K. Gibson, D. A. Walsh, V. Sans and G. N. Newton, *Angew. Chem.*, 2020, **132**, 14437-14441.
79. E. Hampson, J. M. Cameron, S. Amin, J. Kyo, J. A. Watts, H. Oshio and G. N. Newton, *Angew. Chem.*, 2019, **131**, 18449-18453.
80. Y. Hu, Y. Wang, J. Zhao and L. Chen, *Coord. Chem. Rev.*, 2024, **506**, 215724.
81. J. Dong, D. Zhang, P. Zhang, C. Liu, J. Li, J. Bai, Y. Chi and C. Hu, *Coord. Chem. Rev.*, 2024, **517**, 215998.
82. J. Liu, M. Huang, X. Zhang, Z. Hua, Z. Feng, Y. Dong, T. Sun, X. Sun and C. Chen, *Coord. Chem. Rev.*, 2022, **472**, 214785.
83. D. Cheng, K. Li, H. Zang and J. Chen, *EEM*, 2023, **6**, e12341.
84. C. Falaise, *Eur. J. Inorg. Chem.*, 2025, **28**, e202400827.
85. X. Li, X. Liu, Y. Tao, W. Feng, H. Wang, M. Xu, Y. Sun and T. Sun, *ChemistrySelect*, 2025, **10**, e202405001.

86. D. E. S. Marcano and T. N. Parac-Vogt, *Coord. Chem. Rev.*, 2024, **518**, 216086.
87. D. Pakulski, A. Gorczyński, D. Brykczyńska, V. Montes-García, W. Czepa, I. Janica, M. Bielejewski, M. Kubicki, V. Patroniak, P. Samorì and A. Ciesielski, *Angew. Chem. Int. Ed.*, 2023, **62**, e202305239.
88. P.-P. Zhu, L.-J. Sun, N. Sheng, J.-Q. Sha, G.-D. Liu, L. Yu, H.-B. Qiu and S.-X. Li, *Cryst. Growth Des.*, 2016, **16**, 3215-3223.
89. L. Marchetti and M. Levine, *ACS Catal.*, 2011, **1**, 1090-1118.
90. K.-Y. Wang, J. Zhang, Y.-C. Hsu, H. Lin, Z. Han, J. Pang, Z. Yang, R.-R. Liang, W. Shi and H.-C. Zhou, *Chem. Rev.*, 2023, **123**, 5347-5420.
91. K. Song, D. Shi, W. Zhao, Y. Gu, D. Liu and P. K. Chu, *Coord. Chem. Rev.*, 2026, **548**, 217195.
92. N. A. Rey, A. Neves, A. J. Bortoluzzi, C. T. Pich and H. Terenzi, *Inorg. Chem.*, 2007, **46**, 348-350.
93. S. K. Dey and A. Mukherjee, *Coord. Chem. Rev.*, 2016, **310**, 80-115.
94. I. Blain, P. Slama, M. Giorgi, T. Tron and M. Réglier, *Rev. Mol. Biotechn.*, 2002, **90**, 95-112.
95. X. Yu, Y. Wang, J. Zhang, J. Liu, A. Wang and L. Ding, *Adv. Healthc. Mater.*, 2024, **13**, 2302023.
96. D. Heroux, X. X. Sun, Z. Nosrati and M. B. Bally, *Pharmaceutics*, 2026, **18**, 75.
97. T. Klabunde, C. Eicken, J. C. Sacchettini and B. Krebs, *Nat. Struct. Biol.*, 1998, **5**, 1084-1090.
98. M. P. Silva, C. Saibert, T. Bortolotto, A. J. Bortoluzzi, G. Schenk, R. A. Peralta, H. Terenzi and A. Neves, *J. Inorg. Biochem.*, 2020, **213**, 111249.
99. A. W. Smith, A. Camara-Artigas, M. Wang, J. P. Allen and W. A. Francisco, *Biochem.*, 2006, **45**, 4378-4387.
100. M. N. S. Karaboğa and M. K. Sezgintürk, *J. Pharm. Biomed. Anal.* , 2022, **209**, 114479.
101. B. S. Mohd Salleh and M. U. Ahmed, *Nanoscale Horiz.*, 2026, DOI: 10.1039/D5NH00691K.
102. M. D. Hawley, S. V. Tatawawadi, S. Piekarski and R. N. Adams, *J. Am. Chem. Soc.*, 1967, **89**, 447-450.
103. Z. Fredj and M. Sawan, *Journal*, 2023, **13**.
104. A. Gorczyński, D. Pakulski, M. Szymańska, M. Kubicki, K. Bułat, T. Łuczak and V. Patroniak, *Talanta*, 2016, **149**, 347-355.
105. A. Gorczyński, M. Kubicki, K. Szymkowiak, T. Łuczak and V. Patroniak, *RSC Adv.*, 2016, **6**, 101888-101899.
106. P. Uppachai, S. Srijaranai, S. Poosittisak, I. Md Isa and S. Mukdasai, *Molecules*, 2020, **25**, 2528.
107. G. Jiang, M. Wang, X. Gu, T. Chen, Y. Shang, Y. Tang, G. Jiang and Y. Shi, *CrystEngComm*, 2014, **16**, 472-478.
108. X. Gu, X. Li, S. Wu, J. Shi, G. Jiang, G. Jiang and S. Tian, *RSC Adv.*, 2016, **6**, 8070-8078.
109. B. Venkatesagowda and R. F. H. Dekker, *Enzyme Microb. Technol.*, 2021, **147**, 109780.
110. C. Grimm, S. Pompei, K. Egger, M. Fuchs and W. Kroutil, *RSC Adv.*, 2023, **13**, 5770-5777.
111. D. Calabrese, G. Lim, P. Nayyara, M. E. Wolf, P. R. F. Cordero, L. D. Eltis and L. Lauterbach, *Green Chem.*, 2026, DOI: 10.1039/D5GC05054E.

112. A. Bocian, M. Szymańska, D. Brykczyńska, M. Kubicki, M. Wałęsa-Chorab, G. N. Roviello, M. A. Fik-Jaskółka, A. Gorczyński and V. Patroniak, *Molecules*, 2019, **24**, 3173.
113. D. Nowicka, K. Garbaczewski, G. Consiglio, G. Forte, M. Kubicki, T. Łuczak, V. Patroniak and A. Gorczyński, *New J. Chem.*, 2026, DOI: 10.1039/D5NJ04478B.
114. B. Shafaatian, S. S. Mousavi and S. Afshari, *J. Mol. Struct.*, 2016, **1123**, 191-198.
115. D. Mukherjee, S. Reja, K. Sarkar, T. K. S. Fayaz, P. Kumar, A. Kejriwal, P. Das, P. Sanphui and R. Kumar Das, *Inorg. Chem. Commun.*, 2022, **146**, 110190.
116. E. A. Yildiz, Y. Pepe, D. Erdener, A. Karatay, B. Boyacioglu, H. Ünver, G. Yapar, N. Demir, M. Yıldız and A. Elmali, *Phys. Scr.*, 2023, **98**, 085409.
117. L. Hu, L. Yin, F. Wang, D. Yu, C. Wang, M. Hui, L. Chu, X. Zhu and Z. Yan, *Spectrochim. Acta A Mol. Biomol. Spectrosc.*, 2019, **220**, 117130.
118. C. C. Carmona-Vargas, I. Y. Váquiro, L. M. Jaramillo-Gómez, J.-M. Lehn and M. N. Chaur, *Inorganica Chim. Acta*, 2017, **468**, 131-139.
119. M. Wałęsa-Chorab, R. Banasz, D. Marcinkowski, M. Kubicki and V. Patroniak, *RSC Adv.*, 2017, **7**, 50858-50867.
120. E. Smirnova, A. Ankudinov, I. Chepurnaya, A. Timonov and M. Karushev, *Inorganics*, 2023, **11**.
121. G. Ceyhan, C. Celik, S. Uruş, İ. Demirtaş, M. Elmastaş and M. Tümer, *Spectrochim. Acta A Mol. Biomol. Spectrosc.*, 2011, **81**, 184-198.
122. G. Kaur, R. L. Thimes, J. P. Camden and D. M. Jenkins, *Chem. Commun.*, 2022, **58**, 13188-13197.
123. T. Łuczak, *Electroanalysis*, 2014, **26**, 2152-2160.
124. G. Jiang, X. Gu, G. Jiang, T. Chen, W. Zhan and S. Tian, *Sens. Actuators B Chem.*, 2015, **209**, 122-130.
125. D. Nowicka, M. Kubicki, V. Patroniak, T. Łuczak and A. Gorczyński, *Electrochim. Acta*, 2024, **476**, 143754.
126. E. F. Welch, K. W. Rush, R. J. Arias and N. J. Blackburn, *J. Inorg. Biochem.*, 2022, **231**, 111780.
127. Y. Li, M. Liu, C. Xiang, Q. Xie and S. Yao, *Thin Solid Films*, 2006, **497**, 270-278.
128. A. J. Bard, L. R. Faulkner and H. S. White, *Electrochemical methods: fundamentals and applications*, John Wiley & Sons, 2022.
129. A.Kisza, *Electrochemistry II*, Technical Scientific Publishers, Warsaw, 2001.
130. T. Łuczak, *Electrochim. Acta*, 2008, **53**, 5725-5731.
131. A. P. Sandoval-Rojas, L. Ibarra, M. T. Cortés, M. A. Macías, L. Suescun and J. Hurtado, *J. Electroanal. Chem.*, 2017, **805**, 60-67.
132. M. Hyder, G. R. K. Reddy, B. Naveen and P. S. Kumar, *Chem. Phys. Lett.*, 2020, **740**, 137086.
133. U. Amara, S. Riaz, K. Mahmood, N. Akhtar, M. Nasir, A. Hayat, M. Khalid, M. Yaqub and M. H. Nawaz, *RSC Adv.*, 2021, **11**, 25084-25095.
134. C. Liu, P. Goel and P. S. Kaeser, *Nat. Rev. Neurosci.*, 2021, **22**, 345-358.
135. M. I. Awad and T. Ohsaka, *J. Power Sources*, 2013, **226**, 306-312.
136. D. Nowicka, K. Garbaczewski, T. Łuczak, G. Forte, G. Consiglio, M. Kubicki, V. Patroniak and A. Gorczyński, *Dalton Trans.*, 2025, **54**, 1000-1012.
137. M. Singh, N. Kaur and E. Comini, *J. Mater. Chem. C*, 2020, **8**, 3938-3955.

138. M. Ravandeh, D. Thal, H. Kahlert, K. Wende and M. Lalk, *J. Solid State Electr.*, 2020, **24**.
139. F. Chen, X. Li, J. Hihath, Z. Huang and N. Tao, *J. Am. Chem. Soc.*, 2006, **128**, 15874-15881.
140. S. Radenković, M. Antić, N. D. Savić and B. Đ. Glišić, *New J. Chem.*, 2017, **41**, 12407-12415.
141. M. Zohreh, S. M. Ghoreishi, M. Behpour and M. Mohammadhassan, *Arab. J. Chem.*, 2017, **10**, S657-S664.
142. F. Soofiabadi, A. Amiri and S. Jahani, *Anal. Bioanal. Electrochem.*, 2017, **9**, 340-350.
143. S. Shahrokhian, M. Ghalkhani and M. K. Amini, *Sens. Actuators B Chem.*, 2009, **137**, 669-675.
144. C. N. Pecheu, V. K. Tchieda, K. Y. Tajeu, S. L. Z. Jiokeng, A. Lesch, I. K. Tonle, E. Ngameni and C. Janiak, *Molecules*, 2023, **28**, 5487.
145. X. Yang, P. Zhao, Z. Xie, M. Ni, C. Wang, P. Yang, Y. Xie and J. Fei, *Talanta*, 2021, **233**, 122545.
146. N. G. Mphuthi, A. S. Adekunle and E. E. Ebenso, *Sci. Rep.*, 2016, **6**, 26938.
147. J. Tashkhourian, S. F. Nami-Ana and M. Shamsipur, *J. Mol. Liq.*, 2018, **266**, 548-556.
148. N. Lavanya, E. Fazio, F. Neri, A. Bonavita, S. G. Leonardi, G. Neri and C. Sekar, *Sens. Actuators B Chem.*, 2015, **221**, 1412-1422.
149. A. Bocian, W. Drożdż, M. Szymańska, J. Lewandowski, M. Fik-Jaskółka, A. Gorczyński, V. Patroniak and A. R. Stefankiewicz, *Nanoscale*, 2020, **12**, 4743-4750.
150. G. Ulrich, S. Bedel, C. Picard and P. Tisnès, *Tetrahedron Lett.*, 2001, **42**, 6113-6115.
151. R. Contant and A. Teze, *Inorg. Chem.*, 1985, **24**, 4610-4614.
152. B. J. Hornstein and R. G. Finke, *Inorg. Chem.*, 2002, **41**, 2720-2730.
153. R. G. Finke, B. Rapko, R. J. Saxton and P. J. Domaille, *J. Am. Chem. Soc.*, 1986, **108**, 2947-2960.
154. H. Asif, R. B. Bi, M. Tariq, N. Shaheen, M. Khalid, M. Nadeem, M. Ali Khan and T. Ansari, *Russ. J. Inorg. Chem.*, 2021, **66**, 340-347.
155. L. Wang, W. Li, L. Wu, X. Dong, H. Hu and G. Xue, *Inorg. Chem. Commun.*, 2013, **35**, 122-125.
156. S.-M. Wang, J. Hwang and E. Kim, *J. Mater. Chem. C*, 2019, **7**, 7828-7850.
157. S. Vanhaecht, G. Absillis and T. N. Parac-Vogt, *Dalton Trans.*, 2012, **41**, 10028-10034.
158. S. Vanhaecht, T. Quanten and T. Parac-Vogt, *Dalton Trans.*, 2017, **46**, 10215-10219.
159. Y. Sakai, S. Yoshida, T. Hasegawa, H. Murakami and K. Nomiya, *Bull. Chem. Soc. Jpn.*, 2007, **80**, 1965-1974.
160. B. Yan, R. Liang, K. Zheng, R. Li, P. Ma, J. Wang and J. Niu, *Inorg. Chem.*, 2021, **60**, 8164-8172.
161. M.-X. Li, Y. Zhang, Z.-M. Zhu, F. Su, L.-C. Zhang and X.-J. Sang, *J. Coord. Chem.*, 2020, **73**, 2437-2449.
162. J. Guo, D. Zhang, L. Chen, Y. Song, D. Zhu and Y. Xu, *Dalton Trans.*, 2013, **42**, 8454-8459.
163. G. Zhu, E. N. Glass, C. Zhao, H. Lv, J. W. Vickers, Y. V. Geletii, D. G. Musaev, J. Song and C. L. Hill, *Dalton Trans.*, 2012, **41**, 13043-13049.
164. S. Nellutla, J. van Tol, N. S. Dalal, L.-H. Bi, U. Kortz, B. Keita, L. Nadjo, G. A. Khitrov and A. G. Marshall, *Inorg. Chem.*, 2005, **44**, 9795-9806.
165. T. Ueda, M. Suzuki and T. Toya, *J. Clust. Sci.*, 2016, **27**, 501-511.

166. T. Minato, K. Suzuki, K. Kamata and N. Mizuno, *Chem. Eur. J.*, 2014, **20**, 5946-5952.
167. J. Luo, G. Jin, F. Zhang, Y. Liu, L. Chen, S. Xie and J. Zhao, *Eur. J. Inorg. Chem.*, 2018, **2018**, 143-152.
168. G. Cao, J. Xiong, Q. Xue, S. Min, H. Hu and G. Xue, *Electrochim. Acta*, 2013, **106**, 465-471.
169. P. Lapham, L. Vilà-Nadal, L. Cronin and V. P. Georgiev, *J. Phys. Chem. C*, 2021, **125**, 3599-3610.
170. Q. Zheng, M. Kupper, W. Xuan, H. Oki, R. Tsunashima, D.-L. Long and L. Cronin, *J. Am. Chem. Soc.*, 2019, **141**, 13479-13486.
171. Q. Han, X. Sun, J. Li, P. Ma and J. Niu, *Inorg. Chem.*, 2014, **53**, 2006-2011.
172. L. Shi, X.-m. Gao, T.-Y. Liu, X.-H. Huang, Z.-H. Gong, Y.-P. Chen and Y.-Q. Sun, *Dalton Trans.*, 2018, **47**, 1347-1354.
173. S. He, Y. Xin, J. Li, Z. Zhu, P. Zhao and W. You, *Acta Crystallogr., Sec. C: Cryst. Struct. Commun.*, 2018, **74**, 1267-1273.
174. J. Gao, J. Yan, S. Beeg, D. L. Long and L. Cronin, *Angew. Chem. Int. Ed.*, 2012, **51**, 3373-3376.
175. L. Liu, J. Jiang, L. Cui, J. Zhao, X. Cao and L. Chen, *Inorg. Chem.*, 2022, **61**, 1949-1960.
176. U. Kortz and M. T. Pope, *Inorg. Chem.*, 1994, **33**, 5643-5646.
177. M. Bugnola, R. E. Schreiber, Y. Kaufman, G. Leitus, L. J. Shimon and R. Neumann, *Eur. J. Inorg. Chem.*, 2019, **2019**, 482-485.
178. R. E. Schreiber, H. Cohen, G. Leitus, S. G. Wolf, A. Zhou, L. Que Jr and R. Neumann, *J. Am. Chem. Soc.*, 2015, **137**, 8738-8748.
179. L. Vila-Nadal, S. G. Mitchell, D.-L. Long, A. Rodríguez-Fortea, X. López, J. M. Poblet and L. Cronin, *Dalton Trans.*, 2012, **41**, 2264-2271.
180. D. L. Long, Y. F. Song, E. F. Wilson, P. Kögerler, S. X. Guo, A. M. Bond, J. S. Hargreaves and L. Cronin, *Angew. Chem. Int. Ed.*, 2008, **47**, 4384-4387.
181. Y.-Y. Zhang, S.-X. Liu, C.-J. Yu, Q. Tang, D.-D. Liang, C.-D. Zhang, F.-J. Ma, S.-J. Li, W. Zhang and R.-K. Tan, *Inorg. Chem. Commun.*, 2010, **13**, 1418-1420.
182. X. Xu, H.-L. Dong, R.-L. Sang and L. Xu, *Chem. Commun.*, 2012, **48**, 12177-12179.
183. S. Li, G. Li, P. Ji, J. Zhang, S. Liu, J. Zhang and X. Chen, *ACS Appl. Mater. Interfaces.*, 2019, **11**, 43287-43293.
184. A. Müller, E. Krickemeyer, H. Bögge, M. Schmidtmann and F. Peters, *Angew. Chem. Int. Ed.*, 1998, **37**, 3359-3363.
185. O. Oms, A. Dolbecq and P. Mialane, *Chem. Soc. Rev.*, 2012, **41**, 7497-7536.
186. Y. Hayashi, *Coord. Chem. Rev.*, 2011, **255**, 2270-2280.
187. M. Nyman, *Dalton Trans.*, 2011, **40**, 8049-8058.
188. X. Ma, P. Wang, Z. Liu, C. Xin, S. Wang, J. Jia, P. Ma, J. Niu and J. Wang, *Inorg. Chem.*, 2020, **59**, 8690-8698.
189. P. Huang, X.-J. Wang, J.-J. Qi, X.-L. Wang, M. Huang, H.-Y. Wu, C. Qin and Z.-M. Su, *J. Mater. Chem. A*, 2017, **5**, 22970-22974.
190. H. Dridi, A. Boulmier, P. Bolle, A. Dolbecq, J.-N. Rebilly, F. Banse, L. Ruhlmann, H. Serier-Brault, R. Dessapt and P. Mialane, *J. Mater. Chem. C*, 2020, **8**, 637-649.
191. C. P. Pradeep, D. L. Long, G. N. Newton, Y. F. Song and L. Cronin, *Angew. Chem. Int. Ed.*, 2008, **47**, 4388-4391.

192. S. Martín, Y. Takashima, C.-G. Lin, Y.-F. Song, H. N. Miras and L. Cronin, *Inorg. Chem.*, 2019, **58**, 4110-4116.
193. J. Oble, B. Riflade, A. Noël, M. Malacria, S. Thorimbert, B. Hasenknopf and E. Lacôte, *Org. Lett.*, 2011, **13**, 5990-5993.
194. R. Gupta, W. Huang, L. C. Francesconi and T. Polenova, *Solid State Nucl. Magn. Reson.*, 2017, **84**, 28-33.
195. C. P. Pradeep, D.-L. Long, P. Kögerler and L. Cronin, *Chem. Commun.*, 2007, DOI: 10.1039/B707202C, 4254-4256.
196. A. M. Khenkin, D. Kumar, S. Shaik and R. Neumann, *J. Am. Chem. Soc.*, 2006, **128**, 15451-15460.
197. K. Stroobants, G. Absillis, P. S. Shestakova, R. Willem and T. N. Parac-Vogt, *J. Clust. Sci.*, 2014, **25**, 855-866.
198. W. Wang, N. V. Izarova, J. van Leusen and P. Kögerler, *Chem. Commun.*, 2020, **56**, 14857-14860.
199. L. Vandebroek, E. De Zitter, H. G. T. Ly, D. Conić, T. Mihaylov, A. Sap, P. Proost, K. Pierloot, L. Van Meervelt and T. N. Parac-Vogt, *Chem. Eur. J.*, 2018, **24**, 10099-10108.
200. Y.-Q. Jiao, C. Qin, X.-L. Wang, F.-H. Liu, P. Huang, C.-G. Wang, K.-Z. Shao and Z.-M. Su, *Chem. Commun.*, 2014, **50**, 5961-5963.
201. N. V. Izarova, L. Klaß, P. de Oliveira, I. M. Mbomekalle, V. Peters, F. Haarmann and P. Kögerler, *Dalton Trans.*, 2015, **44**, 19200-19206.
202. F. Hussain, U. Kortz, B. Keita, L. Nadjo and M. T. Pope, *Inorg. Chem.*, 2006, **45**, 761-766.
203. S. S. Mal, M. H. Dickman and U. Kortz, *Chem. Eur. J.*, 2008, **14**, 9851-9855.
204. S. Yao, Z. Zhang, Y. Li, Y. Lu, E. Wang and Z. Su, *Cryst. Growth Des.*, 2010, **10**, 135-139.
205. L.-H. Bi and U. Kortz, *Inorg. Chem.*, 2004, **43**, 7961-7962.
206. N. Laronze, J. Marrot and G. Hervé, *Chem. Commun.*, 2003, DOI: 10.1039/B307276B, 2360-2361.
207. S. Matsunaga, Y. Inoue, T. Otaki, H. Osada and K. Nomiya, *ZAAC*, 2016, **642**, 539-545.
208. Israel M. Mbomekalle, B. Keita, L. Nadjo, Wade A. Neiwert, L. Zhang, Kenneth I. Hardcastle, Craig L. Hill and Travis M. Anderson, *Eur. J. Inorg. Chem.*, 2003, **2003**, 3924-3928.
209. L. Ruhlmann, D. Schaming, I. Ahmed, A. Courville, J. Canny and R. Thouvenot, *Inorg. Chem.*, 2012, **51**, 8202-8211.
210. F. Doungmene, P. A. Aparicio, J. Ntienoue, C. S. A. Mezui, P. de Oliveira, X. López and I. M. Mbomekallé, *Electrochim. Acta*, 2014, **125**, 674-682.
211. M. R. Farsani, F. Jalilian, B. Yadollahi and H. A. Rudbari, *Polyhedron*, 2014, **76**, 102-107.
212. R. G. Finke and M. W. Droege, *Inorg. Chem.*, 1983, **22**, 1006-1008.
213. R. Contant and A. Teze, *Inorg. Chem.*, 1985, **24**, 4610-4614.
214. N. I. Gumerova and A. Rompel, *Chem. Soc. Rev.*, 2020, **49**, 7568-7601.
215. L.-Y. Guo, M. Jagodič, S.-Y. Zeng, Z. Wang, Z.-Q. Shi, X.-P. Wang, C.-H. Tung and D. Sun, *Dalton Trans.*, 2016, **45**, 8404-8411.
216. X. Fang and P. Kögerler, *Chem. Commun.*, 2008, DOI: 10.1039/B804111C, 3396-3398.

217. A. Proust, B. Matt, R. Villanneau, G. Guillemot, P. Gouzerh and G. Izzet, *Chem. Soc. Rev.*, 2012, **41**, 7605-7622.
218. J.-X. Liu, X.-B. Zhang, Y.-L. Li, S.-L. Huang and G.-Y. Yang, *Coord. Chem. Rev.*, 2020, **414**, 213260.
219. S. Thorimbert, B. Hasenknopf and E. Lacôte, *Isr. J. Chem.*, 2011, **51**, 275-280.
220. A. J. Kibler and G. N. Newton, *Polyhedron*, 2018, **154**, 1-20.
221. J. Zhang, Y. Huang, G. Li and Y. Wei, *Coord. Chem. Rev.*, 2019, **378**, 395-414.
222. H. Zhang, W.-L. Zhao, H. Li, Q. Zhuang, Z. Sun, D. Cui, X. Chen, A. Guo, X. Ji, S. An, W. Chen and Y.-F. Song, *Polyoxometalates*, 2022, **1**, 9140011.
223. J. Lesage de la Haye, P. Beaunier, L. Ruhlmann, B. Hasenknopf, E. Lacôte and J. Rieger, *Chem. Plus. Chem.*, 2014, **79**, 250-256.
224. M. Glöß, R. Pütt, M. Moors, E. Kentzinger, S. Karthäuser and K. Y. Monakhov, *Adv. Mater. Interfaces*, 2022, **n/a**, 2200461.
225. W. Chen, U. Tong, T. Zeng, C. Streb and Y.-F. Song, *J. Mater. Chem. C.*, 2015, **3**, 4388-4393.
226. P. Yin, C. P. Pradeep, B. Zhang, F.-Y. Li, C. Lydon, M. H. Rosnes, D. Li, E. Bitterlich, L. Xu, L. Cronin and T. Liu, *Chem. – Eur. J.*, 2012, **18**, 8157-8162.
227. M.-P. Santoni, A. K. Pal, G. S. Hanan, A. Proust and B. Hasenknopf, *Inorg. Chem.*, 2011, **50**, 6737-6745.
228. V. Kalyani, V. S. V. Satyanarayana, V. Singh, C. P. Pradeep, S. Ghosh, S. K. Sharma and K. E. Gonsalves, *Chem. – Eur. J.*, 2015, **21**, 2250-2258.
229. B. Matt, C. Coudret, C. Viala, D. Jouvenot, F. Loiseau, G. Izzet and A. Proust, *Inorg. Chem.*, 2011, **50**, 7761-7768.
230. B. Matt, S. Renaudineau, L. M. Chamoreau, C. Afonso, G. Izzet and A. Proust, *J. Org. Chem.*, 2011, **76**, 3107-3112.
231. J. M. Cameron, S. Fujimoto, K. Kastner, R.-J. Wei, D. Robinson, V. Sans, G. N. Newton and H. H. Oshio, *Chem. – Eur. J.*, 2017, **23**, 47-50.
232. A. V. Anyushin, S. Vanhaecht and T. N. Parac-Vogt, *Inorg. Chem.*, 2020, **59**, 10146-10152.

KOPIE PUBLIKACJI NAUKOWYCH WCHODZĄCYCH W ZAKRES ROZPRAWY DOKTORSKIEJ

NJC

New Journal of Chemistry

A journal for new directions in chemistry

Accepted Manuscript

This article can be cited before page numbers have been issued, to do this please use: D. Nowicka, K. Garbaczewski, G. Consiglio, G. Forte, M. Kubicki, T. uczak, V. Patroniak and A. Gorczyski, *New J. Chem.*, 2026, DOI: 10.1039/D5NJ04478B.

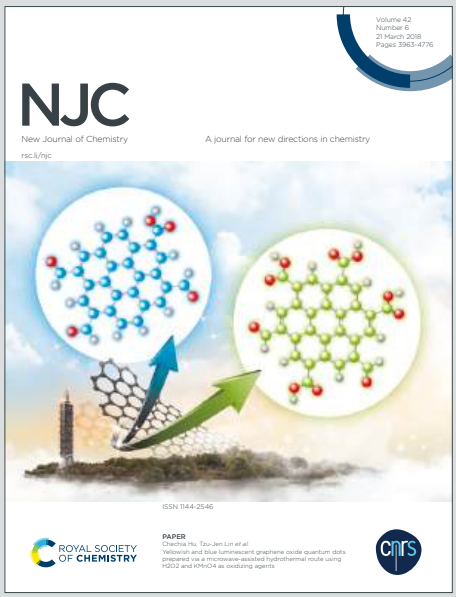

ROYAL SOCIETY OF CHEMISTRY

rsc.li/njc

View Article Online
DOI: 10.1039/D5NJ04478B

ARTICLE

Biomimetic *O*-Demethylation at a Copper(II) Center with Imine Ligand: A Structural and Computational Study

Daria Nowicka,*[a] Karol Garbaczewski,[a] Giuseppe Consiglio,[b] Giuseppe Forte,[c] Maciej Kubicki,[a] Teresa Łuczak,[a] Violetta Patroniak [a] and Adam Gorczyński *[a]

Received 00th January 20xx,
Accepted 00th January 20xx

DOI: 10.1039/x0xx00000x

The catalytic cleavage of C–O bonds is a fundamental transformation in organic synthesis and biomimetic chemistry, with particular relevance to enzymatic *O*-demethylation. Inspired by oxidative *O*-demethylase enzymes, we investigated Cu(II)-mediated *O*-demethylation as a selective and environmentally friendly approach to breaking C–O–C bonds under mild conditions. To probe the electronic effects governing this transformation, we synthesized and characterized a series of Cu(II) complexes based on three imine ligands with varying methoxy substituent patterns. Structural and reaction studies identified key factors influencing the demethylation process, enabling a strategy for controlled *O*-demethylation at the Cu(II) center. Notably, exposure of complex **C1** to a weakly coordinating perchlorate anion, visible light, oxygen and water induced selective demethylation of ligand **L1**, yielding complexes **C2** and **C3**. X-ray crystallography confirmed the demethylated products, while spectroscopic and electrochemical analyses provided mechanistic insights. Additionally, DFT calculations elucidated the regioselectivity, demonstrating why only the methoxy group closest to the metal center undergoes cleavage. This study represents the first example of Cu(II)-mediated *O*-demethylation, revealing the critical interplay of electronic and geometric factors. These findings offer new perspectives for catalytic demethylation strategies and may have broader implications in sustainable lignin valorization, materials science, and environmental chemistry, showing the catalytic potential of Cu(II) ions in this reaction.

1. Introduction

Imine ligands and their metal complexes are widely studied due to their facile synthesis and broad applications in coordination chemistry[1]. Their well-defined ligand backbones, combined with supramolecular interactions such as hydrogen bonding or coordination with d-block metal ions, enable the construction of biomimetic coordination systems that mimic enzymatic activity[2]. Demethylation is a well-studied process catalyzed by various natural enzymes including 2-oxoglutarate (2OG)/Fe(II)-dependent dioxygenases, cytochromes P450 (CYPs), Rieske domain proteins and flavin adenine dinucleotide (FAD)-dependent oxidases. These enzymes play essential roles in diverse biological processes, from histone modification and DNA repair to toxin degradation and plant metabolism[3-7]. Drawing inspiration from nature not only provides deeper insight into enzymatic *O*-demethylation but also facilitates the development of biomimetic synthetic systems capable of replicating such transformations.

Aryl methyl ethers represent a key class of substrates for *O*-demethylation, yielding phenolic derivatives that serve as valuable intermediates in the synthesis of antioxidants, flavor compounds, dyes, and high-value chemicals[8]. Traditional methods rely on strong Brønsted or Lewis acids or bases such as hydrobromic acid, boron tribromide or sodium ethanethiolate[8], which are environmentally hazardous and incompatible with the green chemistry principles. Consequently, significant efforts have been made to develop alternative strategies using metal-based catalysts, yet reports on biomimetic oxidative *O*-demethylation remain scarce. Recent studies have explored metal ion-assisted *O*-demethylation involving Cu(II), Co(II), and Fe(II) complexes bearing methoxy-substituted ligands. These systems offer a promising approach to achieving selective *O*-demethylation under mild conditions while minimizing solvent use and employing environmentally friendly reagents[9-12]. One of the earliest examples was reported by Mandon et al., who demonstrated *O*-demethylation at an Fe(II) center with multiple methoxy groups using molecular oxygen with Zn/Hg amalgam as the reducing agent. Their findings revealed that methoxy coordination to the metal center was not a prerequisite for demethylation but that spatial proximity to the oxidized metal species was essential[11]. More recently, Anjana et al. reported the first *O*-demethylation of non-heme Co(II) complexes featuring tetradentate N-donor ligands in the presence of oxidants[9]. They later extended this work to non-heme Fe(II) complexes,

[a] *Adam Mickiewicz University in Poznań, Faculty of Chemistry, Uniwersytetu Poznańskiego 8, 61-614 Poznań, Poland*
[b] *Department of Chemical Science University of Catania, Via S. Sofia 64, 95125, Italy*
[c] *Department of Drug Science and Health University of Catania, Via S. Sofia 64, 95125, Italy*
* *Correspondence: d.nowicka@amu.edu.pl; adam.gorczynski@amu.edu.pl*
† Footnotes relating to the title and/or authors should appear here.
Electronic Supplementary Information (ESI) available: [details of any supplementary information available should be included here]. See DOI: 10.1039/x0xx00000x

demonstrating that even minor modifications to the ligand backbone could drastically influence reactivity[10]. Notably, Karlin et al. investigated Cu(II) complexes with similar *N,N,N*-donor ligands but observed no *O*-demethylation[12]. However, their work revealed that unobservable Cu_2O_2-derived species actively participated in the oxidation of aliphatic C–H bonds in organic substrates such as toluene and ethylbenzene, further highlighting the sensitivity of metal-mediated oxidative transformations[12].

Copper-catalyzed oxidation reactions are particularly advantageous from a green chemistry perspective due to the natural abundance and biocompatibility of copper[13-15]. This is exemplified by numerous copper-dependent enzymes, including tyrosinase[16-20], phenoxazinone synthase[21-23], catecholase[18, 19, 23-25], galactose oxidase[26, 27] and dopamine β-hydroxylase[28-30], all of which play essential roles in biological oxidation processes. Given the widespread occurrence of copper in nature and its well-documented biomimetic properties, we focused our investigation on copper-based systems paired with ligand frameworks aligned with green chemistry principles. For this reason, we selected imine-based systems, which are not only synthetically accessible and environmentally friendly but also widely utilized in various applications, including catalysis[31-35], biomimetic chemistry[21, 36] and electrochemistry[37-42]. Additionally, Schiff-base imine ligands exhibit significant biological activity, demonstrating antibacterial, antifungal, anticancer, and antimalarial properties, among others[43-46].

Here, we report the first example of Cu(II)-mediated *O*-demethylation of C–O–C bonds in imine-based complexes—a transformation previously unobserved for Cu(II) ions (Scheme 1).

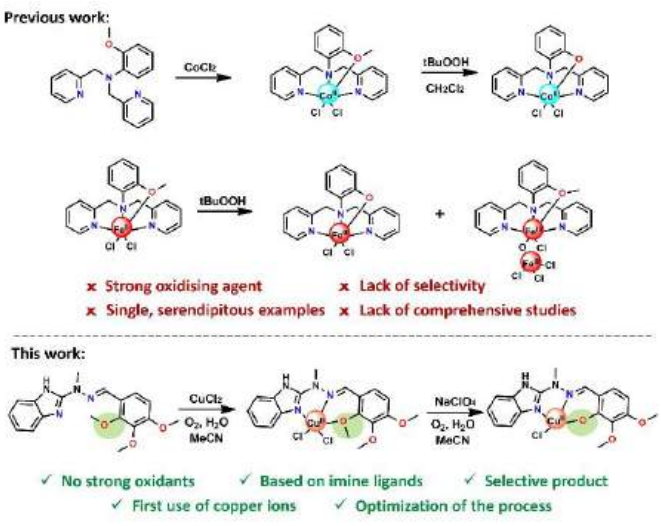

Scheme 1. State-of-the-art of the *O*-demethylation process using biomimetic coordination compounds with different metal ions.

This unprecedented reactivity challenges the established instability of imine systems under oxidative conditions and provides new insights into metal-assisted *O*-demethylation. In particular, the combination of a redox-active Cu(II) center with an electronically tunable imine ligand framework enables efficient electronic communication within the complex, facilitating selective C–O bond cleavage under mild conditions. Our experimental and theoretical investigations reveal that the process is driven by a synergistic interplay between perchlorate anions, water, and molecular oxygen, allowing *O*-demethylation to proceed without the need for strong external oxidants such as *tert*-butyl hydroperoxide[9, 10]. Additionally, the reaction proceeds efficiently in acetonitrile but is completely suppressed in protic solvents such as methanol and ethanol, underscoring the critical role of solvent choice. These findings not only expand the scope of Cu(II) chemistry but also address an important knowledge gap by elucidating the active role of the imine ligand and its structural modifications in directing *O*-demethylation reactivity, thereby providing a deeper mechanistic understanding of biomimetic copper-mediated transformations and paving the way for new catalytic applications.

2. Experimental

2.1 Materials and Instruments

All solvents used for syntheses and all deuterated solvents for NMR studies were purchased from commercial sources and used as received. The reagents for synthesis and studies - including 2-chlorobenzimidazole, methylhydrazine, 2,3,4-trimethoxybenzaldehyde, 2-methoxybenzaldehyde, 2,4-dimethoxy-3-methylbenzaldehyde, $CuCl_2{\cdot}2H_2O$, $MnCl_2$, $Mn(ClO_4)_2{\cdot}6H_2O$, $Zn(ClO_4)_2{\cdot}6H_2O$, $NaClO_4{\cdot}H_2O$, $NaBF_4$, $NaPF_6$, NaOH and $(CH_3CH_2CH_2CH_2)_4N(ClO_4)$ ($TBAClO_4$) were obtained from Sigma-Aldrich and used as received without further purification.

Electrospray ionization mass spectrometry (ESI-MS) was performed using the High-Resolution Bruker QTOF Impact HD spectrometer and Waters Micromass ZQ spectrometer. Fourier-transform infrared (FT-IR) spectra were recorded using a FT-IR IFS 66/s Bruker spectrometer in the range of 4000-400 cm^{-1} in the form of KBr pellets. Microanalyses were obtained using a FLASH 2000 NCH element analyzer. Nuclear magnetic resonance (NMR) spectra were recorded using a Bruker Avance 600 MHz spectrometer, operating at 600 MHz for ^1H NMR and at 151 MHz for ^{13}C NMR. Spectra were measured in DMSO-d_6, with chemical shifts referenced as follows: ^1H NMR - DMSO-d_6 2.50 ppm and 3.33 ppm (H_2O signal); ^{13}C NMR analysis: DMSO-d_6 39.52 ppm. Electronic absorption spectra were recorded in the 200–600 nm range using a JASCO V-770 UV–Vis spectrophotometer, equipped with a Peltier Thermo Cell Holder (water) PAC-743R (Jasco International Co., Tokyo, Japan) using 10×10 mm quartz cells. Electrochemical measurements were carried out at room temperature in a three-electrode system, consisting of a gold working electrode, a platinum wire auxiliary electrode and a saturated calomel electrode (SCE) as a reference electrode. A potentiostat/galvanostat analyzer (AUTOLAB PGSTAT 302N, Eco Chemie, B.V., Utrecht, The Netherlands) was used for data collection.

2.2. Synthesis and characterization of ligands L1 – L3

Scheme 2. Schematic representation of ligands: **L1**, **L2** and **L3**, respectively.

The synthetic approach for ligands **L1** – **L3** follows a two-step procedure. First, a nucleophilic substitution reaction of 2-chlorobenzimidazole (**A**) with methylhydrazine yields 2-(1-methylhydrazinyl)-1H-benzo[d]imidazole (**B**). In the second step, this intermediate undergoes a condensation reaction with 2,3,4-trimethoxybenzaldehyde, 2-methoxybenzaldehyde or 2,4-dimethoxy-3-methylbenzaldehyde, respectively, to give the target ligands: **L1** [benz-$(OMe)_3$], **L2** [benz-$(OMe)_1$] and **L3** [benz-$(OMe)_2$] (Scheme S1, Scheme 2).

The first step in the synthesis of ligands **L1** – **L3** was carried out according to a previously published procedure [21]. In the second step, **B** (0.60 g, 3.70 mmol) was placed in a 250-ml three-necked flask, evacuated and dissolved in absolute ethanol (4 ml). The mixture was stirred on a magnetic stirrer and heated at 80°C for one hour. Subsequently, 2,3,4-trimethoxybenzaldehyde (0.73 g, 3.70 mmol) was added to the first flask, 2-methoxybenzaldehyde (0.50 g, 3.70 mmol) to the second and 2,4-dimethoxy-3-methylbenzaldehyde (0.67 g, 3.70 mmol) to the third. Additional absolute ethanol (10 ml) was added to all three reaction mixtures, which were then heated at 80°C for 3 hours. The resulting solutions were cooled in the refrigerator for 2 hours, then filtered using a Büchner funnel, thoroughly washed with absolute ethanol and dried under vacuum. Yield: **L1**: 76% (0.96 g, 2.82 mmol), **L2**: 86% (0.89 g, 3.17 mmol), **L3**: 78% (0.93 g, 2.87 mmol).

L1 [benz-$(OMe)_3$]: HRMS (ESI) m/z; found: $[(L1)+H]^+$ 341.1607; requires $[(L1)+H]^+$ 341.1614 (2.0 ppm). Anal. calc.: C, 63.52; H, 5.92; N, 16.46; found: C, 63.38; H, 6.00; N, 16.37%. IR (KBr, cm^{-1}): (N-H) 3452; (C-H) 3002, 2930, 2830; $(C=N)_{imine}$ 1624; (C=C) 1574, 1495, 1454; (C-N) 1381; $(C=N)_{ar}$ 1271; (C-H) 1142, 1093, 1004; (C-H) 799, 732. ^1H NMR (600 MHz, DMSO-d_6) δ 11.66 (s, 1 H), 8.03 (d, J = 8.8 Hz, 1 H), 7.85 (d, J = 1.0 Hz, 1 H), 7.33 (dd, J = 7.6, 1.3 Hz, 1 H), 7.30 (dd, J = 6.4 Hz, 1 H), 7.04 – 6.96 (m, 2 H), 6.92 (d, 1 H), 3.87 (s, 3 H), 3.87 (s, 3 H), 3.79 (s, 3 H), 3.64 (s, J = 0.8 Hz, 3 H) ppm. ^{13}C NMR (151 MHz, DMSO-d_6) δ 154.14, 153.96, 152.00, 142.81, 141.57, 134.16, 131.54, 121.31, 120.74, 120.53, 119.56, 116.04, 109.61, 108.47, 61.62, 60.45, 56.03, 31.27 ppm. Crystals suitable for X-ray diffraction in the form of protonated salt of a ligand **L1** were obtained during optimization reactions with $Mn(ClO_4)_2 \cdot 6H_2O$ salt. CCDC 2336936.

L2 [benz-$(OMe)_1$]: ESI-MS(+) m/z (%): 281 (100) $[(L2)+H]^+$; 303 (30) $[(L2)+Na]^+$. ESI-MS(-) m/z (%): 279 (10) $[(L2)-H]^-$. Anal. calc.: C, 68.55; H, 5.75; N, 19.99; found: C, 68.44; H, 5.65; N, 19.87%. IR (KBr, cm^{-1}): (N-H) 3474; (C-H) 3029, 3002, 2963, 2835; $(C=N)_{imine}$ 1630; (C=C) 1605, 1566, 1547, 1489; (C-N) 1384; $(C=N)_{ar}$ 1247; (C-H) 1132, 1025, 1004; (C-H) 934, 908, 740. ^1H NMR (600 MHz, DMSO-d_6) δ 11.70 (s, 1H), 8.29 (d, J = 7.7, 1.8 Hz, 1H), 7.99 (s, 1H), 7.44 – 7.25 (m, 3H), 7.10 (d, 1H), 7.07 – 6.97 (m, 3H), 3.88 (s, 3H), 3.63 (s, J = 0.8 Hz, 3H) ppm. ^{13}C NMR (151 MHz, DMSO-d_6) δ 157.06, 153.90, 142.76, 134.19, 131.29, 130.24, 125.82, 123.07, 120.61, 120.52, 119.71, 116.14, 111.60, 109.71, 55.65, 31.36 ppm. Crystals suitable for X-ray diffraction in the form of protonated salt of a ligand **L2** were obtained during optimization reactions with $Mn(ClO_4)_2 \cdot 6H_2O$ salt. CCDC 2336937.

L3 [benz-$(OMe)_2$]: ESI-MS(+) m/z (%): 325 (100) $[(L3)+H]^+$; 347 (20) $[(L3)+Na]^+$. ESI-MS(-) m/z (%): 323 (50) $[(L3)-H]^-$. Anal. calc.: C, 66.65; H, 6.21; N, 17.27; found: C, 66.83; H, 6.24; N, 17.17%. IR (KBr, cm^{-1}): (N-H) 3449; (C-H) 2994, 2932, 2833; $(C=N)_{imine}$ 1627; (C=C) 1596, 1567, 1490; (C-N) 1380; $(C=N)_{ar}$ 1217; (C-H) 1140, 1107, 1006; (C-H) 941, 803, 737, 697. ^1H NMR (600 MHz, DMSO-d_6) δ 11.66 (s, 1H), 8.16 (d, 1H), 7.85 (s, 1H), 7.36 – 7.21 (m, 2H), 7.08 – 6.93 (m, J = 10.4, 7.4, 1.5 Hz, 2H), 6.88 (d, J = 8.8 Hz, 1H), 3.86 (s, 3H), 3.74 (s, 3H), 3.65 (s, J = 0.8 Hz, 3H), 2.10 (s, 3H) ppm. ^{13}C NMR (151 MHz, DMSO-d_6) δ 159.01, 157.57, 154.04, 142.84, 134.18, 132.08, 129.04, 124.19, 120.54, 119.54, 118.46, 116.02, 109.63, 107.03, 61.58, 55.79, 31.26, 8.76 ppm.

2.3. *O*-demethylation using ligand L1:

2.3.1. Synthesis and characterization of complexes C1 – C3 based on ligand L1

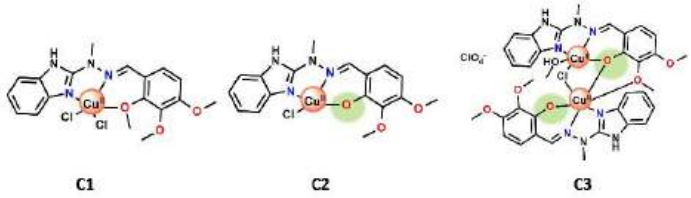

Scheme 3. Schematic representation of complexes **C1**, **C2** and **C3**; *O*-demethylated groups are highlighted. Based on X-ray analysis of **C2** and **C3**

Complex **C1** was synthesized by adding $CuCl_2 \cdot 2H_2O$ (25.6 mg, 0.15 mmol) to a 50 ml flask containing an acetonitrile solution of ligand **L1** (50.0 mg, 0.15 mmol) at a 1:1 molar ratio (ligand:metal). The reaction mixture was stirred at room temperature on a magnetic stirrer for 48 hours. After completion, the solution was concentrated to minimal volume using rotary evaporator and the complex was precipitated by the addition of diethyl ether. The resulting green precipitate was collected using a Büchner funnel, washed with diethyl ether (10 ml in total) and dry in a vacuum desiccator. Yield: 93.3% (69.3 mg, 0.14 mmol) based on ligand **L1**.

C1 $[Cu(L1)Cl_2]$: HRMS (ESI) m/z; found: $[(L1)+H]^+$ 341.1600; requires $[(L1)+H]^+$ 341.1614 (4.1 ppm). Anal. calc.: C, 45.53; H, 4.25; N, 11.80; found: C, 45.48; H, 4.23; N, 11.77%. IR (KBr, cm^{-1}): (N-H) 3381; (C-H) 3022, 2940, 2835; $(C=N)_{imine}$ 1626; (C=C) 1594, 1504, 1464; (C-N) 1377; $(C=N)_{ar}$ 1285; (C-H) 1102, 1059; (C-H) 970, 798, 750.

Complexes **C2** and **C3** were synthesized using a stepwise method following the same synthetic procedure. Complex **C1** (20.0 mg, 0.04 mmol) was dissolved in acetonitrile in two separate 50 ml flasks. To the first solution $NaClO_4 \cdot H_2O$ (5.6 mg, 0.04 mmol) was added, while $Mn(ClO_4)_2 \cdot 6H_2O$ (14.5 mg, 0.04 mmol) was added to the second one. The reactions were conducted at a 1:1 molar ratio (complex:metal) and stirred at

View Article Online DOI: 10.1039/D5NJ04477B

room temperature for 48 hours. After complexation, the reaction mixtures were concentrated to minimal volume using a rotary evaporator and the products were precipitated by the addition of the diethyl ether. The resulting green precipitates were collected by filtration using Büchner funnels, washed with diethyl ether and dried in a vacuum desiccator. Crystals suitable for X-ray diffraction were obtained for **C2** and **C3** through vial-to-vial diffusion crystallization at low temperature (4^0C). CCDC deposit numbers: 2336938 (**C2**) and 2336939 (**C3**). Yield for **C2** and **C3**: 94.6% (16.9 mg), 95.3% (33.8 mg), based on complex **C1**, respectively.

C2 [Cu((L1)-CH_3)Cl]: HRMS (ESI) m/z; found: [Cu((L1)-CH_3)(MeOH)]$^+$ 422.0170; requires [Cu((L1)-CH_3)(MeOH)]$^+$ 422.0179 (2.1 ppm); found: [Cu((L1)-CH_3)Cl(MeOH)+H]$^+$ 456.0412; requires [Cu((L1)-CH_3)Cl(MeOH)+H]$^+$ 456.0426 (3.1 ppm). Anal. calc.: C, 49.55; H, 3.93; N, 12.84; found: C, 49.48; H, 3.99; N, 12.88%. IR (KBr, cm^{-1}): (N-H) 3450; (C-H) 2939, 2837; (C=N)$_{imine}$ 1659; (C=C) 1595, 1499, 1465; (C-N) 1377; (C=N)$_{ar}$ 1269; (C-H) 1116; (C-H) 969, 752, 625.

C3 [Cu_2((L1)-CH_3)$_2$Cl(MeOH)]ClO_4: HRMS (ESI) m/z; found: [Cu_2((L1)-CH_3)$_2$(MeO)]$^+$ 807.1549; requires [Cu_2((L1)-CH_3)$_2$(MeO)]$^+$ 807.1503 (5.7 ppm); found: [Cu_2((L1)-CH_3)$_2$Cl(MeOH)]$^+$ 843.1314; requires [Cu_2((L1)-CH_3)$_2$Cl(MeOH)]$^+$ 843.1364 (5.9 ppm). Anal. calc.: C, 45.87; H, 3.95; N, 11.57; found: C, 45.81; H, 4.00; N, 11.67%. IR (KBr, cm^{-1}): (N-H) 3324, 3214; (C-H) 2945, 2838; (C=N)$_{imine}$ 1631; (C=C) 1593, 1499, 1464; (C-N) 1375; (C=N)$_{ar}$ 1274, 1268; (C-H) 1109, 1006; (C-H) 970, 924, 745, 621.

2.3.2. Stepwise *O*-demethylation attempts with different salts

Using conditions in 2.3.1., other salts were used: $Zn(ClO_4)_2\cdot 6H_2O$ (14.9 mg, 0.04 mmol), $NaBF_4$ (4.4 mg, 0.04 mmol), $NaPF_6$ (6.7 mg, 0.04 mmol) and $MnCl_2$ (5.0 mg, 0.04 mmol). The isolated products were analyzed by mass spectrometry, which showed that a demethylated product (**C2**/**C3** complex) was obtained when $Zn(ClO_4)_2\cdot 6H_2O$ was used. In contrast, reaction with $NaBF_4$, $NaPF_6$ and $MnCl_2$ resulted in formation of non-demethylated complex. Furthermore, the reaction with $NaClO_4\cdot H_2O$ but in the absence of visible light also resulted in the formation of a non-demethylated product. The obtained products were not further analyzed, due to the receipt of products identical to Section 2.3.1.

C1+$Zn(ClO_4)_2\cdot 6H_2O$ ESI-MS (+) m/z (%) = 341 (100) [(L1)+H]$^+$; 728 (60) [Cu(L1)((L1)-CH_3)]$^+$; 813 (10) [Cu_2((L1)-CH_3)$_2$Cl]$^+$. Yield: 89.9% (31.9 mg).

C1+$NaBF_4$ ESI-MS (+) m/z (%) = 341 (100) [(L1)+H]$^+$; 743 (30) [Cu(L1)((L1)-H)]$^+$. Yield: 86.6% (16.6 mg).

C1+ $NaPF_6$ ESI-MS (+) m/z (%) = 341 (100) [(L1)+H]$^+$; 743 (10) [Cu(L1)((L1)-H)]$^+$. Yield: 85.8% (15.9 mg).

C1+$MnCl_2$ HRMS (ESI) m/z; found: [Cu((L1)+H)Cl_2]$^+$ 473.3358; requires [Cu((L1)+H)Cl_2]$^+$ 473.3381 (4.8 ppm). Yield: 85.2% (15.9 mg).

2.3.3. One-pot *O*-demethylation attempts

Using a one-pot approach, following salts were used: $CuCl_2\cdot 2H_2O$, $NaClO_4\cdot H_2O$, $Mn(ClO_4)_2\cdot 6H_2O$ and $MnCl_2$. The ligand **L1** (13.3 mg, 0.04 mmol) was dissolved in three separate 50-ml flasks using MeCN as solvent. Then, $CuCl_2\cdot 2H_2O$ (6.8 mg, 0.04 mmol) was added to all three ligand solutions. To the first solution $NaClO_4\cdot H_2O$ (5.6 mg, 0.04 mmol) was added; to the second and to the third flasks $Mn(ClO_4)_2\cdot 6H_2O$ (14.5 mg, 0.04 mmol) and $MnCl_2$ (5.0 mg, 0.04 mmol) were added, respectively. The reactions were conducted at a 1:1:1 molar ratio (ligand:salt1:salt2) and stirred at room temperature for 48 hours. After completion, the reaction mixtures were concentrated to minimal volume using a rotary evaporator and the products were precipitated by the addition of the diethyl ether. The resulting green precipitates were collected by filtration using Büchner funnels, washed with diethyl ether and left to dry completely in a vacuum desiccator.

Mass spectrometry analysis did not reveal any signals from the demethylated systems, and any attempts to isolate it failed, yielding only the starting material (the **C1** complex).

L1+$CuCl_2\cdot 2H_2O$+$NaClO_4\cdot H_2O$ HRMS (ESI) m/z; found: [Cu((L1)+H)Cl_2]$^+$ 473.3417; requires [Cu((L1)+H)Cl_2]$^+$ 473.3381 (7.6 ppm). IR (KBr, cm^{-1}): (N-H) 3521, 3457; (C-H) 3024, 2947, 2833; (C=N)$_{imine}$ 1627; (C=C) 1608, 1505, 1467; (C-N) 1379; (C=N)$_{ar}$ 1286; (C-H) 1199, 1105, 1057; (C-H) 969, 908, 756, 665. Yield: 85.9% (17.2 mg).

L1+$CuCl_2\cdot 2H_2O$+$Mn(ClO_4)_2\cdot 6H_2O$ HRMS (ESI) m/z; found: [Cu((L1)+H)Cl_2]$^+$ 473.3368; requires [Cu((L1)+H)Cl_2]$^+$ 473.3381 (2.7 ppm). IR (KBr, cm^{-1}): (N-H) 3404; (C-H) 2941, 2836; (C=N)$_{imine}$ 1674; (C=C) 1593, 1498, 1463; (C-N) 1371; (C=N)$_{ar}$ 1291; (C-H) 1143, 1096, 1004; (C-H) 800, 750, 625. Yield: 84.4% (16.9 mg).

L1+$CuCl_2\cdot 2H_2O$+$MnCl_2$ HRMS (ESI) m/z; found: [Cu((L1)+H)Cl_2]$^+$ 473.3374; requires [Cu((L1)+H)Cl_2]$^+$ 473.3381 (1.5 ppm). IR (KBr, cm^{-1}): (N-H) 3429; (C-H) 3020, 2944, 2836; (C=N)$_{imine}$ 1626; (C=C) 1594, 1504; (C-N) 1378; (C=N)$_{ar}$ 1278; (C-H) 1102, 1060, 1008; (C-H) 972, 798, 750. Yield: 80.4% (16.1 mg).

Two separate experiments were also performed between ligand **L1** and $Cu(ClO_4)_2\cdot 6H_2O$ salt or $Cu(BF_4)_2$ salt, where no $CuCl_2\cdot 2H_2O$ is present in the system. Reaction was performed in the same manner as above, while maintaining the 1:1 molar ratio of the reagents. No demethylation products were isolated.

L1+$Cu(ClO_4)_2\cdot 6H_2O$ ESI-MS (+) m/z (%) = 341 (75) [L+H]$^+$; 363 (100) [L+Na]$^+$. ESI-MS (-) m/z (%) = 603 (25) [$CuL(ClO_4)_2$-H]$^-$

L1+$Cu(BF_4)_2$ ESI-MS (+) m/z (%) = 341 (100) [(L1)+H]$^+$. ESI-MS (-) m/z (%) = 577 (60) [Cu(L1)$(BF_4)_2$-H]$^-$.

2.4 *O*-demethylation attempts using ligand L2:

2.4.1 Synthesis and characterization of complex C4 based on ligand L2

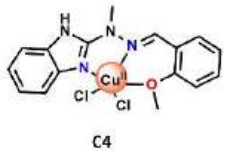

C4

Scheme 4. Schematic representation of complex **C4**, based on X-ray analysis.

Complex **C4** was synthesized by adding $CuCl_2 \cdot 2H_2O$ (30.7 mg, 0.18 mmol) to an acetonitrile solution of the ligand **L2** (50.0 mg, 0.18 mmol) at a molar ratio of 1:1 (ligand:metal). The reaction was carried out in the 50-ml flask for 48 hours at room temperature stirring all the time on a magnetic stirrer. After this time, the reaction mixture was concentrated on an evaporator to minimal volume; a solid was precipitated by addition of Et_2O. The resulting green precipitate was drained using a Büchner funnel, washed with Et_2O (10 ml in total) and left to dry completely in a vacuum desiccator. The crystallization by vial to vial diffusion at low temperature (4^0C) allowed to obtain crystal for complex **C4** proper for X-ray diffraction. CCDC deposit number: 2370350. Yield: 95.4% (71.2 mg, 0.17 mmol) based on ligand L2.

C4 [Cu(L2)Cl_2]: ESI-MS (+) m/z (%): 281 (100) $[(L2)+H]^+$; 343 (10) $[Cu(L2)-H]^+$; 378 (10) $[Cu(L2)Cl]^+$. Anal. calc.: C, 46.33; H, 3.89; N, 13.51; found: C, 46.23; H, 3.96; N, 13.56%. IR (KBr, cm^{-1}): (N-H) 3483; (C-H) 3103, 3003, 2950; $(C=N)_{imine}$ 1624; (C=C) 1601, 1591, 1498, 1466; (C-N) 1371; $(C=N)_{ar}$ 1238; (C-H) 1162, 1122,1046, 1007; (C-H) 970, 902, 827, 751, 611, 552.

2.4.2. Stepwise *O*-demethylation attempts

Using a stepwise method following the same synthetic procedure for complexes in 2.3.1 (instead of **C1** complex, **C4** complex was used), salts: $NaClO_4 \cdot H_2O$ (7.0 mg, 0.05 mmol), $Mn(ClO_4)_2 \cdot 6H_2O$ (18.1 mg, 0.05 mmol) and $MnCl_2$ (6.2 mg, 0.05 mmol) were used. Attempts to isolate it yielded only the complex **C4**, which was confirmed by mass analysis.

C4+$NaClO_4 \cdot H_2O$ ESI-MS (+) m/z (%): 281 (100) $[(L2)+H]^+$; 343 (10) $[Cu(L2)-H]^+$; 378 (30) $[Cu(L2)Cl]^+$. Yield: 96.0% (19.2 mg).

C4+$Mn(ClO_4)_2 \cdot 6H_2O$ ESI-MS (+) m/z (%): 281 (100) $[(L2)+H]^+$; 343 (10) $[Cu(L2)-H]^+$. Yield: 94.5% (18.9 mg).

C4+$MnCl_2$ ESI-MS (+) m/z (%): 281 (100) $[(L2)+H]^+$; 343 (10) $[Cu(L2)-H]^+$. Yield: 89.0% (17.8 mg).

2.5. *O*-demethylation attempts using ligand L3:

2.5.1 Synthesis and characterization of complex C5 based on ligand L3

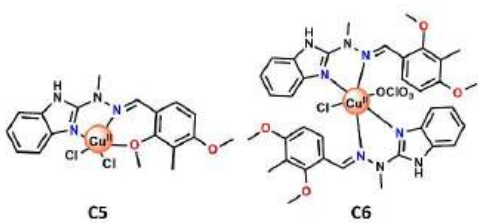

C5 C6

Scheme 5. Schematic representation of complexes **C5** and **C6**, based on X-ray analysis.

Complex **C5** was synthesized by adding $CuCl_2 \cdot 2H_2O$ (25.6 mg, 0.15 mmol) to an acetonitrile solution of the ligand **L3** (50.0 mg, 0.15 mmol) at a molar ratio of 1:1 (ligand:metal). The reaction was carried out in the 50-ml flask for 48 hours at room temperature stirring all the time on a magnetic stirrer. After this time, the reaction mixture was concentrated on an evaporator to minimal volume; a solid was precipitated by addition of Et_2O. The resulting green precipitate was drained using a Büchner funnel, washed with Et_2O (10 ml in total) and left to dry completely in a vacuum desiccator. The crystallization by vial to vial diffusion at low temperature (4^0C) allowed to obtain crystal for complex **C5** proper for X-ray diffraction. CCDC deposit number: 2370351. Yield: 97.2% (64.7 mg, 0.14 mmol) based on ligand **L3**.

C5 [Cu(L3)Cl_2]: ESI-MS (+) m/z (%): 325 (100) $[(L3)+H]^+$; 422 (70) $[Cu(L3)Cl]^+$. Anal. calc.: C, 48.47; H, 4.28; N, 11.90; found: C, 48.39; H, 4.24; N, 11.87%. IR (KBr, cm^{-1}): (N-H) 3404; (C-H) 2945, 2843; $(C=N)_{imine}$ 1674; (C=C) 1596, 1497, 1466; (C-N) 1374; $(C=N)_{ar}$ 1285; (C-H) 1125, 1095, 1004; (C-H) 800, 750, 628.

2.5.2 Stepwise *O*-demethylation attempts

Using a stepwise method following the same synthetic procedure for complexes in 2.3.1 (instead of **C1** complex, **C5** complex was used), salts: $NaClO_4 \cdot H_2O$ (7.0 mg, 0.05 mmol), $Mn(ClO_4)_2 \cdot 6H_2O$ (18.1 mg, 0.05 mmol) and $MnCl_2$ (6.2 mg, 0.05 mmol) were used.

Again, mass spectrometry analysis did not reveal any signals from demethylated systems. Isolation of complexes formed with $NaClO_4 \cdot H_2O$ and $MnCl_2$ salts yielded the complex **C5**. On the other hand, when the $Mn(ClO_4)_2 \cdot 6H_2O$ salt was used, a non-demethylated complex **C6** was obtained.

C5+$NaClO_4 \cdot H_2O$ ESI-MS (+) m/z (%): 325 (100) $[(L3)+H]^+$; 422 (20) $[Cu(L3)Cl]^+$. Yield: 92.0% (18.4 mg).

C5+$MnCl_2$ ESI-MS (+) m/z (%): 325 (100) $[(L3)+H]^+$; 422 (50) $[Cu(L3)Cl]^+$. Yield: 94.5% (18.9 mg).

C6 ESI-MS (+) m/z (%): 325 (100) $[(L3)+H]^+$; 711 (20) $[Cu(L3)_2\text{-}H)]^+$. Anal. calc.: C, 58.49; H, 5.31; N, 14.75; found: C, 58.38; H, 5.26; N, 14.79%. IR (KBr, cm^{-1}): (N-H) 3446; (C-H) 3209, 2936, 2836; $(C=N)_{imine}$ 1635; (C=C) 1600, 1482, 1463; (C-N) 1374; $(C=N)_{ar}$ 1272; (C-H) 1199, 1091, 1004; (C-H) 968, 810, 756, 620. Yield: 88.7% (37.6 mg). CCDC deposit number: 2370352.

2.6. X-ray crystallography

Diffraction data were collected by the ω-scan technique, for **L1** and **C5**: using graphite-monochromated MoK_α radiation (λ=0.71073 Å), at 100(1) on Rigaku XCalibur four-circle diffractometer with EOS CCD detector and for **L2**, **C2**, **C3**, **C4** and **C6** at 130(1) K, with mirror-monochromated CuK_α radiation (λ=1.54178 Å), at 100(1) on Rigaku SuperNova four-circle diffractometer with Atlas CCD detector. The data were corrected for Lorentz-polarization as well as for absorption effects[47]. Precise unit-cell parameters were determined by a least-squares fit of the reflections of the highest intensity, chosen from the whole experiment. The structures were solved with SHELXT[48]

View Article Online DOI: 10.1039/D5NJ04478B

and refined with the full-matrix least-squares procedure on F^2 by SHELXL[49]. All non-hydrogen atoms were refined anisotropically. Hydrogen atoms bonded to N atoms were refined freely with isotropic displacement parameters; all other hydrogen atoms were placed in idealized positions and refined as 'riding model' with isotropic displacement parameters set at 1.2 (1.5 for CH_3) times U_{eq} of appropriate carrier atoms. The crystals of **C4** were of relatively poor quality, resulting in high R values and low data completeness; however, the structure determination remains reliable. Crystallographic data for the structural analysis have been deposited with the Cambridge Crystallographic Data Centre. Copies of this information may be obtained free of charge from: The Director, CCDC, 12 Union Road, Cambridge, CB2 1EZ, UK; e-mail: deposit@ccdc.cam.ac.uk, or www.ccdc.cam.ac.uk.

2.7. Electrode activation

All measurements were performed in laboratory vessels that had been pre-washed with Piranha solution (persulfuric acid, Caro's acid). All test solutions were prepared at room temperature and deaerated with high-purity argon (99.998%) prior to measurement. An argon stream was maintained over the solution surface throughout the measurements to prevent oxygen ingress. For electrochemical experiments, a 0.1 M solution of $TBAClO_4$ in MeCN was used as the supporting electrolyte solution (SES). To prevent contamination of the gold working electrode with water or chloride ions during non-aqueous experiments, the saturated calomel electrode (SCE) was placed in a separate compartment filled with the same SES and connected to the working and counter electrodes via a porous frit. Prior to use, the gold electrode was polished with aluminum slurries of successively decreasing final grades (down to 0.05 µm, Buehler) on polishing cloths (Buehler) and subsequently rinsed with water and acetone, respectively. The electrode was then electrochemically activated by cycling in the potential range between E = -0.8 V and E = 0.6 V vs SCE at dE/dt = 0.1 Vs^{-1} in 0.5 M sodium hydroxide until a stable cyclic voltammogram was obtained. This procedure avoids structural changes on the gold surface[50]. After activation, the electrode was rinsed with water and acetone, dried under an argon stream and was stored in an empty tube at room temperature.

2.8. Computational Methods

To propose a mechanism that could justify the experimental data, simulations were performed using Density Functional Theory (DFT). All calculations were carried out using the Gaussian 16 software package. The exploration of transition state (TS) geometries is crucial for elucidating chemical reaction mechanisms and accurately modeling their kinetics. A TS represents a transient molecular configuration at the peak of the energy barrier that reactants must traverse along the minimum energy path to form products, corresponding to the saddle point on the potential energy surface (PES).

An initial series of simulations was conducted to determine the transition state geometry of complex **C1** in interaction with nucleophiles, including perchlorate (as a representative weakly coordinating anions), hydroxide, and water. The initial geometry of the complex was based on the crystallographic structure, where the methyl group covalently bonded to the oxygen atom O1 was constrained to a planar arrangement. The nucleophiles were positioned on the opposite side to explore their approach and interaction with the metal center (Scheme 6).

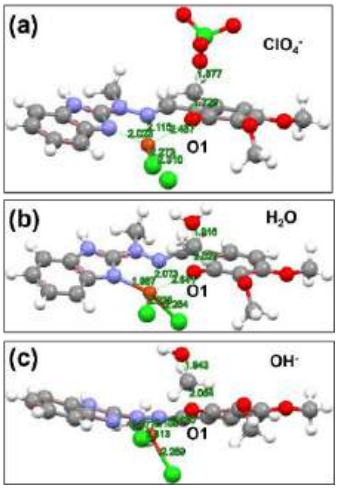

Scheme 6. Initial geometry schemes of **C1** complex used for simulations with (a) ClO_4^-, (b) H_2O and (c) OH^- as the nucleophile source; Me is shown in its planar form.

In the initial step of the procedure, the Berny algorithm was employed in combination with frequency calculations to optimize the TS guess to the saddle point of the PES by utilizing local surface information, including atomic forces and the Hessian matrix [51]. In the second step, the reaction pathway was traced from the TS to the products and reactants using the Intrinsic Reaction Coordinate (IRC) method, which assumes that the initial geometry is a reasonable approximation of the TS[52, 53]. The aforementioned calculations were performed using the cc-PVTZ basis set together with the doubly hybrid functional B2PLYP, which combines exact HF exchange with MP2-like correlation for an accurate description of interactions[54]. To support the results obtained from the IRC simulations, G3 high-level calculations were conducted. This method is commonly used to determine thermodynamic quantities by integrating multiple computational steps. In order to reduce the computational cost we have replaced MP4 calculations with MP2 in the steps 4 and 5 (G3MP2)[55, 56]. All calculations, including G3, were carried out in implicit acetonitrile solvent using the Conductor-like Polarizable Continuum Model (CPCM).

3. Results and discussion

3.1. Discovery and Optimization of Cu(II)-Mediated *O*-Demethylation with Ligand L1

The imine-based ligand **L1**, bearing three methoxy substituents on the aromatic ring, was designed as part of a broader effort to explore oxidative demethylation in copper(II) coordination systems. Its structure, derived from the condensation of 2-(1-methylhydrazinyl)-1H-benzo[d]imidazole[21] **B** with 2,3,4-trimethoxybenzaldehyde, positions electron-donating groups in

View Article Online
DOI: 10.1039/D5NJ04478B

both the *ortho* and *para* positions relative to the imine linkage, potentially activating the C–O–CH_3 bonds toward cleavage under mild oxidative conditions (Scheme S1). Upon complexation of **L1** with $CuCl_2{\cdot}2H_2O$, we observed the formation of a mononuclear precursor complex **C1**, with the formula [Cu(**L1**)Cl_2]. Upon treatment with $NaClO_4{\cdot}H_2O$, the selective *O*-demethylation of the *ortho* methoxy group was observed, yielding complex **C2** [Cu((**L1**)-CH_3)Cl], while the remaining two methoxy groups remained intact. This transformation was initially supported by ESI-MS analysis which revealed characteristic m/z signals corresponding to $[Cu((\mathbf{L1})\text{-}CH_3)(MeOH)]^+$ and $[Cu((\mathbf{L1})\text{-}CH_3)Cl(MeOH)+H]^+$, and was later unambiguously confirmed by single-crystal X-ray analysis of **C2** upon its isolation (see Sections 2.3.1 and 3.3).

Intrigued by this selective transformation, we expanded our study to explore the factors influencing the *O*-demethylation process. When $Mn(ClO_4)_2{\cdot}6H_2O$ was used instead of $NaClO_4{\cdot}H_2O$, the reaction similarly yielded a demethylated product, but this time as a dinuclear complex **C3** with the formula $[Cu_2((\mathbf{L1})\text{-}CH_3)_2Cl(MeOH)]ClO_4$ (see Section 2.3.1 ESI: m/z $[Cu_2((\mathbf{L1})\text{-}CH_3)_2(MeO)]^+$ and $[Cu_2((\mathbf{L1})\text{-}CH_3)_2Cl(MeOH)]^+$ and Section 3.3 for X-ray analysis) was isolated. Reaction with $Zn(ClO_4)_2{\cdot}6H_2O$ also proved the demethylation takes place irrespectively of the chosen cation. Conversely, using manganese chloride $MnCl_2$ salt under identical conditions retrieved the starting material **C1**, indicating that the perchlorate anion together with water molecules are essential for *O*-demethylation, while the identity of the metal ion does not significantly affect the outcome. Interestingly, the presence of other weakly coordinating anions such as BF_4^- and PF_6^- does not lead to demethylation. The reaction also does not proceed under anaerobic conditions, suggesting that molecular oxygen plays a key role, likely through its reduction to H_2O or hydroxide OH^- anions (see Section 3.6.). Intriguingly, the reaction is completely suppressed when MeCN is replaced with protic polar solvents such as MeOH or EtOH (see Section 3.4.), highlighting the critical influence of the reaction medium. Finally, to evaluate the influence of synthetic methodology, we compared the stepwise approach with a one-pot protocol. In the one-pot reactions, $CuCl_2{\cdot}2H_2O$ was combined directly with **L1** and either $NaClO_4{\cdot}H_2O$ or $Mn(ClO_4)_2{\cdot}6H_2O$. Although these reactions yielded the **C1** complex, no demethylation was observed. Additional series of one-pot reactions was carried out using the other screening agents described above, and in each case, **C1** was consistently isolated in high yields (80-86%), as confirmed by ESI-MS and FT-IR analyses (See Section 2.3.3, Fig S17). Use of other Cu(II) salts e.g. $Cu(BF_4)_2$ or $Cu(ClO_4)_2{\cdot}6H_2O$ without $CuCl_2{\cdot}2H_2O$ also does not lead to demethylated product. These results clearly indicate that demethylation occurs exclusively via the stepwise route, with **C1** serving as necessary intermediate for subsequent *O*-demethylation (Scheme 7). The stepwise approach is essential because the preformed Cu–imine complex C1 is structurally organized, allowing effective interaction with perchlorate anions and water molecules to promote selective cleavage of the methoxy group. In contrast, one-pot reactions, where complex formation and demethylation occur simultaneously, do not provide full preorganization of the metal center and fail to produce the demethylated product.

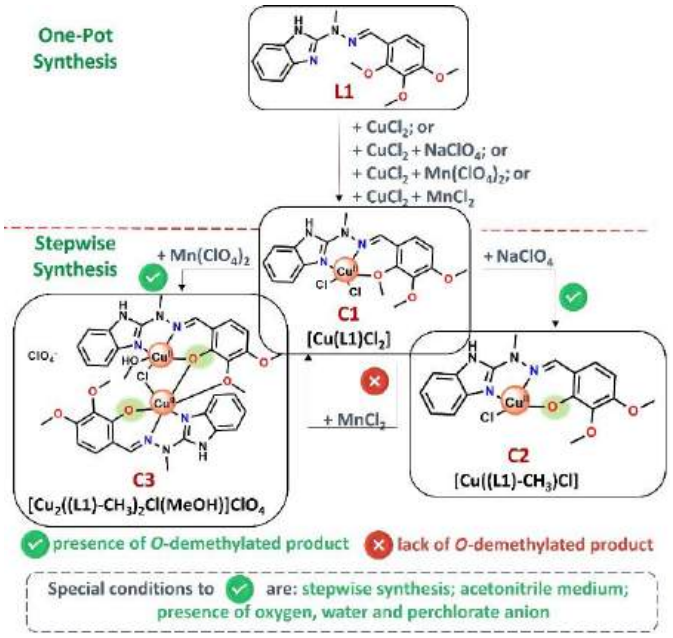

Scheme 7. Schematic representation of the synthetic procedure for Cu(II) complexes **C1**, **C2** and **C3** based on stepwise and one-pot synthesis. Please note that the replacement of Cu^{2+} by Mn^{2+} or Na^+ is not favorable either thermodynamically or kinetically. Therefore, the metal center of the complex remains copper, and the use of various perchlorate salts serves only as a source of ClO_4^- anions, not as metal precursors.

Overall, these findings reveal that *O*-demethylation in Cu(II) complexes proceeded under mild conditions in the presence of perchlorate and water, and does not require strong oxidants like *t*-BuOOH, as seen in prior studies[9, 10]. This represents the first documented example of *O*-demethylation mediated by Cu(II) ions, prompting us to synthesize a series of related imine-based ligands to better define the scope and limitations of this transformation.

3.2. Probing Structure–Reactivity Relationships Using Ligands L2 and L3

To investigate how methoxy group distribution influences the *O*-demethylation process, two additional imine ligands were synthesized: **L2**, containing a single methoxy group in the *ortho*, and **L3**, bearing two methoxy substituents in the *ortho* and *para* positions, along with a methyl group in a *meta* position (Scheme S1). Both ligands were prepared *via* the same two-step route used for **L1**, involving condensation with the appropriately substituted benzaldehydes, and were obtained in 86% (**L2**) and 78% (**L3**) yields. The composition and spectroscopic purity of the compounds were assessed by ^1H NMR (Figs. S3, S5, S7) and ^{13}C NMR (Figs. S4, S6) spectroscopy, confirming the absence of residual starting materials or detectable impurities; notable differences in the aromatic regions attributable to the varying electronic effects of the substituents.

Each ligand was subjected to the stepwise method; first coordinated with $CuCl_2{\cdot}2H_2O$ to form the corresponding mononuclear Cu(II) complexes: **C4** [Cu(**L2**)Cl_2] and **C5** [Cu(**L3**)Cl_2]. These were then subjected to established

View Article Online
DOI: 10.1039/D5NJ04798

demethylation protocol using $NaClO_4 \cdot H_2O$ and $Mn(ClO_4)_2 \cdot 6H_2O$, however no *O*-demethylation was observed in either case (See Section 2.4 and 2.5, Schemes S2 and S3). Interestingly, for **L3**, a non-demethylated complex **C6** [Cu(**L3**)$_2$Cl(ClO_4)]MeOH was isolated, which can be compared to the demethylated bimetallic **C3** complex due to the existence of mixed counterions. Single crystal X-ray diffraction analysis was successfully performed for ligands **L1** and **L2** as well as for complexes **C2**-**C6**, confirming the proposed structures and coordination geometries (see Section 3.3). These results suggest that while the spatial proximity of methoxy group in **L1** is important for enabling the demethylation, it is not the sole determining factor. The lack of reactivity in **L2** and **L3** suggests that insufficient electronic activation or suboptimal orbital alignment in these systems likely hinders C-O bond cleavage under the same conditions.

3.3. X-ray Crystallographic Analysis of Ligands and Complexes

Perspective views of ligands **L1** and **L2** (in the form of protonated salts) are shown in Figures 1a and 1b (see also the schematic representation in Scheme S1), and those of the corresponding Cu(II) complexes are presented in Figures 1c-1g.

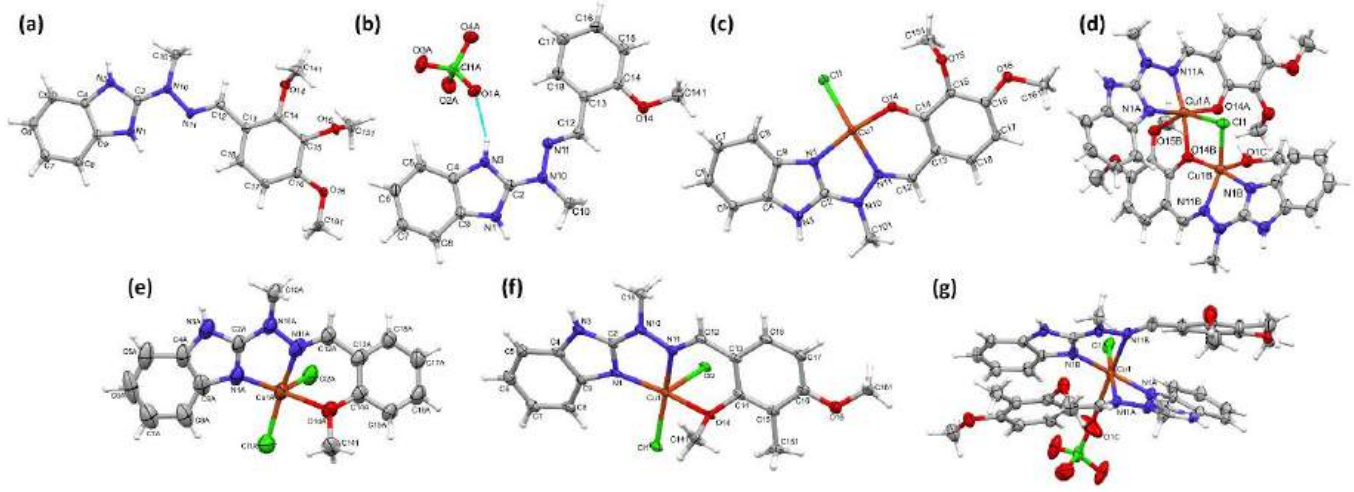

Fig. 1. Perspective views of: (a) cation of ligand **L1**, (b) cation of ligand **L2**, (c) complex **C2**, (d) the cation of complex **C3**, (e) neutral complex **C4**, (f) neutral complex **C5** and (g) neutral complex **C6**. Ellipsoids are drawn at the 50% probability level; hydrogen atoms are represented as spheres of arbitrary radii.

The molecular conformations of ligand cations **L1** and **L2** are nearly planar, with small dihedral angles between the benzimidazole and methoxy-substituted phenyl ring planes: 12.59(7)° for **L1** and 2.34(10)° for **L2**. Both ligands are protonated at the ring nitrogen atom, as confirmed by electron density maps. All NH groups are involved in hydrogen bonding with perchlorate anions, forming infinite chains along the y-axis (Fig. S18) and acting as principal supramolecular motifs. Relevant hydrogen-bonding parameters are listed in Table S2.

In complex **C2** [Cu((**L1**)-CH_3)Cl], the copper(II) center adopts a distorted square-planar geometry, coordinated by two nitrogen atoms and demethylated phenoxide anion from the ligand, along with chloride anion. The Cl^- ligand is displaced 0.78 Å out of the mean plane formed by the remaining donors, contributing to the distortion. Notably, the NH group forms an unexpectedly strong hydrogen bond with the methoxy oxygen, organizing the molecules into infinite chains along the y-axis. Key bond lengths and angles are reported in Table S3.

Complex cation in **C3** adopts a dinuclear structure, [Cu_2((**L1**)-CH_3)$_2$Cl(MeOH)] and unambiguously confirms the *O*-demethylation of the *ortho* methoxy group of **L1**-CH_3. Here, it bridges both Cu(II) centers together with the chloride anion. The perchlorate anion remains uncoordinated and resides in the outer coordination sphere. The two copper(II) centers have distinct coordination environments. Cu1A is six-coordinated and exhibits a distorted octahedral geometry. It is bound to two nitrogen atoms and one phenoxide oxygen from **L1**-CH_3 and to two additional oxygen atoms (from a *meta*-methoxy group and a second phenoxide from another **L1**-CH_3), as well as one chloride anion. Two of these bonds are significantly elongated, giving the appearance of a pseudo-square-planar core with weak axial interactions. Cu1B is five-coordinated, adopting a distorted square-pyramidal geometry. It is coordinated by two nitrogen atoms and one phenoxide anion from **L1**-CH_3, one chloride anion as well as one MeOH solvent molecule. The crystal structure comprises two cations, two perchlorate anions, and four MeOH solvent molecules, forming a complex supramolecular assembly (Fig. S19).

The crystal structure of complex **C4** contains two symmetry-independent but nearly identical molecules of **C4** [Cu(**L2**)Cl_2]. In both, Cu(II) ion is five coordinated (N1, N11 and O14 from the ligand and two Cl^- anions). Interestingly, the Cu-O bonds lengths exceed the Cu-Cl bond lengths, indicating relatively weak Cu-O interactions. The geometry lies between square pyramidal and trigonal bipyramidal, τ_5 values of 0.55 and 0.60 for molecules A and B, respectively. N–H···Cl hydrogen bonds form centrosymmetric AA and BB dimers, with the Cl atom involved in the longer Cu–Cl bond acting as the acceptor. In complex **C5** [Cu(**L3**)Cl_2], the Cu(II) center is also five-coordinated, involving two nitrogen atoms and an *ortho*-methoxy oxygen from the ligand, along with two Cl^- ligands. Unlike **C4**, the Cu–O bond is shorter than the Cu–Cl bonds, and

the coordination geometry is closer to square pyramidal (τ_5 = 0.30). N–H···Cl hydrogen bonding organizes the molecules into infinite chains along the y-axis. This suggests that the electron density on the aldehyde-derived aromatic ring plays a key role for the *O*-demethylation reaction.

Complex **C6**, formulated as [Cu(**L3**)$_2$(Cl)(ClO$_4$)]·MeOH, is the only one that forms the 1:2 (Cu(II):ligand) type system. The coordination environment around the Cu(II) center is particularly interesting. The metal ion forms strong bonds with three nitrogen atoms: N1A, N11A, N1B, and chloride anion Cl1$^-$. In addition, it interacts more weakly with N11B and one oxygen atom from the perchlorate anion. Although these latter contacts are longer, they still fall within the sum of van der Waals radii (Table S3), allowing them to be considered part of the coordination sphere. Taking all six interactions into account, the geometry can be described as distorted octahedral. A hydrogen-bonding network—also involving the methanol solvent—organizes the molecules into chains along the z-direction.

The demethylated nature of **C2** and **C3** was unequivocally confirmed by X-ray crystallography, validating the structural impact of the perchlorate-mediated transformation within the electron rich **L1** scaffold. These findings established **C1** as a key intermediate, with **C2** serving as the primary reference point for mechanistic investigations.

3.4. UV-Vis Spectroscopy: Solvent Effects and Titration Studies

UV-Vis spectra were recorded for ligand **L1** and its Cu(II) complexes **C1**, **C2**, and **C3**, all obtained via stepwise synthesis in acetonitrile at a concentration of 0.02 mM. The spectra confirmed the stability of the complexes in solution, with no decoordination or degradation of the imine ligand **L1** (Fig. 2a). Similar experiments with **L2** and **L3** ligands and their complexes **C4**-**C6** confirmed the absence of demethylated products (Fig. S20). The spectra of **L1** and its complexes exhibited well-defined bands with maxima in the 295–365 nm range, typical of Cu(II) complexes with imine coordination[57, 58] These maxima shifted toward shorter wavelengths: **L1** (339 nm), **C1** (337 nm), and demethylated complexes **C2** (331 nm) and **C3** (327 nm). Additionally, the peak splitting pattern around 400 nm for **C2** and **C3** indicates the presence of phenoxide [59, 60] further confirming the formation of *O*-demethylated products in acetonitrile solution.

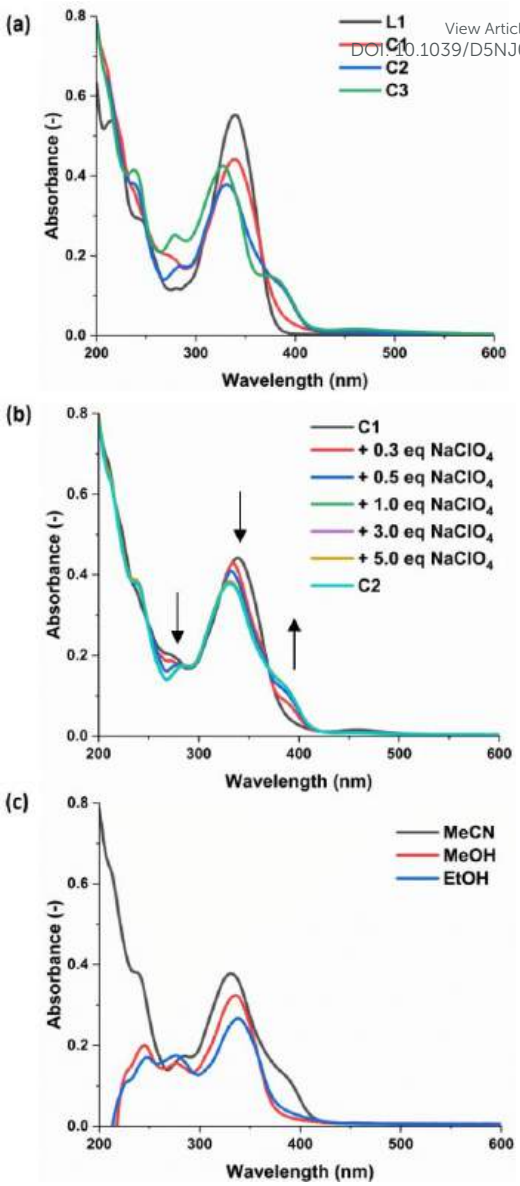

Fig. 2. (a) UV-Vis spectra of ligand **L1** and Cu(II) complexes **C1, C2, C3** recorded in MeCN at c = 0.02 mM. (b) Spectrophotometric titration of complex **C1** (c = 0.02 mM) with increasing amount of NaClO$_4$ and UV-Vis spectra of complex **C2** (c = 0.02 mM). Measurements recorded in MeCN. (c) UV-Vis spectra of complex **C2** recorded in MeCN, MeOH and EtOH at c = 0.02 mM.

To further monitor the *O*-demethylation process, a spectrophotometric titration of **C1** with increasing amounts of NaClO$_4$ in acetonitrile was performed (Fig. 2b). Absorbance spectra were recorded at room temperature after each incremental addition of NaClO$_4$ (from 0.3 to 5.0 equivalents). Upon adding 1.0 equivalent of NaClO$_4$, the intensity of the band in the 375–415 nm range increased, while the bands in the 260–285 nm and 295–365 nm regions decreased. After this point, no further spectral changes were observed, indicating that 1.0 equivalent of NaClO$_4$ is sufficient to form **C2**. This is consistent with the synthesis procedure, and the spectrum of **C2** under the same conditions further confirms this result.

To investigate the effect of solvent type on the product structure, UV-Vis spectra of **C2** were recorded in both aprotic

View Article Online
DOI: 10.1039/D5NJ04478B

(MeCN) and protic (MeOH and EtOH) solvents (Fig. 2c). In all solvents, a band in the 295–365 nm range was observed. However, the spectra recorded in protic solvents showed bathochromic shifts, with maxima at 336 nm for MeOH and 337 nm for EtOH, compared to 331 nm in MeCN. In acetonitrile, an additional band appeared in the 375–415 nm range, likely an indicator of the *O*-demethylation process. The bathochromic shifts observed in MeOH and EtOH, alongside the absence of the additional band, suggest that these solvents are less favorable for observing the *O*-demethylation process. The increase in absorbance in acetonitrile compared to protic solvents further suggests that acetonitrile, as an aprotic solvent, is optimal for studying the *O*-demethylation process.

3.5. Electrochemical Studies: Redox Behavior and Insights into *O*-Demethylation

The electrochemical properties of ligand **L1** and its Cu(II) complexes **C1** and **C2** were studied to gain insights into their redox behavior. Cyclic voltammograms (CVs) were recorded in deaerated acetonitrile containing 0.1 M $TBAClO_4$, within a potential range of -1.30 V to 1.45 V vs SCE (Fig. 3). For 0.1 mM **L1**, three oxidative peaks were observed (Fig. 3a): the first at E = 0.25 V, the second at E = 0.85 V, and the third at E = 1.15 V. Notably, these anodic peaks are irreversible, as they are not accompanied by cathodic counterparts, indicating that the oxidation processes in the system are irreversible in nature. The first oxidation peak, occurring at 0.25 V, is associated with the oxidation of the imine bond in **L1**, confirming the significant influence of the R-N-N=C-R groups on the redox processes in the molecule[61, 62]. The remaining two oxidation peaks likely correspond to the oxidation of the ligand methoxy groups[63, 64]. The benzimidazole group in the ligand does not affect the oxidation or reduction processes, as also reported in the literature[62].

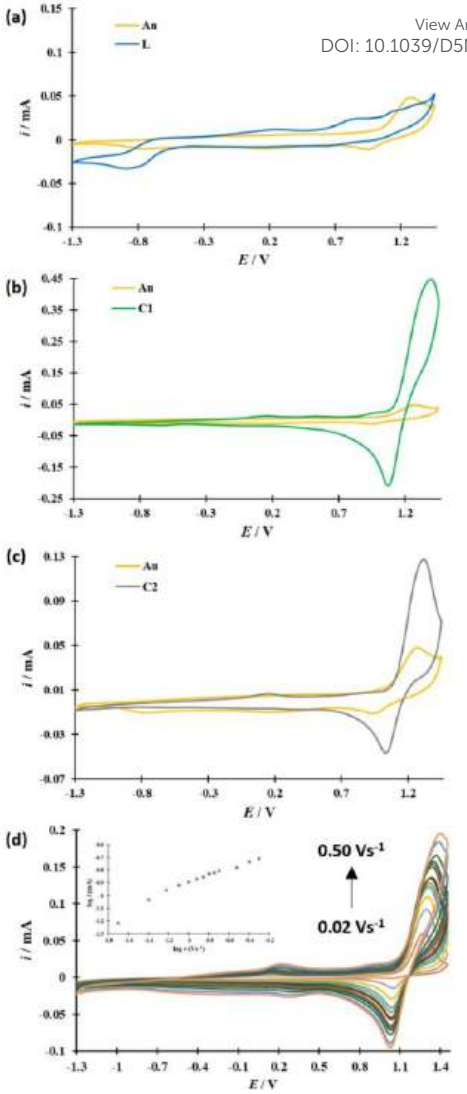

Fig. 3. (a) The cyclic voltammograms of the gold electrode (yellow) in MeCN with 0.1 M $TBAClO_4$ and 0.1 mM L1 (blue), dE/dt = 0.1 Vs-1. (b) Cyclic voltammograms of the gold electrode (yellow) in MeCN with 0.1 M $TBAClO_4$ and 0.1 mM C1 (green), dE/dt = 0.1 Vs-1. (c) Cyclic voltammograms of the gold electrode (yellow) in MeCN with 0.1 M TBAClO4 and 0.1 mM **C2** (grey), dE/dt = 0.1 Vs-1. (d) Cyclic voltammograms of **C2** in MeCN with 0.1 M $TBAClO_4$ at varying scan rates from 0.02 to 0.50 Vs^{-1}. Insert: log i_p vs log v.

For the Cu(II) complexes, the cyclic voltammograms reveal significant changes in the redox behavior after complexation. For **C1** (Fig. 3b), three irreversible anodic peaks are observed at 0.15 V, 0.53 V, and 0.98 V, with an additional quasi-reversible oxidation/reduction peak at 1.40 V and 1.08 V (ΔE = 320 mV). For **C2** (Fig. 3c), two irreversible anodic peaks are observed at 0.15 V and 0.90 V, along with a quasi-reversible peak at 1.32 V and 1.05 V (ΔE = 270 mV). These quasi-reversible peaks are indicative of the oxidation/reduction of the metal center in the complexes[65]. Specifically, the anodic peaks at 1.40 V for **C1** and 1.32 V for **C2** is attributed to the $Cu^{+} \rightarrow Cu^{2+} + e^{-}$ oxidation process, while the cathodic peaks at 1.08 V for **C1** and 1.05 V for **C2** correspond to the reduction of $Cu^{2+} + e^{-} \rightarrow Cu^{+}$.

The shift in oxidation peak potentials between **L1**, **C1**, and **C2** indicates that the oxidation processes are largely due to the same ligand moieties, with the complexation affecting the

View Article Online
DOI: 10.1039/D5NJ04478B

oxidation potentials. The current intensities for **C2** are lower than for **C1**, suggesting a lower electrochemical activity in **C2**. Additionally, the absence of one irreversible anodic peak in **C2** compared to **C1** allows the assignment of the 0.53 V anodic peak to the *ortho*-localized OMe group. The scan rate also affects the electrochemical behavior. For **C2**, cyclic voltammograms were recorded at scan rates ranging from 0.02 V/s to 0.50 V/s (Fig. 3d). The oxidation peak potentials shift positively with increasing scan rate, while the reduction peak potentials shift negatively, consistent with irreversible redox processes. For anodic peaks, a change of the scan rate had no effect on the shape of cyclic voltammetry. Notably, a broad cathodic peak appears at higher scan rates (0.50 V/s) in the range of 0.48 V to 0.10 V, which could indicate reversible oxidation/reduction processes (couple of peaks for 0.50 Vs^{-1} at $E = 0.23$ V and at $E = 0.27$ V vs SCE, ΔE_p = 40 mV), possibly related to the imine group oxidation/reduction[61, 62, 66]. Finally, electrochemical kinetics studies revealed a linear relationship between peak current (i_p) and the square root of scan rate ($v^{1/2}$), suggesting a diffusion-controlled process for the anodic oxidation of copper (Fig. S21). The slope of d log i_p/d log v was found to be less than 0.5, indicating a mixed diffusion-adsorption process, typical of electrode reactions involving both diffusion and adsorption[67, 68].

3.6. Proposed mechanism of *O*-demethylation

Several examples of oxidative *O*-demethylation reactions involving strong oxidants have been reported in the literature. These studies generally propose that the reactions proceed through the formation of a metastable intermediate containing a metal-oxygen-oxygen (M-O-O) bond, which subsequently attacks the C-O bond of the R-O-CH_3 group. This leads to the cleavage of the C-O bond, resulting in formation of the demethylated ligand and the corresponding aldehyde as a by-product[9, 10]. Such transformations were usually based on redox active metal ions such as Co(II/III) and Fe(II/III), but the use of Cu(II) has not been yet demonstrated.

In our work, the Cu^{2+} copper ion from the complex **C1** undergoes a redox reaction with imine under conditions of visible light at room temperature (reaction in the absence of visible light prevented the demethylation), leading to the reduction of the Cu^{2+} ion to Cu^{+} and the formation of the radical form of imine $N^{+\cdot}$(Scheme 8). As a result of this reaction, products are formed which can subsequently react with oxygen or water, leading to the formation of hydroxide ions (see Scheme S4): : (i) 4 Cu^{+} + O_2 + 2 H_2O → 4 Cu^{2+} +4 OH^{-}; (ii) 2 R^1-$N^{+\cdot}$-R^2 + O_2 + 2 H_2O → 2 R^1-N=R^2 + 4 OH^{-}. In these reactions, oxygen acts as a strong oxidizing agent, accepting electrons from Cu^{+} (i) or from the reduced form of imine (ii). In the presence of water, the redox reaction shifts the equilibrium towards the release of OH^{-}, i.e., an alkaline effect [69]. Furthermore, in the presence of oxygen, the Cu^{+} ion oxidizes to Cu^{2+}, confirming the catalytic role of copper ions. Oxygen is also responsible for the regeneration of the oxidizing agent, which re-oxidizes Cu^{+} to Cu^{2+}, closing the redox cycle[70, 71].

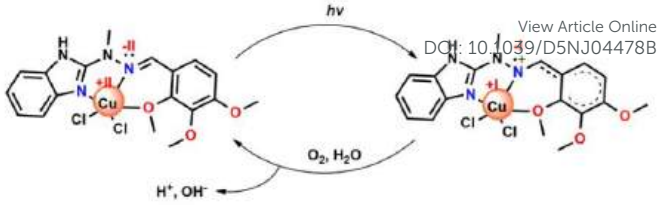

Scheme 8. Schematic representation of the redox reaction of copper(II) ions with imine based on complex **C1**.

To determine the stages of the *O*-demethylation reaction mechanism, we used DFT computations. Based on the experimental findings, it was observed that the ClO_4^- anion alone is insufficient to dissociate the methyl group from oxygen O1. Consequently, the addition of only the weakly coordinating anion does not lead to demethylation (see Scheme 6). However, its presence is crucial for the reaction to occur, since other anions did not produce the desired product. Importantly, the coordination of Cu(II) to the ligand weakens the R-O-CH_3 bond, and a greater number of adjacent methoxy groups enhance this effect, activating the process. Additionally, the reaction is carried out in acetonitrile solvent, which contains significant amounts of water if not anhydrous (reaction with anhydrous MeCN and molecular sieves prevented the reaction). Therefore, the potential impact of water molecules, along with OH^- species (formed as a result of the Cu(II)/Cu(I) redox cycle), was considered in our mechanistic model. Specifically, the OH^- ion can covalently bind to the methyl group, facilitating its detachment from the partially protonated O1 oxygen. The geometries and energy values obtained from the Intrinsic Reaction Coordinate (IRC) method are shown in Figure 4.

The most stable geometry corresponds to the configuration in which the CH_3OH molecule is detached from the complex. This results in Gibbs free energy difference of -0.022 Hartree (approximately -14.19 kcal/mol) between the demethylated complex and **C1**. When considering water as a nucleophile, the reaction pathway indicates that demethylation is disfavored, though the energy difference between the two resulting structures is minimal so it is possible (ΔE = +8.42 kcal/mol, see Figure S22). In contrast, protonation of the oxygens does not result in any structural changes when the perchlorate anion is considered as the nucleophile. As shown in Figure S23, the methylated form remains the most stable, and no potential structure is observed where the perchlorate anion binds to the methyl group, leading to its detachment from the complex. This supports the idea that **C1** is more stable than the **C2** demethylated complex by 14.38 kcal/mol. To further validate these findings, we calculated the relative free energy values for the following reactions using G3 calculations:

$C_{18}H_{20}Cl_2CuN_4O_3$ + OH^- → CH_3OH + $C_{17}H_{17}Cl_2CuN_4O_3^-$ (C2); ΔG = -15.04 kcal/mol

$C_{18}H_{20}Cl_2CuN_4O_3$ + H_2O → $CH_3OH_2^+$ + $C_{17}H_{17}Cl_2CuN_4O_3^-$ (C2); ΔG = +3.51 kcal/mol

$C_{18}H_{20}Cl_2CuN_4O_3$ + ClO_4^- → CH_3O-ClO_3 + $C_{17}H_{17}Cl_2CuN_4O_3^-$ (C2); ΔG = +13.29 kcal/mol

View Article Online
DOI: 10.1039/D5NJ04478B

These values are in strong agreement with the proposed mechanism (Scheme 9).

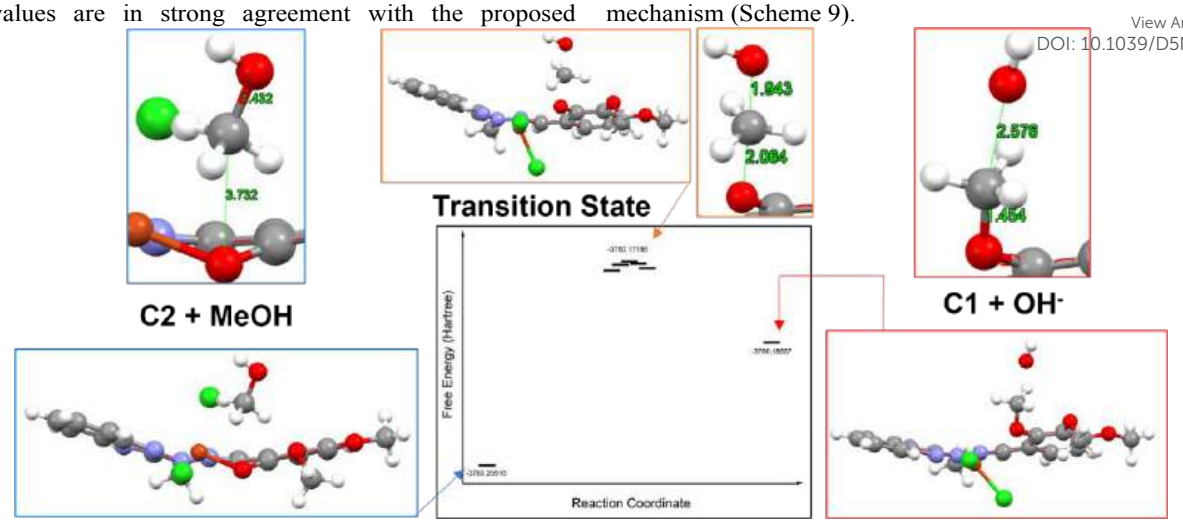

Fig. 4. Gibbs free energy profile for **C1** and the nucleophile OH^- (TS = transition state, measurement in Angstrom).

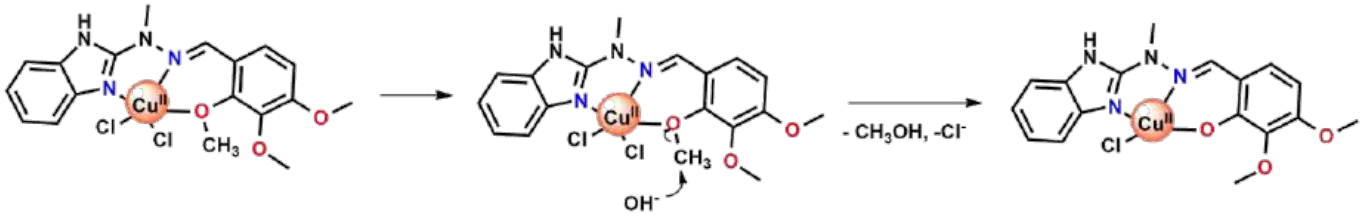

Scheme 9. Proposed mechanistic pathway of the *O*-demethylation of **C1** and the formation of **C2**.

This was also confirmed by calculations done on **C4**/**C5,** where energetic profile disfavored the studied organic transformation. Importantly, they also indicate that the OH^- group is the primary agent responsible for the demethylation process, while the contribution of the water molecule is less significant and the perchlorate anion does not act as agent directly responsible for the S_N2 process. However, the presence of the perchlorate ion is crucial, as it is a weakly coordinating and very weakly basic anion that increases the nucleophilicity of the OH^- ion in an aprotic environment such as acetonitrile[72]. If the reaction environment were polar, the OH^- ion would be strongly solvated, which would reduce its reactivity, which is why the reaction carried out in MeOH did not lead to *O*-demethylation. However, in the case of an aprotic environment and the presence of the ClO_4^- ion, the cation present, in the case of **C2**, Na^+, interacts with ClO_4^-, causing OH^- to be less solvated by the cations present in the solution. A higher proportion of free OH- anions increases the rate of the S_N2 reaction which is consistent with the proposed mechanism[73].

Conclusions

In this study, we present the first example of Cu(II)-mediated *O*-demethylation of C–O–C bonds in imine-based coordination compounds, achieved under mild, environmentally friendly conditions. Through detailed experimental optimization, we identified key parameters such as ligand backbone structure, synthetic method, salt type and solvent choice that significantly influence the reaction's efficiency. Notably, the results suggest that coordination of Cu(II) to the imine ligand plays a pivotal role in weakening the C–O bond, thereby enhancing the reactivity of the methoxy group. DFT calculations provided further mechanistic insights, demonstrating that unexpected nucleophilic S_N2 substitution via the hydroxide anion is responsible for the *O*-demethylation. This work provides a deeper understanding of the Cu(II)-mediated *O*-demethylation mechanism and opens the door for future studies and applications of Cu(II) complexes in biomimetic catalysis, particularly for sustainable processes such as lignin valorization and green chemical synthesis. The development of novel catalysts may enable their use in the catalytic demethylation of alkaloids and drugs and, more importantly, contribute to environmental protection by demethylating methoxy-containing pollutants, reducing their toxicity and persistence.

Author Contributions

Daria Nowicka: Investigation, Methodology, Conceptualization, Formal analysis, Data curation, Visualization, Writing – review & editing, Project administration, Funding acquisition. **Karol Garbaczewski:** Investigation, Formal analysis, Data curation. **Giuseppe Consiglio:** Investigation, Formal analysis, Data curation, Writing – review & editing. **Giuseppe Forte:** Investigation, Formal analysis, Data curation, Writing – review & editing. **Maciej Kubicki:** Formal analysis, Investigation, Data curation, Writing – review & editing, Visualization. **Teresa Łuczak:** Investigation, Methodology, Conceptualization, Formal

analysis, Data curation, Resources, Visualization, Writing – review & editing. **Violetta Patroniak:** Supervision, Resources, Writing – review & editing, Funding acquisition. **Adam Gorczyński:** Conceptualization, Investigation, Methodology, Formal analysis, Writing – review & editing, Project administration, Supervision, Resources, Funding acquisition.

Conflicts of interest

There are no conflicts to declare.

Acknowledgements

This research was financial supported by the National Science Centre, Poland (grant numbers UMO-2022/45/N/ST4/00632 (D.N.), UMO-2020/39/D/ST4/01182 (A.G.), UMO-2022/47/B/ST4/02310 (V.P.)) and by the Foundation for Polish Science (FNP). Daria Nowicka is a scholarship holder of the Adam Mickiewicz University in Poznan Foundation for the academic year 2023/2024. We express gratitude to Anna Orzechowska for help in synthesis of complexes. This work was also supported by the University of Catania, PIACERI 2020/2022, Linea di Intervento 2.

References

1. B. Miroslaw, *Int. J. Mol. Sci.*, 2020, **21**, 3493.
2. J.-N. Rebilly, B. Colasson, O. Bistri, D. Over and O. Reinaud, *Chem. Soc. Rev.*, 2015, **44**, 467-489.
3. J. Hagel and P. Facchini, *Front. Physiol.*, 2010, **1**.
4. S. C. Farrow and P. J. Facchini, *Front. Plant Sci.*, 2014, **5**.
5. S. Martinez and R. P. Hausinger, *J. Biol. Chem.*, 2015, **290**, 20702-20711.
6. E. Erickson, A. Bleem, E. Kuatsjah, A. Z. Werner, J. L. DuBois, J. E. McGeehan, L. D. Eltis and G. T. Beckham, *Nat. Catal.*, 2022, **5**, 86-98.
7. R.-Y. Liu, Z.-H. Liu, B.-Z. Li and Y.-J. Yuan, *Green Chem.*, 2024, **26**, 1770-1789.
8. J. E. Farnberger, N. Richter, K. Hiebler, S. Bierbaumer, M. Pickl, W. Skibar, F. Zepeck and W. Kroutil, *Commun. Chem.*, 2018, **1**, 82.
9. S. S. Anjana, B. Varghese and N. N. Murthy, *Dalton Trans.*, 2020, **49**, 3187-3197.
10. A. S. Suseelan, B. Varghese, P. Edamana and N. N. Murthy, *Eur. J. Inorg. Chem.*, 2018, **2018**, 972-980.
11. L. Benhamou, A. Machkour, O. Rotthaus, M. Lachkar, R. Welter and D. Mandon, *Inorg. Chem.*, 2009, **48**, 4777-4786.
12. H. R. Lucas, L. Li, A. A. N. Sarjeant, M. A. Vance, E. I. Solomon and K. D. Karlin, *J. Am. Chem. Soc.*, 2009, **131**, 3230-3245.
13. N. Chakraborty, J. Banerjee, P. Chakraborty, A. Banerjee, S. Chanda, K. Ray, K. Acharya and J. Sarkar, *Green Chem. Lett. Rev.*, 2022, **15**, 187-215.
14. S. Dutta and K. C. W. Wu, *Green Chem.*, 2014, **16**, 4615-4626.
15. S. Iravani, *Green Chem.*, 2011, **13**, 2638-2650.
16. N. Fujieda, K. Umakoshi, Y. Ochi, Y. Nishikawa, S. Yanagisawa, M. Kubo, G. Kurisu and S. Itoh, *Angew. Chem. Int. Ed. Engl.*, 2020, **59**, 13385-13390.
17. I. Kampatsikas, M. Pretzler and A. Rompel, *Angew. Chem. Int. Ed.*, 2020, **59**, 20940-20945. View Article Online DOI: 10.1039/D5NJ04478B
18. I. Kampatsikas and A. Rompel, *Chem. Bio. Chem.*, 2021, **22**, 1161-1175.
19. Y.-W. Lin, *Coord. Chem. Rev.*, 2021, **434**, 213774.
20. J.-Q. Lai, Z. Li, Y.-H. Lü and Z. Yang, *Green Chem.*, 2011, **13**, 1860-1868.
21. A. Bocian, M. Szymańska, D. Brykczyńska, M. Kubicki, M. Wałęsa-Chorab, G. N. Roviello, M. A. Fik-Jaskółka, A. Gorczyński and V. Patroniak, *Molecules*, 2019, **24**, 3173.
22. M. R. Maurya and A. Chauhan, *New J. Chem.*, 2023, **47**, 2858-2873.
23. S. Reja, D. Sarkar, K. Sarkar, D. Mukherjee, T. K. S. Fayaz, P. Sanphui and R. K. Das, *Inorganica Chim. Acta*, 2024, **560**, 121809.
24. D. Lakk-Bogáth, P. Török, M. Giorgi and J. Kaizer, *J. Mol. Struct.*, 2022, **1262**, 133100.
25. J. Kocábová, M. Sýs, J. Klikarová, M. Novák, M. Bártová, R. Jirásko, H. Tarábková, R. Sokolová and T. Mikysek, *Electrochim. Acta*, 2023, **463**, 142854.
26. C. Figueiredo, A. L. De Lacey and M. Pita, *Electrochem. Sci. Adv.*, 2022, **2**, e2100171.
27. H. Oshita and Y. Shimazaki, *Chem. – A Eur. J.*, 2020, **26**, 8324-8340.
28. M. Liao, C. Li, C. Hu and J. Ding, *Biochem. Biophys. Rep.*, 2023, **34**, 101466.
29. A. N. Hashmi, R. Ahmed Dharejo, U. B. Zubair, N. Khan, I. Kashif, M. Ajmal, R. Taj, R. Qamar and M. Azam, *Int. J. Neurosci.*, 1-9.
30. T. Litwin, A. Antos, J. Bembenek, A. Przybyłkowski, I. Kurkowska-Jastrzębska, M. Skowrońska and A. Członkowska, *Diagnostics (Basel, Switzerland)*, 2023, **13**.
31. Ł. Banach, D. Brykczyńska, A. Gorczyński, B. Wyrzykiewicz, M. Skrodzki and P. Pawluć, *Chem. Commun.*, 2022, **58**, 13763-13766.
32. A. Bocian, M. Skrodzki, M. Kubicki, A. Gorczyński, P. Pawluć and V. Patroniak, *Appl. Catal. A: General*, 2020, **602**, 117665.
33. V. K. Juyal, A. Pathak, M. Panwar, S. C. Thakuri, O. Prakash, A. Agrwal and V. Nand, *J. Organomet. Chem.*, 2023, **999**, 122825.
34. J. Rakhtshah, *Coord. Chem. Rev.*, 2022, **467**, 214614.
35. M. Skrodzki, V. Patroniak and P. Pawluć, *Org. Lett.*, 2021, **23**, 663-667.
36. S. Shahraki, *Colloids Surf. B: Biointerfaces*, 2022, **218**, 112727.
37. A. Gorczyński, D. Pakulski, M. Szymańska, M. Kubicki, K. Bułat, T. Łuczak and V. Patroniak, *Talanta*, 2016, **149**, 347-355.
38. A. Gorczyński, M. Kubicki, K. Szymkowiak, T. Łuczak and V. Patroniak, *RSC Adv.*, 2016, **6**, 101888-101899.
39. É. N. Oiye, M. F. M. Ribeiro, J. M. T. Katayama, M. C. Tadini, M. A. Balbino, I. C. Eleotério, J. Magalhães, A. S. Castro, R. S. M. Silva, J. W. da Cruz Júnior, E. R. Dockal and M. F. de Oliveira, *Crit. Rev. Anal. Chem.*, 2019, **49**, 488-509.
40. D. Marcinkowski, M. A. Fik, T. Łuczak, M. Kubicki and V. Patroniak, *Polyhedron*, 2018, **141**, 125-132.
41. D. Nowicka, M. Kubicki, V. Patroniak, T. Łuczak and A. Gorczyński, *Electrochim. Acta*, 2024, **476**, 143754.
42. D. Nowicka, K. Garbaczewski, T. Łuczak, G. Forte, G. Consiglio, M. Kubicki, V. Patroniak and A. Gorczyński, *Dalton Trans.*, 2025, **54**, 1000-1012.

43. R. Kumar, A. A. Singh, U. Kumar, P. Jain, A. K. Sharma, C. Kant and M. S. Haque Faizi, *J. Mol. Struct.*, 2023, **1294**, 136346.
44. T. Ashraf, B. Ali, H. Qayyum, M. S. Haroone and G. Shabbir, *Inorg. Chem. Commun.*, 2023, **150**, 110449.
45. S. Shekhar, A. M. Khan, S. Sharma, B. Sharma and A. Sarkar, *Emerg. Mater.*, 2022, **5**, 279-293.
46. E. Ewert, I. Pospieszna-Markiewicz, M. Szymańska, A. Kurkiewicz, A. Belter, M. Kubicki, V. Patroniak, M. A. Fik-Jaskółka and G. N. Roviello, *Molecules*, 2023, **28**.
47. *CrysAlis PRO (Version 1.171.38.41)*, 2015.
48. G. Sheldrick, *Acta Crystallogr. Sect. A*, 2015, **71**, 3-8.
49. G. M. Sheldrick, *Acta Crystallogr. Sect. C: Struct. Chem.*, 2015, **71**, 3-8.
50. T. Łuczak, *J. Appl. Electrochem.*, 2007, **37**, 461-466.
51. H. B. Schlegel, *J. Comput. Chem.*, 1982, **3**, 214-218.
52. L. Deng, T. Ziegler and L. Fan, *J. Chem. Phys.*, 1993, **99**, 3823-3835.
53. L. Deng and T. Ziegler, *Int. J. Quantum Chem.*, 1994, **52**, 731-765.
54. T. Schwabe and S. Grimme, *Phys. Chem. Chem. Phys.*, 2007, **9**, 3397-3406.
55. A. G. Baboul, L. A. Curtiss, P. C. Redfern and K. Raghavachari, *J. Chem. Phys.*, 1999, **110**, 7650-7657.
56. G. Forte, I. P. Oliveri, G. Consiglio and S. Failla, *Dalton Trans.*, 2017, **46**, 4571-4581.
57. B. Shafaatian, S. S. Mousavi and S. Afshari, *J. Mol. Struct.*, 2016, **1123**, 191-198.
58. D. Mukherjee, S. Reja, K. Sarkar, T. K. S. Fayaz, P. Kumar, A. Kejriwal, P. Das, P. Sanphui and R. Kumar Das, *Inorg. Chem. Commun.*, 2022, **146**, 110190.
59. E. Akhuseyin, Y. Pepe, D. Erdener, A. Karatay, B. Boyacioglu, H. Ünver, G. Yapar, N. Demir, M. Yildiz and A. Elmali, *Phys. Scr.*, 2023, **98**.
60. L. Hu, L. Yin, F. Wang, D. Yu, C. Wang, M. Hui, L. Chu, X. Zhu and Z. Yan, *Spectrochim. Acta A: Mol. Biomol. Spectrosc.*, 2019, **220**, 117130.
61. C. C. Carmona-Vargas, I. Y. Váquiro, L. M. Jaramillo-Gómez, J.-M. Lehn and M. N. Chaur, *Inorganica Chim. Acta*, 2017, **468**, 131-139.
62. M. Wałęsa-Chorab, R. Banasz, D. Marcinkowski, M. Kubicki and V. Patroniak, *RSC Adv.*, 2017, **7**, 50858-50867.
63. S. Mahato, N. Meheta, M. Kotakonda, M. Joshi, M. Shit, A. R. Choudhury and B. Biswas, *Polyhedron*, 2021, **194**, 114933.
64. E. Smirnova, A. Ankudinov, I. Chepurnaya, A. Timonov and M. Karushev, *Inorganics*, 2023, **11**.
65. K. Pekmez, E. Avci, H. G. Baumgärtel and C. Donner, *Z. Phys. Chem.*, 2012, **226**, 953-963.
66. G. Ceyhan, C. Çelik, S. Uruş, İ. Demirtaş, M. Elmastaş and M. Tümer, *Spectrochim. Acta A: Mol. Biomol. Spectrosc.*, 2011, **81**, 184-198.
67. A. J. Bard and L. R. Faulkner, *Electrochem. methods*, 2001, **2**, 580-632.
68. P. Zanello and N. G. Connelly, *Inorganic Electrochemistry*, The Royal Society of Chemistry, 2003.
69. Q.-Y. Meng, X.-W. Gao, T. Lei, Z. Liu, F. Zhan, Z.-J. Li, J.-J. Zhong, H. Xiao, K. Feng, B. Chen, Y. Tao, C.-H. Tung and L.-Z. Wu, *Science Advances*, 2017, **3**, e1700666.
70. J. P. L. Guerra, D. Penas, P. Tavares and A. S. Pereira, *Int. J. Mol. Sci.*, 2023, **24**.
71. L. Chen, Y. Li, M. Han, Y. Peng, X. Chen, S. Xiang, H. Gao, T. Lu, S.-P. Luo, B. Zhou, H. Wu, Y.-F. Yang and Y. Liu, *J. Org. Chem.*, 2022, **87**, 15571-15581.
72. A. N. Krishnamoorthy, J. Zeman, C. Holm and J. Smiatek, *Physical Chemistry Chemical Physics*, 2016, **18**, 31312-31322.
73. A. M. Erkabaev, T. V. Yaroslavtseva, S. E. Popov and O. V. Bushkova, *Russian Journal of Physical Chemistry A*, 2015, **89**, 76-81.

View Article Online
DOI: 10.1039/D5NJ04478B

The data supporting this article have been included as part of the Supplementary Information and are available in the public open repository Zenodo at https://zenodo.org/uploads/15721744; DOI: 10.5281/zenodo.15721744

Supporting Information

Biomimetic *O*-Demethylation at a Copper(II) Center with Imine Ligand: A Structural and Computational Study

Daria Nowicka,[*a] Karol Garbaczewski,[a] Giuseppe Consiglio,[b] Giuseppe Forte,[c] Maciej Kubicki,[a] Teresa Łuczak,[a] Violetta Patroniak [a] and Adam Gorczyński [*a]

[a] Adam Mickiewicz University in Poznań, Faculty of Chemistry, Uniwersytetu Poznańskiego 8, 61-614 Poznań, Poland

[b] Department of Chemical Science University of Catania, Via S. Sofia 64, 95125, Italy

[c] Department of Drug Science and Health University of Catania, Via S. Sofia 64, 95125, Italy

[*] Correspondence: d.nowicka@amu.edu.pl; adam.gorczynski@amu.edu.pl

Table of contents for Supporting Information

1. Synthesis of ligands **L1** – **L3**……2
2. Synthetic procedure for complexes **C4** – **C6**……2
3. NMR spectra of ligands **L1** – **L3**……4
4. IR spectra of ligands **L1** – **L3** and complexes **C1** – **C6**……8
5. Crystallographic studies……12
6. UV-Vis spectroscopy……17
7. Electrochemical experiments……18
8. Proposed mechanism and DFT computations……19

1. Synthesis of ligands L1 – L3

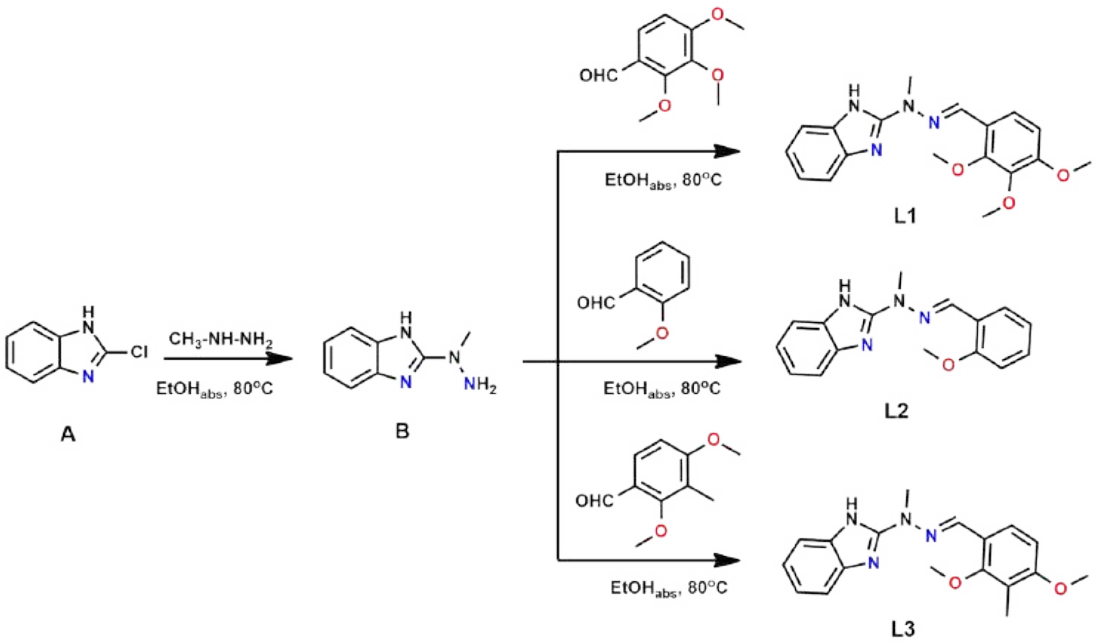

Scheme S1. Scheme of **L1** [$C_{18}H_{20}N_4O_3$], **L2** [$C_{16}H_{16}N_4O$] and **L3** [$C_{18}H_{20}N_4O_2$] ligands synthesis.

2. Synthetic procedure for complexes C4 – C6

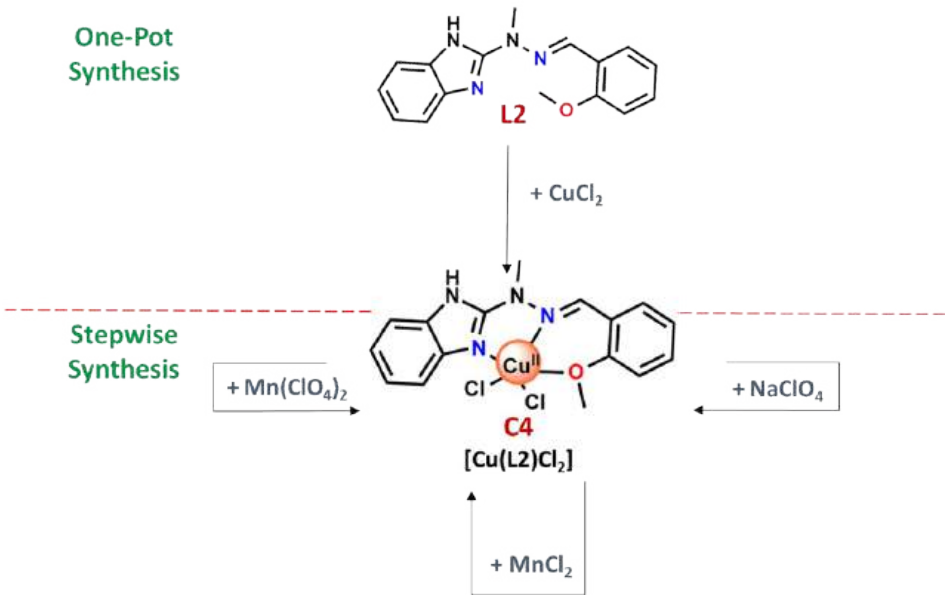

Scheme S2. Schematic representation of the synthetic procedure for Cu(II) complex **C4** based on stepwise and one-pot synthesis. Please note that the replacement of Cu^{2+} by Mn^{2+} or Na^{+} is not favorable either thermodynamically or kinetically. Therefore, the metal center of the complex remains copper, and the use of various perchlorate salts serves only as a source of ClO_4^- anions, not as metal precursors.

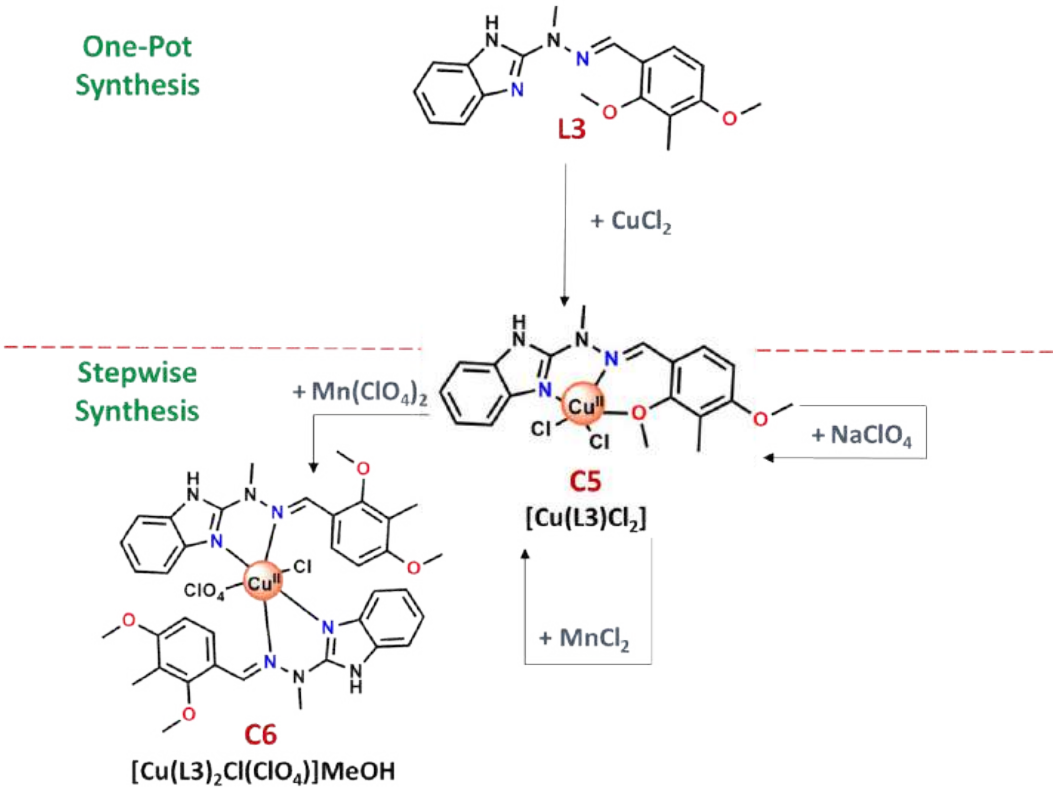

Scheme S3. Schematic representation of the synthetic procedure for Cu(II) complexes **C5** and **C6** based on stepwise and one-pot synthesis. Please note that the replacement of Cu^{2+} by Mn^{2+} or Na^{+} is not favorable either thermodynamically or kinetically. Therefore, the metal center of the complex remains copper, and the use of various perchlorate salts serves only as a source of ClO_4^- anions, not as metal precursors.

3. NMR spectra of ligands L1 – L3

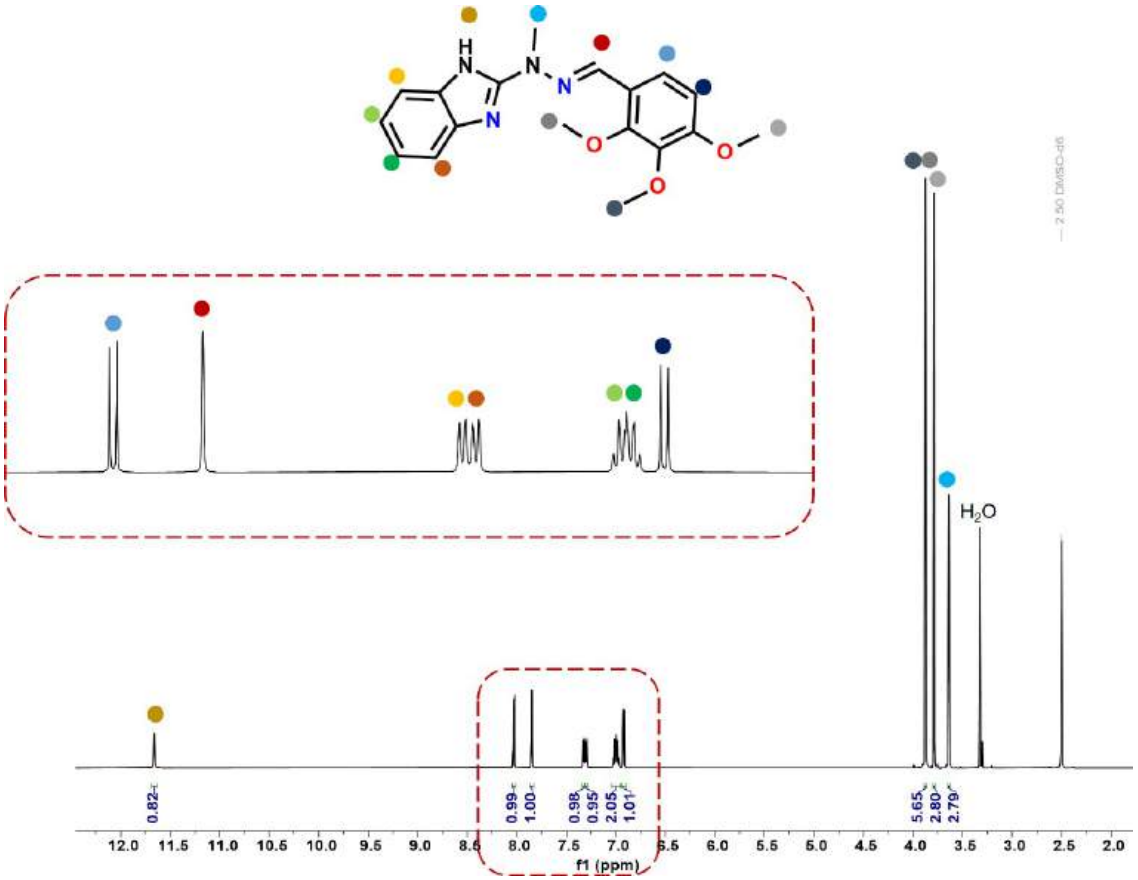

Fig. S1. ^{1}H NMR spectrum for ligand **L1** measured in $(CD_3)_2SO$.

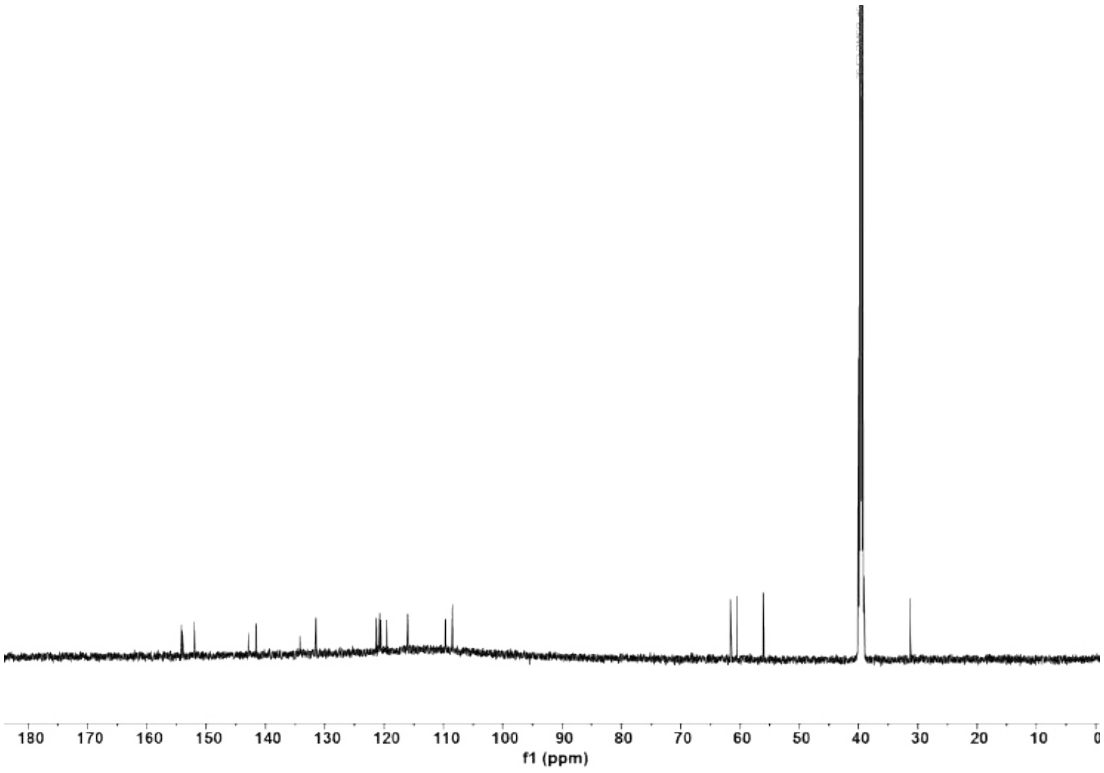

Fig. S2. ^{13}C NMR spectrum for ligand **L1** measured in $(CD_3)_2SO$.

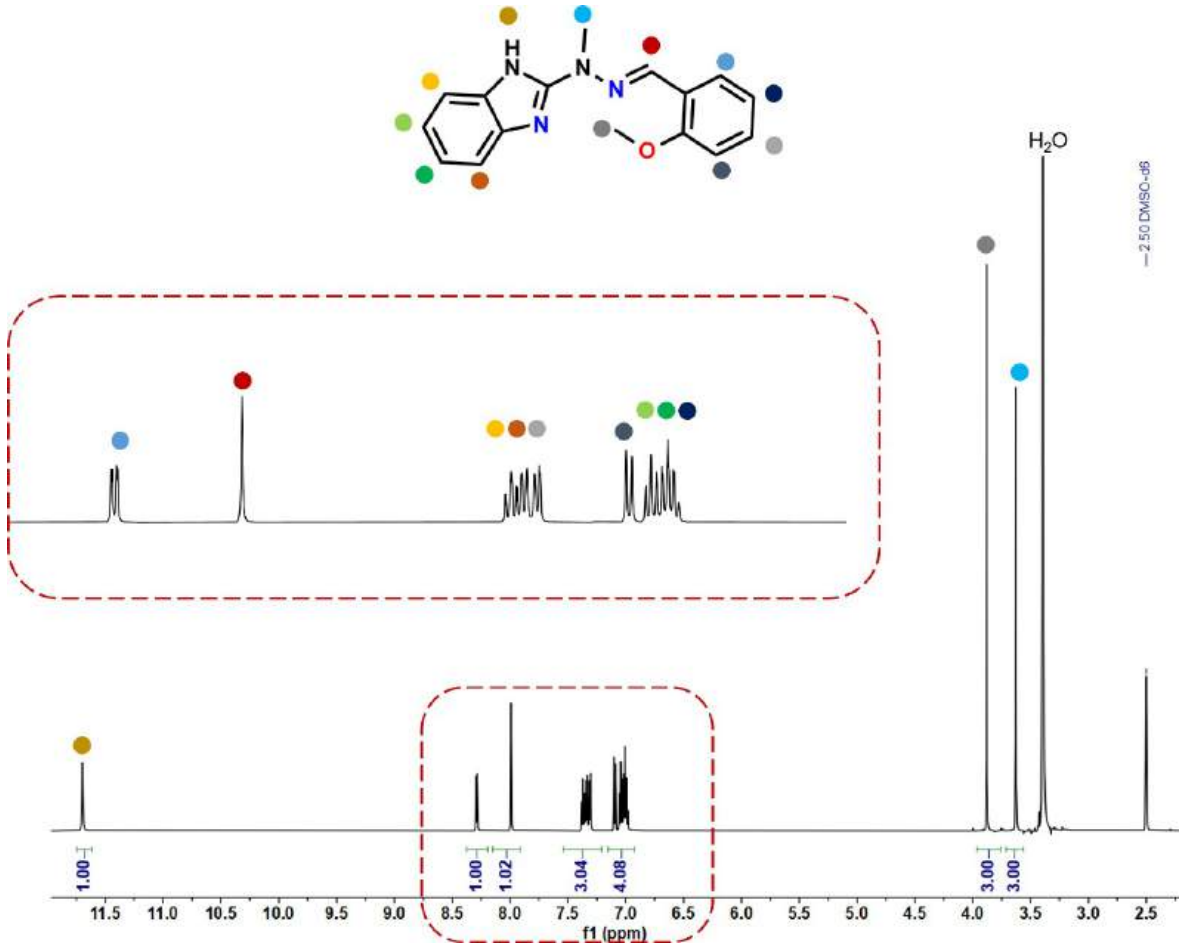

Fig. S3. ^{1}H NMR spectrum for ligand **L2** measured in $(CD_3)_2SO$.

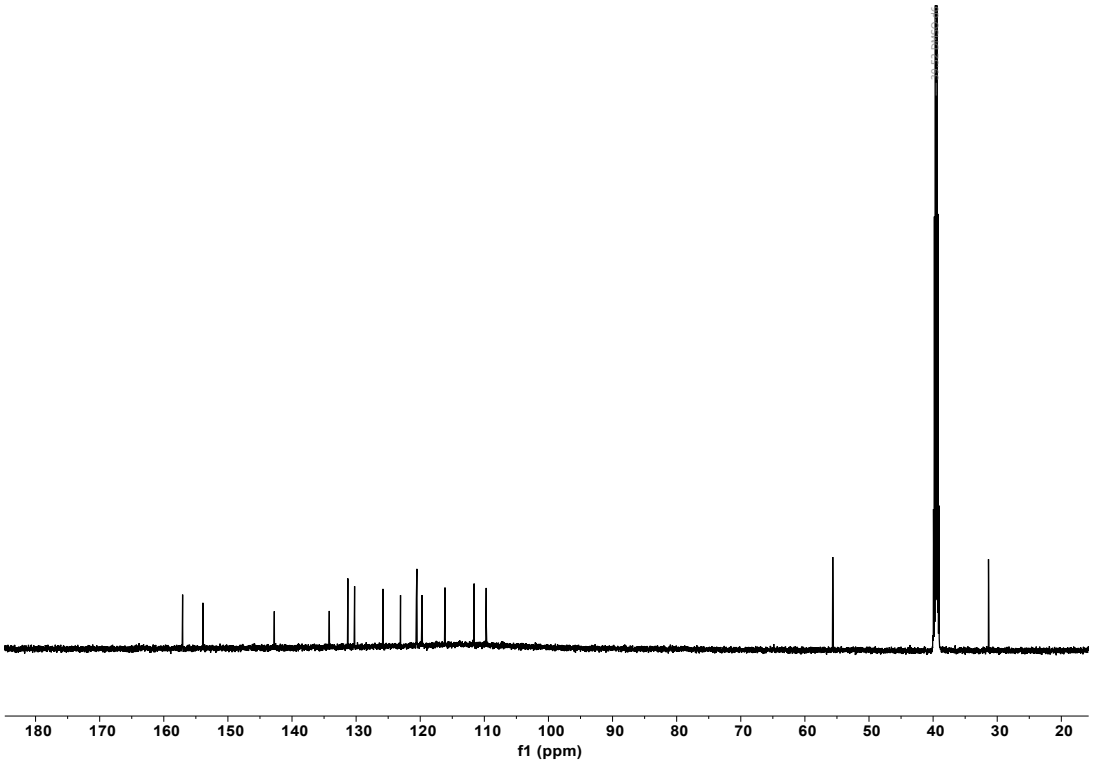

Fig. S4. ^{13}C NMR spectrum for ligand **L2** measured in $(CD_3)_2SO$.

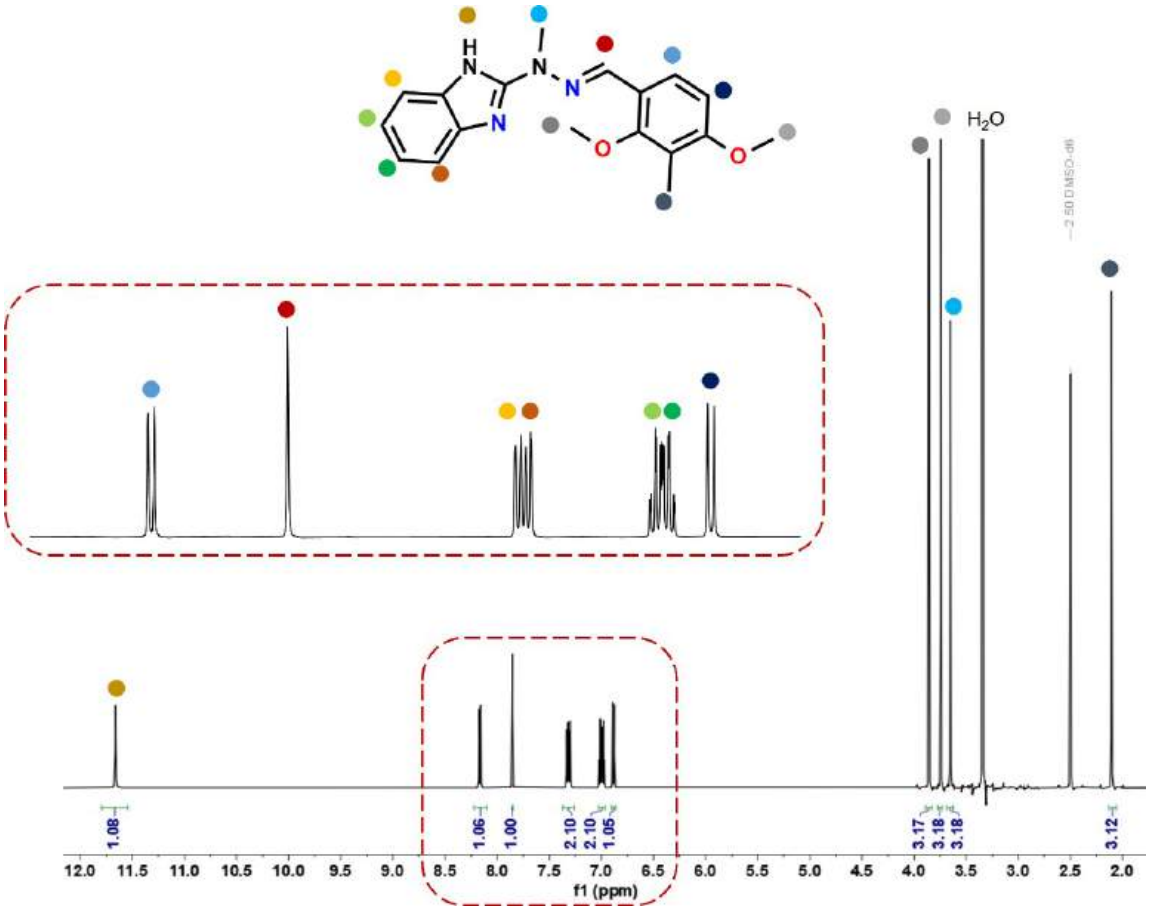

Fig. S5. ^{1}H NMR spectrum for ligand **L3** measured in $(CD_3)_2SO$.

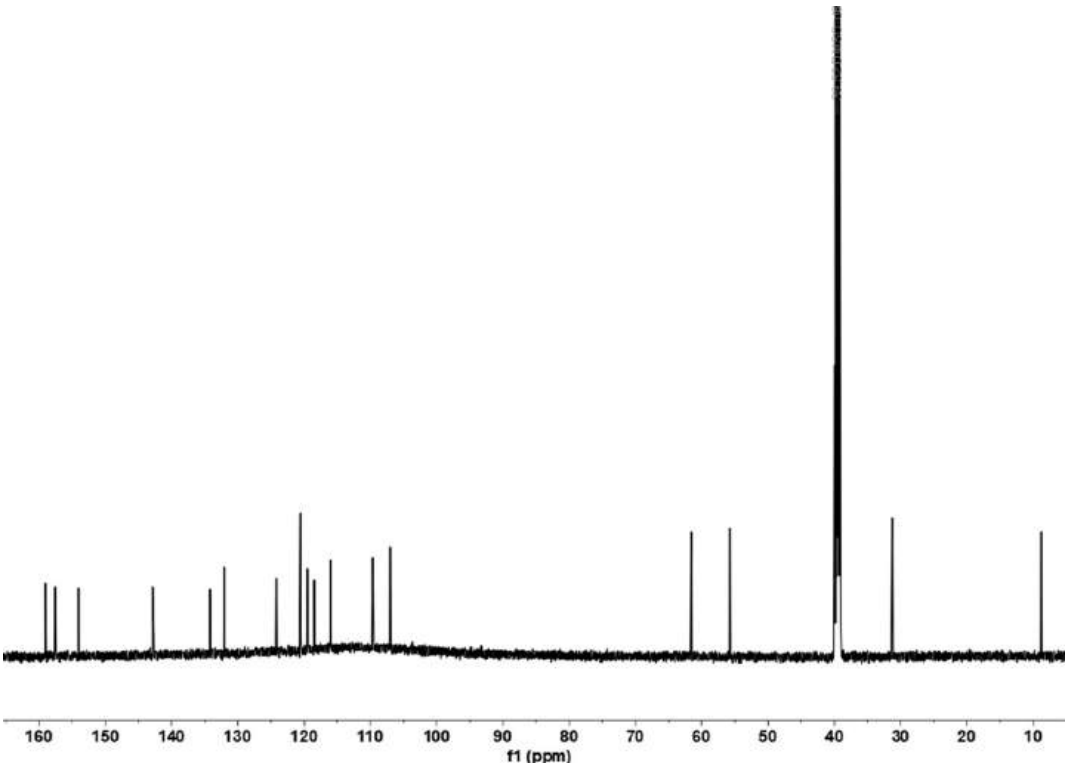

Fig. S6. ^{13}C NMR spectrum for ligand **L3** measured in $(CD_3)_2SO$.

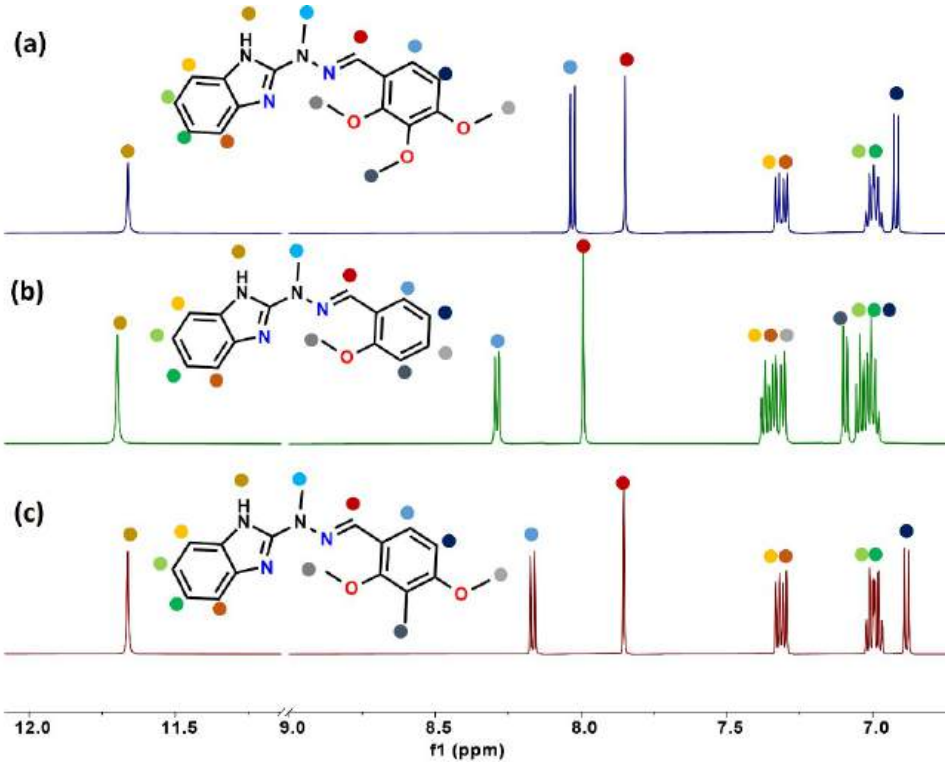

Fig. S7. Comparison of ^{1}H NMR spectra in the aromatic regions for ligands: (a) **L1**, (b) **L2** and (c) **L3** measured in $(CD_3)_2SO$.

4. IR spectra of ligand L1 – L3 and complexes C1 – C6

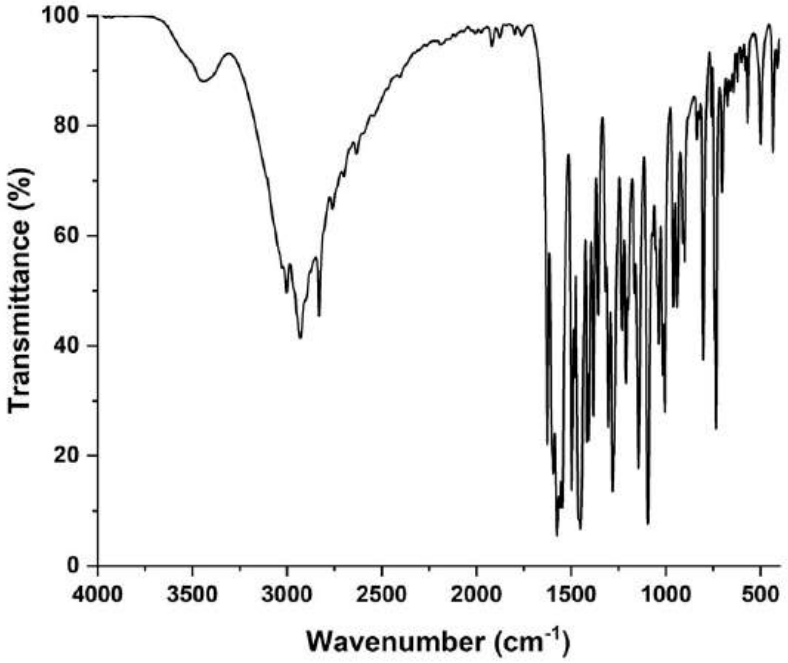

Fig. S8. IR spectrum for ligand **L1**.

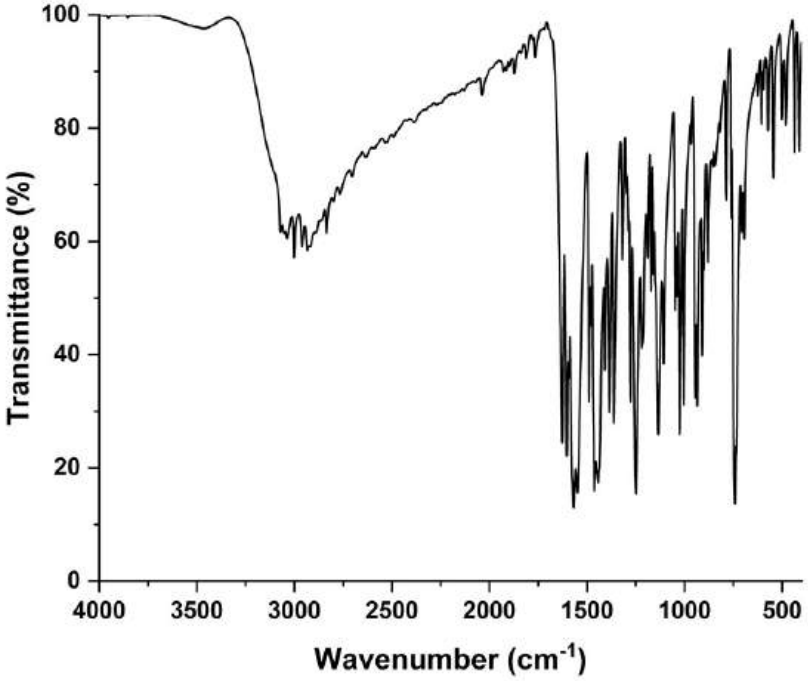

Fig. S9. IR spectrum for ligand **L2**.

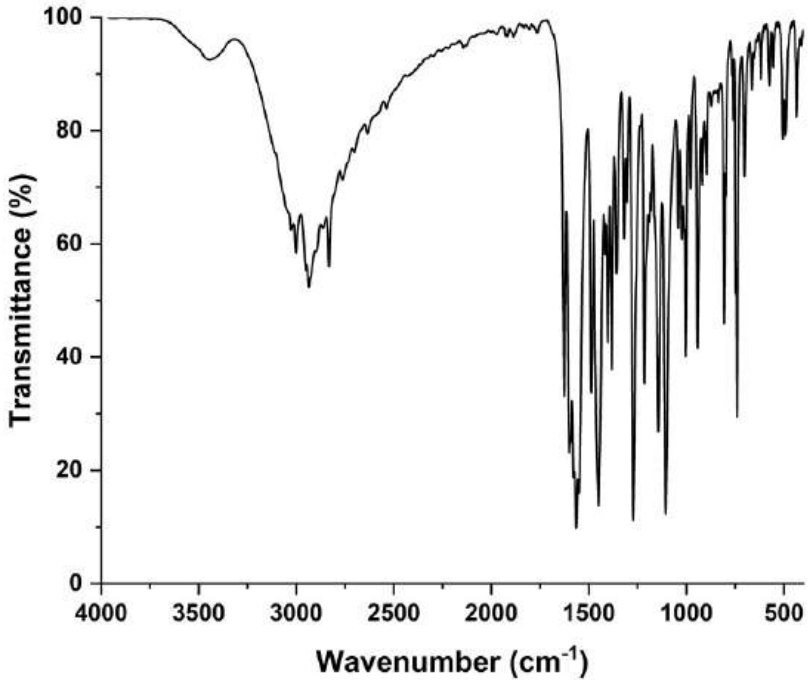

Fig. S10. IR spectrum for ligand **L3**.

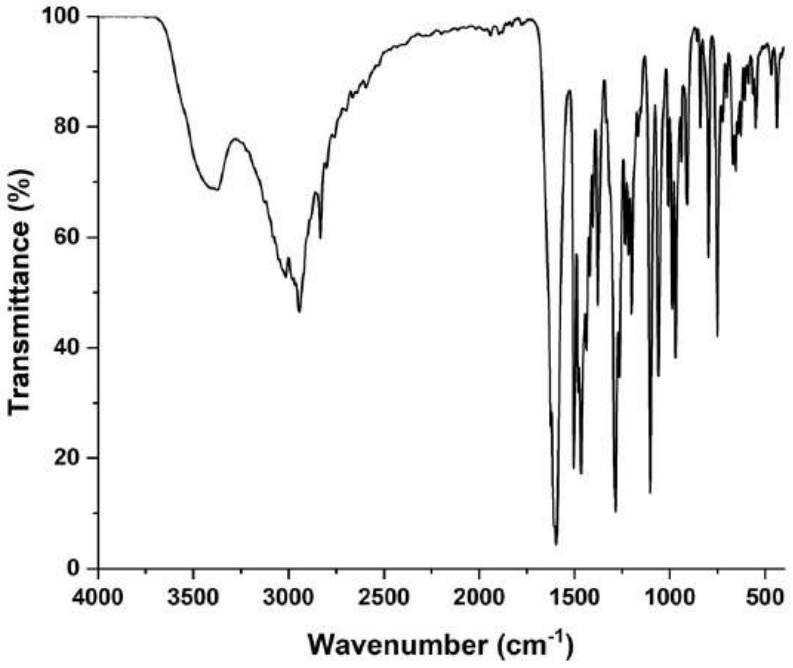

Fig. S11. IR spectrum for **C1** complex.

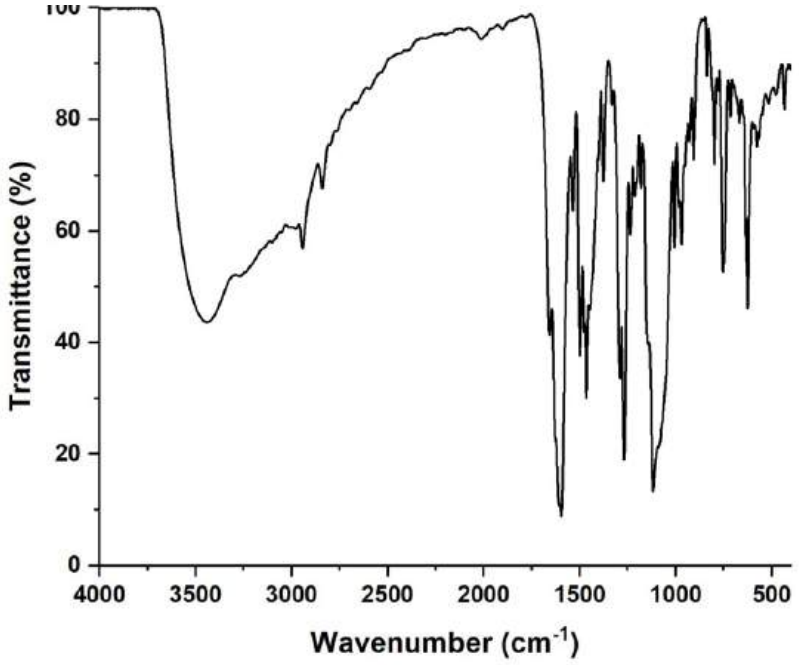

Fig. S12. IR spectrum for **C2** complex.

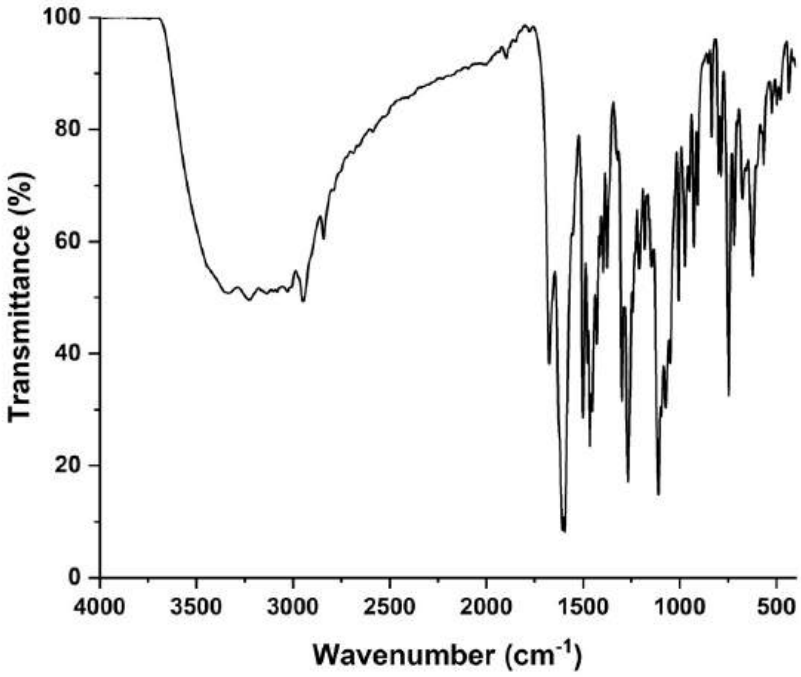

Fig. S13. IR spectrum for **C3** complex.

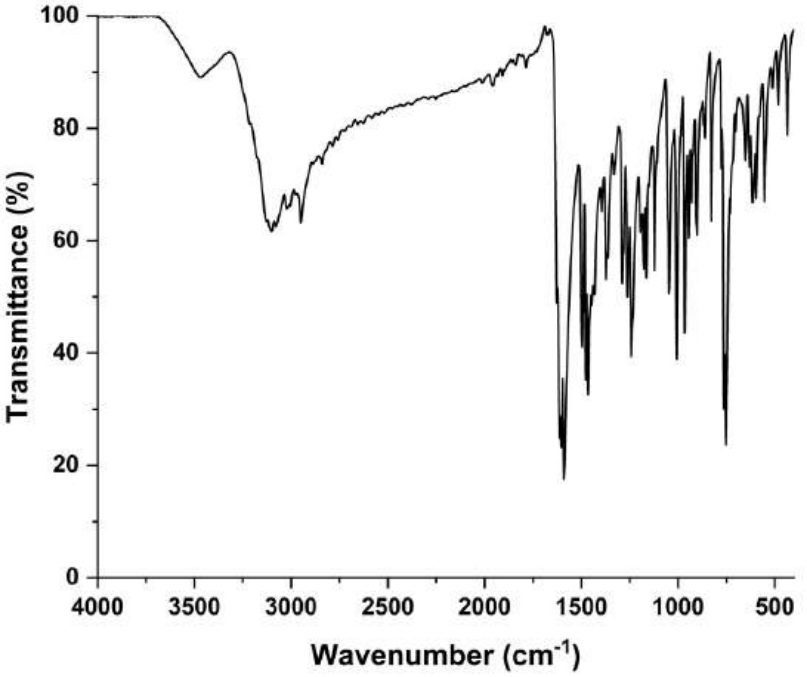

Fig. S14. IR spectrum for **C4** complex.

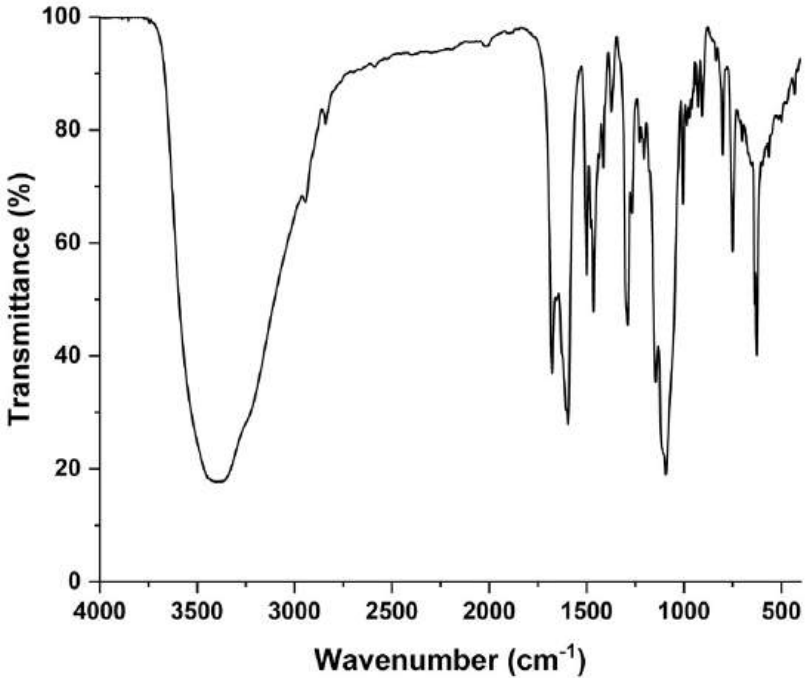

Fig. S15. IR spectrum for **C5** complex.

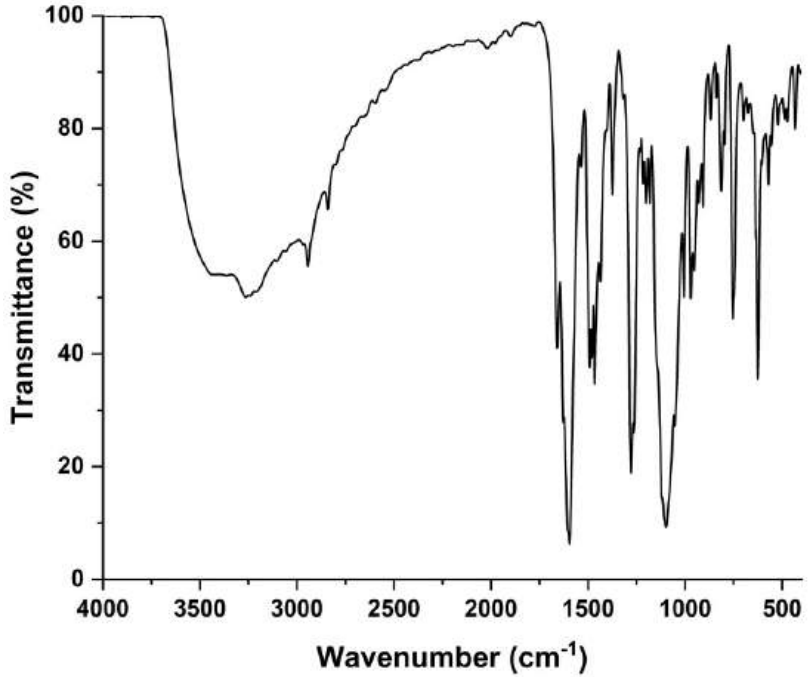

Fig. S16. IR spectrum for **C6** complex.

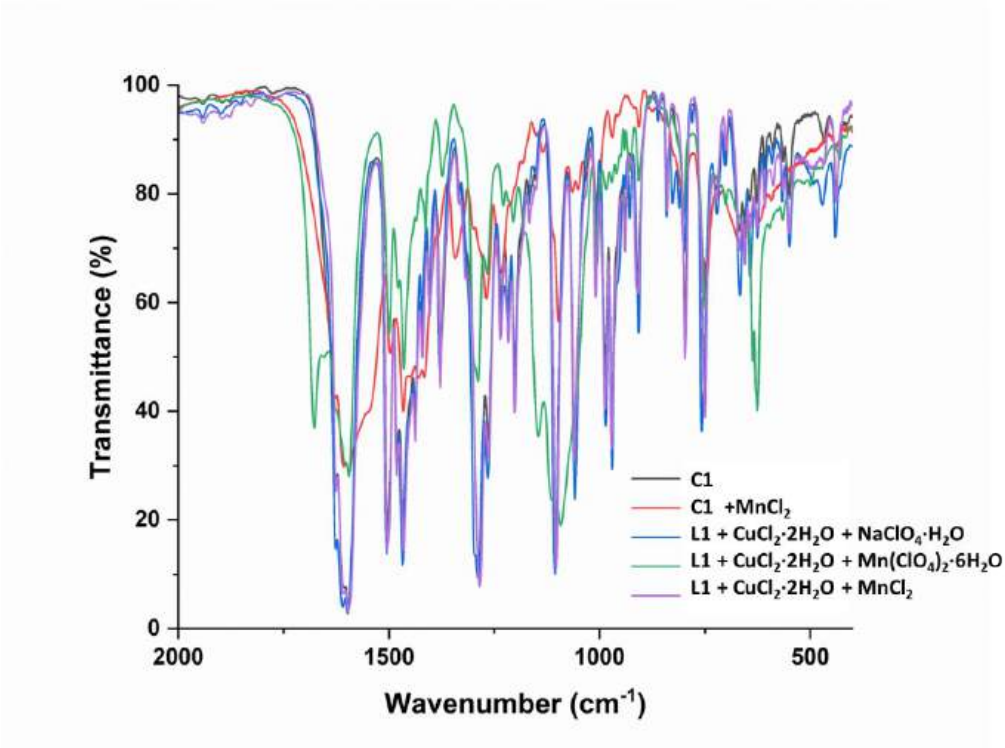

Fig. S17. Comparison of FT-IR spectra for **C1** complexes.

5. Crystallographic studies

Table S1. Crystal data, data collection and structure refinement.

Compound	**L1**	**L2**	**C2**	**C3**	**C4**	**C5**	**C6**
Formula	$C_{18}H_{21}N_4O_3^+ \cdot ClO_4^-$	$C_{16}H_{17}N_4O^+ \cdot ClO_4^-$	$C_{17}H_{17}ClCuN_4O_3$	$C_{35}H_{38}ClCu_2N_8O_{14}^+ \cdot ClO_4^- \cdot 2CH_3OH \cdot H_2O$	$C_{16}H_{16}Cl_2CuN_4O$	$C_{18}H_{20}Cl_2CuN_4O_2$	$C_{36}H_{40}Cl_2CuN_8O_8 \cdot CH_3OH$
Formula weight	440.84	380.78	424.33	1024.80	414.77	458.82	879.24
Crystal system	monoclinic	triclinic	orthorhombic	monoclinic	Triclinic	monoclinic	monoclinic
Space group	$P2_1/c$	P-1	$Pca2_1$	$P2_1/c$	P-1	$P2_1/n$	$P2_1/c$
a(Å)	13.6826(5)	7.5467(5)	18.8457(3)	16.90445(13)	8.2961(7)	14.4376(6)	12.26303(10)
b(Å)	9.7733(3)	9.9377(6)	6.69128(6)	12.18931(8)	13.6909(5)	8.0593(3)	18.89895(16)
c(Å)	15.5906(6)	11.2816(5)	13.29018(11)	22.04368(13)	14.6952(11)	16.8258(7)	17.09492(14)
α(º)	90	77.316(5)	90	90	89.989(5)	90	90
β(º)	109.453(4)	85.652(5)	90	101.9124(7)	88.450(7)	98.442(4)	97.1415(7)
γ(º)	90	88.953(5)	90	90	82.033(6)	90	90
V(Å^3)	1965.83(13)	823.06(8)	1675.91(3)	4444.36(5)	1652.4(2)	1936.59(14)	3931.15(6)
Z	4	2	4	4	4	4	4
D_x(g cm^{-3})	1.490	1.536	1.682	1.532	1.667	1.574	1.486
F(000)	920	396	868	2112	844	940	1828
μ(mm^{-1})	0.245	2.406	3.545	2.918	4.937	1.425	2.587
Reflections:							
collected	7516	6167	23536	51157	7542	7702	38953
unique (R_{int})	3932 (0.0198)	3336 (0.0313)	3492 (0.0409)	9267 (0.0337)	4997 (0.0452)	3853 (0.0295)	8136 (0.0337)
with I>2σ(I)	3295	2943	3488	8481	4500	3202	7345
R(F) [I>2σ(I)]	0.0454	0.0482	0.0258	0.0440	0.1322	0.0430	0.0469
wR(F^2) [I>2σ(I)]	0.1157	0.1368	0.0744	0.1261	0.3014	0.1121	0.1199
R(F) [all data]	0.0558	0.0532	0.0258	0.0475	0.1377	0.0539	0.0534
wR(F^2) [all data]	0.1243	0.1428	0.0744	0.1308	0.3031	0.1210	0.1243
Goodness of fit	1.051	1.097	1.078	1.022	1.002	1.038	1.027
max/min Δρ (e·Å$^-$	0.63/-0.45	0.39/-0.54	0.30/-0.43	1.00/-0.67	2.92/-1.04	0.67/-1.14	1.16/-0.45
CCDC deposition	2336936	2370349	2336938	2336939	2370350	2370351	2370352

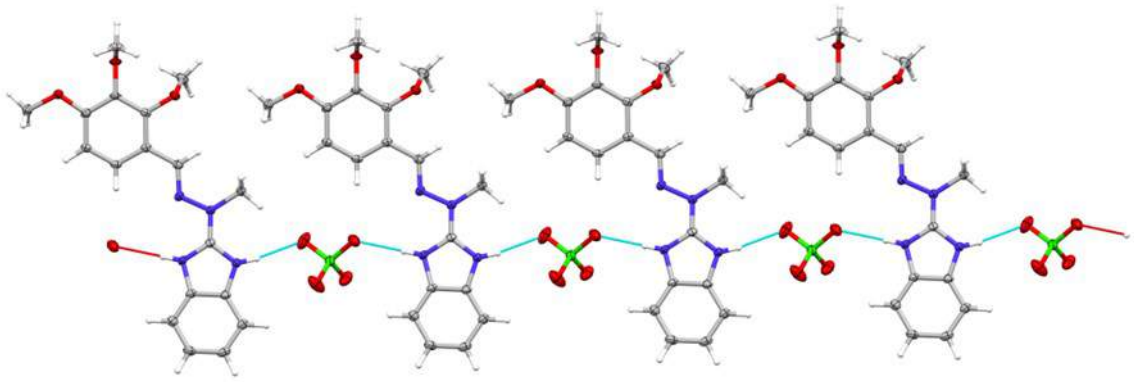

Fig. S18. Supramolecular motifs in crystal structure of ligand' salts: infinite chains (**L1**).

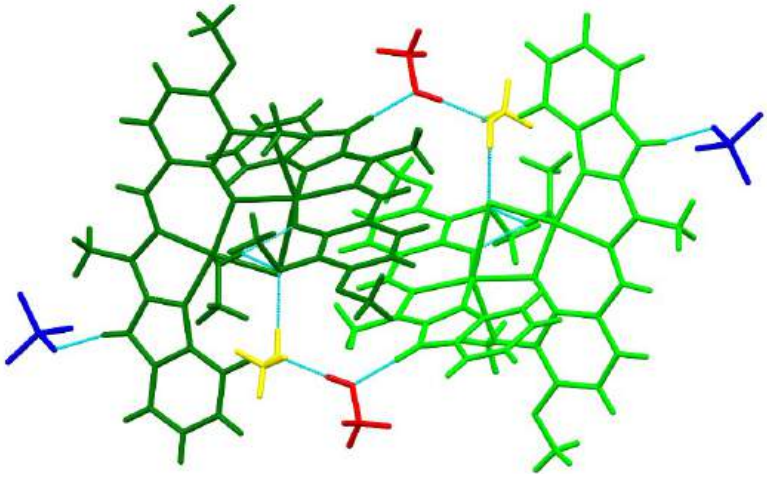

Fig. S19. Hydrogen bond system in the structure of **C3**. Dashed lines show hydrogen bonds, colour code: green – complex cations, blue – perchlorate anions, red and yellow solvent methanol molecules.

Table S2. Hydrogen bond data (Å, °) with s.u.'s in parentheses. Symmetry codes: [i] 1-x,-1/2+y,3/2-z; [ii] 1-x,1/2+y,3/2-z; [iii] x,1+y,z; [iv] -x,-1/2+y,3/2-z, [v] 1-x,1-y,1-z; [vi]1-x,1-y,2-z; [vii] 1-x,2-y,1-z; [viii] x,-1+y,z; [ix] x,3/2-y,-1/2+z.

D	H	A	D-H	H···A	D···A	D-H···A
L1						
N1	H1	O3A^{i}	0.82(3)	2.18(3)	2.977(3)	163(2)
N3	H3	O2A^{ii}	0.84(3)	2.19(3)	2.993(3)	161(2)
L2						
N1	H1	O4A^{iii}	0.89	2.04	2.922(4)	174
N3	H3	O1A	0.88	2.03	2.855(4)	156
C2						
N3	H3	O16^{iv}	0.88	1.97	2.830(2)	164
C3						
N3A	H3A	O1F^{v}	0.88	1.90	2.765(4)	167
N3B	H3B	O4D	0.88	1.92	2.793(3)	169

O1C	H1C	O14A	0.84	1.96	2.776(2)	164
O1E	H1E	O15A	0.84	1.84	2.680(4)	176
O1F	H1F	O15A	0.82	2.05	2.869(3)	170
C4						
N3A	H3A	Cl2A^{vi}	0.88	2.35	3.175(5)	157
N3B	H3B	Cl1B^{vii}	0.88	2.36	3.173(5)	153
C5						
N3	H3	Cl2^{viii}	0.88	2.32	3.199(4)	178
C6						
N3A	H3A	O1D^{ix}	0.88	1.91	2.778(5)	168
N3B	H3B	O4C^{ix}	0.88	2.00	2.841(6)	153
O1D	H1D	Cl1	0.84	2.31	3.120(6)	162

Table S3. Relevant geometrical characteristics of complexes.

C2			
Cu1-N1	1.957(2)	Cu1-O14	1.885(2)
Cu1-N11	2.007(2)	Cu1-Cl1	2.2595(7)
N1-Cu1-O14	168.09(10)	N11-Cu1-Cl1	165.03(7)
C3			
Cu1A-N1A	1.9599(19)	Cu1B-N1B	1.952(2)
Cu1A-N11A	1.9911(19)	Cu1B-N11B	2.0015(19)
Cu1A- O14A	1.9215(16)	Cu1B-O14B	1.9424(16)
Cu1A-O14B	2.0188(16)	Cu1B-O1C	2.2212(17)
Cu1A-O15B	2.4051(17)	Cu1B-Cl3	2.2856(6)
Cu1A-Cl3	2.779(1)		
N1A-Cu1A-O14A	172.53(8)	N1B-Cu1B-O14B	171.71(8)
N11A-Cu1A-O14B	168.91(8)	N11B-Cu1B-Cl3	150.01(6)
O15B-Cu1A-Cl3	149.7(1)		
C4			
Cu1A-N1A	1.982(9)	Cu1B-N1B	1.973(9)
Cu1A-N11A	2.047(11)	Cu1B-N11B	2.042(11)
Cu1A-O14A	2.421(8)	Cu1B-O14B	2.427(7)
Cu1A-Cl1A	2.215(4)	Cu1B-Cl1B	2.305(3)
Cu1A-Cl2A	2.305(4)	Cu1B-Cl2B	2.208(4)
N1A-Cu1A-N11A	79.5(4)	N1B-Cu1B-N11B	79.2(4)
N1A-Cu1A-O14A	121.3(4)	N1B-Cu1B-O14B	127.6(3)
N1A-Cu1A-Cl1A	99.9(3)	N1B-Cu1B-Cl1B	130.4(3)
N1A-Cu1A-Cl2A	132.9(3)	N1B-Cu1B-Cl2B	100.7(3)
N11A-Cu1A-O14A	74.0(3)	N11B-Cu1B-O14B	75.2(3)
N11A-Cu1A-Cl1A	166.2(3)	N11B-Cu1B-Cl1B	92.8(3)
N11A-Cu1A-Cl2A	93.1(3)	N11B-Cu1B-Cl2B	166.3(3)
O14A-Cu1A-Cl1A	95.1(2)	O14B-Cu1B-Cl1B	96.0(2)
O14A-Cu1A-Cl2A	100.2(3)	O14B-Cu1B-Cl2B	94.6(2)
Cl1A-Cu1A-Cl2A	97.20(15)	Cl1B-Cu1B-Cl2B	97.40(15)
C5			
Cu1-N1	1.966(3)	Cu1-N11	2.057(2)
Cu1-O14	2.131(2)	Cu1-Cl1	2.2175(8)

Cu1-Cl2	2.4318(8)		
N1-Cu1-N11	88.08(10)	N1-Cu1-O14	146.66(9)
N1-Cu1-Cl1	100.60(7)	N1-Cu1-Cl2	115.17(7)
N11-Cu1-O14	81.95(9)	N11-Cu1-Cl1	164.65(7)
N11-Cu1-Cl2	94.88(7)	O14-Cu1-Cl1	89.75(6)
O14-Cu1-Cl2	94.11(6)	Cl1-Cu1-Cl2	98.60(3)
C6			
Cu1-N1A	1.9411(19)	Cu1-N1B	1.9325(18)
Cu1-N11A	2.2338(19)	Cu1-Cl1	2.2841(6)
Cu1-O1C	2.703	Cu1-N11B	2.552
N1A-Cu1-N11A	77.91(7)	N1A-Cu1-N1B	168.89(8)
N1A-Cu1-Cl1	97.52(6)	N11A-Cu1-N1B	92.10(7)
N11A-Cu1-Cl1	175.33(5)	N1B-Cu1-Cl1	92.54(6)
N1A-Cu1-N11B	100.2	N1A-Cu1-O1C	79.6
N11A-Cu1-N11B	75.4	N11A-Cu1-O1C	85.6
N1B-Cu1-N11B	72.3	N1B-Cu1-O1C	104.7
Cl1-Cu1-N11B	106.6	Cl1-Cu1-O1C	92.7
N11B-Cu1-O1C	160.5		

6. UV-Vis spectroscopy

The UV-Vis spectra of the ligands **L2**, **L3** and their Cu(II) complexes **C4**, **C5**, **C6** were recorded in acetonitrile at concentration equal to 0.02 mM and confirmed the stability of the complexes in solution, indicating the lack of decoordination of the imine ligands and confirming the absence of demethylated products (Fig. S20). The recorded spectra for ligands **L2**, **L3** and their complexes showed well-defined bands with maxima in the range 295 - 400 nm, which are characteristic of Cu(II) complexes with an imine bond in the ligand backbone. Moreover, for none of the compounds do we observe an additional peak at ~400 nm, characteristic of **C2** and **C3** complexes indicating changes in the ligand backbone, so we confirm the lack of formation of *O*-demethylation products for the studied compounds in acetonitrile solution.

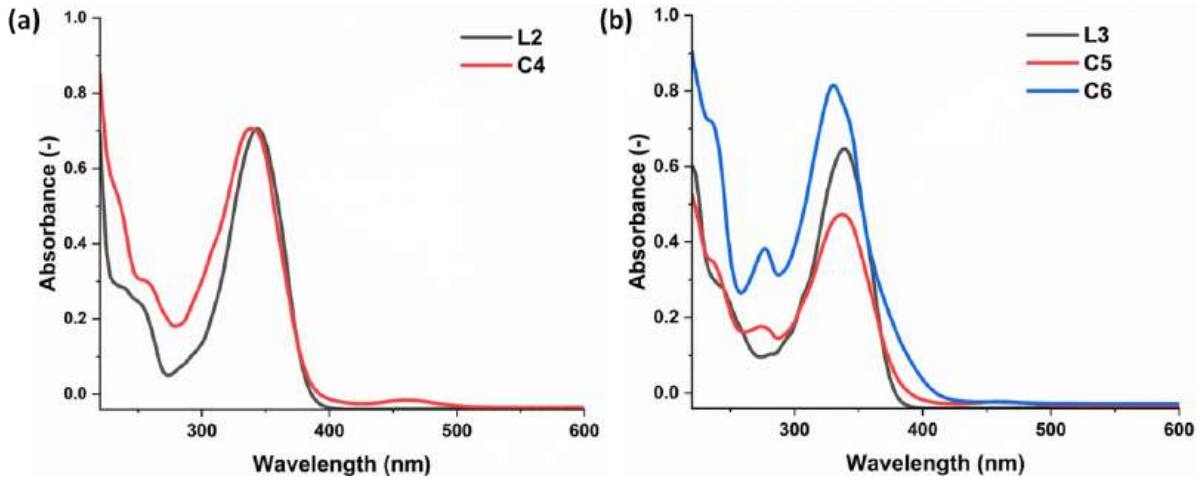

Fig. S20. (a) UV-Vis spectra of ligand **L2** and Cu(II) complex **C4** recorded in MeCN at c = 0.02 mM. (b) UV-Vis spectra of ligand **L3** and Cu(II) complexes **C5** and **C6** recorded in MeCN at c = 0.02 mM.

7. Electrochemical experiments

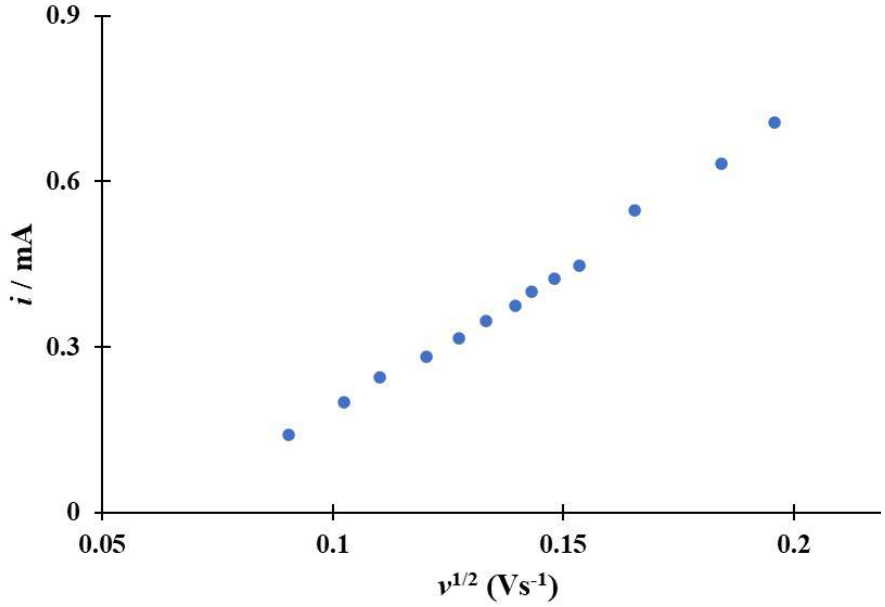

Fig. S21. The relationship between i_p and $v^{1/2}$.

8. Proposed mechanism and DFT computations

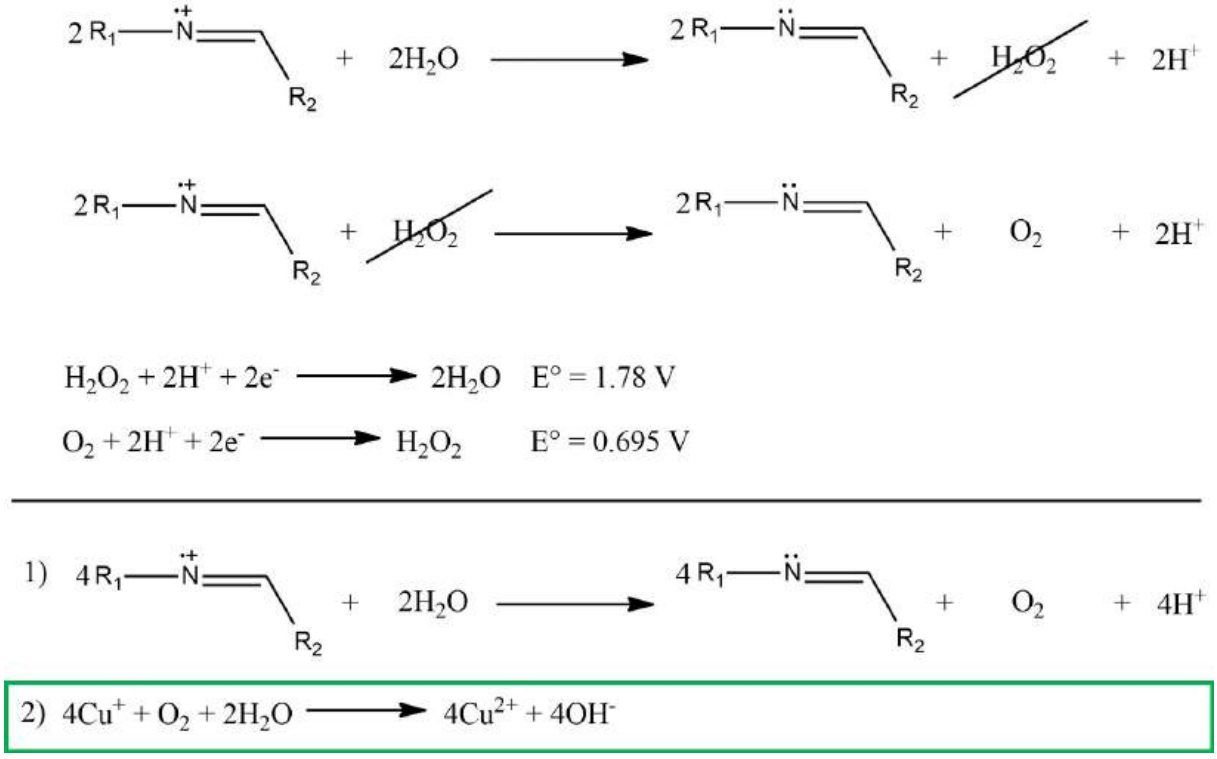

Scheme S4. Proposed reactions for the formed of hydroxide ions acting as a nucleophile in the further reaction stage.

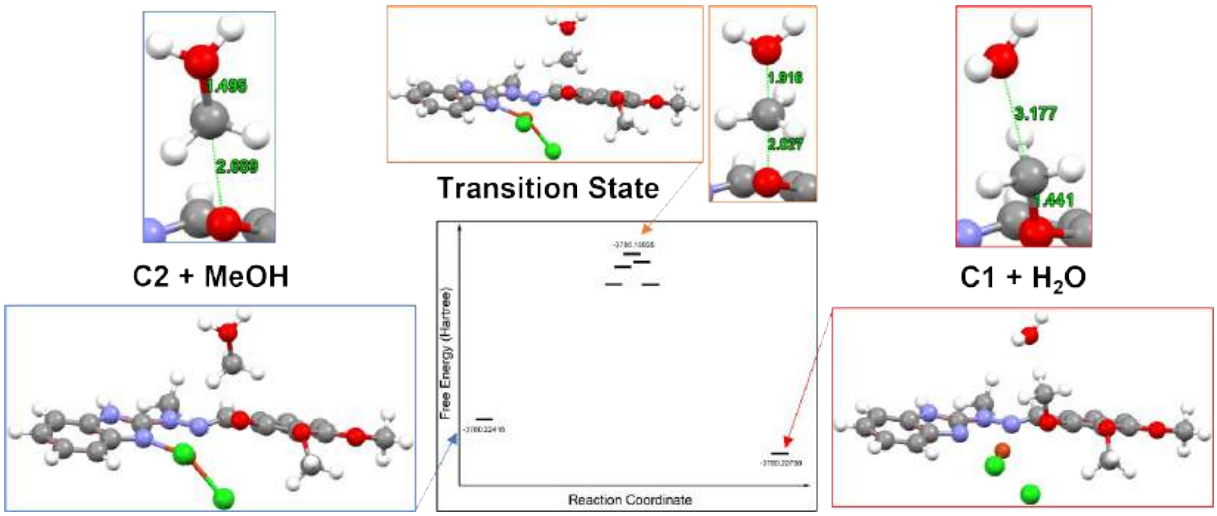

Fig. S22. Gibbs free energy profile for **C1** and the nucleophile H_2O (TS = transition state, measurement in Angstrom).

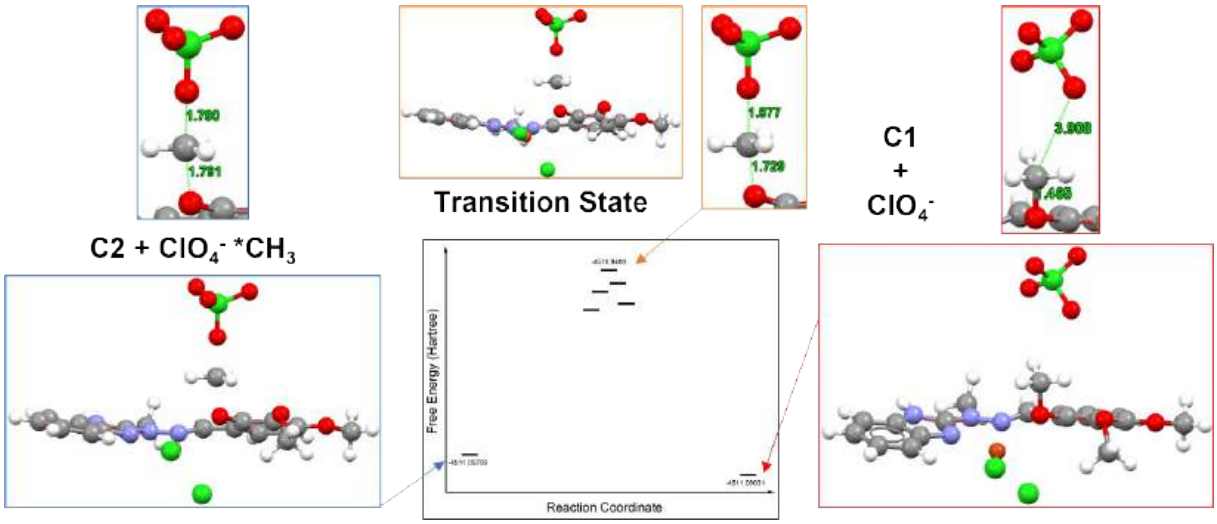

Fig. S23. Gibbs free energy profile for **C1** and the nucleophile OH^- (TS = transition state, measurement in Angstrom).

Electrochimica Acta 476 (2024) 143754

Contents lists available at ScienceDirect

Electrochimica Acta

journal homepage: www.journals.elsevier.com/electrochimica-acta

Self-assembly of simple Schiff base ligand into unique saddle-type [4x4] tetranuclear architecture and its application as selective voltammetric dopamine sensor in aqueous conditions

Daria Nowicka *, Maciej Kubicki, Violetta Patroniak, Teresa Łuczak, Adam Gorczyński *

Faculty of Chemistry, Adam Mickiewicz University in Poznań, Uniwersytetu Poznańskiego 8, 61-614 Poznań, Poland

ARTICLE INFO

Keywords:
Dopamine sensing
Aqueous conditions
Modified gold electrode
Schiff base
Cu(II) complexes

ABSTRACT

Dopamine, a crucial catecholamine neurotransmitter, plays essential roles in the operation of the central nervous system in humans. Disrupted dopamine release is associated with neurological disorders and depression, therefore monitoring of dopamine levels is imperative for preliminary disease detection. Development of sensitive and selective sensors for neurotransmitters that function under aqueous conditions is however still challenging, mostly due to the complexity of hybrid nanomaterials that are interacting with the electrode. Here we provide a coordination compound constructed from simple substrates, where subcomponent self-assembly leads to a unique, discrete [4 × 4] saddle-type complex $[Cu_4(L\text{-}H)_4(BF_4)_2(MeOH)_2](BF_4)_2$, which was characterized by ESI-MS and FT-IR techniques, including single crystal X-ray diffraction. The Cu_4L_4 complex was subsequently used for modification of the bare Au electrode based on its accumulation on the electrode surface. The new voltammetric sensor (Au/complex) was applied for dopamine detection alone and in the presence of interfering ascorbic acid by using the Differential Pulse Voltammetry (DPV) techniques under aqueous conditions. In the linear dynamic range (LDR) range from 0.0001 mM to 0.75 mM the dependence of the peak current on dopamine concentration satisfied the following linear regression equation: i_p [mA] = $17 \bullet 10^{-2}$ c_{DA} [mM] + $8 \bullet 10^{-2}$ (R^2 = 0.998). Moreover, the excellent limit of dopamine detection (LOD) and the limit of its quantification (LOQ) were established at the level of 5.4 nM and 18.0 nM with accomplished high sensitivity 0.17 A M^{-1}, repeatability as well as reproducibility. Clear separation of the voltammetric signal of dopamine from this one of ascorbic acid, even in the presence of a 100-fold excess of interfering ions found in water, consequently proves that the new prepared sensor can be used as an excellent analytical tool for selective detection of dopamine and ascorbic acid coexisting in the tested samples.

1. Introduction

Dopamine (DA), naturally produced in the human body, is one of the most important neurotransmitters in the central nervous system. It plays a key role in transmitting information between neurons and is responsible for emotional behavior and responses to stimuli. Abnormal levels of dopamine in the body can cause a number of problems, such as Parkinson's, Alzheimer's, Huntington's, schizophrenia and Tourette's syndrome [1–7]. Due to the issues associated with inadequate dopamine levels in the body, it is important to develop a simple and effective method for detecting and determining it. The use of electrochemical methods for this purpose allows for high accuracy, sensitivity and precision. However, detectioning and selectively determining dopamine in the body is challenging due to the coexistence of dopamine with other biogenic compounds, such as ascorbic acid (AA) [8–10], which oxidize at bare electrodes within almost the same potential region [4–7]. Therefore, it is necessary to separate the oxidation potentials of these compounds to enable accurate determination of the neurotransmitter. Solving this problem may be facilitated by using modified electrodes as sensors. Among the many ways of modifying electrodes, the use of gold electrodes modified by self-assembled monolayers composed of complex layers for neurotransmitter detection has recently garnered attention in the literature [11–14]. Research has shown that such modification not only facilitates electron exchange between the biomolecule and the electrode surface but also provides effective protection of the metal surface against the adsorption of reaction intermediates and/or end

* Corresponding authors.
E-mail addresses: d.nowicka@amu.edu.pl (D. Nowicka), adam.gorczynski@amu.edu.pl (A. Gorczyński).

https://doi.org/10.1016/j.electacta.2023.143754
Received 29 August 2023; Received in revised form 13 November 2023; Accepted 31 December 2023
Available online 1 January 2024

products, which can be harmful and even poisonous to the electrode surface and thus affect the qualitative and quantitative efficiency of neurotransmitter detection [15].

Transition metal complex compounds, owing to their ability to accept or deliver electrons, have become a flagship in many fields of research and are among the most widely used compounds in electrochemical processes, including applications in the modification of the gold template for dopamine detection [12]. A very important aspect influencing the utilization of compounds in electrochemistry is their structure, more specifically, the scaffold of organic ligands and the structure of complexes, which is influenced by the coordination preference of the selected transition metal ion [11,16]. Among these, copper complex compounds hold particular significance. Copper ions are frequently employed to coordinate with proteins in multicore complexes, playing a pivotal role in generating active sites of specific proteins, such as dopamine monooxygenase [16–18]. Consequently, electrochemical studies of di-, tri- and tetranuclear transition metal complex compounds, particularly those involving copper, have garnered substantial interest. Additionally, polymetallic compounds are employed due to the presence of metal–oxygen–metal and direct metal–metal linkages, which enhance the redox centers in oxidation/reduction processes [16]. Despite this interest, the existing literature on the utilization of copper complexes for electrode modification in terms of dopamine detection is still now rather scarce. For instance, Jiang et al. described the mercapto-terminated binuclear Cu(II) complex that was applied to modify an Au electrode and revealed an improved selectivity for dopamine detection [16]. In another research group, Boulkroune et al. modified an Au/complex electrode using a Cu(II) complex based on a bis-pyrazolyl N-tripodal ligand, which showed high stability and selectivity toward detection of dopamine in the presence of ascorbic and uric acids [19]. These systems however necessitated utilization of the modified thiol groups, which enhance the affinity of the complex to the gold electrode, but render such systems unnecessarily complicated in terms of synthesis, toxicity and overall economy.

Bearing in mind our research group previous experience in the selective detection of neurotransmitters [11,15] and in the synthesis of polymetallic compounds [20–23], in the present study we synthesized a novel tetrametallic complex $[Cu_4(L\text{-}H)_4(BF_4)_2(MeOH)_2](BF_4)_2$ based on the *N*-heterocyclic Schiff base ligand (HL) reported previously [24] (Fig.1). Below, in the remainder of the manuscript, the resulting complex will be denoted as Cu_4L_4.

The composition of the supramolecular architecture allows its adsorption on the gold surface without the need to utilize the thiolic moieties. The newly developed voltammetric sensor (Au/complex) was applied for both standalone dopamine detection and in the presence of interfering ascorbic acid under PBS aqueous conditions, demonstrating excellent selectivity, sensitivity and reproducibility.

2. Experimental section

2.1. Chemicals

Dopaminum hydrochloricum WXF 1 % (specified as 10 mg cm^{-3}, 5 cm^3) solution for infusion was purchased from local chemist's. Other synthesis reagents: $Cu(CH_3CN)_4BF_4$, MeOH, EtOH, Et_2O and reagents for electrochemical studies: KCl, $Na_2HPO_4 \bullet 2H_2O$, KH_2PO_4, $K_3[Fe(CN)_6]$, NaCl, Na_2SO_4, KNO_3, $Mg(NO_3)_2 \bullet 6H_2O$, $Ca(NO_3)_2 \bullet 4H_2O$, $Zn(NO_3)_2 \bullet 6H_2O$, NaOH, citric acid monohydrate, glycine, dopamine hydrochloride (DA) and L-ascorbic acid (AA) were purchased from commercial sources (Sigma-Aldrich, Fluka and POCh-Gliwice) and used as received without further purification.

2.2. Instrumentation

Infrared spectra were recorded in the range from 400 to 4000 cm^{-1} using FT-IR IFS 66/s Bruker spectrometer and ATR-IR Nicolet iS 50. Electrospray ionisation mass spectroscopy (ESI-MS) for methanol solutions in concentration $\sim 10^{-4}$ M was performed using Mas ZQ Water spectrometer. Scanning electron microscopy (SEM) analysis were carried out by using Quanta 250 FEG, FEI scanning electron microscope with energy dispersive X-ray analysis (EDAX). The electrochemical measurements were carried out at room temperature in a three-electrode system with a gold (unmodified or modified) electrode as a working electrode with a geometric area of 0.33 cm^2, a platinum wire as an auxiliary electrode and a saturated calomel electrode (SCE) as a reference electrode using the potentiostat/galvanostat analyzer (AUTOLAB PGSTAT 302 N, Eco Chemie, B.V., Utrecht, The Netherlands). The pH measurements were performed using pH meter (Model-ULAB 2002).

2.3. Synthesis of ligand HL $[C_{10}H_{11}N_5]$

Ligand HL was prepared in a two-steps synthetic method according to the synthetic protocol reported previously [24] (Scheme S1). The first step was nucleophilic substitution reaction between 2-bromopyridine and an excess of methylhydrazine, and second step, the condensation between obtained primary amine 2-(1-methylhydrazinyl)pyridine with 4-imidazolecarboxaldehyde.

2.4. Synthesis of complex $[Cu_4(L\text{-}H)_4(BF_4)_2(MeOH)_2](BF_4)_2$

Cu_4L_4 complex was synthesized in a one pot complexation reaction. Ligand HL (15.0 mg, 0.075 mmol) and $Cu(CH_3CN)_4BF_4$ (23.5 mg, 0.075 mmol) were dissolved in 15 mL methanol. The reaction mixture was magnetically stirred for 24 h at room temperature to give green solution. The reaction mixture was concentrated and added Et_2O. The dark-green precipitate was obtained, filtered *via* suction filtration and washed with Et_2O (2 × 5 ml) and dried under vacuum. The crystallization by vial to vial diffusion at low temperature (4 °C) of diisopropyl ether to a methanolic solution allowed to obtain crystals proper for X-ray diffraction. Yield: 32.80 mg, 85.3 % based on ligand HL.

ESI-MS (+) *m/z* (%): 264 (100) $[CuL]^+$; ESI-MS (-) *m/z* (%): 1490 (90) $[Cu_4HL_4(BF_4)_5]^-$. IR (KBr cm^{-1}): ν(N—H) 3440; ν(C—H)$_{ar}$ 3124, 3067; ν(C═N)$_{imin.}$ 1610; ν(C═C)$_{ar}$ 1552, 1490; ν(C—N) 1446, 1322; ν(C═N)$_{ar}$ 1285, 1224; $\nu(BF_4)$ 1110, 1083; γ(C—H)$_{ar}$ 850, 765, 647, 521.

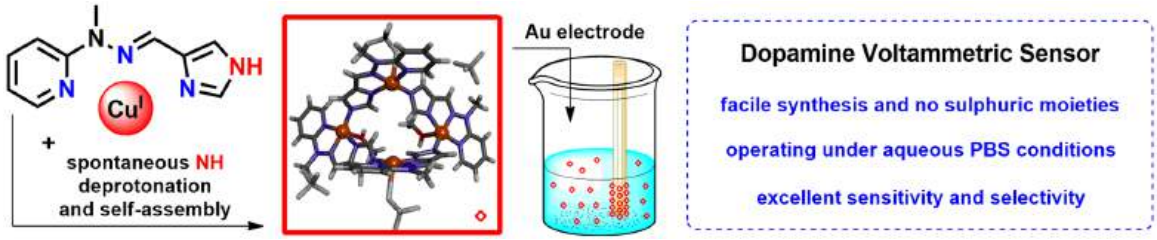

Fig. 1. Self-assembly of ligand HL into its Cu_4L_4 saddle-type complex and application as voltammetric sensor for dopamine neurotransmitter.

2.5. Electrode activation and modification

All solutions under investigated were prepared at room temperature using ultra-pure deionized water and were deareted with highly pure argon before use. All measurements were conducted in pre-washed laboratory vessels in Piranha solution (persulfuric acid, Caro acid).

Prior to use, the bare gold electrode was polished with aluminum slurries of successively decreasing final grades (down to 0.05 μm, Buehler) on polishing cloths (Buehler). Then, the electrode was electrochemically activated by cycling in the potential range between $E = -0.8$ V and $E = 0.6$ V vs SCE at $dE/dt = 0.1$ Vs^{-1} in 0.5 M sodium hydroxide until the cyclic voltammogram was stable. This procedure avoids structural changes on the gold surface [25]. Then, the activated gold electrode was subjected to modification processes by an accumulation of Cu_4L_4 complex on its surface. In order to do this the activated gold electrode was immersed in phosphate-buffered solution (PBS) (0.06 M; pH 7.0) as the supporting electrolyte solution with addition of 0.01 mM Cu_4L_4 complex and electrochemically cycled in the range of potential from $E = -0.80$ V to $E = 1.15$ V vs SCE at $dE/dt = 0.1$ Vs^{-1} for 10 min with a continuous flow stream of argon over the solution. After obtaining a stable cyclic voltammogram (~15 cycles), the electrode was removed from the cell, washed copiously with water, dried in a stream of argon gas and used in further electrochemical measurements. The obtained modified gold electrode has been marked as Au/complex and this designation will be used bellow in the text. After electrochemical measurements the electrode was washed with water, dried in an argon streaming and was stored in empty tube at room temperature. To confirm the durability of the adsorbed complex layer on the electrode surface, a series of separate experiments were performed in which the modified Au/complex electrode was cycled in PBS, then rinsed copiously with water, immersed in fresh PBS and CVs were recorded (experiment repeated once a day for 5 days). It has been observed that obtained cyclic voltammograms did not alter from the first one CV indicating strong adsorption of the Cu_4L_4 complex on the gold template. To remove accumulated Cu_4L_4 complex from the modified gold surface, the electrode was dipped in a Piranha solution for ~5 min and rinsed with water.

2.6. Electrochemical active surface area

The electroactive surface areas of the gold electrode and the Au/complex electrode were evaluated by cyclic voltammetry in 0.1 M KCl with addition of 1 mM $[Fe(CN)_6]^{3-}$ as a probe at different scan rates, by applying the Randles-Ševčik equation: $i_p = 2.69\ 10^5 \bullet A \bullet D^{1/2} \bullet n^{3/2} \bullet v^{1/2} \bullet c$ where i_p [in A] is a peak current, n is a number of electrons involved in the reaction, $A = 0.33$ [in cm^2] is an electrode active surface area, $D = 7.6 \bullet 10^{-6}$ [in $cm^2\ s^{-1}$] is diffusion coefficient of ferricyanides ions in 0.1 M KCl solution, c [in M] is the concentration of $K_4[Fe(CN)_6]$ and v is the potential scan rate [in $V \bullet s^{-1}$] [26]. According to the scan rate analysis, the peak current obtained on both electrodes were found to be proportional to the square root of the scan rate in the range 0.01–05 $V \bullet s^{-1}$. From the slopes of i_p versus $v^{1/2} \bullet$plots, the electroactive surface area was calculated to be 0.38 cm^2 and 0.495 cm^2 for Au and Au/complex electrode, respectively.

3. Results and discussion

3.1. Crystal structure description

The tetracationic complex Cu_4L_4 is C_2-symmetrical (Fig. 2). Coordination of both Cu^{II} ions can be described as square-pyramidal, with four N atoms from two different deprotonated L ligand molecules as a base; however there are some significant differences. In a case of Cu1, the fifth position (axial) is occupied be F atom of BF_4 anion, and the Cu-F distance is relatively large (2.609 Å; relevant geometric data are listed in Table S1). The CSD analysis shows that such distances are found quite often for Cu···F_4B contacts, while general, for Cu—F bonds the typical distances are much shorter (Fig.S3). For Cu1, four N atoms are almost coplanar (max deviation from the least-squares plane is 0.015(1) Å), the Cu atom is also only slightly displaced 0.055(1) Å, while the F atom is displaced in the same direction by 2.619 Å. For second Cu^{II} ion, Cu2, the fifth coordination place is occupied by water oxygen, and the distance is much shorter; also, the geometry is more distorted: maximum deviation from the four-atoms plane is 0.085(1) Å, Cu is 0.198(1) Å and O(water) – 2.476(2) Å out of the mean plane.

Unlabeled part is related to the label one by symmetry operation *1-x, y, ½-z*. Cu···F contacts are drawn as thin lines. (b) Channels in the crystal structure of Cu_4L_4 complex (see text).

In the crystal structure there are huge channels (Fig. 2b), filled with the highly disordered solvent molecules; the attempts to model this electron density have not improved the quality of the structure. The voids take as much as 19 % of the volume of the unit cells.

3.2. Electrochemistry of prepared complex on a gold electrode

Cyclic voltammogram of the bare gold electrode recorded in PBS as

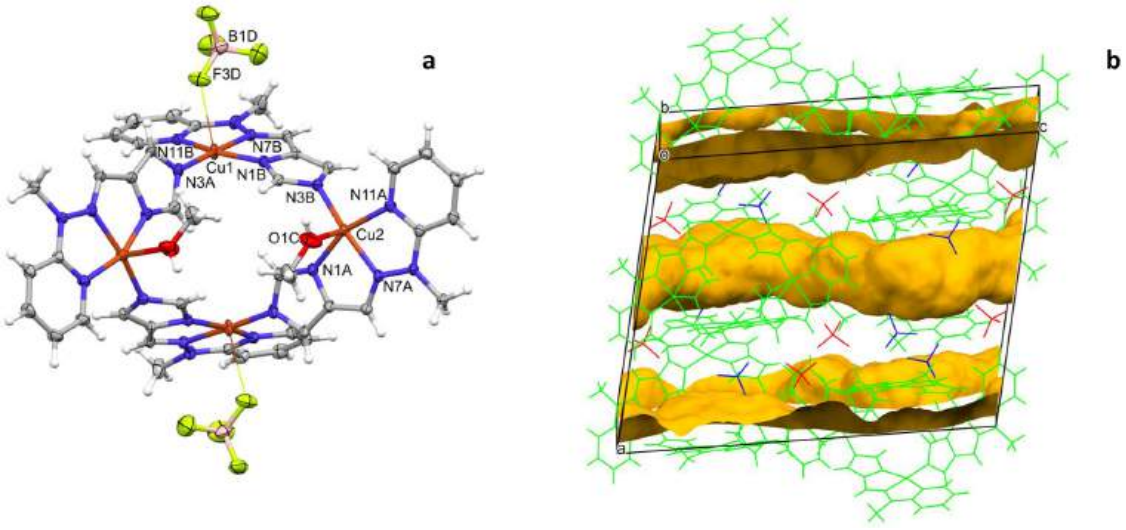

Fig. 2. (a) Perspective view of the asymmetric part of the unit cell; the ellipsoids are drawn at the 50 % probability level, hydrogen atoms are represented by spheres of arbitrary radii.

supporting electrolyte in the potential range from $E = -0.8$ V to $E = 1.15$ V vs SCE at $dE/dt = 0.1$ Vs^{-1} is shown in Fig. 3ab. As can be seen, over a wide potential range ranging from $E = -0.8$ V to $E = 0.6$ V vs SCE, no electrochemical reactions occur. A well-defined anodic peak visible on the CV at 0.93 V vs SCE and cathodic peak at 0.45 V vs SCE are assigned to the gold oxide formation and to its reduction, respectively [27]. In Fig. 3c, an electrochemistry of studied complex (Cu_4L_4) and ligand (HL) is presented. The synthesized ligand is inactive on the gold electrode. Its addition to the supporting electrolyte solution does not alter the cyclic voltammogram. Otherwise, changes in the course of the *i* - *E* relationship were noted when the 0.01 mM complex has been added to the solution.

In the potential range of the electrical double layer of gold electrode a well-defined pair of reversible peaks located at 0.25 V and 0.17 V vs SCE is visible. According to the literature this couple of peaks is indicative of electrochemical process of Cu(I)/Cu(II) oxidation and Cu(II)/Cu (I) reduction, respectively [16]. A set of consecutive CVs recorded in the presence of 0.01 mM Cu_4L_4 complex in the potential limits of the electrical double layer is shown on Fig. 3d. It is noteworthy that with increasing number of the successive potential scans (up to 12th cycle) both anodic and cathodic peaks decrease. This indicates formation of an adsorbed layer of complex on the bare gold electrode surface. The conclusion about the Cu_4L_4 complex being adsorbed on the gold electrode surface has been confirmed by the results at various sweep rates (Fig. 4). A linear relationship of the peak current (i_p) versus the scan rate (v) with high value of the correlation coefficient ($R^2 = 0.9996$) was obtained in the range from 0.02 Vs^{-1} to 0.50 Vs^{-1}. Moreover, the adsorption of Cu_4L_4 complex at the studied electrode was confirmed by a linear correlation of log i_p versus log v with a slope of di_p/dv close to 1.

3.3. Characterization of the modified electrode

The use of accumulation of Cu_4L_4 complex method for modification of gold electrode brings many benefits, one of the most important of which is to ensure protection of the surface against adsorption of intermediate and/or final reaction products which are harmful and even poisonous for the surface of the bare electrode [15,28]. In order to obtain accumulated Cu_4L_4 complex on the gold electrode surface it is necessary to choose a suitable system with appropriate features for deposition such as redox transformable, transition metal complexes [12]. Suitable (metallo)supramolecular architectures provide the opportunity to construct artificial compounds that play a key role as a redox center in oxidation/reduction processes. A very important aspect affecting the use of compounds in electrochemistry is their structure, more specifically, the scaffolding of organic ligands and the structure of complexes, which is influenced by the coordination preference of the selected transition metal ion [11,16].

We have chosen copper ion since it is most often used to coordinate with proteins in multicore complexes, which contribute to the generation of active sites of selected proteins, such as dopamine monooxygenase [16]. In addition, the choice of tetrametallic architectures complex is also of great importance because the presence of more metal ions can strengthen the redox centers in oxidation/reduction processes while the application of monometallic systems show difficulties in electrode coating and in the process of chemisorption, which is confirmed in the literature [16,19]. The Cu_4L_4 complex was designed by us to form two active regions, one having affinity for the gold surface and the other providing active sites for dopamine oxidation (Fig. 5).

Moreover, our prediction of the resulting structure was unambiguously confirmed by X-ray characterization and furthermore allow us to determine the nature of Cu_4L_4 complex layer accumulated on the electrode surface. In agreement with our anticipation, one of two areas of the structure involves two methanol molecules coordinated to the metal center and N-heterocycles. In aqueous solution, previously coordinated methanol molecules can be transferred to the solution, as confirmed by ESI-MS analysis. According to the literature, aromatic nitrogen-containing heterocycles can exhibit high affinity for the gold surface [29]. The second area, on the other hand, is a cavity surrounded by four copper ions that constitute an active redox center catalyzing the oxidation of dopamine.

Most importantly, the complex compound we obtained does not contain thiol groups in its structure, which, despite their numerous and well-known disadvantages (susceptible to pH changes, oxidants, organic solvents) [30] are commonly used in modification of gold surface due to

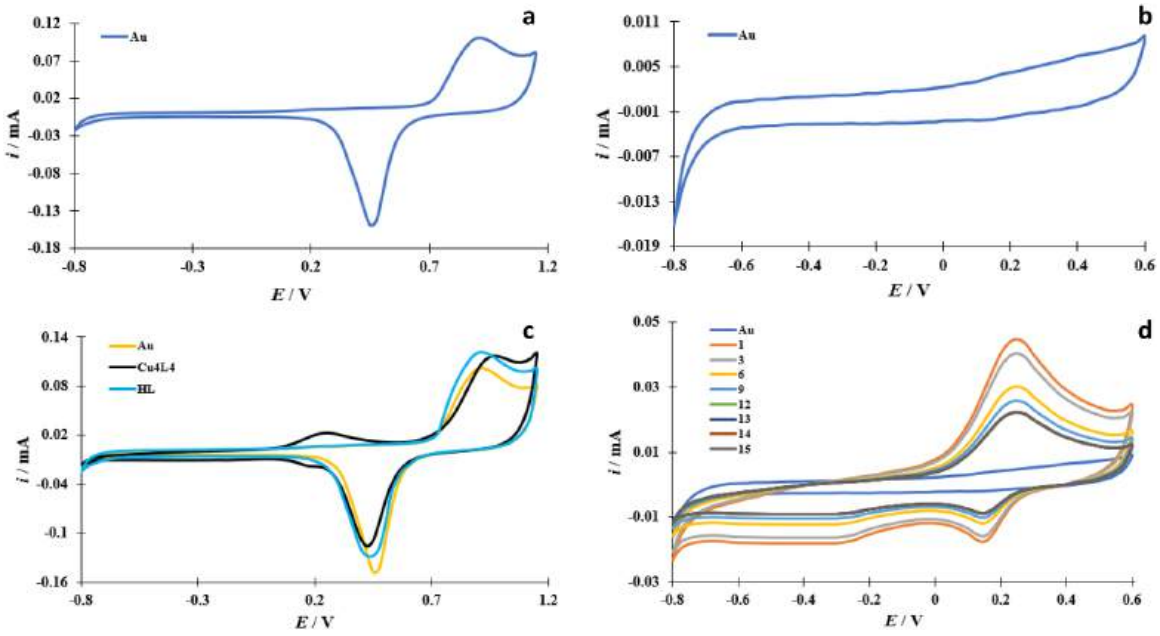

Fig. 3. (a) Cyclic voltammogram of the bare gold electrode in PBS, $dE/dt = 0.1$ Vs^{-1}. (b) the same as in the (a) but in the potential range involved electrical double layer of the gold electrode. (c) The cyclic voltammograms of the bare gold electrode (yellow) in PBS and in the presence of 0.01 mM Cu_4L_4 complex (black) and 0.01 mM ligand (blue), $dE/dt = 0.1$ Vs^{-1}. (d) A set of cyclic voltammograms recorded at the gold electrode during successively cycles in PBS with 0.01 mM Cu_4L_4 complex, $dE/dt = 0.1$ Vs^{-1}.

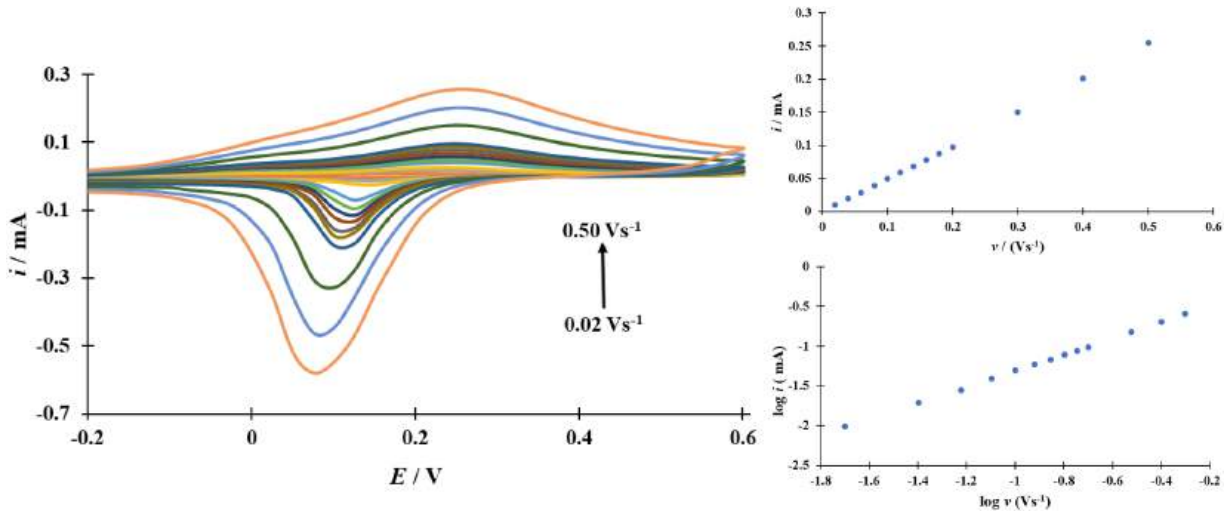

Fig. 4. The cyclic voltammograms of the Au/complex electrode recorded in PBS at scan rate ranging from 0.02 to 0.50 Vs^{-1}. Insert: the relationships between $i_p - v$ and log $_{ip}$ versus log v.

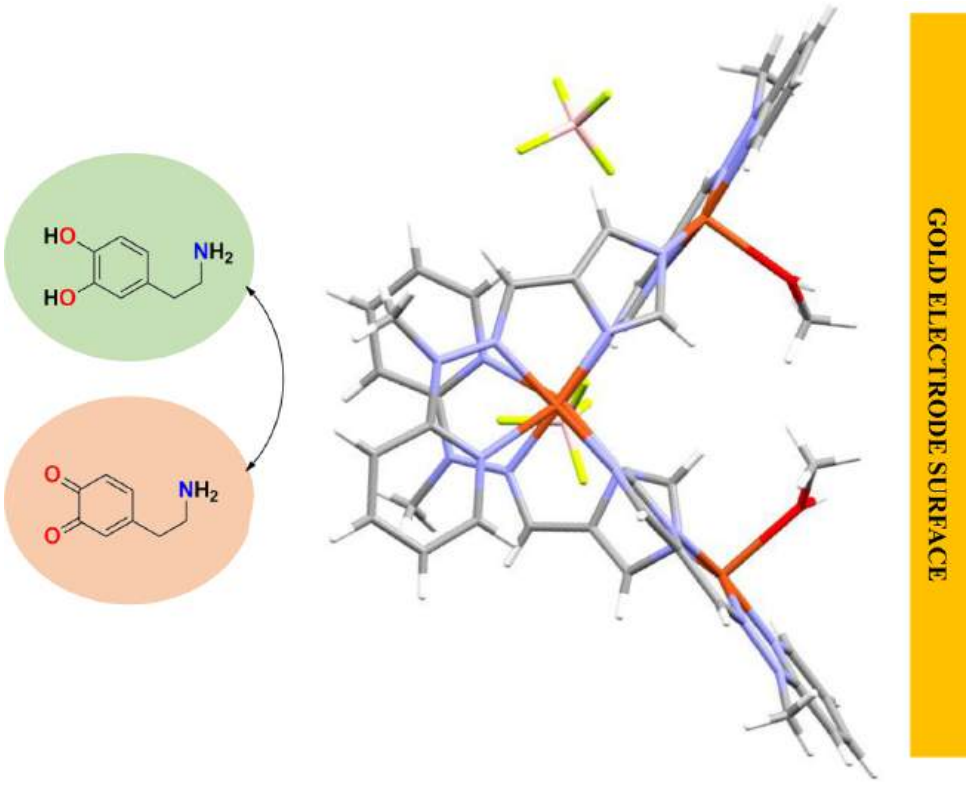

Fig. 5. A representative schematic of the arrangement of the complex during electrochemical measurements highlighting two regions, one associated with the gold electrode surface and the other providing active sites for the oxidation of dopamine.

S-Au bonding. This structural feature makes our system capable of modifying the gold surface and selectively detecting dopamine even more attractive due to, among other things, higher stability. A confirmation on the interaction between the Cu_4L_4 complex and the gold surface is provided by the surface coverage (Γ) calculation by integration of the charge (Q) flowing through the working electrode during the Cu_4L_4 complex electrodeposition from the equation: $Q = n\,F\,A\,\Gamma$ [31] (where: n - the number of electrons involved in the electron transfer process; F - the Faraday's constant; A - geometric area of the electrode). The surface coverage was estimated to be about 10.8 nmol cm^{-2}. The obtained Γ value allowed estimating the area per adsorbed molecule of the Cu_4L_4 which was 0.17 nm^2 and it is in agreement with the above findings. Moreover, it should be underlined that the calculated values of the surface coverage and the area per one adsorbed molecule of the Cu_4L_4 are compatible with the observed increase in the active surface area obtained by the modifying the gold electrode which demonstrates an improvement in the electroactivity of the electrode surface after modification in comparison with active surface area before modification. It is worth adding that adsorption of the Cu_4L_4 complex not only effectively protects the electrode surface from adsorption of poisonous reaction products, but also increases the electrode surface area and facilitates target transfer of electrons between the oxidized compound and

the gold electrode.

The surface morphology and chemical composition of both the bare gold electrode and the modified Au/complex electrode were investigated using scanning electron microscopy (SEM) with energy dispersive X-ray analysis (EDAX), which confirmed the modification of the bare gold electrode with Cu_4L_4 complex (Fig. 6). It can be clearly seen that the modification of the bare gold template with Cu_4L_4 complex drastically affects its morphology. The surface of the unmodified Au electrode is characterized by uniform surface material (Fig. 6a). Meanwhile the SEM image of the modified Au/complex electrode shows the process of accumulation of the complex on its surface, resulting in a relatively wide size distribution (Fig. 6b) and the formation of an irregular system with a tendency to aggregation. According to previously published [11], nitrogen-functionalized organic compounds form well-organized and compact monolayers on Au electrode. Most likely, such a structure provides easier access for possible reactants to the electrode surface. In addition, the EDAX analysis nicely showed the homogeneous distribution of elements in the tested sample, which is another proof of confirming that the adsorption of the used complex on the gold electrode surface has taken place (Fig. 6c–h). The latter is additionally proved by X-ray energy dispersion spectrum (see, Figs. S5, S6). Next, gold electrode surface modification by Cu_4L_4 complex has been confirmed by Attenuated Total Reflectance Infrared Spectroscopy (ATR-IR) spectra, where the C═N/C—N bands shifts observed in 1500–1200 cm^{-1} regions (Fig. S7) are evidence of the high affinity of aromatic nitrogen-containing heterocycles to the gold template. The adsorbed layer of the Cu_4L_4 complex on the surface of the electrode can effectively protect poisoning of the modified electrode surface by intermediate and/or final products of the redox processes under study.

3.4. Electrochemical behavior of dopamine at modified electrode

The modified Au/complex electrode has been used to study the electrochemical behavior of dopamine. The difference between the cyclic voltammograms recorded at the bare and at the Au/complex electrode in the presence of 0.5 mM dopamine is depicted at Fig. 7.

As can be seen, electrooxidation/electroreduction processes of dopamine at Au as well as at Au/complex electrode occur in two potential ranges as evidenced by the presence of 2 pairs of quasi-reversible peaks on the CVs. This is in accordance with the commonly known mechanism [32] presented below (Fig. 8).

At the bare gold electrode, according to the above scheme, an oxidation peak at $E = 0.32$ V is responsible to quasi-reversible oxidation of dopamine to o-dopaminoquinone which in the reverse scan undergoes reduction at $E = 0.17$ V. The peak-to-peak separation (ΔE_p) for these processes is equal to 150 mV. The change of the bare Au electrode to the Au/complex modified one shifts potentials of the two above aforementioned processes toward lower values and so oxidation/reduction process occur at $E = 0.23$ V and at $E = 0.13$ V, respectively. In the case of the Au/complex electrode, ΔE_p for processed occurred in the first step of the above adopted mechanism is approximately 100 mV. The second stage of the mechanism includes transformation of dopaminequinone to

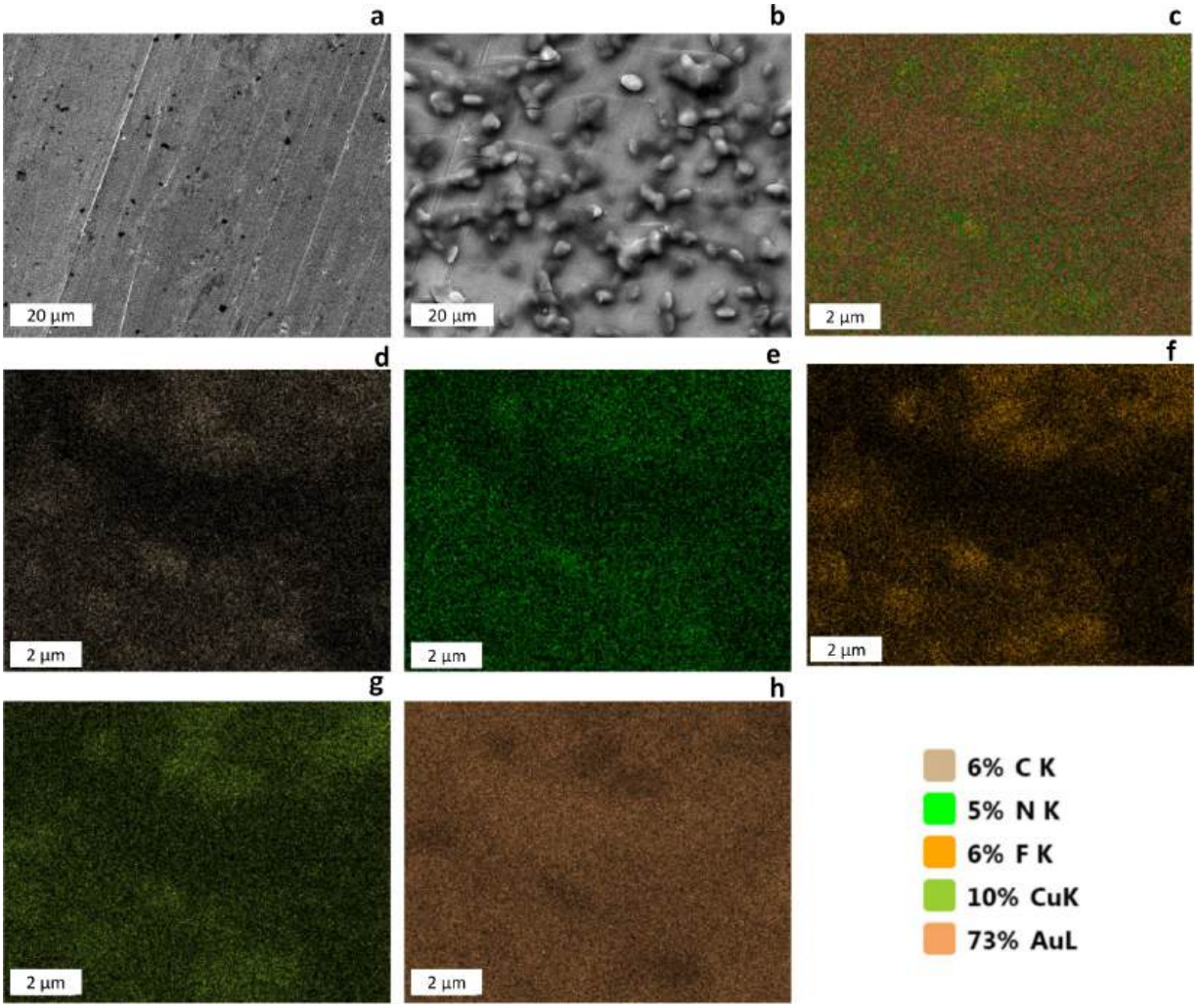

Fig. 6. SEM images of (a) the bare gold surface and (b) modified Au/complex electrode. (c-h) EDAX analysis of Au/complex electrode.

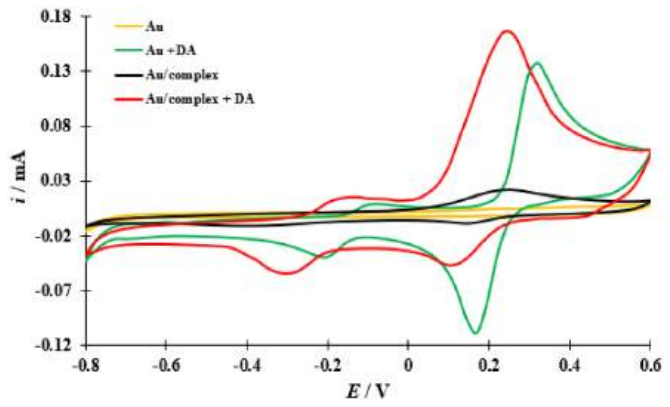

Fig. 7. Second scans of CVs recorded at the bare gold electrode (yellow) in PBS and in the presence of 0.5 mM DA (green), second scans of CVs recorded at the Au/complex electrode in PBS (black) and in the presence of 0.5 mM DA (red), $dE/dt = 0.1\ Vs^{-1}$.

leucodopaminochrome and it is not associated with electron exchange, it is chemical in nature. The subsequent couple of peaks at $E = -0.08$ V and at $E = -0.20$ V (ΔE_p= 120 mV) visible on the CV obtained for Au electrode is associated with quasi-reversible process of dopaminochrome formation. The location of these peaks shifts when the process occurs on the electrode modified by Cu_4L_4 and the pair of peaks under consideration appears at $E = -0.12$ V and at $E = -0.30$ V (ΔE_p = 180 mV). For clarity of the picture for Au + DA and Au/complex + DA systems, the second scans are shown in Fig. 7. This kind of presentation makes it easier to show both above described electrochemical steps. It should be noted that in addition to the potential shift of the observed redox processes, the replacement of the bare gold electrode with the modified one also results in an increase in the intensity of current signals. The latter together with the shift of the considered redox processes towards lower potentials, undoubtedly testifies to the catalytic effect of the Cu_4L_4 complex being accumulated at the electrode surface on the considered processes of dopamine. Note that the potential range at which the peak pair associated with the electrooxidation/electroreduction of dopamine to o-dopaminoquinone visible on CV overlaps with potential range of the oxidation/reduction of the Cu_4L_4 complex (Fig. 7), while at the same time the current response of dopamine at the Au/complex modified electrode is about 7.5 times higher. This observation strongly proves that the voltammetric response of dopamine is catalytically mediated by the Cu_4L_4 complex modified gold template.

3.5. Effect on pH on the electrocatalytic activity of dopamine at modified electrode

To examine the effect of pH on the position and intensity of oxidation signal of DA pH of the supporting electrolyte solution was varied from 3 to 11. An observation in Fig. 9 reveals a strong pH dependence of current signal with a maximum in the range of 6–8. Thus, supporting electrolyte solution at pH 7.0 close to physiological pH in human fluids was chosen for subsequent investigations. As it could be expected peak potential moves linearly toward less positive values with pH increasing and in the pH range from 3 to 11 the following equation is fulfilled: E_p= −0.060 pH + 0.64, (R^2 = 0.9996). The value of dE_p/dpH slope equal 0.06 indicates that during oxidation of DA on the Au/complex electrode the number of electrons exchanged is equal to the number of protons released [33].

3.6. Effect on scan rate on the electrocatalytic activity of dopamine at modified electrode

The dependence of the potential scan rate on the redox process provides some important kinetic information. A set of cycle voltammograms recorded on the Au/complex electrode with different scan rates is shown in Fig. 10a. As established, a linear relationship between the peak current and the square root of scan rate was obtained in the range from 0.02 Vs^{-1} to 0.50 Vs^{-1}, Fig. 10b. Analysis of the experimental data generated the following linear regression equation: i_p [mA] = 0.45 $v^{1/2}$ + 0.02 (R^2 = 0.993). This result proves that under the experimental conditions used, the overall rate of DA oxidation is limited by diffusion being slower than both adsorption of DA and following charge transfer at the electrode/solution interface. This conclusion is additionally supported by the value of d log i/d log v slope being very close to 0.5 [26]. It should be stressed that a diffusion-controlled electrode process is favorable for quantitative determination of analyte concentration in electrolyte solution.

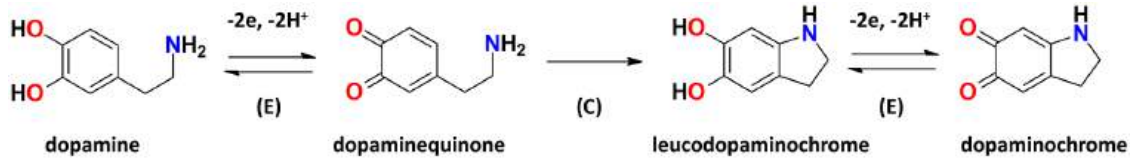

Fig. 8. Mechanism of dopamine electrooxidation.

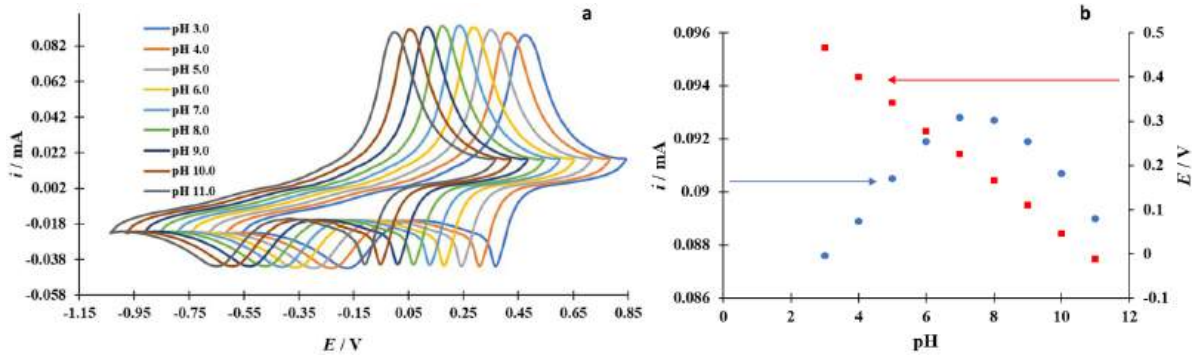

Fig. 9. (a) CVs of Au/complex electrode in supporting electrolyte with various pH in the presence of 0.05 mM DA, $dE/dt = 0.1\ Vs^{-1}$. (b) effect of pH on the peak current (blue) and the peak potential (red) during DA electrooxidation.

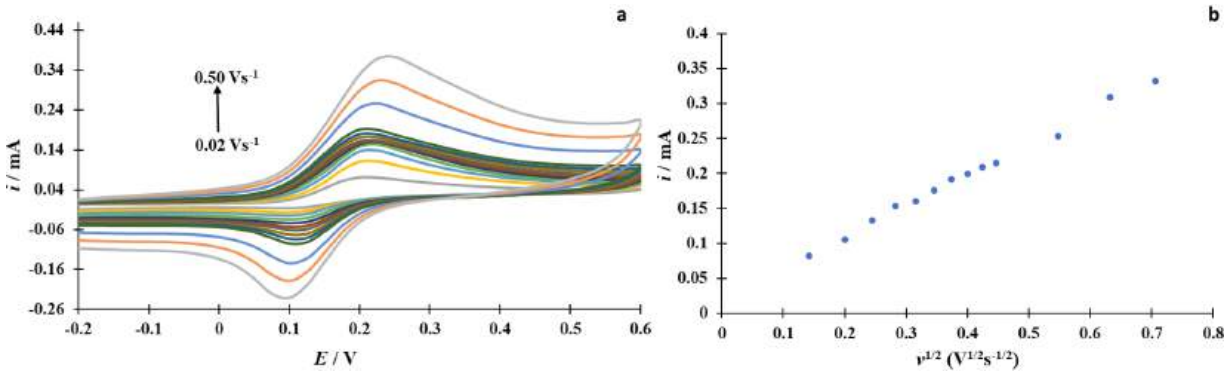

Fig. 10. (a) The CVs recorded at the modified gold electrode containing 0.5 mM of dopamine in PBS at various scan rates (0.02 and 0.50 Vs^{-1}). (b) the relationship between $i_p - v^{1/2}$ for the oxidation signal.

3.7. Electrochemical determination of dopamine

In the next stage of the study, the analytical sensitivity of the Au/complex electrode was determined for the quantification of dopamine by differential pulse voltammetry (DPV) in the DA concentration range from 0.0001 to 1.5 mM. The corresponding DPV voltammograms are presented in Fig. 11a (for the picture clarity only some DPV curves for selected DA concentrations are shown).

As follows from the course of DPVs, with increasing dopamine content in the bulk of solution the anodic peak current increases (for each tested concentration measurements were triplicated). The relationship between the peak current and the DA concentration is presented in Fig. 11b. According to Fig.11b, the peak current increased linearly from 0.0001 mM to 0.75 mM of dopamine. In this linear dynamic range (LDR), as established by using the at least square method, the following linear regression equation is satisfied: i_p [mA] = $17 \bullet 10^{-2}$ c_{DA} [mM] + $8 \bullet 10^{-2}$ ($R^2 = 0.9989$). At the DA concentration higher than 0.875 mM, the oxidation current started to diminish, which may be evidence that above this concentration DA begins to adsorb on the modified electrode surface [34]. At the same time the detection sensitivity (i_p/c_{DA}) at dE/dt = 0.1 Vs^{-1} was determined to be equal to 0.17 A M^{-1}. Moreover, the limit of detection (LOD) and the limit of quantification (LOQ) estimated according to formulas: LOD = 3 S_b / S and LOQ = 10 S_b / S, where: S_b is the standard deviation of current in the supporting electrolyte solution evaluated on the basis of 10 times repeated DPV measurements, S is the slope of the linear i vs $c_{analyte}$ dependence [35], were established at the level of 5.4 nM and 18.0 nM, respectively. The values of electroanalytical parameters obtained for the prepared electrochemical sensor based on the Au/complex conductive material are collected in Table 1 and are compared with these ones evaluated for other sensors published in the literature. This comparison gives rise to the conclusion that the Au/complex is a promising platform for the electrochemical determination of DA in real samples.

Table 1
Representative results of the DA sensing at various modified electrodes.

Type of electrode	Range of linearity [μM]	LOD [nM]	Sensitivity	Ref.
Au electrode modified by binuclear Cu(II) complex	0.2–30	80	–	[16]
Au electrode modified by Mn(II) complex	0.0001–850	6.8	4.11 A M^{-1} cm^{-2}	[11]
Graphite electrode modified by Cu(II) complex	–	500	2.01 A M^{-1} cm^{-2}	[36]
MWCNT/[Cu(sal-ala)bpy] nanocomposite modified GCE	0.1–300	160	2.3455 A M^{-1} cm^{-2}	[37]
PGE modified by Cu/Cu_xO nanoparticles	0.3–53	1060	0.51 A M^{-1}	[38]
Dopamine polymer film	1–600	200	–	[34]
CPE/ $K_2[Co^{II}(HL^{NNN})_2]$	0.25–100	12	0.180 A M^{-1}	[12]
GR-SWCNT-Ce-Cu-Tween 20/GCE	0.1–100	7.2	–	[6]
GPE modified by PDI-CuO	5–500	6	4 A M^{-1} cm^{-2}	[39]
GPE modified by La@CuO-DMT	10–1500	21	13.9 A M^{-1} cm^{-2}	[40]
GPE modified by Cu-Ag bimetallic	0.1–200	26	1.56 A M^{-1} cm^{-2}	[41]
Au electrode modified by tetranuclear Cu(II)	0.1–750	5.4	0.17 A M^{-1}	This work

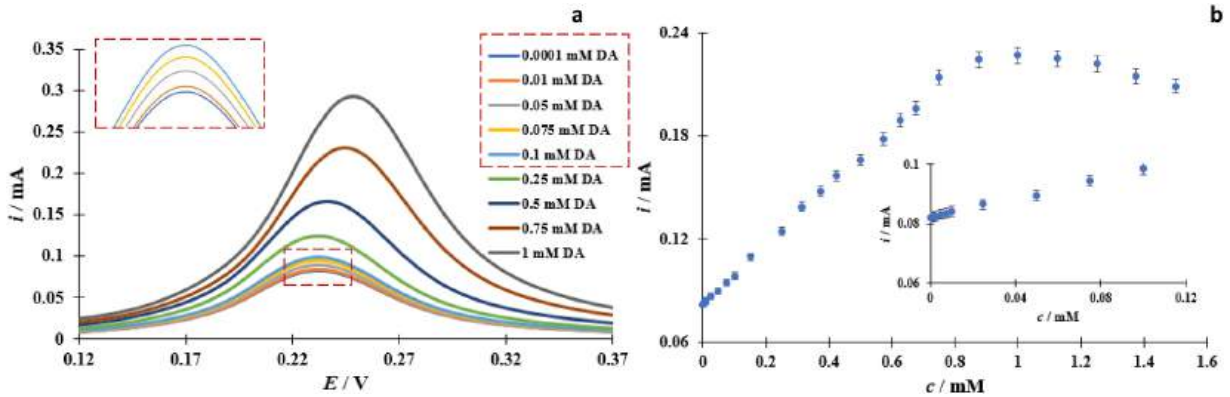

Fig. 11. (a) The DPVs recorded at the Au/complex electrode in addition of various concentration of dopamine in PBS, $dE/dt = 0.1$ Vs^{-1}. Insert: The excerpts of DPVs recorded for the lowest concentrations (red dashed line). (b) the relationship $i_p - c_{DA}$ in the dopamine concentration range (0.0001–1.5 mM). Insert: $i_p - c_{DA}$ in the narrow dopamine concentration range (0.0001 to 0.1 mM). Error bars correspond to the standard deviations of the measurements ($n = 3$).

The practical application of the developed Au/complex sensor was tested by DPV voltammetry for determination of DA in a commercially available DA solution for infusion. For this purpose, the calibration method was used [42]. To do so the content of the ampoule with this solution (specified as 10 mg cm^{-3}, 5 cm^3) was diluted and spiked with known amount of DA standard solution. For each tested solution the measurements were triplicated. The calibration curve was used to determine the concentration of each solution. The results are summarized in Table 2 together with the recovery and RSD. As can be seen, the concentrations found are very close to their nominal content in each sample. The recovery values varied from 98.9 % to 100.7 % confirm that the developed sensor is reliable and effective for DA determination in commercial samples. Moreover, the low values of RSD ranging from 1.7 % to 2.5 % show good precision of the proposed method.

3.8. Interference studies

The precise quantification of dopamine on the bare gold electrode is practically hampered in fluids containing some other biogenic molecules like for example ascorbic acid. As shown in Fig. 12a these two compounds oxidize on the unmodified Au electrode almost in the same potential range. Therefore, the subsequent objective of the study was to test the suitability of the developed Au/complex sensor for analytical study of DA in the mixture with AA. The corresponding voltammetric responses obtained with the Au/complex sensor are shown in Fig. 12b.

It can be observed that the deposition of Cu_4L_4 on the gold surface causes an increase of voltammetric signals of both analyzed substances and moreover significantly affects the peak-to-peak separation of considered processes. In the case of the Au/complex electrode, ΔE_p is 267 mV, while on the bare ΔE_p is equal to 56 mV. Thus, there is no doubt that the Au/complex electrode is suitable for simultaneous selective detection and analytical determination of dopamine in the presence of ascorbic acid and therefore also for determination of ascorbic acid in the presence of dopamine coexisting in a binary mixture.

In the binary mixture, the negative shift observed during dopamine oxidation and the positive shift recorded during AA oxidation on the Au/complex electrode can be attributed to electrostatic attraction and repulsion, which are caused by the presence of Cu_4L_4 complex, where the copper(II) ions are positively charged, the tridentate Schiff-base ligand is negative in charge, as is also the tetrafluoroborate anion. When referring to the representative schematic arrangement of the complex during electrochemical measurements (Fig. 5) the region that provides active sites for the oxidation of dopamine is exposed to the tetrafluoroborate anion, which would also explain the observed negative shifts. It is worth noting that similar behavior has been observed by Jiang et al., where acetate anions were the exposed negatively charged groups (while still coordinated to positively charged copper(II) ions) [16]. The effect of this process is to exclude most of the AA anions from the Cu_4L_4 modified electrode surface, causing a shift in the peak potential of the AA current toward a higher AA overpotential. At the same time, a reduction in the DA oxidation overpotential can be observed, the cause of which is the electrostatic attraction between Cu_4L_4 and positively charged DA cations.

The analytical sensitivity of the Au/complex sensor toward quantification of DA and AA in a binary mixture was determined by using the DPV technique and varying the concentration of one compound with that of the other kept constant. The DA concentration was changed in the range from 0.0001 mM to 1.5 mM and selected DPV voltammograms recorded in the presence of 0.5 mM of AA are shown at Fig. 13a. And conversely, the concentration of AA was varied from 0.5 mM to 5 mM, and selected DPV curves obtained in the presence of 0.5 mM DA are presented in Fig. 13b.

As expected, due to electrostatic interactions, the peaks corresponding to oxidation of the individual components of the tested binary mixture under investigation appear on the DPV at different potential values. An increase in the concentration of each component of the binary mixture results in an increase in the DPV signal corresponding to the oxidation of individual components of the tested mixture. Moreover, it should be noted that an increase in the concentration of each component in the studied mixture does not affect the peak potential at which DA and AA oxidize. This means that certainly the Au/complex electrode can be successfully applied for the analytical purposes intended in this work.

Fig. 14a and b shows the analysis of the peak currents versus concentration of individual compounds in the binary mixture under investigation.

By using the at least square method, the following linear regression equation was obtained for DA in the presence of constant amount of AA: i_p [mA] = $17\bullet10^{-2}$ c_{DA} [mM] + $8\bullet10^{-2}$ (R^2 = 0.9989) in the LDR between 0.0001 mM and 0.75 mM. The LOD and LOQ values for DA quantification in this system were estimated as 5.4 nM and 18.0 nM, respectively. Note that LOD and LOQ values are analogous to those estimated for dopamine alone (see above). Meanwhile for AA in the presence of constant amount of DA in the LDR between 0.5 mM and 5 mM the rectilinear relationship is represented by the following linear regression equation: i_p [mA] = $19\bullet10^{-3}$ c_{AA} [mM] + $17\bullet10^{-2}$ (R^2 = 0.9986), whereas the LOD and LOQ values are equal to 0.37 mM and 1.11 mM, respectively.

As above for DA alone, the practical application of the new Au/complex electrode for determination of DA in the presence of AA has been tested by the calibration method. For each studied sample, the measurements were repeated three times. The concentrations evaluated from calibration curves for both components of double mixture under investigation are very close to their nominal content in each sample, Table S2. On this basis, it is concluded that the presence of the interfering compound in the mixture with DA does not affect the quality of the quantitative analysis.

In addition to studying the effect of AA on DA quantitative determination, the effect of other possible interfering species on dopamine quantification at the Au/complex electrode has been investigated. For this purpose, various species (Na^+, K^+, Mg^{2+}, Ca^{2+}, Zn^{2+}, NO_3^-, SO_4^{2-}) at concentration of 5 mM were added to the supporting electrolyte solution (pH 7.0) containing 0.05 mM DA. It was observed that 100-fold excess of the aforementioned interferences had no effect on the DPV voltammetric signal derived from DA. The collected results are summarized in Table S3, and once again confirm that the designed modified Au/complex electrode shows good ability to specifically detect DA without any interference from the above species.

3.9. Electrode reproducibility and long-term stability of the modified electrode

To determine the reproducibility of the Au/complex electrode, five measurements were carried out in separate PBS solutions containing 0.05 mM dopamine. The calculated RSD values did not differ by more than 2.8 %, indicating the excellent reproducibility of the prepared new electrochemical sensor.

The long-term stability of the Au/complex electrode was examined every 8 days for 24 days in PBS solution containing 0.05 mM DA. Before and after each electrochemical measurement, the electrode was washed with water and dried in a stream of argon gas. For the time between

Table 2
Determination of DA in a commercially available DA solution for infusion (n = 3).

Initial amount [mM]	Spiked amount [mM]	Found amount [mM]	Recovery [%] (Mean±SD)	RSD [%]
0.150	0	0.149	99.3 ± 2.0	2.0
0.150	0.01	0.161	100.6 ± 1.8	1.9
0.150	0.02	0.168	98.8 ± 2.3	2.4
0.150	0.05	0.199	99.5 ± 1.7	1.7
0.150	0.1	0.252	100.8 ± 2.0	2.2
0.150	0.15	0.302	100.7 ± 2.5	2.5

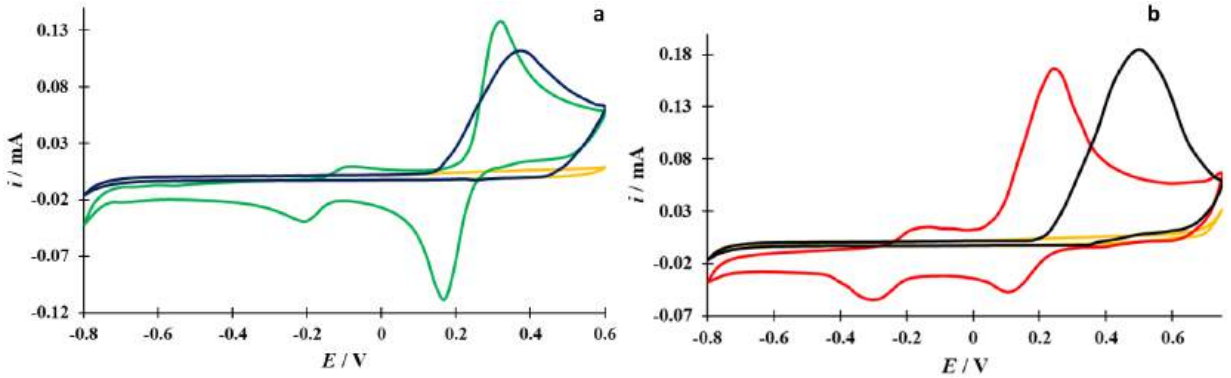

Fig. 12. (a) CVs recorded at the bare Au electrode in PBS (yellow) containing 0.5 mM DA (green) and 0.5 mM AA (blue), $dE/dt = 0.1$ Vs^{-1}. (b) CVs recorded at Au/complex electrode in PBS (yellow) containing 0.5 mM DA (red), 0.5 mM AA (black), $dE/dt = 0.1$ Vs^{-1}.

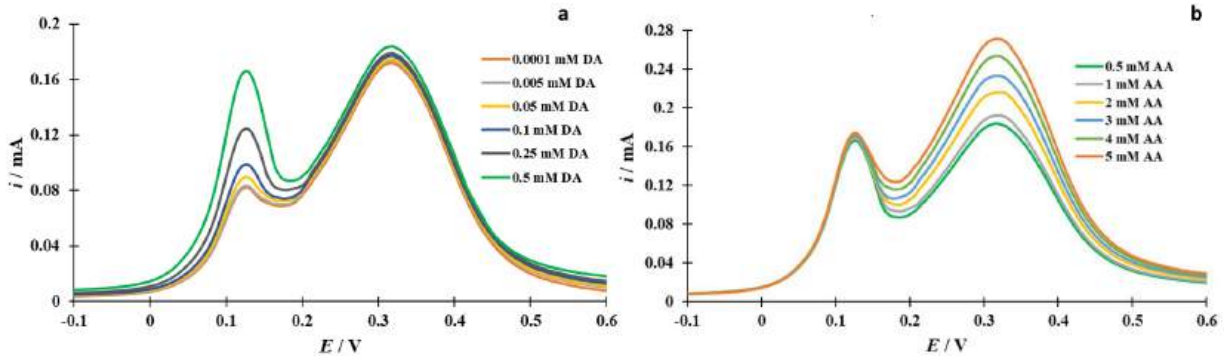

Fig. 13. DPVs recorded at the Au/complex electrode in PBS solution containing (a) 0.5 mM AA and increasing concentrations of DA (from 0.0001 mM to 0.5 mM) (b) 0.5 mM DA and increasing concentrations of AA (from 0.5 mM to 5 mM). $dE/dt = 0.1$ Vs^{-1}.

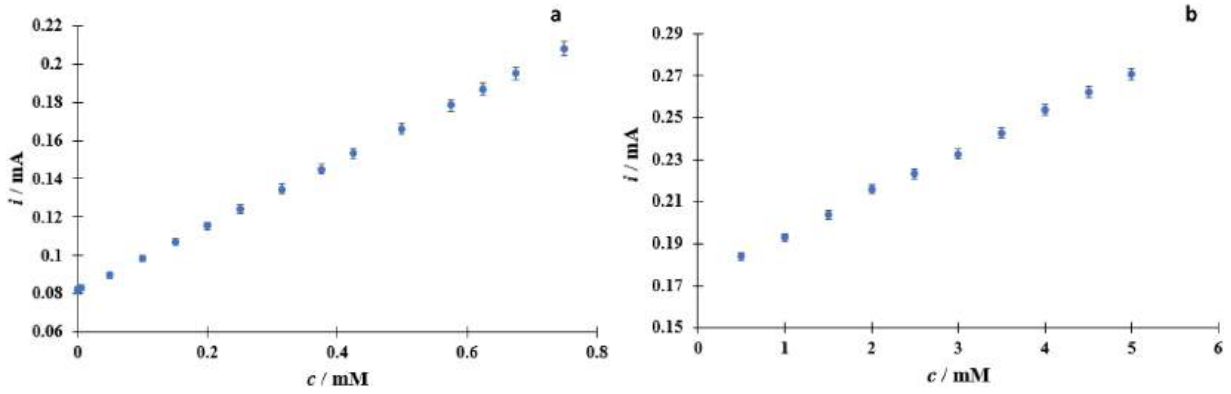

Fig. 14. (a) The relationship between the peak current and concentration of DA in the presence of 0.5 mM AA (b) The relationship between the peak current and concentration of AA in the presence of 0.5 mM DA in a binary mixture. $dE/dt = 0.1$ Vs^{-1} Error bars correspond to the standard deviations of the measurements ($n = 3$).

measurements, the electrode was stored in an empty tube at room temperature. After 24 days, the voltammetric response decreased by about 4.9 % compared to the first measurement.

4. Conclusions

In summary, the tetrametallic copper(II) discrete [4 × 4] complex $[Cu_4(L\text{-}H)_4(BF_4)_2(MeOH)_2](BF_4)_2$ has been obtained and characterized. In addition, it was proven that the saddle-type complex promotes the formation of two regions, one having affinity for the gold electrode surface due to N-heterocycles and the other constituting a cavity with four copper ions as active centers for the catalytic oxidation of dopamine. The prepared complex was used for modification of the gold electrode surface forming an excellent electrochemical sensor for dopamine sensing in aqueous medium, thus creating conditions similar to physiological ones. The measurements showed that the modified electrode has good selectivity, sensitivity, long-term stability and reproducibility. In addition, the Au/complex electrode is capable of detecting dopamine in the presence of interfering biogenic compounds such as ascorbic acid with low LOD and LOQ value of 5.4 nM and 18.0 nM, respectively. Additionally, other possible interfering species that may occur in the aqueous medium did not interfere with the dopamine detection. These results pave the way for further investigation of polymetallic copper(II) complexes based on Schiff base ligands capable of

accumulation on the electrode surface and with an emphasis on their use as sensors for detecting neurotransmitters in the presence of interferents.

Supplementary materials

Supplementary material associated with his article can be found, in the online version, at doi:

CRediT authorship contribution statement

Daria Nowicka: Investigation, Formal analysis, Data curation, Visualization, Writing – review & editing, Funding acquisition. **Maciej Kubicki:** Formal analysis, Investigation, Data curation, Writing – review & editing, Visualization. **Violetta Patroniak:** Supervision, Resources, Visualization, Writing – review & editing. **Teresa Łuczak:** Investigation, Methodology, Conceptualization, Formal analysis, Data curation, Resources, Visualization, Writing – review & editing, Project administration. **Adam Gorczyński:** Conceptualization, Methodology, Writing – review & editing, Project administration, Supervision, Resources, Funding acquisition.

Declaration of competing interest

The authors declare that they have no known competing financial interests or personal relationships that could have appeared to influence the work reported in this paper.

Data availability

Data will be made available in the open data repository.

Acknowledgments

This work was supported by the National Science Centre, Poland (grant numbers UMO-2022/45/N/ST4/00632, UMO-2020/39/D/ST4/01182). Daria Nowicka is a scholarship holder of the Adam Mickiewicz University in Poznan Foundation for the academic year 2023/2024. We express gratitude to Dr. Aleksandra Bocian for help in synthesis of ligand and the complex.

Supplementary materials

Supplementary material associated with this article can be found, in the online version, at doi:10.1016/j.electacta.2023.143754.

References

[1] S.J. Lee, B. Lodder, Y. Chen, T. Patriarchi, L. Tian, B.L. Sabatini, Cell-type-specific asynchronous modulation of PKA by dopamine in learning, Nature 590 (2021) 451–456.
[2] S.M. Siddeeg, Electrochemical detection of neurotransmitter dopamine, Int. J. Electrochem. Sci. 15 (2020) 599–612.
[3] S. Srinivas, A. Senthil Kumar, Surface-activated pencil graphite electrode for dopamine sensor applications: a critical review, Biosensors 13 (2023) 353–370.
[4] R.P. Bacil, L. Chen, S.H.P. Serrano, R.G. Compton, Dopamine oxidation at gold electrodes: mechanism and kinetics near neutral pH, Phys. Chem. Chem. Phys. 22 (2020) 607–614.
[5] K. Schmack, M. Bosc, T. Ott, J.F. Sturgill, A. Kepecs, Striatal dopamine mediates hallucination-like perception in mice, Science 372 (2021) 1–9.
[6] C. Liu, P. Goel, P.S. Kaeser, Spatial and temporal scales of dopamine transmission, Nat. Rev. Neurosci. 22 (2021) 345–358.
[7] M. Lakshmanakumar, N. Nesakumar, A.J. Kulandaisamy, J.B.B. Rayappan, Principles and recent developments in optical and electrochemical sensing of dopamine: a comprehensive review, Measurement 183 (2021) 109873.
[8] M. Sajid, M.K. Nazal, M. Mansha, A. Alsharaa, S.M.S. Jillani, C. Basheer, Chemically modified electrodes for electrochemical detection of dopamine in the presence of uric acid and ascorbic acid: a review, TrAC Trends Anal. Chem. 76 (2016) 15–29.
[9] N. Tukimin, J. Abdullah, Y. Sulaiman, Review—electrochemical detection of uric acid, dopamine and ascorbic acid, J. Electrochem. Soc. 165 (2018) B258.
[10] S.I. Kaya, S. Kurbanoglu, S.A. Ozkan, Nanomaterials-based nanosensors for the simultaneous electrochemical determination of biologically important compounds: ascorbic acid, uric acid, and dopamine, Crit. Rev. Anal. Chem. 49 (2019) 101–125.
[11] A. Gorczyński, D. Pakulski, M. Szymańska, M. Kubicki, K. Bułat, T. Łuczak, V. Patroniak, Electrochemical deposition of the new manganese(II) Schiff-base complex on a gold template and its application for dopamine sensing in the presence of interfering biogenic compounds, Talanta 149 (2016) 347–355.
[12] E. Turunc, I. Gumus, H. Arslan, Redox active Co(II) complex modified carbon paste electrode for the determination of dopamine, Mater. Chem. Phys. 243 (2020) 122597.
[13] A.S. Butt, N. Baig, M. Khan, A. Ul-Hamid, M. Sher, M. Altaf, M. Sohail, HfO2-CoO nanoparticles for electrochemical dopamine sensing, Electrochem. Sci. Adv. 2 (2022) e2100013.
[14] M.I. Awad, B. Al-jahdaly, M. Kassem, O. Hazazi, Nickel oxide nanoparticles modified gold electrode for fractional determination of dopamine and ascorbic acid, J. Anal. Chem. 73 (2018) 1188–1194.
[15] A. Gorczyński, M. Kubicki, K. Szymkowiak, T. Łuczak, V. Patroniak, Utilization of a new gold/Schiff-base iron(iii) complex composite as a highly sensitive voltammetric sensor for determination of epinephrine in the presence of ascorbic acid, RSC Adv. 6 (2016) 101888–101899.
[16] G. Jiang, X. Gu, G. Jiang, T. Chen, W. Zhan, S. Tian, Application of a mercapto-terminated binuclear Cu(II) complex modified Au electrode to improve the sensitivity and selectivity for dopamine detection, Sens. Actuators B: Chem. 209 (2015) 122–130.
[17] E.F. Welch, K.W. Rush, R.J. Arias, N.J. Blackburn, Copper monooxygenase reactivity: do consensus mechanisms accurately reflect experimental observations? J. Inorg. Biochem. 231 (2022) 111780.
[18] N. Puentes-Díaz, D. Chaparro, D. Morales-Morales, A. Flores-Gaspar, J. Alí-Torres, Role of metal cations of copper, iron, and aluminum and multifunctional ligands in Alzheimer's disease: experimental and computational insights, ACS Omega 8 (2023) 4508–4526.
[19] M. Boulkroune, A. Lemaire, A. Chibani, F. Geneste, Monocopper complex based on N-tripodal ligand immobilized in a Nafion® film for biomimetic detection of catechols: application to dopamine, Electrochim. Acta 221 (2016) 80–85.
[20] M. Szymańska, M. Kubicki, G.N. Roviello, G. Consiglio, M.A. Fik-Jaskółka, V. Patroniak, New Cu(i) square grid-type and Ni(ii) triangle-type complexes: synthesis and characterization of effective binders of DNA and serum albumins, Dalton Trans. 51 (2022) 15648–15658.
[21] M. Szymańska, I. Pospieszna-Markiewicz, M. Mańka, M. Insińska-Rak, G. Dutkiewicz, V. Patroniak, M.A. Fik-Jaskółka, Synthesis and spectroscopic investigations of Schiff base ligand and its bimetallic Ag(I) complex as DNA and BSA binders, Biomolecules 11 (2021) 1449.
[22] S. Napierała, M. Kubicki, V. Patroniak, M. Wałęsa-Chorab, Electropolymerization of [2 × 2] grid-type cobalt(II) complex with thiophene substituted dihydrazone ligand, Electrochim. Acta 369 (2021) 137656.
[23] A. Bocian, A. Gorczyński, D. Marcinkowski, S. Witomska, M. Kubicki, P. Mech, M. Bogunia, J. Brzeski, M. Makowski, P. Pawluć, V. Patroniak, New benzothiazole based copper(II) hydrazone Schiff base complexes for selective and environmentally friendly oxidation of benzylic alcohols: the importance of the bimetallic species tuned by the choice of the counterion, J. Mol. Liq. 302 (2020) 112590.
[24] A. Bocian, M. Szymańska, D. Brykczyńska, M. Kubicki, M. Wałęsa-Chorab, G. N. Roviello, M.A. Fik-Jaskółka, A. Gorczyński, V. Patroniak, New Artificial Biomimetic Enzyme Analogues Based on Iron(II/III) Schiff Base Complexes: an Effect of (Benz)imidazole Organic Moieties on Phenoxazinone Synthase and DNA Recognition ‡, Molecules 24 (2019) 3173–3196.
[25] T. Łuczak, Activity of gold towards methylamine electrooxidation, J Appl Electrochem 37 (2007) 461–466.
[26] A. Kisza, Electrochemistry II, Technical Scientific Publishers, Warsaw, 2001.
[27] T. Łuczak, Gold and nanogold electrodes modified with gold nanoparticles and meso-2,3-dimercaptosuccinic acid for the simultaneous, sensitive and selective determination of dopamine and its biogenic interferents, Electroanalysis 26 (2014) 2152–2160.
[28] S. Watcharinyanon, Structure of self-assembled monolayers on gold studied by NEXAFS and photoelectron spectroscopy, 2008.
[29] S. Radenković, M. Antić, N.D. Savić, B.Đ. Glišić, The nature of the Au–N bond in gold(iii) complexes with aromatic nitrogen-containing heterocycles: the influence of Au(iii) ions on the ligand aromaticity, New J. Chem. 41 (2017) 12407–12415.
[30] G. Kaur, R.L. Thimes, J.P. Camden, D.M. Jenkins, Fundamentals and applications of N-heterocyclic carbene functionalized gold surfaces and nanoparticles, Chem. Commun. 58 (2022) 13188–13197.
[31] E. Laviron, The use of linear potential sweep voltammetry and of a.c. voltammetry for the study of the surface electrochemical reaction of strongly adsorbed systems and of redox modified electrodes, J. Electroanal. Chem. Interfacial Electrochem. 100 (1979) 263–270.
[32] M.D. Hawley, S.V. Tatawawadi, S. Piekarski, R.N. Adams, Electrochemical studies of the oxidation pathways of catecholamines, J. Am. Chem. Soc. 89 (1967) 447–450.
[33] A.J. Bard, L.R. Faulkner, H.S. White, Electrochemical methods: Fundamentals and Applications, John Wiley & Sons, 2022.
[34] T. Łuczak, Preparation and characterization of the dopamine film electrochemically deposited on a gold template and its applications for dopamine sensing in aqueous solution, Electrochim. Acta 53 (2008) 5725–5731.
[35] C. Analytical Methods, Recommendations for the definition, estimation and use of the detection limit, Analyst 112 (1987) 199–204.
[36] A.P. Sandoval-Rojas, L. Ibarra, M.T. Cortés, M.A. Macías, L. Suescun, J. Hurtado, Synthesis and characterization of copper(II) complexes containing acetate and N,N-donor ligands, and their electrochemical behavior in dopamine detection, J. Electroanal. Chem. 805 (2017) 60–67.

[37] S. Sakthinathan, S.-M. Chen, W.C. Liao, Multiwalled carbon nanotube supported Schiff base copper complex inorganic nanocomposite for enhanced electrochemical detection of dopamine, Inorg. Chem. Front. 4 (2017) 809–819.
[38] E. Bahrami, R. Amini, S. Vardak, Electrochemical detection of dopamine via pencil graphite electrodes modified by Cu/CuxO nanoparticles, J. Alloys Compd. 855 (2021) 157292.
[39] U. Amara, S. Riaz, K. Mahmood, N. Akhtar, M. Nasir, A. Hayat, M. Khalid, M. Yaqub, M.H. Nawaz, Copper oxide integrated perylene diimide self-assembled graphitic pencil for robust non-enzymatic dopamine detection, RSC Adv. 11 (2021) 25084–25095.
[40] U. Amara, K. Mahmood, M. Hassan, M. Hanif, M. Khalid, M. Usman, Z. Shafiq, U. Latif, M.M. Ahmed, A. Hayat, M.H. Nawaz, Functionalized thiazolidone-decorated lanthanum-doped copper oxide: novel heterocyclic sea sponge morphology for the efficient detection of dopamine, RSC Adv. 12 (2022) 14439–14449.
[41] M. Hyder, G.R.K. Reddy, B. Naveen, P.S. Kumar, Copper-silver bimetallic nanoelectrocatalyst on pencil graphite substrate for highly selective amperometric dopamine sensor, Chem. Phys. Lett. 740 (2020) 137086.
[42] W. Szczepaniak. Instrumental Methods of Chemical Analysis, Polish Scientific Publishers PWN, Warsaw, 2010.

Supporting Information

Self-assembly of Simple Schiff base Ligand into unique Saddle-type [4x4] Tetranuclear Architecture and Its Application as Selective Voltammetric Dopamine Sensor in Aqueous Conditions

Daria Nowicka [a]*, Maciej Kubicki [a], Violetta Patroniak [a], Teresa Łuczak [a], Adam Gorczyński [a]*

[a] Faculty of Chemistry, Adam Mickiewicz University in Poznań, Uniwersytetu Poznańskiego 8, 61-614 Poznań, Poland

* corresponding author.

Email address: d.nowicka@amu.edu.pl (D.N.); adam.gorczynski@amu.edu.pl (A.G.)

1. Synthesis and physical characterization

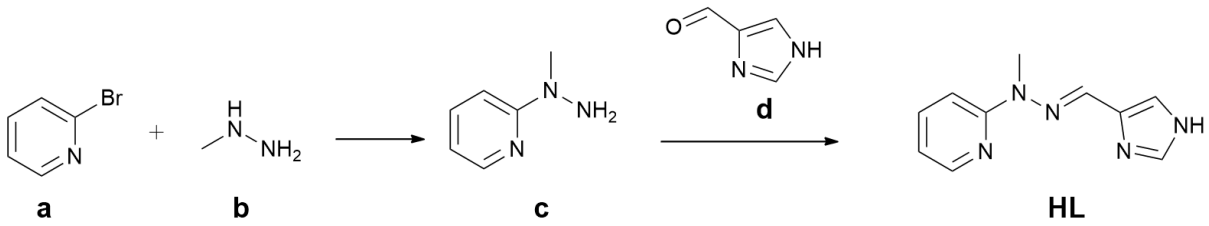

Fig. S1. Scheme of HL [$C_{10}H_{11}N_5$] ligand synthesis.

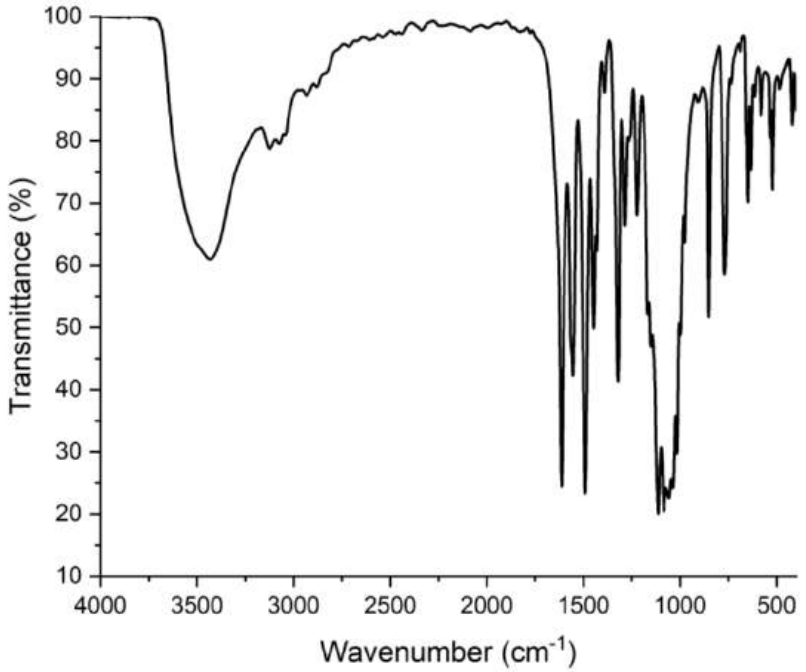

Fig. S2. FT-IR spectrum of Cu_4L_4 complex.

2. Crystallographic studies

X-ray diffraction data were collected at 100(1) K by the ω-scan technique on Rigaku four-circle XCalibur diffractometer (Eos detector) with graphite-monochromatized MoK_α radiation (λ=0.71073 Å). The data were corrected for Lorentz-polarization and absorption effects [1]. The structure was solved with SHELXT [2] and refined with the full-matrix least-squares procedure on F^2 by SHELXL [3]. All non-hydrogen atoms were refined anisotropically,

hydrogen atoms were placed in the calculated positions and refined as 'riding model' with the isotropic displacement parameters set at 1.2 (1.5 for methyl) times the U_{eq} value for appropriate non-hydrogen atom. As the structure contains large voids with heavily disordered solvent molecules, and the attempts to model the guests did not lead to improvement of the model, SQUEEZE procedure [4] has been applied.

Crystal data: $(C_{42}H_{48}Cu_4N_{20}O_2)^{4+}\cdot 4(BF_4)^-$, M_r = 1466.40, monoclinic, C2/c, a = 19.6488(4) Å, b = 13.7738(3) Å, c = 24.5401(4) Å, β = 102.3957(19)º, V = 6486.7(2) Å^3, Z = 4, d_x = 1.502 g·cm^{-3}, F(000) = 2944, μ = 1.390 cm^{-1}, 19245 reflection collected, 6873 symmetry independent (R_{int} = 2.21%), 5937 with I>2σ(I). Final R[I>2σ(I)] = 0.0361, wR2[I>2σ(I)] = 0.1084, R [all reflections] = 0.0434, wR2[all reflections] = 0.1138, S = 1.039, ($\Delta\rho_{max}$/ $\Delta\rho_{min}$) = 1.06/-0.55 e·Å^{-3}. CCDC deposition number: 2267914.

Crystallographic data for the structural analysis has been deposited with the Cambridge Crystallographic Data Centre, Nos.. Copies of this information may be obtained free of charge from: The Director, CCDC, 12 Union Road, Cambridge, CB2 1EZ, UK. Fax: +44(1223)336-033, e-mail:deposit@ccdc.cam.ac.uk, or www: www.ccdc.cam.ac.uk.

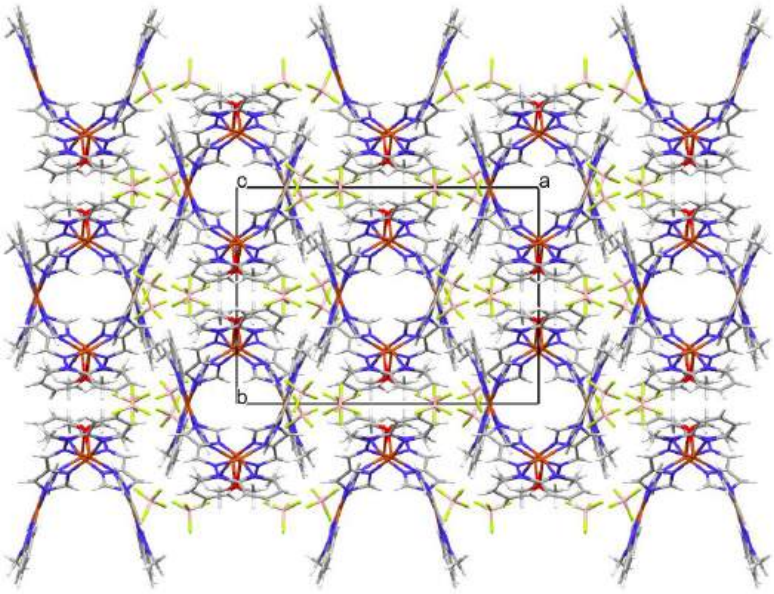

Fig. S3. An example of the crystal packing of a structure of Cu_4L_4 complex.

Table S1. Selected geometrical data (Å, º); [i] denotes symmetry operation *1-x,y,1/2-z*.

Cu1-N3A	1.9328(19)	Cu2-N3B	1.9638(19)
Cu1-N1B	1.9918(19)	Cu2-N1A^{i}	1.9773(19)
Cu1-N7B	1.9456(19)	Cu2-N7A^{i}	1.9753(19)
Cu1-N11B	2.0003(19)	Cu2-N11A^{i}	1.9857(19)
Cu1-F3D^{i}	2.609(2)	Cu2-O1C	2.287(2)
N3A-Cu1-N7B	177.47(9)	N3B-Cu2-N7A^{i}	163.97(8)
N1B-Cu1-N11B	160.11(8)	N1A^{i}-Cu2-N11A^{i}	159.03(8)

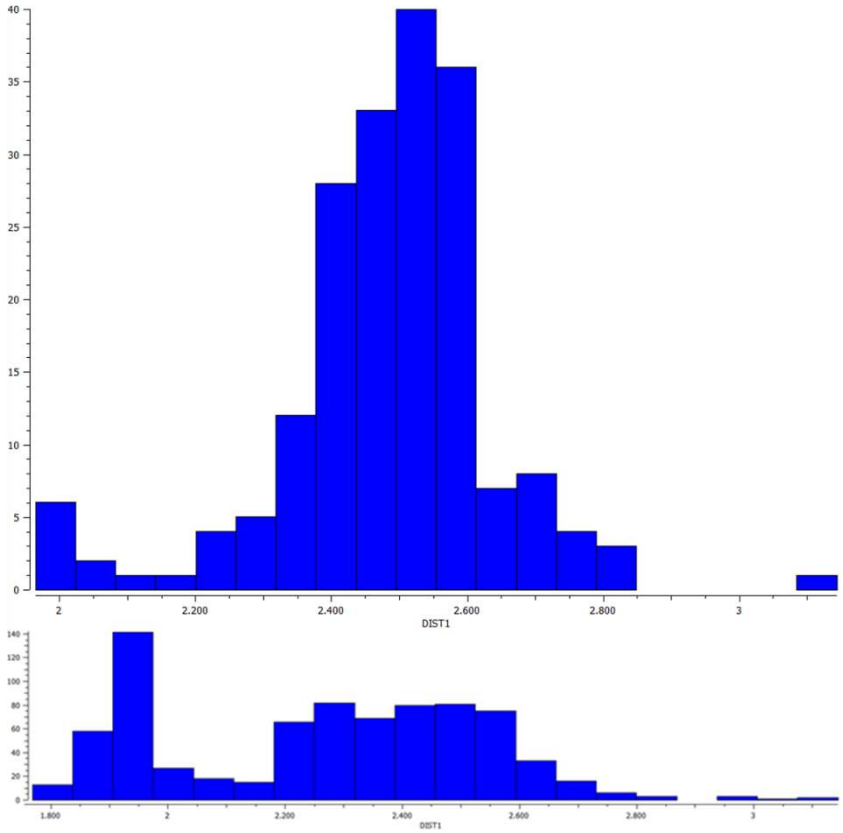

Fig. S4. Histograms showing numbers of certain Cu-F distances for BF_4 (upper) and for all contacts (lower).

3. Characterization of the modified electrode

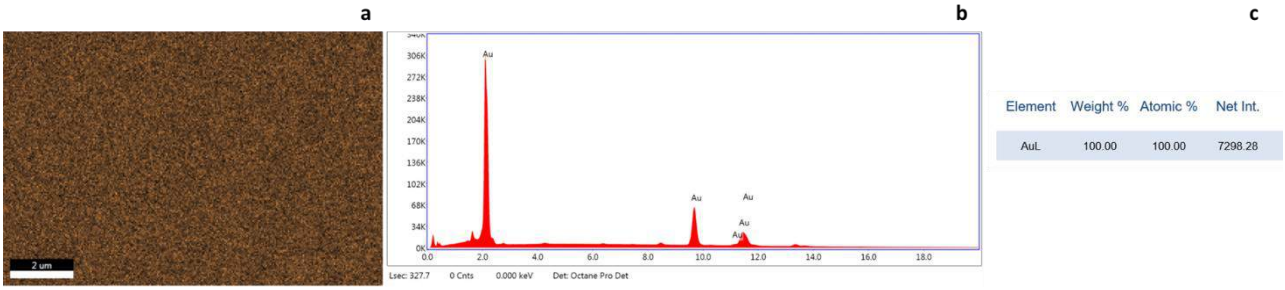

Fig. S5. (a) EDAX analysis of the bare Au electrode (2 μm) and its (b, c) X-ray energy dispersion spectrum.

a

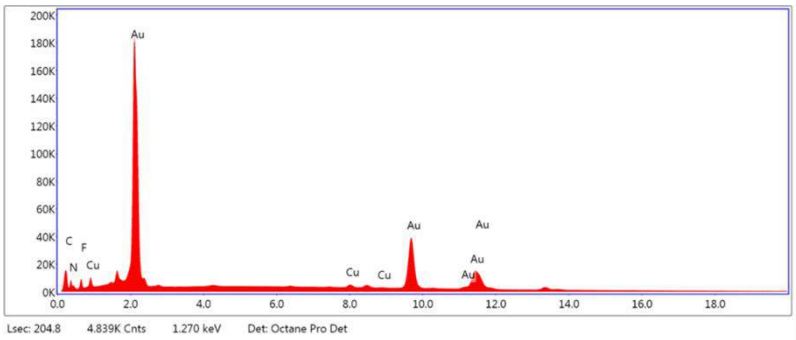

b

Element	Weight %	Atomic %	Net Int.
C K	24.71	61.35	1365.83
N K	10.47	22.29	239.68
F K	4.46	6.99	456.65
CuK	0.74	0.35	348.85
AuL	59.62	9.02	6954.79

Fig. S6. (a, b) X-ray energy dispersion spectrum of the Au/complex electrode.

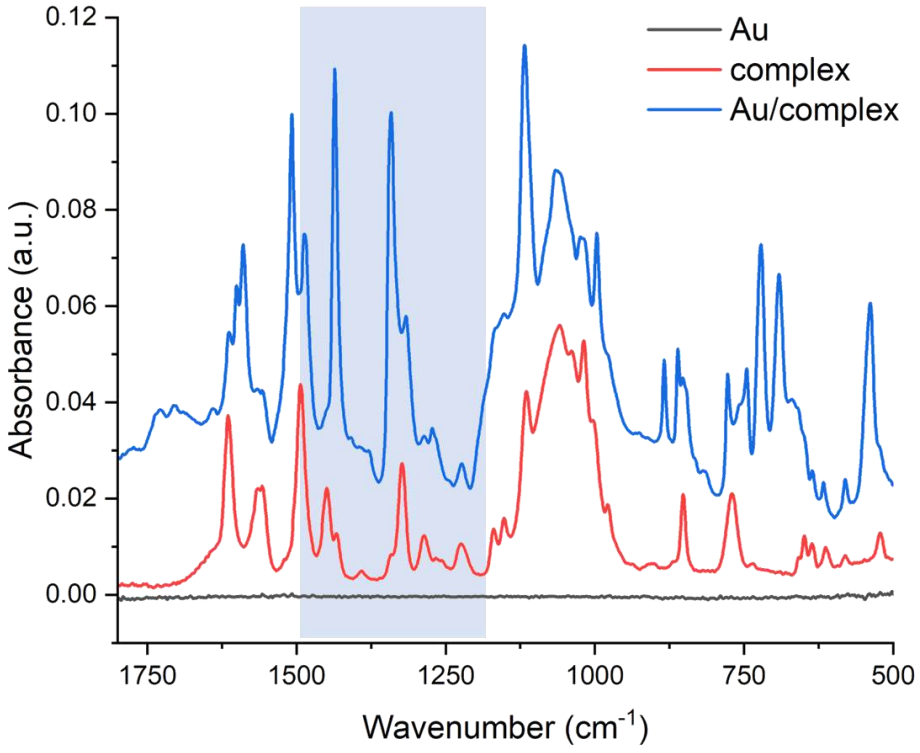

Fig. S7. Comparison of ATR-IR spectra of the bare Au electrode, Cu_4L_4 complex and Au/complex electrode.

4. Electrochemical experiments

Table S2. Determination of DA in the presence of AA (n = 3).

Initial amount [mM]		Spiked amount [mM]		Found amount [mM]		Recovery [%]		RSD [%]	
DA	AA	DA	AA	DA	AA	DA	AA	DA	AA
0.150	0.50	0	0	0.148	0.48	98.7	96.0	2.1	1.9
0.150	0.50	0.01	0	0.162	0.51	108.0	102.0	1.8	1.8
0.150	0.50	0.02	0	0.168	0.52	98.8	104.0	2.4	1.9
0.150	0.50	0.05	0	0.199	0.49	99.5	98.0	1.7	2.0
0.50	0.50	0	0.1	0.51	0.61	102.0	101.7	2.0	1.6
0.50	0.50	0	0.4	0.49	0.89	98.0	98.9	1.2	1.1
0.50	0.50	0	0.7	0.48	1.22	96.0	101.7	1.7	1.2
0.50	0.50	0	1.0	0.49	1.47	98.0	98.0	2.0	1.5

Table S3. Sensing of 0.05 mM DA with addition of 5 mM of some interferents (n = 3) at the Au/complex electrode.

Type of interference	Found DA [mM]	Recovery [%]	RSD [%]
Na^+	0.0479	95.8	2.5
K^+	0.0516	103.2	3.8
Mg^{2+}	0.0531	106.2	2.5
Ca^{2+}	0.0490	98.0	2.2

Zn^{2+}	0.0537	107.4	1.9
NO_3^-	0.0522	104.4	2.3
SO_4^{2-}	0.0474	94.8	3.0

References:

[1] Rigaku Oxford Diffraction CrysAlis PRO (Version 1.171.38.41), (2015).

[2] G. Sheldrick, SHELXT - Integrated space-group and crystal-structure determination, Acta Crystallographica Section A, 71 (2015) 3-8.

[3] G.M. Sheldrick, Crystal structure refinement with SHELXL, Acta crystallographica. Section C, Structural chemistry, 71 (2015) 3-8.

[4] A.L. Spek, PLATON SQUEEZE: a tool for the calculation of the disordered solvent contribution to the calculated structure factors, Acta Crystallographica Section C: Structural Chemistry, 71 (2015) 9-18.

Dalton Transactions

ROYAL SOCIETY OF CHEMISTRY

PAPER

Cite this: *Dalton Trans.*, 2025, **54**, 1000

Application of a simple copper(II) complex compound as an epinephrine selective voltammetric sensor in the presence of uric acid under aqueous conditions†

Daria Nowicka,*[a] Karol Garbaczewski,[a] Teresa Łuczak,[a] Giuseppe Forte,[b] Giuseppe Consiglio,[c] Maciej Kubicki,[a] Violetta Patroniak[a] and Adam Gorczyński*[a]

Received 23rd September 2024,
Accepted 10th November 2024

DOI: 10.1039/d4dt02702g

rsc.li/dalton

Developing sensors with high sensitivity and selectivity for detecting neurotransmitters under near-physiological conditions is a major challenge and is crucial for preventing diseases of the nervous, cardiovascular, and endocrine systems. Most existing systems that meet these requirements involve either complicated synthesis processes, require sulfur groups, or are not functional under aqueous conditions. Herein, we report that the self-organisation of a simple imine ligand L with copper(II) tetrafluoroborate leads to the formation of a $[CuL_2](BF_4)_2$ complex (CuL_2) with a 2 : 1 ligand-to-metal ratio, as confirmed by high-resolution electrospray ionization mass spectrometry (HR ESI-MS), Fourier-transform infrared (FT-IR) spectroscopy and single-crystal X-ray analysis. Surprisingly, modifying a gold surface with a self-assembled monolayer of the CuL_2 complex created a stable sensor for selective detection of epinephrine (EP) using differential pulse voltammetry (DPV) in phosphate buffer solution (PBS) at pH 7.0. A linear correlation between the current response and the concentration of EP was observed with a detection limit of 0.03 μM, high reproducibility and good stability in the range of 0.0001 to 0.875 mM. These results show that the new sensor (Cu/Au) can serve as a reliable analytical tool to selectively detect EP alone and in a mixture with coexisting uric acid (UA) in tested samples.

1. Introduction

Epinephrine (EP), otherwise known as adrenaline, is classified as an important catecholamine neurotransmitter necessary for the proper functioning of the central nervous, cardiovascular and endocrine systems of mammals.[1,2] Abnormal levels of EP in living organisms result in health problems. Thus, too high levels of EP may be associated with stress or hypothyroidism, while too low levels may indicate Parkinson's disease. Furthermore, epinephrine is commonly used in medicine as a drug to treat allergic reactions, glaucoma, asthma, sepsis, heartbeat stimulation or myocardial infarction.[3–7]

To avoid the problems associated with abnormal EP concentrations, the development of a rapid, efficient and selective method for the quantification of this neurotransmitter in living organisms is needed. Numerous studies have led to advances in analytical procedures for EP sensing using spectroscopic,[8] chromatographic[9] and fluorescence[10] methods. Unfortunately, their use is associated with high costs, prolonged analysis times and, most importantly, a lack of selectivity. A review of the literature shows that, as EP is readily oxidized, the most cost-effective methods for its quantification are electrochemical methods. EP determinations performed by the latter methods feature high selectivity, sensitivity, accuracy, precision and relatively low instrumentation costs.[11] Unfortunately, EP occurs in the natural environment along with some small biomolecules, such as uric acid (UA), which oxidize at bare electrodes in almost the same potential range.[12] Therefore, separation of the oxidation potentials of these compounds is necessary for accurate neurotransmitter determination.

Among miscellaneous attempts to overcome the above-mentioned problem, much attention has been paid to the appli-

[a]*Faculty of Chemistry, Adam Mickiewicz, University in Poznań, Uniwersytetu Poznańskiego 8, 61-614 Poznań, Poland. E-mail: d.nowicka@amu.edu.pl, adam.gorczynski@amu.edu.pl*

[b]*Department of Drug Science and Health, University of Catania, Via S. Sofia 64, 95125, Italy*

[c]*Department of Chemical Science, University of Catania, Via S. Sofia 64, 95125, Italy*

† Electronic supplementary information (ESI) available: Synthesis and analysis of the CuL_2 complex, additional characterization of the bare gold electrode and supplementary electrochemical experiments. CCDC 2346925. For ESI and crystallographic data in CIF or other electronic format see DOI: https://doi.org/10.1039/d4dt02702g

cation of altered electrodes to develop suitable EP sensors. Hence, in EP electrooxidation, a variety of chemically and/or electrochemically modified electrode templates was prepared and examined. Many modification attempts were devoted to electrodes made of various carbon materials, *e.g.* a carbon paste electrode (CPE) that was altered with carbon nanofibers[13] or graphene quantum dot chitosan[14] and used for EP detection. Subsequently, application of a glassy carbon electrode (GCE) coated with a biopolymer,[15] catechol,[16] polyrutin,[17] Au nanoparticles[18–20] or nanocomposites prepared from various nanoparticles and functionalized multiwalled carbon nanotubes[21] for EP sensing was reported. In the literature there are also papers demonstrating modification of a screen printing electrode (SPE), including with dysprosium tungstate nanoparticles[22] and Cu(II) nanocomplexes,[23] for EP detection. In addition, there are also examples of selective EP sensing in the presence of UA, which were carried out on CPE coated with iron(II) phthalocyanine[6] or graphene oxide (GO),[24] and on SPE altered with a nanocomposite film combined with electrochemically reduced GO and NiO nanoparticles,[25] among others. Concomitantly, the literature supports the possibility of selective EP determination using Au electrodes decorated with a self-assembled monolayer (SAM). Effective protection of the electrode surface from toxic reaction products is the major advantage of this type of modification.[4,5,18,26–28] An Au electrode modified with SAM layers consisting of a Schiff base with thiol moieties[27] or metallo-octacarboxyphthalocyanine complexes and cysteamine[18] was used as a sensor for EP determination. The same interference was described on a gold electrode coated with 2-(2,3-dihydroxyphenyl)-1,3-dithiane SAM[29] or AgNPs–penicillamine[30] and on an Au nanoporous electrode.[31] Moreover, the detection of EP in the presence of UA on the Au electrode modified with SAM layers formed by an iron(III) complex $[Fe_2(H_3L)_2(CH_3OH)_2(\mu\text{-}OCH_3)_2](ClO_4)_4$ based on a Schiff base[4] has been reported by us.

The limited examples of gold electrode modification with SAMs of complex compounds prompted us to develop a Schiff base system that could serve as an inexpensive, environmentally friendly and stable epinephrine sensor with low detection and quantitation limits. By using well-defined small molecules, we aimed to address the reproducibility challenges typically associated with nanoparticle-based or hybrid systems. Herein, we synthesized a new copper(II) complex $[CuL_2](BF_4)_2$ based on the N,N,N-donor imine ligand L, referred to here as CuL_2. Due to its –NH groups, this complex readily forms SAMs on a bare gold surface through chemisorption. The resulting voltammetric sensor (Cu/Au) demonstrated effective EP detection both independently and in the presence of interfering UA under aqueous PBS conditions.

2. Experimental section

2.1. Materials and apparatus

Adrenaline (epinephrine) WZF 0.1% (300 mcg per 0.3 ml and 1 pre-filled syringe, 1 ml) for injections was bought from a local pharmacy. The remaining chemical substances and all solvents for synthesis, characterization and electrochemical measurements were bought from commercial sources (Sigma-Aldrich, Fluka, POCh-Gliwice) and used as delivered without any additional purification.

Fourier-transform infrared (FT-IR) spectra were collected using a FT-IR IFS 66/s Bruker spectrometer and attenuated total reflection infrared spectra (ATR-IR) were recorded using a Nicolet iS 50 spectrometer, both in the range from 400 to 4000 cm^{-1}. Electrospray ionization mass spectrometry (ESI-MS) was obtained utilizing a High-Resolution Bruker QTOF Impact HD spectrometer by dissolution of a powder sample of complex in a methanolic solution. Microanalyses were performed using a PerkinElmer 2400 CHN microanalyser. Thermogravimetry (TG) analysis was conducted on a Netzsch TG 209 Libra analyzer under a nitrogen atmosphere in the temperature range of 24–1000 °C. UV-vis absorption spectra with a concentration of 2.0×10^{-5} M in appropriate solution (MeOH or aqueous PBS with pH = 7.4) were recorded in the range of 250̀600 nm using cuvettes of 1 cm path length by a JASCO V-770 spectrophotometer (JASCO, Japan). Scanning electron microscopy (SEM) analyses were performed using a Quanta 250 FEG, FEI scanning electron microscope with energy dispersive X-ray analysis (EDAX). The electrochemical measurements were performed with a potentiostat/galvanostat analyzer (AUTOLAB PGSTAT 302N, Eco Chemie, B.V., Utrecht, The Netherlands) at room temperature in a three-electrode system with a (unmodified or modified) gold electrode (99.999%, Polish State Mint) as a working electrode with a geometric area of 0.33 cm^2, a saturated calomel electrode (SCE) as a reference electrode and a platinum wire as an auxiliary electrode. A pH meter (Model-ULAB 2002) was used to record pH measurements.

2.2. Synthesis of ligand L

Ligand L was obtained using a two-step synthesis process according to a synthesis report published earlier.[32] The first step was a nucleophilic substitution reaction between two components: 2-bromopyridine and methylhydrazine in an excess, and the second step was the condensation between the product synthesized in the first step: primary amine 2-(1-methylhydrazinyl)pyridine and 4-imidazolecarboxaldehyde (Fig. S1†).

2.3. Synthesis of copper(II) complex $[CuL_2](BF_4)_2$

Complex $[CuL_2](BF_4)_2$ was synthesized by adding $Cu(BF_4)_2 \cdot xH_2O$ (17.90 mg, 0.075 mmol) to a methanolic solution of the imine ligand L (30.00 mg, 0.15 mmol) at a molar ratio of 1 : 2 (ligand : metal) (Fig. S2†). The reaction mixture was stirred using a magnetic stirrer in a 50 ml round-bottom flask for 24 h at room temperature to give a dark-green solution. The reaction mixture was concentrated and then Et_2O was added. The precipitate was obtained, filtered *via* suction filtration, washed with Et_2O (2 × 5 ml) and dried under vacuum. Yield: 42.53 mg, 88.7% based on ligand L.

$[CuL_2](BF_4)_2$: HRMS (ESI) *m*/*z*; found: $[CuL(BF_4)(MeCN)]^+$ 393.2050; requires $[CuL(BF_4)(MeCN)]^+$ 393.2027 (5.85 ppm); found: $[Cu(L–H)L(BF_4)Na]^+$ 575.1980; requires $[Cu(L–H)L(BF_4)Na]^+$ 575.1955 (4.35 ppm); found: $[CuL_2(BF_4)MeCN]^+$ 593.2958; requires $[CuL_2(BF_4)MeCN]^+$ 593.2931 (4.55 ppm). Elemental analysis calc. for $C_{27}H_{40}B_2CuF_8N_{10}O_2$ $[CuL_2](BF_4)_2{\cdot}MeOH{\cdot}iPr_2O$ (773.83): C, 41.91; H, 5.21; N, 18.10; found: C, 42.00; H, 5.16; N, 18.16%. FT-IR (KBr cm^{-1}): ν(N–H) 3527, 3343; ν(C–H)$_{ar}$ 3141; ν(C–H) 2896; ν(C═N)$_{imine}$ 1643; ν(C═C)$_{ar}$ 1608, 1569, 1490, 1447; ν(C–N) 1323; ν(C═N)$_{ar}$ 1214; ρ(C–H)$_{ar}$ 1056; γ(C–H)$_{ar}$ 849, 768, 613.

2.4. X-ray crystallography

Diffraction data were collected on a Rigaku XCalibur four-circle diffractometer with an EOS CCD detector using the ω-scan technique at 100(1) K with graphite-monochromated MoK_α radiation (λ = 0.71073 Å). The data were adjusted for Lorentz-polarization and for absorption effects.[33] Precise unit-cell parameters were obtained by least-squares fitting. The highest intensity reflections were selected from the entire experiment. The structure was solved with SHELXT[34] and improved with the full-matrix least-squares procedure on F^2 by SHELXL.[35] All non-hydrogen atoms were refined anisotropically, while hydrogen atoms were posted in idealized positions and enhanced as a 'riding model' with isotropic displacement parameters set at 1.2 (1.5 for methyl groups) times U_{eq} of appropriate carrier atoms.

Structural analysis crystallographic data were deposited at the Cambridge Crystallographic Data Centre.

2.5. Electrode activation and modification

All solutions were arranged using ultra-pure deionized water and were deaerated with highly pure argon (99.998%) prior to measurements, which were carried out at room temperature in pre-washed laboratory vessels in peroxymonosulfuric acid (Piranha solution, Caro acid). Before use, the bare Au electrode was polished with alumina slurries of successively decreasing final grades down to 0.05 μM (Buehler) on polishing cloths (Buehler). Then, the polished gold template was rinsed carefully with acetone and water and next, it was electrochemically activated by cycling within the range of E = −0.8 V and E = 0.6 V *vs*. SCE at dE/dt = 0.1 V s^{-1} in 0.5 M sodium hydroxide until the stable cyclic voltammogram was obtained. This described procedure evades structural changes on the Au surface.[36] To modify the surface of the gold electrode with the self-assembling monolayer of CuL_2, the activated bare Au electrode was immersed in 0. 01 mM CuL_2 dissolved in PBS (0.06 M; pH 7.0) for 16 h at room temperature. After this time, the electrode was washed profusely with water to remove unadsorbed compounds from the electrode surface, dried in a stream of argon and stored at room temperature in an empty tube. The modified electrode thus prepared was ready-to-use for electrochemical measurements (denoted as Cu/Au in the manuscript).

2.6. Molecular simulations

Molecular simulations of the studied complexes were performed using the Gaussian 16 software package.[37] The geometries were fully optimized by employing the B3LYP functional in conjunction with the 6-311+G(2d,p) basis set. To calculate the absorption spectra, the TD-DFT method was applied with the same basis set, considering the lowest 20 singlet–singlet transitions employing the long-range corrected CAM-B3LYP functional.[38,39] Solvent effects were modeled using the conductor-like polarizable continuum model (CPCM).[40,41]

3. Results and discussion

3.1. Synthesis of the complex and theoretical analysis

Copper(II) complex was synthesized *via* direct reaction of copper(II) tetrafluoroborate with ligand L and was isolated in very high yield *via* precipitation. Its structure was unambiguously determined to be *mer*-$[CuL_2](BF_4)_2$, using single-crystal X-ray analysis (see section 3.2), whereas elemental analysis, high-resolution mass spectrometry together with FT-IR spectroscopy (Fig. S3†) and thermogravimetric analysis (Fig. S4†) confirmed the purity of the synthesized sample.

To verify that the *mer*-configuration of the complex is retained in the solution and does not convert into the *fac*-isomer, density functional theory analysis was performed. The CuL_2 complex, as obtained from X-ray crystallography, was subjected to an optimization procedure, and the resulting geometry is shown in Fig. 1A. In order to investigate the possibility of the *mer*-isomer converting into the *fac*-isomer, a study was conducted on the rotational barrier around the dihedral angle formed by atoms 1, 2, 3, and 4 (Fig. 1B-left), which the ligand must overcome to adopt the favorable geometry for the formation of the *fac*-isomer. For this purpose, the considered dihedral angle should assume a value close to 90°, as illustrated in Fig. 1B-right. The results obtained are shown in Fig. 1C and highlight that the absolute energy minimum of the monomer corresponds to the geometry with a dihedral angle of 177.20°, while a relative minimum is observed with a dihedral angle of −2.80°. However, this rotation is associated with a $\Delta G°$ of 5.29 kcal mol^{-1}. Analysis of the population corresponding to some of these dihedral angle values is presented in Table 1, revealing a significant steric hindrance to the formation of a conformer at 90°, and consequently to the possibility of *mer*- to *fac*-isomer conversion, in agreement with the experimental synthetic results (*vide infra*).

To further support the prohibiting of *mer*- to *fac*-isomer conversion, an optimization was carried out based on the geometry of the *fac*-isomer shown in Fig. 1D-left. The optimized structure so obtained is reported in Fig. 1D-right. As shown, it exhibits a tetrahedral coordination, which is markedly different from the initial octahedral geometry, confirming that the formation of the *fac*-isomer would be energetically unfavorable. Finally, experimental UV-vis spectra of the *mer*-isomer were measured in water (PBS solution used for electrochemical measurements) and methanol. They were then compared with

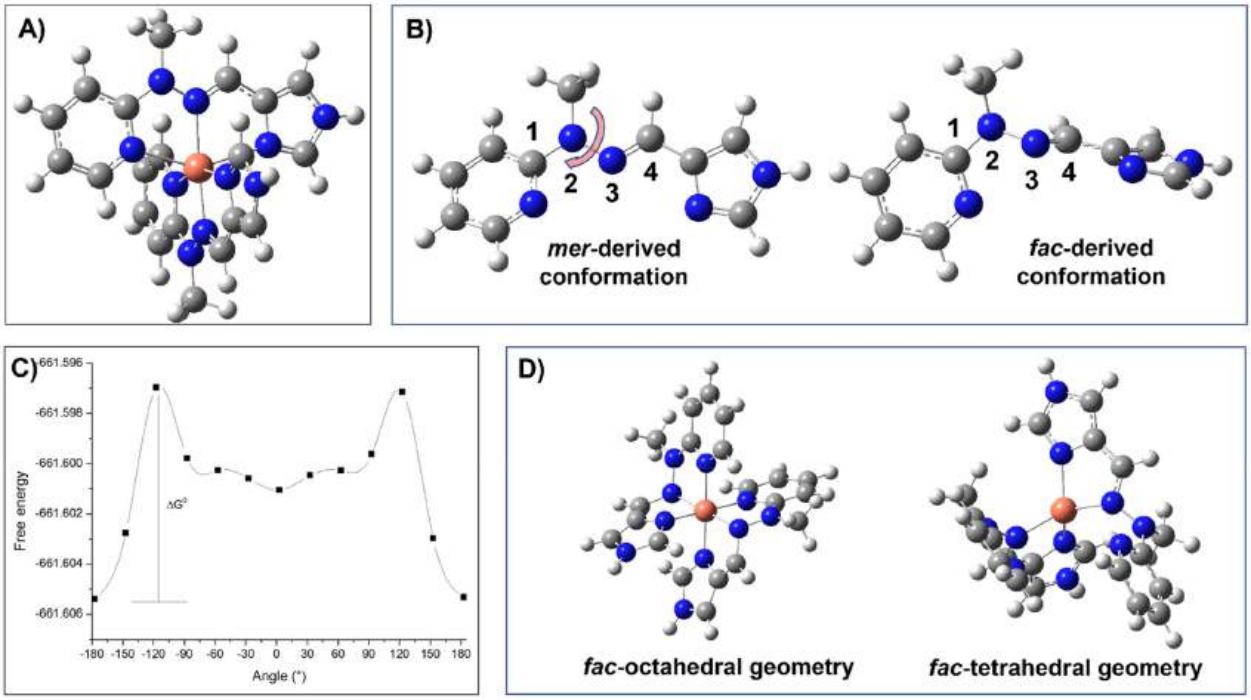

Fig. 1 (A) Optimized geometry of CuL_2 in methanol at the B3LYP/6-311+G(2d,p)/CPCM level; (B) definition of the dihedral angle of the ligand for the rotational barrier study (left) and geometry associated with the ligand conformation required for the formation of the *fac*-isomer (right); (C) energy *vs*. dihedral angles formed by atoms 1, 2, 3 and 4, which are kept fixed during each optimization; and (D) starting geometry for the optimization of the *fac*-isomer (left) and optimized geometry of the *fac*-isomer at the B3LYP/6-311+G(2d,p)/CPCM level (right).

Table 1 Parameters used for the calculation of *mer*- and *fac*-complex fraction population distributions

Dihedral angle (°)	Gibbs free energy (Hartree)	% of population $(N_i/N_{tot})^a$
177.20	−661.6053986	93.93
147.20	−661.6027662	5.79
117.20	−661.5969627	0.01
87.20	−661.5997828	0.27

[a] Fraction population distribution is calculated as: $\frac{N_i}{N_{tot}} = \frac{e^{-\frac{\Delta G_i}{RT}}}{\sum_{j=1}^{N} e^{-\frac{\Delta G_j}{RT}}}$.

TD-DFT calculated spectra and are in good agreement (Fig. S5†). Notably, a bathochromic shift is observed in methanol, and the trend in the absorption intensities of the two main calculated bands is consistent with that of the experimental results. These altogether prove that the solid state structural representation of the complex is retained in the solution in the *mer*-configuration.

3.2. Crystallographic analysis

A description of an anisotropic displacement ellipsoid of the cationic complex is shown in Fig. 2a, while some relevant geometrical characteristics are presented in Table S1.†

The Cu^{2+} ion in the cationic complex is coordinated in a distorted octahedral arrangement by six nitrogen donor atoms

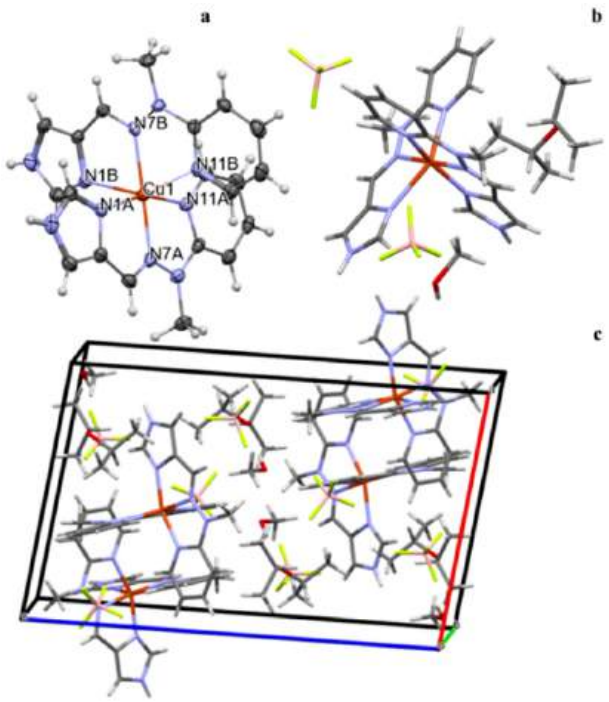

Fig. 2 (a) Cation complex anisotropic ellipsoid representation. (b) Crystal structure of the CuL_2 complex including the cationic part of the compound and the two BF_4 counterions, along with the solvent molecules, methanol and diisopropyl ether. (c) An example of the crystal packing of a structure of the CuL_2 complex.

Table 2 Relevant geometrical characteristics (Å, °)

Distances (Å)	Angles (°)
Cu1–N1A	2.016(4)
Cu1–N1B	2.402(4)
Cu1–N7A	1.999(4)
Cu1–N7B	2.049(4)
Cu1–N11A	2.019(4)
Cu1–N11B	2.246(4)
N1A–Cu1–N11A	158.36(15)
N1B–Cu1–N11B	149.22(13)
N7A–Cu1–N7B	175.95(15)

from two molecules of ligands (three from each). Interestingly there seems to be a difference in the interactions between the metal cation and the ligands as the Cu–N bonds are much shorter for one of the ligands (A, *cf.* Table 2). The ligand molecules are in a good approximation plane, and they are almost perpendicular in the complex; the dihedral angle between the mean planes of the ligand molecules is equal to 86.75°.

In the crystal structure, besides the two BF_4^- counteranions, there are also solvent molecules of methanol and diisopropyl ether (Fig. 2b). The crystal structure is an effect of different interactions, from the electrostatic interaction between the charged species through stronger N–H···F and weaker C–H···F hydrogen-bond-like interactions to really weak but ubiquitous van der Waals interactions.

3.3. Electrochemistry of obtained copper(II) complex on Au electrode and its characterization

Cyclic voltammogram (CV) of the bare Au electrode recorded in PBS (0.06 M, pH 7.0) as a supporting electrolyte solution (SES) in the potential range of E = −0.8–1.15 V *vs.* SCE at dE/dt = 0.1 V s^{-1} is presented in Fig. 3a. A well-defined pair of reversible peaks located at 0.83 V and 0.48 V *vs.* SCE is responsible for the gold oxide formation and for its reduction, respectively. In a wide range of potentials (E = −0.8 V to E = 0.6 V relative to the SCE) no electrochemical reactions take place on the Au electrode surface. Further electrochemical measurements can be analyzed in this potential window.

The CV of the Au electrode after its modification in a 0.01 mM solution of the CuL_2 complex in the range of potential from E = −0.8 to −1.15 V *vs.* SCE at dE/dt = 0.1 V s^{-1} is presented in Fig. 3b. For comparison CVs of the bare Au electrode in PBS and in the sight of ligand L are shown too. As can be seen from the obtained cyclic voltammetry, the prepared ligand L is inactive on the Au electrode, and its addition to the SES does not change the shape of the CV. Alterations in the *i–E* course were noted after modification of the Au surface. For the prepared modified Cu/Au electrode a well-defined anodic peak at 0.25 V *vs.* SCE and cathodic peak at 0.18 V *vs.* SCE is visible.

This pair of oxidation/reduction peaks according to the literature data[42–44] was assigned to Cu(I)/Cu(II) oxidation and Cu(II)/Cu(I) reduction, respectively.

The electrochemical activity of these processes was studied at various scan rates ranging from 0.02 to 0.50 V s^{-1} (Fig. 4a).

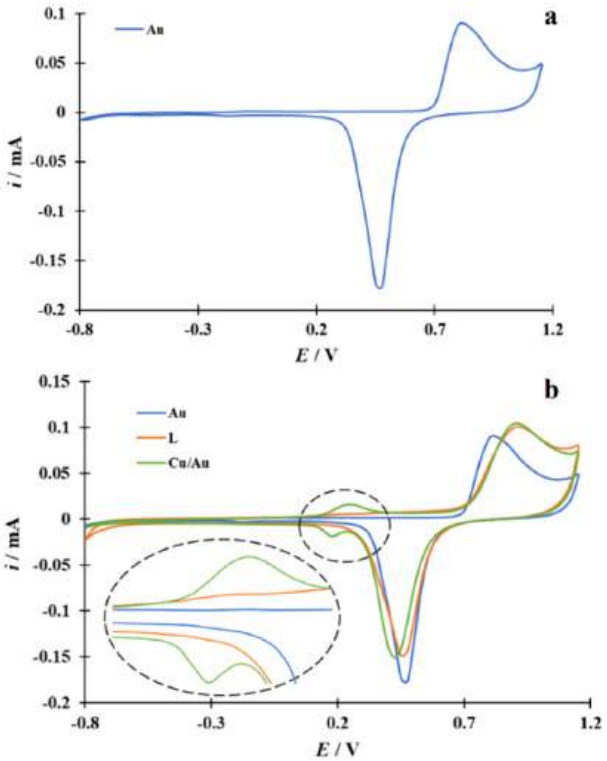

Fig. 3 (a) CV of the bare Au electrode in PBS at dE/dt = 0.1 V s^{-1}. (b) CVs of the bare gold electrode in PBS (blue) and in PBS with 0.01 mM ligand L (orange), and the cyclic voltammogram of the gold electrode after modification with 0.01 mM CuL_2 complex (green), dE/dt = 0.1 V s^{-1}. Inset: approximation of an excerpt of CV (black dashed line).

The dependence of $\log i_p$ on $\log \nu$ was linear with a slope of $d \log i_p / d \log \nu$ close to 1. On this basis, it was concluded that the CuL_2 complex used adsorbs on the Au surface during the modification procedure. The linear correlation i_p *versus* ν defined by the linear equation i_p [mA] = 0.2 ν [V s^{-1}] + 0.0006 with a high correlation coefficient value (R^2 = 0.9979) confirmed the conclusion that the CuL_2 complex is adsorbed on the surface of the gold electrode (Fig. 4b).

SAMs attached to the gold surface can facilitate the oxidation/reduction processes that occur at the interface between the electrode and the solution, but most importantly, effectively protect the metal surface from the adsorption of intermediate and/or final reaction products poisonous to the electrode surface.[45–48] Importantly, there are no thiol groups in the structure of the SAM monolayer-forming complex compound we obtained, which, despite their copious and well-known drawbacks such as susceptibility to pH changes, oxidants and organic solvents,[49] are widely used in gold surface alteration due to the ease of S–Au binding. In addition, the CuL_2 complex is characterized by the simplicity of the system, being monometallic and facile to synthesize, which further enables our system to make the Au surface modification and selective detection of epinephrine even more attractive. The formation of SAM with CuL_2 on the gold surface has been verified by considering the crystal structure of the complex discussed in more

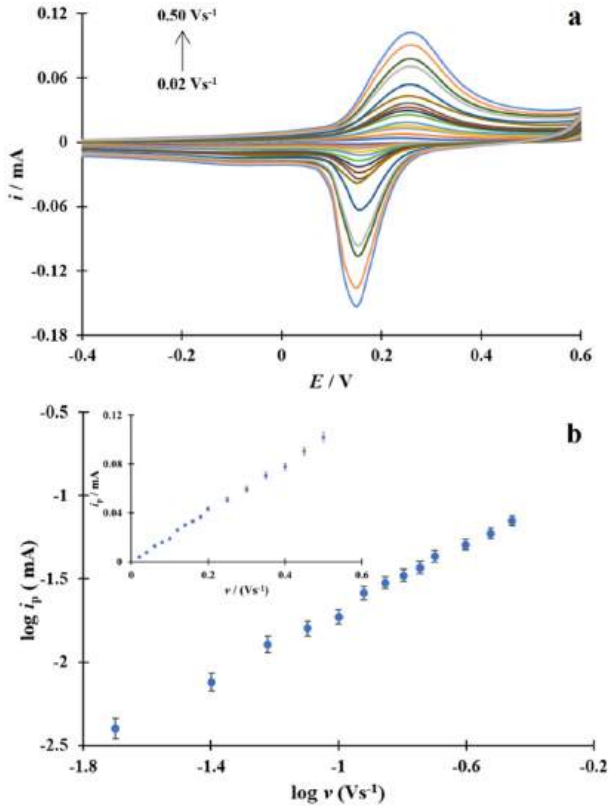

Fig. 4 (a) Cu/Au electrode CVs recorded in PBS at a scan rate of 0.02 to 0.50 V s^{-1}. (b) The relationship between log i_p and log v. Inset: the relationship i_p–v.

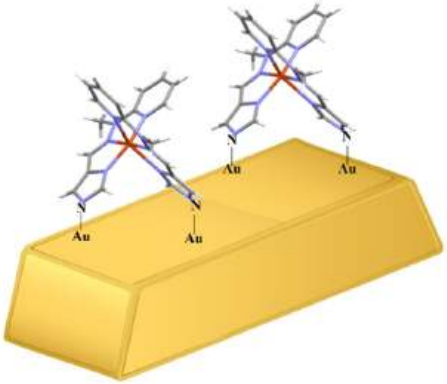

Fig. 5 A representative schematic presenting the bonding between nitrogen atoms from the complex CuL_2 structure and gold atoms from the electrode surface.

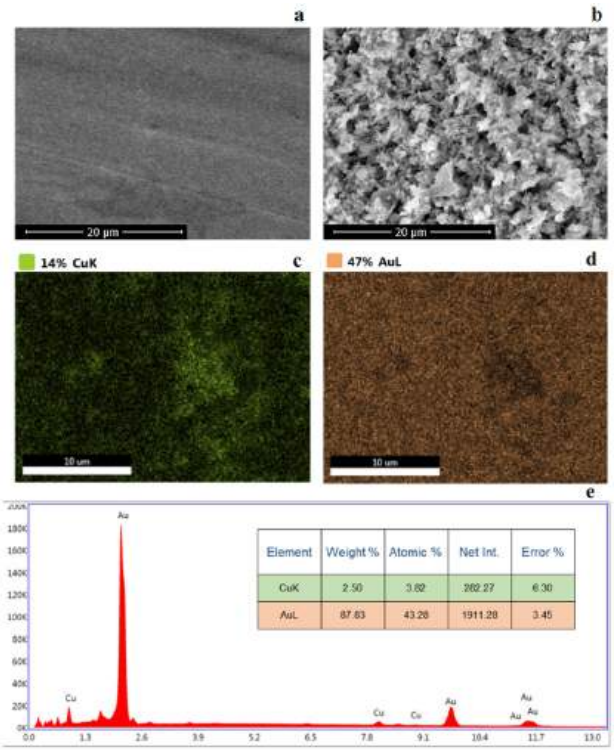

Fig. 6 SEM micrographs showing (a) the unmodified Au electrode and (b) the modified Cu/Au electrode. The EDAX analysis of the Cu/Au electrode (c and d) and its (e) X-ray energy dispersion spectrum.

detail in the crystallographic part. The surface of the gold electrode has a good affinity for nitrogen when nitrogen is present in the form of both the NH groups and the N-heterocycles.[50,51] In the complex we describe, nitrogen is present in both of these forms, which further improves its candidacy for SAM formation. The self-assembly of each molecule of CuL_2 on the gold surface is achieved by forming covalent bonds between N atoms of two amino groups, which have previously undergone hydrogen oxidative abstraction, and the surface Au atoms. A proposed scheme for associating the CuL_2 complex with the gold surface is shown in Fig. 5.

The adsorption of the CuL_2 complex and the generation of a monolayer on the gold template were also proved by scanning electron microscopy (SEM) with energy dispersive X-ray analysis (EDAX). The examined morphology and chemical composition of the surface allowed for the comparison of the unmodified and modified gold electrodes, at the same time confirming the formation of a monolayer of a CuL_2 complex on the gold electrode surface (Fig. 6). The surface of the bare gold electrode features a uniform arrangement (Fig. 6a), while the Cu/Au electrode surface represents a regular surface material formed by self-assembling and adsorbing the complex on its surface (Fig. 6b). It can be clearly seen that the surface of the bare gold electrode is smooth and devoid of any irregularities (Fig. 6a), while the surface of the modified Cu/Au electrode shows a regular arrangement of adsorbed material resulting from adsorption and self-organization of the complex on the surface (Fig. 6b). An additional EDAX analysis performed for the unmodified electrode (Fig. S6a†) and for the Cu/Au electrode (Fig. 6c and d) showed a uniform distribution of the contained chemical elements (Au and Cu), which is further evidence that CuL_2 adsorption occurs on the gold electrode surface. The latter further confirms the X-ray energy dispersion spectrum presented at Fig. 6e and S6b.† Subsequently, the change of the gold electrode surface with the CuL_2

complex was verified by attenuated total reflection infrared spectroscopy (ATR-IR), where the absence of a band in the 4000–3000 cm^{-1} range for the Cu/Au electrode is indicative of the disappearance of the NH groups through nitrogen binding to gold from the electrode surface (Fig. S7†).

3.4. Epinephrine electrooxidation at unmodified and modified gold electrodes

In order to determine whether the newly obtained modified Cu/Au electrode fulfils the assumed intended role during EP detection and determination, electrochemical experiments involving this neurotransmitter were carried out first on the unmodified gold electrode and then on the Cu/Au modified gold electrode. According to the literature,[52] the oxidation of EP consists of three steps, which are schematically shown in Fig. 7.

Fig. 8a shows second scans of the voltammetric responses of the bare Au electrode during EP oxidation, which were recorded for solutions with increasing analyte concentration in PBS, starting at 0.0001 mM EP and ending at 1 mM EP. The assumed mechanism of the EP oxidation is reflected in the shape of the CVs shown in Fig. 8a. It can be seen that the oxidation of EP on the unmodified gold electrode takes place in two potential ranges. A broad irreversible current wave with a maximum at E = 0.36 V *vs.* SCE, dE/dt = 0.1 V s^{-1} represents irreversible EP electrooxidation yielding epinephrinequinone, which is known to convert to leucoepinephrinechrome *via* an intramolecular cyclization reaction (1,4-Michael addition). The latter nonelectrochemical step is possible because of the structure of an epinephrinequinone, which includes both an electron-poor aromatic ring and an electron-rich amine group. Deprotonation of the NH group allows the molecule to perform a 1,4-Michael addition reaction.[11] According to the adopted mechanism of EP oxidation, the subsequent pairs of peaks visible on the CVs at about 0.01 V and −0.07 V with a peak-to-peak separation (ΔE_p) equal to 80 mV are associated with the third step, *i.e.* the reversible oxidation of leucoepinephrinechrome to epinephrinechrome. An increase in the concentration of the analytical substance in the bulk of the solution does not influence the course of the cyclic voltammograms.

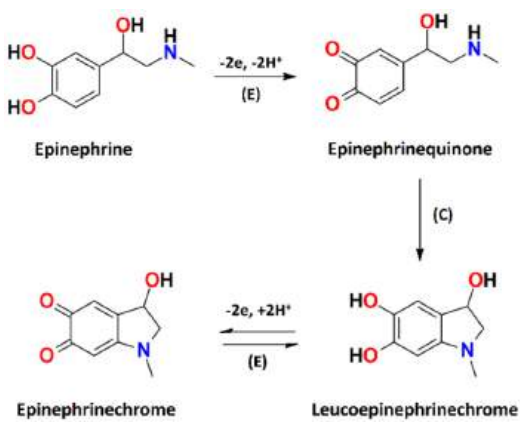

Fig. 7 Scheme of epinephrine electrooxidation.

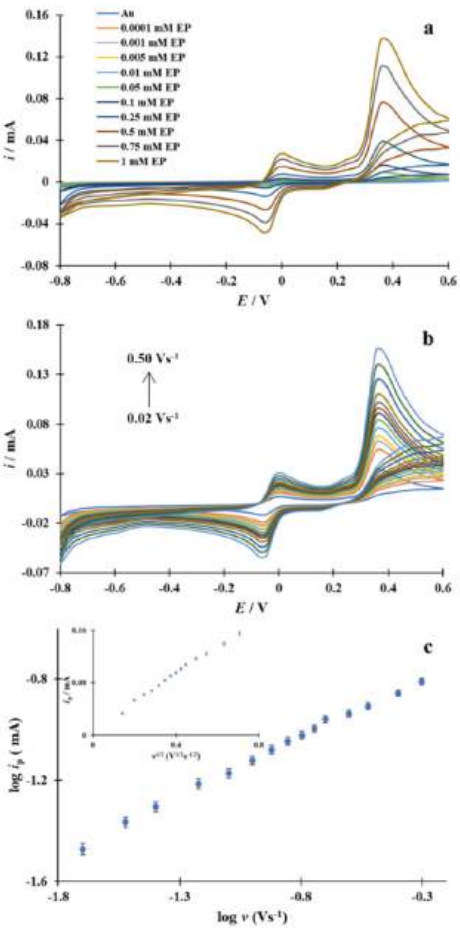

Fig. 8 (a) Second scans of CVs of the unmodified gold electrode recorded in PBS containing EP at different concentrations ranging from 0.0001 mM to 1 mM at dE/dt = 0.1 V s^{-1}. (b) The set of CVs of the unmodified Au electrode recorded in PBS containing 0.5 mM of EP at scan rates of 0.02 to 0.50 V s^{-1}. (c) The relationship between log i_p and log v. Inset: the relationship i_p–$v^{1/2}$.

For the unmodified gold electrode in the presence of 0.5 mM EP, one set of CVs was recorded at different scan rates between 0.02 V s^{-1} and 0.50 V s^{-1} (Fig. 8b). As established, a linear correlation between log i_p and log v with a concentration limit from 0.02 V s^{-1} to 0.20 V s^{-1} was obtained with a $d \log i_p / d \log v$ slope being equal to 0.49. In addition, the following linear regression equation was obtained: i_p [mA] = 0.23 $v^{1/2}$ + 0.0041 (R^2 = 0.9939) (Fig. 8c) by analyzing the experimental data of the linear correlation between i_p and $v^{1/2}$. Therefore, the overall rate of the EP oxidation is controlled by diffusion of substrate molecules towards the gold electrode surface.[53]

Having the characteristics of epinephrine electrooxidation on the bare Au electrode, the next stage of measurements was undertaken to study the electrooxidation of EP on a gold electrode modified with a prepared CuL_2 complex, as shown in Fig. 9. On the Cu/Au electrode the anodic peak corresponding to the oxidation of epinephrine to epinephrinequinone appears at E = 0.23 *vs.* SCE at dE/dt = 0.1 V s^{-1}, while the couple of peaks corresponding to the reversible oxidation/

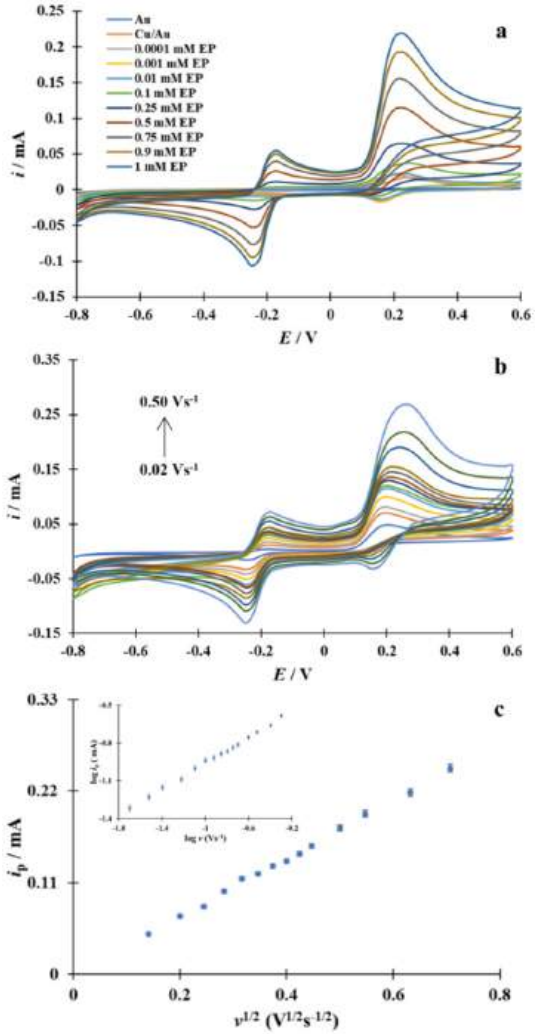

Fig. 9 (a) Second scans of CVs of the Cu/Au electrode recorded in PBS including EP concentrations from 0.0001 mM to 1 mM of EP at dE/dt = 0.1 V s^{-1}. (b) The set of CVs of the Cu/Au electrode recorded in PBS in the presence of 0.5 mM of EP at scan rates of 0.02 to 0.50 V s^{-1}. (c) The relationship between i_p and $v^{1/2}$. Inset: the relationship log i_p–log v.

reduction processes described in the third step of the electrooxidation mechanism adopted above for the analyte under consideration are visible at $E = -0.18$ V and $E = -0.24$ V (ΔE_p = 60 mV), respectively. On the prepared modified Cu/Au electrode, as on the bare Au electrode, an increase in the EP concentration in the supporting electrolyte solution does not change the shape of the CVs. It is conspicuous from Fig. 9a that an exceptional catalytic effect on the EP electrooxidation is achieved for the Au electrode modified with the SAM of CuL_2. This manifests itself as a significant shift of the corresponding voltammetric peaks to the negative direction, accompanied by an increase in the current responses compared to the characteristics of the unmodified electrode (Fig. 8a). It is important to emphasize that the potential range at which the peak involving the electrooxidation of epinephrine to epinephrinequinone is seen on the CV overlaps with that of the oxidation/reduction potential of the CuL_2 complex (Fig. 3b), whilst the current response of epinephrine is about seven times higher. This observation provides strong evidence that the epinephrine voltammetric response is catalyzed by the CuL_2 complex, which modifies the surface of the gold electrode. It should be noted that similar patterns were found during the electrooxidation of dopamine on an Au electrode coated with the Cu complex $[Cu_4(L–H)_4(BF_4)_2(CH_3OH)_2](BF_4)_2$, which was prepared by us earlier.[42]

The effect of composition of the electrode on the rate of this process is shown in Fig. 9b and c. Replacement of the gold electrode with the Cu/Au modified electrode did not affect the linear correlation between the peak current associated with EP (0.5 mM) oxidation and the square root of the scan rate ($v^{1/2}$) in the range from $v = 0.02$ V s^{-1} to $v = 0.50$ V s^{-1} (Fig. 9c) and is described by the following equation: i_p [mA] = 0.35 $v^{1/2}$ + 0.002 (R^2 = 0.9981). Furthermore, throughout the entire range of scan rates, a linear relationship between log i_p and log v was established and revealed a slope of $d \log i_p / d \log v$, which was equal to 0.51. In line with this, the overall rate of oxidation of epinephrine at the peak maximum potential under the above experimental conditions is controlled by the process of diffusion, which is slower than both the adsorption of the EP and the subsequent charge transfer at the interface between the electrode and the solution. At this point, it is worth emphasizing that the diffusion-controlled electrode process is beneficial for the quantitative determination of the concentration of an analyte in electrolyte solutions.[54]

Moreover, it was observed that the anodic current peaks assigned to EP electrooxidation at the Cu/Au electrode are shifted towards lower electrode potentials as the concentration of proton ions in the electrolyte solution decreases (Fig. S8).† Analysis of the experimental data revealed that the potential of the peak maximum (E_p) decreased in a linear manner with increasing pH over the range from 3 to 11 and shift can be expressed by the equation of linear regression: E_p = −0.0596 pH + 0.6428. The resulting slope $d E_p/d$ pH close to the theoretical Nernstian value of 0.059 V implies that an equal number of electrons and protons are exchanged during the oxidation of EP at the Cu/Au electrode.[53] This is in agreement with the theory of electrochemical kinetics,[53] and confirms the above assumed mechanism of EP electrooxidation.

Moreover, as shown in Fig. S8,† the current peak of epinephrine oxidation increases up to a pH of approximately 7–8, at which point a decrease in the recorded voltammetric responses is seen. This observation may be related to the fact that the epinephrine molecule has two active sites: one is an aromatic ring with two hydroxyl groups, and the other is a secondary amine group. According to the literature,[55] at pH lower than 5.8 the NH group can undergo protonation, forming a HEp^+ cation. At pH higher than 9.0, deprotonation of the hydroxyl group can result in problems to effectively accumulate at the surface of the electrode, hence a decrease in the current density. The latter observation together with considering the future practical application of the Cu/Au electrode as sensors

in physiological systems was the reason why pH 7 was selected in all our further studies presented below.

3.5. Epinephrine electrochemical determination

Both the decrease in oxidation potential and the increase in the current intensity found during the EP oxidation at the Cu/Au electrode undoubtedly make the prepared modified electrode suitable for analytical applications. The differential pulse voltammetry (DPV) technique was used to determine the analytical sensitivity of the Cu/Au electrode for the quantitative determination of EP. The analyte concentration was varied in a range of 0.0001 mM to 1.375 mM. The DPVs recorded at the Cu/Au electrode for selected concentrations of EP from the above range are shown in Fig. 10a.

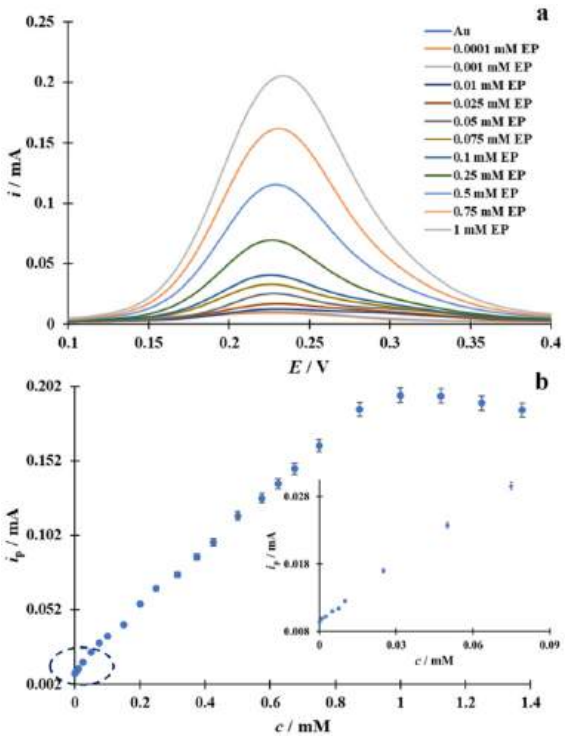

Fig. 10 (a) The DPVs recorded at the modified Cu/Au electrode with the addition of different EP concentrations in PBS at dE/dt = 0.1 V s^{-1}. (b) The correlation i_p *vs.* c in the EP concentration range from 0.0001 to 1.375 mM. Inset: i_p *vs.* c in the narrow concentration range of the EP (0.0001–0.075 mM).

The recorded DPVs demonstrate a clear correlation between the increasing EP concentration in the SES and the increasing current intensity. As can be seen from Fig. 10b, the relationship between the current peak i_p, which corresponds to the electrooxidation of EP (c_{EP}), and its concentration is within the concentration interval between 0.0001 mM and 0.875 mM, and the resulting linear regression equation is as follows: i_p [mA] = 0.20 c_{EP} [mM] + 0.01 (R^2 = 0.9988). At a higher concentration of EP outside the linear relationship, the value of the current response decreases, which may indicate that above the concentration of 1 mM, EP begins to accumulate on the altered surface of the gold electrode.[56] The limit of detection (LOD) and the limit of quantification (LOQ), calculated from the following IUPAC recommended formulas: LOD = 3 S_b/S and LOQ = 10 S_b/S (where S_b is the standard deviation of the current in the SES evaluated on the basis of 10 times repeated DPV measurements, S is the slope of the linear i_p *vs.* c dependence),[57] were 0.03 μM and 0.1 μM, respectively. Table 3 compares the value of LOD and that of the linearity range of EP quantification obtained with the modified Cu/Au electrode prepared in the present with analogue parameters obtained from other electrodes published in the literature. This comparison led to the conclusion that the Cu/Au electrode could undoubtedly be a successful sensor for the electrochemical determination of EP in real samples.

For the determination of EP in a commercial epinephrine injection solution, the practical application of the Cu/Au sensor was tested using the calibration method[61] and the DPV technique. To do this, the contents of each pre-filled syringe with the test solution (concentration 300 mcg per 0.3 ml) were diluted to 10 ml, and then spiked with a known amount of 0, 0.01, 0.02, 0.05, 0.1 and 0.15 mM EP standard solution. Three repeated measurements were made for each solution studied. The averaged results of the analytical test determinations, together with the recovery and relative standard deviation (RSD), are summarized in Table 4. As can be seen, in each of the test samples, the amounts of the substances are very close

Table 3 Representative results of EP determination on modified electrodes

Type of electrode	Range of linearity [μM]	LOD [μM]	Ref.
Au electrode modified with a Cu(II) complex	0.1–875	0.03	This work
Au electrode modified with an Fe(III) complex	0.01–900	0.0074	4
Au electrode modified with TMBH	1.7–24.9; 24.9–91.7	0.19	27
SPE modified with a Cu(II) nanocomplex	10–600	2.5	23
CPE modified with Fe(II) phthalocyanine	1–300	0.5	6
CPE modified with graphene quantum dots	0.36–380	0.0003	14
GCE modified with a SnO_2/graphene nanocomposite	0.5–200	0.017	58
GCE modified with an OMC–NiO nanocomposite	0.8–50	0.085	59
GCE modified with a MO/Pc/MWCNT composite	20–48	12.3	60
IPGE modified with a thin layer of a La clay mineral	0.8–10	0.26	3

TMBH: 2-hydroxy-*N*′1-[(*E*)-1-(3-methyl-2-thienyl)methylidene]benzohydrazide; OMC–NiO: ordered mesoporous carbon/nickel oxide; MO/Pc/MWCNT: metal oxide (MO = Fe_3O_4, ZnO) nanoparticles, doped phthalocyanine (Pc) and functionalized MWCNTs; La: LAPONITE®.

Table 4 Epinephrine determination in a commercial solution of EP for infusion (n = 3)

Initial amount [mM]	Spiked amount [mM]	Found amount [mM]	Recovery [%]	RSD [%]
0.164	0	0.165	100.6	2.1
0.164	0.01	0.177	101.7	1.8
0.164	0.02	0.183	99.5	2.3
0.164	0.05	0.211	98.6	1.8
0.164	0.1	0.267	101.1	2.4
0.164	0.15	0.312	99.4	2.7

to their nominal content. The feasibility of the developed Cu/Au sensor for EP determination in commercial samples is confirmed by recoveries ranging from 98.6 to 101.7% and the low RSD values from 1.8 to 2.7%, indicating the satisfactory accuracy of the proposed method.

3.6. Study of interferences

As underlined in the Introduction section and as shown in Fig. 11a, accurate sensing of EP on the unmodified gold electrode is virtually impossible in physiological samples containing some interferents such as UA because of the overlap of the cyclic voltammetric responses of these compounds. This problem is eliminated when the Cu/Au electrode developed in this work was used to analyze a binary mixture containing EP and UA.

It is evident from the CVs in Fig. 11a that the current density at the peak maximum potential is higher for both EP and UA oxidation on the Cu/Au electrode. Simultaneously, the current peaks corresponding to the oxidation of these compounds are noticeably separated from each other after using the Au electrode modified with the CuL_2 complex. It should be distinguished that the peak potential separation between EP and UA is greater for the Cu/Au electrode (ΔE_p = 220 mV) than for the bare Au electrode (ΔE_p = 20 mV). The negative shift corresponding to the EP oxidation peak and the positive shift occurring during the UA oxidation recorded on the Cu/Au electrode can be attributed to CuL_2 complex chemisorption on the gold surface leading to SAM formation. The monolayer formed is characterized by the presence of free electron pairs located on two nitrogen atoms of each molecule of the CuL_2 complex (Fig. 5), the presence of which results in an excess of negative charge, thus causing electrostatic repulsion and attraction. Owing to electrostatic repulsion of anionic forms, most UA anions are excluded from the Cu/Au electrode, which results in a shift of the peak potential of UA in the direction of the higher overpotential. Concomitantly, the attraction of the cationic form of epinephrine by the electrostatic interaction between them and the Cu/Au electrode results in a reduction of the EP oxidation overpotential. Thus, this electrode appears to be advantageous for the selective EP sensing and analytical determination in the presence of UA and *vice versa*.

Information on the detection sensitivity of the Cu/Au electrode for the EP and UA determination in the presence of each other was obtained from DPV experiments in which the concentration of one compound was diverse while that of the other was kept constant (Fig. 11b and 10c). Analysis of the DPVs for the Cu/Au electrode showed that the current intensity (i_p) corresponding to the electrooxidation of EP in the presence of a constant amount (0.5 mM) was proportional to the reactant concentration (c_{EP}) over the range from 0.0001 mM to 0.5 mM (see inset in Fig. 11b) and was described by the following equation: i_p [mA] = 0.20 c_{EP} [mM] + 0.01 (R^2 = 0.9988). It should be noted that the calculated LOD and LOQ values are the same as those calculated for EP without the presence of UA in the bulk solution (see above). Undoubtedly, this modified electrode is suitable for the accurate determination of the EP concentration without UA interference. Furthermore, when

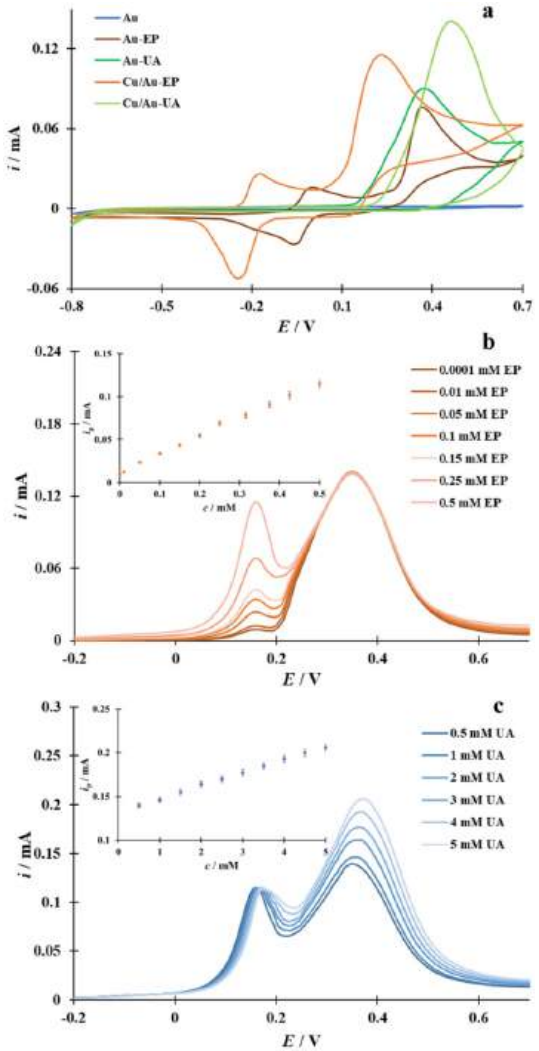

Fig. 11 (a) Second scans of the CVs recorded at the unmodified gold electrode in PBS (blue) in the presence of 0.5 mM EP (brown) and 0.5 mM UA (dark green), and second scans of the CVs recorded in PBS at the modified Cu/Au electrode including 0.5 mM EP (orange) and 0.5 mM UA (light green) at dE/dt = 0.1 V s^{-1}. (b) DPVs recorded at the Cu/Au electrode in PBS with 0.5 mM UA and increasing EP concentrations (from 0.0001 mM to 0.5 mM) at dE/dt = 0.1 V s^{-1}. Inset: the relationship i_p–c_{EP}. (c) DPVs recorded at the Cu/Au electrode in PBS with 0.5 mM EP and increasing UA concentrations (from 0.5 mM to 5 mM) at dE/dt = 0.1 V s^{-1}. Inset: the relationship i_p–c_{UA}.

UA was analyzed quantitatively in the presence of a fixed amount of EP in solution, the linear i_p–c_{UA} relationship was found to be satisfied over the analyte concentration interval from 0.5 mM to 5.0 mM and is described by the equation: i_p [mA] = 0.015 c_{UA} [mM] + 0.13 (R^2 = 0.9988). In this case, the LOD and LOQ values are 40 μM and 133 μM, respectively.

A further experiment was carried out on the practicality of the Cu/Au electrode for EP determination in the presence of UA, for which the calibration method was used. Each measurement was repeated three times and the results are presented in Table S2† as in the EP alone experiment. As expected, the concentrations of both components of the studied binary mixture in each sample are very close to their nominal content. For an accurate determination of the EP concentration without interference from UA and *vice versa*, there is no doubt that this modified Cu/Au electrode is adequate.

To ensure that the presence of additional interfering compounds did not affect the quantification of epinephrine using a Cu/Au electrode, a further experiment was carried out. The samples to be tested were prepared by adding 5 mM of the following salts: Na^+, K^+, Ca^{2+}, NH_4^+, Mg^{2+}, SO_4^{2-}, and $C_2O_4^{2-}$ to 0.5 mM EP solution in 5 mM PBS. The results presented in Table S3† show that the addition of the above disturbances did not alter the DPV voltammetric signal coming from the EP and did not influence the quality of the quantitative analysis.

Considering the above results, it can be concluded that the prepared Cu/Au electrode can be used with great success for the analytical purposes that are intended in this work.

3.7. Reproducibility and stability of the modified gold electrode

Reproducibility tests determined that the RDS values of five measurements performed on the new Cu/Au modified electrode in separate PBS solutions containing 0.5 mM EP were below 2.7%, suggesting high reproducibility of the obtained sensor (Fig. S9a†).

The stability of the modified gold electrode was investigated four times over a period of 24 days in PBS with 0.5 mM EP. Prior to each of the following measurements, the electrode was washed with water only and dried in a stream of argon. Over a period of more than 3 weeks, the voltammetric responses for the tested system decreased by approximately 3.5% from the initial measurement (Fig. S9b†).

4. Conclusions

The present results indicate that the newly synthesized and characterized CuL_2 complex $[CuL_2](BF_4)_2$ forms a self-assembled monolayer on the gold electrode surface by the chemisorption process. The oxidation kinetics of epinephrine, a biologically important molecule, on the modified Cu/Au electrode surface was improved compared to the electrochemical activity of EP on the bare Au electrode. The measurements showed that the modified Cu/Au electrode is a promising electrochemical sensor for the detection of EP under aqueous conditions with good selectivity, long-term stability and reproducibility. The EP quantification method thus developed features simplicity and low cost, while the obtained linear relationship between i_p and c of EP in the range of 0.0001 mM to 0.875 mM is comparable to or broader than that described in the literature using other modified electrodes. Furthermore, the Cu/Au electrode is capable of detecting EP in the presence of biogenic interferents, such as UA. These findings pave the way for further studies of Schiff-base Cu(II) complex compounds that can accumulate on a gold template and their application as sensors for the sensing of neurotransmitters in the presence of interfering substances.

Author contributions

Daria Nowicka: investigation, data curation, formal analysis, visualization, project administration, writing – review & editing, and funding acquisition. Karol Garbaczewski: investigation, data curation and formal analysis. Teresa Łuczak: investigation, data curation, conceptualization, methodology, formal analysis, resources, visualization, writing – review & editing, and project administration. Giuseppe Forte: data curation, formal analysis, visualization, and writing – review & editing. Giuseppe Consiglio: data curation, formal analysis, visualization, and writing – review & editing. Maciej Kubicki: investigation, data curation, formal analysis, writing – review & editing, and visualization. Violetta Patroniak: supervision, visualization, resources, and writing – review & editing. Adam Gorczyński: supervision, conceptualization, writing – review & editing, project administration, resources, and funding acquisition.

Data availability

The data supporting this article have been included as part of the ESI† and are available in the public open repository Zenodo at **https://zenodo.org/uploads/14045170**; **10.5281/zenodo.14045170**.

Conflicts of interest

There are no conflicts to declare.

Acknowledgements

This work was supported by the National Science Centre, Poland (grant numbers UMO-2022/45/N/ST4/00632, UMO-2022/47/B/ST4/02310, and UMO-2020/39/D/ST4/01182). Daria Nowicka is a scholarship holder of the Adam Mickiewicz University in Poznan Foundation for the academic year 2023/2024. Adam Gorczyński is a scholarship holder of the Polish Ministry of Education and Science for outstanding young

scientists. We would like to thank Dr Aleksandra Bocian for her help in ligand and complex synthesis.

References

1 K. E. Barrett, S. Boitano, S. M. Barman, W. F. Ganong and H. L. Brooks, *Ganong's Review of Medical Physiology*, McGraw-Hill Medical, 2012.
2 M. Müller, *Clinical pharmacology: current topics and case studies*, Springer, 2010.
3 C. N. Pecheu, V. K. Tchieda, K. Y. Tajeu, S. L. Jiokeng, A. Lesch, I. K. Tonle, E. Ngameni and C. Janiak, *Molecules*, 2023, **28**, 5487.
4 A. Gorczyński, M. Kubicki, K. Szymkowiak, T. Łuczak and V. Patroniak, *RSC Adv.*, 2016, **6**, 101888–101899.
5 E. Honarmand and M. H. Motaghedifard, *Anal. Methods*, 2015, **7**, 4995–5005.
6 S. Shahrokhian, M. Ghalkhani and M. K. Amini, *Sens. Actuators, B*, 2009, **137**, 669–675.
7 A. Bhattacharya, K. B. Patel, R. Ghosh, D. N. Srivastava and P. B. Chatterjee, *Sens. Actuators, B*, 2024, **398**, 134772.
8 M. V. Gorbunova, S. V. Gutorova, D. A. Berseneva, V. V. Apyari, V. D. Zaitsev, S. G. Dmitrienko and Y. A. Zolotov, *Appl. Spectrosc. Rev.*, 2019, **54**, 631–652.
9 J. Bicker, A. Fortuna, G. Alves and A. Falcão, *Anal. Chim. Acta*, 2013, **768**, 12–34.
10 A. Moslehipour, *J. Chem. Rev.*, 2020, **2**, 130–147.
11 M. D. Hawley, S. V. Tatawawadi, S. Piekarski and R. N. Adams, *J. Am. Chem. Soc.*, 1967, **89**, 447–450.
12 Z. Fredj and M. Sawan, *Biosensors*, 2023, **13**, 211.
13 B. Soleymani, B. Zargar and S. Rastegarzadeh, *J. Iran. Chem. Soc.*, 2020, **17**, 1013–1025.
14 J. Tashkhourian, S. F. Nami-Ana and M. Shamsipur, *J. Mol. Liq.*, 2018, **266**, 548–556.
15 G. Pallam, S. Sam, S. Sreekumar and K. G. Kumar, *Ionics*, 2023, **29**, 819–831.
16 M. Mazloum-Ardakani, F. Alvansaz-Yazdi, F. Hoseynidokht and A. Khoshroo, *Anal. Bioanal. Chem. Res.*, 2023, **10**, 387–394.
17 G.-P. Jin, Q.-Z. Chen, Y.-F. Ding and J.-B. He, *Electrochim. Acta*, 2007, **52**, 2535–2541.
18 B. O. Agboola and K. I. Ozoemena, *Phys. Chem. Chem. Phys.*, 2008, **10**, 2399–2408.
19 Z. Yang, G. Hu, X. Chen, J. Zhao and G. Zhao, *Colloids Surf., B*, 2007, **54**, 230–235.
20 B. Jin and H. Zhang, *Anal. Lett.*, 2002, **35**, 1907–1918.
21 S. Agrahari, A. K. Singh, R. K. Gautam and I. Tiwari, *Environ. Sci. Pollut. Res.*, 2023, **30**, 124866–124883.
22 H. Beitollahi, Z. Dourandish, S. Tajik, M. R. Ganjali, P. Norouzi and F. Faridbod, *J. Rare Earths*, 2018, **36**, 750–757.
23 F. Soofiabadi, A. Amiri and S. Jahani, *Anal. Bioanal. Electrochem.*, 2017, **9**, 340–350.
24 T. Joseph, T. Thomas and N. Thomas, *Electroanalysis*, 2020, **32**, 2463–2473.
25 O. Gunes, A. Sarilmaz, S. Z. Bas, M. Ozmen, F. Ozel and M. Ersoz, *Electroanalysis*, 2021, **33**, 2460–2468.
26 N. F. Atta, A. Galal and E. H. El-Ads, *Analyst*, 2012, **137**, 2658–2668.
27 M. Zohreh, S. M. Ghoreishi, M. Behpour and M. Mohammadhassan, *Arabian J. Chem.*, 2017, **10**, S657–S664.
28 S. Ramirez, N. Silva, M. P. Oyarzun, J. Pavez and J. F. Silva, *J. Electroanal. Chem.*, 2017, **799**, 349–357.
29 M. Mazloum-Ardakani, H. Beitollahi, M. K. Amini, B.-F. Mirjalili and F. Mirkhalaf, *J. Electroanal. Chem.*, 2011, **651**, 243–249.
30 K. Barman and S. Jasimuddin, *RSC Adv.*, 2016, **6**, 99983–99988.
31 E. Wierzbicka and G. D. Sulka, *Sens. Actuators, B*, 2016, **222**, 270–279.
32 A. Bocian, M. Szymańska, D. Brykczyńska, M. Kubicki, M. Wałęsa-Chorab, G. N. Roviello, M. A. Fik-Jaskółka, A. Gorczyński and V. Patroniak, *Molecules*, 2019, **24**, 3173.
33 O. Rigaku, *CrysAlis PRO*, Rigaku Oxford Diffraction, Yarnton, England, 2015.
34 G. M. Sheldrick, *Acta Crystallogr., Sect. A:Found. Adv.*, 2015, **71**, 3–8.
35 G. M. Sheldrick, *Acta Crystallogr., Sect. C: Struct. Chem.*, 2015, **71**, 3–8.
36 T. Łuczak, *J. Appl. Electrochem.*, 2007, **37**, 461–466.
37 M. J. Frisch, G. W. Trucks, H. B. Schlegel, G. E. Scuseria, M. A. Robb, J. R. Cheeseman, G. Scalmani, V. Barone, G. A. Petersson, H. Nakatsuji, X. Li, M. Caricato, A. V. Marenich, J. Bloino, B. G. Janesko, R. Gomperts, B. Mennucci, H. P. Hratchian, J. V. Ortiz, A. F. Izmaylov, J. L. Sonnenberg, D. Williams-Young, F. Ding, F. Lipparini, F. Egidi, J. Goings, B. Peng, A. Petrone, T. Henderson, D. Ranasinghe, V. G. Zakrzewski, J. Gao, N. Rega, G. Zheng, W. Liang, M. Hada, M. Ehara, K. Toyota, R. Fukuda, J. Hasegawa, M. Ishida, T. Nakajima, Y. Honda, O. Kitao, H. Nakai, T. Vreven, K. Throssell, J. A. Montgomery Jr., J. E. Peralta, F. Ogliaro, M. J. Bearpark, J. J. Heyd, E. N. Brothers, K. N. Kudin, V. N. Staroverov, T. A. Keith, R. Kobayashi, J. Normand, K. Raghavachari, A. P. Rendell, J. C. Burant, S. S. Iyengar, J. Tomasi, M. Cossi, J. M. Millam, M. Klene, C. Adamo, R. Cammi, J. W. Ochterski, R. L. Martin, K. Morokuma, O. Farkas, J. B. Foresman and D. J. Fox, *Gaussian 16*, Rev C.01, Gaussian Inc., Wallingford CT, 2016.
38 T. Yanai, D. P. Tew and N. C. Handy, *Chem. Phys. Lett.*, 2004, **393**, 51–57.
39 G. Consiglio, A. Gorcyński, S. Petralia and G. Forte, *RSC Adv.*, 2023, **13**, 1019–1030.
40 M. Cossi, N. Rega, G. Scalmani and V. Barone, *J. Comput. Chem.*, 2003, **24**, 669–681.
41 J. Tomasi, B. Mennucci and R. Cammi, *Chem. Rev.*, 2005, **105**, 2999–3094.
42 D. Nowicka, M. Kubicki, V. Patroniak, T. Łuczak and A. Gorczyński, *Electrochim. Acta*, 2024, **476**, 143754.

43 M. I. Awad and T. Ohsaka, *J. Power Sources*, 2013, **226**, 306–312.
44 G. Jiang, X. Gu, G. Jiang, T. Chen, W. Zhan and S. Tian, *Sens. Actuators, B*, 2015, **209**, 122–130.
45 M. Singh, N. Kaur and E. Comini, *J. Mater. Chem. C*, 2020, **8**, 3938–3955.
46 M. Ravandeh, D. Thal, H. Kahlert, K. Wende and M. Lalk, *J. Solid State Electrochem.*, 2020, **24**, 3003–3011.
47 A. Ulman, *Chem. Rev.*, 1996, **96**, 1533–1554.
48 S. Watcharinyanon, *Structure of self-assembled monolayers on gold studied by nexafs and photoelectron spectroscopy*, Karlstads Universitet, 2008.
49 G. Kaur, R. L. Thimes, J. P. Camden and D. M. Jenkins, *Chem. Commun.*, 2022, **58**, 13188–13197.
50 F. Chen, X. Li, J. Hihath, Z. Huang and N. Tao, *J. Am. Chem. Soc.*, 2006, **128**, 15874–15881.
51 S. Radenković, M. Antić, N. D. Savić and B. Đ. Glišić, *New J. Chem.*, 2017, **41**, 12407–12415.
52 Y. Yao, R. Shen, J. Xu and Z. Feng, *Int. J. Electrochem. Sci.*, 2024, **19**, 100750.
53 A. J. Bard, L. R. Faulkner and H. S. White, *Electrochemical methods: fundamentals and applications*, John Wiley & Sons, 2022.
54 A. Kisza, *Electrochemistry II*, WNT Warsaw, 2001, p. 94.
55 Z. Kun, C. Hongtao, Y. Yue, B. Zhihong, L. Fangzheng and L. Sanming, *Ionics*, 2015, **21**, 1129–1140.
56 T. Łuczak, *Electrochim. Acta*, 2008, **53**, 5725–5731.
57 C. Analytical Methods, *Analyst*, 1987, **112**, 199–204.
58 N. Lavanya, E. Fazio, F. Neri, A. Bonavita, S. G. Leonardi, G. Neri and C. Sekar, *Sens. Actuators, B*, 2015, **221**, 1412–1422.
59 X. Yang, P. Zhao, Z. Xie, M. Ni, C. Wang, P. Yang, Y. Xie and J. Fei, *Talanta*, 2021, **233**, 122545.
60 N. G. Mphuthi, A. S. Adekunle and E. E. Ebenso, *Sci. Rep.*, 2016, **6**, 26938.
61 W. Szczepaniak, *Instrumental methods in chemical analysis*, PWN Scientific Publishers, Warsaw, 2010.

Electronic Supporting Information

Application of a simple copper(II) complex compound as an epinephrine selective voltammetric sensor in the presence of uric acid in aqueous conditions

Daria Nowicka,*[a] Karol Garbaczewski,[a] Teresa Łuczak,[a] Giuseppe Forte,[b] Giuseppe Consiglio,[c] Maciej Kubicki,[a] Violetta Patroniak [a] and Adam Gorczyński *[a]

a. Faculty of Chemistry, Adam Mickiewicz University in Poznań, Uniwersytetu Poznańskiego 8, 61-614 Poznań, Poland

b. Department of Drug Science and Health University of Catania, Via S. Sofia 64, 95125

c. Department of Chemical Science University of Catania, Via S. Sofia 64, 95125, Italy

*Correspondence** d.nowicka@amu.edu.pl; adam.gorczynski@amu.edu.pl

Table of contents for Supporting Information

1. Synthesis and physical characterization……..……...……...……...2
2. Crystallographic studies……..……..……..….4
3. Characterization of the bare gold electrode…….……...……...……...5
4. Electrochemical experiments…….……...……...……....6

1. **Synthesis and physical characterization**

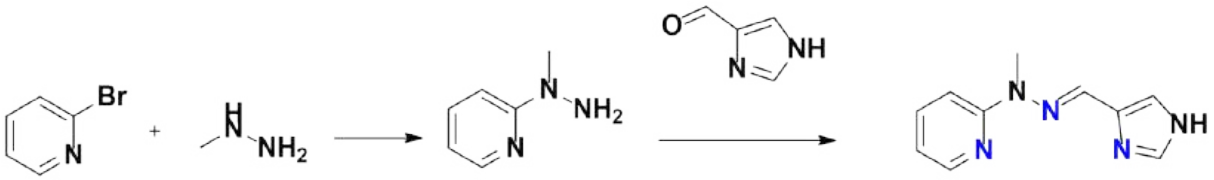

Fig. S1. Scheme of ligand L [$C_{10}H_{11}N_5$] synthesis.

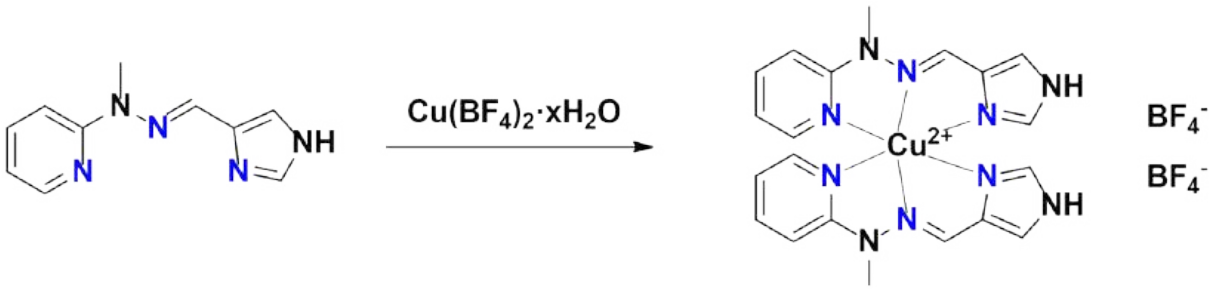

Fig. S2. Scheme of copper(II) complex $[CuL_2](BF_4)_2$ synthesis.

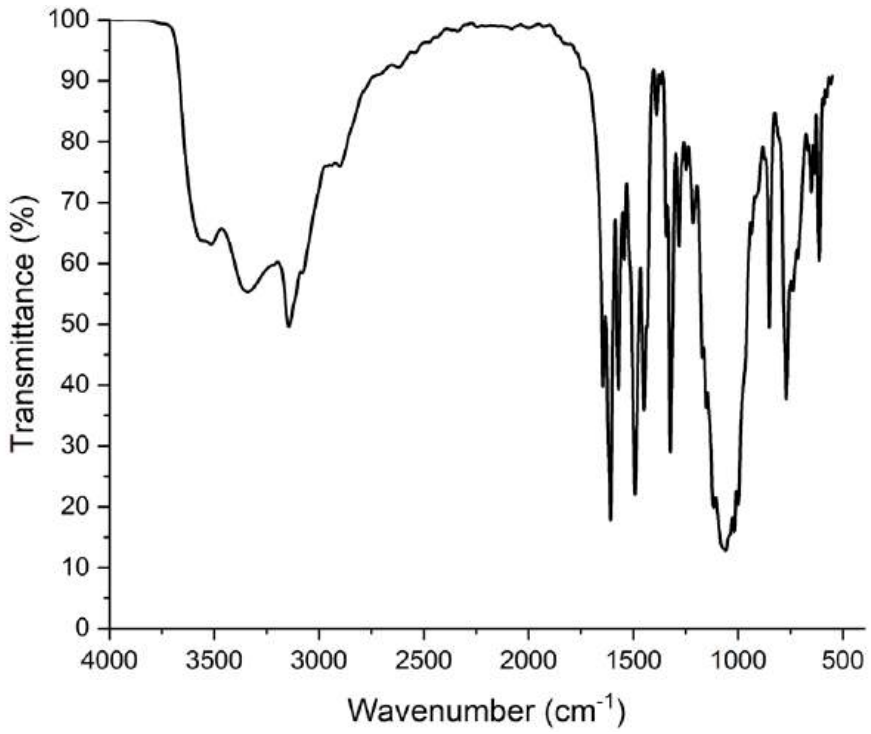

Fig. S3. FT-IR spectrum of copper(II) complex $[CuL_2](BF_4)_2$.

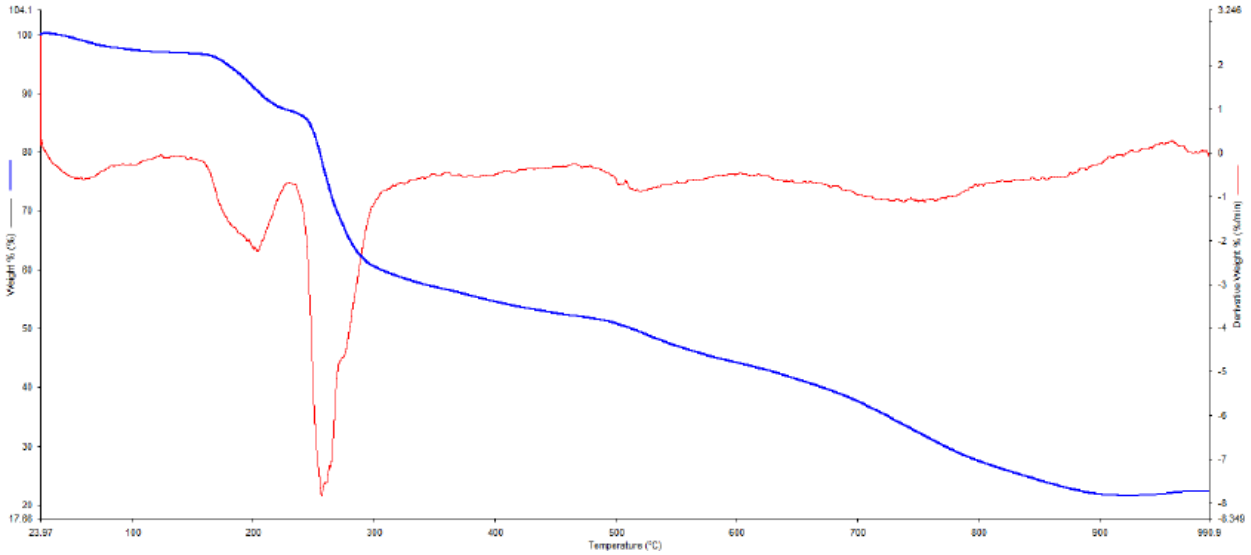

Fig. S4. Thermogravimetric analysis of compound **1**.

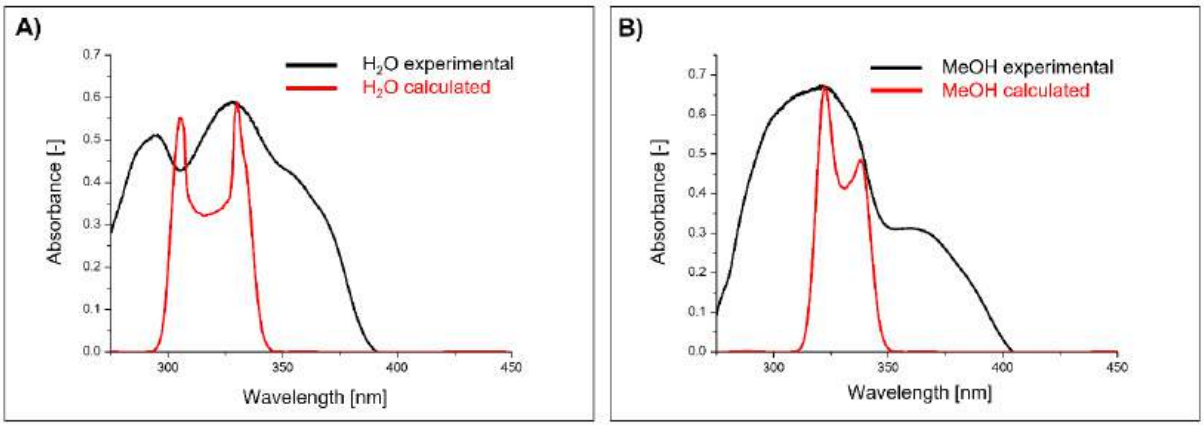

Fig. S5. Comparison of experimentally measured and theoretically calculated UV-Vis spectra of CuL_2 in water (A) and methanol (B), at the CAM-B3LYP/6-311+G(2d,p)/CPCM level.

2. **Crystallographic studies**

Table S1. Crystal data, data collection and structure refinement.

Compound	**CuL_2**
Formula	$C_{20}H_{22}CuN_{10}^{2+}\cdot 2BF_4\text{-}\cdot CH_3OH\cdot O(C_3H_7)_2$
Formula weight	773.85
Crystal system	monoclinic
Space group	$P2_1/n$
a(Å)	12.4491(4)
b(Å)	13.8403(3)
c(Å)	19.8972(6)
β(º)	97.153(3)
V(Å^3)	3401.59(17)
Z	4
D_x(g cm^{-3})	1.511
F(000)	1596
μ(mm^{-1})	0.729
Reflections:	
collected	19089
unique (R_{int})	6945 (0.0401)
with I>2σ(I)	4856
R(F) [I>2σ(I)]	0.0692
wR(F^2) [I>2σ(I)]	0.1582
R(F) [all data]	0.1054
wR(F^2) [all data]	0.1777
Goodness of fit	1.042
max/min Δρ (e·Å^{-3})	1.91/-0.80
CCDC deposition	2346925

3. **Characterization of the bare gold electrode**

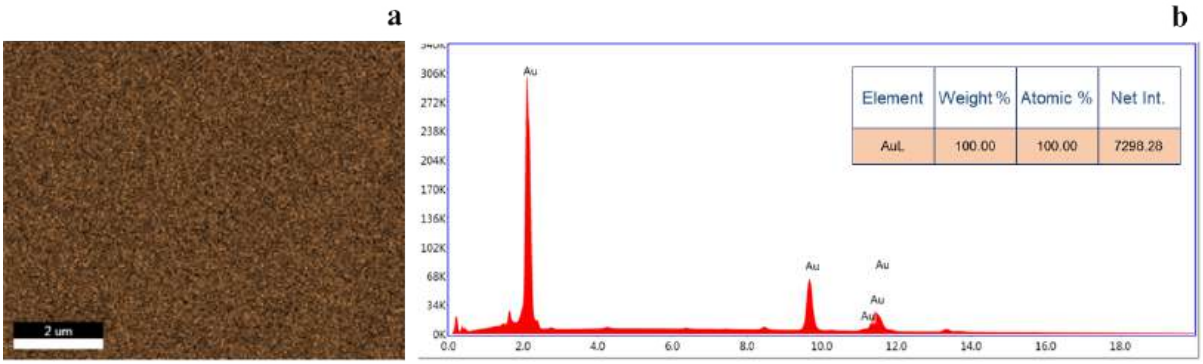

Fig. S6. (a) EDAX analysis of the bare Au electrode (2 μm) and its (b) X-ray energy dispersion spectrum.

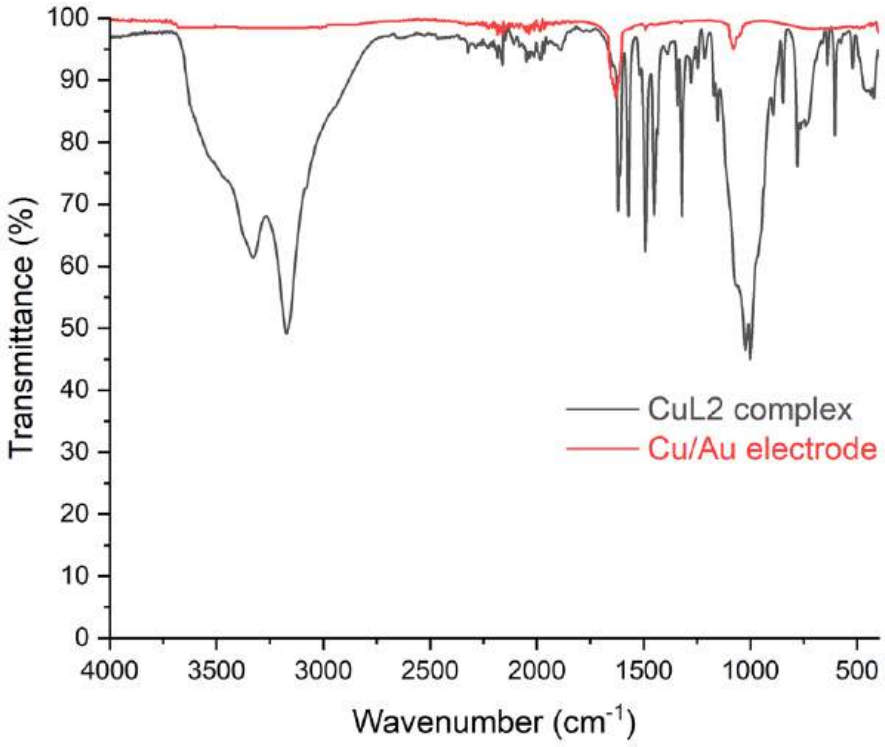

Fig. S7. Comparison of ATR-IR spectra of the CuL_2 complex and Cu/Au electrode.

4. **Electrochemical experiments**

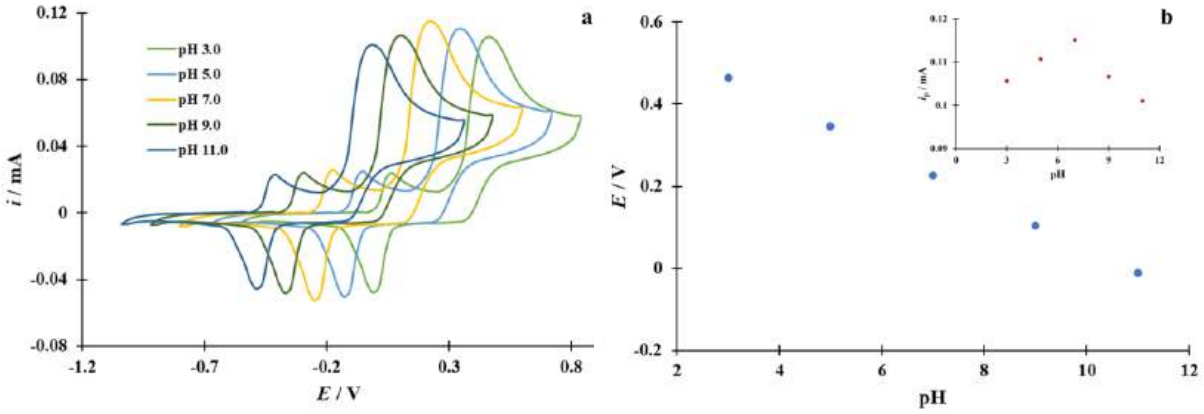

Fig. S8. (a) CVs of the Cu/Au electrode in supporting electrolyte solution at various pH in the range from pH 3.0 = pH 11.0 in the presence of 0.5 mM EP, dE/dt = 0.1 Vs^{-1}. (b) Effect of pH on the peak potential during EP electrooxidation. Insert: effect of pH on the peak current.

Table S2. Determination of EP in the presence of UA (n = 3) at the Cu/Au electrode.

Initial amount [mM]		Spiked amount [mM]		Found amount [mM]		Recovery [%]		RSD [%]	
EP	UA	EP	UA	EP	UA	EP	UA	EP	UA
0.100	0.50	0	0	0.102	0.49	102.0	98.0	2.0	1.8
0.100	0.50	0.01	0	0.111	0.51	100.9	102.0	1.9	1.9
0.100	0.50	0.03	0	0.133	0.48	99.3	96.0	2.6	1.8
0.100	0.50	0.05	0	0.148	0.51	98.7	102.0	1.6	2.2
0.50	0.50	0	0.1	0.52	0.59	104.0	98.3	2.2	1.7
0.50	0.50	0	0.3	0.48	0.84	96.0	105.0	1.6	1.5
0.50	0.50	0	0.6	0.49	1.14	98.0	103.6	1.8	1.7
0.50	0.50	0	1.0	0.51	1.52	102.0	101.3	2.1	1.8

Table S3. Sensing of 0.5 mM EP with addition of 5 mM of some interferents (n = 3) at the Cu/Au electrode.

Type of interference	Found EP [mM]	Recovery [%]	RSD [%]
Na^+	0.489	97.8	2.4
K^+	0.512	102.4	3.5
Ca^{2+}	0.491	98.2	2.1
NH_4^+	0.533	106.6	1.8
Mg^{2+}	0.529	105.8	2.7
SO_4^{2-}	0.479	95.8	3.2
$C_2O_4^{2-}$	0.518	103.6	2.1

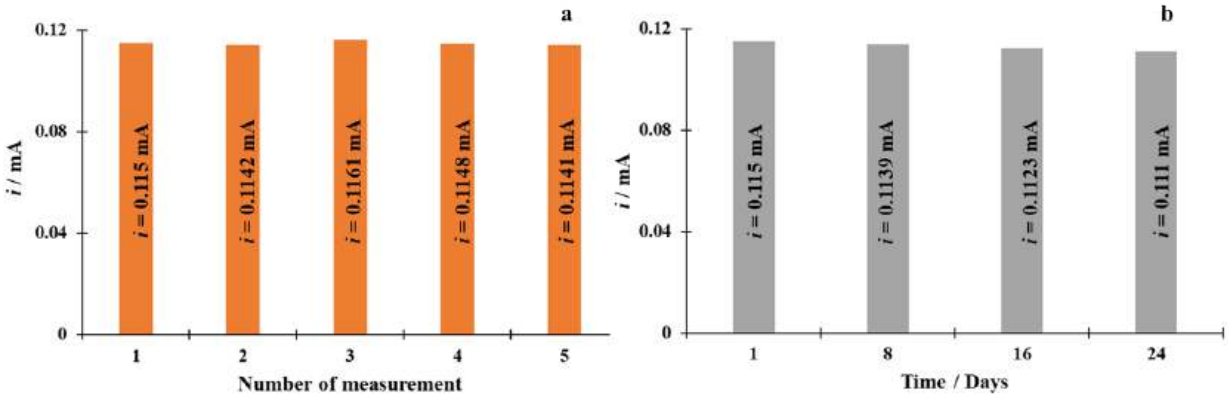

Fig. S9. Graphs presenting (a) reproducibility and (b) long-term stability of the Cu/Au electrode.

Volume 53
Number 28
28 July 2024
Pages 11587-12008

Dalton Transactions

An international journal of inorganic chemistry

rsc.li/dalton

ISSN 1477-9226

ROYAL SOCIETY OF CHEMISTRY

PAPER

Marta Fik-Jaskółka, Adam Gorczyński *et al.*

The effect of ionic *versus* covalent functionalization of polyoxometalate hybrid materials with coordinating subunits on their stability and interaction with DNA

Dalton Transactions

ROYAL SOCIETY OF CHEMISTRY

PAPER

View Article Online
View Journal | View Issue

Cite this: *Dalton Trans.*, 2024, **53**, 11678

The effect of ionic *versus* covalent functionalization of polyoxometalate hybrid materials with coordinating subunits on their stability and interaction with DNA†

Daria Nowicka,‡[a] Dawid Marcinkowski, ‡[a] Nahir Vadra,[b] Martyna Szymańska,[a] Maciej Kubicki,[a] Giuseppe Consiglio,[c] Wojciech Drożdż,[a,d] Artur R. Stefankiewicz,[a,d] Violetta Patroniak,[a] Marta Fik-Jaskółka *[a] and Adam Gorczyński *[a]

Received 2nd April 2024,
Accepted 9th May 2024

DOI: 10.1039/d4dt00965g

rsc.li/dalton

Inorganic–organic hybrid materials that combine both Polyoxometalates (POMs) and metal ion coordinating subunits (CSUs) represent promising multifunctional materials. Though their individual components are often biologically active, utilization of hybrid materials in bioassays significantly depends on the functionalization method and thus resulting stability of the system. Quite intriguingly, these aspects were very scarcely studied in hybrid materials based on the Wells–Dawson POM (WD POM) scaffold and remain unknown. We chose two model WD POM hybrid systems to establish how the functionalization mode (ionic *vs.* covalent) affects their stability in biological medium and interaction with nucleic acids. The synthetic scope and limitations of the covalent POM-terpyridine hybrids were demonstrated and compared with the ionic Complex-Decorated Surfactant Encapsulated-Clusters (CD-SECs) hybrids. The nature of POM and CSU binding can be utilized to modulate the stability of the hybrid and the extent of DNA binding. The above systems show potential to behave as model cargo-platforms for potential utilization in medicine and pharmacy.

Introduction

Polyoxometalates (POMs) can be described as a group of transition metals in their highest oxidation state linked together by oxygen atoms with a general formula $[MO_x]_n$, where M = Mo, W, V, and Nb, and x = 4–7,[1–3] which can form different structures of varying sizes by gradual condensation. Besides, heteroatoms such as P, Si, Al, or S and transition metal ions such as Co, Fe, Ni, Cu, Zn, or Ln may be present, resulting in more stable systems commonly named as archetypical groups as *e.g.*, Keggin, Wells Dawson (WD), Anderson or Preyssler.[4] In addition, vacancies in the structure can be generated by controlled hydrolysis (*e.g.*, lacunary POMs), giving new reactive centers that can be linked using electrophiles to form larger aggregates or utilized for postfunctionalization.[5,6] Given their anionic characteristics, POMs can also bind different cations,[7] and the final architecture and the physicochemical properties of the complex formed depend on the participating components of the complex.[8]

Self-assembly and functionalization processes in POMs are not always straight-forward, and they are highly influenced by small changes in reaction conditions such as pH, temperature or stoichiometry and therefore, it is not always easy to predict the architecture and have a preprogrammed design.[4] In the last few years, there have been numerous efforts to find new approaches to control the structure of POMs, some of the reported strategies have pointed to controlling self-assembly using classical approaches (such as trapping of functional metallic cores, molecular nanoparticles, or incorporation of active sites),[8] while the latest ones focus on using Machine learning[9] and automated chemistry.[10]

[a]*Adam Mickiewicz University in Poznań, Faculty of Chemistry, Uniwersytetu Poznańskiego 8, 61-614 Poznań, Poland. E-mail: marta.fik@amu.edu.pl, adam.gorczynski@amu.edu.pl*
[b]*Universidad de Buenos Aires, Facultad de Ciencias Exactas y Naturales, Departamento de Química Inorgánica, Analítica y Química Física and CONICET–Universidad de Buenos Aires, Instituto de Química Física de los Materiales, Medio Ambiente y Energía (INQUIMAE), Buenos Aires C1428EGA, Argentina*
[c]*Università di Catania, Dipartimento di Scienze Chimiche, I-95125 Catania, Italy*
[d]*Adam Mickiewicz University in Poznań, Center for Advanced Technology, Uniwersytetu Poznańskiego 10, 61-614 Poznań, Poland*

†Electronic supplementary information (ESI) available: Spectroscopic analysis of synthesized hybrids and chosen biological spectra. CCDC 2078396. For ESI and crystallographic data in CIF or other electronic format see DOI: https://doi.org/10.1039/d4dt00965g

‡Equal contribution.

The versatility and variety of properties in these systems have led in the recent years to exploring ways to diversify the physicochemical properties, for example, by generating hybrid inorganic–organic architectures.[11] In general terms, hybrid inorganic–organic POMs may be obtained by different approaches such as (1) nanostructurization of small POMs into larger ones;[12] (2) covalent linking of organic moieties onto the POM cluster surface;[13] (3) non-covalent functionalization (ionic interaction or hydrogen bonding) through the formation of the Surfactant-Encapsulated-Clusters (SECs).[13] We have also presented a new pathway (4) to generate a novel family POMs inorganic–organic systems to form Complex-Decorated Surfactant-Encapsulated-Cluster (CD-SEC) materials.[14] It is a multilevel functionalization based on the decoration of WD POMs with organic cation surfactant, which could simultaneously act as a metal ion complexing agent allowing for high versatility and tunable functionality. As a result, extensive exploration has been carried out for those systems concerning applications in fields such as catalysis,[15,16] electrocatalysis,[17,18] hydrogen generation,[19] protein crystallography,[20] elaboration of functional materials.[21–23]

Biological applications are also promising in terms of the potential of POMs to modify and enhance interaction with biomacromolecules.[24–26] Indeed, a high negative charge accompanied by a large number of oxo-ligands results in POMs that can be treated as water-soluble macroanions, thus representing perfect models for studying the biomacromolecular interactions in polyelectrolyte solutions.[27] Iso and heteropolyanions were studied in terms of hydrolytic cleavage of peptides,[28] nucleotides,[29] and saccharides,[30] along with analysis of the POM-biomolecule mechanisms that govern the observed outcomes.[31] Consequently, systematic studies on potential applications, such as antiviral,[32] antidiabetic,[33] antibiotic[34] or anticancer[35] effects, have been reported. Nevertheless, high toxicity in normal cells and unclear biochemical pathways indicate the need for further studies. Recently recognized organic–inorganic hybrid systems have been shown to enhance the anticancer activity[35] and exhibit more effective antibacterial properties than the inorganic analogues.[34] Both derivatization with organic moieties *via* covalent bonds and their encapsulation inside non-toxic organic macromolecules could lead to systems with enhanced biocompatibility, higher stability at physiological pH and lower toxicity.[36–39] However, these results are still scarcely understood, and the need to construct such systems and studies is therefore justified.

Herein, we have chosen WD POMs to study due to their ability to undergo a variety of modifications and formation of organic–inorganic hybrids that exhibit potential biological activity. In this work we have studied how the ionic *vs.* covalent functionalization of the hybrid WD POM based system affects their stability in the presence of DNA and interacts with this biological system. To establish this, two distinct systems were preprogrammed: (i) previously demonstrated CD-SECs; (ii) covalently bound POM-tpy, and chosen, together with the construction algorithms that demonstrate the potential feasibility of such systems, to act as the drug carrier models.

Experimental section

Materials and methods

The metal salts, organic compounds and solvents were supplied by Aldrich and POCH. All chemicals mentioned above were of analytical grade quality and were used as obtained without further purification. The precursor **V_3POM-TBA** $TBA_5H_4[P_2W_{15}V_3O_{62}]$ POM was synthesized and characterized following published procedures ($K_6[\alpha\text{-}P_2W_{18}O_{62}]\cdot 14H_2O$[40] → $Na_{12}[\alpha\text{-}P_2W_{15}O_{56}]\cdot 18H_2O$[41] → $K_8H[P_2W_{15}V_3O_{62}]\cdot 9H_2O$[42] → $TBA_5H_4[P_2W_{15}V_3O_{62}]$).[42]

V_3POM + TRIZMA $(TBA)_4H_2[H_2NC(CH_2O)_3P_2V_3W_{15}O_{59}]\cdot 3C_3H_7NO$ was synthesized following published procedure.[43] All reactions were performed under an argon atmosphere condition unless otherwise stated with magnetic stirring and in the dark to prevent photoreduction of the V^{5+} containing POM to mixed valence V^{5+}/V^{-4+} POMs. Ligand $\mathbf{L^{tpy}}$ was obtained according to the previously reported procedure.[44] IR spectra were obtained with a PerkinElmer 580 spectrophotometer and peak positions are reported in cm^{-1}. ESI mass spectra were determined in methanolic solution with $c = \sim 10^{-4}$ M using a Waters Micromass ZQ spectrometer. NMR spectra were run on a Varian VNMR-S 400 MHz spectrometer and were calibrated against the residual protonated solvent signals (DMSO-d_6, δ 2.50; D_2O, δ 3.33) which are given in parts per million. In ^{31}P NMR 25% H_3PO_4 was used as an external reference. Electronic absorption titrations and stability tests of compounds were performed on JASCO V-770 spectrophotometer equipped with a Peltier PAC-743R at a temperature of 20 °C in 10 × 10 mm quartz cells in the range of 800–200 nm. pH measurements were tested on Mettler Toledo Seven Compact S210 pH meter.

Synthetic procedure of complex K1 $[Zn(L^{tpy})Cl_2]$

Ligand $\mathbf{L^{tpy}}$ (100.0 mg, 0.30 mmol) was placed in a 50 ml round-bottom flask and dissolved in the mixture methanol/acetonitrile (1 : 1, v : v) (10 ml). The $ZnCl_2$ (40.9 mg, 0.30 mmol) was dissolved in a mixture of methanol/acetonitrile (1 : 1, v : v) (10 ml). Then the salt solution was added to the ligand and the solution changed colour from transparent to light yellow. The resulting mixture was stirred for 24 hours at room temperature. After this time, the reaction mixture was evaporated to dryness under reduced pressure. The residue was dissolved in a minimal amount of methanol/acetonitrile (1 : 1, v : v) (*ca.* 1 ml) and precipitated by the adding an excess of diethyl ether (approx. 30 ml). The resulting white precipitate was filtered off with suction and dried in a vacuum. Yield: 80.0 mg, 57.0%. ESI-MS(+) *m*/*z* (%): 335 (100) $[\mathbf{L^{tpy}} + H]^+$, 433 (30) $[ZnL^{tpy}Cl]^+$. Anal. calc.: C, 51.15; H, 4.08; N, 8.95; found: C, 51.05; H, 3.98; N, 9.02%. IR (KBr, cm^{-1}): $\nu(C\text{–}H)_{ar}$ 3392; $\nu_s(CH_3)$ 2449; $\nu(C{=}O)$ 1627; $\rho(C\text{–}H)_{ar}$1040; $\gamma(C\text{–}H)_{ar}$ 553. ^1H NMR (400 MHz, DMSO-d_6): δ = 9.06 (s, 1H), 8.71 (d, J = 7.9 Hz, 1H), 8.17 (t, J = 7.8 Hz, 1H), 7.69 (d, J = 7.7 Hz, 1H), 4.58–4.45 (m, 1H), 3.01 (s, 4H), 1.46 (t, J = 7.1 Hz, 2H). Solubility problems result in a mixture of "open" (metal ion : ligand; 1 : 1) and "closed" (metal ion : ligand; 1 : 2) systems.

Synthetic procedure of complex K2 $[Zn(L^{tpy})_2](ClO_4)_2$

Ligand L^{tpy} (100.0 mg, 0.30 mmol) was placed in a 50 ml round-bottom flask and dissolved in the mixture methanol/acetonitrile (1 : 1, v : v) (10 ml). The $Zn(ClO_4)_2{\cdot}6H_2O$ (55.9 mg, 0.15 mmol) was dissolved in a mixture of methanol/acetonitrile (1 : 1, v : v) (10 ml). Then the salt solution was added to the ligand solution. The resulting transparent mixture was stirred for 24 hours at room temperature. After this time, the reaction mixture was evaporated to dryness under reduced pressure. The residue was dissolved in a minimal amount of methanol/acetonitrile (1 : 1, v : v) (about 1 ml) and precipitated by adding an excess of diethyl ether (approx. 30 ml). The resulting white precipitate was filtered off with suction and dried in a vacuum. White solid residue was recrystallized by slow diffusion method from diisopropyl ether into methanol/acetonitrile (1 : 1, v : v) system at lowered temperature. Yield: 105.0 mg, 75.0%. ESI-MS(+) *m*/*z* (%): 335 (30) $[L^{tpy} + H]^+$, 356 (50) $[L^{tpy} + Na]^+$, 366 (80) $[ZnL^{tpy}_2]^{2+}$, 831 (10) $[ZnL^{tpy}_2(ClO4)]^+$. IR (KBr, cm^{-1}): ν(C–H)$_{ar}$ 3104; $\nu_s(CH_3)$ 2980, 2931; ν(C=O) 1773; ν(C=C)$_{ar}$ 1604, 1570, 1478, ν(C–N) 1442, 1372; ν(C=N)$_{ar}$ 1269, 1249; ρ(C–H)$_{ar}$ 1139, 1089; γ(C–H)$_{ar}$ 810, 769, 740; γ(ClO) 622. ^{1}H NMR (400 MHz, DMSO-d_6): δ = 8.82 ppm (s, 2H), 8.44 ppm (d, 2H), 7.91 ppm (t, 2H), 7.40 ppm (d, 2H), 4.46 ppm (q, 2H), 2.62 ppm (s, 6H), 1.40 ppm (t, 3H).

Synthetic procedure of hybrid $H1^{cov}$ (POM + L^{tpy}) [V_3POM + TRIZMA + L^{tpy}]TBA_6

V_3POM + TRIZMA (50 mg, 0.01 mmol) was dissolved in 15 ml of acetonitrile and added to a two necked 50 ml flask equipped with a condenser. Ligand L^{tpy} (3.2 mg, 0.01 mmol) was dissolved in 5 ml of acetonitrile and was added to solution of **V_3POM + TRIZMA**. The solution changed colour from brown-orange to yellow-green. Then the mixture was heated under reflux for 3 days. The resulting yellow-green precipitate was filtered off with suction, washed with acetonitrile and dried in a vacuum. Yield: 41.5 mg, 78.0%. ESI-MS(−) *m*/*z* (%): 716 (20) $[L^{tpy}$(**V_3POM + trizma**)$]^{6-}$. Anal. calc.: C, 25.03; H, 4.25; N, 2.43; found: C, 25.01; H, 4.31; N, 2.38%. IR (KBr, cm^{-1}): ν(N–H) 3446; $\nu_s(CH_3)$ 2932, 2872; ν(C=O) 1633; ν(C–N) 1465, 1379; ρ(C–H)$_{ar}$ 1086; γ(C–H)$_{ar}$ 952, 910, 817, 528. ^{1}H NMR (400 MHz, DMSO-d_6): δ = 8.85 ppm (s, 2H, HL), 8.49 ppm (d, 2H, HL), 7.99 ppm (m, 2H, HL), 7.46 ppm (d, 2H, HL), 5.39 ppm (s, 6H, O-CH_2-C), 3.16 ppm (m, 48H, HTBA), 2.65 ppm (s, 6H, HL), 1.57 ppm (p, 48H, HTBA), 1.31 ppm (h, 48H, HTBA), 0.98 ppm (t, 72H, HTBA). ^{31}P NMR (162 MHz, DMSO-d_6): δ = −6.65 ppm, −12.70 ppm.

Synthetic procedure of hybrid $H2^{cov}$ (POM + K1) [Zn(V_3POM + TRIZMA + L^{tpy})Cl_2]TBA_6

V_3POM + TRIZMA (50 mg, 0.01 mmol) was dissolved in 8 ml of acetonitrile and added to two necked 50 ml flask. **K1** (4.5 mg, 0.01 mmol) was added to solution of **V_3POM + TRIZMA**. The homogeneous mixture was heated under reflux for 24 hours. After this time clear yellow solution was condensed on rotavapor and diethyl ether was added. The resulting yellow precipitate was centrifuged, washed with diethyl ether and dried in a vacuum. Yield: 50.8 mg, 87.6%. ESI-MS(−) *m*/*z* (%): 962 (30) $[L^{tpy}$(**V_3POM + trizma**)Cl + 2TBA$]^{5-}$, 1638 (40) [Zn L^{tpy}(**V_3POM + trizma**)Cl_2 + H + 2TBA$]^{3-}$. Anal. calc.: C, 25.45; H, 4.15; N, 2.38; found: C, 25.58; H, 4.21; N, 2.31%. IR (KBr, cm^{-1}): ν(N–H) 3436; $\nu_s(CH_3)$ 2963, 2873; ν(C=O) 1644; ν(C–N) 1473, 1391; ρ(C–H)$_{ar}$ 1079; γ(C–H)$_{ar}$ 952, 900, 804, 737, 514. ^{1}H NMR (400 MHz, DMSO-d_6): δ = 8.84 ppm (s, 2H, H_L), 8.38 ppm (s, 2H, H_L), 7.95 ppm (s, 2H, H_L), 7.28 ppm (s, 2H, H_L), 5.39 ppm (s, 6H, O-CH_2-C), 3.17 ppm (t, 48H, H_{TBA}), 2.59 ppm (s, 6H, H_L), 1.56 ppm (p, 48H, H_{TBA}), 1.23 ppm (h, 48H, H_{TBA}), 0.94 ppm (t, 72H, H_{TBA}). ^{31}P NMR (162 MHz, DMSO-d_6): δ = −6.65 ppm, −12.70 ppm.

Synthetic procedure of hybrid $H3^{cov}$ (POM + K2) [Zn(V_3POM + TRIZMA + L^{tpy})$_2$(ClO_4)$_2$]$TBA_{(12-x)}H_x$; x = 11.5

V_3POM + TRIZMA (100 mg, 0.02 mmol) was dissolved in 15 ml of acetonitrile and added to two necked 50 ml flask. **K2** (7.0 mg, 0.01 mmol) was added to solution of **V_3POM + TRIZMA**. The heterogeneous mixture was heated under reflux for 24 hours. After this time a clear yellow solution was condensed on a rotavapor and placed at 4° deg overnight. The resulting yellow precipitate was filtered off with suction, washed with acetonitrile and dried in a vacuum. Yield: 38.0 mg, 71.7%. ESI-MS(−) *m*/*z* (%): 795 (30) [Zn(**L^{tpy}**(**V_3POM + trizma**))$_2ClO_4]^{11-}$, 1089 (70) [ZnL^{tpy}(**V_3POM + trizma**)$]^{4-}$. IR (KBr, cm^{-1}): ν(N–H) 3465; $\nu_s(CH_3)$ 2952, 2863; ν(C=O) 1629; ν(C=C)$_{ar}$ 1570; ν(C–N) 1458, 1384; ν(C=N)$_{ar}$ 1272; ρ(C–H)$_{ar}$ 1079; γ(C–H)$_{ar}$ 975, 900, 818, 730, 514. ^{1}H NMR (400 MHz, DMSO-d_6): 8.85 ppm (s, 4H, H_L), 8.50 ppm (d, 4H, H_L), 7.99 ppm (m, 4H, H_L), 7.48 ppm (d, 4H, H_L), 5.40 ppm (s, 6H, O-CH_2-C), 3.16 ppm (m, 3H, H_{TBA}), 2.65 ppm (s, 12H, H_L), 1.57 ppm (s, 3H, H_{TBA}), 1.30 ppm (p, 3H, H_{TBA}), 0.93 ppm (t, 5H, H_{TBA}). ^{31}P NMR (162 MHz, DMSO-d_6): δ = −6.65 ppm, −12.70 ppm.

Synthetic procedure of hybrid $H4^{cov}$ ($H1^{cov}$ + $ZnCl_2$) [Zn(V_3POM + TRIZMA + L^{tpy})Cl_2]H_2TBA_4

Hybrid $H1^{cov}$ (30 mg, 0.005 mmol) was dissolved in 5 ml of acetonitrile and added to two necked 50 ml flask. Next, solution of **$ZnCl_2$** (0.7 mg, 0.005 mmol) was added to solution of hybrid $H1^{cov}$. The heterogeneous mixture was heated under reflux for 24 hours. After this time the solution changed colour from violet to grey-green. The mixture was condensed on rotavapor and diethyl ether was added. The resulting grey-green precipitate was filtered *via* suction filtration, washed with diethyl ether and dried in a vacuum. Yield: 21.0 mg, 43.9%. ESI-MS(−) *m*/*z* (%): 915 (20) [L^{tpy}(**V_3POM + trizma**)Cl + H + TBA$]^{5-}$, 1204 (10) [L^{tpy}(**V_3POM + trizma**)Cl + H + 2TBA$]^{4-}$. Anal. calc.: C, 19.53; H, 3.22; N, 2.07; found: C, 19.75; H, 3.29; N, 2.10%. IR (KBr, cm^{-1}): ν(N–H) 3443; $\nu_s(CH_3)$ 2960, 2878; ν(C=O) 1644; ν(C–N) 1466, 1377; ν(C=N)$_{ar}$ 1272; ρ(C–H)$_{ar}$ 1087; γ(C–H)$_{ar}$ 952, 915, 812, 722, 536. ^{1}H NMR (400 MHz, DMSO-d_6): δ = 8.85 ppm (s, 2H, H_L), 8.48 ppm (d, 2H, H_L), 7.96 ppm (m, 2H, H_L), 7.45 ppm (d, 2H, H_L), 5.39 ppm (s, 6H, O-CH_2-C), 3.16 ppm (t, 32H, H_{TBA}), 2.64 ppm (s, 6H, H_L),

1.56 ppm (p, 32H, H_{TBA}), 1.32 ppm (h, 32H, H_{TBA}), 0.94 ppm (t, 48H, H_{TBA}). ^{31}P NMR (162 MHz, DMSO-d_6): δ = −6.65 ppm, −12.70 ppm.

Synthetic procedure of hybrid H5^{cov} (H1^{cov} + Zn(ClO$_4$)$_2$) [Zn(V$_3$POM + TRIZMA + L^{tpy})$_2$(ClO$_4$)$_2$]H$_{12}$

Hybrid **H1^{cov}** (30 mg, 0.005 mmol) was dissolved in 5 ml of acetonitrile and added to two necked 50 ml flask. Next, **Zn(ClO$_4$)$_2$·6H$_2$O** (1.0 mg, 0.0026 mmol) was added to solution of hybrid **H1^{cov}**. The heterogeneous mixture was heated under reflux for 24 hours. The resulting yellow precipitate was centrifuged, washed with acetonitrile and dried in a vacuum. Yield: 25.8 mg, 98.7%. ESI-MS(−) *m*/*z* (%): 575 (10) [**L^{tpy}(V$_3$POM + trizma)**(ClO$_4$)$_3$ + H]$^{8-}$, 604 (30) [**L^{tpy}(V$_3$POM + trizma)**(ClO$_4$)$_3$ + TBA]$^{8-}$. IR (KBr, cm^{-1}): ν(N–H) 3465; ν_s(CH$_3$) 2982, 2915; ν(C═O) 1607; ν(C═C)$_{ar}$ 1540; ν(C–N) 1435, 1391; ν(C═N)$_{ar}$ 1287; ρ(C–H)$_{ar}$ 1087; γ(C–H)$_{ar}$ 960, 900, 797, 722, 522. ^{1}H NMR (400 MHz, DMSO-d_6): 8.85 ppm (s, 4H, H_L), 8.48 ppm (d, 4H, H_L), 7.97 ppm (m, 4H, H_L), 7.45 ppm (d, 4H, H_L), 5.39 ppm (s, 12H, O-CH$_2$-C), 2.64 ppm (s, 12H, H_L). ^{31}P NMR (162 MHz, DMSO-d_6): δ = −6.67 ppm, −12.70 ppm.

Synthetic procedure of hybrid H6^{cov} (POM + L^{tpy} + ZnCl$_2$) [Zn(V$_3$POM + TRIZMA + L^{tpy})Cl$_2$]TBA$_{(6-x)}$H$_x$; *x* = 5.75

V$_3$POM + TRIZMA (50 mg, 0.01 mmol) was dissolved in 8 ml of acetonitrile and added to two necked 50 ml flask. **L^{tpy}** (3.2 mg, 0.01 mmol) and **ZnCl$_2$** (1.3 mg, 0.01 mmol) were added to solution of **V$_3$POM + TRIZMA**. The mixture changed colour to dark violet. The heterogeneous mixture was heated under reflux for 24 hours. After 3 hours the mixture turned yellow again. The resulting gray-green precipitate was centrifuged, washed with acetonitrile and dried in a vacuum. Yield: 17.4 mg, 36.4%. ESI-MS(−) *m*/*z* (%): 962 (30) [**L^{tpy}(V$_3$POM + trizma)**Cl + 2TBA]$^{5-}$, 1089 (30) [Zn **L^{tpy}(V$_3$POM + trizma)**]$^{4-}$. Anal. calc.: C, 6.48; H, 0.75; N, 1.26; found: C, 6.51; H, 0.80; N, 1.31%. IR (KBr, cm^{-1}): ν(N–H) 3458; ν(C–H)ar 3086; ν_s(CH$_3$) 2960, 2863; ν(C═O) 1636; ν(C═C)$_{ar}$ 1577, 1517; ν(C–N) 1428, 1384; ν(C═N)$_{ar}$ 1265; ρ(C–H)$_{ar}$ 1071; γ(C–H)$_{ar}$ 960, 908, 812, 737, 522. ^{1}H NMR (400 MHz, DMSO-d_6): δ = 8.85 ppm (s, 2H, H_L), 8.50 ppm (d, 2H, H_L), 7.98 ppm (d, 2H, H_L), 7.49 ppm (d, 2H, H_L), 5.40 ppm (s, 6H, O-CH$_2$-C), 3.16 ppm (m, 2H, H_{TBA}), 2.66 ppm (s, 6H, H_L), 1.57 ppm (p, 2H, H_{TBA}), 1.31 ppm (h, 2H, H_{TBA}), 0.94 ppm (t, 3H, H_{TBA}). ^{31}P NMR (162 MHz, DMSO-d_6): δ = −6.65 ppm, −12.70 ppm.

Synthetic procedure of hybrid H7^{cov} (POM + L^{tpy} + Zn(ClO$_4$)$_2$) [Zn(V$_3$POM + TRIZMA + L^{tpy})$_2$(ClO$_4$)$_2$]TBA$_{(12-x)}$H$_x$; *x* = 11.5

V$_3$POM + TRIZMA (50 mg, 0.01 mmol) was dissolved in 8 ml of acetonitrile and added to two necked 50 ml flask. **L^{tpy}** (3.2 mg, 0.01 mmol) and **Zn(ClO$_4$)$_2$·6H$_2$O** (1.8 mg, 0.005 mmol) were added to solution of **V$_3$POM + TRIZMA**. The heterogeneous mixture was heated under reflux for 24 hours. The resulting yellow precipitate was centrifuged, washed with acetonitrile and dried in a vacuum. Yield: 34.3 mg, 64.7%. ESI-MS(−) *m*/*z* (%): 716 (20) [**L^{tpy}(V$_3$POM + trizma)**]$^{6-}$, 732 (20) [**L^{tpy}(V$_3$POM + trizma)**ClO$_4$ + H]$^{6-}$, 772 (40) [**L^{tpy}(V$_3$POM + trizma)**ClO$_4$ + TBA]$^{6-}$, 976 (60) [**L^{tpy}(V$_3$POM + trizma)**ClO$_4$ + 2TBA]$^{5-}$. IR (KBr, cm^{-1}): ν(N–H) 3458; ν(C–H)ar 3086; ν_s(CH$_3$) 2952, 2863; ν(C═O) 1644; ν(C═C)$_{ar}$ 1554; ν(C–N) 1428, 1384; ν(C═N)$_{ar}$ 1272; ρ(C–H)$_{ar}$ 1094; γ(C–H)$_{ar}$ 960, 923, 812, 752, 581, 522. ^{1}H NMR (400 MHz, DMSO-d_6): 8.85 ppm (s, 4H, H_L), 8.49 ppm (d, 4H, H_L), 7.97 ppm (m, 4H, H_L), 7.46 ppm (d, 4H, H_L), 5.41 ppm (s, 6H, O-CH$_2$-C), 3.17 ppm (m, 4H, H_{TBA}), 2.64 ppm (s, 12H, H_L), 1.58 ppm (m, 4H, H_{TBA}), 1.31 ppm (m, 4H, H_{TBA}), 0.94 ppm (m, 6H, H_{TBA}). ^{31}P NMR (162 MHz, DMSO-d_6): δ = −6.65 ppm, −12.70 ppm.

X-ray crystallography

X-ray diffraction data were collected at 100(1) K by the ω-scan technique on Rigaku four-circle XCalibur diffractometer (Eos detector) with graphite-monochromatized MoK$_\alpha$ radiation (λ = 0.71073 Å). The data were corrected for Lorentz-polarization and absorption effects.[45] The structure was solved with SHELXT[46] and refined with the full-matrix least-squares procedure on F^2 by SHELXL.[47] Non-hydrogen atoms were refined anisotropically (*vide infra*), hydrogen atoms were placed in the calculated positions and refined as 'riding model' with the isotropic displacement parameters set at 1.2 (1.5 for methyl) times the U_{eq} value for appropriate non-hydrogen atom. The structure has been found disordered, in both ligand molecules the ethyl groups have been refined in two alternative positions, and in both cases the terminal methyl carbon atoms were left isotropic. Some constraints for C–C distances were applied. Additionally, there are regions of diffused electron density in the voids, apparently connected with the disorder solvent molecules. The attempts to model the solvent failed, so it has been refined with the SQUEEZE method.[48]

Crystal data: $(C_{40}H_{38}ZnN_6O_4)^{2+}\cdot 2(ClO_4)$, M_r = 931.03, triclinic, $P\bar{1}$, a = 12.9401(8) Å, b = 13.1181(8) Å, c = 13.9436(6) Å, α = 68.923(5), β = 80.861(4), γ = 66.577(6), V = 2026.2(2) Å^3, Z = 2, d_x = 1.523 g·cm^{-3}, F(000) = 958, μ = 0.743 cm^{-1}, 14 264 reflection collected, 7131 symmetry independent (R_{int} = 3.36%), 5905 with $I > 2\sigma(I)$. Final $R[I > 2\sigma(I)]$ = 0.0779, wR_2[I > 2σ(*I*)] = 0.1993, R [all reflections] = 0.0928, wR_2[all reflections] = 0.2088, S = 1.102, ($\Delta\rho_{max}/\Delta\rho_{min}$) = 1.45/−0.76 e Å^{-3}. Crystallographic data for the structural analysis has been deposited with the Cambridge Crystallographic Data Centre, CCDC 2078396.†

General for biological activities

CT-DNA, Tris and NaCl were supplied from Merck and used without further purification. CT-DNA was dissolved in Tris Buffer (5 mM Tris HCl, 50 mM NaCl, pH 7.4) prior to use. The CT-DNA solution gave a ratio of UV absorbance at 260 and 280 nm and the value is lower than 1.82 : 1, indicating that the CT-DNA sample was sufficiently free from protein. CT-DNA concentration per nucleotide was determined from the UV absorbance at 260 nm using the extinction coefficient ε_{260} = 6600 dm^3 mol^{-1} cm^{-1}. Stock solutions of compounds in DMSO at concentration 2 × 10^{-3} M were prepared prior to use. All electronic absorption spectra were performed in 10 × 10 mm quartz cells on Jasco V-770 between 800 and 200 nm

using solutions ~2×10^{-5} M with respect to the compound concentration in Tris Buffer (5 mM Tris HCl, 50 mM NaCl, pH 7.4) with 1% DMSO content.

Stability tests

Samples were prepared by diluting aqueous stock solutions (2 mM) of compounds (25 μl) in Tris Buffer (2475 μl; 5 mM Tris HCl, 50 mM NaCl, pH 7.4). UV-Vis absorbance spectra were measured in time intervals until stabilization of spectra has been reached. The obtained data indicate that the compounds remain stable[49] and reach equilibrium within 60 minutes.

Electronic absorption titration with DNA

The absorbance titrations were performed in a fixed concentration of compounds (20 μM) while gradually increasing the concentration of CT-DNA within the range from 0 to 100 μM. Identical aliquots of CT-DNA stock solution were added to the sample and the blank solutions and a new baseline was recorded before each titration step in order to not observe the bands corresponding to CT-DNA alone in the subsequent spectra. Each sample solution was allowed to equilibrate 5 min before the spectra were recorded. Using the absorption titration data, the binding constant K_b was determined according to the equation:[50] $[DNA]/(\varepsilon_a - \varepsilon_f) = [DNA]/(\varepsilon_b - \varepsilon_f) + 1/K_b\,(\varepsilon_b - \varepsilon_f)$, where [DNA] is the concentration of CT-DNA in the base pairs, ε_a corresponds to the extinction coefficient observed ($A_{obsd}/[M]$), ε_f corresponds to coefficient of free compound, ε_b is the extinction coefficient of the compound fully bound to CT-DNA, and K_b is the intrinsic binding constant. The K_b value was given by the ratio of slope to intercept in the plot of $[DNA]/(\varepsilon - \varepsilon_f)$ *versus* [DNA].

pH driven decomposition of hybrids and electronic absorption titration of $H1^{cov}$, $H2^{cov}$, $H3^{cov}$ with DNA in alkaline solutions

Solutions were prepared by adding stock solutions of compounds (20 μM) to MiliQ water (4 ml solution volume). The pH of each of the solutions was measured and the absorption spectra were performed by taking 2.5 ml of the solution. 2 M NaOH (1.5 μl) was then added to the test solutions to adjust the pH to alkaline. The pH of the solutions and the UV spectrum were measured. The next step was to add 100 μM CT-DNA to each sample including reference and the absorption measurement was made after 10 min, 60 min and 24 h.

Results and discussion

General rationale

WD POM hybrids with terpyridine-type ligands are known in the literature from both covalent and ionic approaches. The majority of papers focus on the covalent bonding of terpyridine ligands to WD POM, where organosilyl[51,52] or organophosphonate[53,54] functionalized WD POMs can be post-functionalized with terpyridine ligand-based complexes. In contrast, a distinct minority can be found in the literature showing ionic bonding between WD POM and terpyridine ligand. Among the few articles, the most commonly presented is the binding of a common P_2W_{18} subunit or modified cap WD POM to a pentaerythritol-based metallodendrimer with Ru^{II} terpyridine units.[55,56]

Herein, the hybrid systems based on WD POM were obtained *via* ionic and covalent functionalization to compare if the type of POM-complex interactions affect the stability of the hybrids and whether this can be used in the presence of DNA to demonstrate the possible interactions with a simple biological system. Hybrid materials constructed *via* ionic interactions were prepared using WD POM and tridentate acylhydrazone N_2O ligand $\mathbf{L^{N2O}}$ with NR_4^+ cationic moiety and was reported by us in 2020[14] (Scheme 1b). The simplicity of the system lies in the fact that WD counterpart is non-functionalized, easily available and its highly negative charge is responsible for interactions with ligand $\mathbf{L^{N2O}}$ or its complexes, ultimately forming (CD)-SEC materials. Please note that it was previously demonstrated in the literature that introduction of the cationic moiety in the acyl-hydrazone group can influence the binding propensity of the system to the DNA.[57] These hybrid materials termed $\mathbf{H1^{ion}}$–$\mathbf{H3^{ion}}$ are studied for their interactions with DNA (see Section: interaction of ionic hybrids with DNA). Herein, we constructed new class of WD hybrid materials based on the inorganic WD POM and 6,6″-dimethyl-2,2′:6′,2″-terpyridine-type ligand $\mathbf{L^{tpy}}$, which is based on the covalent functionalization. Tris(hydroxymethyl)aminomethane (TRIZMA) was chosen as the anchoring group, given its wide and successful utilization in the POM chemistry.[58]

Onto the TRIZMA-modified mono-substituted WD POM ($\mathbf{V_3POM + TRIZMA}$), $\mathbf{L^{tpy}}$ ligand was chemically grafted through the ester group in the *p*-position of the central tpy N-heterocyclic ring (Scheme 1c). We have previously demonstrated that the methylated version of the tpy ligand can efficiently form bimetallic $[Ag_2L_2]^{2+}$ helicates, which demonstrated cytotoxic character towards chosen cancer cell lines,[59] hence we envisaged that the formed POM covalent hybrids $\mathbf{H1^{cov}}$–$\mathbf{H3^{cov}}$ have the potential to exhibit related properties and therefore interaction with DNA were studied and compared with $\mathbf{H1^{ion}}$–$\mathbf{H3^{ion}}$ materials. Please note that irrespectively of the chosen type of connection (ionic or covalent), **H1** denotes POM-ligand hybrid, whereas **H2** and **H3** its complex with zinc(II) chloride and perchlorate, respectively.

Synthetic considerations for substrates

The synthetic pathway was divided into independent groups: preparation of TRIZMA-functionalized Wells–Dawson system $\mathbf{V_3POM + TRIZMA}$ (Scheme 1a), synthesis of ligand $\mathbf{L^{tpy}}$ and its two zinc(II) complexes **K1** $[Zn(\mathbf{L^{tpy}})Cl_2]$, **K2** $[Zn(\mathbf{L^{tpy}})_2](ClO_4)_2$ (Scheme 1e). After preparing the precursors, the synthesis of the seven hybrid materials $\mathbf{H1^{cov}}$–$\mathbf{H7^{cov}}$ was carried out using different routes (Scheme 1c). Details, including synthetic procedures and characterization are included in the Experimental section and ESI,† respectively.

The general procedure (Scheme 1a) involves selective lacunarization of the parent $K_6[P_2W_{18}O_{62}]$ WD POM and

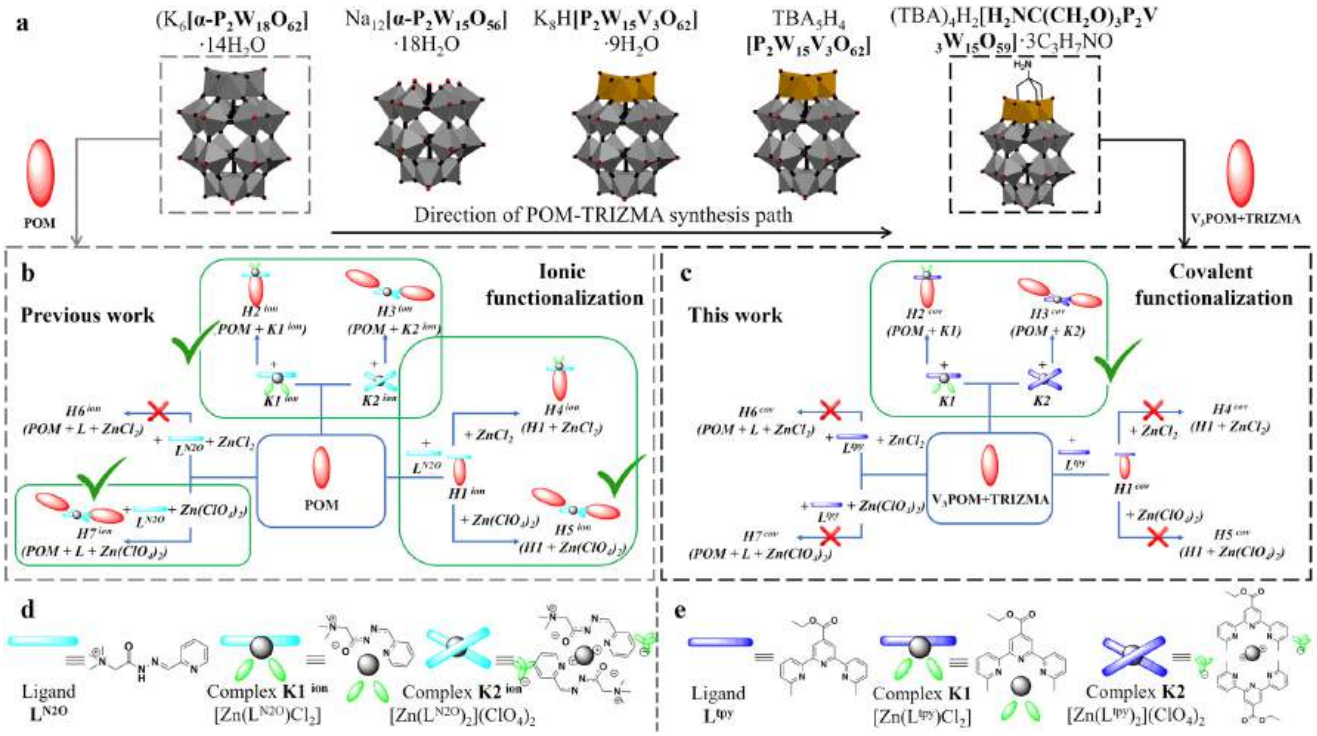

Scheme 1 (a) Scheme of synthesis path of WD POM in their polyhedral representations; schematic representation of hybrids constructed *via* (b) ionic[14] and (c) covalent interactions; schematic representation structures of (d) ligand L^{N2O} and complexes $K1^{ion}$ $[Zn(L^{N2O})Cl_2]$, $K2^{ion}$ $[Zn(L^{N2O})_2](ClO_4)_2$, respectively; and (e) ligand L^{tpy} $[C_{20}H_{19}N_3O_2]$ and complexes **K1** $[Zn(L^{tpy})Cl_2]$, **K2** $[Zn(L^{tpy})_2](ClO_4)_2$, respectively.

subsequent implementation of the vanadium cap, which renders the system prone to selective integration of the TRIZMA linker. Such amino-functionalized POM allows one to graft the tpy ligand in a robust, covalent manner through the amide bond, which was demonstrated to be feasible approach.[60,61]

Ligand L^{tpy} was obtained according to the slightly modified reported procedure[44] *via* the Stille coupling protocol (Scheme S1†) and was used for complexation reactions with $ZnCl_2$ and $Zn(ClO_4)_2$, thus allowing formation of complexes **K1** $[Zn(L^{tpy})Cl_2]$ and **K2** $[Zn(L^{tpy})_2](ClO_4)_2$, respectively. In both cases, the reaction was conducted in a mixture of methanol/acetonitrile (1 : 1, v : v) for 24 hours at room temperature. The purity of the compound and the repeatability of the desired product were confirmed by ESI-MS, elementary analysis, FT-IR, ^{1}H NMR and ^{31}P NMR spectroscopy are described in detail in the Experimental section and ESI.† X-ray crystal structure of complex **K2** is described in Section: X-ray crystal characterization of complex **K2**.

X-ray crystal characterization of complex K2

Fig. 1a shows the perspective view of the $[Zn(L^{tpy})_2]^{2+}$ cation in structure **K2**. The Zn^{II} ion is 6-coordinated, by six nitrogen atoms – three from each ligand molecule. The coordination might be described as distorted octahedral, with the Zn–N distances within the range 2.054(5) Å–2.311(4) Å, and the three largest.

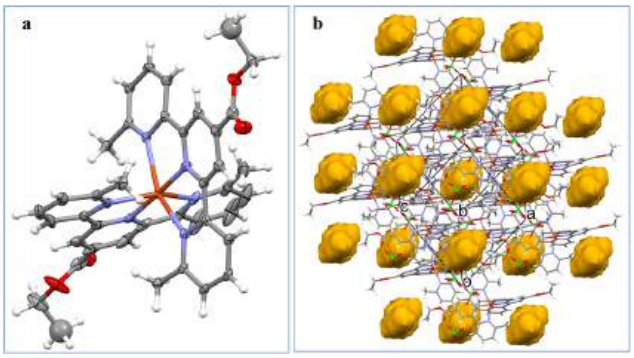

Fig. 1 (a) Perspective view of the dicationic complex **K2** $[Zn(L^{tpy})_2]^{2+}$; (b) the ellipsoids are drawn at the 30% probability level, hydrogen atoms are represented by spheres of arbitrary radii.

N–Zn–N angles equal 176.17(17)°, 151.07(19)°, and 151.63 (15)°. The crystal architecture is determined mainly be electrostatic interactions between charged species; there are voids filled with diffused electron density (Fig. 1b).

Synthesis and characterization of hybrid materials

The obtained precursors, both **V_3POM + TRIZMA**, ligand L^{tpy} and Zn(II) complexes **K1** and **K2**, were reacted to obtain three distinct families of hybrid materials $H1^{cov}$–$H3^{cov}$ ($H1^{cov}$ – POM with grafted ligand; $H2^{cov}$ – POM with grafted complex **K1**; $H3^{cov}$ – POM with grafted complex **K2**) that can be potentially

formed *via* seven different routes – depicted in Scheme 1c. Since we observed in our previous study[14] that not every route is feasible for the construction of ionic assemblies **H1^{ion}**–**H3^{ion}**, the same approach needs to be performed for the covalent class. Please note that for clarity purposes, each process was termed as **H1^{cov}**–**H7^{cov}**, where **H1^{cov}**–**H3^{cov}** denote reactions of POM with ligand **L^{tpy}** or its complexes; **H4^{cov}** and **H5^{cov}** denote reaction of **H1^{cov}** with metal salts (so called step-by-step approach) and **H6^{cov}** and **H7^{cov}** denote one-pot reaction of all substrates (POM, **L^{tpy}** and metal ion salts).

Synthesis of H1^{cov}–H3^{cov} hybrids

Synthesis of hybrids of **H1^{cov}**–**H3^{cov}** through direct reaction of amino-functionalized WD POM synthesis with **L^{tpy}** (**H1^{cov}**) or its zinc complexes **K1** (**H2^{cov}**) and **K2** (**H3^{cov}**) was performed through heating of substrates under reflux and successfully confirmed by a series of analytical methods (ESI-MS, elementary analysis, FT-IR, ^{1}H NMR spectroscopy, ^{31}P NMR spectroscopy) and is described in detail in the Experimental section and ESI.† Comparison of ^{1}H NMR spectra of respective substrates and their products (**H1^{cov}** – Fig. S24 and S25; **H2^{cov}** – Fig. S26 and S27; **H3^{cov}** – Fig. S28 and S29†) shows changes that are consistent with covalent bonding of the organic counterparts with the inorganic POM core (see also Fig. 2 of the aromatic region). FT-IR spectra (Fig. S4–S6†) also confirm the conducted reactions *via* the NH and C=O frequency shifts but importantly, together with ^{31}P NMR (Fig. S40–S42†) confirms that the WD POM retained its structural integrity. ESI-MS analyses also prove formation of the desired products. Interestingly, while the sole complex **K1** shows the ^{1}H NMR signature of the solution speciation between the 1 : 1 M : L [Zn(**L^{tpy}**)Cl$_2$] and the 1 : 2 M : L [Zn(**L^{tpy}**)$_2$]$^{2+}$ complexes – which is also observed in the literature for other tpy systems[62] – the **H2^{cov}** hybrid does not exhibit such a character. The *n*Bu$_4$N$^+$ cations inherent to the negatively charged POM species are also observed in the hybrid materials and integrated accordingly (6 for **H1^{cov}** and **H2^{cov}**, 12 for **H3^{cov}** hybrid). These were demonstrated to be inter-exchangeable,[63] which provides additional means for future functionalization.

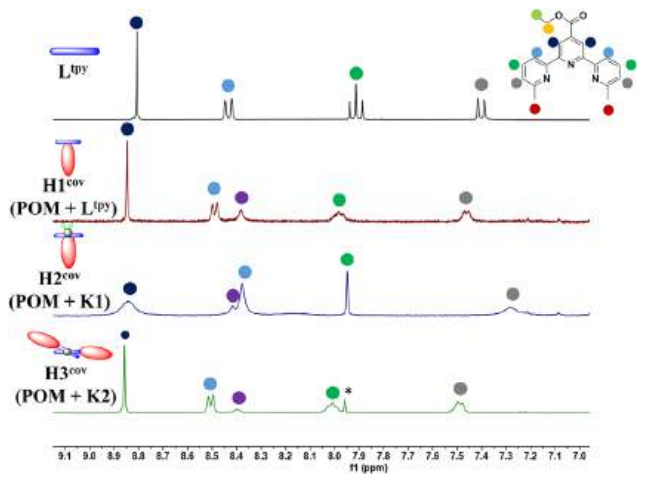

Fig. 2 Comparison of aromatic region of ^{1}H NMR spectra of **L^{tpy}** and hybrids: **H1^{cov}**, **H2^{cov}** and **H3^{cov}** in *d*^{6}-DMSO. Counterions are omitted for clarity.

Synthesis of H4^{cov} and H5^{cov} hybrids

Synthesis of **H4^{cov}** and **H5^{cov}** hybrids was anticipated to form analogues of **H2^{cov}** and **H3^{cov}** hybrids respectively, attempted from **H1^{cov}** hybrid *i.e.* system with **L^{tpy}** ligand covalently grafted onto the WD POM. While changes indicative of the molecular transformations were observed during the synthetic procedure, the isolation and characterization of hybrids (**H4^{cov}** – Fig. S7, S18, S30, S31 and S43; **H5^{cov}** – Fig. S8, S19, S32, S33 and S44†) showed that $ZnCl_2$ and $Zn(ClO_4)_2$ salts are not readily coordinated in the tpy pocket, but lead to partial hydrolysis resulting in the exchange of *n*Bu$_4$N$^+$ counteractions for the acidic protons – partial in the case of **H4^{cov}** (2H$^+$ and 4*n*Bu$_4$N$^+$ remain ionically bound to the POM hybrid) and complete in the case of **H5^{cov}** (12H$^+$ and no *n*Bu$_4$N$^+$ cations). What needs to be noted is the fact that in both cases the covalently bound tpy ligand remained grafted on the POM cluster and the polyoxometalate remained its plenary character. This is interesting, given the fact that in the presence of ionic hybrids,[14] we did observe the possibility of retrieving **H2^{ion}** and **H3^{ion}** analogues *via* this synthetic route to the certain extent (**H3^{ion}** perchlorates being more stable than the **H2^{ion}** chloride analogues) and that **H1^{ion}** hybrid was ultimately the most stable system.

Synthesis of H6^{cov} and H7^{cov} hybrids

Synthesis of **H6^{cov}** and **H7^{cov}** hybrids was expected to form analogues of **H2^{cov}** and **H3^{cov}** hybrids, respectively, attempted in the form of the one-pot reaction *i.e.* from which means combination of both POM, ligand **L^{tpy}** and appropriate Zn(II) salt in one vessel. Isolation and characterization of products (**H6^{cov}** – Fig. S9, S20, S34, S35 and S45; **H7^{cov}** – Fig. S10, S21, S36, S37 and S46†) and comparison with previously synthesized samples (Fig. S38, S39 and S47†) allowed us to establish that covalent grafting of the tpy ligand was successful (per analogy to the **H1^{cov}** hybrid) and zinc(II) cations did not coordinate to the N_3 tridentate pocket but resulted in an almost complete counterion exchange from *n*Bu$_4$N$^+$ cations to the acidic protons (**H6^{cov}** – TBA$_{(6-x)}$H$_x$; x = 5.75; **H7^{cov}** – TBA$_{(12-x)}$H$_x$; x = 11.5). This further confirms that in order for the covalent WD hybrids to retain Zn(II) ions in their molecular composition, one has to use the preformed complexes in the form of **K1** or **K2** compounds. As in previous instances, integrity of the WD POM counterpart was confirmed *via* ^{31}P NMR (Fig. S47†). The remarkable stability of the **H1^{cov}** and **H1^{ion}** (previously demonstrated[14]) hybrids combined with excellent water solubility led us to focus on the domain of bioassays.

Biological activities – general considerations

Polyoxometalates,[64,65] organic multidentate ligands and their Zn(II) complexes[57,66,67] were demonstrated in the literature to exhibit promising biological properties. Utilization of such

materials in bioassays significantly depends on the functionalization method and stability of the system, yet these aspects were very scarcely studied in hybrid materials based on WD POM scaffold and remain unknown, and only relatively recently such a niche was highlighted upon the fact that organic functionalization of the POM inorganic clusters alleviates some of the drawbacks that are inherent to the sole POM within the context of biotoxicity.[24] One of the primary cellular targets of drugs in cancer cells is the DNA present in the nuclei. Owing to the large size and the negative charge of both unfunctionalized POMs and DNA assemblies they are expected to rather repulse than interact between each other. It was however demonstrated that functionalization of POM clusters may reverse this trend or at least provide an alternative interaction path. For instance, Wang and co-workers[68] have reported cyclopentadienyltitanium substituted polyoxotungstate $[CoW_{11}O_{39}(CpTi)]^{7-}$ (Cp = η^5-C_5H_5) that is able to cleave the supercoiled DNA macrostructure. In addition, Dianat *et al.*[69] showed $K_6H[CoW_{11}O_{39}CpZr]$, $K_6H[CoW_{11}O_{39}CpTi]$ and $K_7H_2[CoW_{11}O_{39}CpFe]$ Keggin-type POMs, that tend to interact with the phosphate backbone of the DNA *via* electrostatic interactions.

Herein, we aimed to elucidate the affinity of the hybrid compounds (ionic **Hx^{ion}** *vs.* covalent **Hx^{cov}**) toward CT-DNA (deoxyribonucleic acid sodium salt from calf thymus), a model reagent used for routine DNA studies.[70] Since the electrostatic character of **Hx^{ion}–H1** (neutral), **H2** (anionic) and **H3** (anionic) is structure dependent, the interplay between them and DNA scaffold may be dissimilar to those previously described. At the same time, covalent functionalization of the POM hybrid can also be anticipated to help, especially since we did demonstrate previously that the silver(I) helical complexes of the related tpy ligand bind nucleic acids.[59] Both types of hybrids reach equilibrium within *ca.* 60 min and remain stable in the buffered medium (Fig. S48 and S49†).[49] Therefore, in order to probe the interactions between the synthesized hybrid materials **H1^{ion}**, **H2^{ion}**, **H3^{ion}**, **H1^{cov}**, **H2^{cov}**, **H3^{cov}** and also the corresponding complexes with the nucleic acid, a solution of the corresponding compound was titrated with CT-DNA samples.

Interaction of ionic hybrids with DNA

Significant changes in the shape of the spectra were observed for a series of CD-SEC hybrids **H2^{ion}** and **H3^{ion}**, contrary to the **H1^{ion}** system, which remained unchanged (Fig. 3 and Fig. S50†). In particular, the MLCT bands at 345 nm for **H2^{ion}** and 339 nm for **H3^{ion}** characteristic for the CD-SEC entities disappeared. Simultaneously, new bands, peculiar for **H1^{ion}**, at 257 nm and 290 nm appear. We surmise that this means that **H2^{ion}** and **H3^{ion}** undergo a structural transformation to **H1^{ion}** in the presence of DNA (compare Fig. 3) with the binding constant K_b of 2.5×10^5 M^{-1} (Fig. S50†) through decomplexation mechanism. Further experiments confirmed that the substrate complexes **K1^{ion}** and **K2^{ion}**, in fact, interact with DNA what is manifested by the moderately high binding constants of K_b = 6.7×10^4 and 1.2×10^5 M^{-1}, respectively (Fig. S51†). In case of both complexes, a hypsochromic shifts of *ca.* 10 nm of ILCT bands (*ca.* 295 nm) were observed. Changes in the intensity and position of the ligand-derived bands may suggest electrostatic interaction with CT-DNA. On the other hand, isosbestic points at *ca.* 305 nm as well as hypochromism of MLCT bands at *ca.* 345 nm are present and, together with the reported K_b values, indicate binding to DNA, possibly, by intercalation.[71,72] This indicates that the **H2^{ion}** and **H3^{ion}** are able to rearrange themselves to **H1^{ion}**. It also highlights the stability of the **H1^{ion}** in a cellular-like environment, making it a potential drug delivery platform.

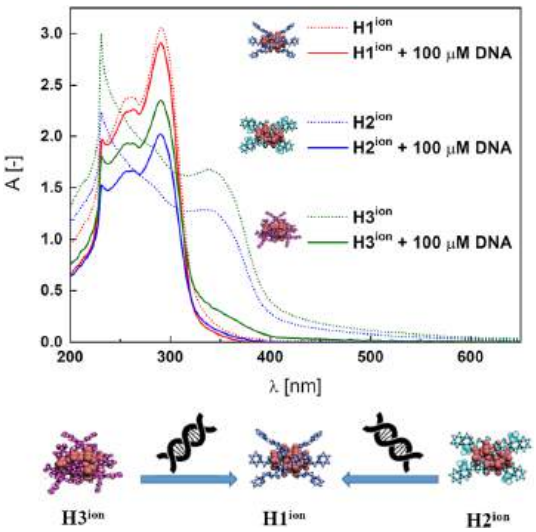

Fig. 3 **H1^{ion}**, **H2^{ion}** and **H3^{ion}** alone and the effect of CT-DNA addition.

Potential drugs such as platinum complexes[73] bound in SEC system as CD-SEC systems may be released in the presence of cellular DNA and then interact with its backbone *via* covalent binding thus inhibiting the cells vital processes as replication and transcription.

Interaction of covalent hybrids with DNA

It should be noted that in order to gain a deeper insight into the nature of the counterions present in the system and the changes associated to the POM transformations (Scheme 1a), a much larger number of substrates were tested for stability – including the V_3-capped WD POM with varying countercations (K^+ (**V_3POM-K8**), nBu$_4$N$^+$ (**V_3POM-TBA**), nBu$_4$N$^+$ functionalized with TRIZMA (**V_3POM + trizma**)), including the **L^{tpy}** ligand and its **K2** complex (**K1** is very poorly soluble in aqueous media). It occurred that functionalization of the WD POM with TRIZMA renders the system more stable that its non-substituted counterparts **V_3POM-K8** and **V_3POM-TBA** (Fig. S49†).

The covalently linked **H1^{cov}–H3^{cov}** hybrids did not bind to the DNA scaffold (Fig. S51†). However, the substrate ligand **L^{tpy}** and **K2** complex easily bound to DNA what is reflected in the high binding constants, respectively, 2.6×10^6 M^{-1} and 1.1×10^5 M^{-1} (Fig. 4 and Fig. S52†).

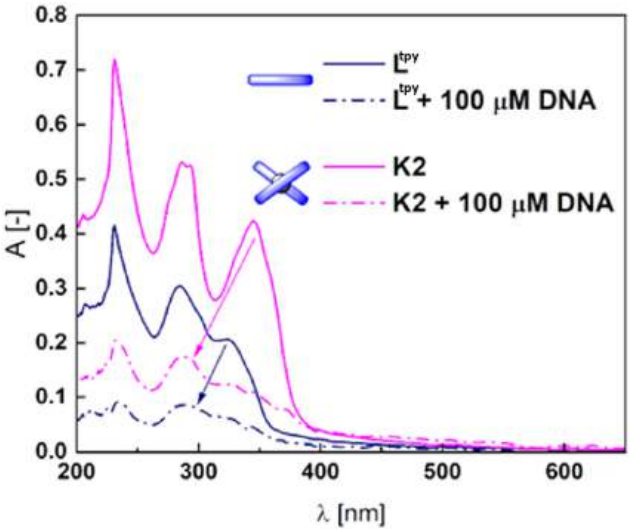

Fig. 4 L^{tpy} and **K2** alone and the effect of CT-DNA addition. Arrows indicate the trend of changes.

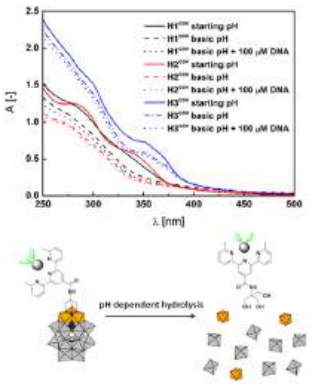

Fig. 5 $H1^{cov}$, $H2^{cov}$ and $H3^{cov}$ alone in miliQ water (starting pH *ca.* 5.9) and the effect of basification (up to pH ~ 8.6) and CT-DNA addition. Scheme below – schematic illustration using the example of $H2^{cov}$ of pH dependent hydrolysis leading to the breakdown into basic inorganic building subunits.

Addition of DNA to both compounds caused significant hypochromic changes in the spectra implying the intercalation.[71,72] **K1** complex is insoluble in buffer with DMSO, therefore the K_b was not calculated. However, its derivatization with POM increased its solubility (Fig. S52†) and the structure similarity to L^{tpy} and **K2** allows to surmise it could interfere with the DNA after the exchange of monovalent ligands. The stability of $H1^{cov}$–$H3^{cov}$ hybrids in acidic (*cf.* synthesis) and normal cellular pH (7.4) opens a path to a controlled release of the ligand and complexes in basic pH in the duodenum and small intestine (pH ~ 8). Basification of the acidic solutions of $H1^{cov}$–$H3^{cov}$ (*ca.* 5.9) to pH ~ 8.2–8.6 led to some morphological changes within 1 h in the UV spectra indicating slow decomposition of the hybrids in the POM region[63] (Fig. 5 and Fig. S53†). Then, to the partially decomposed covalent hybrids, the DNA was added and some subtle changes in the band's intensity were detected (Fig. 5 and Fig. S53†). One can observe that the $H2^{cov}$ is more readily decomposed than $H3^{cov}$ probably due to the insolubility of **K1** and the lower stability of the complexes of 1 : 1 ligand : metal ratio in comparison to 2 : 1 complexes as **K2**. We find it as evidence for the facilitation of the DNA binding process, possibly, due to the detaching of the POM octahedrons.[63,74] Changes are less abrupt that in the case of Hx^{ion} hybrids (Fig. 3).

This means that depending on the character of the chosen hybrid (covalent *vs.* ionic) one can envisage those systems to become cargo-loading drug candidates, with functionalization mode ultimately affecting the stability and eventual pharmacotherapeutic effect – which was demonstrated for the anchored organic ligand/complex (interaction constant K_b = 2.5×10^5 M^{-1}, insets in Fig. S50†). The ultimate mechanism is however different; for Hx^{ion} hybrids, the ionic interactions make it very fast system, where POM remains intact in its $H1^{ion}$ form and the disturbance of ionic interactions results in cargo-release of the appended molecules; for Hx^{cov} hybrids the POM hydrolyses through the pH dependent mechanisms, therefore ligand/complex is released together with disintegration of WD POM into the basic inorganic building subunits (Fig. 4).

Conclusions

In summary, we have presented the effect of various synthetic methods on the synthesis of three different families of $H1^{cov}$–$H3^{cov}$ hybrid materials. The first synthetic method involved the reaction of POM with the ligand L^{tpy} or its complexes: **K1** or **K2**; the second synthetic method involved the reaction of $H1^{cov}$ with metal salts (step-by-step approach), and the third involved the reaction between POM, L^{tpy} and metal ion salts (one-pot approach). As a result, the desired hybrid materials were obtained using the first synthetic method and we have demonstrated for the first time how hybrid materials based on Wells–Dawson Polyoxometalates interact with DNA and how their functionalization mode (ionic/covalent) modulates the stability of the hybrid and the extent of DNA binding. This was done by comparing the ionic Hx^{ion} hybrids synthesized previously[14] and newly prepared covalent Hx^{cov} hybrids. Protocols for the latter ones were also developed, giving therefore different means for their functionalization and demonstrating which molecular parts of the hybrids are amenable to further synthetic changes. Specifically, the acidic character of the zinc(II) salts is responsible for part of those transformations.

In the presence of DNA, the synthesized ionic and covalent hybrids undergo reorganizations, which in both instances lead to the release of the bound ligands/complexes, nonetheless the ultimate mechanism is different. For Hx^{ion} ionic hybrids, fast elimination of the coordinated zinc(II) ions/ligands from $H2^{ion}$ and $H3^{ion}$ hybrids is observed, concomitant with transformation to the $H1^{ion}$ hybrid due to the significant stability of the latter one. For Hx^{cov} covalent hybrids, slow pH mediated hydro-

lysis of the polyoxometalate was observed, which leads to release of the grafted ligand/complex to the surrounding aqueous medium. High binding constant of terpyridine ligand and its complex $[Zn(\mathbf{L}^{tpy})_2](ClO_4)_2$ to the DNA was also demonstrated. This overall shows that the WD POM has the potential to act as the cargo-loading system, which we anticipate to study further.

Author contributions

Daria Nowicka: investigation, methodology, formal analysis, data curation, visualization, writing – review & editing, funding acquisition. Dawid Marcinkowski: investigation, methodology, formal analysis, data curation, visualization, writing – review & editing, funding acquisition. Nahir Vadra: investigation, methodology, formal analysis, data curation, visualization, writing – review & editing. Martyna Szymańska: investigation, methodology, formal analysis, data curation, visualization, writing – review & editing. Maciej Kubicki: formal analysis, investigation, data curation, writing – review & editing, visualization. Giuseppe Consiglio: conceptualization, visualization, writing – review & editing. Wojciech Drożdż: investigation, formal analysis, data curation, writing – review & editing. Artur R. Stefankiewicz: resources, visualization, writing – review & editing. Violetta Patroniak: supervision, resources, writing – review & editing, funding acquisition. Marta Fik-Jaskółka: investigation, conceptualization, methodology, writing – review & editing, project administration, supervision, resources, funding acquisition. Adam Gorczyński: conceptualization, methodology, writing – review & editing, project administration, supervision, resources.

Conflicts of interest

There are no conflicts to declare.

Acknowledgements

We express gratitude to Dr Aleksandra Bocian for help in synthesis of ionic hybrids $\mathbf{H1}^{ion}$–$\mathbf{H7}^{ion}$. This work was supported by the National Science Centre, Poland (grant numbers UMO-2022/45/N/ST4/00632 (D. N.), UMO-2022/45/N/ST4/00344 (D. M.), UMO-2019/32/C/ST4/00565 (W. D.), UMO-2022/47/B/ST4/02310 (V. P.)). Daria Nowicka is a scholarship holder of the Adam Mickiewicz University in Poznan Foundation for the academic year 2023/2024. Adam Gorczyński is a scholarship holder of the Polish Ministry of Education and Science for outstanding young scientists. MFJ: the work was supported by IDUB-UAM (project no. 038/04/NŚ/0023). This work was also supported by the University of Catania, PIACERI 2020/2022, Linea di Intervento 2.

References

1 D.-L. Long, R. Tsunashima and L. Cronin, *Angew. Chem., Int. Ed.*, 2010, **49**, 1736–1758.
2 S. Lentink, D. E. Salazar Marcano, M. A. Moussawi and T. N. Parac-Vogt, *Angew. Chem., Int. Ed.*, 2023, **62**, e202303817.
3 X.-K. Lian, H.-B. Chen, Y.-D. Lin, X.-X. Li and S.-T. Zheng, *Coord. Chem. Rev.*, 2023, **497**, 215440.
4 L. Vilà-Nadal and L. Cronin, *Nat. Rev. Mater.*, 2017, **2**, 17054.
5 L. Cronin, *Ann. Rep. Prog. Chem., Sect. A: Inorg. Chem.*, 2004, **100**, 323–383.
6 L.-L. Liu, L. Wang, X.-Y. Xiao, P. Yang, J. Zhao and U. Kortz, *Coord. Chem. Rev.*, 2024, **506**, 215687.
7 A. Misra, K. Kozma, C. Streb and M. Nyman, *Angew. Chem., Int. Ed.*, 2020, **59**, 596–612.
8 H. N. Miras, J. Yan, D.-L. Long and L. Cronin, *Chem. Soc. Rev.*, 2012, **41**, 7403–7430.
9 V. Duros, J. Grizou, W. Xuan, Z. Hosni, D.-L. Long, H. N. Miras and L. Cronin, *Angew. Chem., Int. Ed.*, 2017, **56**, 10815–10820.
10 D. S. Salley, G. A. Keenan, D. L. Long, N. L. Bell and L. Cronin, *ACS Cent. Sci.*, 2020, **6**, 1587–1593.
11 A. V. Anyushin, S. Vanhaecht and T. N. Parac-Vogt, *Inorg. Chem.*, 2020, **59**, 10146–10152.
12 Q. Liu and X. Wang, *Matter*, 2020, **2**, 816–841.
13 A. Dolbecq, E. Dumas, C. R. Mayer and P. Mialane, *Chem. Rev.*, 2010, **110**, 6009–6048.
14 A. Bocian, W. Drożdż, M. Szymańska, J. Lewandowski, M. Fik-Jaskółka, A. Gorczyński, V. Patroniak and A. R. Stefankiewicz, *Nanoscale*, 2020, **12**, 4743–4750.
15 S.-S. Wang and G.-Y. Yang, *Chem. Rev.*, 2015, **115**, 4893–4962.
16 S. Li, Y. Ma, Y. Zhao, R. Liu, Y. Zhao, X. Dai, N. Ma, C. Streb and X. Chen, *Angew. Chem., Int. Ed.*, 2023, **62**, e202314999.
17 M. Yang, X. Wang, C. J. Gómez-García, Z. Jin, J. Xin, X. Cao, H. Ma, H. Pang, L. Tan, G. Yang and Y. Kan, *Adv. Funct. Mater.*, 2023, **33**, 2214495.
18 X. Chen, C. Ma, Z. Tan, X. Wang, X. Qian, X. Zhang, J. Tian, S. Yan and M. Shao, *Chem. Eng. J.*, 2022, **433**, 134504.
19 J.-J. Chen, M. D. Symes and L. Cronin, *Nat. Chem.*, 2018, **10**, 1042–1047.
20 A. Bijelic and A. Rompel, *Acc. Chem. Res.*, 2017, **50**, 1441–1448.
21 Y. Martinetto, B. Pégot, C. Roch-Marchal, B. Cottyn-Boitte and S. Floquet, *Eur. J. Inorg. Chem.*, 2020, **2020**, 228–247.
22 S.-M. Wang, J. Hwang and E. Kim, *J. Mater. Chem. C*, 2019, **7**, 7828–7850.
23 U. Kortz, A. Müller, J. van Slageren, J. Schnack, N. S. Dalal and M. Dressel, *Coord. Chem. Rev.*, 2009, **253**, 2315–2327.
24 J. T. Rhule, C. L. Hill, D. A. Judd and R. F. Schinazi, *Chem. Rev.*, 1998, **98**, 327–358.
25 B. Hasenknopf, *Front. Biosci.*, 2005, **10**, 275–287.
26 M. Arefian, M. Mirzaei, H. Eshtiagh-Hosseini and A. Frontera, *Dalton Trans.*, 2017, **46**, 6812–6829.
27 T. Liu, *Langmuir*, 2010, **26**, 9202–9213.

28 P. Gao, Y. Wu and L. Wu, *Soft Matter*, 2016, **12**, 8464–8479.
29 S. Vanhaecht, G. Absillis and T. N. Parac-Vogt, *Dalton Trans.*, 2012, **41**, 10028–10034.
30 K.-i. Shimizu, H. Furukawa, N. Kobayashi, Y. Itaya and A. Satsuma, *Green Chem.*, 2009, **11**, 1627–1632.
31 J. Zhang, *Trends in Polyoxometalates Research*, 2015.
32 A. Flütsch, T. Schroeder, M. G. Grütter and G. R. Patzke, *Bioorg. Med. Chem. Lett.*, 2011, **21**, 1162–1166.
33 K. Nomiya, H. Torii, T. Hasegawa, Y. Nemoto, K. Nomura, K. Hashino, M. Uchida, Y. Kato, K. Shimizu and M. Oda, *J. Inorg. Biochem.*, 2001, **86**, 657–667.
34 A. Bijelic, M. Aureliano and A. Rompel, *Chem. Commun.*, 2018, **54**, 1153–1169.
35 A. Bijelic, M. Aureliano and A. Rompel, *Angew. Chem., Int. Ed.*, 2019, **58**, 2980–2999.
36 L. Fu, H. Gao, M. Yan, S. Li, X. Li, Z. Dai and S. Liu, *Small*, 2015, **11**, 2938–2945.
37 D. Li, P. Yin and T. Liu, *Dalton Trans.*, 2012, **41**, 2853–2861.
38 X. Wang, J. Liu and M. Pope, *Dalton Trans.*, 2003, 957–960.
39 S. K. Petrovskii, E. V. Grachova and K. Y. Monakhov, *Chem. Sci.*, 2024, **15**, 4202–4221.
40 R. Contant and A. Tézé, *Inorg. Chem.*, 1985, **24**, 4610–4614.
41 B. J. Hornstein and R. G. Finke, *Inorg. Chem.*, 2002, **41**, 2720–2730.
42 R. G. Finke, B. Rapko, R. J. Saxton and P. J. Domaille, *J. Am. Chem. Soc.*, 1986, **108**, 2947–2960.
43 C. P. Pradeep, D.-L. Long, G. N. Newton, Y.-F. Song and L. Cronin, *Angew. Chem., Int. Ed.*, 2008, **47**, 4388–4391.
44 G. Ulrich, S. Bedel, C. Picard and P. Tisnès, *Tetrahedron Lett.*, 2001, **42**, 6113–6115.
45 *CrysAlis PRO (Version 1.171.38.41)*, 2015.
46 G. M. Sheldrick, *Acta Crystallogr., Sect. A: Found. Adv.*, 2015, **71**, 3–8.
47 G. M. Sheldrick, *Acta Crystallogr., Sect. C: Struct. Chem.*, 2015, **71**, 3–8.
48 A. L. Spek, *Acta Crystallogr., Sect. C: Struct. Chem.*, 2015, **71**, 9–18.
49 J. Skiba, T. Bernaś, D. Trzybiński, K. Woźniak, G. Ferraro, D. Marasco, A. Merlino, M. Z. Shafikov, R. Czerwieniec and K. Kowalski, *Molecules*, 2017, **22**, 809.
50 L. Shivakumar, K. Shivaprasad and H. D. Revanasiddappa, *Spectrochim. Acta, Part A*, 2012, **97**, 659–666.
51 G. Izzet, B. Abécassis, D. Brouri, M. Piot, B. Matt, S. A. Serapian, C. Bo and A. Proust, *J. Am. Chem. Soc.*, 2016, **138**, 5093–5099.
52 B. Matt, C. Coudret, C. Viala, D. Jouvenot, F. Loiseau, G. Izzet and A. Proust, *Inorg. Chem.*, 2011, **50**, 7761–7768.
53 E. Hampson, J. M. Cameron, S. Amin, J. Kyo, J. A. Watts, H. Oshio and G. N. Newton, *Angew. Chem.*, 2019, **131**, 18449–18453.
54 E. Hampson, J. M. Cameron, J. A. Watts and G. N. Newton, *Chem. Commun.*, 2020, **56**, 8237–8240.
55 M. Zynek, M. Serantoni, S. Beloshapkin, E. Dempsey and T. McCormac, *Electroanalysis*, 2007, **19**, 681–689.
56 R. I. Nooney, D. Thirunavukkarasu, Y. Chen, R. Josephs and A. E. Ostafin, *Chem. Mater.*, 2002, **14**, 4721–4728.
57 W. Drożdż, A. Walczak, Y. Bessin, V. Gervais, X.-Y. Cao, J.-M. Lehn, S. Ulrich and A. R. Stefankiewicz, *Chem. – Eur. J.*, 2018, **24**, 10802–10811.
58 A. V. Anyushin, A. Kondinski and T. N. Parac-Vogt, *Chem. Soc. Rev.*, 2020, **49**, 382–432.
59 M. A. Fik, A. Gorczyński, M. Kubicki, Z. Hnatejko, A. Fedoruk-Wyszomirska, E. Wyszko, M. Giel-Pietraszuk and V. Patroniak, *Eur. J. Med. Chem.*, 2014, **86**, 456–468.
60 A. Proust, B. Matt, R. Villanneau, G. Guillemot, P. Gouzerh and G. Izzet, *Chem. Soc. Rev.*, 2012, **41**, 7605–7622.
61 M. Najafi, *ChemCatChem*, 2023, **15**, e202201045.
62 M. Wałęsa-Chorab, A. R. Stefankiewicz, D. Ciesielski, Z. Hnatejko, M. Kubicki, J. Kłak, M. J. Korabik and V. Patroniak, *Polyhedron*, 2011, **30**, 730–737.
63 D. E. Salazar Marcano, S. Lentink, M. A. Moussawi and T. N. Parac-Vogt, *Inorg. Chem.*, 2021, **60**, 10215–10226.
64 N. I. Gumerova and A. Rompel, *Inorg. Chem.*, 2021, **60**, 6109–6114.
65 L. S. Van Rompuy and T. N. Parac-Vogt, *Curr. Opin. Biotechnol.*, 2019, **58**, 92–99.
66 W. Drożdż, Y. Bessin, V. Gervais, X. Y. Cao, J. M. Lehn, A. R. Stefankiewicz and S. Ulrich, *Chem. – Eur. J.*, 2018, **24**, 1518–1521.
67 F. Nachon, X. Brazzolotto, J. Dias, C. Courageux, W. Drożdż, X.-Y. Cao, A. R. Stefankiewicz and J.-M. Lehn, *ChemBioChem*, 2022, **23**, e202200456.
68 X. Wang, J. Liu, J. Li, Y. Yang, J. Liu, B. Li and M. T. Pope, *J. Inorg. Biochem.*, 2003, **94**, 279–284.
69 S. Dianat, A. K. Bordbar, S. Tangestaninejad, B. Yadollahi, S. H. Zarkesh-Esfahani and P. Habibi, *J. Photochem. Photobiol., B*, 2013, **124**, 27–33.
70 M. Szymańska, M. Kubicki, G. N. Roviello, G. Consiglio, M. A. Fik-Jaskółka and V. Patroniak, *Dalton Trans.*, 2022, **51**, 15648–15658.
71 S. Tabassum, S. Amir, F. Arjmand, C. Pettinari, F. Marchetti, N. Masciocchi, G. Lupidi and R. Pettinari, *Eur. J. Med. Chem.*, 2013, **60**, 216–232.
72 A. A. Almaqwashi, T. Paramanathan, I. Rouzina and M. C. Williams, *Nucleic Acids Res.*, 2016, **44**, 3971–3988.
73 S. Ghosh, *Bioorg. Chem.*, 2019, **88**, 102925.
74 N. I. Gumerova and A. Rompel, *Chem. Soc. Rev.*, 2020, **49**, 7568–7601.

Electronic Supporting Information

The effect of ionic versus covalent functionalization of Polyoxometalate hybrid materials with coordinating subunits on their stability and interaction with DNA

Daria Nowicka[#a], Dawid Marcinkowski[#a], Nahir Vadra[b], Martyna Szymańska[a], Maciej Kubicki[a], Giuseppe Consiglio[c], Wojciech Drożdż[ad], Artur R. Stefankiewicz[ad], Violetta Patroniak[a], Marta Fik-Jaskółka*[a] and Adam Gorczyński*[a]

[a] *Adam Mickiewicz University in Poznań, Faculty of Chemistry, Uniwersytetu Poznańskiego 8, 61-614 Poznań, Poland*

[b] *Universidad de Buenos Aires, Facultad de Ciencias Exactas y Naturales, Departamento de Química Inorgánica, Analítica y Química Física and CONICET–Universidad de Buenos Aires, Instituto de Química Física de los Materiales, Medio Ambiente y Energía (INQUIMAE), Buenos Aires C1428EGA, Argentina*

[c] *Università di Catania, Dipartimento di Scienze Chimiche, I-95125 Catania, Italy*

[d] *Adam Mickiewicz University in Poznań, Center for Advanced Technology, Uniwersytetu Poznańskiego 10, 61-614 Poznań, Poland*

** Correspondence: marta.fik@amu.edu.pl; adam.gorczynski@amu.edu.pl*

 # equal contribution†

Table of contents for Electronic Supporting Information

1. Schematic synthesis of ligand, complexes and hybrids……...……..2
2. FT-IR spectra of ligand, complexes and hybrids ……....…….8
3. Comparison of FTIR spectra of compounds…….……..……13
4. ^{1}H NMR spectra of ligand, complexes and hybrids ……...……..……..14
5. Comparison of ^{1}H NMR spectra of compounds ……...……..…..……19
6. ^{31}P NMR spectra of hybrids……...…….…….……28
7. Comparison of ^{31}P NMR spectra of hybrids ……...…….…..……..31
8. Biological measurements ……..……...…….....32

References…….……..35

1. Schematic synthesis of ligand, complexes and hybrids

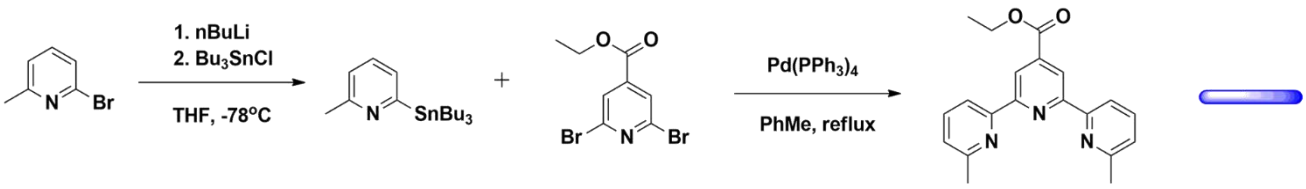

Scheme S1. Scheme of synthesis of ligand $\mathbf{L^{tpy}}$ [$C_{20}H_{19}N_3O_2$] according to publication [1].

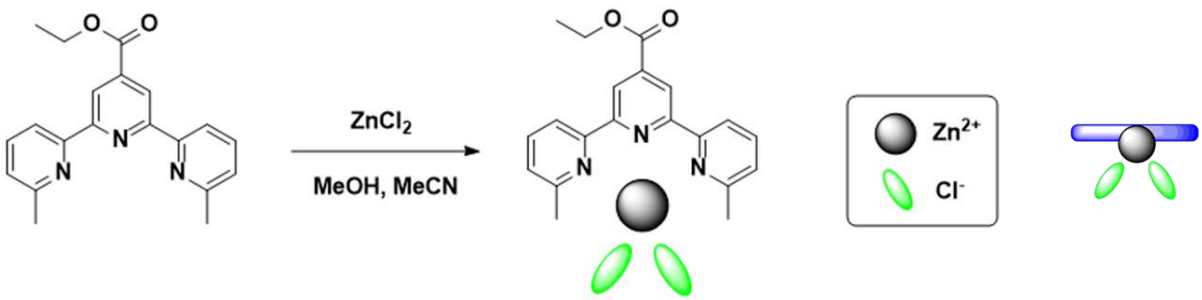

Scheme S2. Scheme of synthesis of complex **K1 [$\mathbf{ZnL^{tpy}Cl_2}$]**.

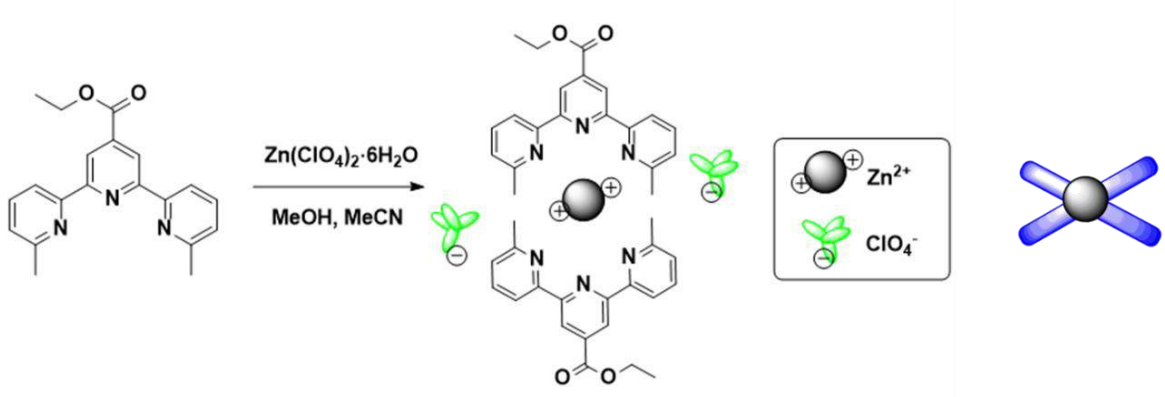

Scheme S3. Scheme of synthesis of complex **K2 [$\mathbf{Zn(L^{tpy})_2](ClO_4)_2}$**.

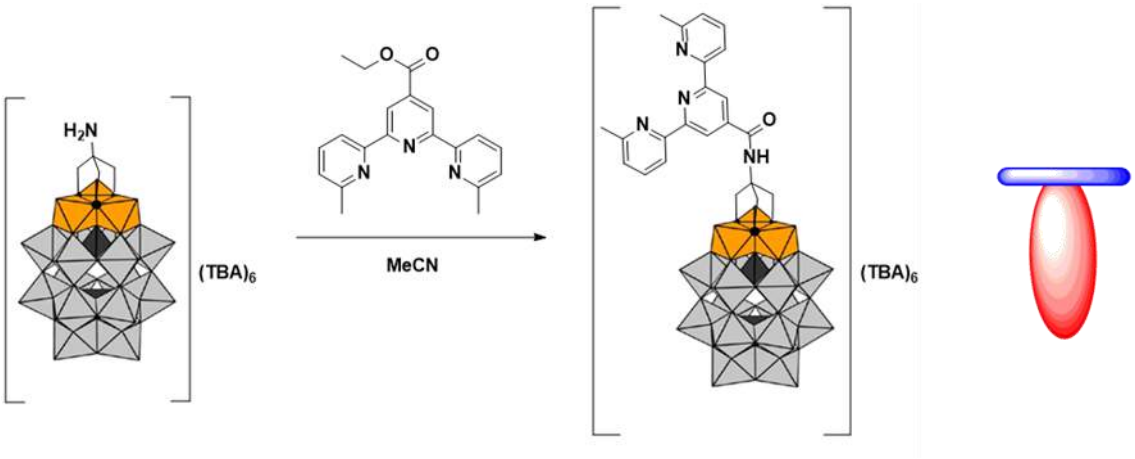

Scheme S4. Scheme of synthesis of hybrid **H1^{cov} (POM + L^{tpy})**.

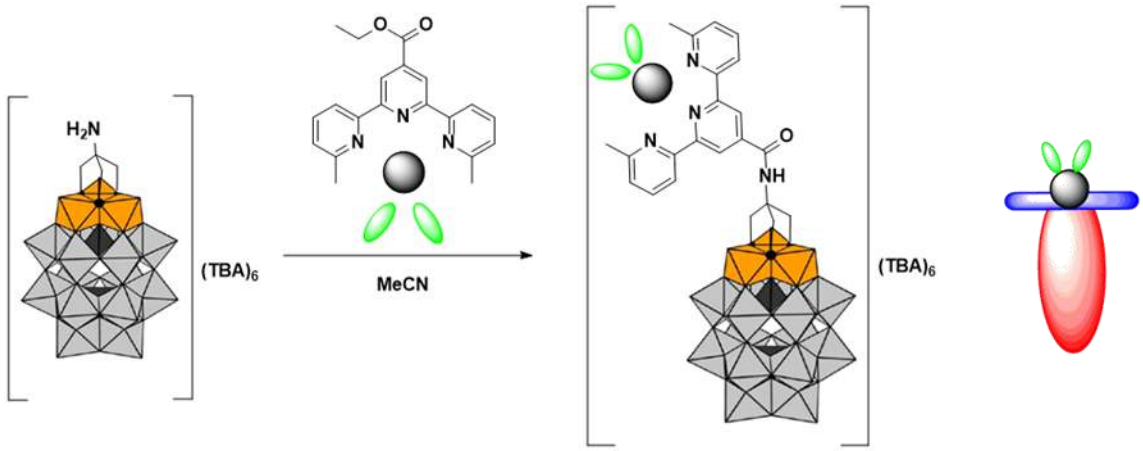

Scheme S5. Scheme of synthesis of hybrid **H2^{cov} (POM + K1)**.

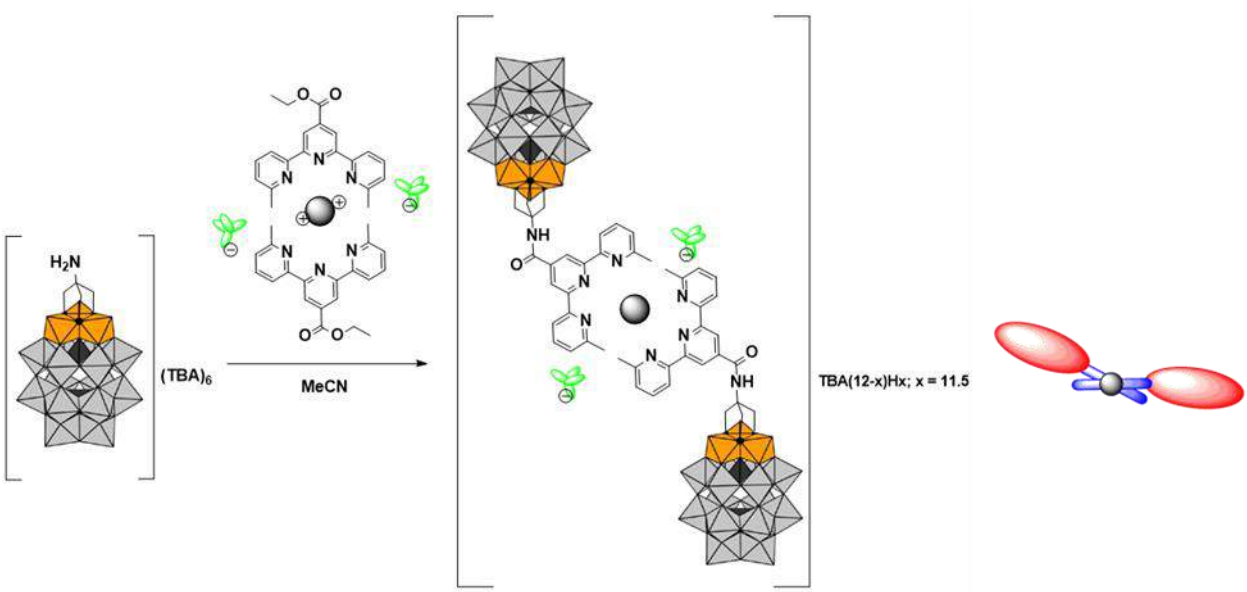

Scheme S6. Scheme of synthesis of hybrid **H3^{cov} (POM + K2)**.

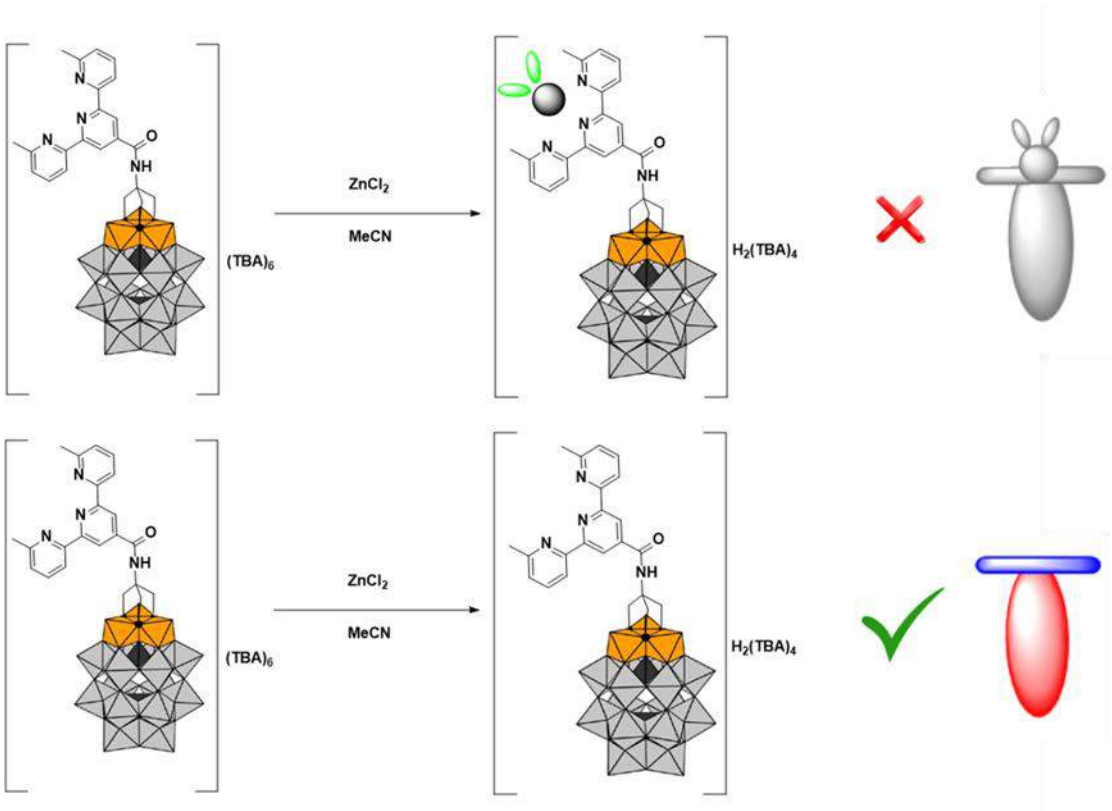

Scheme S7. Scheme of synthesis of hybrid **H4^{cov} (H1^{cov} + $ZnCl_2$)**.

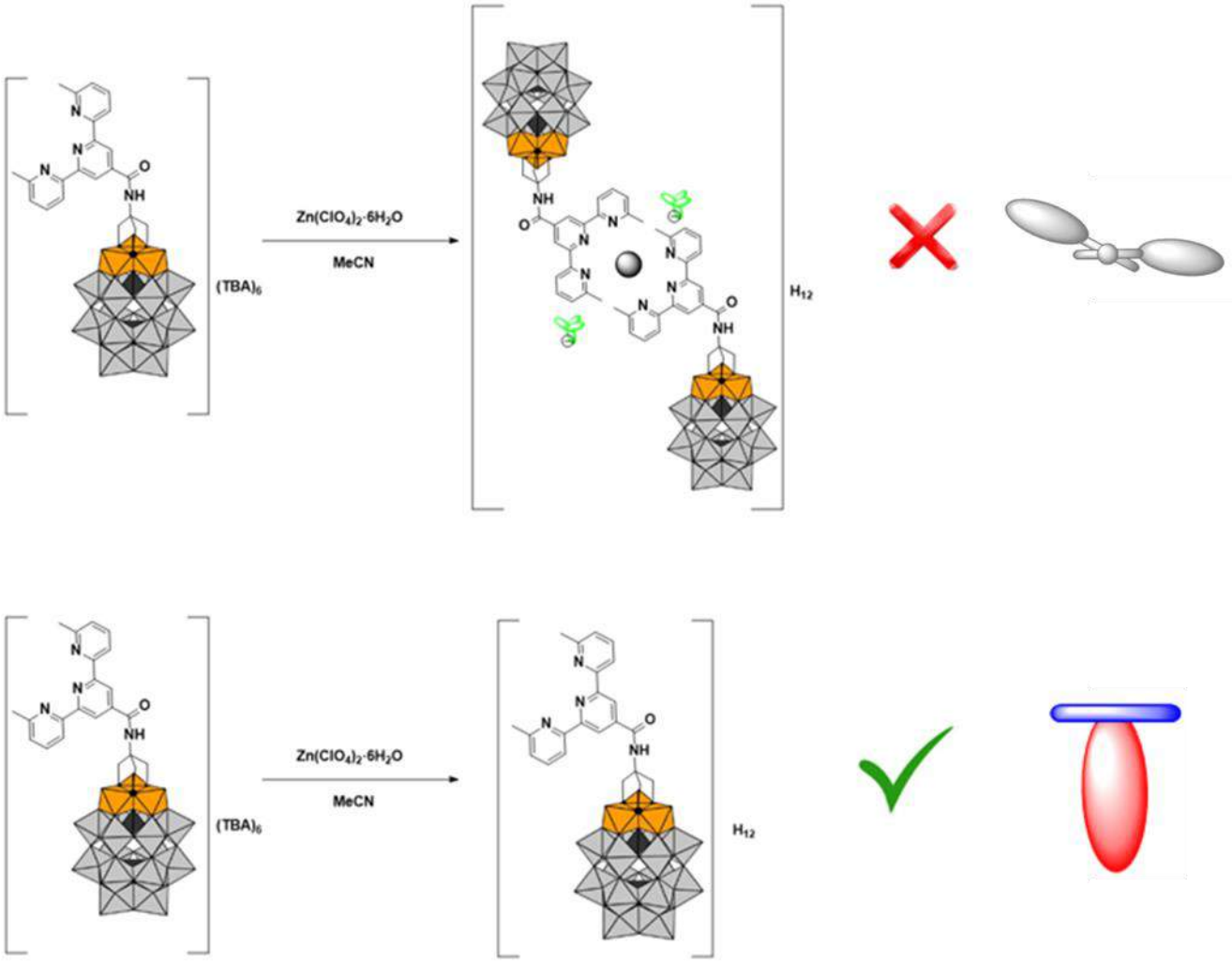

Scheme S8. Scheme of synthesis of hybrid **H5^{cov} (H1^{cov} + Zn(ClO$_4$)$_2$)**.

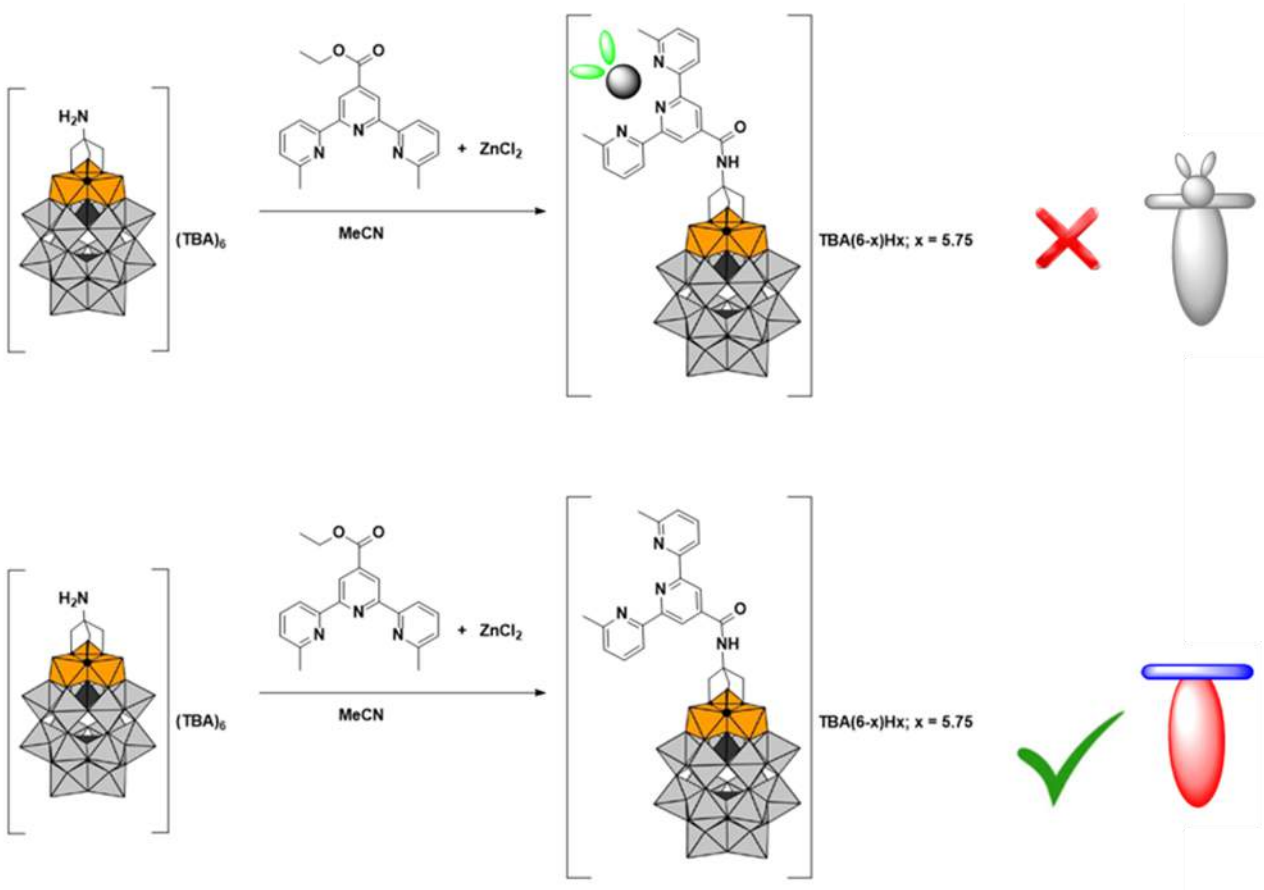

Scheme S9. Scheme of synthesis of hybrid **H6^{cov} (POM + L^{tpy} + ZnCl$_2$)**.

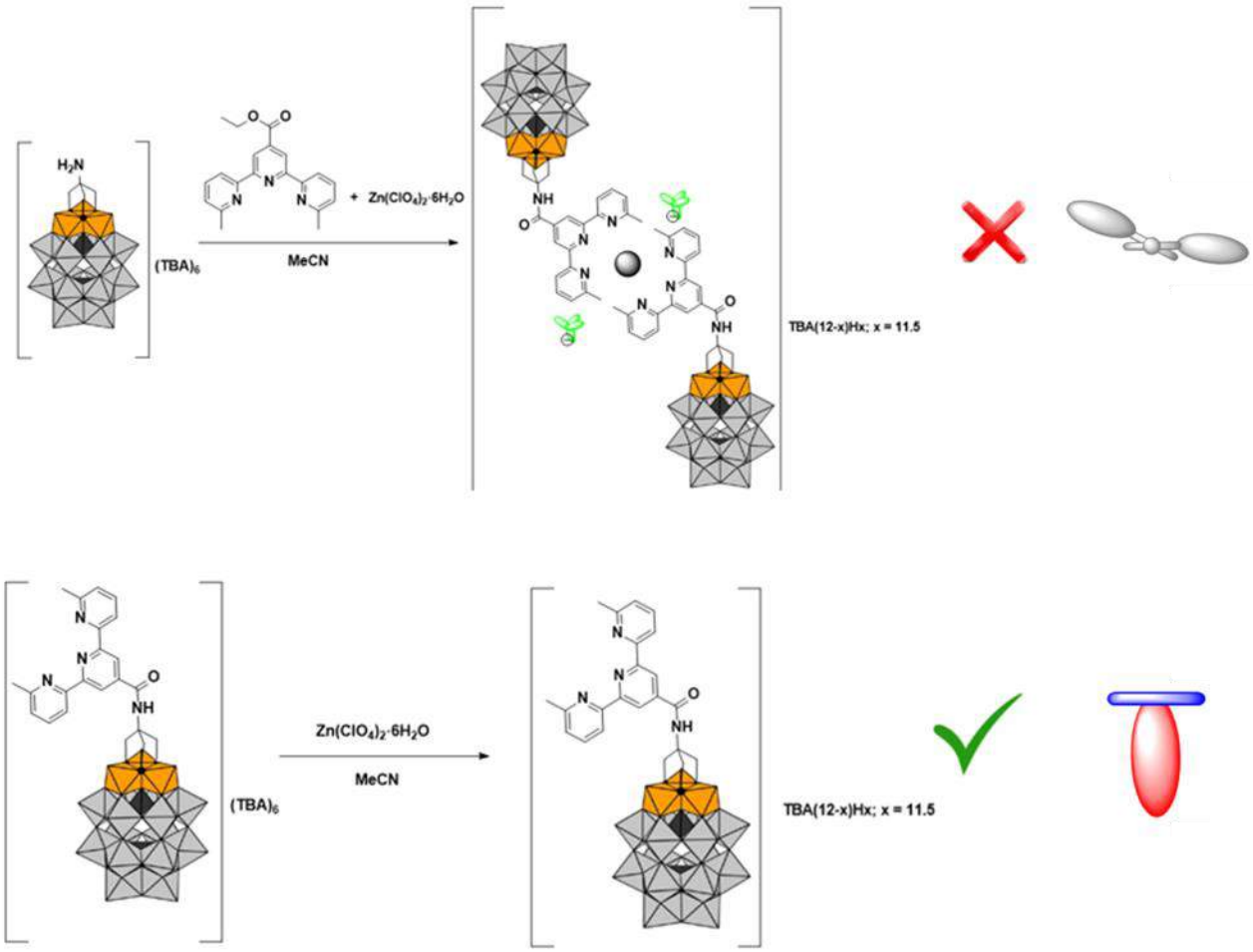

Scheme S10. Scheme of synthesis of hybrid **H7^{cov} (POM + L^{tpy} + Zn(ClO$_4$)$_2$)**.

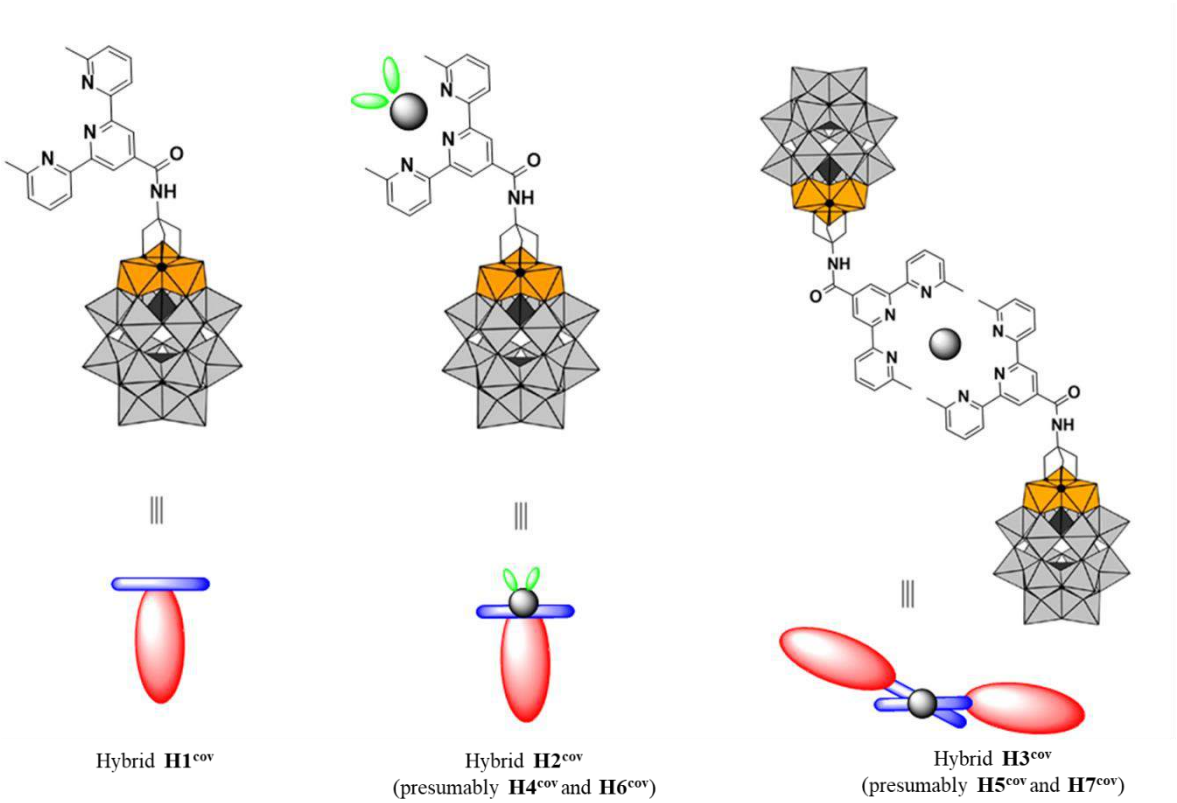

Scheme S11. Schematic representation structures of hybrids **H1^{cov} - H7^{cov}**.

2. FT-IR spectra of ligand, complexes and hybrids

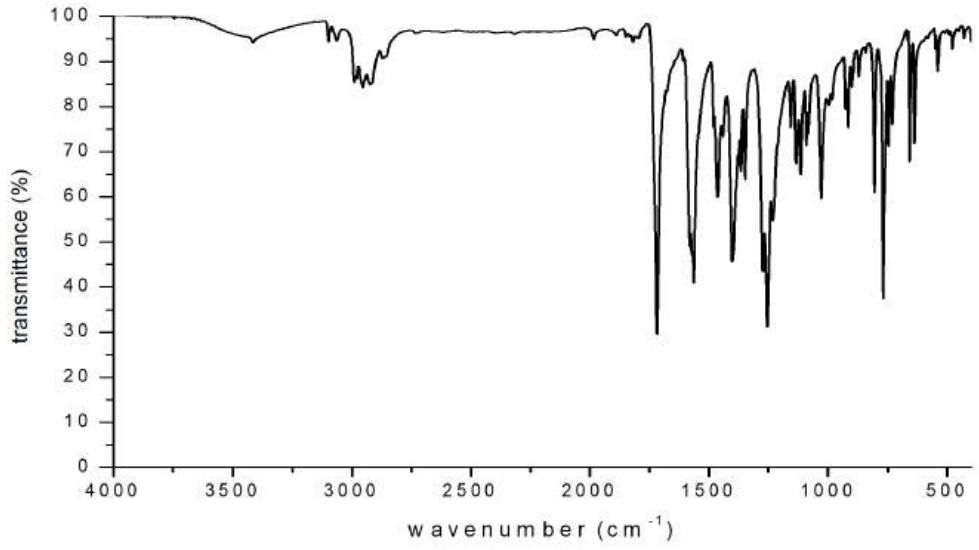

Fig. S1. IR spectrum of ligand **L^{tpy}**.

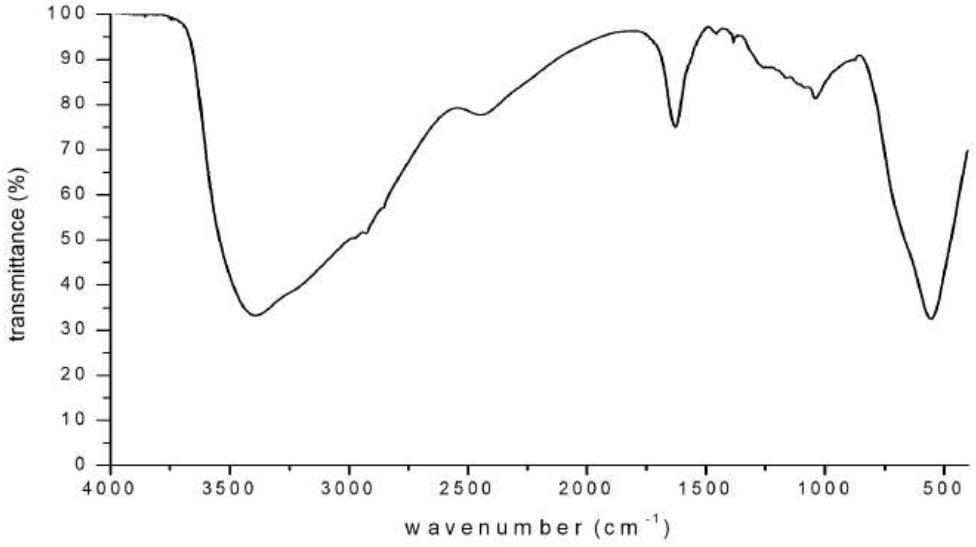

Fig. S2. IR spectrum of complex **K1**.

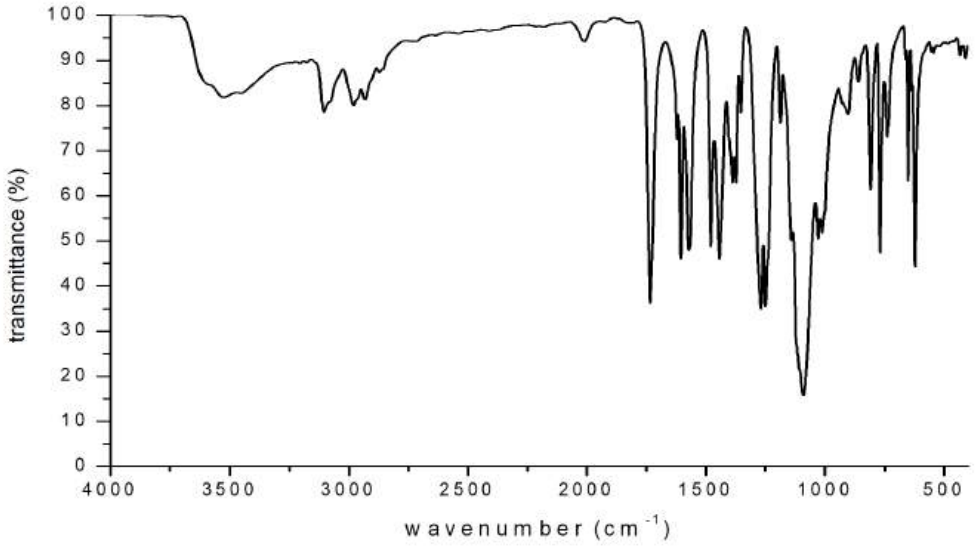

Fig. S3. IR spectrum of complex **K2**.

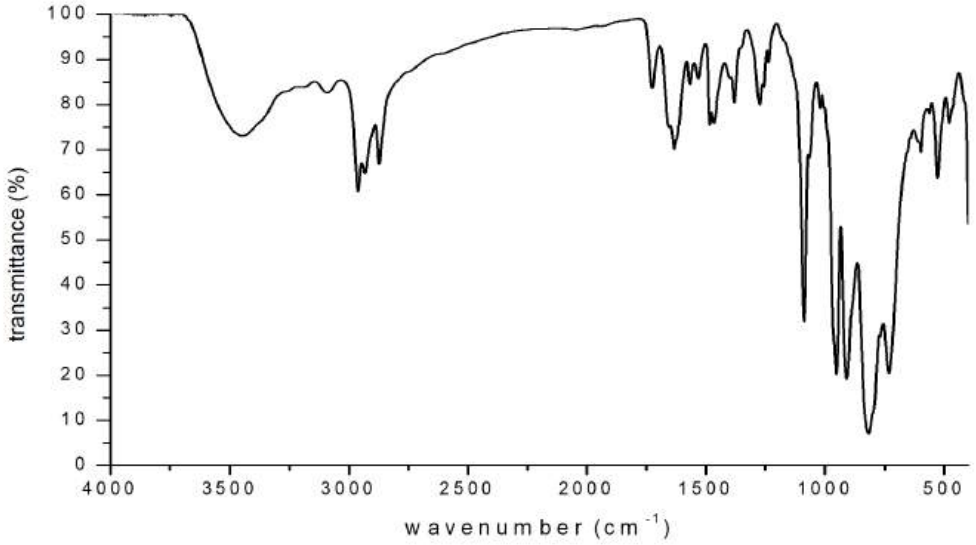

Fig. S4. IR spectrum of hybrid **H1^{cov} (POM + L^{tpy})**.

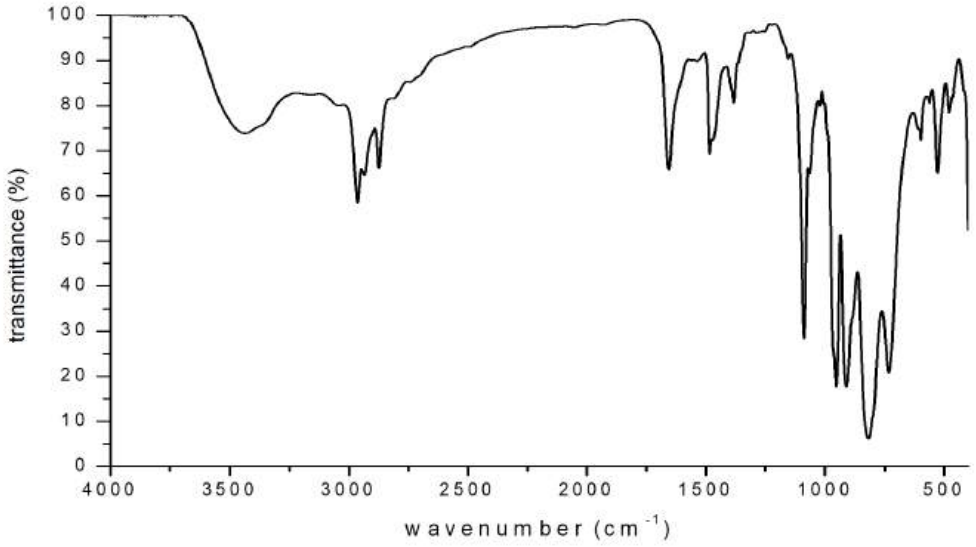

Fig. S5. IR spectrum of hybrid **H2^{cov} (POM + K1)**.

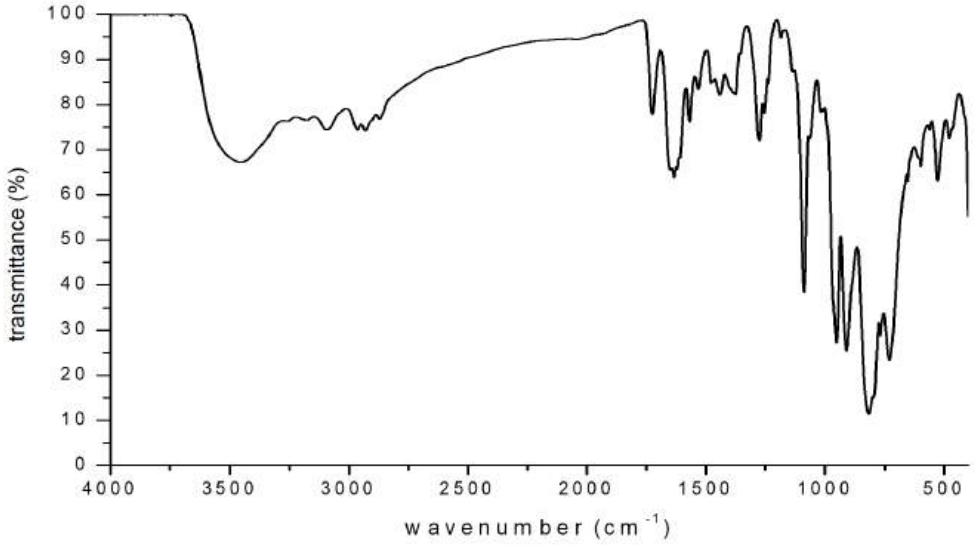

Fig. S6. IR spectrum of hybrid **H3^{cov} (POM + K2)**.

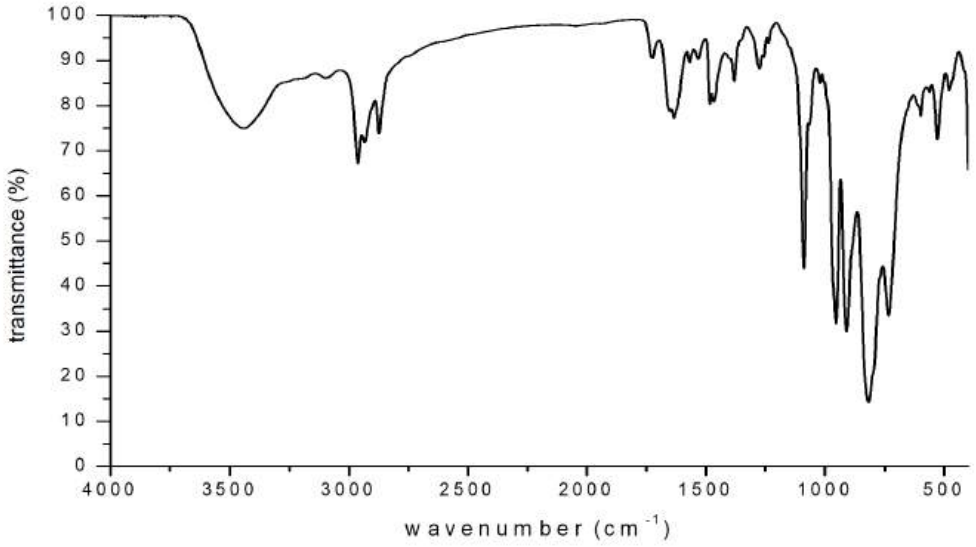

Fig. S7. IR spectrum of hybrid **H4^{cov} (H1^{cov} + $ZnCl_2$)**.

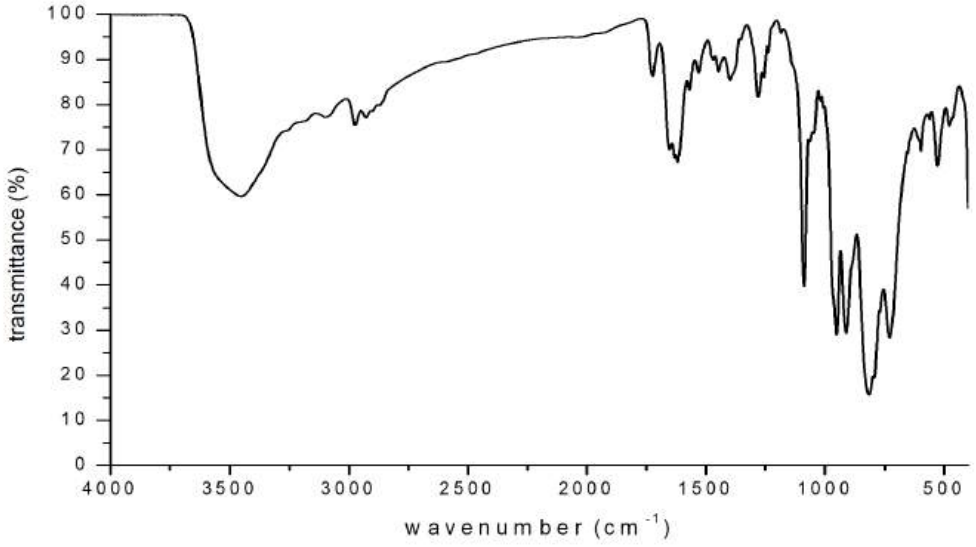

Fig. S8. IR spectrum of hybrid **H5^{cov} (H1^{cov} + Zn(ClO$_4$)$_2$)**.

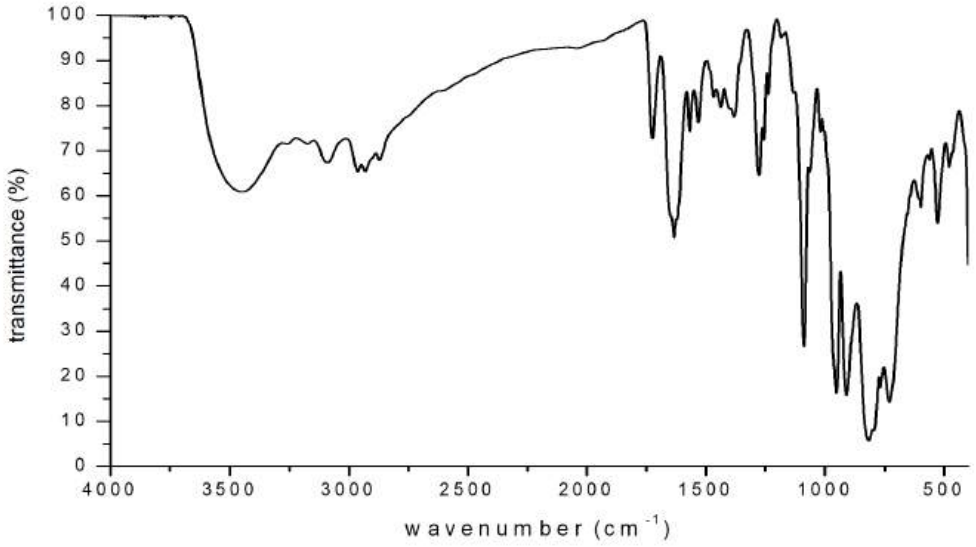

Fig. S9. IR spectrum of hybrid **H6^{cov} (POM + L^{tpy} + ZnCl$_2$)**.

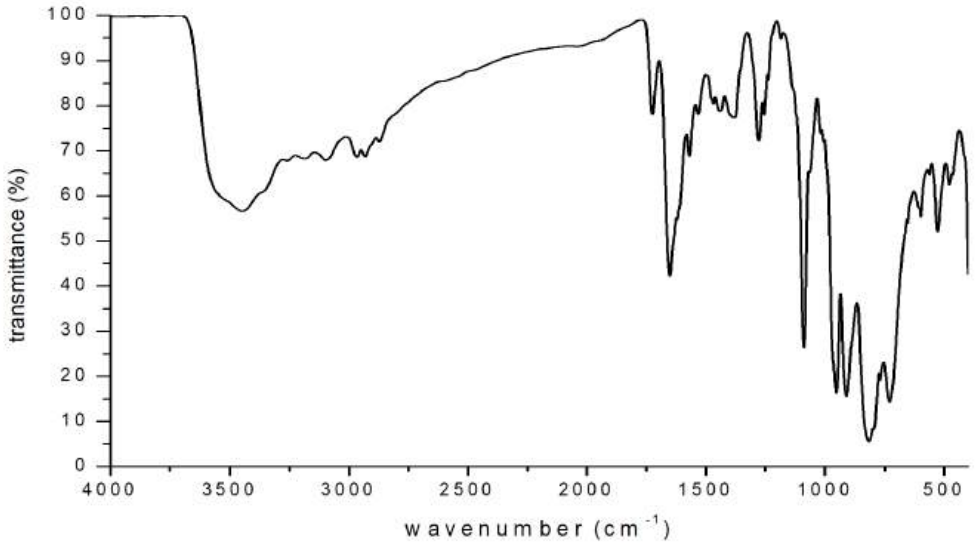

Fig. S10. IR spectrum of hybrid **H7^{cov} (POM + L^{tpy} + Zn(ClO$_4$)$_2$)**.

3. Comparison of IR spectra of compounds

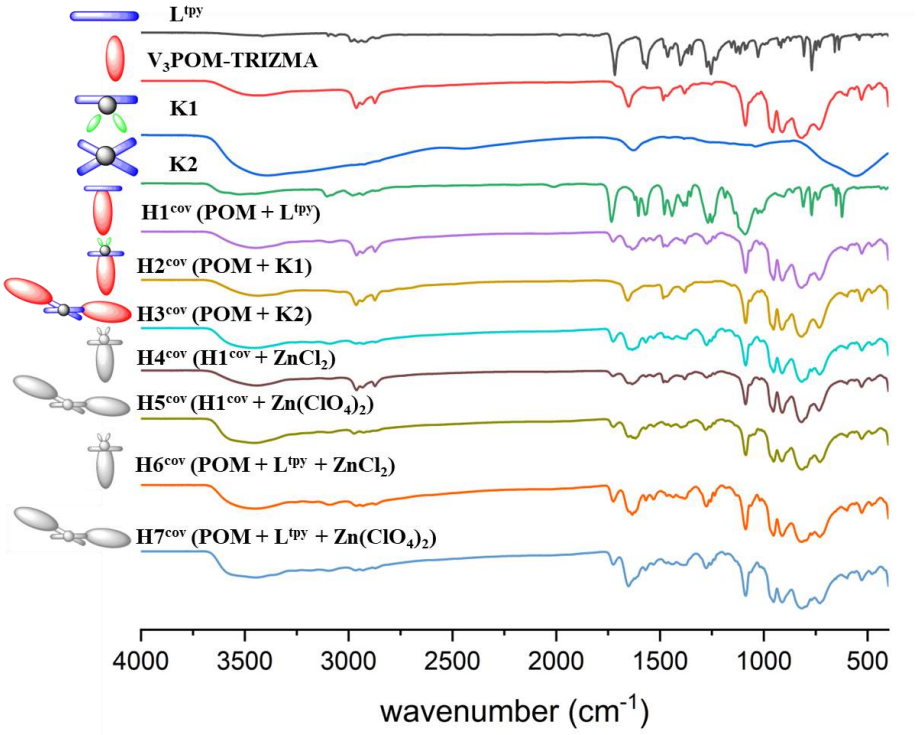

Fig. S11. Comparison of IR spectra of compounds: **L^{tpy}**, **V$_3$POM-TRIZMA**, **K1**, **K2**, **V$_3$POM-TBA, H1^{cov} (POM + L^{tpy}), H2^{cov} (POM + K1), H3^{cov} (POM + K2), H4^{cov} (H1^{cov} + ZnCl$_2$), H5^{cov} (H1^{cov} + Zn(ClO$_4$)$_2$), H6^{cov} (POM + L^{tpy} + ZnCl$_2$), H7^{cov} (POM + L^{tpy} + Zn(ClO$_4$)$_2$)**, respectively.

4. ^{1}H NMR spectra of ligand, complexes and hybrids

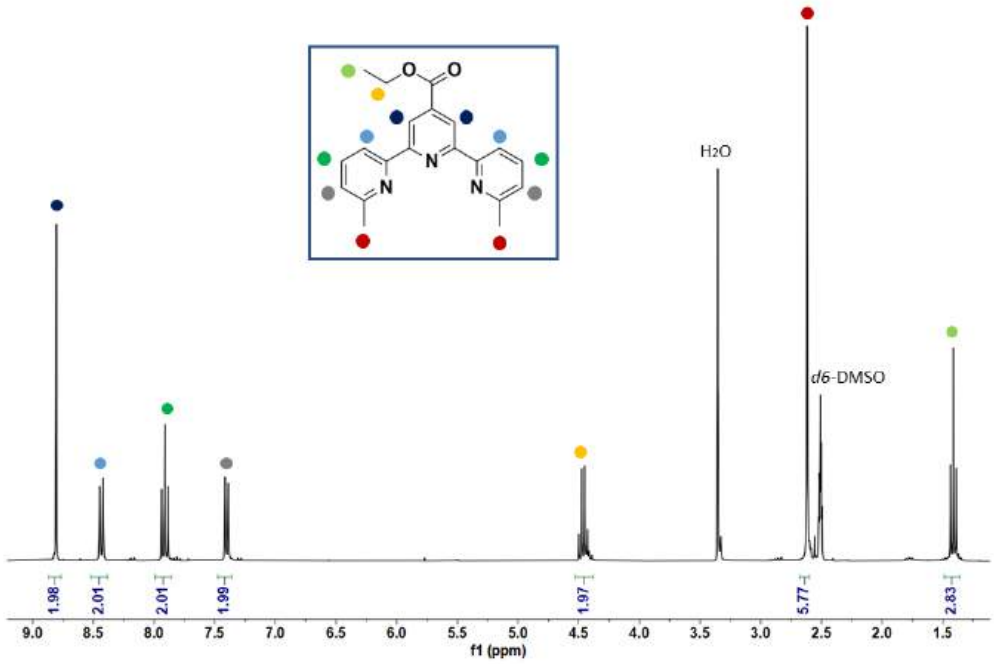

Fig. S12. ^{1}H NMR spectrum of ligand $\mathbf{L^{tpy}}$ in $CDCl_3$ at 400 MHz.

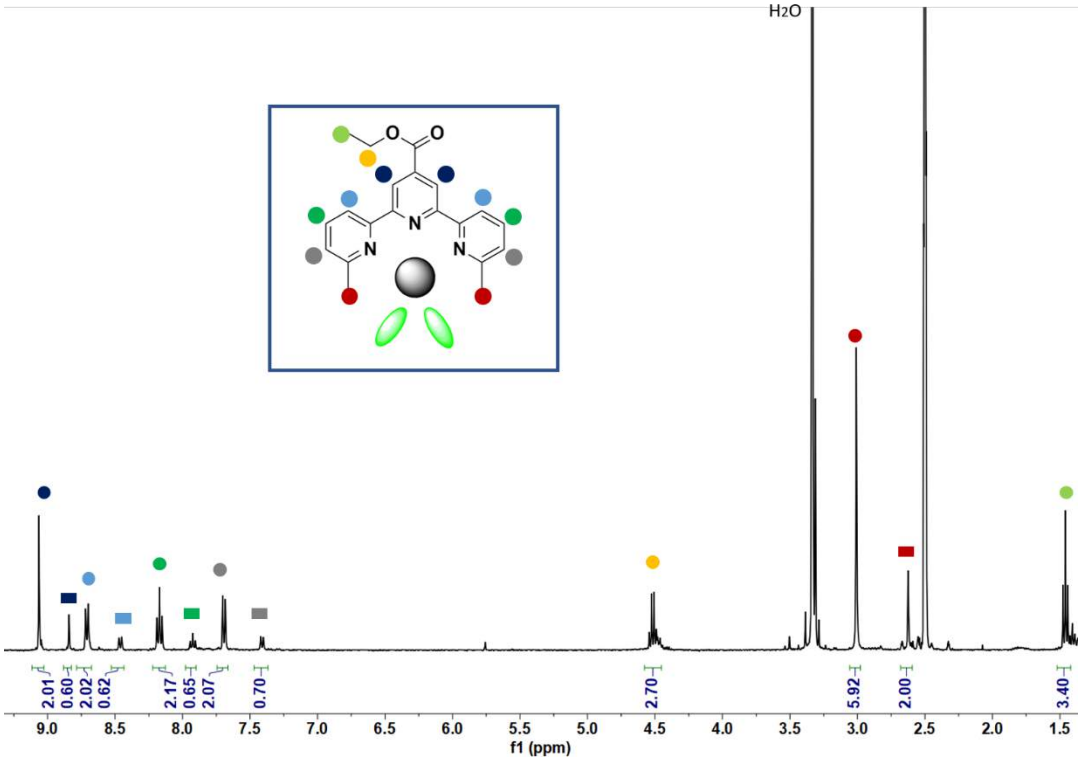

Fig. S13. ^{1}H NMR spectrum of complex **K1** in *d6*-DMSO at 400 MHz.

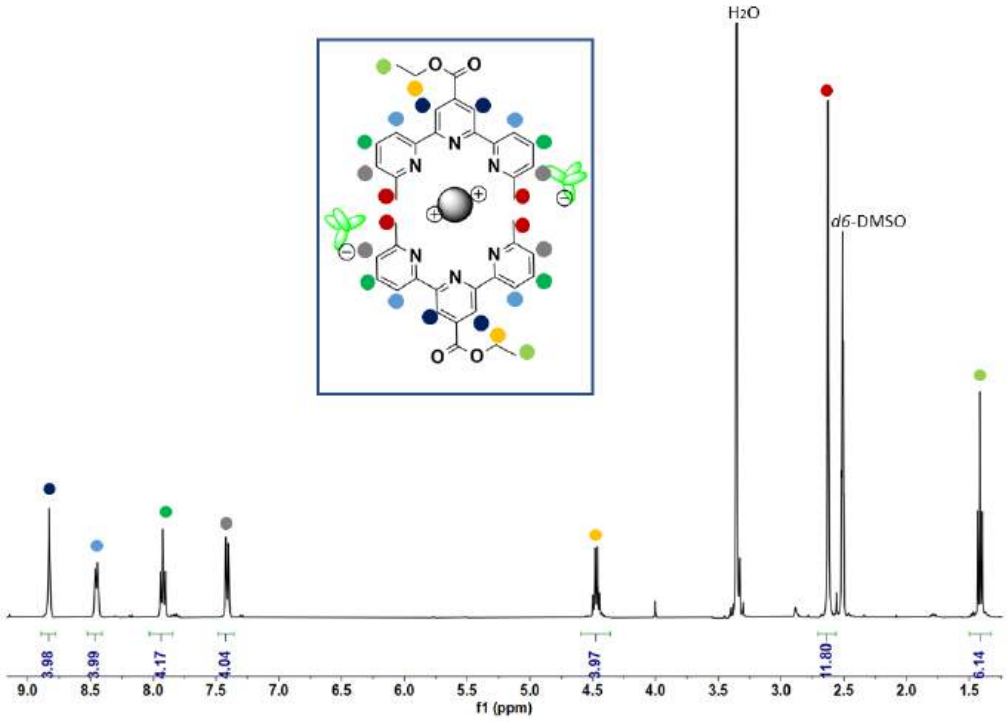

Fig. S14. ^{1}H NMR spectrum of complex **K2** in *d6*-DMSO at 400 MHz.

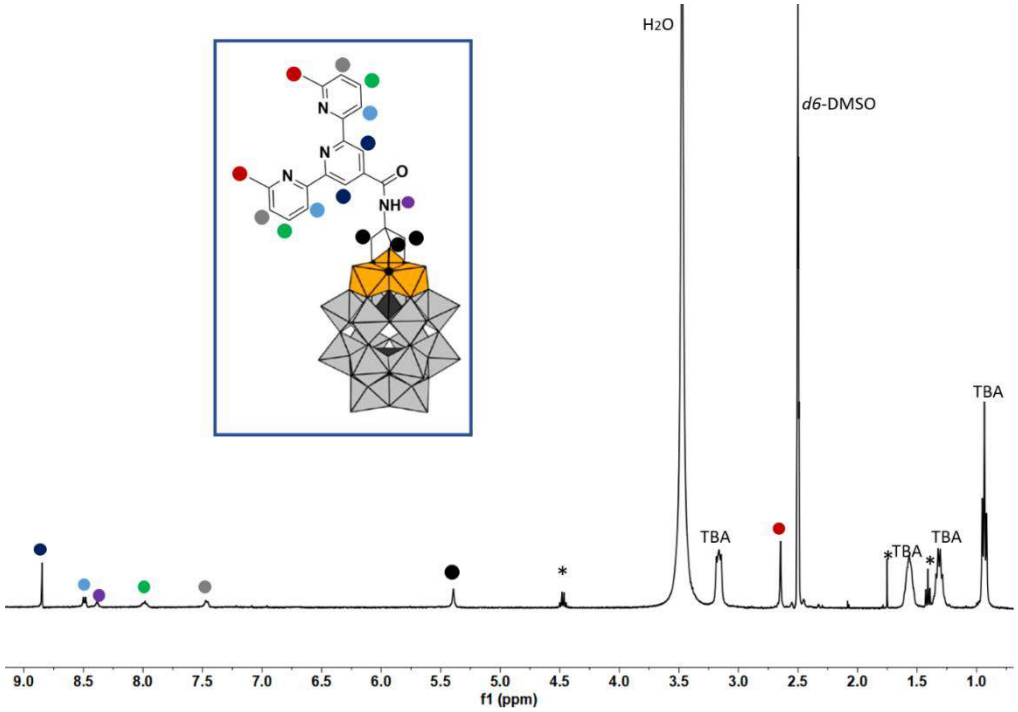

Fig. S15. ^{1}H NMR spectrum of hybrid **H1^{cov} (POM + L^{tpy})** in DMSO-d_6 at 400 MHz.

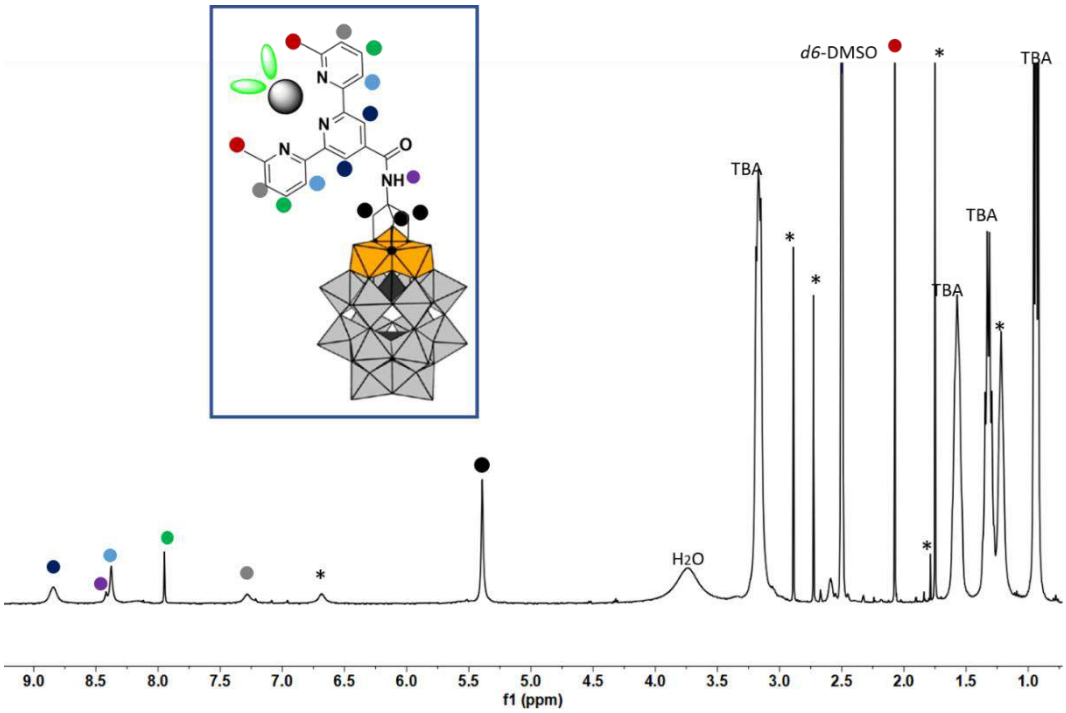

Fig. S16. ^{1}H NMR spectrum of hybrid **H2^{cov} (POM + K1)** in DMSO-d_6 at 400 MHz.

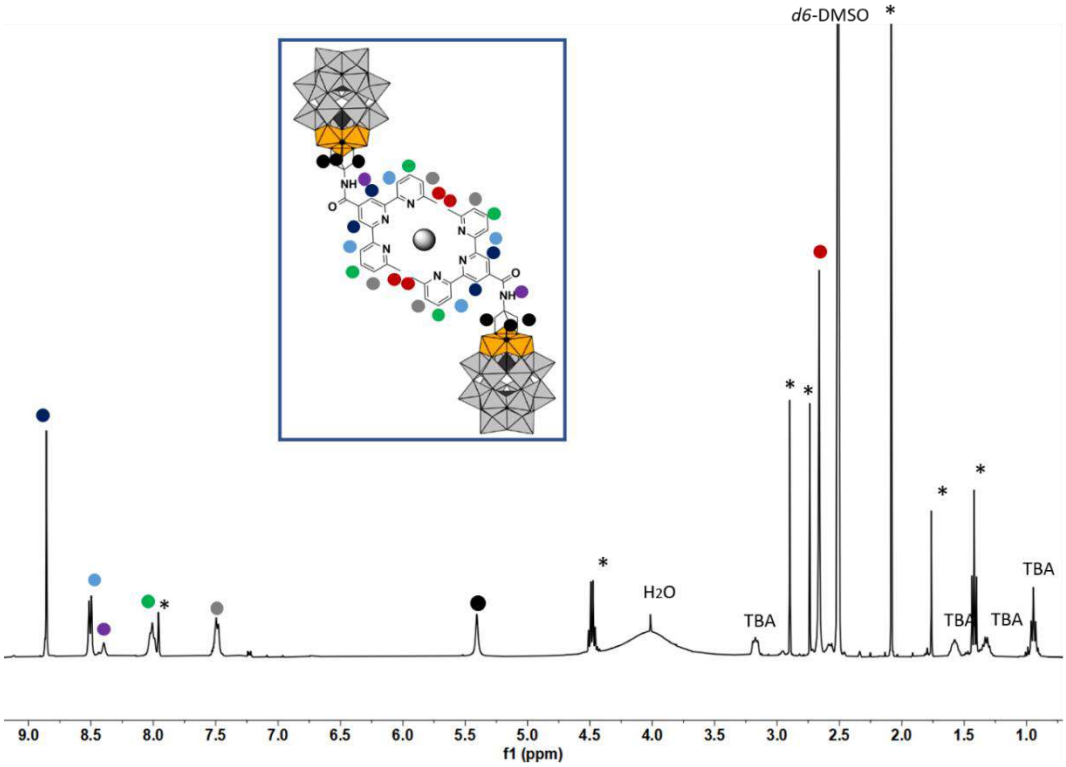

Fig. S17. ^{1}H NMR spectrum of hybrid **H3^{cov} (POM + K2)** in DMSO-d_6 at 400 MHz.

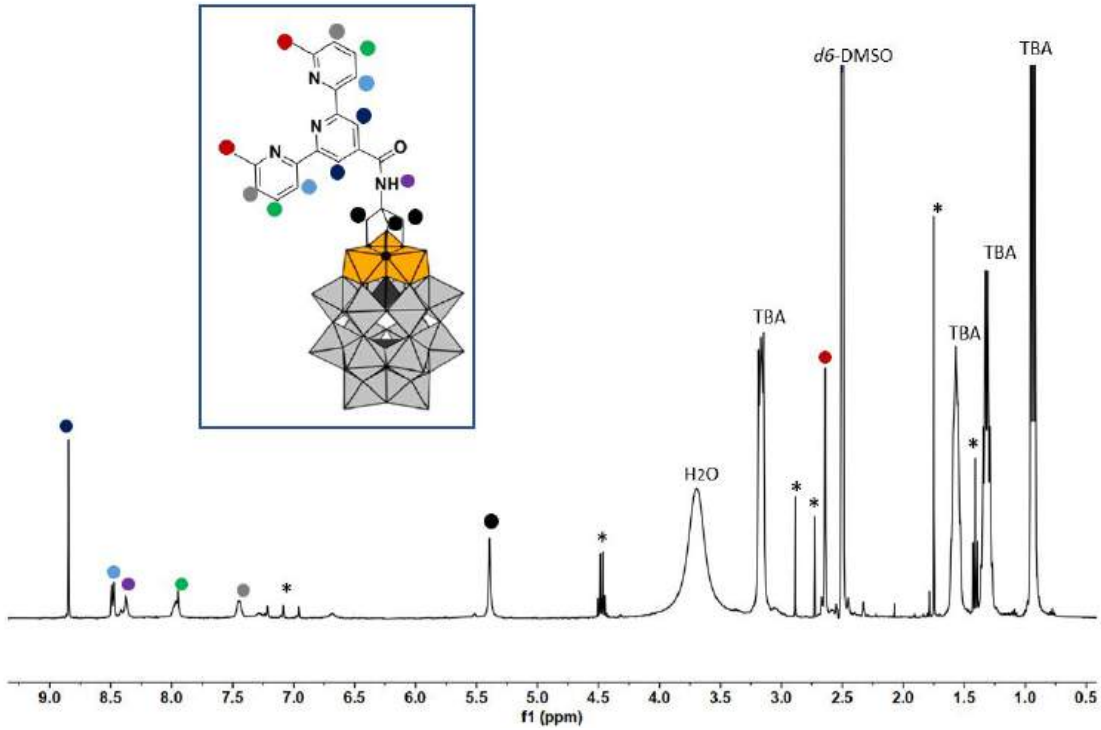

Fig. S18. ^{1}H NMR spectrum of hybrid **H4^{cov} (H1^{cov} + ZnCl$_2$)** in DMSO-*d*$_6$ at 400 MHz.

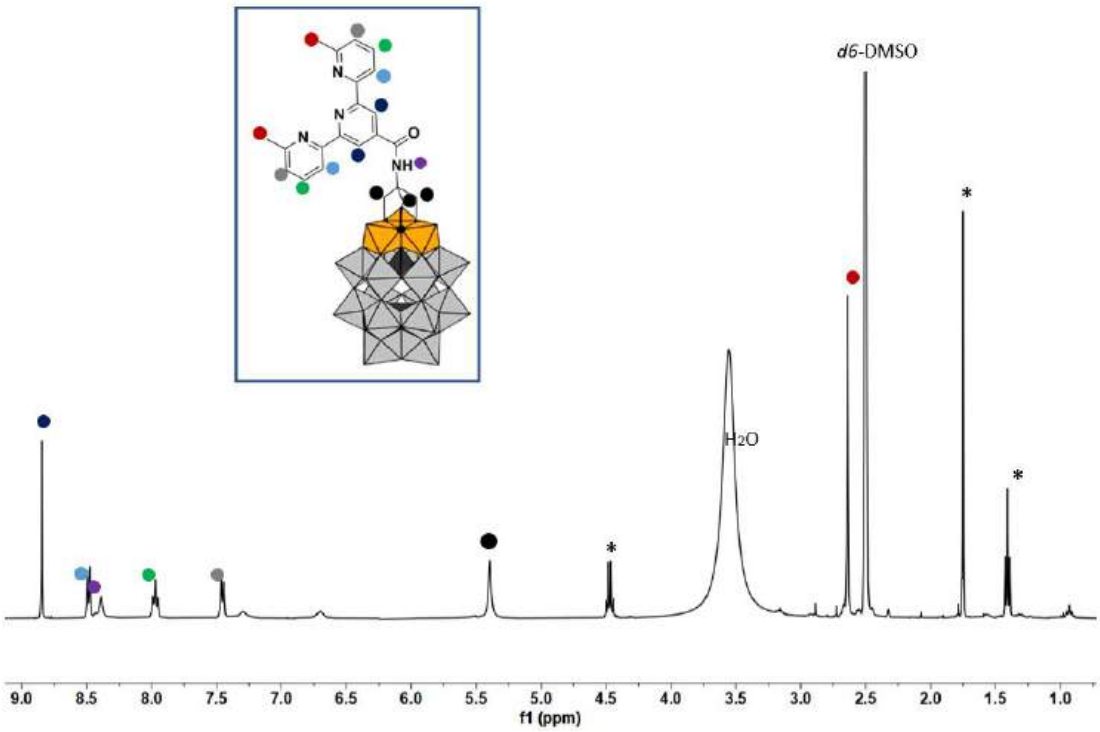

Fig. S19. ^{1}H NMR spectrum of hybrid **H5^{cov} (H1^{cov} + Zn(ClO$_4$)$_2$)** in DMSO-*d*$_6$ at 400 MHz.

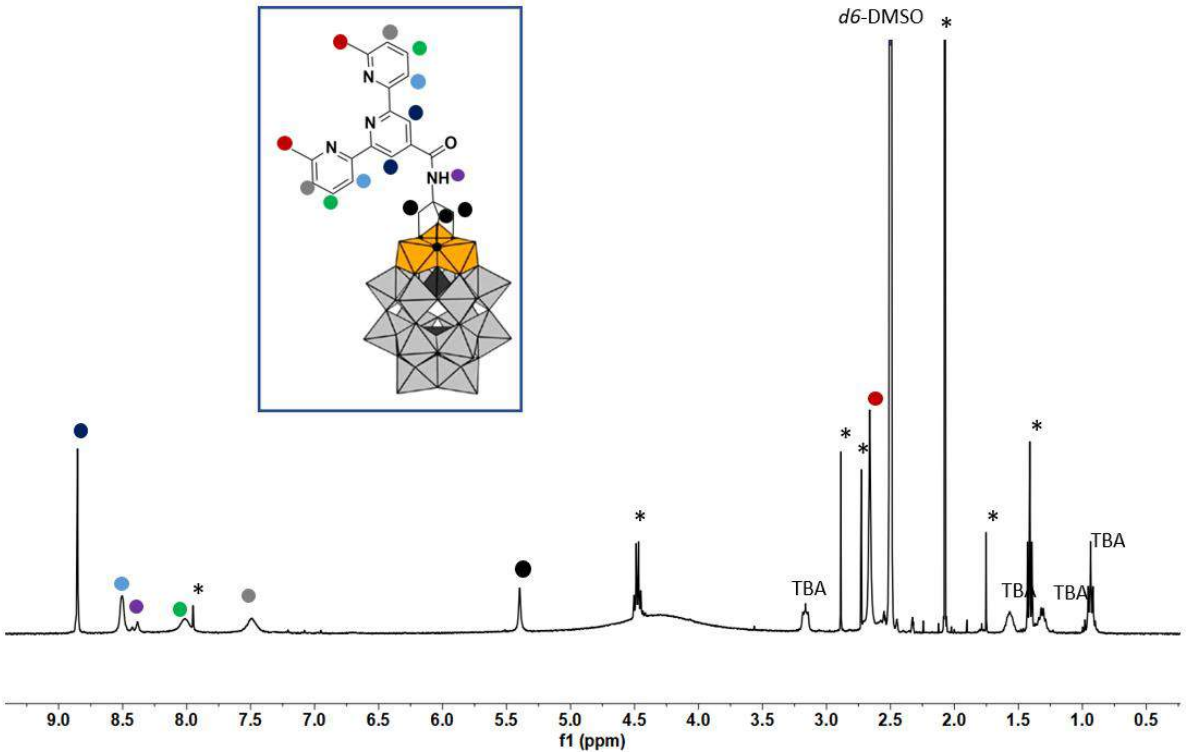

Fig. S20. ^{1}H NMR spectrum of hybrid **H6^{cov} (POM + L^{tpy} + ZnCl$_2$)** in DMSO-*d*$_6$ at 400 MHz.

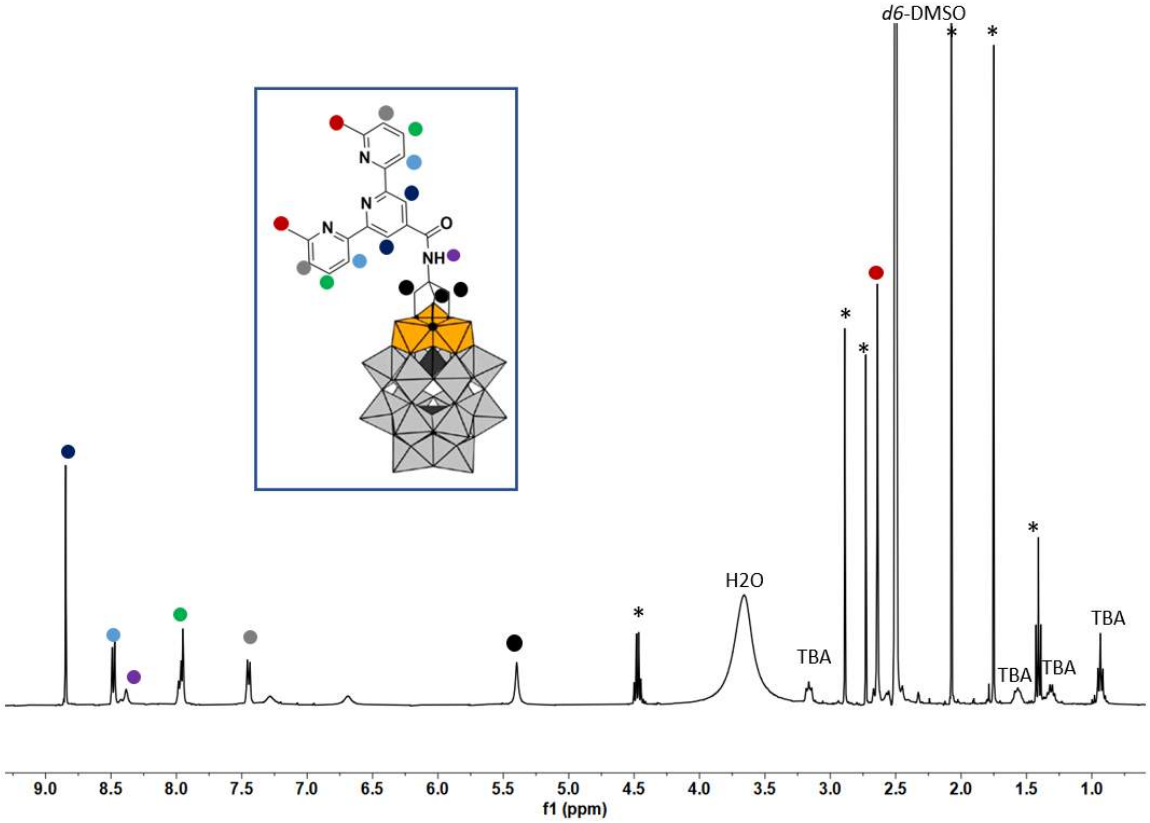

Fig. S21. ^{1}H NMR spectrum of hybrid **H7^{cov} (POM + L^{tpy} + Zn(ClO$_4$)$_2$)** in DMSO-*d*$_6$ at 400 MHz.

5. Comparison of ^{1}H NMR spectra of compounds

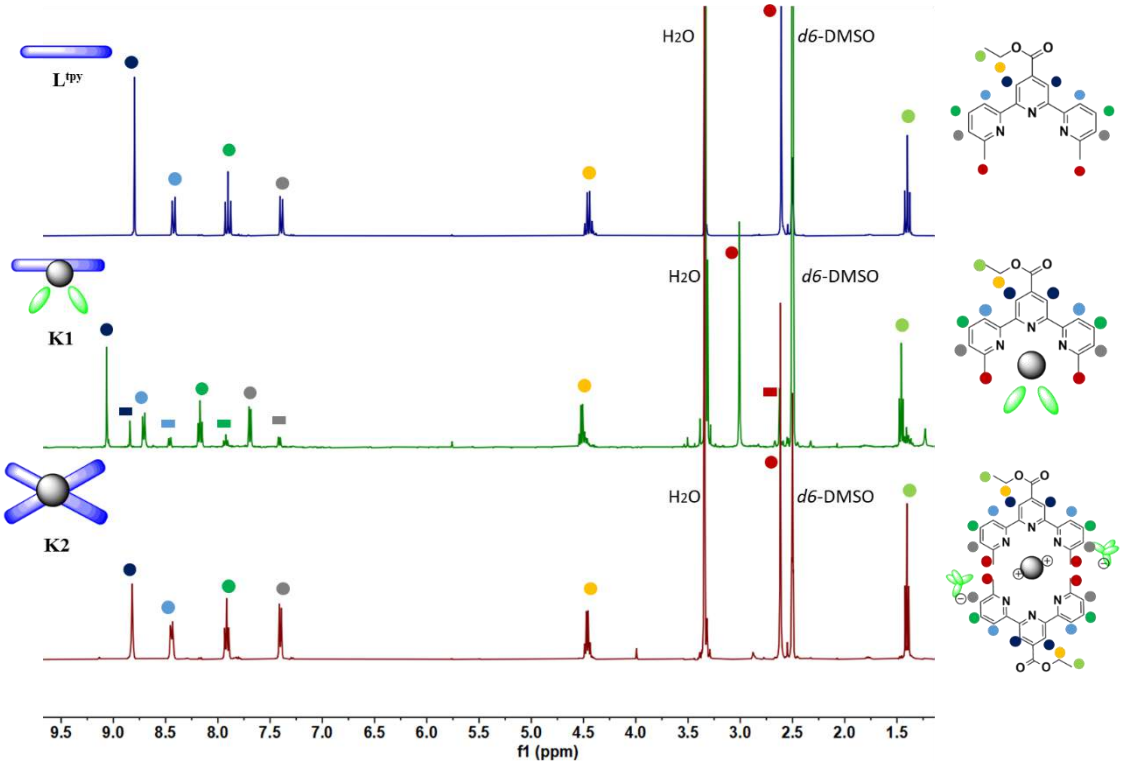

Fig. S22. Comparison of ^{1}H NMR spectra of ligand $\mathbf{L^{tpy}}$ (blue), complex **K1** (green) and complex **K2** (red) in DMSO-d_6 at 400 MHz.

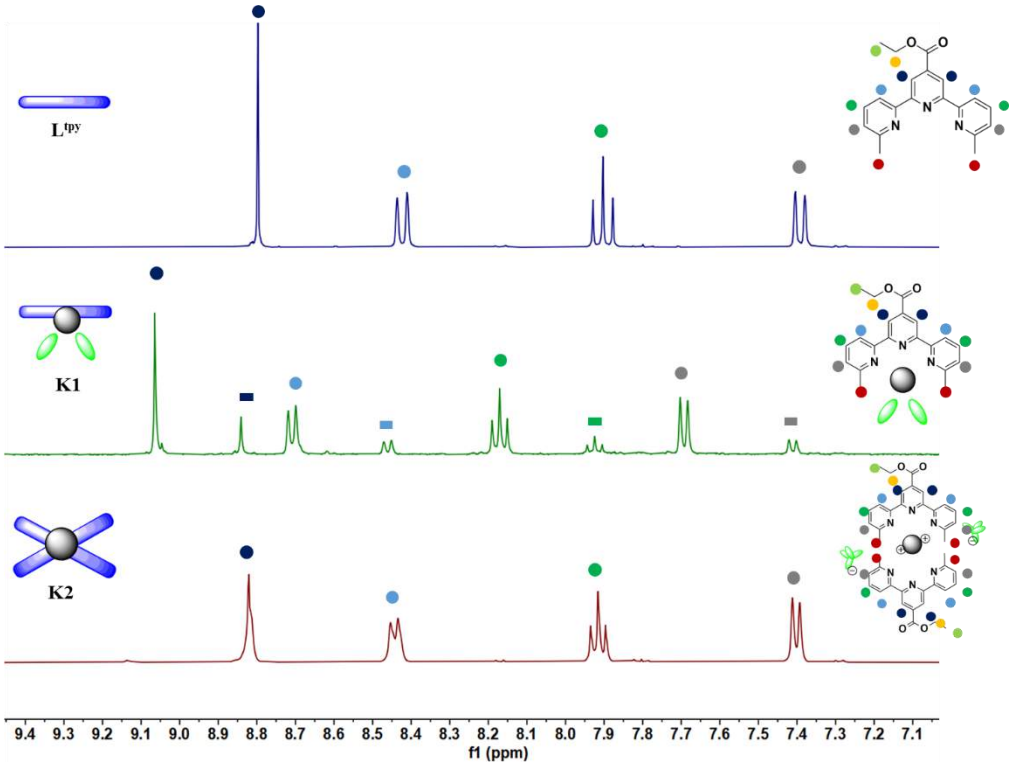

Fig. S23. Comparison of ^{1}H NMR spectra of ligand **L^{tpy}** (blue), complex **K1** (green) and complex **K2** (red) in DMSO-d_6 at 400 MHz (aromatic region).

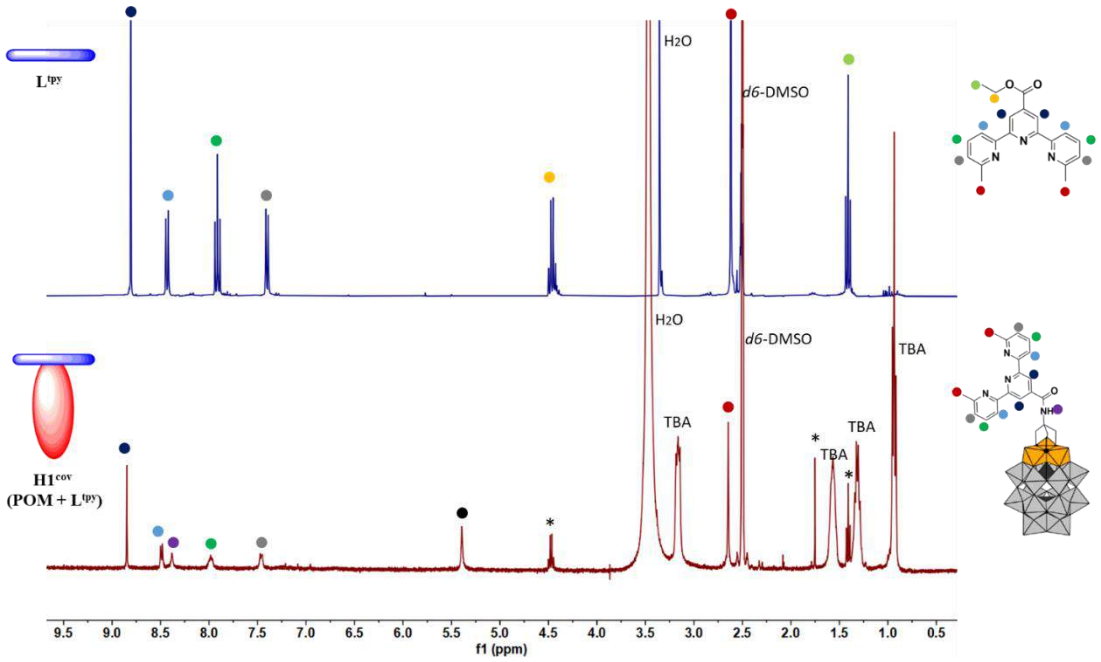

Fig. S24. Comparison of ^{1}H NMR spectra of ligand **L^{tpy}** (blue) and hybrid **H1^{cov} (POM + L^{tpy})** (red) in DMSO-d_6 at 400 MHz.

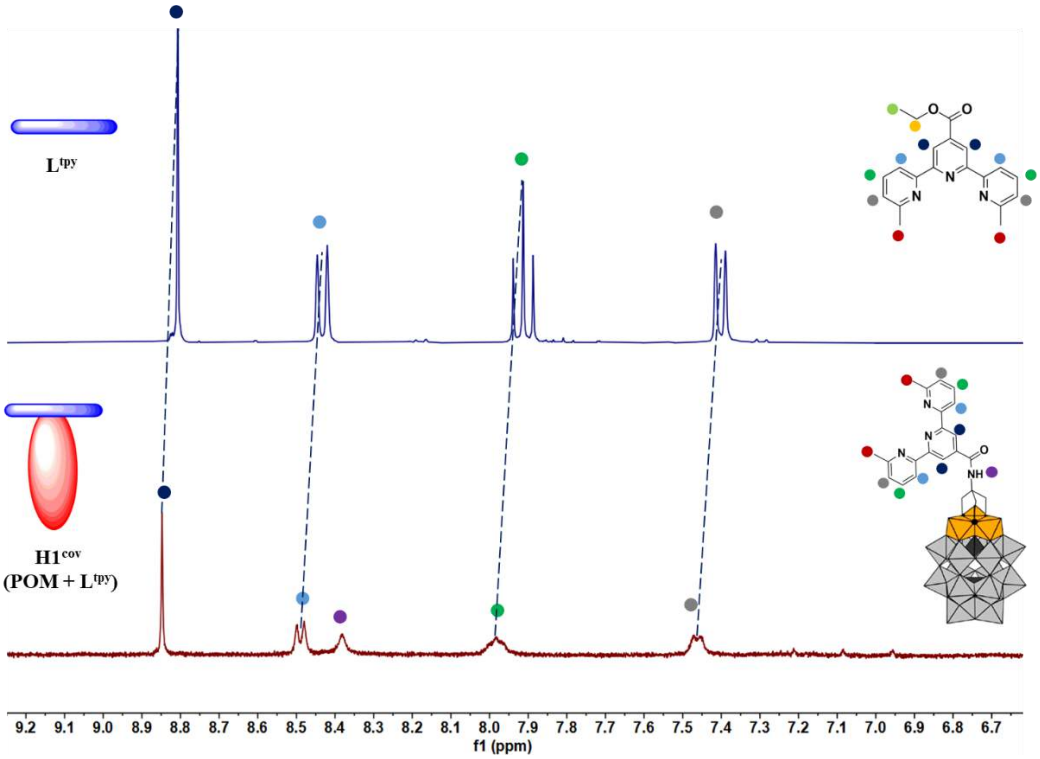

Fig. S25. Comparison of ^{1}H NMR spectra of ligand **L^{tpy}** (blue) and hybrid **H1^{cov} (POM + L^{tpy})** (red) in DMSO-d_6 at 400 MHz (aromatic region).

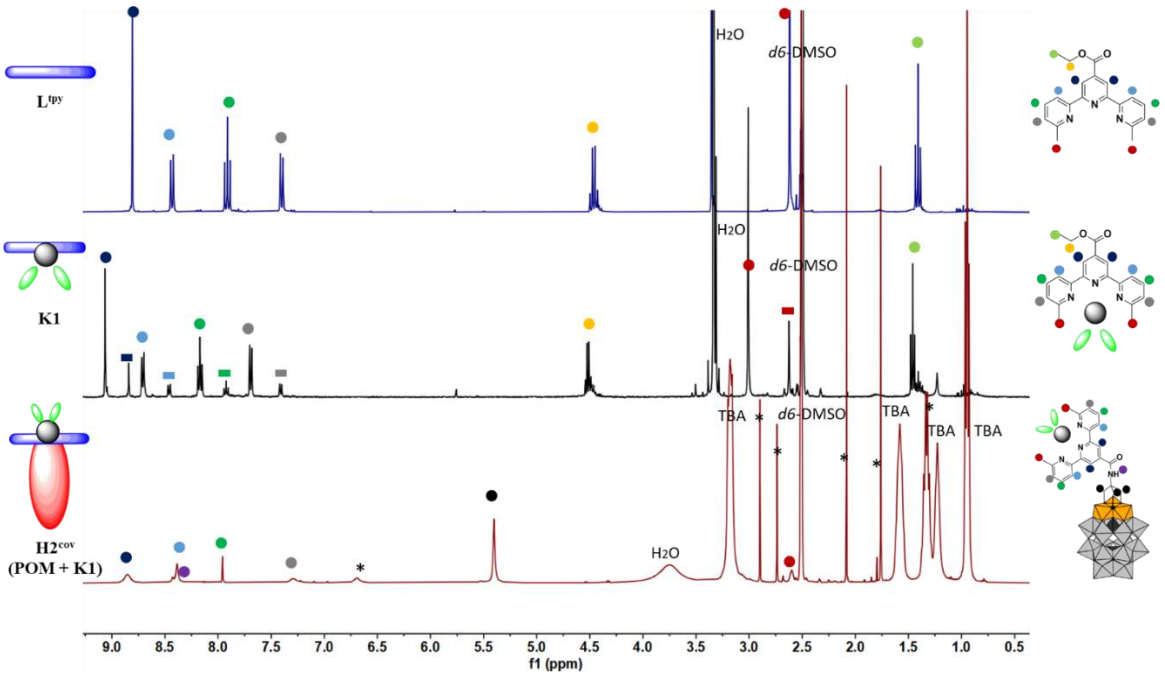

Fig. S26. Comparison of ^{1}H NMR spectra of ligand **L^{tpy}** (blue), complex **K1** (black) and hybrid **H2^{cov} (POM + K1)** (red) in DMSO-d_6 at 400 MHz.

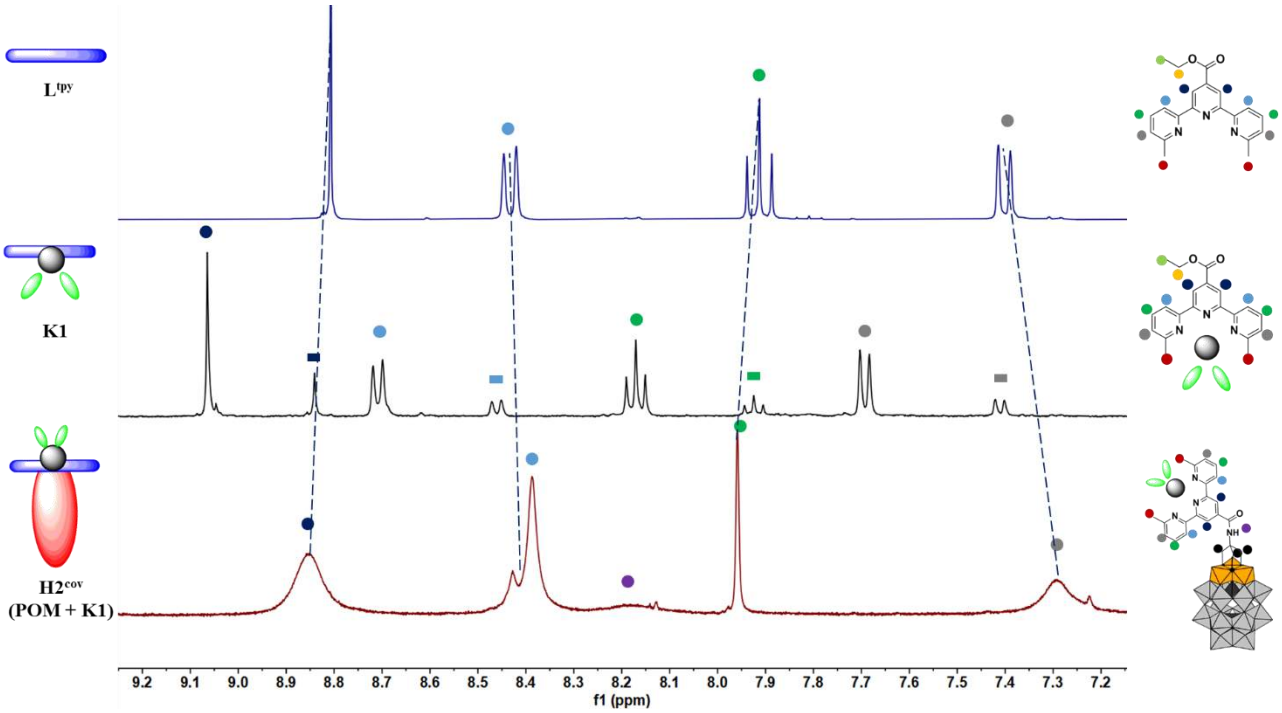

Fig. S27. Comparison of ^{1}H NMR spectra of ligand **L^{tpy}** (blue), complex **K1** (black) and hybrid **H2^{cov} (POM + K1)** (red) in DMSO-d_6 at 400 MHz (aromatic region).

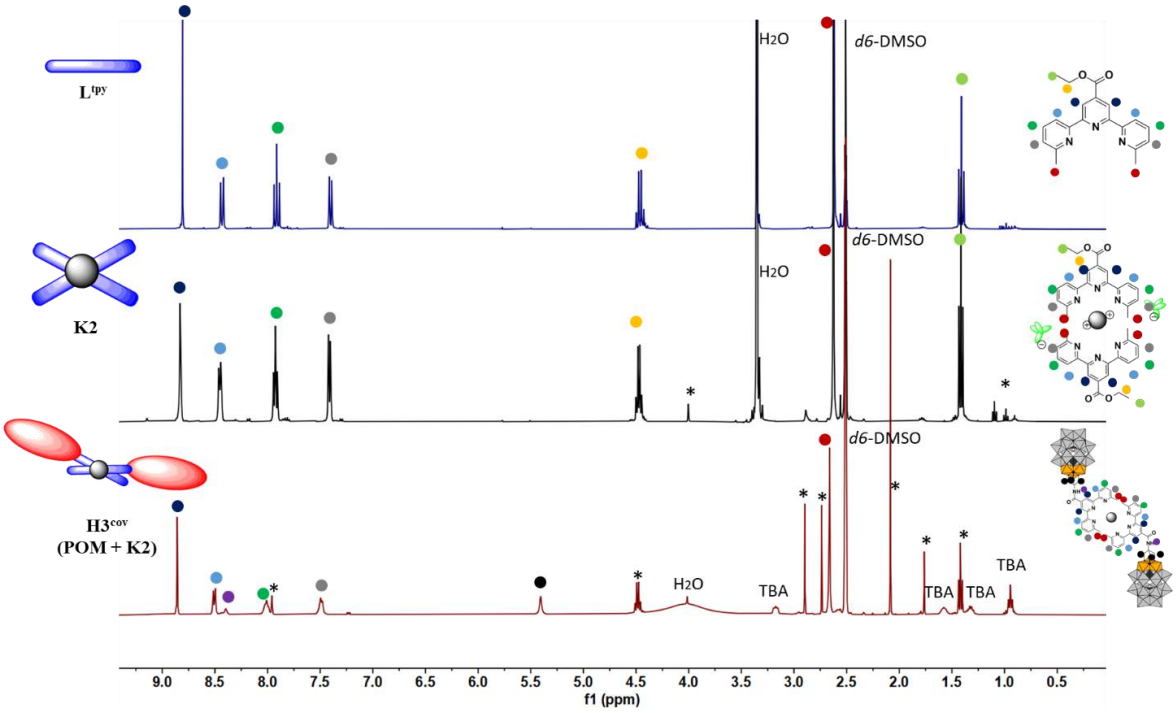

Fig. S28. Comparison of ^{1}H NMR spectra of ligand **L^{tpy}** (blue), complex **K2** (black) and hybrid **H3^{cov} (POM + K2)** (red) in DMSO-d_6 at 400 MHz.

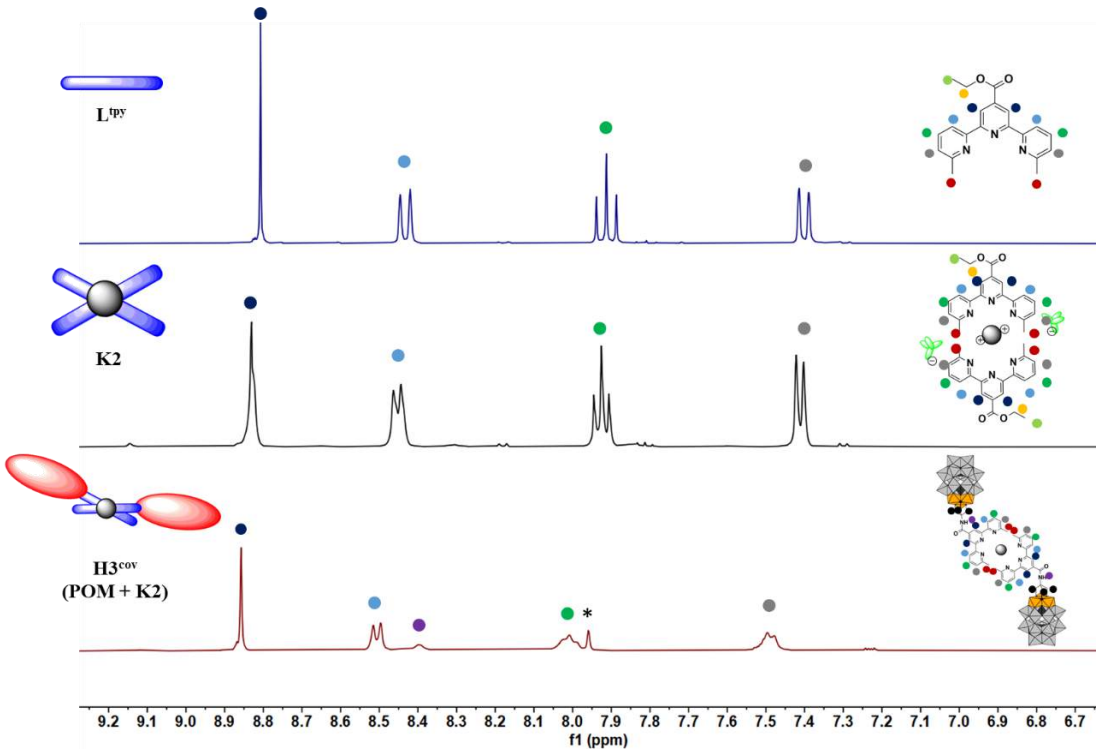

Fig. S29. Comparison of ^{1}H NMR spectra of ligand **L^{tpy}** (blue), complex **K2** (black) and hybrid **H3^{cov} (POM + K2)** (red) in DMSO-*d*$_6$ at 400 MHz (aromatic region).

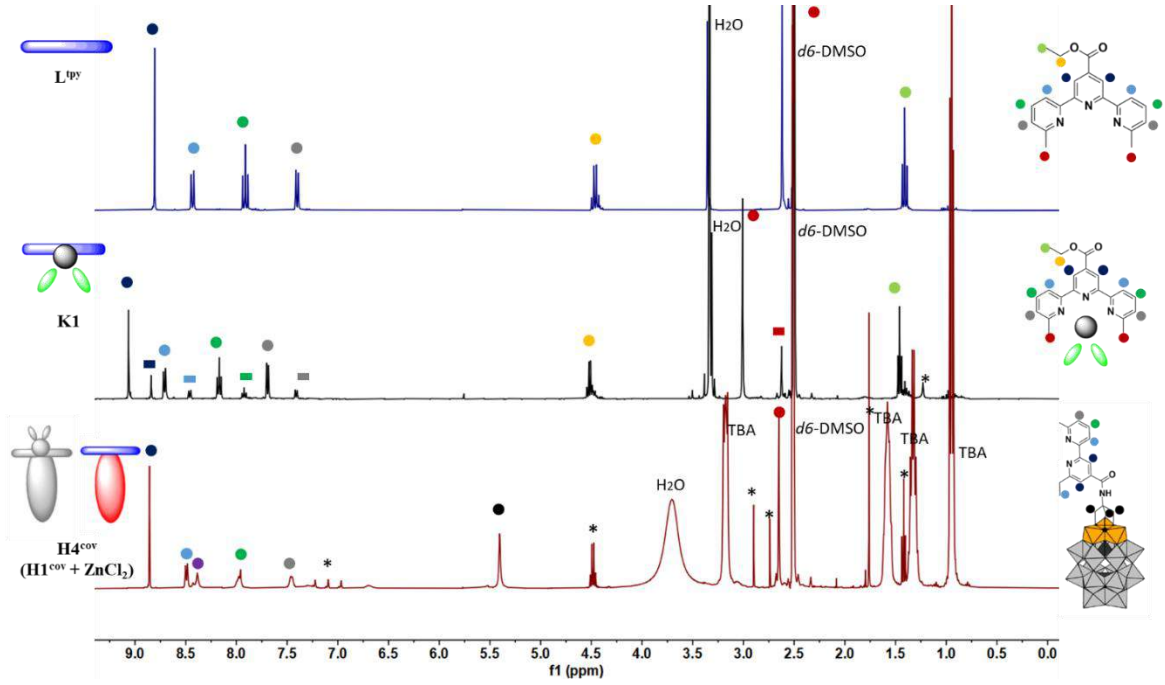

Fig. S30. Comparison of ^{1}H NMR spectra of ligand **L^{tpy}** (blue), complex **K1** (black) and hybrid **H4^{cov} (H1^{cov} + ZnCl$_2$)** (red) in DMSO-*d*$_6$ at 400 MHz.

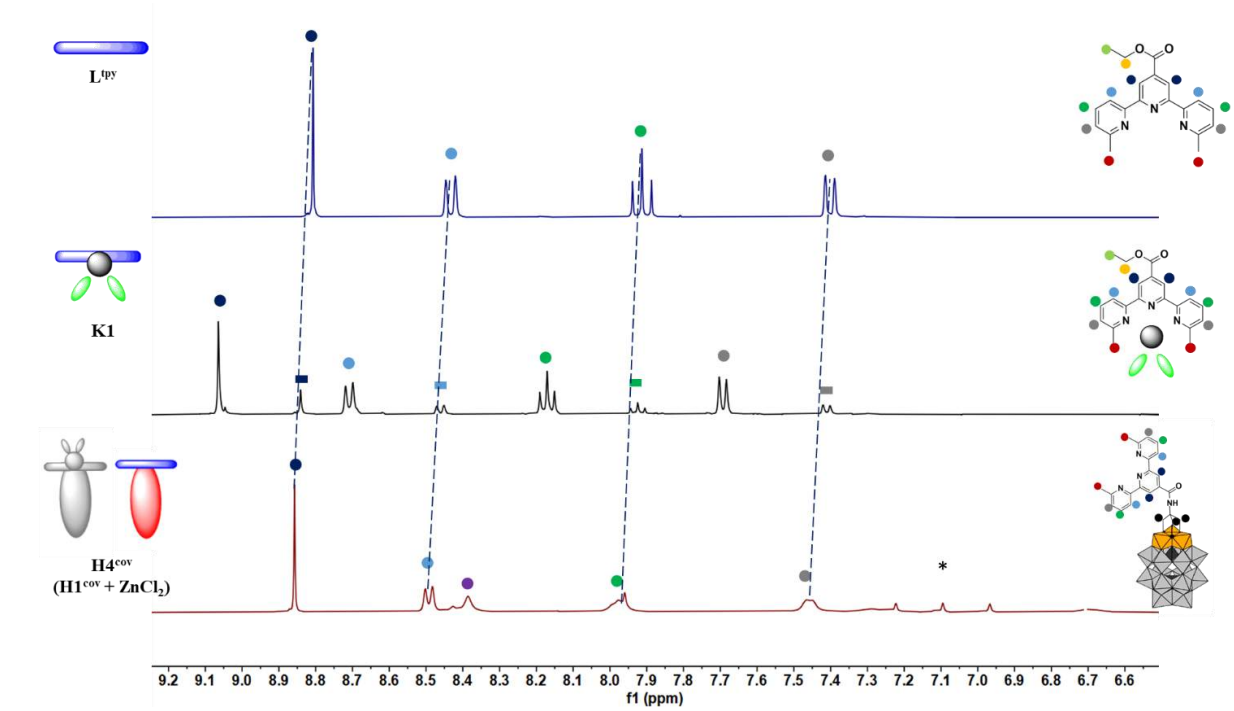

Fig. S31. Comparison of ^{1}H NMR spectra of ligand **L^{tpy}** (blue), complex **K1** (black) and hybrid **H4^{cov} (H1^{cov} + ZnCl$_2$)** (red) in DMSO-*d*$_6$ at 400 MHz (aromatic region).

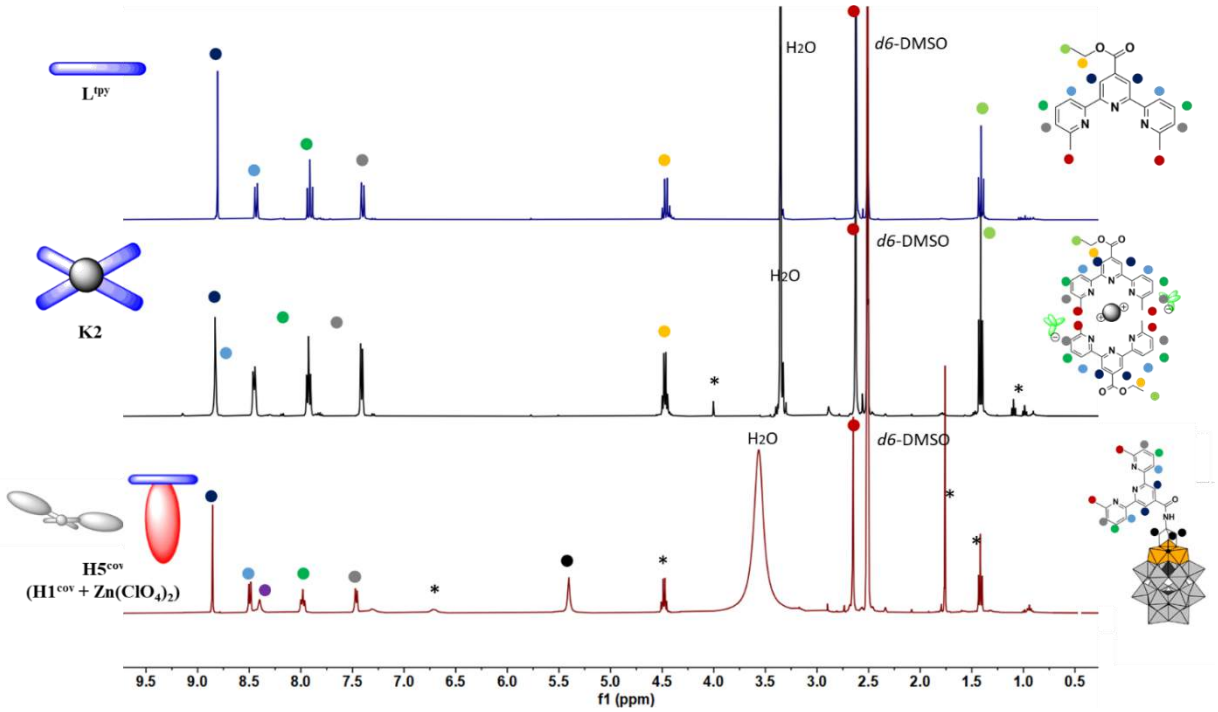

Fig. S32. Comparison of ^{1}H NMR spectra of ligand **L^{tpy}** (blue), complex **K2** (black) and hybrid **H5^{cov} (H1^{cov} + Zn(ClO$_4$)$_2$)** (red) in DMSO-*d*$_6$ at 400 MHz.

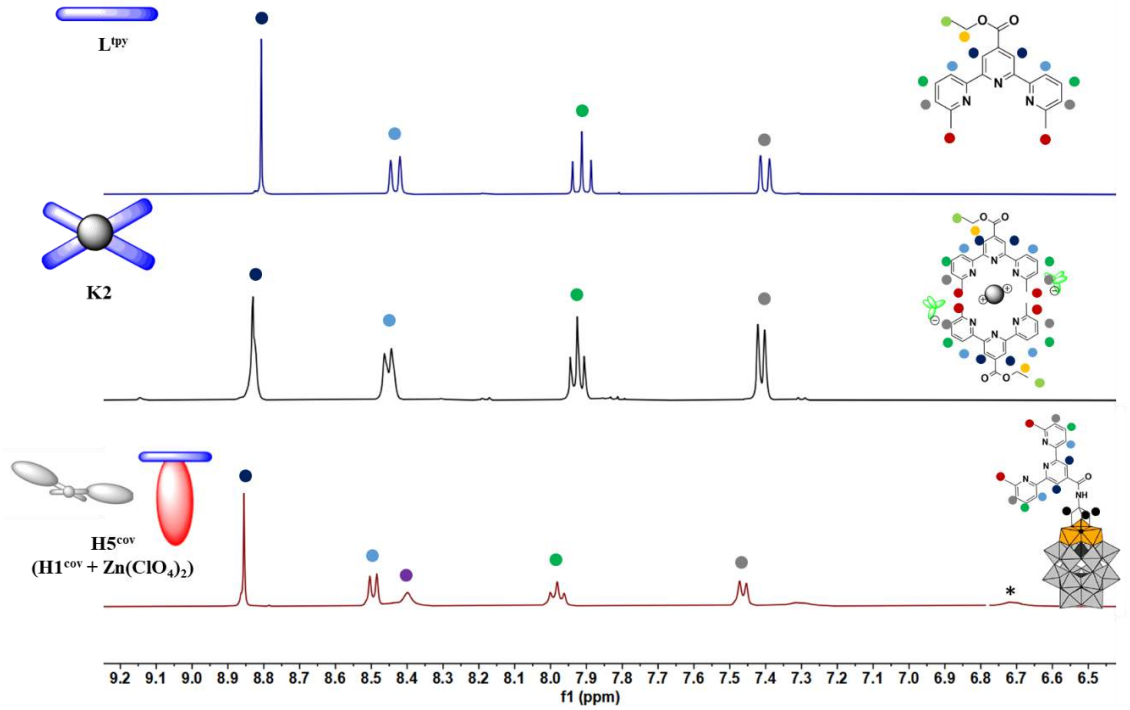

Fig. S33. Comparison of ^{1}H NMR spectra of ligand **L^{tpy}** (blue), complex **K2** (black) and hybrid **H5^{cov} (H1^{cov} + Zn(ClO$_4$)$_2$)** (red) in DMSO-*d*$_6$ at 400 MHz (aromatic region).

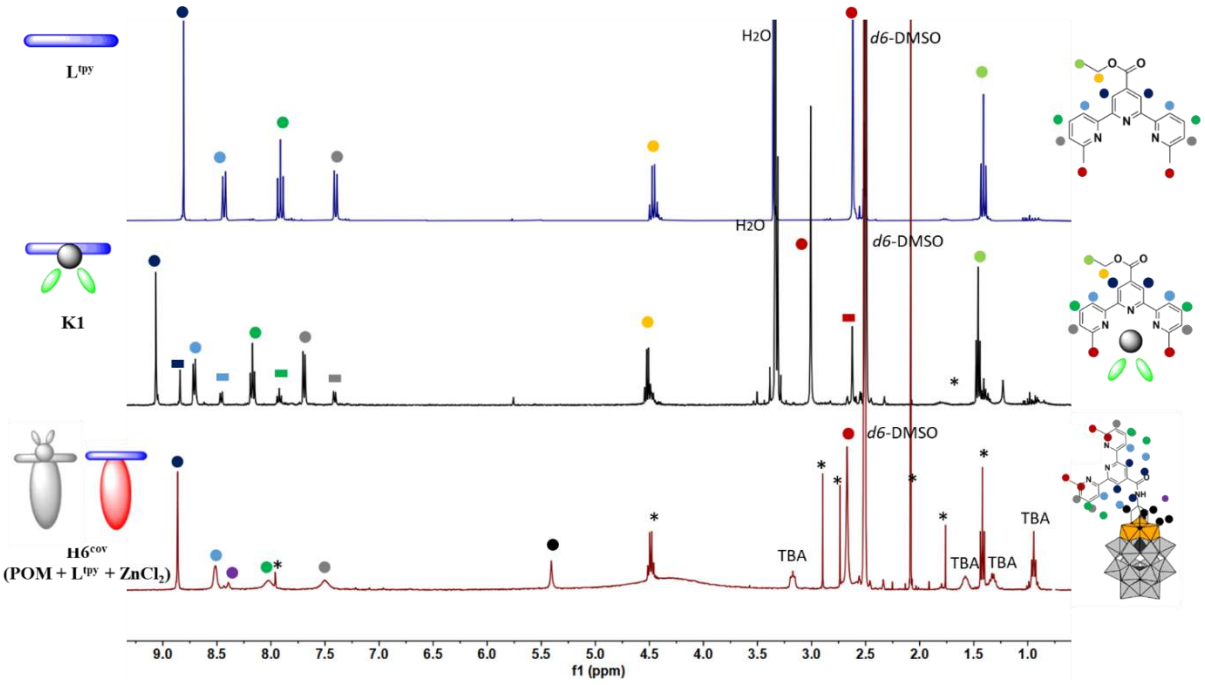

Fig. S34. Comparison of ^{1}H NMR spectra of ligand **L^{tpy}** (blue), complex **K1** (black) and hybrid **H6^{cov} (POM + L^{tpy} + ZnCl$_2$)** (red) in DMSO-*d*$_6$ at 400 MHz.

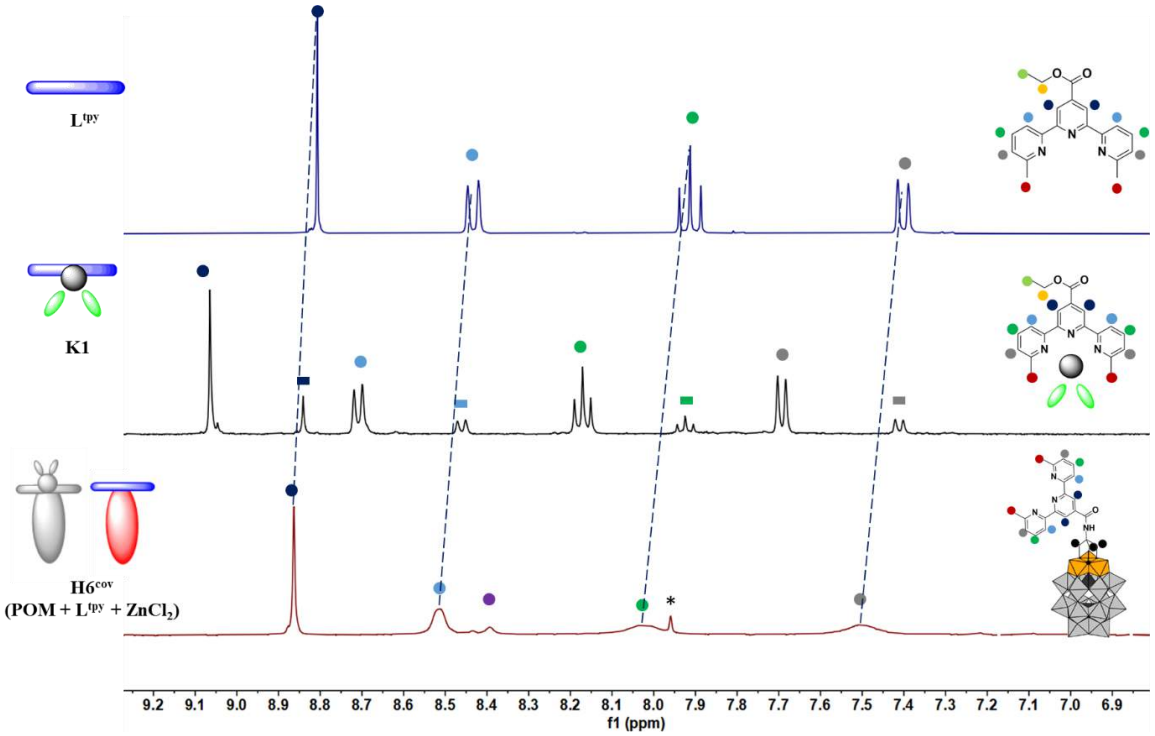

Fig. S35. Comparison of ^{1}H NMR spectra of ligand **L^{tpy}** (blue), complex **K1** (black) and hybrid **H6^{cov} (POM + L^{tpy} + ZnCl$_2$)** (red) in DMSO-*d*$_6$ at 400 MHz (aromatic region).

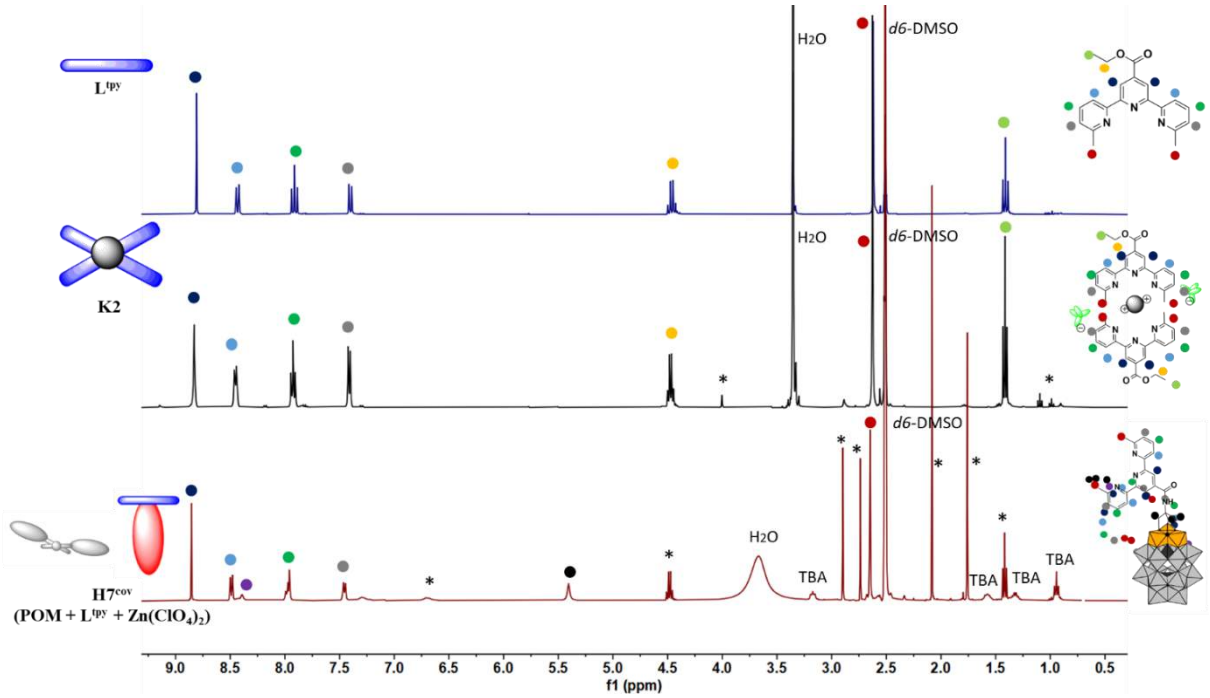

Fig. S36. Comparison of ^{1}H NMR spectra of ligand **L^{tpy}** (blue), complex **K2** (black) and hybrid **H7^{cov} (POM + L^{tpy} + Zn(ClO$_4$)$_2$)** (red) in DMSO-*d*$_6$ at 400 MHz.

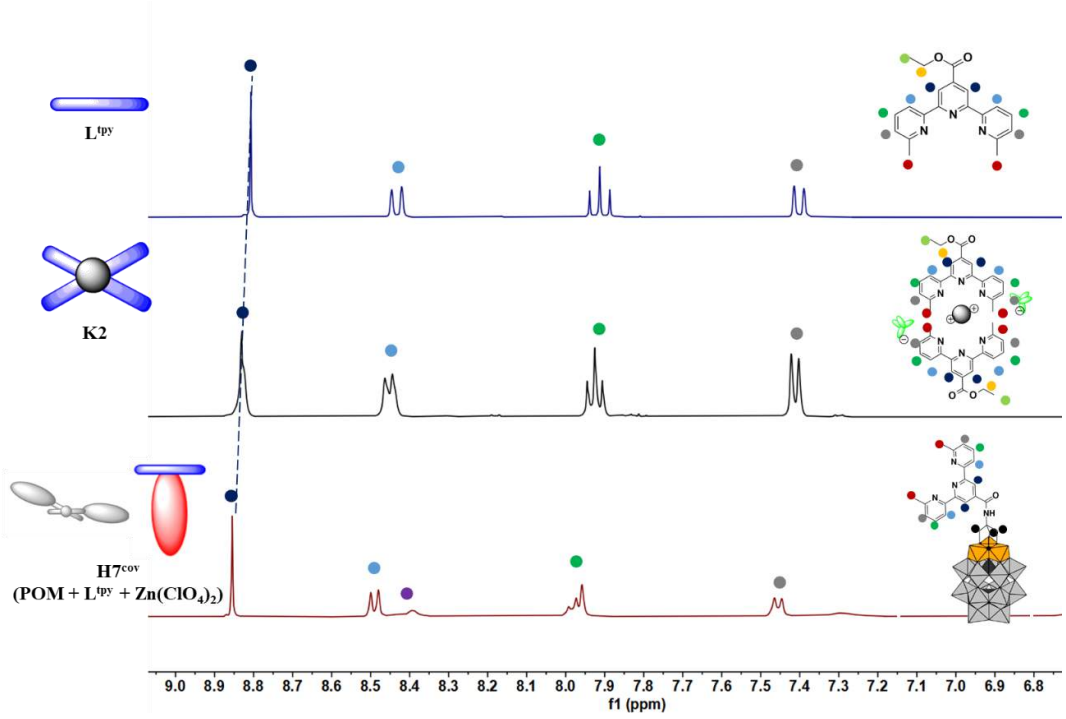

Fig. S37. Comparison of ^{1}H NMR spectra of ligand **L^{tpy}** (blue), complex **K2** (black) and hybrid **H7^{cov} (POM + L^{tpy} + Zn(ClO$_4$)$_2$)** (red) in DMSO-*d*$_6$ at 400 MHz (aromatic region).

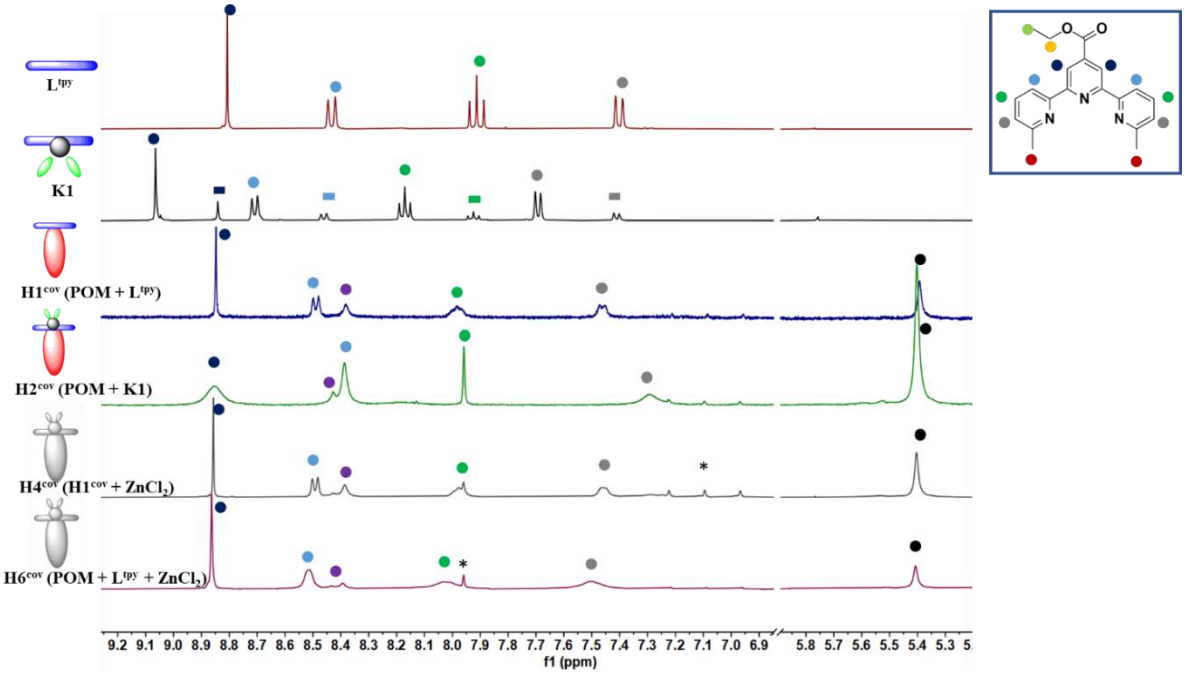

Fig. S38. Comparison of ^{1}H NMR spectra of ligand **L^{tpy}**, complex **K1** and hybrids: **H1^{cov} (POM + L^{tpy}), H2^{cov} (POM + K1), H4^{cov} (H1^{cov} + ZnCl$_2$), H6^{cov} (POM + L^{tpy} + ZnCl$_2$)**, respectively in DMSO-*d*$_6$ at 400 MHz.

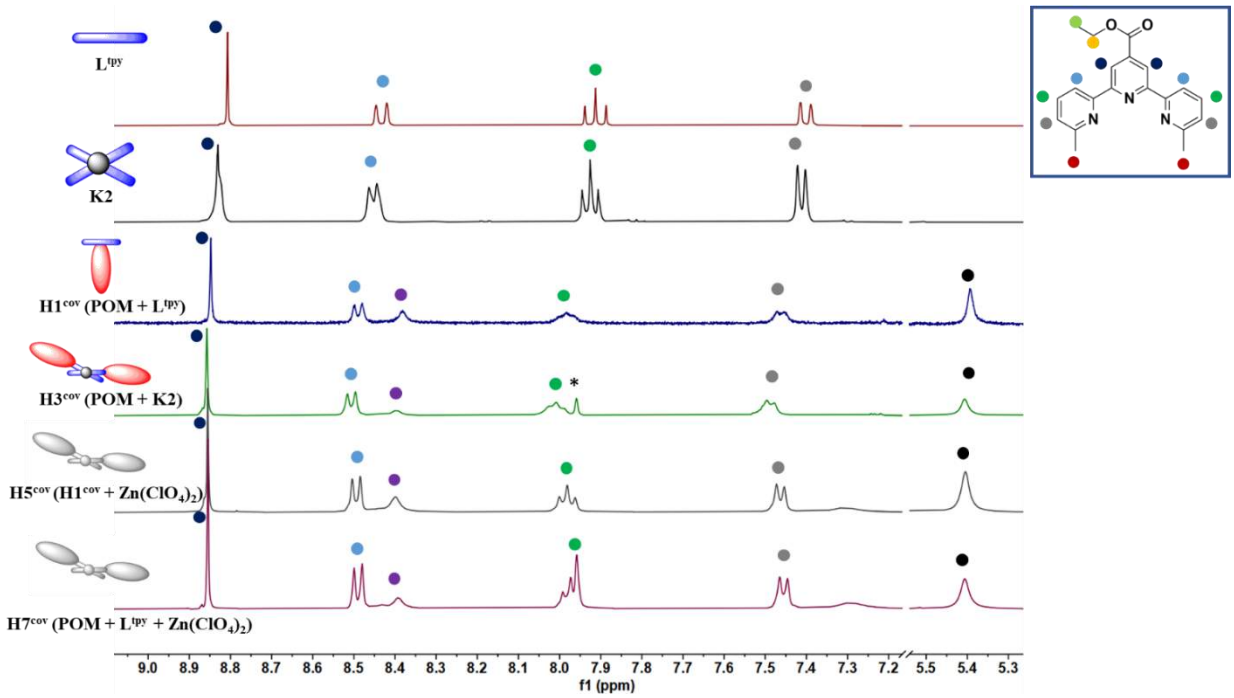

Fig. S39. Comparison of ^{1}H NMR spectra of ligand **L^{tpy}**, complex **K1** and hybrids: **H1^{cov} (POM + L^{tpy}), H3^{cov} (POM + K2), H5^{cov} (H1^{cov} + Zn(ClO$_4$)$_2$), H7^{cov} (POM + L^{tpy} + Zn(ClO$_4$)$_2$)**, respectively in DMSO-*d*$_6$ at 400 MHz.

6. ^{31}P NMR spectra of hybrids

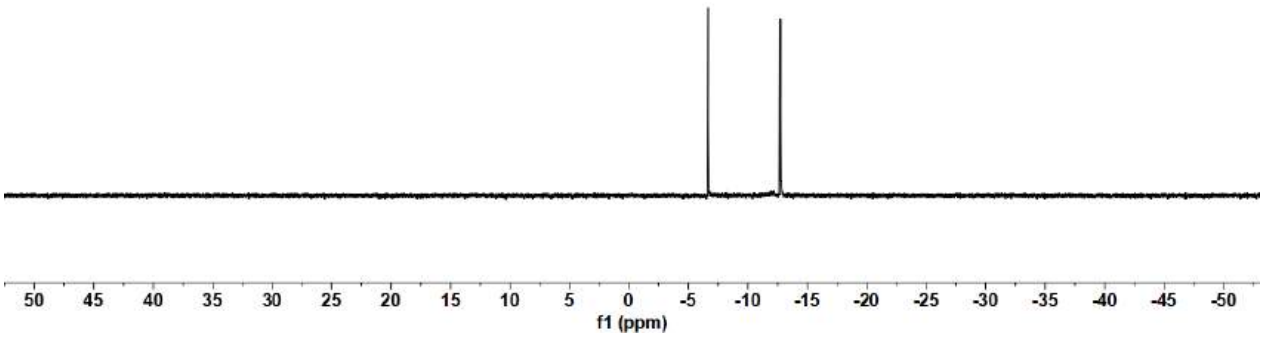

Fig. S40. ^{31}P NMR spectrum of hybrid **H1^{cov} (POM + L^{tpy})** in DMSO-*d*$_6$ at 400 MHz.

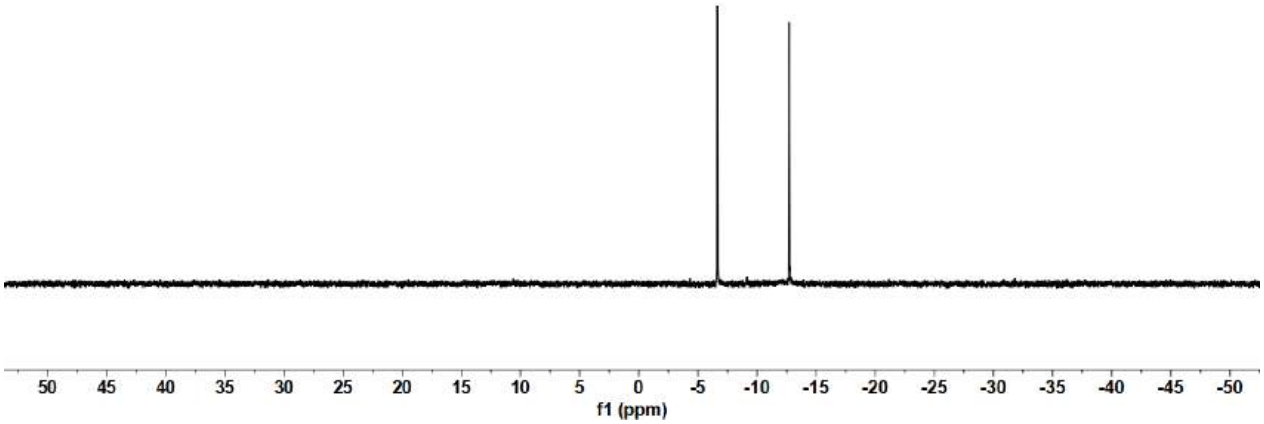

Fig. S41. ^{31}P NMR spectrum of hybrid **H2^{cov} (POM + K1)** in DMSO-d_6 at 400 MHz.

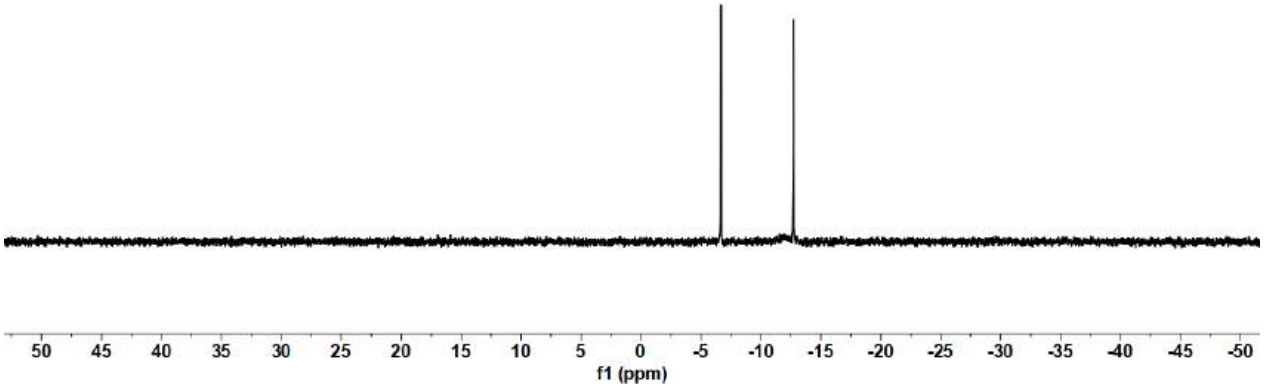

Fig. S42. ^{31}P NMR spectrum of hybrid **H3^{cov} (POM + K2)** in DMSO-d_6 at 400 MHz.

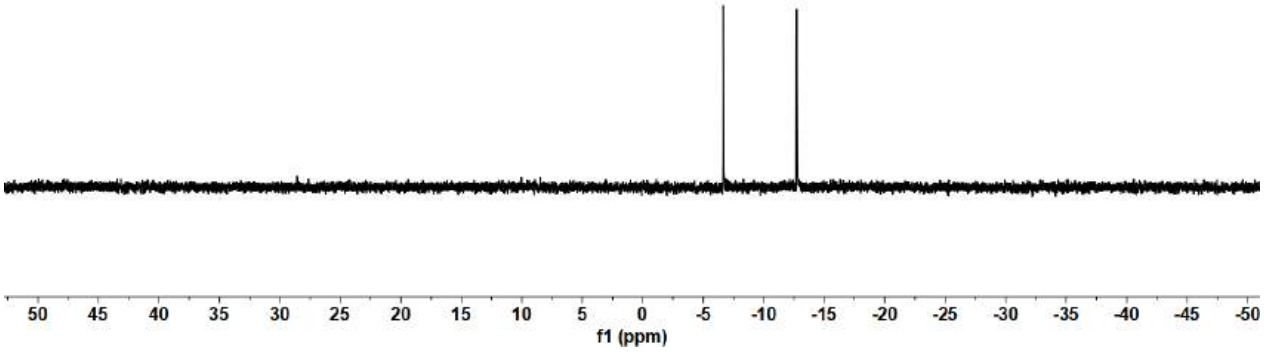

Fig. S43. ^{31}P NMR spectrum of hybrid **H4^{cov} (H1^{cov} + ZnCl$_2$)** in DMSO-d_6 at 400 MHz.

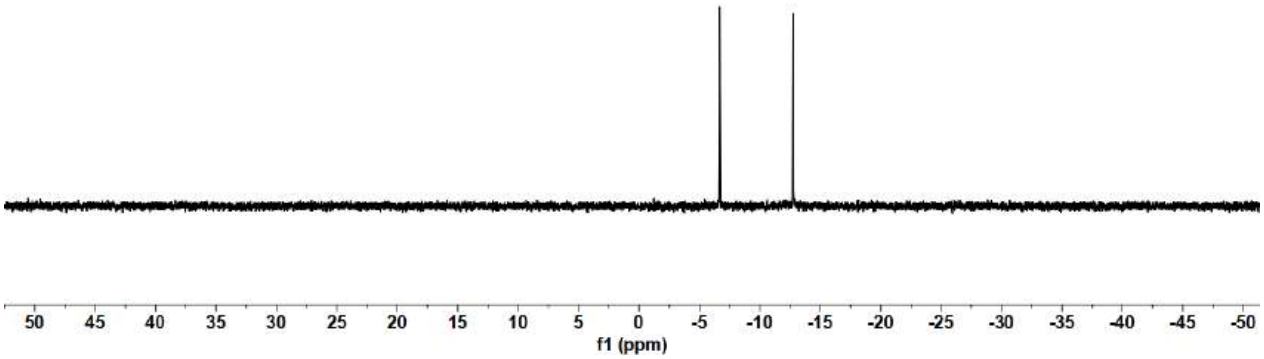

Fig. S44. ^{31}P NMR spectrum of hybrid **H5^{cov} (H1^{cov} + Zn(ClO$_4$)$_2$)** in DMSO-*d*$_6$ at 400 MHz.

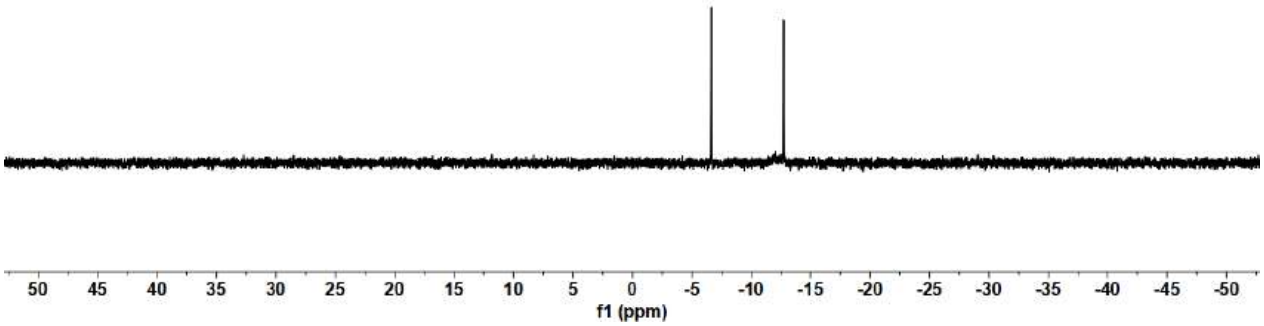

Fig. S45. ^{31}P NMR spectrum of hybrid **H6^{cov} (POM + L^{tpy} + ZnCl$_2$)** in DMSO-*d*$_6$ at 400 MHz.

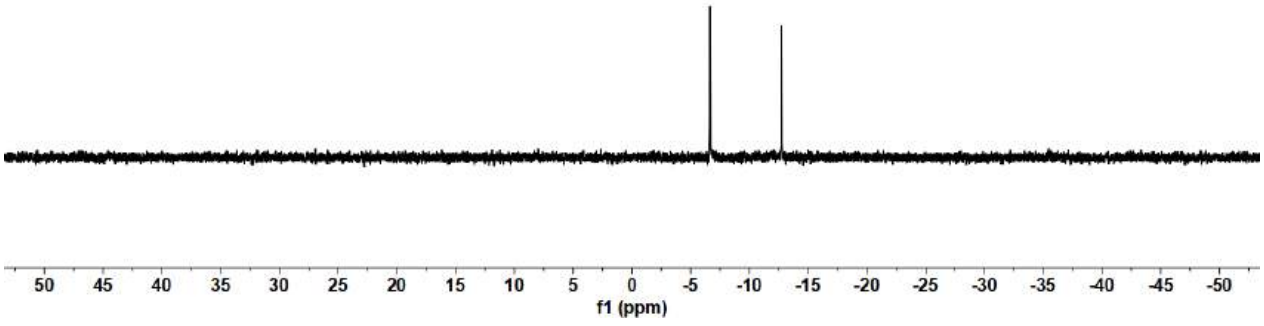

Fig. S46. ^{31}P NMR spectrum of hybrid **H7^{cov} (POM + L^{tpy} + Zn(ClO$_4$)$_2$)** in DMSO-*d*$_6$ at 400 MHz.

7. Comparison of ^{31}P NMR spectra of hybrids

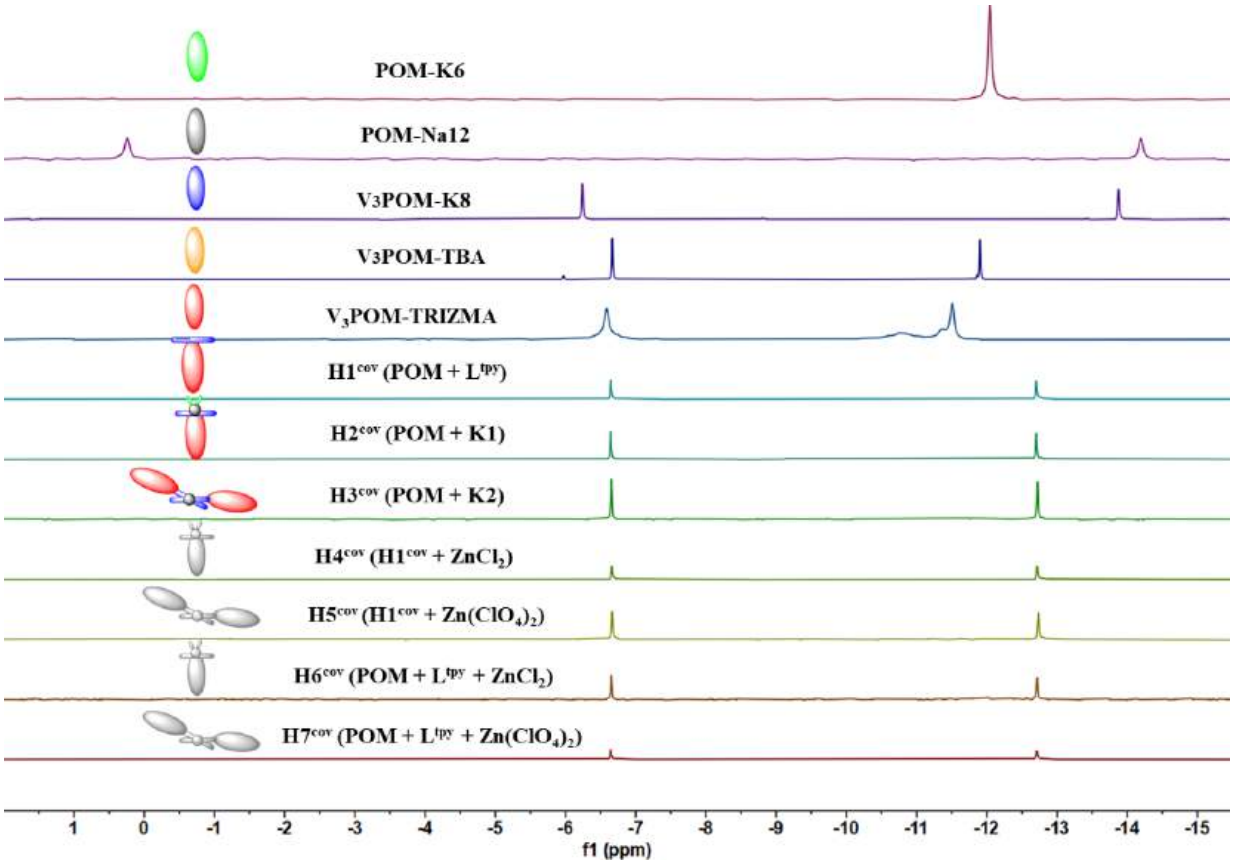

Fig. S47. Comparison of ^{31}P NMR spectra of hybrids: **POM-K6, POM-Na12, V_3POM-K8, V_3POM-TBA, V_3POM-TRIZMA, H1^{cov} (POM + L^{tpy}), H2^{cov} (POM + K1), H3^{cov} (POM + K2), H4^{cov} (H1^{cov} + $ZnCl_2$), H5^{cov} (H1^{cov} + $Zn(ClO_4)_2$), H6^{cov} (POM + L^{tpy} + $ZnCl_2$), H7^{cov} (POM + L^{tpy} + $Zn(ClO_4)_2$)**, respectively in DMSO-d_6 at 400 MHz.

8. Biological measurements

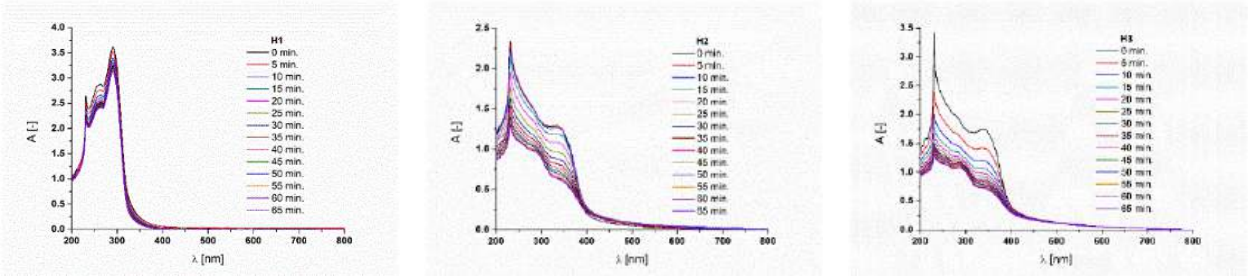

Fig. S48. Time-dependent equilibration of **H1^{ion}** and **H2^{ion}** and **H3^{ion}** in Tris Buffer with 1% DMSO content.

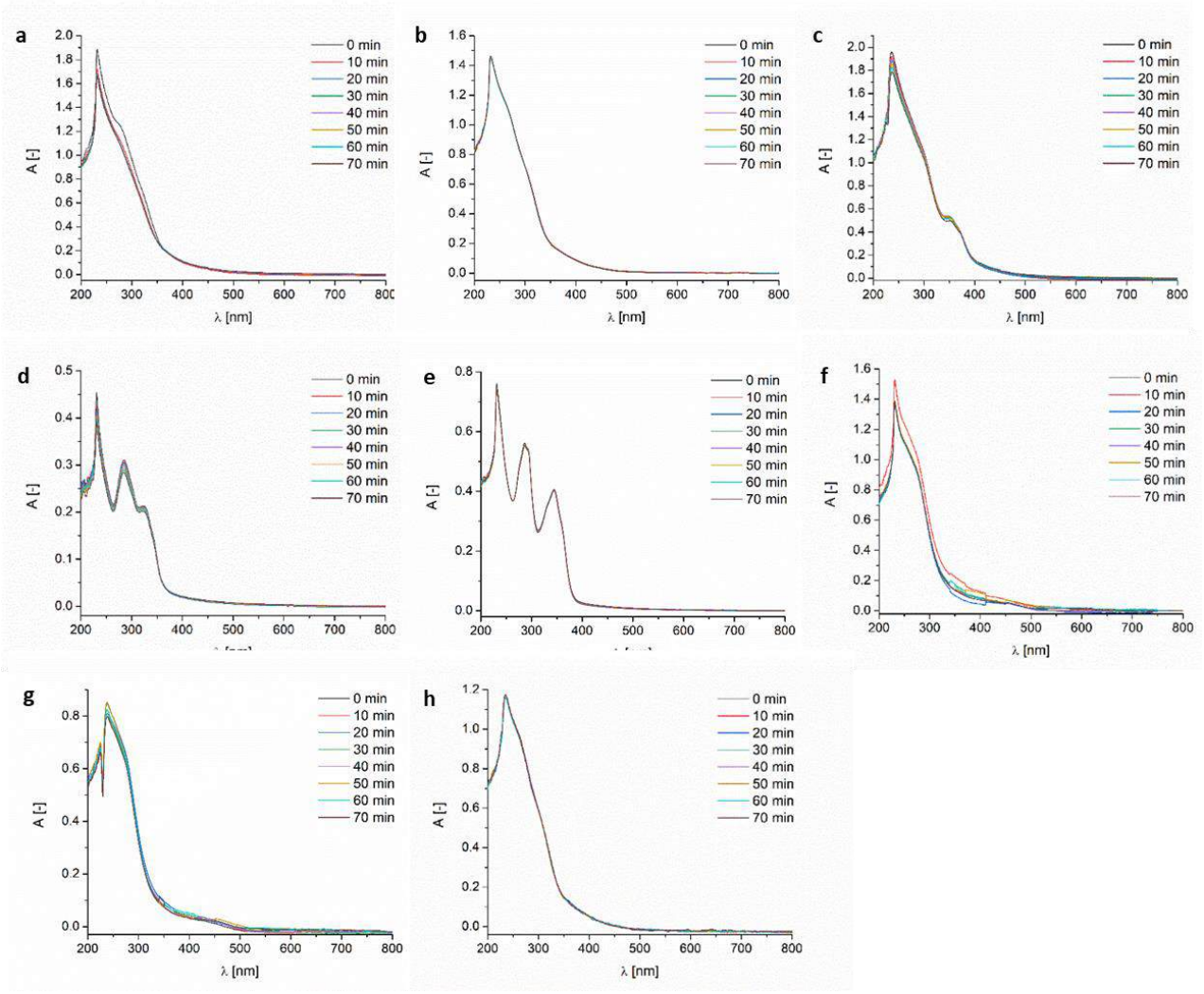

Fig. S49. Time-dependent equilibration of (a) **H1^{cov}**, (b) **H2^{cov}**, (c) **H3^{cov}**, (d) **L**, (e) **K2**, (f) **V$_3$P-K8**, (g) **V$_3$P-TBA** and (h) **V$_3$P+trizma** in Tris Buffer (5 mM Tris, 50 mM NaCl, pH = 7.4) with 1% DMSO content.

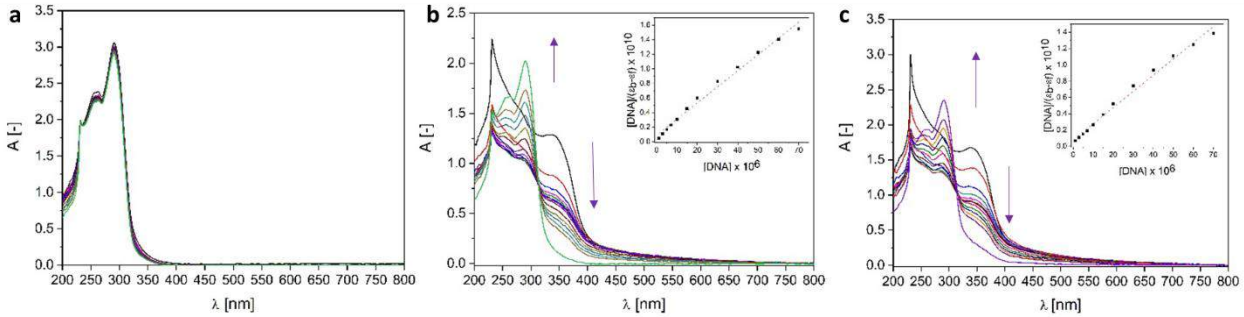

Fig. S50. Titration of (a) **H1^{ion}** and (b/c) **H2^{ion} / H3^{ion}** CD-SECs with aliquots of CT-DNA in (5 mM Tris, 50 mM NaCl, pH = 7.4) with 1% DMSO content. Arrows show changes upon increasing CT-DNA concentration. Insets in **b** and **c**: plot of [DNA]/(ε_a-ε_f) versus [DNA]; ■, experimental data points; solid line, linear fitting of the data.

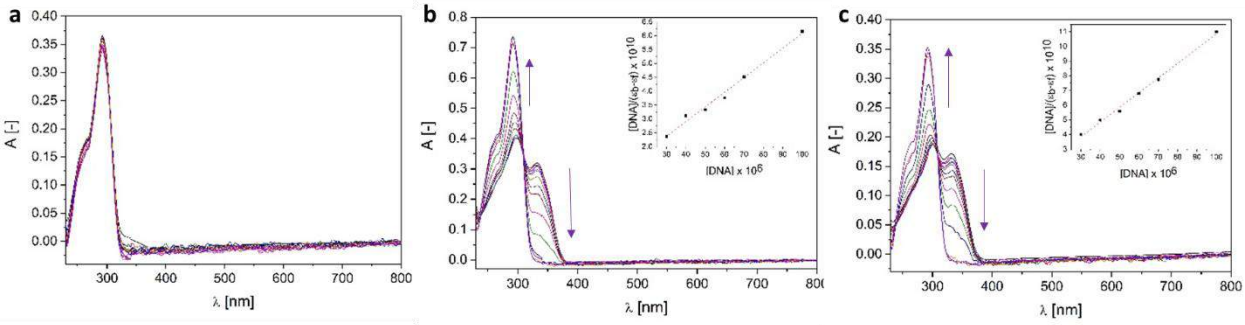

Fig. S51. Titration of (a) **L^{N2O}**, (b) **K1^{ion}** and (c) **K2^{ion}** with aliquots of CT-DNA in (5 mM Tris, 50 mM NaCl, pH = 7.4) with 1% DMSO content. Arrows show changes upon increasing CT-DNA concentration. Insets in **b** and **c**: plot of [DNA]/(ε_a-ε_f) versus [DNA]; ■, experimental data points; solid line, linear fitting of the data.

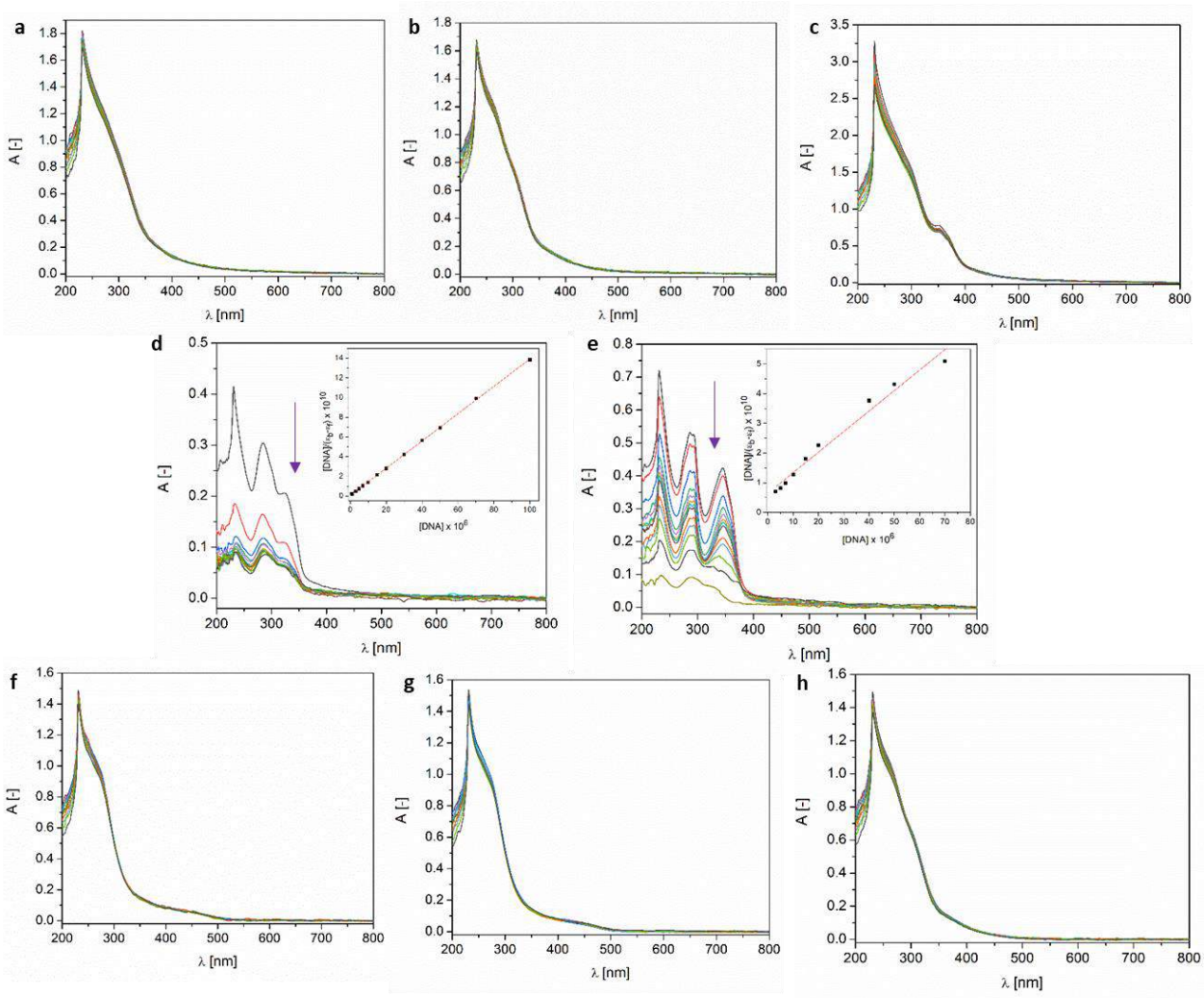

Fig. S52. Titration of (a) **H1^{cov}**, (b) **H2^{cov}**, (c) **H3^{cov}**, (d) **L^{tpy}**, (e) **K2**, (f) **V$_3$P-K8**, (g) **V$_3$P-TBA** and (h) **V$_3$P+trizma** with aliquots of CT-DNA in (5 mM Tris, 50 mM NaCl, pH = 7.4) with 1% DMSO content. Arrows show hypochromic changes upon increasing CT-DNA concentration. Insets in **d** and **e**: plot of [DNA]/(ε_a-ε_f) versus [DNA]; ■, experimental data points; solid line, linear fitting of the data.

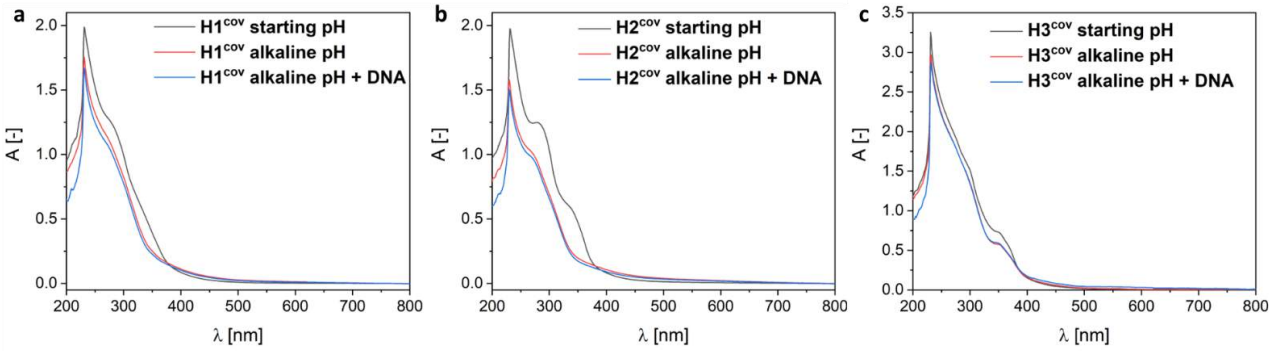

Fig. S53. Investigation on the influence of pH change (to ~8.6) on the stability of (a) **H1^{cov}**, (b) **H2^{cov}** and (c) **H3^{cov}** with subsequent addition of the 100 μM CT-DNA aliquots in miliQ water with 1% DMSO content after 1 h equilibration period.

References

1. G. Ulrich, S. Bedel, C. Picard and P. Tisnès, *Tetrahedron Letters*, 2001, **42**, 6113-6115.

Coordination Chemistry Reviews 519 (2024) 216091

Contents lists available at ScienceDirect

Coordination Chemistry Reviews

journal homepage: www.elsevier.com/locate/ccr

Review

Overview of Wells-Dawson Polyoxometalates: from structure and functionalization to application

Daria Nowicka [a], Nahir Vadra [a,b], Ewelina Wieczorek-Szweda [a], Violetta Patroniak [a], Adam Gorczyński [a,*]

[a] Adam Mickiewicz University in Poznań, Faculty of Chemistry, Uniwersytetu Poznańskiego 8, 61-614 Poznań, Poland
[b] Universidad de Buenos Aires, Facultad de Ciencias Exactas y Naturales, Departamento de Química Inorgánica, Analítica y Química Física and CONICET–Universidad de Buenos Aires, Instituto de Química Física de los Materiales, Medio Ambiente y Energía (INQUIMAE), Buenos Aires C1428EGA, Argentina

ARTICLE INFO

Dedicated to Professor Jean-Marie Lehn on the occasion of his 85th birthday.

Keywords:
Wells-Dawson POM
Polyoxometalates
Hybrid organic-inorganic
Functional materials
Post-functionalization approaches

ABSTRACT

Wells-Dawson polyoxometalates (WD POMs) are an important subgroup within the diverse family of POMs. In the last two decades, there has been remarkable progress in the structure modification and post-functionalization of WD POMs, which has unlocked their enormous potential across various domains, including energy materials, catalysis (photocatalysis, electrocatalysis), functional materials (sensors, optical materials, electrochromic materials, magnetic materials) or biology/medicine (anticancer and antibacterial activities). What makes these systems particularly captivating is their highly adaptable topological structure, combined with the versatile functionalization methods and consequently their precise design and control, which transfers into a wide range of applications. In our comprehensive review, we focus on the exploration of their intricate structural characteristics which play a pivotal role in their functional properties. Moreover, the exciting and promising applications of WD POMs across various areas of science disciplines are highlighted. Our aim is to shed light on the current state of the art, identify emerging trends, and provide insights into the potential future directions of WD POM research, which are still being expanded, especially given the rapid development and continuous progress in the design of novel WD POM subunit functionalities. By doing so, we hope to contribute to a better understanding of these remarkable materials and inspire further innovation in their utilization.

1. Introduction

Polyoxometalates (POMs) are a group of metal-oxo nanoclusters in the class of inorganic compounds, represented by the general formula $[X_xM_mO_o]^{n-}$, where X = heteroatom, M = early transition metal (TM) ion in the highest oxidation state (W^{6+}, Mo^{6+}, V^{5+}) [1–16]. In general, POMs are formed by the condensation of oxygen atoms and an early TM ion under appropriate conditions (pH, solvent, reducing agents, temperature, rate and sequence of addition, type of heteroatoms, type of cations, etc.) thus forming polyhedra, which are linked to each other via edge and corner sharing [17–22]. Metal–oxo nanoclusters are classified into different types, with the principal ones being Lindqvist $[M_6O_{19}]^{n-}$ [23], Keggin $[XM_{12}O_{40}]^{n-}$ [24], Wells-Dawson $[XM_{18}O_{62}]^{n-}$ [25], Silverton $[XM_{12}O_{42}]^{n-}$ [26], Preyssler $[X^{n+}P_5W_{30}O_{110}]^{(15-n)-}$ [27] and Anderson-Evans $[XM_6O_{24}]^{n-}$ [28,29] types (Fig. 1). The possibility of self-assembly in various geometric archetypes and sizes contributes to the diverse nature of the compounds and affects their characteristics such as charge density and redox properties [20,30]. The versatility and variety of POM properties have led to the publication of numerous papers and reviews in the last decades. An important area of research focuses on POM nanoclusters as precursors to forming organo-inorganic hybrid materials [2]. The process of POM functionalization occurs in a covalent and/or ionic manner. The combination of inorganic precursors with organic functionalities via covalent binding is a significant branch of hybrid materials chemistry due to synergistic interactions between organic and inorganic parts [18]. Moreover, published works have explored ways to diversify physicochemical properties for potential applications as well as to understand structure–function relationships in a wide variety of areas such as catalysis [31–43], photocatalysis [44–52], magnetism [53–57], energy [58–70], biology/medicine [71–80], and others [81–87].

However, although comprehensive and recent reviews of several of the archetypical POM systems have been reported [88–97], an in-depth discussion of Wells-Dawson POMs (WD POMs) has been unexpectedly

* Corresponding author.
E-mail address: adam.gorczynski@amu.edu.pl (A. Gorczyński).

https://doi.org/10.1016/j.ccr.2024.216091
Received 5 April 2024; Accepted 10 July 2024
Available online 30 July 2024

missing. In fact, the latest published review that focuses on WD nanoclusters dates as far back as 2003 [31] and it summarized related developments in this group for the period 1990–2002. The versatility of WD structures has led in the last decades to exploring ways to diversify their physicochemical properties: for example, modification of the internal counterions or templates (Se, P, S, Te, Sb, Ge), modification of addenda atoms (V, Mo, W) by other coordination metals leading to CAP (trilacunar or monolacunar) or belt modification, and the formation of non-conventional WD POMs such as open or sandwich WD POMs. Furthermore, besides the changes that typically occur in the WD POM structure, the properties are also influenced by post-functionalization processes, such as for example single-, double-linker modularity-generating hybrid materials and others leading to the formation of for example polymeric systems based on WD POMs. Structurally modified and post-functionalized WD POMs show an unparalleled range of properties, from systems capable of mimicking enzymes to materials for supercapacitors or batteries. Despite the numerous limitations associated with speciation in solution at different pH ranges, the modification of POM structures, such as the adjustment of the electronic properties of acidity or polarity and post-functionalization, researchers started to probe into biological properties, such as anticancer and antibacterial activity. Thanks to their valuable redox properties, they find numerous applications in catalysis, be it photocatalysis or electrocatalysis. Modified WD POMs have gained features such as stability in solution and in the solid, have shown potential host roles for magnetic ions, and their structure has become rigid and highly symmetric, all of which has made them encouraging compounds in the design of new molecular magnetic devices. Owing to dynamic developments in the synthesis, characterization and application of new WD POMs since the most recent review, 567 papers have been published on WD POMs, of which 293 have appeared in the last 10 years (Fig. 2).

The purpose of this work is to provide a comprehensive review of developments related to WD POMs centered on the growing interest in this class of compounds. Firstly, structural modifications made in this family of POMs are analyzed in a rational and orderly form, followed by the synthetic strategies used for these modifications. Subsequently, the post-functionalization processes of WD POMs together with the synthetic strategies are thoroughly discussed. Finally, the properties and recent applications in areas such as energy transfer, photo- or electrocatalysis, sensors, magnetism, biology and other functional materials are critically evaluated.

2. Structure of WD POMs

WD POMs are one of the more common types of POMs of the general formula $[X_2M_{18-n}Y_nO_{62}]^{n-}$, where X = heteroatom/template (P, Si, S, As, etc.), M = early transition metal ion/addenda atom (Mo, W), Y = other metal coordinate (V, Cr, Sn, Co, etc.), n = 1, 2 or 3 [98–101] (Fig. 3) and interestingly enough, the first example of a WD POM was developed and published as early as in 1953 [25].

The overall structure can be grouped according to the exterior cap and belt positions, which are mostly oxometallates of molybdenum, tungsten or vanadium at their highest oxidation states, and the internal *p*-block elements which form so-called templating oxoanion heteroatoms. A modification to the original WD POM structure by incorporating another metal ion in the cap position contributes to building variable structures such as dimers or tetramers and facilitates functionalization [101–104]. Nonetheless, belt modification is also important as it leads to the formation of non-classical POMs such as open WD POMs [105–108] (Fig. 4).

2.1. Templates/Heteroatoms

WD clusters may differ from each other in their inner heteroatoms which are enclosed in the 3D structure of POMs [98,99,109–112] (Fig. 5). Unlike the classical WD POMs containing two $[XO_4]^{n-}$ moieties in their structures, e.g. $[PO_4]^{3-}$ [113–116], $[AsO_4]^{3-}$ [113,114,117,118], $[SO_4]^{2-}$ [119–122], $[ClO_4]^{-}$ [123], non-classical types are generated by the incorporation of non-tetrahedral moieties, such as pyramidal $[XO_3]^{n-}$ groups, e.g. $[SO_3]^{2-}$ [124–127], $[AsO_3]^{3-}$ [128], $[SbO_3]^{3-}$ [129,130], $[BiO_3]^{3-}$ [131], $[TeO_3]^{2-}$ [132], $[SeO_3]^{2-}$ [99,127,133,134], ditetrahedral $[P_2O_7]^{4-}$ [135], trigonal-hexafluorosodate $[NaF_6]^{5-}$ [136–139], trigonal-prismatic $[WO_6]^{6-}$ [140–142] or other octahedral $[XO_6]^{n-}$, such as $[TeO_6]^{6-}$ [141,142], $[IO_6]^{5-}$ [142,143], $[SbO_6]^{7-}$ [144] (Table 1). It is noted that owing to the introduction of various heteroatoms into the interior of the structure, the physicochemical properties are effectively modulated and fine-tuned [110], e.g. solubility, conductivity, functionalizing flexibility, specific surface area, degradation, and aggregation.

Classical WD POMs are one of the most well-known and researched types of POMs owing to their interesting properties and auspicious utilization [110]. $[PO_4]^{3-}$ [113–115] moieties are most frequently encountered in the literature as the inner counterions in POM structures, considering the basic POM group. The unusual resemblance to the

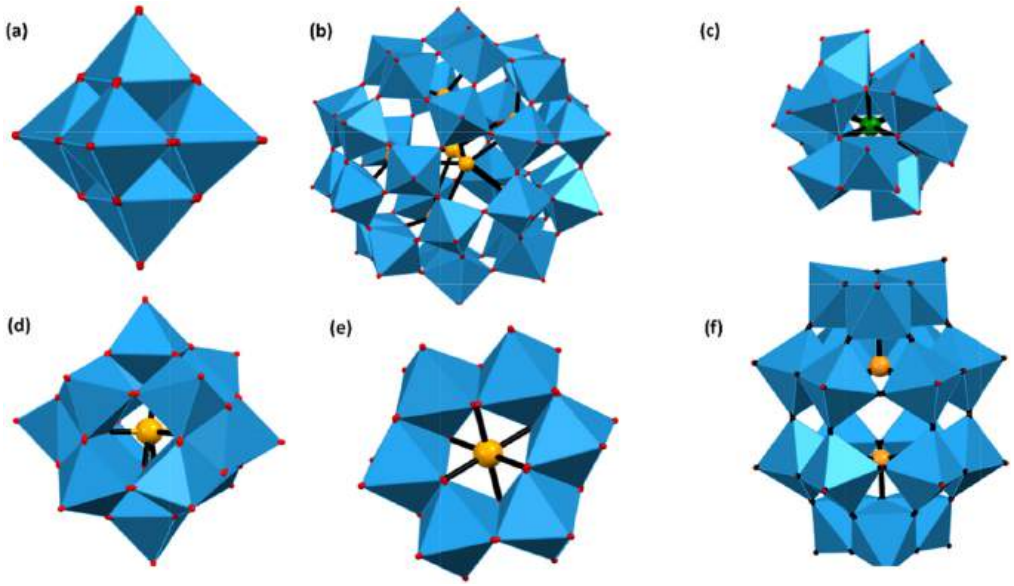

Fig. 1. The most common POM structures: (a) Lindqvist, (b) Preyssler, (c) Silverton, (d) Keggin, (e) Anderson-Evans, and (f) Wells-Dawson.

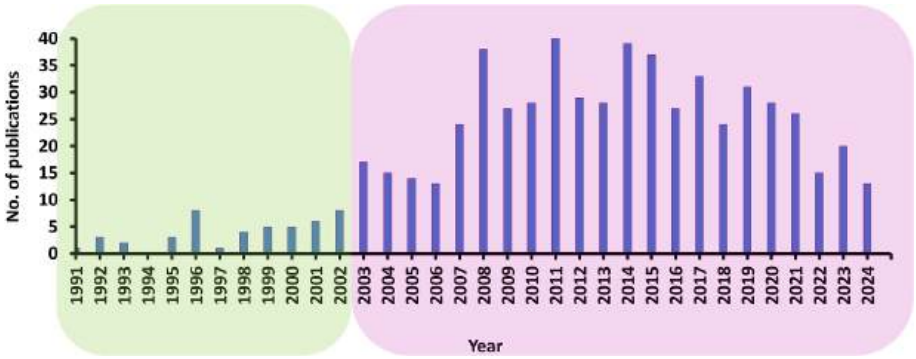

Fig. 2. Number of publications on WD POMs vs. time. Green: Papers summarized in the previous review; pink: papers summarized in this paper.

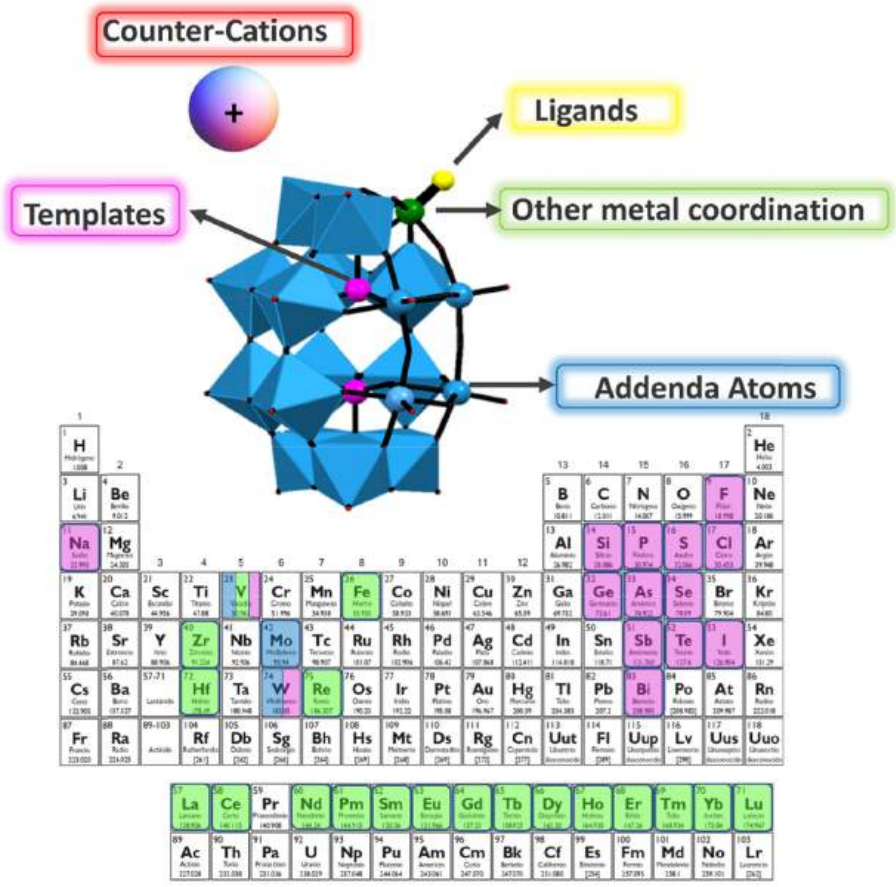

Fig. 3. WD POM structure with modifiable groups highlighted and the periodic table showing elements selected for specific modifications.

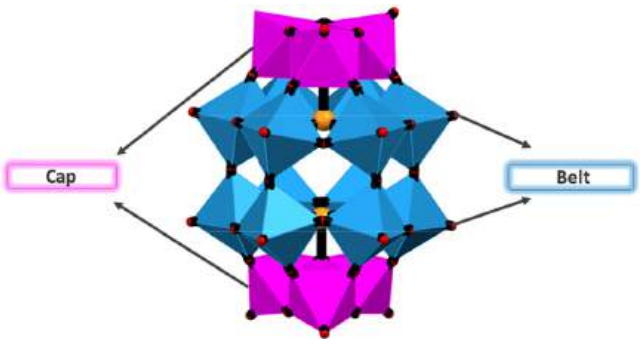

Fig. 4. WD POM structure with cap and belt positions.

phosphorus-centered POM can be seen when arsenic is introduced as the heteroatom. However, the differences between these heteroatoms, such as the larger atomic radius of arsenic and easy oxidation between the As^{III}/As^{V} states, modify the electronic properties of the POMs, which can be important for catalysis [113,117]. Remarkably, both arsenic and phosphorus can form a mixed WD POM system, such as arsenate – phosphate – tungstate α-$[AsPW_{18}O_{62}]^{6-}$ as reported by Haouas et al. [147]. Sulfur is the subsequent neighboring element to phosphorus in the periodic table, the introduction of which into the interior of a WD POM structure has a promising effect on its oxidizing properties [121]. Interestingly, WD POM silicotungstates are rarely reported; nonetheless, according to the available literature most of them do not contain any organic compound and no more than five paramagnetic metal atoms can be introduced. This type of POM can be formed by the dimerization of

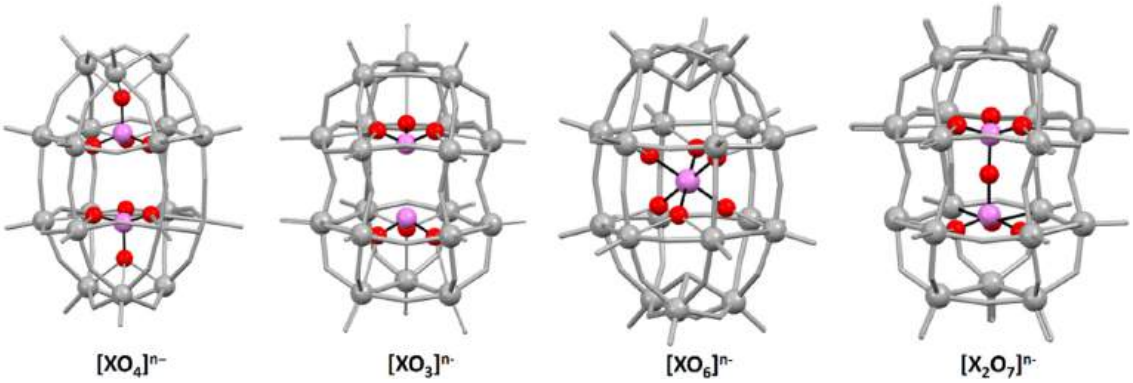

Fig. 5. General structures of classical and non-classical WD POMs with $[XO_4]^{n-}$, $[XO_3]^{n-}$, $[X_2O_7]^{n-}$ and $[XO_6]^{n-}$ moieties.

Table 1
Representation of the classical and non-classical WD POM structures containing $[XO_m]^{n-}$ moieties (m = 3, 4 or 6) and $[X_2O_7]^{n-}$.

General formula of the moiety	Moiety	General formula of the compound	Ref.
$[XO_4]^{n-}$	$[PO_4]^{3-}$	αββα-$Na_{16}(Mn^{II}OH_2)_2(Mn^{II})2(P_2W_{15}O_{56})_2$	[116,115]
		$TBA_6[\alpha\text{-}P_2W_{18}O_{62}]\cdot H_2O$	
	$[AsO_4]^{3-}$	αββα-$Na_{16}(Mn^{II}OH_2)_2\text{-}Mn^{II}_2(As_2W_{15}O_{56})_2\cdot 55H_2O$	[113,117,118]
		$Na_{16}[Cu_4(H_2O)_2(As_2W_{15}O_{56})_2]\cdot 47H_2O$	
		$K_{14}[As_2W_{19}O_{67}(H_2O)]$	
	$[SO_4]^{2-}$	$[C_{19}H_{18}N_3]_4[\alpha\text{-}S_2Mo_{18}O_{62}]$	[119,120,121,122]
		$(MB)_5[S_2Mo^{V}Mo^{VI}_{17}O_{62}]\cdot CH_3CN$ (MB = $C_{16}H_{18}N_3S$) $[Bu_4N]_5[S_2W_{18}O_{62}]$	
		$[Ru^{II}(bpy)_3]_2[\alpha\text{-}S_2M_{18}O_{62}]$	
	$[ClO_4]^-$	$[NBu^{n}_4]_3[Cl_2W^{V}W^{VI}_{17}O_{62}]$	[123]
	$[SiO_4]^{2-}$	$TBA_8[\alpha\text{-}Si_2W_{18}O_{62}]\cdot 3H_2O$	[115,105,145]
		$K_7H_2[K(Co(H_2O)_4)_2Co(H_2O)_2(Si_2W_{18}O_{66})]\cdot 22H_2O$	
		$[Dy_2(H_2O)_{6.5}(C_2H_4O_2)_{0.5}Si_2W_{18}O_{66}]^{10-}$	
	$[VO_4]^{2-}$	$[Cu_2(2,2'\text{-bpy})_2(Inic)_2(H_2O)_2][Y(Inic)_2(H_2O)_5]H_3[V_2W_{18}O_{62}]\cdot 5.5H_2O$	[146]
$[XO_3]^{n-}$	$[SO_3]^{2-}$	$(Bu_4N)_4[W^{VI}_{18}O_{54}(SO_3)_2]$	[124,125,125,126,127]
		$(TEAH)_6[H_2W_{18}O_{57}(SO_3)]$	
		$(DMAH)_8[W_{18}O_{56}(SO_3)_2(H_2O)_2]$	
		$[W_{18}O_{54}(SO_3)_2]^{4-}$	
		$[W_{18}O_{56}(SO_3)_2(H_2O)_2]^{8-}$	
	$[AsO_3]^{3-}$	$\beta\text{-}[W_{18}O_{54}(AsO_3)_2]^{6-}$	[128]
	$[SbO_3]^{3-}$	$[SbW_{18}O_{60}]^{9-}$	[130,129]
		$[Cu(phen)(H_2O)]_2[Cu(phen)(H_2O)_3]_2H[SbW_{18}O_{60}]\cdot 5H_2O$	
	$[BiO_3]^{3-}$	$[H_3BiW_{18}O_{60}]^{6-}$	[131]
	$[TeO_3]^{2-}$	$(C_2H_8N)_{19}Na_{13}[(WO_2)_4(Te_2W_{15}O_{54})_4]\cdot 57H_2O$	[132,132]
		$(C_2H_8N)_{19}Cs_2Na_{11}[(WO_2)_4(Te_2W_{15}O_{54})_4]\cdot 77H_2O$	
	$[SeO_3]^{2-}$	$[H_2Se^{IV}W_{18}O_{60}]^{6-}$	[99,133,134,127]
		$[Se_2W_{18}O_{62}(H_2O)_2]^{8-}$	
		$[W_{18}O_{54}(SeO_3)_2]^{4-}$	
		$[W_{18}O_{56}(SeO_3)_2(H_2O)_2]^{8-}$	
$[X_2O_7]^{n-}$	$[P_2O_7]^{4-}$	$(N(C_4H_9)_4)_4[(P_2O_7)Mo_{18}O_{54}]$	[135]
$[XO_6]^{n-}$	$[NaF_6]^{5-}$	$[(NaF_6)W_{18}O_{54}(OH)_2]^{7-}$	[109,136,137,139]
		$K_9[NaH_2Zn(H_2O)W_{17}F_6O_{55}]$	
		$K_8[NaH_2Mn^{II}(H_2O)W_{17}F_6O_{55}]\cdot 19H_2O$	
		$K_9[NaH_2Ni(H_2O)W_{17}F_6O_{55}]\cdot 15H_2O$	
	$[WO_6]^{6-}$	$(TEAH)_6[H_4W_{19}O_{62}]$	[140,142]
		$\alpha\text{-}[W_{18}O_{56}(WO_6)]^{10-}$	
	$[TeO_6]^{6-}$	$Na(DMAH)_6[H_3W_{18}O_{56}(Te^{VI}O_6)]\cdot 14H_2O$	[141,141]
		$(TBA)_7[H_3W_{18}O_{56}(Te^{VI}O_6)]\cdot 4CH_3CN$	
	$[IO_6]^{5-}$	$K_6[H_3W_{18}O_{56}(IO_6)]\cdot 9H_2O$	[143,143,143]
		$(TPA)_6[H_3W_{18}O_{56}(IO_6)]$	
		$(TBA)_6[H_3W_{18}O_{56}(IO_6)]$	
	$[SbO_6]^{7-}$	$[(SbO_6)W_{18}O_{54}(OH)_2]^{9-}$	[109,144]
		$(NH_4)_9[Sb^{V}W_{18}O_{60}(OH)_2]\cdot 25H_2O$	

TBA: tetrabutylammonium; bpy: 2,2'-bipyridine; TEAH: protonated triethanolamine; DMAH: protonated dimethylammonium; phen: 1,10-phenanthroline; TPA: tetrapropylammonium.

tri-lacunary Keggin-type $[\alpha\text{-}SiW_9O_{34}]^{10-}$ anions [106,115]. There are only a few examples in the literature where other metals, such as selenium or vanadium, were introduced as heteroatoms; however, these metal-oxo nanoclusters are little known and studied [146,148–150]. It is yet noted that despite the fact that they have been little studied, papers are available that discuss their interesting applications. The work of Cronin's group is such an example, in which a core–shell cluster of POM $[W_{18}O_{54}(SeO_3)_2]^{4-}$ has been shown to act as a potential storage node for metal–oxide–semiconductor (MOS) flash memory [134].

Non-classical WD nanoclusters containing only non-tetrahedral moieties affect the properties and can modulate the physicochemical nature of POMs. Admittedly, almost for all of non-classical WD POMs (except for pyramidal $[XO_3]^{n-}$ and di-tetrahedral $[P_2O_7]^{4-}$), six Baker–Figgis isomers have been observed (α, β, γ, α*, β* and γ*) (for

explanation and description, see Sections 2.2.1 and 2.2.2) [109]. The first structure of this group of POMs is α-$[(NaF_6)(OH)_2W_{18}O_{54}]^{7-}$containing $[NaF_6]^{5-}$ moieties, reported in 1980 by Chauveau et al. [138] and determined in 1990 by Baker's group [151]. In 1994, Kortz and Pope identified the second WD POM, γ-$[(P_2O_7)Mo_{18}O_{54}]^{4-}$, which embeds di-tetrahedral $[P_2O_7]^{4-}$ [135]. In the next decade, Cronin and co-workers reported a library of WD POMs with octahedral $[XO_6]^{n-}$ moieties with the general formula $[H_mW_{18}O_{56}(XO_6)]^{n-}$, where m = 3 or 4; n = 6 or 7; X = I, W or Te [141–143]. Moreover, the possibility of the occurrence of $[WO_6]^{6-}$ moieties was proved in two forms: octahedral and trigonal-prismatic [109,140,141,143]. Noteworthy, in the archetypes with octahedral geometry, the heteroatoms are located at the center of the cluster, unlike in other archetypes [142]. It is noted that Cronin's group developed a stepwise synthesis method using a robotic workflow for discovering new metal clusters which led for example to the discovery of three new tetrametallic POMs with the formula $TBA_5[(A\text{-}\alpha\text{-}SiW_9O_{34})_2FeMn_4O_2(Lu(acac)_2)_2A_2]$ (A = Ag, Na, K; acac = acetylacetonate) reported in [152].

2.2. Addenda atoms

An important aspect of POMs are addenda atoms, i.e. transition metals that are part of POM structures, typically Mo, W, V, Nb, and Ta. The metals are of remarkable importance for reactivity and type of displayed function [98,153]. The first group, polyoxomolybdates (POMos), are characterized by their size and shape, being giant clusters in the shape of spheres, wheels and hedgehogs due to the presence of building blocks composed of $[Mo_2O_4]$ and $[(Mo)Mo_5]$ subunits under reducing conditions [154]. A distinctive feature of the second group, polyoxotungstates (POTs), is their occurrence as lacunar precursors which are stable and act as inorganic multidentate ligands, so that they can coordinate with different active species leading to the formation of abundant POM structures [155]. The third group, polyoxovanadates (POVs), provide rich redox chemistry and organometallic frameworks or cages can be formed owing to their structure. In addition, the oxidation of reduced POVs provides a new pathway for the generation of lacunar POVs, which in turn can act as host molecules [156]. The last two groups of POMs are polyoxoniobates (PONbs) and polyoxotantalates (POTas); their chemistry is hindered and they are characterized by their neutral redox nature, have high negative charge density, their behavior under aqueous conditions is poorly understood and they are base-dependent [157]. Substitution of various addenda atoms is a useful method to modulate the electronic structure of hybrids. For instance, Amin et al. investigated the effects of molybdenum substitution in a wolframium-based cluster and confirmed the significant effect of this modification on the energies of the frontier orbitals of the hybrid [158].

The original WD POM structure is composed of two $[XM_3]$ moieties that form the cap (3x$[XM_3]$ per each cap) and two $[XM_6]$ moieties that form the belt (6x$[XM_6]$ per each belt). Both the cap and the belt can be modified and rotated resulting in six theoretical rotational isomers: α, β, γ, α*, β*, and γ*. As shown in the study of Contant and Thouvenot, the most stable form of these isomers is isomer α, and isomer α* is less stable (α > β > γ > γ* > β* > α*) [159]. The α-$[X_2M_{18}O_{62}]^{6-}$ anion is composed of two halves of $[XM_9]$; subsequently two isomers are formed: β and γ form at high temperatures; the β-isomer forms through a rotation by 60° around the axis leading through both heteroatoms X and the γ-isomer forms through a second rotation by 60° [100,147,160,161] (Fig. 6).

According to calculations by Zhang et al., among the six isomers α, β, γ, α*, β* and γ*, a form of D_{3h}-symmetric $M_{18}O_{54}$, where M=W, Mo, V, etc. cages, for α, γ and β* isomers, and a form of D_{3d}-symmetric $M_{18}O_{54}$ for β, α* and γ* isomers are possible. In addition, α, β and γ isomers incorporate two eclipsed D_{3h} anions, while α*, β* and γ* isomers encapsulate two staggered XO_4^{n-} D_{3d} anions [162]. In summary, the α and γ isomers have D_{3h} symmetry, α* and γ* have D_{3d} symmetry and β and β* have C_{3v} symmetry due to the mismatch of the inner anions and the outer cage, as confirmed in the report from Poblet's group [163].

Of the six isomers predicted by Baker and Figgis in 1970, only four isomers (α, β, γ, and γ*) have actually been observed [162,164]. It is noted that the incorporation of non-tetrahedral moieties into a WD structure (see Section 2.1) enhances the complexity of cap-rotational isomerism [162] which was underscored in a paper by Cronin's group with a WD species including trigonal-prismatic WO_6^{6-} moieties as heteroatoms, which confirmed the greatest stability for the γ isomer using DFT calculations, different from the stability of isomers in classic WD

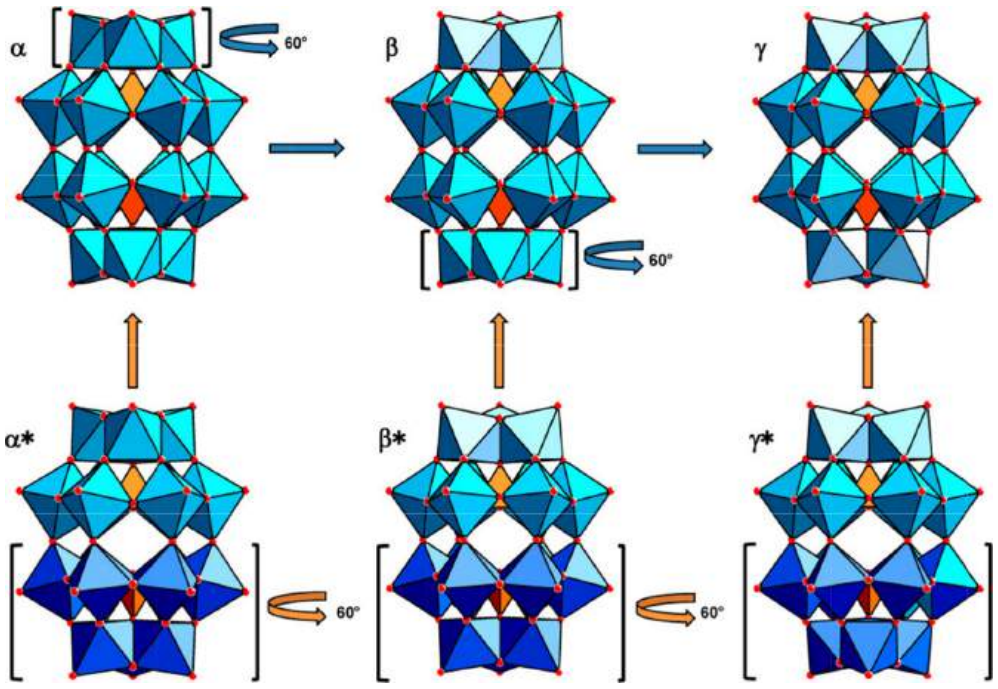

Fig. 6. Theoretical rotational WD POM isomers (α, β, γ, α*, β*, and γ*) and their structural relationships. Reproduced from [147] with permission of the copyright holders.

POMs [140]. It is difficult to obtain the most stable isomer α of a classic WD with the general formula $K_6[\alpha\text{-}P_2W_{18}O_{62}]\cdot 14H_2O$ with high purity by selective synthesis due to possible intermediate products [165]. In 2004, Nadjo's group reported the most successful synthesis of a highly pure α-isomer, $K_6[\alpha\text{-}P_2W_{18}O_{62}]\cdot 14H_2O$, and they produced over 200 g with more than 97% (by ^{31}P NMR) of the pure isomer α and with no side products other than isomer β [166]. Additionally, Graham and Finke again obtained $K_6[\alpha\text{-}P_2W_{18}O_{62}]\cdot 14H_2O$ using the synthesis method described by Nadjo's group and after one recrystallization they obtained a product with purity increased to 99% of isomer α [165]. Conducted over the years and by many research groups, the investigation into WD isomers confirms the hypothesis of Contant and Thouvenot [159] on the stability of individual isomers of classical WD species, with the following order of stability: $\alpha > \beta > \gamma > \gamma^* > \beta^* > \alpha^*$.

Possible structural modifications of classic WD POMs are shown in the scheme below (Fig. 7) and they are discussed in detail in sections that follow about the modification of cap and belt positions.

2.2.1. *CAP modification: Trilacunar modification*

One of the limitations of WD POM synthesis and their further functionalization is the presence of oxo groups on the WD POM surface which can only bind to a limited number of organic groups to form hybrid materials for further post-functionalization. Therefore, modification of the POM structure is extremely important. One of the most common types of WD modifications is the cap modification in which the WD POM structure, $[M_3P_2W_{15}O_{62}]^{n-}$, is composed of a $[\alpha\text{-}P_2W_{15}O_{56}]^{12-}$ precursor and M (M = V^V, Ta^V, Nb^V, etc.) [102,167–169]. Inarguably, due to the easier synthetic method, the size of the introduced metal ion and charge of the POM, high-valence *d*-block metal ions are usually used to modify the structure. Nonetheless, there are known examples of POMs in which low-valence *d*-block metal ions have been used to modify the original structure [167,170].

Among the aforementioned structural motifs, the most popular is the WD POM cap modified by vanadium ions, V^V (PWV). It is noted that this type of modification has a considerable impact on subsequent functionalization. Moreover, further functionalization is extremely important, given the limitations of the POM subunit itself, in particular poor chemical stability. The importance and usefulness of this type of modification are evidenced in the large number of publications reporting the synthesis and structure of PWVs [18,98,102,169,171–182]. The incorporation of three vanadium ions in the cap position of POMs adjusts photochemical and electrochemical properties, but most importantly it allows selective modification at the cap position with linkers, for instance using tris-alcohol organic derivatives or other organic groups. Here we report selected examples of vanadium-substituted WD POMs selected based on their potential in further post-synthetic modification. Cronin's group described a benchmark example of the PWV cluster, $TBA_5H_4[P_2V_3W_{15}O_{62}]$, which has been often used for subsequent functionalization with other linkers especially in terms of their single modularity, discussed in detail in Section 2.2 [18,171,172].

Furthermore, the presence of the V_3 cap in the POM structure contributes to sensitivity to external factors, for instance reducing agents, pH, and nucleophiles [102]. Arguably, due to the three capping vanadium atoms in the $[P_2V_3W_{15}O_{62}]^{9-}$ cluster PWV becomes an oxidant, and the WD POM cluster acquires catalytic properties [174,183]. Hence, the WD cluster with the vanadate cap is more reactive in comparison to the tungstate cap [173], which allows selective modification toward hybrid materials *via* post-functionalization, for instance connecting the WD POM with a chosen organic group through the M−O−C bond [102]. Interestingly, depending on the synthetic method a cluster with a different location of one, two or three V^v metal ions of the vanadium polyhedral can be obtained [183,184].

Tantalum is a different example of a high-valence metal ion which can be used for the cap modification of a WD cluster. It turns out that Ta^V incorporation in the WD POM cap results in enhanced reactivity due to an increased polyoxoanion charge and basicity of oxygen atoms bound to Ta^V [168]. The investigation into the effect of niobium, another metal from the fifth group of the periodic table, has been reported. Research confirms improved catalytic properties of $P_2W_{15}Nb_3O_{62}^{9-}$ in comparison to $P_2W_{18}O_{62}^{6-}$ and a high level of kinetic control obtained [185]. In addition, Xiao et al. reported a cluster consisting of three Nb_3POM units connected by four $[M(H_2O)_x]^{2+}$ groups as an example of a mixed POM with Lewis acid metal centers enhancing catalytic activity [186]. Moreover, apart from catalytic activities, a di-Nb^V substituted cluster of WD POM can effectively form coiled polymers not previously reported in the literature [187].

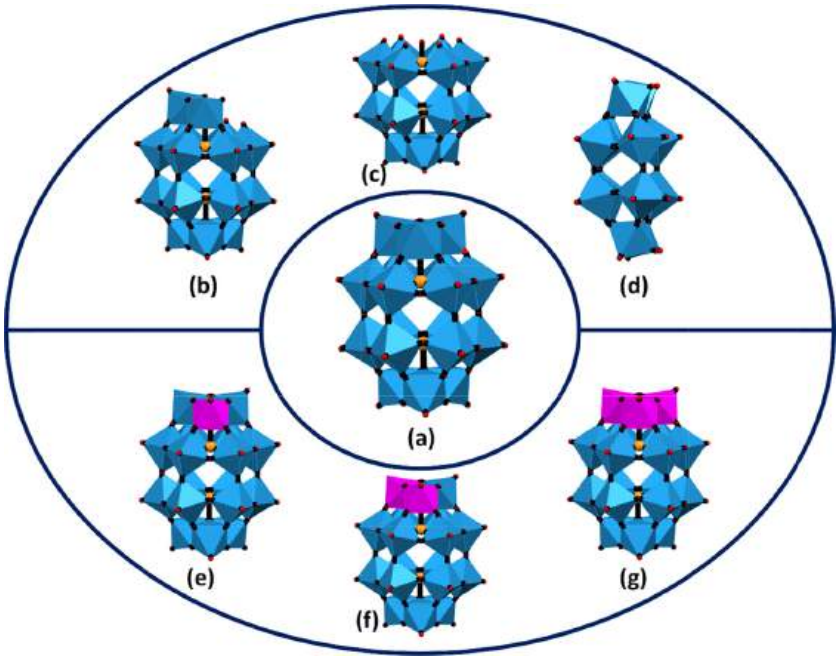

Fig. 7. Modified structures of WD POMs: (a) saturated WD, (b) mono-lacunary WD, (c) tri-lacunary WD, (d) *hexa*-lacunary WD, (e) mono-substituted WD, (f) bi-substituted WD, (g) tri-substituted WD.

To our knowledge, scientists reported examples of cap modification using a low-valence *d*-block metal ion (Co^{II}, Mn^{III}, Ni^{II}, Fe^{III}, Re^{IV}, Ti^{IV}) [103,167,188–193]. The substitution of the transition metal ion for tungsten increases the negative charge of the polyoxoanion, which results in improved catalytic ability and thermodynamical stabilization of the structure. An example of the $Mn_3^{III}Mn^{IV}$cluster can be mentioned in which a cuban-type system was obtained [188] with single molecule magnet (SMM) magnetic properties (Fig. 8a). Interestingly, it is possible to integrate the cuban type into a WD POM cluster lacunary POM, and while the structural Mn_4 core geometry is retained, an unexpected change in the sequence of the lowest magnetic levels causes transformation of the Mn_4 core into a high-spin system without observable slow magnetic relaxation [188].

An interesting example of cap modification was reported by Li et al. who synthesized a series of *hexa*-Ni-substituted WD POM clusters *via* a hydrothermal method (Figs. 8b-d). This technique significantly differs from the conventional synthesis technique of WD clusters and results in a shift from a thermodynamic product toward a kinetic one, owing to increased temperature and pressure, which shifts the above chemical equilibrium [190,191]. Three structures of modified WD POMs were determined via single-crystal X-ray and good stability of Ni_6 clusters was confirmed, in spite of changes in the cap position in the structure. All of those three systems are stabilized via ethylenediamine ligands or their methylated analogs and, noteworthy, the two clusters (the left and middle ones) are isolated compounds but the last one (on the right) is based on Ni_6-substituted WD POM segments, $[Ni(enMe)_2]^{2+}$ bridges and acetate anions. Interestingly, only for the latter were ferromagnetic magnetic interactions observed, thus confirming how important even subtle structural changes can be [190].

Noteworthy is also the structure of a transition metal-substituted POM $[M_3P_2W_{15}O_{62}]^{n-}$ (M = Ti^{IV}) [α-1,2,3-$P_2W_{15}(TiO_2)_3O_{56}(OH)_3]^{9-}$ due to the generation of multicenter octahedral TiO_6 active sites which can have semiconductive and photocatalytic properties [192]. Additionally, there is another example of a POM with substitution of W^{VI} atoms in a cluster by Ti^{IV} atoms forming giant "tetrapod"-shaped POMs composed of three main parts: four Ti_3-capped WD subunits, four bridging groups of octahedral $Ti(H_2O)_3$ and one encapsulated anion: Br^-, I^- or NO_3^- [103]. It is noted that similar giant "tetrapod"-shaped polyoxoanions can be obtained using a different transition metal substituent, such as Fe^{III}, with the formula $[KFe_{12}(OH)_{18}$(α-1,2,3-$P_2W_{15}O_{56})_4]^{29-}$, published by Cronin's group [193] (Fig. 8e).

POMs can also be combined into larger superstructures, as shown in a paper by Li et al. [194]. They used a synthetic concept based on exploiting the chemical nature of the boron atom in boronic acids (electrophilicity and electron deficiency) and features of metal-oxo groups in POMs (nucleophilicity and high electron density) to connect multiple WD POM anions $[M_3P_2W_{15}O_{62}]^{9-}$ (M = Ta^V or Nb^V) into POM-based nanostructures using aromatic boronic acid linkages, resulting in giant POM-based nanocapsules with diameters of up to 4 nm, internal cavities and unique high-symmetry architectures [194]. The same research group published other examples of a polymer based on covalently linked POM-organoboronic acid [195,196]. In 2021, they reported for the first time the preparation of polymers with high proton conductivity by the controlled covalent polymerization of Nb_3-WD POM and organoboronic acid monomers and the potential for using the resulting polymer as a solid proton conductor [195].

2.2.2. CAP modification: monolacunar modification

Apart from the widespread interest in tri-substituted WD POMs resulting from the ability to manipulate the building blocks, control the growth of the structure and modulate the functionalization process [193], there are many literature examples of mono-substituted WD POMs formed by the incorporation of metal ions with high Lewis acid strength, such as Mn^{III}, Ni^{II}, Co^{II} etc. [20,101,197], or a high coordination number, such as Zr^{IV}, Sn^{IV}, Hf^{IV}, Ln^{III} etc. [17,20,101,104,198–201], to form mono-lacunary WD POMs.

The first group of the ions (the first row transition metal ions) have a tendency to form monomeric POM structures as exemplified by $[Co^{II}(\alpha_2$-$P_2W_{17}O_{61})]^{10-}$, $[Ni^{II}(\alpha_2$-$P_2W_{17}O_{61})]^{10-}$, $[Cu^{II}(\alpha_2$-$P_2W_{17}O_{61})]^{10-}$ [20] and $[Mn^{III}(\alpha_2$-$P_2W_{17}O_{61}]^{9-}$ [197]. Interestingly, this first group of modifications tend to coordinate with the four terminal oxygen atoms in the lacunar site of the α_2-$[P_2W_{17}O_{61}]^{10-}$ unit in a planar manner due to the typical octahedral coordination expected for the first row transition metals, which may affect the less favorable applications of these systems compared to WD POMs mono-substituted by metal ions with a high coordination number described below [101].

On the other hand, transition metal ions, such as Zr^{IV}, Hf^{IV}, have enhanced Lewis-acid strength and additionally also have a high coordination number [101]. The incorporation of Zr^{IV}, Hf^{IV} metal ions into mono-lacunary WD POMs affects the biological properties of modified POMs (see also Section 6.4). Both Zr^{IV}-substituted and Hf^{IV}-substituted WD POMs exist in several forms: 2:2 dimers, 1:1 monomers and 1:2 species, as shown in Fig. 9 [101,198,199,202].

It is noted that the coordination of a lanthanide ion is more likely than that of the first row transition metal ion due to more flexible geometries and a higher coordination number. To the best of our

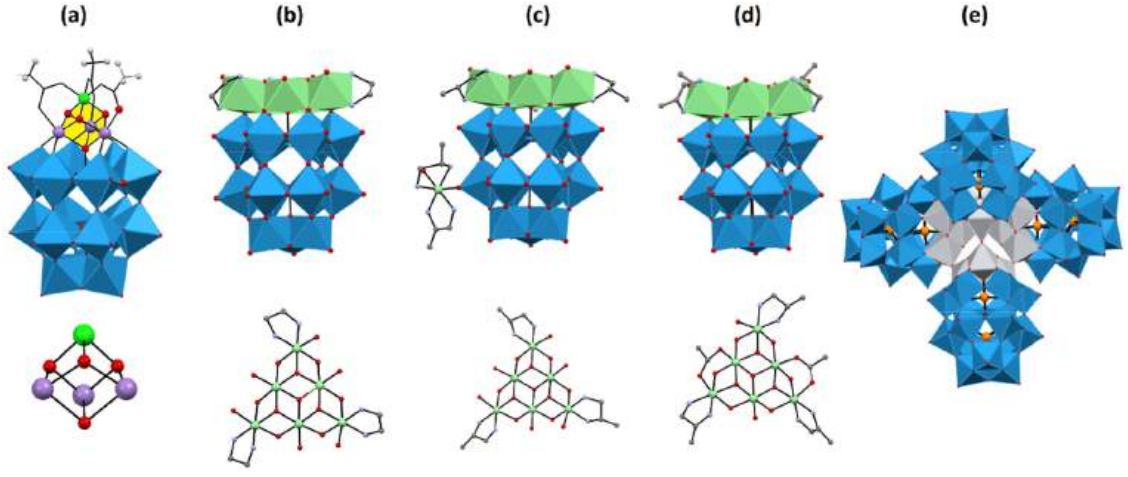

Fig. 8. Polyhedral representation and coordination environment of the (a) $[(\alpha$-$P_2W_{15}O_{56})Mn_3^{III}Mn^{IV}O_3(CH_3COO)_3]^{8-}$ cluster and (b-d) *hexa*-Ni cap in three clusters: (b) $[Ni_6(en)_3(H_2O)_6(\mu_3$-$OH)_3(H_3P_2W_{15}O_{56})]\cdot 14H_2O$; (c) $[Ni(enMe)_2(H_2O)][Ni_6(enMe)_3(\mu_3$-$OH)_3(H_2O)_6(HP_2W_{15}O_{56})]\cdot 10H_2O$; (d) $[Ni(enMe)_2]_3[Ni(enMe)_2(H_2O)][Ni(enMe)(H_2O)_2]$-$[Ni_6(enMe)_3(\mu_3$-$OH)_3(Ac)_2(H_2O)(P_2W_{15}O_{56})]_2\cdot 6H_2O$; (en = ethylenediamine; enMe = 1,2-diaminopropane; Ac = CH_3COO). (e) Polyhedral representation of giant "tetrapod"-shaped polyoxometalates $[KFe_{12}(OH)_{18}(\alpha$-1,2,3-$P_2W_{15}O_{56})_4]^{29-}$.

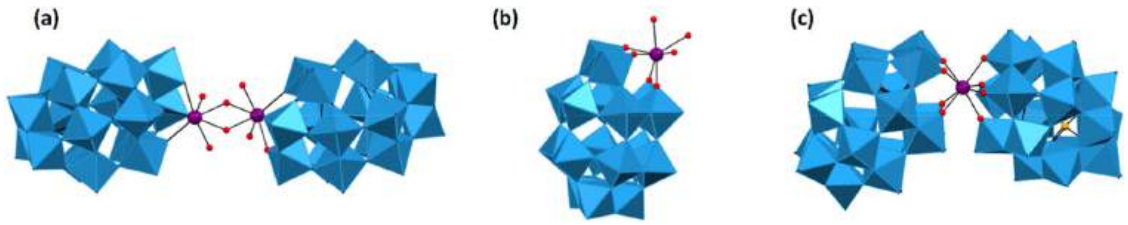

Fig. 9. Representative structures of Zr^{IV}-substituted and Hf^{IV}-substituted WD POMs in various forms: (a) 2:2 dimer; (b) 1:1 monomer and (c) 1:2 species.

knowledge, different monosubstituted $[Ln^{III}(\alpha_2\text{-}P_2W_{17}O_{61})_2]^{17-}$ WD POMs (Ln = La, Sm, Gd, Dy, Nd, Eu, Er, Ho, Lu, Ce, Pr) [101,104,203–216] have been reported. When comparing different lanthanide ions, slight variation in the distances in the structures of the published compounds between the metal ions and the nearest oxygen atoms is typical of the lanthanide contraction effect [203]. Interestingly, owing to those features, lanthanides are able to coordinate more than one subunit of mono-lacunary WD POMs and generate more complex structures [101,104,213–216]. It is also noted here that two different L and D isomers of the monosubstituted POM subunit can be obtained (Fig. 10a and Fig. 10b). In the dimeric form of POM clusters presented by Wang et al., two lacunary sites existed [200]. $Cs_{7.5}K_{0.5}[((H_2O)_7Dy^{III}_2(\alpha_2,\alpha_2'\text{-}P_2W_{16}O_{60})(C_6H_5PO)_2)_2]\cdot 42H_2O$ and $Cs_{7.5}K_{0.5}[((H_2O)_7Y^{III}_2(\alpha_2,\alpha_2'\text{-}P_2W_{16}O_{60})(C_6H_5PO)_2)_2]\cdot 42H_2O$ were synthesized in mild conditions to form one lacunar site (α_2) in one of the outer caps (Fig. 10c). Metal ion coordination (M = Dy^{III}, Y^{III}) and the phenylphosphonate induce the opening of the second lacuna (α_2') in the opposite cap. The resulting clusters assemble in a dimeric form connected via M^{III} cap-belt bridges [200] (Fig. 10d).

2.2.3. *Belt modification*

The second significant type of WD modification is related to the belt part, which sparks less interest among scientists than the above-noted cap modification, most plausibly due to more serious problems with the selective etching of XO polyhedra. This alteration involves the replacement of the WD metal ions (Mo^{VI}, W^{VI}) by surface heterometals such as Cu^{II} [110] (the most common strategy) and rarely by Co^{II} [217], Mn^{III} [218], etc. at the belt position. Xu et al. reported in 2012 a new WD isomer, δ-$[(WO_5)W_{17}Cu(H_2O)O_{65}]^{-}$, with considerable yields of 55%; they modified the belt site by Cu^{II} incorporation and formation of a $[WO_5]$ moiety with a square pyramid shape which causes a 45° rotation of the four-belt square-pyramidal $[CuO_5]/[WO_5]$ (Fig. 11) thus establishing a new type of WD isomerism involving rotation of the belt polyhedra, previously believed to remain unchanged. Jiao, et al. reported the first example of an isomer modified by the $[(WO_5)_3W_{14}Mn^{III}_2O_{44}Cl_2]^{12-}$ Jahn-Teller distortion δ-WD POM via the incorporation of two Mn^{III} ions which resulted in the formation of a square pyramid in the belt position. The resulting WD POM modified in the belt position using manganese ions, compared to the classical WD POM subunit, showed higher photocatalytic activity toward H_2 evolution [218].

In the literature, it can be noted that combined cap and belt modifications within the *hexa*-lacunary $[H_2P_2W_{12}O_{48}]^{12-}$ WD is also feasible, and it is characterized by the lack of the six octahedra, more precisely one from each cap position and two from each belt part of the structure [219–225]. Combination of *hexa*-lacunary WD POMs with transition metal and alkali metal ions usually leads to the formation of a macrocyclic tetramer of $[P_8W_{48}O_{184}]^{40-}$ [219,220,222,225] but dimers $[P_4W_{24}O_{94}]^{24-}$ [224], U-shaped trimers $[(PO_3OH)_2P_6W_{36}O_{136}]^{46-}$ [226] and cyclic trimers $[(H_2O)_3P_6W_{39}O_{147}]^{30-}$ [221,223] have also

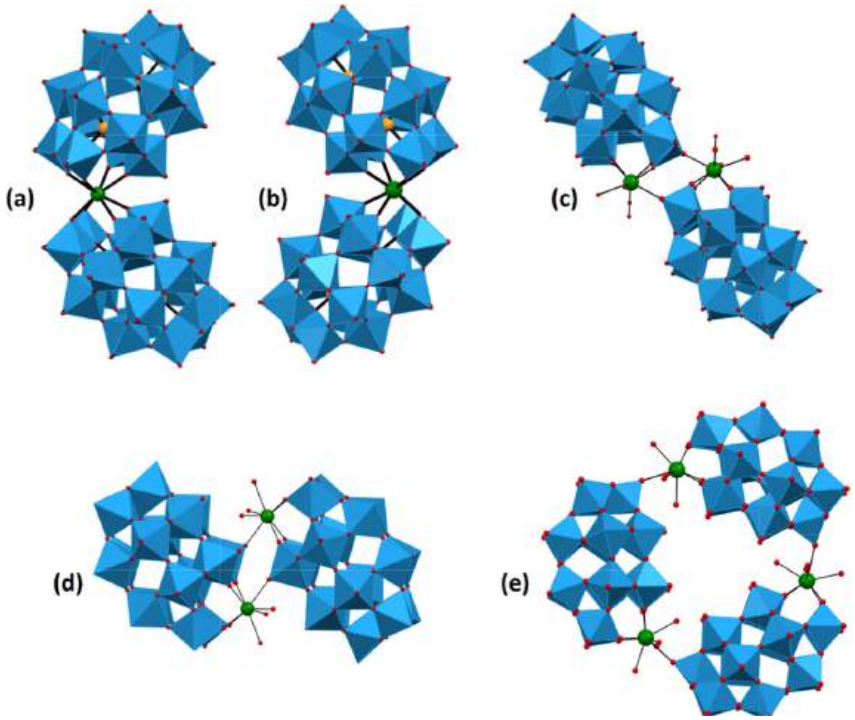

Fig. 10. Representative structures of lanthanide polyanion modifications of (a) L-isomers of cis-$[Ln^{III}(\alpha_2\text{-}P_2W_{17}O_{61})_2]^{17-}$, (b) D-isomers of cis-$[Ln^{III}(\alpha_2\text{-}P_2W_{17}O_{61})_2]^{17-}$, (c) "cap to cap", (d) "cap to belt", (e) 2:2 type dimeric and trimeric.

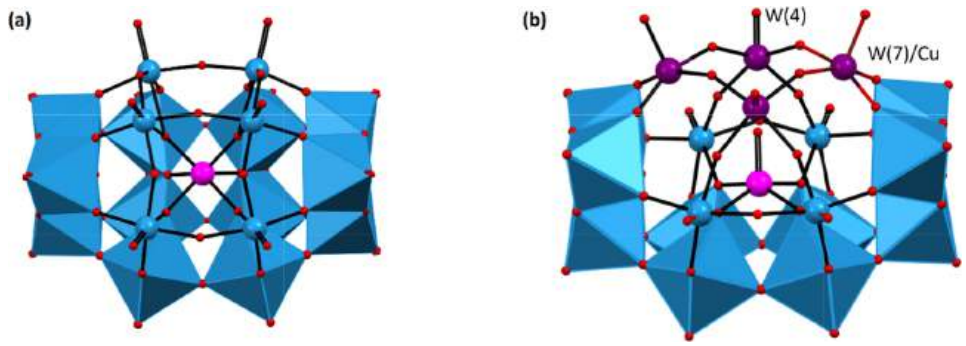

Fig. 11. Comparison of WD structures between the known isomer, (a) α-$[(WO_6)W_{18}O_{66}]^{10-}$ (color code: the central WO_6: pink; rest WO_6: blue octahedra), and the new isomer, (b) δ-$[(WO_5)W_{17}Cu(H_2O)O_{65}]^{-}$ (color code: the central WO_5: pink; the belt square-pyramidal metal atoms (W(4), W(7)/Cu) and their equivalents: purple; rest WO_6: blue octahedra), as an example of belt modification.

been reported (Fig. 12).

To summarize this section, WD POMs can be modified in several ways by removing atoms and forming lacunary WD POMs or substituting original atoms by other elements. Additionally, the reported syntheses allowed a better understanding of the formation mechanism of WD POM polyanions and provided new information on the design of new multifunctional materials that exhibit more effective properties (magnetic properties, photocatalytic activity toward H_2 evolution, electrocatalytic reduction of NO_x) through modification [100,218,220–223].

2.3. Non-conventional WD POM motifs

POM nanoclusters can undergo condensation in a variety of different ways, based on which they are classified into the archetypical POMs, including the classic WD system, as discussed above. Below, we report on the so-called non-conventional or non-typical WD systems which bear certain resemblance to the classical WDs but exhibit enough structural integrity and differences that a separate section is needed.

2.3.1. Open WD POMs

Open WD POMs are an example of the non-conventional modification of POM structures. They are formed by the fusion process of two trivacant Keggin-type $[\alpha\text{-}SiW_9O_{34}]^{10-}$ polyoxoanion units combined *via* W-O-W bonds. The most common in the literature are open WDs containing silicon as the heteroatom, characterized by the ease of capturing transition metal ions in the pocket between the two trivacant Keggin units or as an open container for metals [105]. In these modified compounds five metal atoms are commonly introduced which are paramagnets [106–108,227], such as Mn^{II}, Fe^{III}, Co^{II}, Ni^{II}, Cu^{II}, Zn^{II}, Al^{III}, Ho^{III}, Gd^{III}, Ga^{III}, etc., but modifications are known in which their number is two [228,229], three [105], four [230] or rarely more than five [106] (Fig. 13). The first example of an open WD was reported by Laronze et al. in 2003: the pocket contained potassium and two copper ions [228]. After one year, Kortz's group announced the first example of polyoxotungstate with five Cu^{2+} ions incorporated into the pocket between two Keggin units [227]. In the following years, papers began to appear with further novel open WD POMs in which the effect of

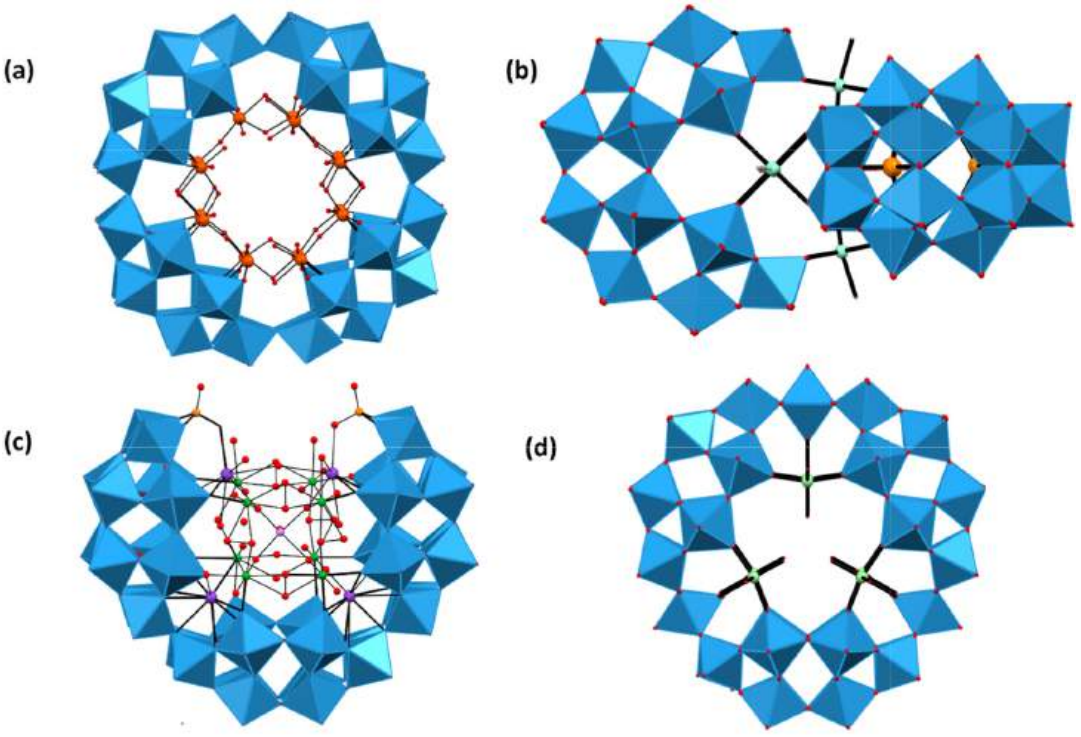

Fig. 12. Combined polyhedral/ball-and-stick representation examples of (a) a macrocyclic tetramer of a WD POM $[P_8W_{48}O_{184}Fe_{16}(OH)_{28}(H_2O)_4]^{20-}$; (b) dimers $[P_4W_{24}O_{94}]^{24-}$; (c) U-shaped trimers $[(PO_3OH)_2P_6W_{36}O_{136}]^{46-}$ and (d) cyclic trimers $[(H_2O)_3P_6W_{39}O_{147}]^{30-}$.

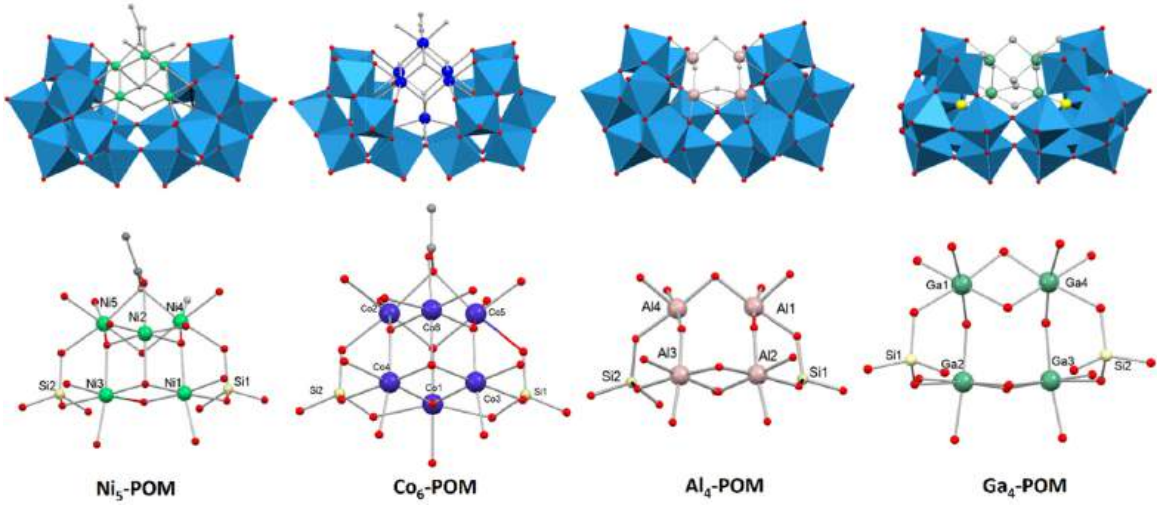

Fig. 13. Polyhedral representations and partial structures of the center of metal ions: Ni_5-POM: $Na_2(C_3N_2H_{12})_4([Ni_5(OH)_3(H_2O)_4(CH_3CO_2)]$-$[Si_2W_{18}O_{66}])\bullet 12.5H_2O$, Co_6-POM: $(C_3N_2H_{12})_3([Co_2^{II}\ CO_4^{III}(OH)_5(H_2O)_2(CH_3CO_2)]$-$[Si_2W_{18}O_{66}])\bullet 6H_2O\bullet(C_3N_2H_{10})$, Al_4-POM: $K_{10}([Al_4(m\text{-}OH)_6([a,a\text{-}Si_2W_{18}O_{66}])\bullet 28H_2O$ and Ga_4-POM: $K_{10}([Ga_4(OH)_6([a,a\text{-}Si_2W_{18}O_{66}])\bullet 28H_2O$.

increasing the opening angle of the $[Si_2W_{18}O_{66}]^{16-}$ open WD skeleton was proved, affecting magnetic properties, and magnetization measurements showed that the multi-metallic core of metal ions in open WD POMs induced strong antiferromagnetic interactions [106,108].

Wang's group reported an interesting example of two open WD POMs: they constructed S-shaped tetrameric germanotungstates with cobalt and nickel in the open pocket in a two-step synthetic procedure shown in Fig. 14. In addition, it is noted that both compounds in the solid state and in aqueous solution had almost identical Raman spectra, confirming the stability of the studied compounds in solution. In addition, the ESI-MS spectra of negative ions and UV spectra showed that both open WD compounds remained stable over a wide range of pH values of 2.7–9.3 and 2.6–9.8, respectively, suggesting their broad applicability [231].

In addition to the incorporation of transition metals into the pocket in the open system of a WD, the introduction of *f*-block metals has been reported in the literature. In 2011, Patzke's group reported five examples of lanthanoid-containing silicotungstates $[Ln_2(H_2O)_7Si_2W_{18}O_{66}]_n^{10n-}$ (Ln = Gd^{III}, Tb^{III}, Ho^{III}) and an example with $Dy^{III}[Dy_2(H_2O)_{6.5}(C_2H_4O_2)_{0.5}Si_2W_{18}O_{66}]_n^{10n-}$ [145]. The challenge is to obtain open-system WD POMs containing metal ions from the *p*-block, for instance Al^{III} and Ga^{III} ions, in their structures, and this was first described in 2016 by Nomiya's group [230]. These are difficult to obtain due to synthetic and structural problems. Arguably, interactions between oxygen atoms in the open WD units and potassium cations in the crystal structures of the Al_4- and Ga_4-open structures play a pivotal role in the formation of open WDs with aluminum and gallium ions [230].

2.3.2. *Sandwich-type WD POMs*

Sandwich-type POMs are a large group of transition metal-substituted POMs derivatives (TMSPs) with applications in many areas, e.g. catalysis, biology and materials science [113,167,232–234]. Five principal families of POMs with a sandwich-type arrangement are known, and four of them are derivatives of the trivacant Keggin type polyoxoanion and one is a derivative of the WD structure (Fig. 15). The first group of the four modifications are formed by the combination of two trivacant types: $MW_9O_{34}^{n-}$ or $MW_9O_{33}^{n-}$ (M = Fe^{III}, Cu^{II},Co^{II}, Zn^{II}, P^V, As^{III}, As^V, Si^{IV},Sb^{III}, Bi^{III}, Se^{IV} or Te^{IV}), while the fifth modification consists of two encapsulated units of trivacant α-$X_2W_{15}O_{56}^{12-}$ (X = As^V or P^V) with potential incorporation of transition-metal cations between two subunits (M = Mn^{II}, Fe^{III}, Co^{II}, Ni^{II}, Cu^{II}, Zn^{II}, and Cd^{II}), forming compounds of the formula $[M_4(H_2O)_2(P_2W_{15}O_{56})_2]^{n-}$.The latter are among the most thoroughly described systems by virtue of easy ^{31}P NMR analysis [232,235–238].

In 1983, Finke and Droege reported the first example of a sandwich-type POM with the formula $P_4W_{30}M_4(H_2O)_2O_{112}^{16-}$ (M = Co^{II}, Cu^{II}, Zn^{II}) [239] which resulted in a rapidly developing group of non-conventional POMs owing to their catalytic and physicochemical properties that are attracting increased interest [235]. The presence of subunits in the form of a tetranuclear cluster $[M_4O_{14}(OH_2)_2]$ where water molecules are attached to the center of the cluster improves the effectiveness of the compounds in applications in electrochemistry, catalysis and materials science [113,117,236,240]. Ruhlmann et al. reported sandwich-type WD POMs with a tetranuclear cluster with Co^{II} forming complex ββ-$[Co_4(H_2O)_2(P_2W_{15}O_{56})_2]^{16-}$ at low pH (pH~3) for which isomers

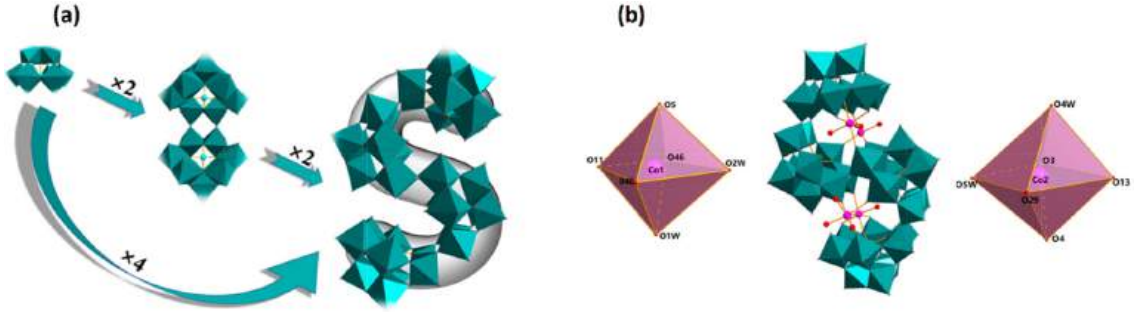

Fig. 14. Scheme of S-shaped tetrameric germanotungstates (a) and polyhedral/ball-and-stick scheme of the $K_{10}H_{10}([Co\text{–}(H_2O)_2]_2[Co(H_2O)_3]_2(Ge_4W_{36}O_{130}))\cdot 32H_2O$ polyanion (b). Reproduced from [231] with permission of the copyright holders.

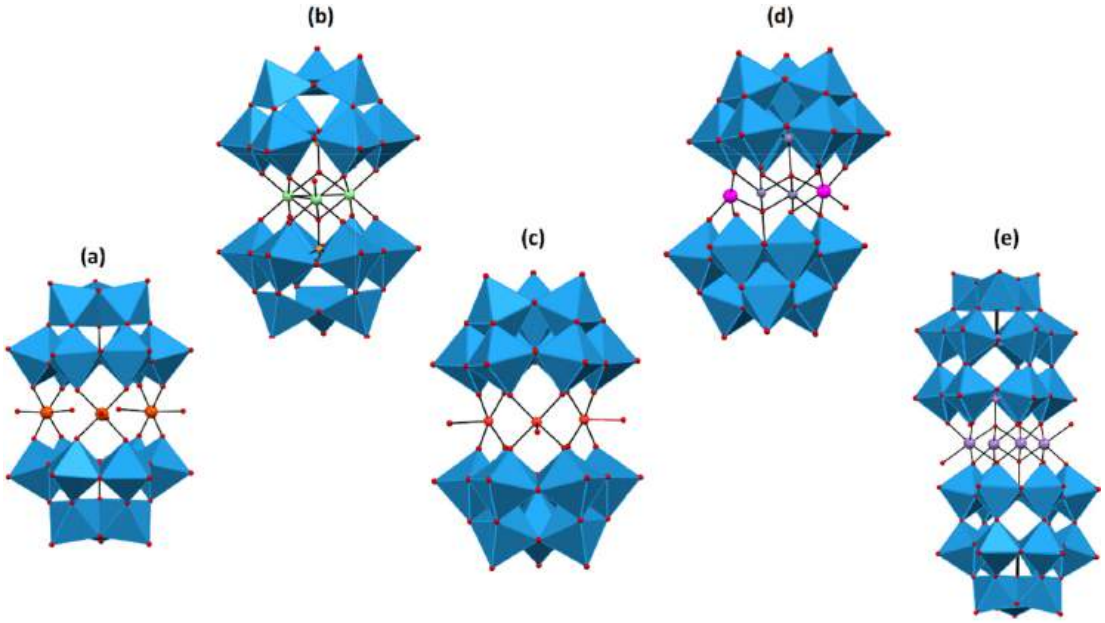

Fig. 15. Polyhedral representations of the five principal families of POMs with the sandwich-type arrangement: conventional A-type Keggin sandwich; conventional B-type Keggin sandwich; B-type Keggin sandwich with pyramidal heteroatoms; Tourné B-type Keggin sandwich (transition metal heteroatoms); WD sandwich.

based on α-$[P_2W_{15}O_{56}]^{12-}$ units and relationships between them are presented in Fig. 16. The type of connectivity (ββ, αβ or αα) depends on synthesis conditions (pH, concentration, ratio of TM to trivacant moieties), and the number and nature of transition metal ions in the central sheet. Moreover, in connection with the lability of Na^+ (due to sodium salts in aqueous solution) and their weak binding to the POM unit $Co_4(P_2W_{15})_2$ (blue frame), monovacant $NaCo_3(P_2W_{15})_2$ (violet frame) and divacant $Na_2Co_2(P_2W_{15})_2$ (yellow frame) lacunary species can be

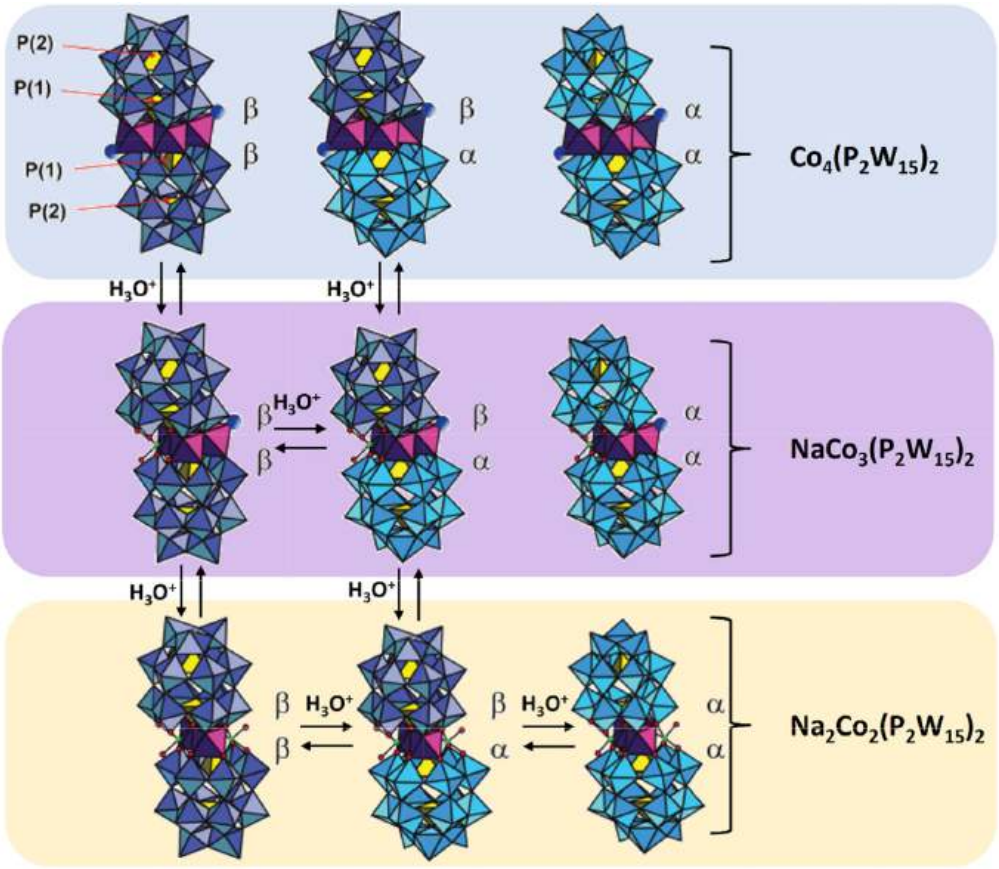

Fig. 16. Relationships between isomers of different sandwich-type WD POMs with cobalt-based α-$[P_2W_{15}O_{56}]^{12-}$ subunits. Reproduced from [235] with permission of the copyright holders.

distinguished. The interconversion between the isomers is strongly influenced by the pH value, which has been investigated using ^{31}P NMR, UV–Vis spectroscopy and electrochemistry. In a medium at pH of more than 3.5, αβ-$Co_4(P_2W_{15}O_{56})_2$, ββ-$Co_4(P_2W_{15}O_{56})_2$ and αβ-$NaCo_3(P_2W_{15})_2$ are stable but, interestingly, the $Na_2Co_2(P_2W_{15})_2$ they obtained underwent isomerization. On the other hand, isomerization of αβ-$Co_4(P_2W_{15}O_{56})_2$ *via* αβ-$NaCo_3(P_2W_{15})_2$ to ββ-$Co_4(P_2W_{15}O_{56})_2$ was observed in lower pH in a range from 2.5 to 3.5.

It is noted that complexes based on electrostatic interactions between zinc tetracationic porphyrin $[ZnTMePyP]^{4+}$ and the aforementioned sandwich-type WD $[M_4(H_2O)_2(P_2W_{15}O_{56})_2]^{n-}$ containing four transition metal ions are known [241–243]. Shaming et al. reported films formed *via* the layer-by-layer method between different porphyrins, $[ZnTMePyP]^{4+}$or $[ZnOEP(py)_4]^{4+}$, and tetracobalt WD sandwich POMs with the formula αββα-$[Co_4(H_2O)_2(P_2W_{15}O_{56})_2]^{16-}$ useful in photocatalysis [242].

3. Solution and pH speciation in solution

In aqueous solution, numerous and highly negative-charged species are most frequently formed, hence the determination of dominant POM species is difficult. Therefore, individual speciation profiles need to be investigated in applications in a specific solution [244,245] (Fig. 17).

Stability studies by Contant and Thouvenot show that only the α-isomer of a WD POM is stable in aqueous solution and all the other isomers undergo transformation to the α-isomer in the order of $\gamma \rightarrow \beta \rightarrow \alpha$ [159]. In addition, the rate of WD POM hydrolysis is also dependent on the counterions and follows the trend of $K^+ > Na^+ > Li^+$ [244].

The common structure of WD POMs with the general formula $[P_2^VW_{18}^{VI}O_{62}]^{6-}$ is stable in acidic media at pH lower than 6 and it degrades at higher pH forming three different species such as mono-lacunary $[P_2^VW_{17}^{VI}O_{61}]^{10-}$, tri-lacunary $[P_2^VW_{15}^{VI}O_{56}]^{12-}$ and *hexa*-lacunary $[H_2P_2^VW_{12}^{VI}O_{48}]^{12-}$ WDs [244,246]. The aforementioned studies from 1985 were also confirmed in the other paper in which Mbomekalle et al. reported that within the POM of the WD family, compounds with the formula $[X_2W_{18}O_{62}]^{6-}$ (X = P^V or As^V) in acidic media were stable but monolacunary WD POMs with the formula $[X_2MW_{17}O_{61}]^{n-}$ (X = P^V or As^V) were more stable in higher pH [232]. Moreover, the pH value also affects the formation of functionalized structures and is associated with partial or complete transformation from trivacant P_2W_{15} with the formula α-$[P_2W_{15}O_{56}]^{12-}$ into rarely occurring divacant P_2W_{16} with the formula α-$[P_2W_{16}O_{57}]^{8-}$ [247,248] (Fig. 18a). Interestingly, formed by *hexa*-lacunary species, the macrocyclic tetramer of $[P_8W_{48}O_{184}]^{40-}$ is stable at lower pH at a range from 1 to 8 [244,246]. The mutual transformations of the different forms of WDs depending on the environment are shown in Fig. 18b.

Moreover, as can be seen in Fig. 19, WD formation depends on the [Mo]/[P] ratio and slows down as the [Mo] to [P] ratio increases. In addition, in an acidic environment, comparing solutions immediately after preparation ("fresh") with solutions after up to one month ("aged"), it can be seen that in"fresh" solutions, only the Keggin POM polyanion with the formula $[P^VMo_{12}^{VI}O_{40}]^{3-}$ is found, and no polyanion of the WD type is observed, but after some time in the"aged" solution, both in the case of the [Mo]/[P] ratio = 9 and [Mo]/[P] = 12, a polyanion of the formula $[P_2^VMo_{18}^{VI}O_{62}]^{6-}$ is formed. In addition, for observable anions formed in a pH range of from 6 to 8, a relationship can be seen, arising from the balance of anions $[HP^VO_4]^{2-}$ and $[P^VO_4]^{3-}$ whose occurrence is independent of the [Mo]/[P] ratio and of whether the solution is "fresh" or "aged" [249,250].

4. Ionic interactions with counter-cations

Crucial for the self-assembly, solubility, stabilization and function of POMs are the mutual interactions between anionic POMs and organic or inorganic cations [8,251]. Therefore, papers have been published that show the effect of the type of cation and solvent on self-assembly and, consequently, on applications. Given the effect of cations and solvent on the structure in Anderson-Evans POMs [252], it is expected that it is

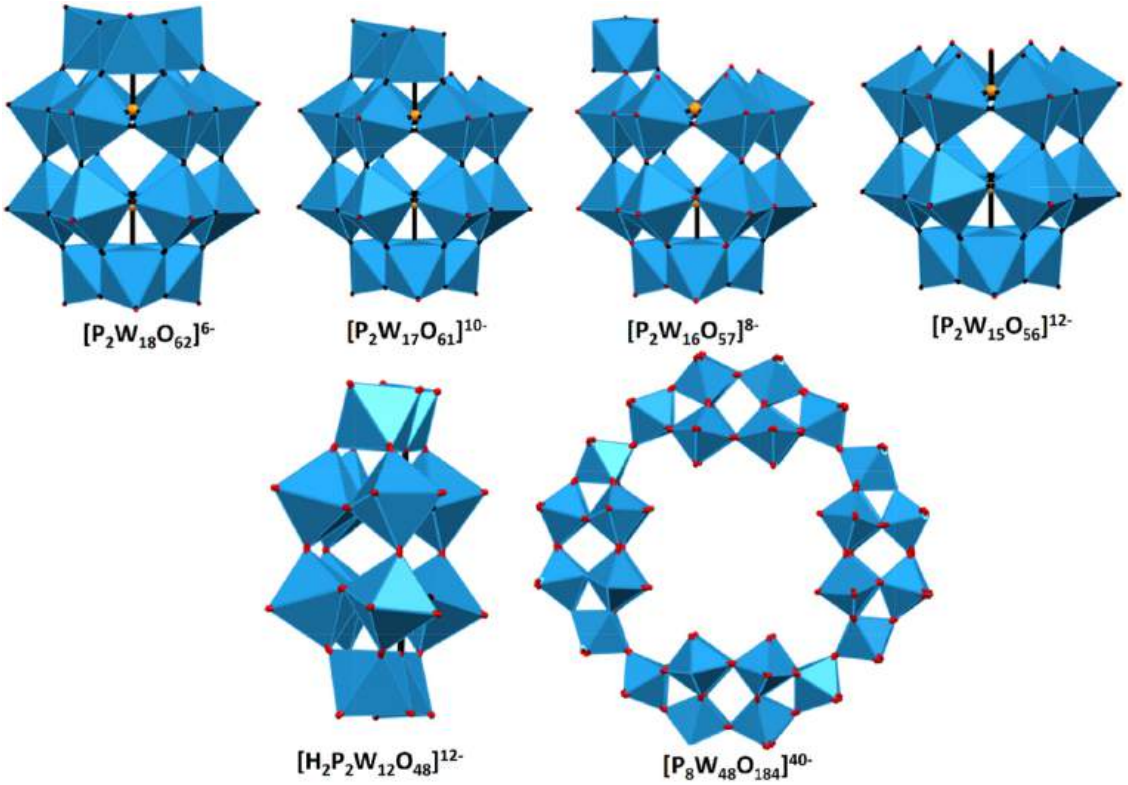

Fig. 17. Polyhedral representation of the classical structure of the $[P_2W_{18}O_{62}]^{6-}$ WD POM and its species such as mono-lacunary $[P_2W_{17}O_{61}]^{10-}$, di-lacunary $[P_2W_{16}O_{57}]^{8-}$, tri-lacunary $[P_2^VW_{15}^{VI}O_{56}]^{12-}$, *hexa*-lacunary $[H_2P_2^VW_{12}^{VI}O_{48}]^{12-}$ and the macrocyclic tetramer of $[P_8W_{48}O_{184}]^{40-}$.

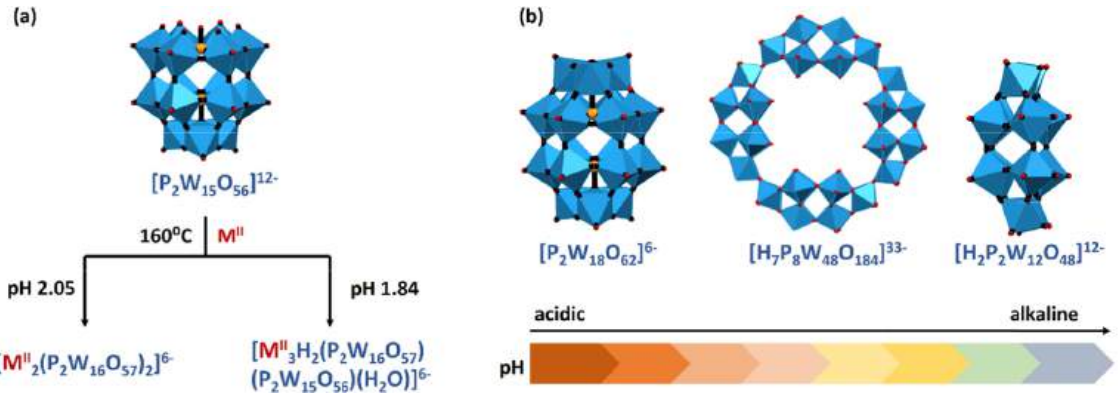

Fig. 18. Scheme of (a) in situ transformation of the trivacant to the divacant form of WD POMs (M^{II} – transition metal ion); (b) hydrolytic transformation of $[P_2^VW_{18}^{VI}O_{62}]^{6-}$ with an increasing pH value.

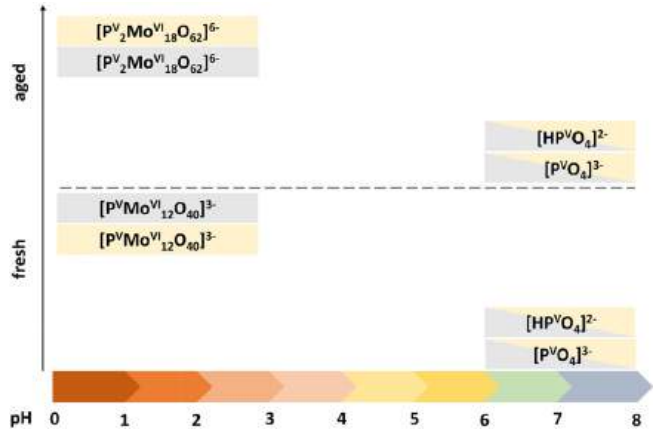

Fig. 19. Scheme of the speciation of selected phosphomolybdates ($[P_2^VMo_{18}^{VI}O_{62}]^{6-}$, $[P^VMo_{12}^{VI}O_{40}]^{3-}$, $[HP^VO_4]^{2-}$ and $[P^VO_4]^{3-}$) in fresh prepared and aged (up to 1 month) aqueous solution with a ratio of [Mo]/[P] = 9 (gray filling) and [Mo]/[P] = 12 (yellow filling) in specific pH ranges corresponding to the width of the filling.

similar for WD POMs, but to the best of our knowledge, this requires further research to be confirmed. The self-assembly process of polyanionic POMs can result from their association with the long chains of alkyl-constituting hydrophobic tails. In the literature the amphiphilic feature of POM hybrids is discussed, which may affect the formation of surfactant-encapsulated POMs (SEPs) [9,21]. To the best of our knowledge, WD POMs can form only one type of the molecular structure of amphiphilic POMs, such as classical 'head-tail'-type surfactants (Fig. 20a). Various amphiphilic structures of hybrid-POMs can be distinguished depending on the shape and packing parameter of the surfactant, such as micelles, vesicles and bilayers which can be observed using microscopy analyses, for instance STM, TEM, etc. (Fig. 20b) [9].

5. Post-functionalization approaches as a means to forming hybrid WD POM assemblies

Hybrid POM platforms, also known as hybrid POM scaffolds, are compounds that consist of reactive organic groups or sites of ligand-like species combined with POMs *via* covalent, ionic, hydrogen and coordination bonds, etc. [2,3,94,253–256]. In addition, these systems can be used as building blocks in further functionalization aimed to obtain discrete or network materials. The possibility of forming such modified compounds prompted a lot of research groups to develop hybrid POM materials using subsequent organic groups, such as amide, sulfonamide, ester, and thioester groups, and based on organic reactions (Huisgen, Sonogashira, Suzuki coupling, polymerization, metal coordination, etc.) [2] (Fig. 21, Table 2). In essence, two main groups of WD POM functionalization can be distinguished: the first group based on single-linker modularity and the other one based on double-linker modularity, each of which divided into several subgroups.

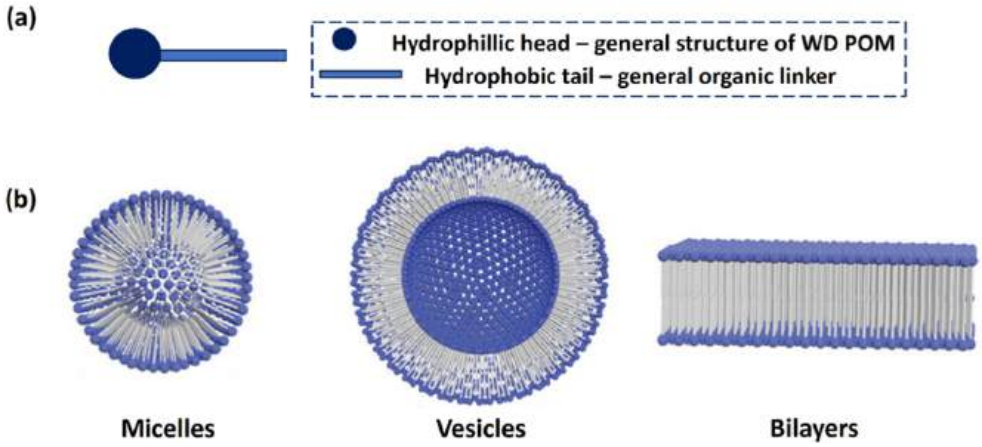

Fig. 20. (a) Scheme of a representative example of the classical 'head-tails' type of WD surfactant. (b) Representative examples of various types of the amphiphilic POM structure: micelles, vesicles and bilayers. Partially reproduced from [9] with permission of the copyright holders.

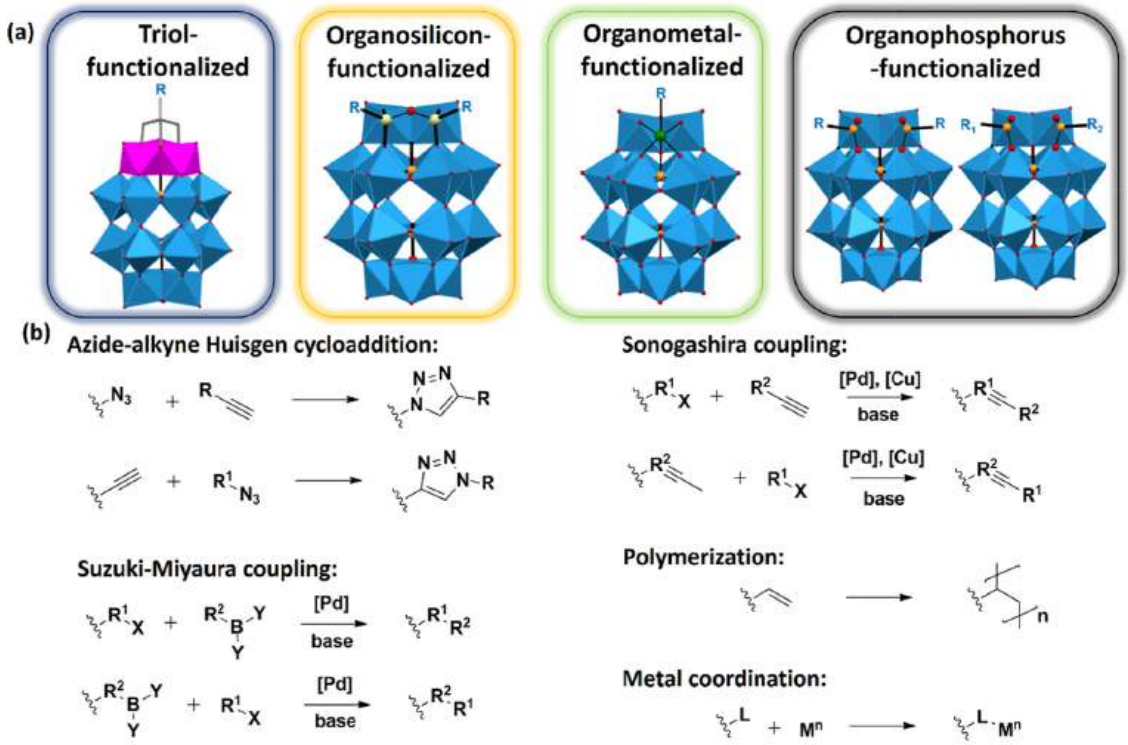

Fig. 21. (a) Selected most commonly studied hybrid WD platforms and functionalization strategies. (b) Typical post-functionalization reactions based on WD POM subunits, where R, R^1, R^2 = organic moieties; X = halogen; BY_2 = organoborane; L = ligand; M^n = metal ion.

5.1. Single-linker modularity

The first main group of WD POM functionalization (single modification) constitutes a vast group leading to diverse structural hybrid materials with interesting applications. The incorporation of organic moieties into POM backbones ensures facile structural modifications aimed at obtaining anticipated compounds with specific properties [17,174,254–256,258] (Fig. 22).

5.1.1. Trilacunary WD POMs

POMs with organic groups introduced into the cap site are more frequently reported, especially WD tri-vanadium substituted POMs (V_3POM) due to the easy modulation of structure, stable WD POM scaffolds for the incorporation of redox-active vanadium centers and expanded properties [174,275]. It is noted that the presence of the V_3 substituent improves oxidative properties, thus providing more opportunities in biological [254] and catalytical applications [174]. The major way to this functionalization is the generation of a M−O−C bond connecting the WD POM and an organic group from the second substrate [102]. In 1993 Hill and Hou reported the first alkoxy-POMs obtained through functionalized POMs *via* the tris(hydroxymethyl) group [276]. Owing to the functionalization of the cap site *via* tris-alcohol organic derivatives these compounds can be used as building blocks leading to the formation of hybrids via covalent functionalization [173,177,181,254,255,258]. Since the pioneering publication, many papers have been published on using this modification method, and after 16 years, a paper reporting on the modification of the previously developed method appeared in 2009. The new procedure made it possible to insert an organic compound with two hydroxyl groups and an amide group. This work paved the way for new modifications by substituting the POM with carbonyl oxygen from the amide group, making it possible to communicate electron effects between the organic group and the inorganic unit (POM) [175] (Fig. 23). Since 2009, a large number of approaches that use this functionalization to obtain particular hybrids can be found in published works. Dridi et al. reported a series of novel POMs modified with spironaphthoxazine and spiropyran derivatives [176]. Riflade et al. showed an example of a tri-substituted WD POM modified with picolinamide-diols and formation of a pincer complex using palladium as the catalyst for Mizoroki-Heck coupling [178]. It is noted that not only the amide group is inserted to the POM structure but also different organic groups with carbonyl moieties are used, such as carbamates, thiocarbamates, ureas etc. [174]. Vilona et al. reported several functionalized WD POMs with inserted urea groups and they proved that carbonyl incorporation to WD building blocks caused activation of the urea toward H-bond catalysis [277]. It is noted that Santoni et al. used WD species substituted by the dipyridyl group for complexation with Re^I that resulted in the formation of a covalently bond hybrid material [180].

Grafting linear ligands, such as bis(TRIS), tris(TRIS) etc., onto V_3-capped WD POM leads to the formation of a separate class of hybrids. These materials consist of two or more $[P_2V_3W_{15}O_{62}]^{9-}$ units and depending on the amount of subunits known as dumb-bells (two units), triangular (three units) (Fig. 24) and higher species can be obtained which are the most frequently reported by Hill, Hasenknopf and Cronin groups and the main reason for the interest in this class of hybrids is their amphiphilic properties [18,171,278].

An example of the dumbbell modification linked by the bipyridine subunit has been reported by Cronin's research group; they reported a bipyridine-based dumbbell WD hybrid coordinating Zn^{2+}. Interestingly, they proved formation of a *trans*-dumbbell WD species and transformation to the *cis* form of the hybrid in DMSO solution upon the coordination of Zn^{2+} ions, which returned to the original form after adding EDTA which removed Zn^{2+} ions. The authors suggested that this transformation could be further used to manipulate its self-assembly behavior, which arguably mimicked the behavior of protein folding and assembly under the guidance of metal ions [279] (Fig. 25).

5.1.2. Monolacunary WD POMs

A single modification of the WD POM structure includes functionalization by organic groups connected not only with the trilacunary but

Table 2
Representation of functionalized WD hybrids with organic functional groups or metal centers.

General formula of the modularity	General formula of the compound	Ref.
$[P_2W_{15}V_3O_{59}((\mathbf{OCH_2})_3\mathbf{CNH\text{-}CO\text{-}R})]$	$[P_2W_{15}V_3O_{59}(OCH_2)_3C_{11}H_9N_4O]^{6-}$ $[P_2V_3W_{15}O_{59}(OCH_2)_3CNHCOC_{15}H_{31}]^{6-}$ [COHNC $(CH_2O)_3P_2V_3W_{15}O_{59}(C_{44}H_{29}N_4)]^{6-}$ $TBA_{10}H_2[(P_2V_3W_{15}O_{59}(OCH_2)_3CNHCO)_2]$ $TBA_5H[P_2W_{15}V_3O_{62}(C_{20}H_{17}N_4O)]$ $TBA_4H_2[C_{12}H_9O_4NHC(CH_2O)_3P_2W_{15}V_3O_{59}]$ $TBA_5H[C_{16}H_{16}N_3O_{63}P_2V_3W_{15}]$ $TBA_5H[C_{19}H_{16}N_3BrO_{66}P_2ReV_3W_{15}]$ $TBA_5H[P_2V_3W_{15}O_{59}((OCH_2)_3CNHCO(CH_3)C{=}CH_2)]$ $TBA_5H[P_2V_3W_{15}O_{66}C_{19}H_{16}N_3ReBr]$	[102,173,257,171,258,177,180,180,181,259]
$[P_2W_{15}V_3O_{59}((\mathbf{OCH_2})_3\mathbf{C\text{-}R})]$	$TBA_{10}H_2[(P_2V_3W_{15}O_{59}(OCH_2)_3CCH_2)_2O]$ $TBA_{10}H_2[C_7H_{14}O_4C(CH_2O)_3P_2V_3W_{15}O_{59}]$ $TBA_5H_2[C_2H_4OC(CH_2O)_3P_2V_3W_{15}O_{59}]$ $TBA_5[HP_2V_3W_{15}O_{59}((OCH_2)_3CCH_2OCH_2C_6H_4I)]$	[171,98,98,260]
$[P_2W_{15}V_3\text{-}\mathbf{SP}])$	$TBA_5[(P_2V_3W_{15}O_{59}(OCH_2)_2C(Et)\text{–}NHCO(C_{20}H_{19}N_2O_3))]$	[176]
$[P_2W_{15}V_3O_{59}((\mathbf{OCH_2})_2\mathbf{(R)\text{–}CNH\text{-}C(=)\text{-}R'})]$	$TBA_{5.95}H_{0.05}[C_{22}H_{21}N_3O_{62}P_2V_3W_{15}]$ $TBA_5[P_2V_3W_{15}O_{59}((OCH_2)_2C\text{–}(Et)NHC(=O@POM)R)]$	[261,262]
$[P_2W_{17}O_{61}(\mathbf{Sn\text{-}R})]$	$[P_2W_{17}O_{61}SnCH_2CH_2C(=O)]^{6-}$ $[P_2W_{17}O_{61}SnCH_2CH_2C(=O)NHCH_2\text{-poly(N,N-diethylacrylamide)}]^{7-}$ $TBA_7[P_2W_{17}O_{61}(Sn(CH_2)_2C(O)NH(CH_2)_3(N_3C_2H)CH_2OC(O)C(CH_3)_2SC(S)SC_{12}H_{25}]$ $TBA_7[\alpha_1\text{-}P_2W_{17}O_{61}(Sn(CH_2)_2C(O)NH(CH_2)_3N_3)]$ $TBA_7[\alpha_2\text{-}P_2W_{17}O_{61}SnCH_2CH_2CON(CH_2)_5]$ $[P_2W_{17}O_{61}(SnCH_2CH_2COOH)]^{7-}$	[17,263,264,264,265,266]
$[P_2W_{16}O_{59}(\mathbf{Zr\text{-}R})]$	$Na_{14}[Zr_4(P_2W_{16}O_{59})_2(_{\mu3}\text{-}O)_2(OH)_2(H_2O)_4]\cdot 57H_2O$	[267]
$[P_2W_{17}O_{61}(\mathbf{O(Si\text{-}R)_2})]$	$[P_2W_{17}O_{61}(PhSi)_2O]^{6-}$ $[P_2W_{17}O_{61}(O(Si\text{-}C_{29}H_{18}N_3)_2)]^{6-}$ $TBA_6[\alpha_2\text{-}P_2W_{17}O_{61}(SiC_6H_4CH_2N_3)_2O]$ $TBA_6[P_2W_{17}O_{62}(Si\text{-}PhI)_2O]$ $TBA_6[P_2W_{17}O_{61}(Si\text{-}Ph\text{-}ethynyl\text{-}TMS)_2O]$ $TBA_6[P_2W_{17}O_{61}(Si\text{-}Ph\text{-}ethynylpyrene)_2O]$ $TBA_6[P_2W_{17}O_{61}(Si\text{-}Ph\text{-}acetylene)_2O]$ $TBA_6[P_2W_{17}O_{61}(SiC_3H_6\text{-}I))_2O]$	[268,19,269,270,270,270,270,271]
$[P_2W_{17}O_{61}(\mathbf{P(O)\text{-}R})_2]$	$TBA_6[\alpha_2\text{-}P_2W_{17}O_{61}(P(O)CH_2CH_2N_3)_2]$ $K_6[P_2W_{17}O_{57}(PO_5H_5C_7)_2]\cdot 6C_4H_9NO$ $K_7(C_2H_8N)_3(Fe[P_2W_{17}O_{57}(PO_3C_{21}H_{14}N_3)(PO_4C_{24}H_{41})]_2)$ $K_4(C_2H_8N)_2[P_2W_{17}O_{61}(P(O)C_{21}H_{14}N_3)(P(O)OC_{24}H_{41})]$ $H_6[P_2W_{17}O_{57}(H_{27}C_{17}O_4PS)_2]\cdot 3C_4H_9NO$	[269,44,272,273,274]

SP: spiropyran group; TMS: tetramethylsilane.

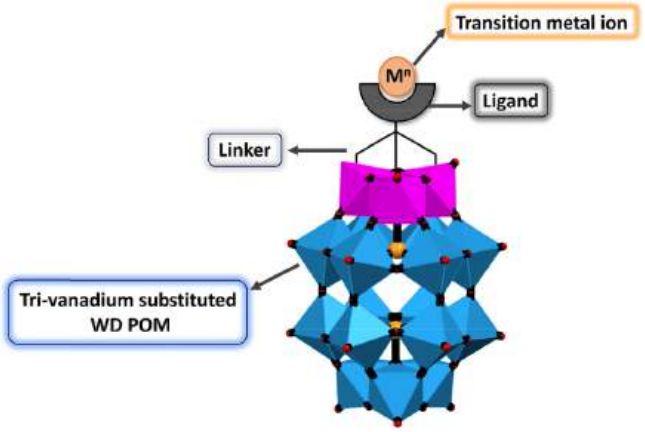

Fig. 22. Scheme of a functionalized tri-vanadium WD POM *via* an organic ligand capable of coordinating the transition metal ion.

also with the monolacunary site of a WD POM, such as organotin, organosilicon, organophosphorus, etc. functionalization (see Fig. 21a) [9,254,255].

Mayer et al. reported in 2004 the first example of two monolacunary WD POMs with an Si-O-Si anchorage which was confirmed by ^{29}Si NMR studies [268]. Izzet et al. showed the a covalently bond POM-hybrid can consist of two terpyridine subunits connected with $\alpha_2\text{-}[P_2W_{17}O_{61}]^{10-}$ *via* the Si-O-Si anchorage. This system leads to discrete metallomacrocycles through the self-assembly process with metal ions [19,280]. It is also noted that an organosilicon WD hybrid covalently bonded with an iridium complex having photophysical properties [281]. In the same paper, Matt et al. reported an example of an organotin hybrid WD species covalently grafted to an iridium(III) complex [281]. Monolacunary tin-substituted WD species form a comprehensive group of functionalized hybrids. The first example of organotin hybrids was reported in 1979 [282] and a number of papers related to this type of functionalization have been published since then [17,263–266]. Boglio et al. reported an example of a tin-substituted WD POM in the cap and belt position that formed two isomers: $\alpha_2\text{-}[P_2W_{17}O_{61}(SnCH_2CH_2COOH)]^{7-}$ (mono-substituted in the cap position) and $\alpha_1\text{-}[P_2W_{17}O_{61}(SnCH_2CH_2COOH)]^{7-}$ mono-substituted in the belt position). The tin-substituted WD hybrids obtained by their research group were subsequently used in a regioselective acylation reaction owing to the nucleophilic character of the W-O-Sn bond and acyl-hybrids were isolated and proved experimentally and computationally [266] (Fig. 26).

Unlike the organotin hybrids, organophosphorus WD hybrids occur very rarely. This type of functionalization is characterized by the presence of two organophosphorus moieties that fill the single vacancy, aligned parallel to the mirror plane, and by the lack of P-O-P anchoring with features that set the organophosphorus hybrids apart from both the organotin and organosilicon species [255]. Even though rare, organophosphorus hybrids are characterized by rich redox chemistry combined with strong electron conjugation between the units and, therefore, they are mainly studied for their electronic properties. In 2008, Boujtita et al. performed the first electrochemical study on a hybrid with a phosphonate moiety with the general formula $TBA_6[P_2W_{17}O_{61}(POC_6H_5)_2]$. They proved a reversible redox process involving the organophosphorus hybrid in acetonitrile as solvent [283]. Kastner et al. reported an

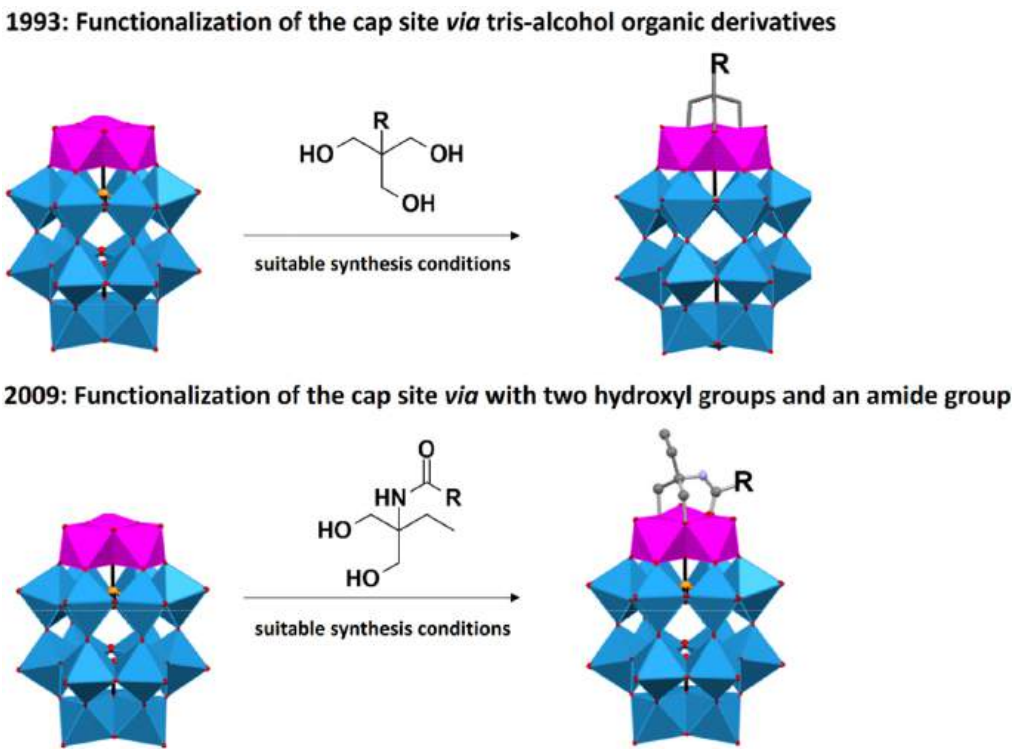

Fig. 23. Comparison of functionalization methods between the pioneering modification of 1993 and the new modification procedure published in 2009.

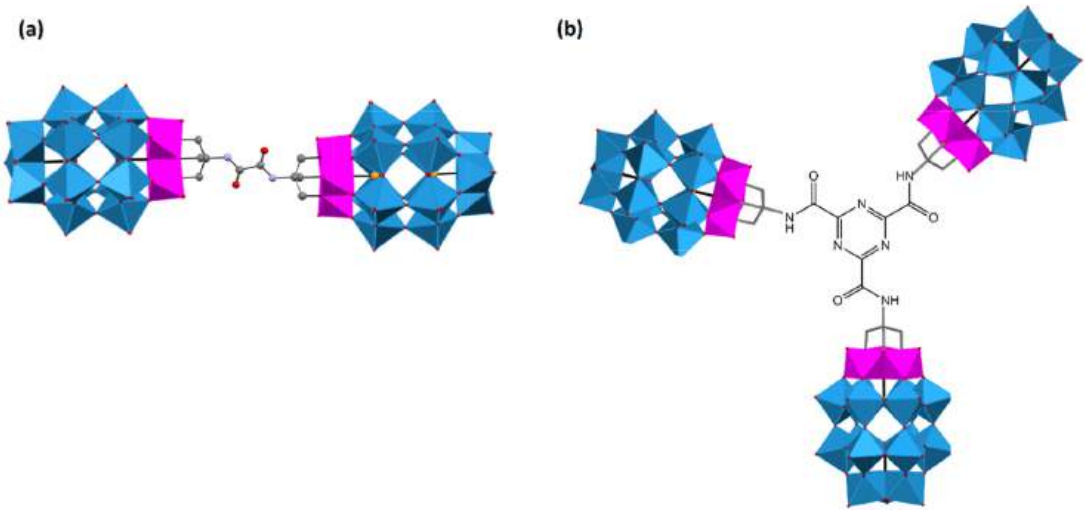

Fig. 24. Scheme of an example of (a) dumbbell (two units) and (b) triangular (three units) species.

example of a redox-active WD POM surfactant consisting of thiol chains which was grafted to a WD structure by phosphonate linkers to form supramolecular aggregates, and this resulted in changes in the redox chemistry of the WD species. In water as solvent, the novel hybrid surfactant formed regular micellar assemblies but the effect of the DMF solvent caused the aggregation to break down to the monomeric form which proved reversible redox chemistry for the aggregates. This transition of the monomeric to the supramolecular form and the accompanying change in physical properties offers opportunities for applications in photocatalysis, catalysis and advanced switchable materials [274].

It is noted that in the case of the formation of hybrid materials by a single linker to the monolacunary site of a POM, there have also been cases of POM-polymer formation as for the modifications discussed above (see Section 5.3 for more information).

5.1.3. *Various mixed types of POMs*

In addition, an interesting example of functionalization reported in 2022 by the group of Tatjana N. Parac-Vogt concerned the combination of subunits of different POM types functionalized with dipentaerythritol ($R = (OCH_2)_3CCH_2OCH_2C(CH_2OH)$) and the formation of four heterometallic hybrids of the general formula (POM_2-R-POM_1-R-POM_2) that combined Lindqvist [V_6] and Anderson-Evans [XMo_6] (X = Cr, Al) structures and tri-substituted [$P_2V_3W_{15}$] WD POM structures [90] (Fig. 27).

5.2. *Double-linker modularity*

The second main group of functionalized WD POMs have double linkers in various sites. Furthermore, three types of this modification are

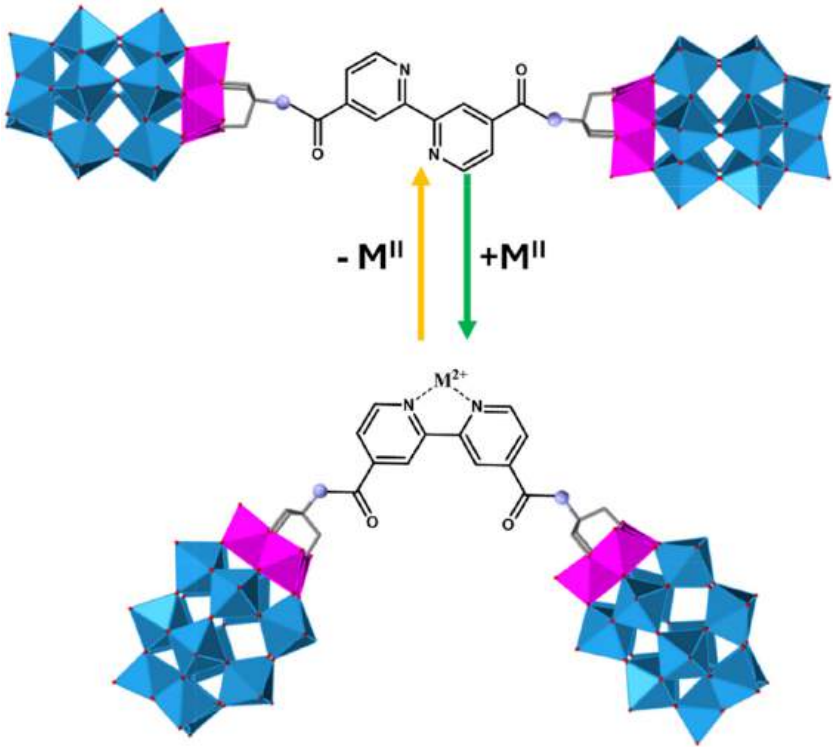

Fig. 25. Scheme of an example of a reversible conformational transformation involving a complexation reaction.

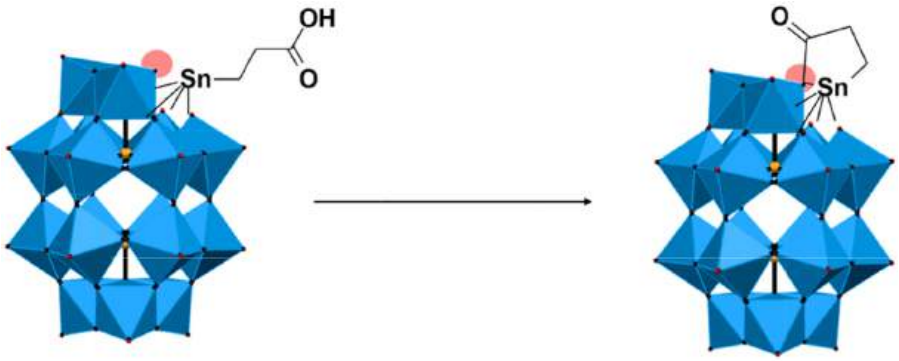

Fig. 26. Demonstration of the use of a tin-substituted WD hybrid for the regioselective acylation of an oxo reaction.

known, such as bent, linear and asymmetrical (Fig. 28). The possibility of functionalization of the primary POM unit gives the opportunity for further post-functionalization, thus improving the activity of compounds in various areas of chemistry.

Pre-functionalized POMs forming hybrids of disilylated WD species are further post-functionalized with additional organic groups to form a bent structure [9,269]. This combination is prepared using effective means, such as Sonagashira coupling reactions most frequently used in the post-functionalization of this type as they provide a rigid connection between the POM and the organic group with photoactive centers [270,284]. Matt et al. reported bent double functionalization in which the POM unit was covalently bond with chromophores to open up a possibility of the potential implementation of this system in photocatalytic devices [270]. Cameron et al. obtained organophosphonate functionalized POMs with photoactive properties. Enhanced photoactivity through the presence of the POM unit was proved in this paper [44].

The second type of WD POM functionalization is the linear modification with double post-functionalization of the POM *via* a coupling reaction in suitable reaction conditions. The research group of Tatjana N. Parac-Vogt reported an example of the post-functionalization of a previously prepared iodine-functionalized WD POM with amine substrates in a linear fashion [271]. He et al. showed a copper complex based on POM units formed through the linear functionalization of primary inorganic subunits [131] and another research group, of Han et al., reported linear double post-functionalized WD POMs forming a Cu (II) complex with octahedral and tetragonal pyramidal structure [129].

The last type of double functionalization is asymmetrical POM modification which involves a synthetic challenge and, therefore, the access to such hybrid materials is difficult. In essence, these compounds are desirable as they offer a greater possibility of function and physicochemical activity control of these systems, thus leading to specific and strictly defined applications [272,273]. Hampson et al. reported an example of a cluster consisting of two units with organophosphonate groups with various properties: one of them was terpyridine as a chelating group and the second one was an aliphatic, long-chain subunit [272]. In the following year, Hampson et al. reported an asymmetrical hybrid also based on POM units and two different organic groups: one

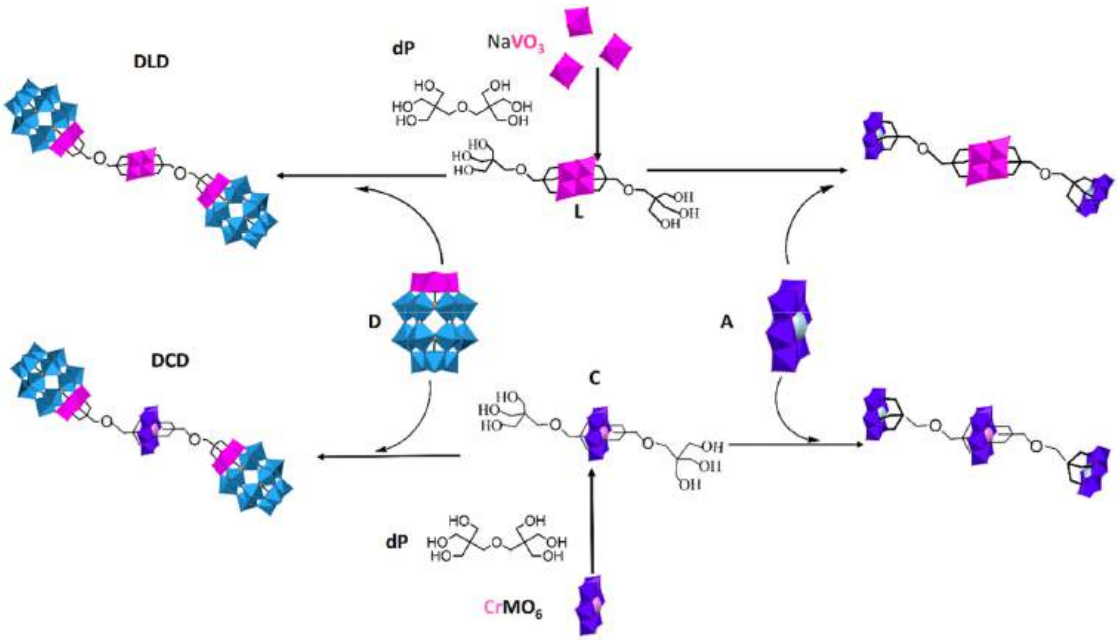

Fig. 27. Scheme of heterometallic hybrids with the general formula (POM_2-R-POM_1-R-POM_2) that combine Lindqvist [V_6], Anderson-Evans [XMo_6] (X = Cr, Al) and trisubstituted WD POM structures [$P_2V_3W_{15}$]. L: $[V_6O_{13}((OCH_2)_3CCH_2OCH_2C(CH_2OH)_3)_2]_2$; A: $[Al(OH)_6Mo_6O_{18}]^{3-}$; C: $[CrMo_6O_{18}((OCH_2)_3CCH_2OCH_2C(CH_2OH)_3)_2]_3$; D: $[P_2V_3W_{15}O_{62}]^{9-}$; dP: $(HOCH_2)_3CCH_2OCH_2(CH_2OH)_3$; ALA: $TBA_8[V_6O_{13}((OCH_2)_3CCH_2OCH_2C(CH_2O)_3(Al(OH)_3Mo_6O_{18}))_2]$; ACA: $TBA_9[CrMo_6O_{18}((OCH_2)_3CCH_2OCH_2C(CH_2O)_3(Al(OH)_3Mo_6O_{18}))_2]$; DCD: $TBA_{12.4}H_{2.6}[CrMo_6O_{18}((OCH_2)_3CCH_2OCH_2C(CH_2O)_3(P_2V_3W_{15}O_{59}))_2]$; DLD: $TBA_{11.4}H_{2.6}[V_6O_{13}((OCH_2)_3CCH_2OCH_2C(CH_2O)_3(P_2V_3W_{15}O_{59}))_2]$. Partially modified and reproduced from [90] with permission of the copyright holders.

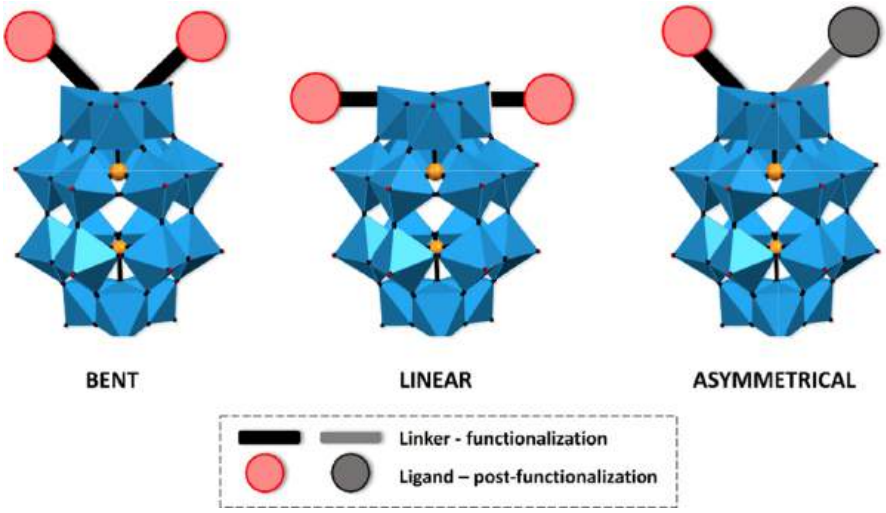

Fig. 28. Scheme of the double functionalization of WD POMs involving three types: bent, linear and asymmetrical.

group with terpyridine-coordinating Pt^{2+} ions, and the other one without changes, with a long aliphatic chain [273] as in the previously published paper by the same research group [272]. It is noted that it is very difficult to obtain asymmetric functionalized hybrids, and Hampson et al. first obtained a mixture of symmetric and asymmetric products, and then carried out purification to separate the components of the mixture (*via* addition of a different solvent, centrifugation, and filtration several times) and obtained pure products of hybrid functionalization as confirmed by ^{31}P NMR analyses (Fig. 29) [272].

5.3. Different linker modularity polymers with POMs

5.3.1. Covalent polymeric systems based on POM monomers

Organically functionalized POMs offer the opportunity to incorporate POMs into polymeric networks. Typically, POM structures are used as components in polymers and self-assembly materials [21]. Miao et al. reported organic polymers with WD POM pendants. The POM was functionalized *via* a direct M−O−C bond by linking with a norbornene derivative. A study of Ring Opening Metathesis Polymerization (ROMP) revealed that Macromonomers can be polymerized in a controllable manner under mild conditions in the presence of a Grubbs catalyst. The architecture resulting from this process exhibits a well-defined hybrid structure, consisting of an organic backbone and pendant POM groups [285] (Fig. 30). Moreover, a hybrid block copolymer (H-BCP) composed of poly-POM and organic polynorbornene blocks was prepared *via* living ROMP. The self-assembly properties of H-BCP were investigated, and it was found that in acetonitrile, H-BCP formed micelles with a poly-POM shell and a polynorbornene core,

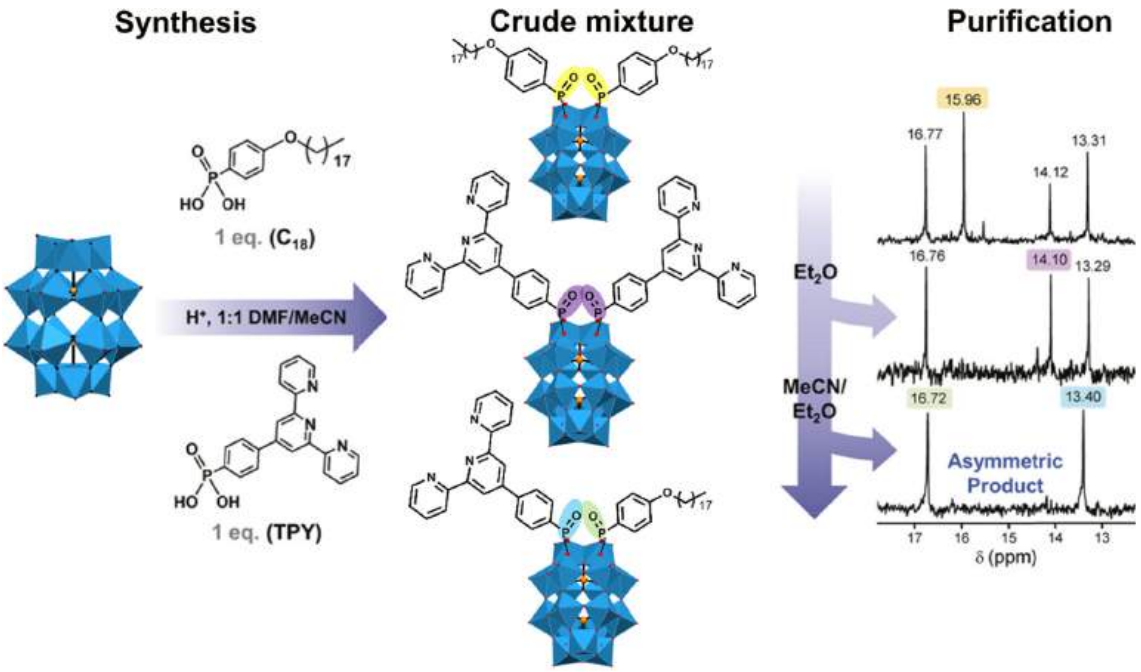

Fig. 29. Scheme of the reaction and purification of the asymmetric functionalized organophosphorus WD hybrid. Partially modified and reproduced from [272] with permission of the copyright holders.

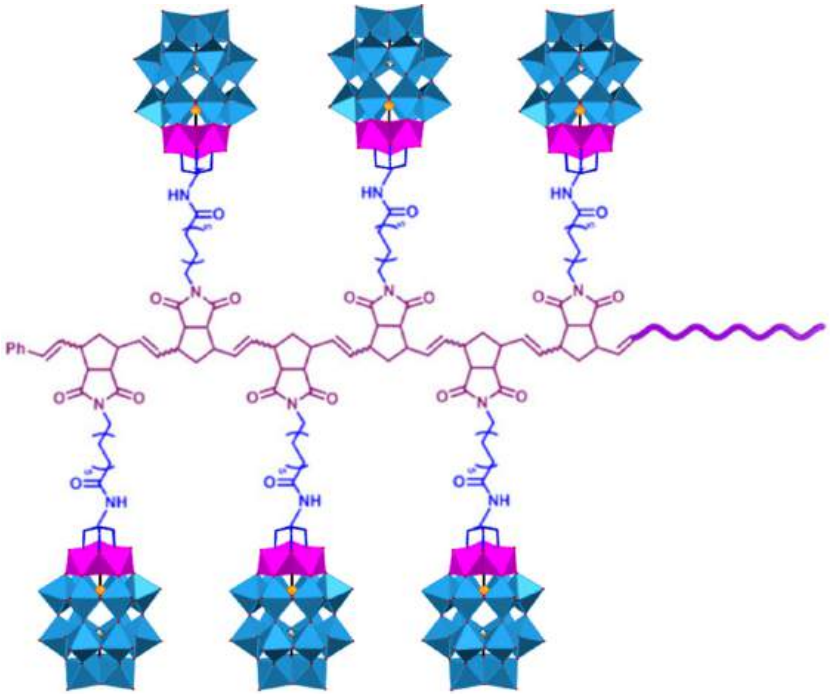

Fig. 30. Scheme of the three-dimensional structure of the hybrid. Partially modified and reproduced from [285] with permission of the copyright holders.

which then formed a hexagonal close-packed pattern [286].

Other interesting materials are copolymer films based on POM-porphyrin hybrids obtained via electrooxidation between porphyrin derivatives and different dipyridyl-substituted WD POMs [179]. Hasenknopf, Lacôte, Ruhlmann et al. published several papers in which they showed a connection between two substituents from the benzene ring with the pyridyl group, and one substituent with POM units [179,261,287].

A POM-based coordination polymer $(Hbpe)_2([Cu(pzta)(H_2O)][P_2W_{18}O_{62}])$ (pztaH = 5-(2-pyrazinyl) tetrazolate; bpe = bis(4-pyridyl) ethylene) reported by Pang, Ma et al. [288] forms a 3D supramolecular architecture and shows an improved electronic behavior explained in Section 6.1. In this structure each of $[Cu(pzta)(H_2O)]_2^{4+}$ complexes connects four neighboring P_2W_{18} anions and forms a straight chain, further interconnected through hydrogen bonds among the terminal oxygen atoms of P_2W_{18} anions to create a polymeric network.

5.3.2. WD POM-based polymerization initiators

Because the POM surface can be modified with organic domains, they can be used as inorganic polymerization macroinitiators. There are several examples of research into WD POM-based macroinitiators in Atom Transfer Radical Polymerization (ATRP) and Reversible Addition-Fragmentation chain-Transfer (RAFT).

5.3.2.1. ATRP macroinitiators. ATRP, also known as Reverse-Deactivation Radical Polymerization (RDRP) or Controlled Radical Polymerization (CRP), has recently been recognized as one of the ten groundbreaking chemical innovations set to revolutionize our world. This emerging chemical technology holds the potential to contribute significantly to the sustainability of our planet [289]. In 1995, almost simultaneously yet independently, Mitsuo Sawamoto [290] and Krzysztof Matyjaszewski [291] developed one of the earliest and most robust CRP methodologies known as living Atom Transfer Radical Polymerization in the presence of metal complexes. Unlike conventional radical-based polymer manufacturing methods, ATRP stands out by enabling the creation of intricate polymer structures. This is achieved through the use of a special catalyst that incrementally adds one or a few subunits (monomers) at a time to a growing polymer chain. Notably, this living synthetic process can be controlled, allowing the polymerization to be suspended or resumed when needed. Manipulation of the reaction conditions, such as temperature, plays a pivotal role in this capability. ATRP provides an exceptionally resilient means of precisely controlling the chemical composition and architecture of polymers. It ensures the uniform growth of each polymer chain, employing a diverse range of monomers [292]. With over 20,000 citations, ATRP is the most widely used RDRP technique in approximately 40,000 RDRP systems. Its success is attributed to its simplicity and the extensive availability of commercially accessible monomers, initiators, and catalysts.

The first example of well-defined POM-polymer hybrid materials composed of a trivanadium-substituted heteropolytungstate WD POM ($(Bu_4N)_5[H_4P_2W_{15}V_3O_{62}]$) and a conventional polystyrene chain obtained by in situ by the ATRP method was reported by Han et al. in 2009. The macroinitiator was synthesized *via* a reaction of 2-hydroxyethyl 2-bromoisobutyrate with tris(hydroxymethyl)aminomethane (Tris) in DMF at 70°C. Tris can be covalently linked to a POM cluster, while the 2-methylpropionyl group can initiate the ATRP of styrene (Fig. 31) *via* the normal (high copper) ATRP methodology. The resulting linear POM-polymer assembled in solution to give hybrid vesicles [293].

Further studies on the POM-polymer hybrid in DMF showed evolution from single macromolecules to vesicles, then to micelles, nanotubes and finally to micelle-stacked domains. The conversion of single macromolecules to vesicles can occur by changing the hydrophobic POM head to a hydrophilic POM head. In contrast, in the further alteration of vesicles into tubular aggregates, an annealing-driven process is necessary [294] (Fig. 32). A recent study demonstrated that the self-assembly of the POM-polystyrene polymer depended on the concentration and differing solubility of the POM and the polymer in DMF [295].

5.3.2.2. RAFT macroinitiators. The RAFT method is another form of living radical polymerization providing an excellent platform for the formation of products with high molar mass and controlled properties. In 2013 Lesage de la Haye et al. synthesized for the first time an organo-POM trithiocarbonate RAFT agent in which the macroinitiator was

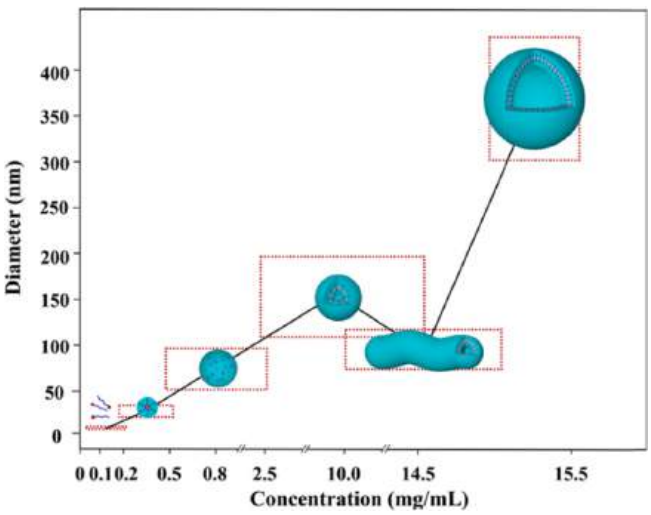

Fig. 32. Morphology of self-assembled aggregates of H_6^+-POM-polystyrene hybrids, the size of which depends on the concentration. The red dotted rectangles correspond to the concentration range of the solutions in which the aggregates formed and the diameter distribution of the aggregates formed, respectively. Reproduced from [294] with permission of the copyright holders.

obtained using trithiocarbonate acid (TTCA) as a classical RAFT agent to enable control of the acrylamide polymerization process. The polymerization reaction was initiated by azobisisobutyronitrile (AIBN) in acetonitrile, with different molar ratios of the monomer while keeping the concentration of the macroinitiator and AIBN constant (Fig. 33a). The polymer hybrid showed photocatalytic activity for the synthesis of silver nanoparticles under UV irradiation [264]. In a further study using the same macroinitiator stable polystyrene–POM composite latex nanoparticles with a size in a range of 50–100 nm were prepared. Core-shell nanoparticles underwent self-assembly during emulsion polymerization. The POM-polymer hybrid latexes were synthesized in the presence of either an amphiphilic organo-POM derivative or a RAFT macroinitiator. 4,4′-Azobis-4-cyanopentanoic acid (ACPA) used as the initiator reacts through the RAFT mechanism with a POM macroinitiator having TTCA in aqueous solution (Fig. 33b). The POM-based RAFT agent stabilized polystyrene nanoparticles. Moreover, the surface of the latexes mediated by POM hybrids retained its photocatalytic activity, as confirmed by using a spatially controlled process involving the germination of silver nanoparticles on the edge of the studied composites, thus confirming the presence of POM moieties at the surface of the nanoparticles in aqueous media [296].

The findings presented above suggest that such WD POM-based polymer hybrids may be used as well-controlled structures in functional materials and lead to the development of the precise control and hierarchical structural construction of the functional aggregates of POM-polymer hybrids.

5.3.3. Polymeric POM assemblies

The ability to precisely control the size and topology of hybrid WD POMs as well as their interaction with other components makes them excellent building blocks for the large-scale assembly of supramolecular

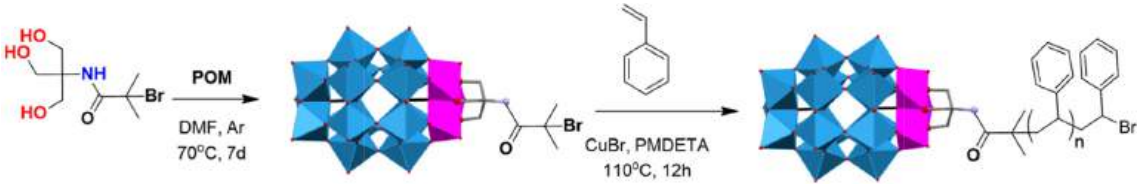

Fig. 31. The first example of POM-polymer hybrid synthesis based on a trivanadium-substituted WD POM.

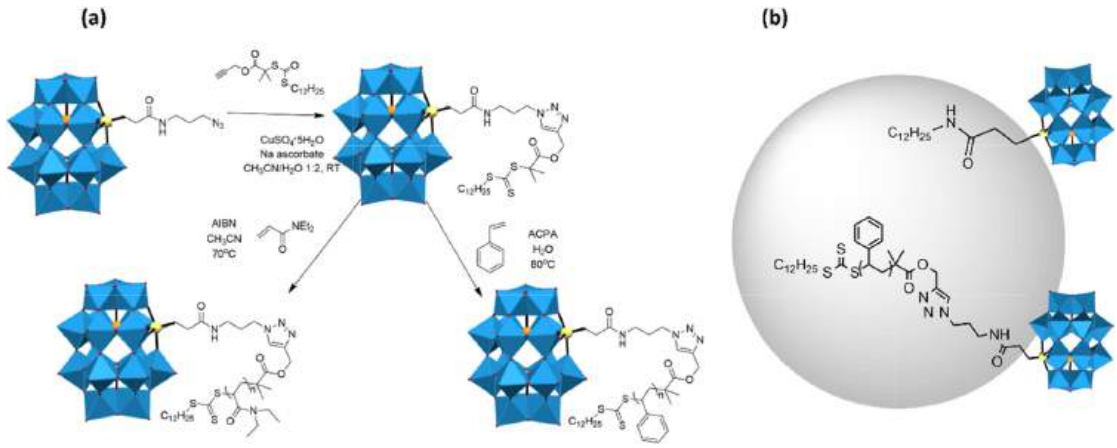

Fig. 33. (a) Example of the synthesis of a WD POM-based polymer using the RAFT method. AIBN: azobisisobutyronitrile; ACPA: 4,4′-azobis-4-cyanopentanoic acid. (b) Examples of polystyrene-POM latexes obtained by the surfactant-free radical emulsion polymerization of styrene in the presence of WD POM derivatives.

hybrid materials.

In 2009, Han et al. presented the first example of a hybrid vesicle assembly composed of a WD POM and polymer chains. The hybrid vehicles were formed by a previously described H^+-POM polymer obtained *via* ATRP polymerization, with a hydrophilic inner ring and a hydrophobic shell and core [293]. He and co-workers presented POM-based supramolecular gels through self-assembly formed by nanorolls with lamellar structure. Surfactants such as TBA and triacetate (CTA) encapsulated the $K_6P_2W_{18}O_{62}$ WD structure and assembled into nanorolls in butanone and ethyl acetate and the presence of nanorolls constructed from $(CTA)_3(TBA)_3P_2W_{18}O_{62}$ and gel formation was confirmed by TEM images [297]. Using a similar approach with a palladium-substituted WD POM, $K_{15}[Pd_2(\alpha_2\text{-}P_2W_{17}O_{61})_2H]$, promoted the formation of nanorolls constructed from $[(CTA)_x(TBA)_{(16\text{-}x)}Pd_2(\alpha_2\text{-}P_2W_{17}O_{61})_2$ and hollow spindles, $(DTA)_x(TEA)_{(16\text{-}x)}Pd_2(\alpha_2\text{-}P_2W_{17}O_{61})_2$ (DTA = decyltrimethylammonium; TEA = tetraethylammonium). The nanorolls and the spindles were formed in chloroform and in aqueous solution, respectively. The authors found an interesting application of such Pd-POM assemblies in Suzuki-Miyaura coupling reactions [298]. A three-component supramolecular hybrid composed of a WD POM, a $[Ta_6Br_{12}(H_2O)_6]^{2+}$ cluster and γ-cyclodextrin (γ-CD) formed in a specific multi-step recognition was reported by Moussawi et al. Hydrogen bonding and electrostatic interaction enables the formation of a tightly packed cationic cluster between two γ-CDs which bind to the electron-poor POM and form a tubular chain (Fig. 34) [299].

Yin and co-workers reported the formation of monolayer vesicles constructed from a bipyridine-based dumbbell-shaped WD POM [279]. An interesting approach to the formation of novel supramolecular nanostructures self-assembling into a lamellar arrangement was presented by Hu and co-workers. In their work, a WD POM structure was linked *via* a short organic bond with polyhedral oligomeric silsesquioxane (POSS), resulting in hybrid molecules assembled into layers composed of WD POM and POSS blocks [300]. The combination of WD POM with terpyridine units enables the construction of multiscale nanostructures through metal-driven self-assembly processes. In the presence of $[Co(H_2O)_6](NO_3)_2$, the building block, $(TBA)_6[P_2W_{17}O_{61}(O(SiC_{29}H_{18}N_3)_2)]$, formed nano-organizations, such as a triangle or a square, and assembled into dense nanoparticles with a specific orientation. POM units combined with Co^{III} display a different aggregate structure, resulting in worm-like assemblies with enhanced electrostatic interactions (Fig. 35) [301].

In 2019 Lui et al. demonstrated that substitution of a single metal atom in the POM cluster leads to 15 types of clusters, and they used transition metals (Ti, V, Cr, Mn, Co, Ni, Cu, and Zn) and lanthanides (La, Ce, Pr, Nd, Sm, Eu, and Gd). The authors reported a series of single-cluster nanowires, single-cluster nanorings and three-dimensional (3D) superstructure assemblies. Nanostructure formation depends on pH, and pH 4.0 leads to nanoring formation while nanowires form at pH 6.5. The catalytic activity of P_2W_{17}-Mn nanowires toward olefin epoxidation and sensitivity toward H_2O_2 detection of P_2W_{17}-Eu 3D superstructures presented in this report show different application possibilities of such cluster assemblies [302].

Flexible inorganic polymer chains were also obtained by Zhang et al. in 2020 from K^+ and THA salts of a di-Nb^V-substituted WD POM through the formation of *μ-oxo* linkage between Nb^v = O inorganic blocks. Following the formation of intermolecular Nb-μ-O-Nb linkages, each WD anion repeating unit had a 6- charge [187]. Glöß et al. demonstrated a new surfactant based on a V_3-capped WD POM structure with a specific linker. In low volumes of water, the POM units were surrounded by nBu_4N^+ ions to form a micellar structure and were deposited in the liquid phase on a highly oriented pyrolytic graphite, resulting in the formation of two-dimensional molecular layers [260]. Further studies by Glöß et al. on two tris(alkoxo)-ligated polyoxoanions $[HP_2V_3W_{15}O_{59}((OCH_2)_3C\text{-}R)]^{5-}$ (R = CH_2SMe, $NHCOC_6H_4SMe$) focused on differences in self-assembly on gold depending on ligand functionality. WD POMs with a shorter ligand form a small island on Au(1 1 1) and grow vertically, whereas POMs with a longer chain form larger clusters of similar length (Fig. 36) [275].

Zhang and co-workers studied linear poly-POM chains formed with tris(hydroxymethyl)aminomethane cations as substituents on the WD

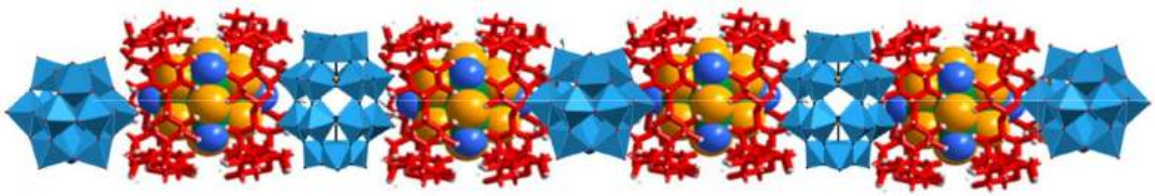

Fig. 34. Structural representation based on the X-ray diffraction analysis of a single crystal of the tubular chain showing periodic alternation of a ditopic cation $(Ta_6@2CD)^{2+}$ and $[P_2W_{18}O_{62}]^{6-}$. Partially modified and reproduced from [299] with permission of the copyright holders.

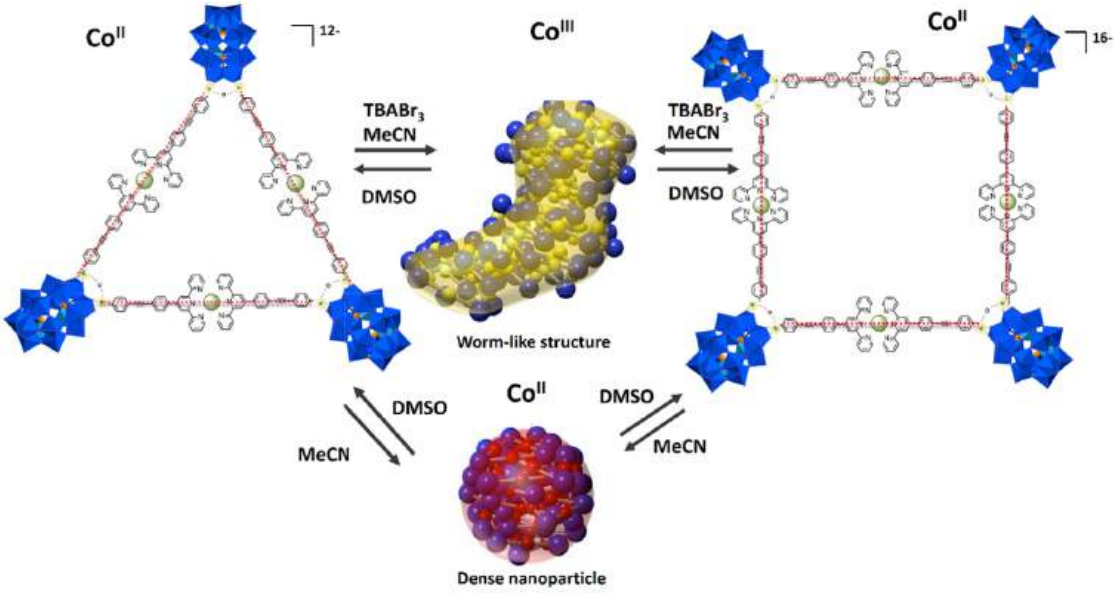

Fig. 35. Metal (Co^{II})-driven formation of a molecular triangle and a square in DMSO (Co^{II}) and the formation of nanosized aggregates through hierarchical metal-driven self-assembly depending on solvent composition (DMSO/CD_3CN mixtures) and the metal linker charge. For clarity, the supramolecular structures contain only triangles.

Fig. 36. Scheme of the self-assembly of a post-functionalized WD POM on Au(1 1 1).

POM anionic core. The authors observed multi-shaped aggregates of single chains of poly-POM units. The shapes of the chains depended on intramolecular interactions. Short-range interactions mimicked straight chains, while long-range interactions mimicked curved and disc-shaped chains [303].

6. Different uses of WD POMs

WD POMs are used in many scientific fields: energy-related applications, catalysis, functional materials and biology/medicine (Fig. 37).

6.1. POMs as candidates for energy-related applications

Recently, research into new materials for green and sustainable energy sources has increased significantly due to the demand for renewable alternatives and new storage technologies. POMs have gained prominence and have been the subject of several articles and reviews on energy-related applications due to their unique capabilities (e.g., a high number of metallic centers, high oxidation states, reversible redox processes, multiple electron transfer reactions without altering their structures, etc.) [58,304–307]. However, WD POMs have not been as extensively explored/investigated in this area compared to other types of POMs.

This motivation has led to developments in energy storage technology, such as the use of WD POMs in supercapacitors, which can lead to remarkable results in terms of improved energy storage and delivery capabilities. Using an adsorption method, Madhusree et al. integrated a WD POM with an activated carbon surface. The hybrid electrode showed a capacitance of 289 F g^{-1} and achieved cycle stability of 89% over 4000 cycles [308]. An interesting example of the use of WD POMs as redox materials was shown by Mughal et al. Carbon black (Vulcan XC-72R) used as a stabilizing anchor for $K_6[P_2W_{18}O_{62}]$ enhanced charge and discharge stability during electrochemical cycling. In voltammetric analysis, the redox activity of a POM and oxidized Vulcan carbon was retained after 500 cycles, while non-oxidized POM-Vulcan lost its redox activity at 250 cycles [309].

An example of hybrid POM nanostructures assembled on a carbon surface was presented by Amin et al. A POM organofunctionalized by (4-(icosyloxy)phenyl)phosphonic acid forms a polar POM head group and non-polar long-chain alkane tails which spontaneously create monodisperse micelles in aqueous media. The deposition of micelles occurs on three different carbon surfaces: (i) glassy carbon (GC), (ii) graphene oxide (GO), where the micelles form a monolayer, and (iii) highly ordered pyrolytic graphite (HOPG) to form a multilayer lamellar structure. Electrochemical analysis showed that GC with multi-redox properties coated with a POM micelle layer is stable and active for up to 100 measurements [310] (Fig. 38).

Deposition of a pseudo-WD-type POM cluster $[Mo_{18}O_{54}(SO_3)_2]$ on a nanogold surface activates thermally controlled redox behavior, activated by a local electric field, and it accelerates reversible intramolecular redox reactions within the cluster shell. POM nanoclusters containing redox agents are able to eject electrons from the sulfite anion and delocalize them over the POM cage, leading to a reduced state. This process shows potential for applications in molecular electronic devices [311].

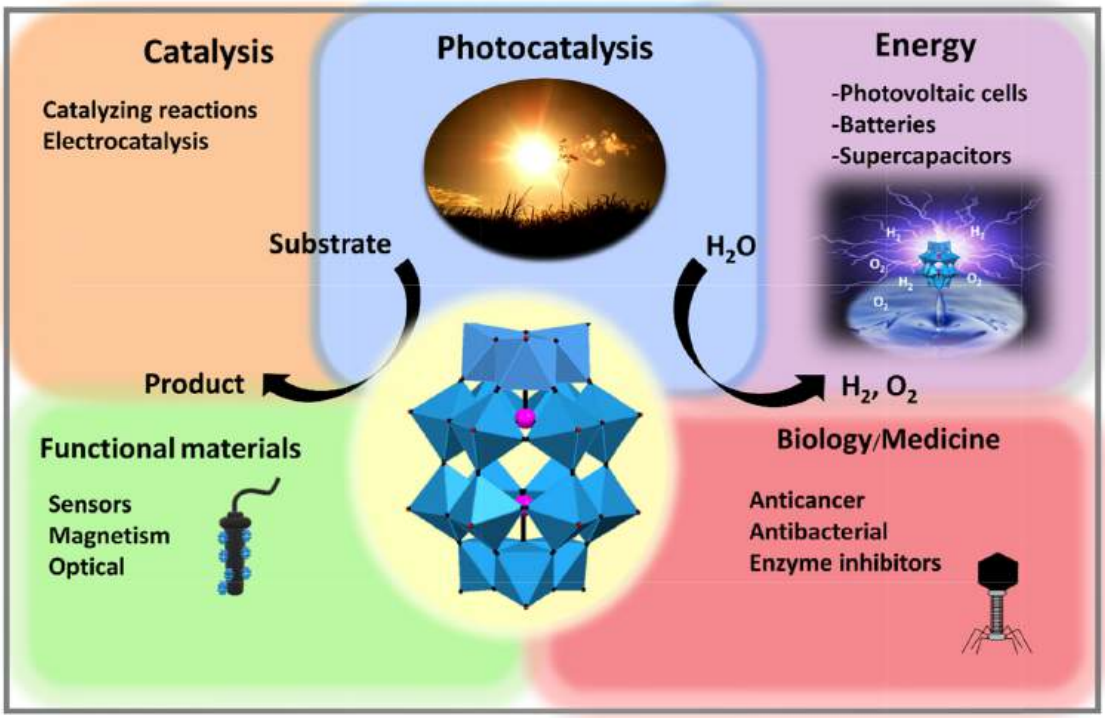

Fig. 37. Scheme of the various applications of WD POMs.

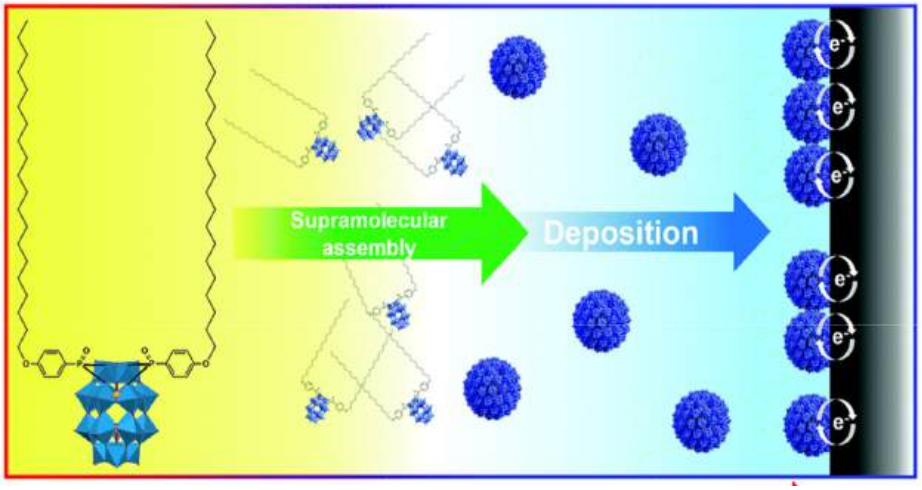

Fig. 38. The model of self-assembly and deposition of a WD POM nanostructure on the carbon surface. Reproduced from [310] with permission of the copyright holders.

A study of the interaction of WD POM films with an aluminum electrode as a POM/Al cathode showed that six electrons were transferred from the electrode to the $(NH_4)_6[P_2W_{18}O_{62}]$ and $(NH_4)_6[P_2Mo_{18}O_{62}]$ WD POM cluster after reduction. The device presented in this article has demonstrated applicability in optoelectronics as a cathode interlayer material with improved electron injection/extraction efficiency and reduced recombination losses [312]. The multi-electron reduction of films based on both POM ammonium salts on the aluminum and semiconductor surface was studied several years later by the same research group. They found that the presence of ammonium counterions, POM's LUMO position and Fermi substrate levels affected multi-electron reduction and enabled spontaneous electron transfer [313]. An interesting approach was presented by Bushe et al. in their paper, in which they considered the potential application of POM molecules as flash memory devices. The core–shell WD POM cluster $[W_{18}O_{54}(SeO_3)_2]^{4-}$ can be repeatedly reduced, and the selenium moieties can be oxidized. Such a metal-oxide semiconductor can serve as a floating gate and inhibit flash memory charge trapping after the initial excitation step [134]. The role of POMs as an active material in the engineering of resistive random-access memory (RRAM) has been explored by Sterin et al. They demonstrated resistive switching behavior in redox-active POM clusters $[V_{10}O_{28}]^{6-}$ deposited on the top of a glass/ITO layer and coated with Cr/Au contact pads. The new RRAM appliance was capable of storing as well as releasing a large number of electrons and exhibited high endurance, retention, and resistance ratio. Stability of the device was confirmed after as long as 12 months [314].

WD POMs are well-known photosensitive materials with the potential to facilitate multiple electron transfer reactions using light

[218,315]. Unfortunately, most of the excited states of WD POMs can only be generated under UV irradiation (typically at wavelengths of 200–400 nm). Therefore, only a small fraction of sunlight can be converted into electrical energy. Indeed, this has limited applications in the field of photoelectric energy. However, new approaches involving photosensitization of visible light by chromophores have improved photocurrent generation. Among the photosensitization strategies investigated for WD POMs, the most relevant include: (i) electrostatic interactions between anionic POMs and cationic sensitizers [316–318] and (ii) covalent or coordination chromophores coupled to POMs [269,284,319,320].

A significant part of the field has focused on porphyrin [317,319,321–323] which is known to have high absorbance in the visible and near-infrared range. However, most of these photophysical studies have focused on exploring the first light-induced electron transfer and not on the transfer of a second electron, a crucial aspect for solar energy transformation into storable energy such as H_2 or O_2. In this sense, it is extremely important to carry out a rational design to adapt the hybrid systems to achieve more effective change transfer properties. Harriman, Odobel et al. [322] described a multi-porphyrin complex consisting of two components, one being ZnTPP-based donors and the other a free porphyrin intermediate compound. Their study was instrumental in promoting directional charge transfer and simultaneously preventing too rapid recombination of the charge between the molecules: WD POM and ZnTPP donors. This enabled POM to store multiple electrons in a single group, an essential requirement for its energetic application. Subsequently, Izzet, Artero, and Proust [324] showed efficient photoreduction of a WD POM hybrid with an iridium complex: ($[P_2W_{17}O_{61}$-$(O(SiC_{36}H_{23}N_3O_2Ir)_2)]^{6-}$) in the presence of a sacrificial electron donor. Sequential formation of one-electron and two-electron reduced species was observed with a significantly higher reaction rate for the first reduced species. This hybrid also generated hydrogen under visible light without significant yield loss for more than one week of continuous photolysis.

Hydrogen generation in non-covalently sensitized systems has also been reported. Douvas, Argitis, and Coutsolelos studied the sensitization of W and Mo WD POMs with *meso*-tetrakis(N-methyl-pyridinium-4-yl) porphyrin ($ZnTMPyP_4^+$) [325]. Both sensitized WD POMs showed higher hydrogen generation efficiency compared to those obtained by direct photoreduction. Moreover, the $[P_2Mo_{18}O_{62}]^{6-}$ (Fig. 39a (left)) catalyst (after sensitization with $ZnTMPyP_4^+$) showed higher efficiency for H_2 evolution than $[P_2W_{18}O_{62}]^{6-}$ (Fig. 39a (right)). The authors attributed this fact to the lower LUMO position of the $[P_2Mo_{18}O_{62}]^{6-}$ anion and its higher degree of reduction.

In addition to porphyrins and iridium complexes, metal organic frameworks (MOFs) and supramolecular MOFs (SMOFs) derived from $[Ru(bpy)_3]^{2+}$ were used as photosensitizers (e.g. UiO MOF [326], MIL-101 [327] or SMOF-cucurbit[8]uril [328]) which showed improved hydrogen evolution. This effect can be attributed to increased three-dimensional organization and enhanced association between the cationic photosensitizer and the anionic catalyst in these systems. However, a disadvantage of these strategies consists in the use of precious metals such as ruthenium. Recently, Lv and co-workers reported noble metal-free POM@MOF systems with efficient hydrogen

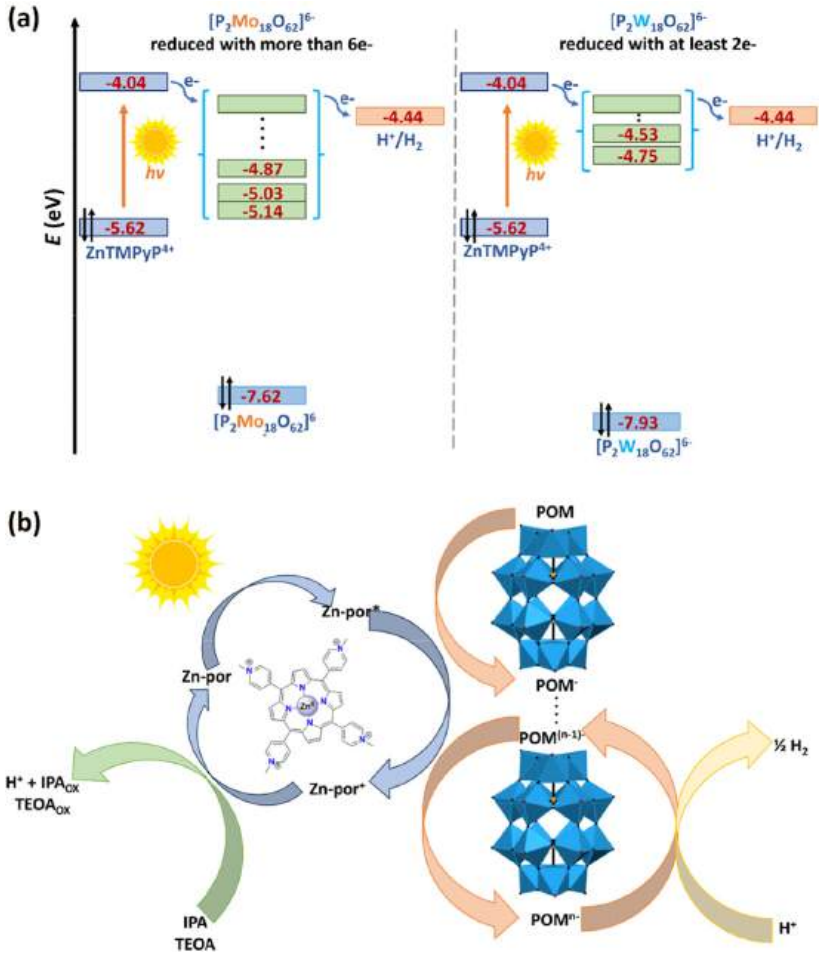

Fig. 39. (a) Scheme of a simplified molecular orbitals diagram presenting the $ZnTMPyP_4^+$-sensitized multi-electron reduction of two WD-type POM catalysts: $[P_2Mo_{18}O_{62}]^{6-}$ and $[P_2W_{18}O_{62}]^{6-}$, for efficient H_2 evolution. (b) Illustration of highly efficient H_2 evolution by the $ZnTMPyP_4^+$-sensitized multi-electron reduction of WD POM catalysts using 2-propanol (IPA) or triethanolamine (TEOA) as the sacrificial electron donor in a water-soluble system; based on [325].

generation using visible light [329]. The compounds were prepared by incorporating Ni-containing POMs (Ni_3PW_{10} and $Ni_3P_2W_{16}$) into the Zr-based MOF (NU-1000). Both compounds showed reproducible photocatalytic hydrogen generation, which was higher in the WD POM@MOF system.

Water oxidation catalysts (WOCs) are also a critical topic for solar fuel production. Hill and co-workers synthesized an open complex of $[Ni_5(OH)_6(OH_2)_3(Si_2W_{18}O_{66})]_{12}$ WD POMs containing penta-nickel and silicotungstate, showing an ability to generate oxygen by oxidizing water in the presence and absence of light by forming complexes with $[Ru(bpy)_3]^{n+}$ (n = 2 or 3) [107].

The unique and tunable electronic properties of POMs have led to the construction of photovoltaic cells for solar cell applications using POMs. It has been observed, for example, that the incorporation of P_2W_{18} films on ITO in organic photovoltaic cells has improved power conversion efficiency [330]. On the other hand, mono-substituted POMs with transition metals, P_2W_{17}-Co and P_2W_{17}-Mn, have been used to co-sensitize NiO electrodes, showing higher overall power conversion efficiency compared to other inorganic photosensitizers [331].

Lithium batteries (LiBs) are also in the spotlight in the energy research field because they offer an alternative source of new energy due to their high specific energy density and long lifetime. Energy storage in rechargeable batteries results from reversible redox reactions in active electrode materials. Due to their multi-electron reversible transfer, POMs have received a lot of interest as electrode materials in LiBs [304]. POM can be activated by the coordination of conductive materials and can significantly modify the electronic structure of the clusters. The formation of WD helical hybrids has been shown to improve performance when used as electrodes in LiB [332]. Thus, by having a high number of oxygen atoms and with a lower spatial symmetry, WD POMs are attractive building blocks for different structures and functionalities. For example, Sha and Wang [333] reported complex multi-fold Mesohelices in the structure of a WD POM-based hybrid. The resulting hybrids, $[Ag_{26}(Trz)_{16}(OH)_4][P_2W_{18}O_{62}]$ and $Na[Ag_{16}(Trz)_9(H_2O)_4][P_2W_{18}O_{62}]$ ($P_2W_{18}O_{62}$] (Trz = 1,2,3 triazole), were used as anode materials for LiBs, showing higher discharge capacities than those obtained for unfunctionalized $(NBu_4)_6[P_2W_{18}O_{62}]$ or commercial graphite commonly used as reference anodes. Both POM hybrids show excellent performance after 100 cycles and the authors conclude that the regular helical conformation of the composites provides stable charge transmission channels during the discharge–charge process. The surface of GO, a commonly used building block for various nanocomposites, was effectively modified by the covalent binding of ionic liquids and loaded with a WD POM. The use of the prepared nanocomposite as a LiB anode material enhances charge transfer and provides high specific capacitance with a long cycle life over 1000 cycles [334]. A new class of hybrid materials has emerged by introducing the WD POM cluster $[As_2Mo_{18}O_{62}]^{6-}$ into MOF architectures based on Cu(btp)$_2$ (btp = 1,3-bis(1,2,4-triazol-1-yl)propane) generating a POMOF. Such a 3D network exhibits stability in air and at different pH values in aqueous solutions and organic solvents. Based on the assessment of reversible capacity and cycling stability, it is a promising anode material for LiBs [335].

Recent studies, from 2022, on lithium-sulfur batteries (LiSBs) based on WD POMs present a solution for dendrite formation and polysulfide conversion. A WD POM-modified polypropylene membrane improves the electrochemical performance of LiSBs and shows initial high specific capacity with excellent cycling stability [336]. A surface modification of MIL-88A(Fe) by a WD POM enables the carbonization of the material to produce a capsule coating with a carbon and Fe_3O_4 component. The hollow capsule acts as a sulfur host and can significantly improve the efficiency of the sulfur electrode during the charging and discharging process [337].

The use of an addenda WD POM for energy storage may be challenging. A study of Pratt et al. shows that clusters with higher charge density exhibit poor stability. Consequently, charge storage in a laboratory-scale flow cell demonstrated the worst performance of all tested addenda POMs [338].

Supercapacitors are also energy storage devices that are gaining importance. They have the ability to deliver a large amount of energy in a short time. Energy storage is based on the combination of electrostatic charge separation (double layer capacitance) and electrochemical charge separation (pseudo capacitance). Ammam et al. synthesized WD POM hybrids with Ru and evaluated the performance of the hybrids deposited on electrodes to be used as supercapacitors in physiological electrolytes as potential storage devices for powered implanted biomedical devices [339]. The hybrid synthesis was carried out in the presence and absence of KI, and two different stoichiometries were obtained: $[Ru(bpy)_3]_3PMo_{18}O_{62}{\cdot}nH_2O$ and $[Ru(bpy)_3]_{3.33}PMo_{18}O_{62}{\cdot}mH_2O$, respectively. The authors showed that there was a strong influence of hybrid composition and supercapacitor behavior. It was found that a hybrid with a higher proportion of Ru(bpy) performed better as a supercapacitor in physiological conditions.

Stretchable supercapacitors reported by Mu et al. constructed with 3-(2-naphthyl)-L-alanine, the $[H_6P_2W_{18}O_{62}]$ WD POM and silver powder reveal underwater adhesion properties. In addition, this type of flexible material shows advantages such as adhesion to electrolytes, conductivity, reversible redox behavior and fast electron transfer/storage abilities [340]. The P_2W_{18} WD POM integrated with activated carbon (AC) was studied as a nanohybrid electrode for high-performance supercapacitors in a two-electrode system. The results showed excellent specific capacitance (289 F g^{-1}) with good energy and power density (40 W h kg^{-1}) and demonstrated a cycling stability of 89% over 4000 cycles [308].

The use of polymer hybrids is a strategy to reduce POM solubility in electrolytes and increase conductivity in supercapacitors, for example by adding nitrogen compounds to the polymer. Pang, Ma et al. reported and investigated a new coordination polymer, $(Hbpe)_2([Cu(pzta)(H_2O)][P_2W_{18}O_{62}])$ (bpe = bis(4-pyridyl)ethylene; pzta = 5-(2-pyrazinyl) tetrazolate) [288]. The authors showed that the formation of a polymeric WD hybrid had better electronic performance than the α-$K_6P_2W_{18}O_{62}$ inorganic analog and other electrodes made of POMs (see Section 5.3.1).

Research into energy storage, either in the form of electrical charge or conversion into chemical fuels, has undoubtedly been a major focus in recent years. In this sense, battolysers (integrated battery-electrolyzers) can function as both batteries and fuel generators and could have a transformative effect on how renewable energy is used [341]. Moreover, finding new mediators capable of accepting more electrons per molecule is crucial for practical applications. Cronin et al. recently showed that the $[P_2W_{18}O_{62}]^{6-}$ polyoxoanion had remarkable proton-coupled electron redox activity [342]. Under those conditions, the molecule could reversibly accept up to 18 protons and electrons in aqueous solution. The authors showed that the highly reduced $[P_2W_{18}O_{62}]^{6-}$ WD POM can be used in two ways: firstly it can act as high-performance electrolyte of a flow redox battery (practical discharge energy density: 225 Wh l^{-1}; theoretical energy density: more than 1000 Wh l^{-1}) and can be used as a mediator in an electrolytic cell to produce hydrogen on demand.

6.2. Catalysis

POMs are widely used as catalysts due to their high efficiency, resistance to oxidation, degradation and hydrolysis, ability to stabilize ions, and environmental compatibility [31]. POMs and heteropolyacids (HPAs) (containing protons as cations) represent one of the most versatile catalysts due to the multiple active sites, including protons, oxygen, and metals [32]. The protons in HPAs can act as Brønsted acids and participate in acid-catalyzed reactions. Some oxygens are sufficiently basic and are capable of reacting or even abstracting protons from organic substrates. Lewis cation incorporation (in a lacunar POM or through a suitable ligand in a hybrid POM) converts them into catalysts as Lewis acids. However, the most active sites in POMs are on the metal atoms, which are involved in many distinct types of reactions (such as oxidations, acid-catalyzed reactions or other reactions). In turn, the Lewis acidity of POMs may be achieved using high-valent metals [32]. A

wide variety of WD POMs have been extensively used as catalysts in organic transformations, such as chemical oxidation [167,174], in many classical reactions: Diels-Alder, Mannich and Mukaiyama-type [343], Suzuki–Miyaura cross-coupling reactions [344], amide formation [345], cyclization of 1,3-diketones with hydrazines/hydrazides or diamines [346], epoxidation [113], allylation of sulfonyl imines and aldehydes [178], hydrolysis of peptides [199], hydrogenolysis reactions [347], Friedel-Crafts acylation [348], and so on. As in all homogeneous reactions, recovery and reuse of the catalyst can be difficult. In this regard, the inclusion of POM anions as inorganic building units to construct WD POM-based MOFs represents a successful strategy to recover the catalyst at the end of the organic transformation [150].

The catalytic ability of POMs is undoubtedly altered and in many cases enhanced by the introduction of transition metal/lanthanide heteroatoms into their structure (see Section 2.2.2). Cronin et al. investigated the phosphoesterase activity of α_2-$[P_2W_{17}O_{61}]^{10-}$ type WD POMs, containing various metals such as Mn^{III}, Fe^{III}, Co^{II}, Ni^{II}, and Cu^{II}, and other ions such as Y^{III}, La^{III}, Eu^{III}, Zr^{IV}, and Hf^{IV} [101]. Catalytic activity was studied on 4-nitrophenyl (NPP) and bis-4-nitrophenyl phosphate (BNPP), well-studied model substrates that mimic the phosphoester bond in DNA. The incorporation of the first-row transition metals showed no catalytic activity. In contrast, the second and third groups of POMs modified with lanthanides and Zr^{IV} and Hf^{IV}, respectively, showed catalytic activity. In the former case, the activity was reported only in NPP and those with Zr and Hf also showed catalytic activity on the more resistant BNPP. The authors attributed these differences to the higher coordination numbers and the capacity to form complexes with flexible geometries of the lanthanides, Zr and Hf. Another consequence of the high oxidation number is the ability to form organized dimeric POM structures. On the other hand, the enhanced Lewis-acid strength from Zr^{IV} and Hf^{IV} compared to Ln^{III} ions enabled more efficient NPP hydrolysis and catalytic activity in more resistant BNPP. In the same way, Wynne et al. showed the potential of WD-substituted hetero-metals, $[Zr(\alpha_2\text{-}P_2W_{17}O_{61})_2]^{16-}$ and $[Ni(\alpha_2\text{-}P_2W_{17}O_{61})]^{8-}$, to be used as catalysts in the rapid oxidation of a persistent organophosphorus chemical warfare agent analog [349]. A novel decontamination method was employed by the direct application of aqueous POM solutions on the CWA analog and 15 wt% hydrogen peroxide. WD incorporation with Ni^{II} and Zr^{IV} increased the oxidation rate significantly and reduced the reaction half-lives compared to the slower oxidation without a POM. In the first case, the mechanism involved a direct Ni^{II} reaction with hydrogen peroxide generating a reactive species that then the substrate was oxidized. In the case of Zr^{IV}-POMs, the process was more complex, with additional active species present in the solution that influenced the rate of substrate oxidation.

6.2.1. Photocatalysis

The photocatalytic behavior of POM hybrid materials is the result of UV light irradiation which excites electrons from low-energy states to high-energy states, from oxygen-binding 2p orbitals to (HOMO) metal-binding anti-binding d orbitals (LUMO) [350]. The photoexcitation offers several advantages, such as homogeneous photocatalysis or a light-induced active redox reagent in multi-step photoredox-systems.

Photocatalysis focused on POMs is not only interesting for its energy-related applications but also for its use in the degradation of organic and inorganic pollutants. The major advantage of photocatalysis processes is that experiments can be conducted under mild conditions such as atmospheric pressure and room temperature. As previously noted, many efforts have been made to modify the electronic properties of POMs to take advantage of visible light (see Section 6.1). Newton, Oshio et al. showed that WD POM functionalization with an organophosphonate derivative (4-carboxyphenyl phosphonic acid) reduced the energy gap between HOMO and LUMO [44]. It also shifted the LMCT band to the visible region as compared to non-functionalized WD POMs. This hybrid can photocatalyze the indigo dye (a model impurity) using visible light, unlike non-functionalized POMs. Subsequently, the authors demonstrated that catalytic activity can be modulated by modifying the substituent at the *para* position of the phenyl ring [130]. They found that catalytic activity depended on the inductive properties of the substituent. Mousavi et al. used a sodium polytungstate POM cluster as an efficient agent to remove toxic auramine-O from aqueous media. The results showed that up to 100% of impurities were degraded within 110 min irradiation time of the WD POM cluster [351].

Photocatalytic capacity has also been explored using non-classical WD POMs, or "WD-like" (similar to WD POMs but with a non-tetrahedral group added to each $[M_{18}]$ cluster). These include inorganic–organic hybrids containing the SbO_3 pyramidal group in a WD POM based on an organic ligand $((Ni(phen)_3)[SbW_{18}O_{60}](H_3O)_3{\cdot}7H_2O)$ [130]. This hybrid showed excellent catalytic activity and selectivity in the degradation of RhB at pH 3 using visible light. The authors suggest that this type of structure may have enhanced catalytic activity as it contains a lone pair of electrons in $[W_{18}]$.

The high solubility of WD POMs and the growing interest in designing efficient and recyclable heterogeneous catalysts have prompted the exploration of a variety of approaches to this problem. Several selected supports to immobilize POMs have been shown to play a dual role by modifying some of the physicochemical characteristics of the POM and enhancing the adsorption capacity of the substrates to react with the active species [352]. Metal oxides, for example, are a widely studied group with several types of POMs. In this respect, Wu, Guo, and co-workers showed the effect of immobilizing $H_6P_2W_{18}O_{62}$ on TiO_2 [353]. These composites were successful in the photocatalytic degradation process of aqueous parathion-methyl insecticide solution using visible light. This effect was attributed to the synergy effect between the POM and anatase TiO_2, porous structures, and the narrow bandgap of the composites. The coupling of $H_6[P_2W_{18}O_{62}]$ and TiO_2 produces a decrease in conductivity band levels, resulting in a smaller bandgap than the POM or the support alone. This group later showed a similar effect by coupling $H_6[P_2W_{18}O_{62}]$ to tantalum pentoxide (Ta_2O_5) [354]. In addition to metal oxides, the effect on heterogeneous photocatalytic properties was investigated using hybrid organic–inorganic POMs. The reported organic–inorganic hybrids were based on cucurbituril derivatives and WD POMs which showed photocatalytic activity in the degradation of methyl orange and rhodamine-B using visible light [355].

6.2.2. Electrocatalysis

POMs are also widely used as electrocatalysts (mediators) in electrochemical reactions, and they catalyze electron transfer between the electrode and electrolyte solution. Undoubtedly, the functional versatility of WD POMs is evidenced by the large number of papers reporting a wide range of modified WD POMs as electrocatalysts [356]. Among the modifications of WD POMs that present interesting electrocatalytic properties, noteworthy is the introduction of vanadium into the structure of a tungstic or molybdo-tungstic POM [356–358]. The electrocatalytic capacity of non-conventional WD POM structures (e.g. WD-sandwiched clusters [247], open WD-tungstosilicates [105] or metal–organic framework based on WD POM [359,360]) has also been studied. Some of the major electrocatalytic processes using WD POMs include the reduction and oxidation of nitrogen oxides [120,357,361–364], reduction processes resulting in molecules of biological interest (e.g. $NADP^+$, L-cysteine) [356,357], oxyanions (such as chlorate, bromate, iodate) [120,247,355,363,365] or hydrogen peroxide [105,360,363,365,366]. A recent study on the mechanism responsible for the super-reduction of fully inorganic POM salts by Chen et al. showed that the protonation and agglomeration of WD structures in aqueous solution promoted H_2 production [367].

6.3. Functional materials

6.3.1. Sensors

The most salient features of a POM sensor include sensitivity,

selectivity, detection limit, stability and linear range. The remarkable electrocatalytic properties of WD POMs and the numerous works reported in this field have made it possible to understand and study many fundamental aspects for using these systems as electrochemical sensors. In addition, other methods such as colorimetric or fluorescence have been investigated [368]. Some examples of WD POMs used for sensing are summarized in Table 3.

6.3.2. Optical materials

POMs are potential candidates as novel nonlinear optical (NLO) materials. For example, WD POMs modified with transition metals have been prepared to obtain non-centrosymmetric structures (a requirement for second-order NLO materials). Su, Wang et al. [82] have shown in a theoretical study that trisubstituted α-$[P_2M_{15}M'_3O_{62}]^{m-}$ (M=W^{VI}, Mo^{VI}, and M′ = V^{V}, Mo^{VI}) display good second-order NLO properties. On the other hand, since porphyrins exhibit significant NLO responses, porphyrin-WD POM hybrid systems have been prepared by covalent interactions [257,379]. These systems show remarkable enhancement of the nonlinearity of the hybrids over their corresponding porphyrin precursors.

Tetrameric WD POMs containing lanthanide ions, shown in Fig. 40 [104], exhibit reversible photochromic behavior. After UV irradiation, they can change from white to blue within 6 min and restore their color in the dark for 30 h. The switchable luminescent behavior of Sm-POMs induced by their photochromism opens up a new perspective for the development of optical materials. A WD POM ($[H_2N(CH_3)_2]_{10}H_3[SeO_4M_5(H_2O)_7(Se_2W_{14}O_{52})_2]\cdot 40H_2O$ M = Dy, Gd) was encapsulated by CTA and formed a nanoscale material with photoluminescent properties. The authors showed that CTA, a cationic surfactant, can regulate morphology and tune multicolor optical behavior [380].

6.3.3. Electrochromic materials

Electrochromic (EC) materials are characterized by color change after electrochemical reduction or oxidation. POMs exhibit this property and can be modulated through molecular design [100]. Organic cations, such as poly(stryenesulfonate) (PSS) and polyallylamine hydrochloride (PAH), have been used to prepare films based on WD POMs with different modifications to explore their electrochromic properties. For example, a film formed by incorporating Neutral Red (NR) $[P_2W_{17}/PAH/P_2W_{17}/NR]_{35}$ [83] showed color changes from deep pink to dark violet-blue depending on the reduction rate of P_2W_{17} in response to different applied potentials. It was also observed that the electrochromic properties were affected by the degree of the lacunar structure (PSS/PAH/(P_2W_{18-x}/PAH) [381]. Another example is the adjustable color of PSS/$Cu^{II}(phen)_2$/$[(P_2W_{17}/Cu^{II}(phen)_2)]_n$ and PSS/$Fe^{II}(phen)_3$/$[(P_2W_{17}/Fe^{II}(phen)_3)]_n$ through the reduction of both the transition metal and the POM at different potentials [382].

An interesting approach to detecting weak visible light induced by an LED source and converted into an electrical signal was reported by Zhang et al. [383]. The introduction of covalently linked Pb^{2+} ions formed a new POM-Pb_3Mo_{18} chain complex. The revealed new mechanism promoting the ligand-to-metal charge-transfer (LCMT) process and enhanced electrical conductivity was related to the stabilization of the hole of oxygen atoms due to O → Mo charge transfer.

Wang, Chen and co-workers formed films through the electrodeposition of P_2W_{18} and P_2W_{17} on TiO_2 to fabricate high-performance smart windows. The authors observed, as in the case of (PSS/PAH/(P2W18-x/PAH) systems, that the degree of lacunar structure affected the performance of smart windows [83]. Mono-vacant lacunary WD-type P_2W_{17} had high optical contrast and higher coloration efficiency than P_2W_{18} [384] (Fig. 41).

6.3.4. Magnetic materials

Features such as stability in solution and in the solid-state, the potential role as a host for magnetic ions, rigid and highly symmetric structure and structural integrity after accepting several electrons, have been encouraging characteristics to explore POMs in the design of new molecular magnetic devices [53]. Although numerous papers reported magnetic properties and potential applications in single-molecule magnetism (SMM) or single-ion magnetism (SIM) using POMs, reports using WD POMs are scarcer than the Keggin, Peacock-Weakley, or Anderson-Evans POMs [53,385]. Table 4 shows some examples of WD POMs and their magnetic properties.

Cubane-type ($Mn^{III}_3Mn^{IV}O_3X$) assemblies constitute a well-known family of SMMs. Fang and co-workers condensed cubane-type

Table 3
Sensors constructed from WD POMs. Coordination water was omitted.

Compound	Substrate	Detection method	Detection limit [μM]	Linear range [μM]	Ref.
H_{10}[Cu(bix)$_2$(**$P_2W_{18}O_{62}$**)$_2$](bix)$_6$	UA	Electrochemistry	0.497	0.259–679	[81]
[**$P_2W_{17}O_{61}$**M]$_n$; M=Cu^{II}, Fe^{III} insertion during the electropolymerization of polypyrrole	Hydrogen peroxide	Electrochemistry	M=Cu^{II}: 0.3 M=Fe^{III}: 0.6	100–2000	[369]
K_8**$P_2W_{16}V_2O_{62}$** and monodisperse bimetallic nanoparticles (Au–Pd)	DA, AA	Electrochemistry	DA: 0.83 AA: 0.43	DA: 2.1–2060 AA: 1.2–1610	[370]
FAD-GDH($C_4H_{10}N)_6$[**$P_2Mo_{18}O_{62}$**]/PMA /MWCNT	Glucose	Electrochemistry	–	1000—20000	[371]
$(HDA)_3(TBA)_3$**$P_2W_{18}O_{62}$** (on GO)	Hydrogen peroxide	Electrochemistry	12.0	500–20000	[372]
αK_8[**$P_2W_{17}O_{61}$**$Ni^{II}H_2O$]	Protons	Electrochemistry	–	pH: 3–7	[373]
AgNPs@**DHPA**/GO/PGE	LD	Electrochemistry	0.00076	0.003 – 10	[374]
$(H_2N(CH_3)_2]_{10}H_3${$SeO_4Eu_5(H_2O)_8$[**$Se_2W_{14}O_{52}$**]	Cu^{II}Cys	Fluorescence	Cu^{II}: 1.24 Cys: 0.217	Cu^{II}: 10–250 Cys: 20 – 140	[149]
$[Cu_9(FKZ)_{12}(H2O)_8][H_3$**$P_2W_{18}O_{62}$**$]_2$ /PPy	Hydrogen peroxide, AA	Colorimetry	H_2O_2: 0.07 AA: 0.627	–	[375]
MIL-101(Fe)@H_6**$P_2W_{18}O_{62}$**@SWNT	Hydrogen peroxide Glc	Colorimetry	H_2O_2: 0.3 Glc: 0.2	H_2O_2: 80 Glc: 150	[376]
K_8[Co**$P_2W_{17}O_{61}$**·H_2O]·16H_2O/CNTFs	Glucose, AA	Electrochemistry	Glc: 0.42 AA: 0.1	–	[377]
[(*n*-$C_3H_7)_4N]_4$**$S_2W_{18}O_{62}$** doped PEDOT	bromate	Chronoampero-metry		100–2000	[378]

UA: uric acid; DA: dopamine; AA: ascorbic acid; Glc: glucose; LD: levodopa; bix: 1,4-bis(imidazol-1-ylmethyl)benzene; PEI: poly(ethylenimine); FAD-GDH: FAD-dependent glucose dehydrogenase; MWCNT: multiwalled carbon nanotube; HDA: hexadecyltrimethylammonium; GO: graphene oxide; DHPA: WD heteropolyacid; Cys: cysteine; HFKZ: 1-(2,4-difluorophenyl)-1,1-bis[(1H-1,2,4-triazol-1-yl)methyl] ethanol; ppy: polypyrrole; PGE: pencil graphite electrode; MIL-101(Fe): Tris [μ-[1,4-benzenedicarboxylato(2-)-κO1:κO'1]]chloro-μ3-oxotriiron; SWNT: single-walled carbon nanotube; CNTFs: carbon nanotube (CNTs) fibers; PEDOT: poly(3,4-ethylenedioxythiophene).

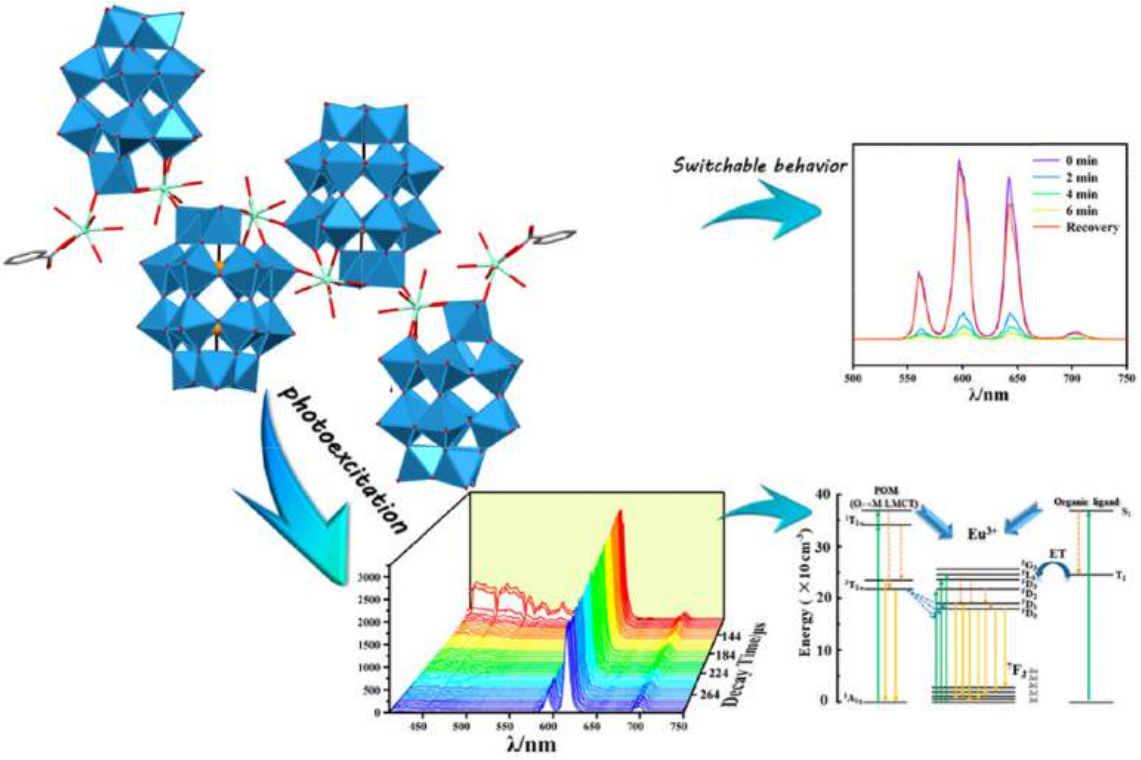

Fig. 40. Scheme of photoexcitation and switchable behavior observed for centrosymmetric tetrameric WD POMs containing samarium ions, ([$(P_2W_{17}O_{61})Sm(H_2O)_3Sm(C_6H_5COO)(H_2O)_6][(P_2W_{17}O_{61})Sm(H_2O)_3$]). Partially modified and reproduced from [104] with permission of the copyright holders.

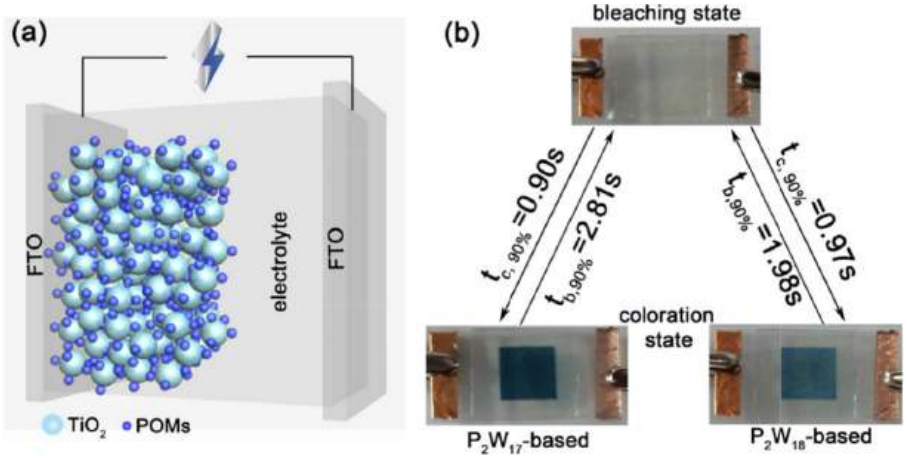

Fig. 41. (a) Structure of a POM-based smart window. (b) Images of POM-based smart windows at bleaching and coloration states. Reproduced from [384] with permission of the copyright holders.

$Mn_3^{III}Mn^{IV}O_4$ in the $[\alpha\text{-}P_2W_{15}O_{56}]^{12-}$ lacunar plane to obtain a polyanion, $[(\alpha\text{-}P_2W_{15}O_{56})Mn_3^{III}Mn^{IV}O_3(CH_3COO)]^{8-}$ (Fig. 42, Compound 1) with a spin S = 9/2 [188]. Surprisingly the polyanion did not exhibit any slowing of magnetization relaxation. The authors attributed the results to the existence of positive axial anisotropy D = +0.36 cm^{-1} that led to the reverse order of the zero-field split substrates, and thus an absence of slow magnetization relaxation. Subsequently, the authors synthesized a sandwich-type polyanion, $[(\alpha\text{-}P_2W_{15}O_{56})_2Mn_6^{III}Mn^{IV}O_6(H_2O)_6]^{14-}$ [386] (Fig. 42, Compound 2), whose magnetic measurements revealed a system with a spin S=21/2 and D = −0.143 cm^{-1}. The formation of the sandwich-type structure restored the slow magnetization relaxation characteristics typical of $[Mn_4O_4]^-$ based SMMs. The differences observed between these two compounds were attributed to the unexpected sign change in the D parameter, a consequence of a pronounced dipole moment of 1 vs. the absence of a dipole moment in 2.

Two types of $P_2V_3W_{15}$ WD POMs with a metalated (M = Y^{III}, Yb^{III}) phthalocyanine moiety (MPc) connected *via* an exposed organic linker (tris(alkoxo)pyridine) were synthesized by Pütt et al. A SQUID study of the resulting functionalized POMs confirmed intramolecular charge transfer between the MPc and the POM unit and the MPc of one molecule to the POM unit from another molecule [391].

Magnetic properties of $Cs_{7.5}K_{0.5}[((H_2O)_7Dy_2^{III}(\alpha_2,\alpha_2'\text{-}P_2W_{16}O_{60})(C_6H_5PO)_2)_2]\cdot 42H_2O$ and $Cs_{7.5}K_{0.5}[((H_2O)_7Y^{III}{}_2(\alpha_2,\alpha_2'\text{-}P_2W_{16}O_{60})(C_6H_5PO)_2)_2]\cdot 42H_2O$ (see section 2.2.2) were analyzed by Wang et al. and the magnetic susceptibility of the Dy derivative had the characteristics of a single ion magnet [200].

Table 4
Compounds based on WD POMs with magnetic properties.

Compound	Magnetic properties	Ref.
$Na_2(C_3N_2H_{12})_4([Ni_5(OH)_3(H_2O)_4(CH_3CO_2)][\mathbf{Si_2W_{18}O_{66}}])$	Antiferromagnetic interaction	[106]
$(H_2bpz)_6[Co_2(\mathbf{P_2W_{16}O_{57}})_2]$[a]	Weak ferromagnetic exchange interaction between Co	[247]
$(H_2bpz)_6[Co_3H_2(\mathbf{P_2W_{16}O_{57}})$ $(\mathbf{P_2W_{15}O_{56}})$		
$(C_{16}H_{18}N_3S)_5[S_2Mo_1^{V}\mathbf{Mo_{17}^{VI}O_{62}}]CH_3CN.$	Weak inter-cluster antiferromagneticinteraction	[120]
$H_4Li_6[\beta\text{-}P_2Co\mathbf{W_{17}O_{62}}]$	Antiferromagnetic Co–Co coupling	[217]
Na_{14} $[(\alpha\text{-}\mathbf{P_2W_{15}O_{56}})_2Mn_6^{III}Mn^{IV}O_6$	Ferromagnetic	[386]
	Mn^{III}–Mn^{III} interaction and antiferromagnetic Mn^{III} and Mn^{IV}, SMM	
$Na_{32.5}Rb_{1.5}$ $[Ni_{14}(OH)_6(H_2O)_{10}(HPO_4)_4(P_2\mathbf{W_{15}O_{56}})_4]$	Coexistence of both ferro andantiferromagnetic coupling	[387]
$Na_{12}[Mn_4^{III}(H_2O)_2(P_2\mathbf{W_{15}O_{56}})2]$	Antiferromagnetic interaction between the four Mn^{III}	[388]
$(NH_2Me_2)_{13}Na_3[(Er(H_2O)(CH_3COO)(\alpha2\text{-}\mathbf{P_2W_{17}O_{61}}))_2]$	Antiferromagnetic intramolecular dipolar interaction between the Er^{III} ions	[389]
$Na(NH_4)_5[\mathbf{P_2W_{15}O_{56}Ni_3}(H_2O)_3(\mu3\text{-}OH)_3(Re(CO)_3)_3]$	Ferromagnetic coupling	[390]
	interaction between adjacent Ni^{II}	
$(_nBu_4N)_4[HP_2V_3\mathbf{W_{15}O_{59}}(OCH_2)_3C(C_5H_4N)(YC_{32}H_{16}N_8)]$	Non-photoinduced charge transfer between electron donor and acceptor centers	[391]
$(_nBu_4N)_4[HP_2V_3\mathbf{W_{15}O_{59}}(OCH_2)_3C(C_5H_4N)(YbC_5H_4$ $N_8)]$		
$Cs_{7.5}K_{0.5}[((H_2O)_7Dy^{III}$ $_2(\alpha_2,\alpha_2'\text{-}P_2W_{16}O_{60})(C_6H_5PO)_2)_2]\cdot42H_2O$	Two predominant slow relaxation process ranges at separate temperature intervals	[200]

Bpz: 3,3′,5,5′-tetramethyl-4,4′-bipyrazo.

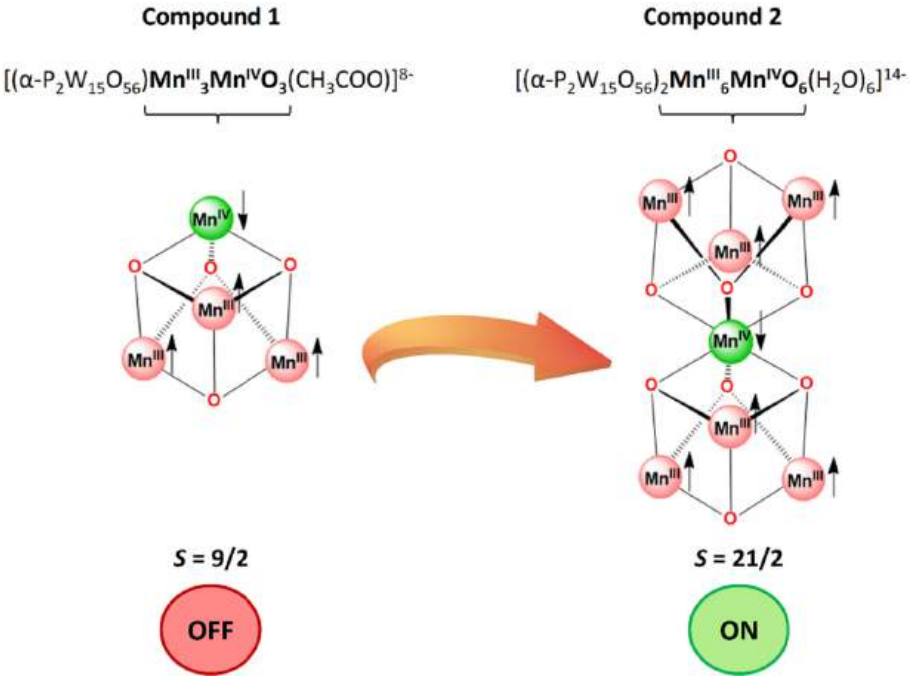

Fig. 42. Scheme of the proposed spin arrangement in the ground state for Compound **1** and **2**.

6.4. *Biology/Medicine*

Tunable POM-macromolecular interaction results from the modification of the POM structure, such as adjustment of electronic properties of acidity or polarity, POM encapsulation, post-functionalization with organic molecules or with metals and other species, and it has inspired several studies on the use of these compounds as therapeutic agents such as for Alzheimer's disease, antibacterial, anticancer, and the like (Table 5).

6.4.1. *Anticancer activity*

Numerous studies have been reported using POMs as potential anticancer drugs [71]. Antitumor activity against various tumor cell types has been found using inorganic WD POMs [392,393], WD organometallic hybrids [394,395] or WD POMs encapsulated in covalent [396] and supramolecular [397,398] polymeric networks. The proposed mechanisms of POM antitumor activity are diverse and are still under discussion/being investigated [71]. However, WD POMs inhibit processes that play pivotal roles in the proliferation of several types of cancer, for example in angiogenesis (in particular through binding the fibroblast growth factor [399], CK2 inhibitors [400], inhibition of the DNA-binding activity of AP-2gamma [393] and Sox2 [401], or aquaporin-3 (AQP3) activity [402]. These studies have shown that the size and type of POMs affect inhibitory activity, and the WD type was one of the most efficient inhibitors compared to other POM types.

Additionally, a gadolinium-containing WD POM ($Gd_2P_2W_{18}O_{62}$) was evaluated *in vitro* and *in vivo* as a magnetic resonance imaging (MRI) contrast agent [229]. Recent studies on WD POMs in combined photothermal and immune anticancer therapy (PTT) show promising results. The authors presented *in vivo* and *in vitro* studies on $P_2Mo_{18}O_{62}$ in the free form and in a gellan gum hydrogel formulation. Moreover, POM hydrogel incorporation into resiquimod (R848) showed a synergy effect against the 4 T1 cell line. Photothermal agent R848/POM@GG is stable in water, degrades to a nontoxic form in the physiological environment and minimizes POM toxicity against normal tissues [403].

6.4.2. *Antibacterial activity*

Similarly, it has also been observed that POMs have interesting

Table 5
Activity of selected WD POMs in the *in vitro* and *in vivo* experiments.

POM	Cell line	Activity	Ref.
$Na_6[P_2Mo_{18}O_{62}]$	KB	IC_{50} = 34.5 μg/mL	[392]
$Na_6[As_2Mo_{18}O_{62}]$	KB	IC_{50} = 52.3 μg/mL	
$Na_{12}[P_2W_{15}O_{56}]\cdot 24H_2O$	HeLa	cell viability- 85%	[398]
	MCF-7	cell viability- 79%	
	Vero	cell viability- 37%	
PMAA-ChCl-$[P_2W_{15}O_{56}]$	HeLa	cell viability- 75%	
	MCF-7	cell viability -77%	
	Vero	cell viability- 15%	
PMAA-CMCh-$[P_2W_{15}O_{56}]$	HeLa	cell viability- 68%	[397]
	MCF-7	cell viability- 72%	
	Vero	cell viability- 10%	
$K_4H_3[(CH_3OOCCH_2CH_2Sn)P_2W_{17}O_{61}]\cdot 11H_2O$	HeLa	IC_{50} = 90.2 μg/mL	[394]
	SSMC-7721	IC_{50} = 86.3 μg/mL	
$K_4H_3[(CH_3OOCCH(CH_3)CH_2Sn)P_2W_{17}O_{61}]\cdot 11H_2O$	HeLa	IC_{50} = 86.7 μg/mL	
	SSMC-7721	IC_{50} = 79.1 μg/mL	
$K_7H_2[(CpTi)_3P_2W_{15}O_{59}]\cdot 5H_2O$	HeLa	IC_{50} = 47.2 μg/mL	[395]
	SSMC-7721	IC_{50} = 20.8 μg/mL	
$(Bu_4N)_9[(CpZr)_3P_2W_{15}O_{59}]$	HeLa	IC_{50} = 63.3 μg/mL	
	SSMC-7721	IC_{50} = 40.6 μg/mL	
$K_4H_5[(CH_3OOCCH_2CH_2Sn)_3P_2W_{15}O_{59}]\cdot 10H_2O$	HeLa	IC_{50} = 50.1 μg/mL	
	SSMC-7721	IC_{50} = 30.6 μg/mL	
$K_4H_5[(CH_3OOCH(CH_3)CH_2Sn)_3P_2W_{15}O_{59}]\cdot 10H_2O$	HeLa	IC_{50} = 48.3 μg/mL	
	SSMC-7721	IC_{50} = 30.1 μg/mL	
α_2-$K_7[P_2W_{17}(NbO_2)O_{61}]\cdot 13H_2O$	HeLa	cell viability- 10.0%	[413]
TMC-$[P_2W_{17}(NbO_2)O_{61}]$	HeLa	cell viability- 5.0%	
$[(n\text{-}C_4H_9)_4N]_6[P_2W_{18}O_{62}]$	CT26	cell viability- 80.0%	
	MC38	cell viability- 80.0%	[30]
	CT26 – tumor-bearing mice	TGI 55.5%	
	MC38 – tumor-bearing mice	TGI 64.3%	
$[P_2W_{18}O_{62}]$@Hf_{12}-DBB-Ir	CT26	IC_{50} = 3.21 μM	
	MC38	IC_{50} = 2.51 μM	
	CT26 – tumor-bearing mice	TGI- 99.7%	
	MC38 – tumor-bearing mice	TGI- 99.0%	
$(NH_4)_6[P_2Mo_{18}O_{62}]\cdot 14H_2O$	4 T1	cell viability- 90.0%	[403]
$[P_2Mo_{18}O_{62}]$@GG	4 T1 – tumor-bearing mice	inhibition rate- 90.0%	
R848/$[P_2Mo_{18}O_{62}]$@GG	4 T1 – tumor-bearing mice	inhibition rate- 99.3%	
$K_6[P_2W_{18}O_{62}]\cdot 14H_2O$	PC12	cell viability- 95.0%	[408]
$K_8[P_2W_{17}O_{61}(Co^{II}\cdot OH_2)]\cdot 16H_2O$		cell viability- 90.0%	
$K_8[P_2W_{17}O_{61}(Ni^{II}\cdot OH_2)]\cdot 17H_2O$		cell viability- 95.0%	
Aβ- $K_6P_2W_{18}O_{62}$		cell viability- 80.8%	
Aβ- $K_6P_2W_{18}O_{62}$-Co		cell viability- 90.0%	
Aβ- $K_6P_2W_{18}O_{62}$-Ni		cell viability -105.0%	
Aβ- $K_6P_2W_{18}O_{62}$@AuNPs	PC12	cell viability- 65.0%	[409]
Aβ- $K_6P_2W_{18}O_{62}$@AuNPs-pep		cell viability- 90.0%	[411]
MSNs-$K_5P_2W^{V}W^{VI}_{17}O_{62}$-copolymer	PC12	cell viability- 92.6%	
MSNs- $K_5P_2W^{V}W^{VI}_{17}O_{62}$-copolymer upon NIR irridation		cell viability- 54.8%	[407]
$K_8[P_2CoW_{17}O_{61}]$	PC12	cell viability- 90.0%	
CeONP-$K_6P_2W_{18}O_{62}$	PC12	cell viability- 75.0%	[410]

PMAA-ChCl: poly(methacrylic acid)-chitosan hydrochloride; PMAA-CMCh: poly (methacrylic acid)-carboxymethyl chitosan; TMC: trimethyl chitosan; DBB: 4,4′-di(4-benzoato)-2,2′-bipyridine; R848: resiquimod; GG: gellan gum hydrogel; pep: peptide CLPFFD; CeONP: cerium oxide nanoparticles.

antibacterial properties [404]. In particular, the WD type has shown synergy effects with conventional antibiotics such as β-lactam antibiotics against *Staphylococcus aureus* [405,406].

In addition to the anticancer and antibacterial effects, transition metal-substituted WD POMs ($K_7P_2W_{17}O_{61}M$; M = Co^{II}, Ni^{II}) have shown the greatest inhibition effect on amyloid β (Aβ) aggregation and Aβ-heme peroxidase-like activity (critical steps in the development of Alzheimer's disease) [407,408]. WD POM-type structures built on nanoplatform-like gold nanoparticles (AuNPs), mesoporous silica nanoparticles (MSNs) or cerium oxide nanoparticles (CeONPs) were used as novel Aβ inhibitors [409–411]. WD POMs built in MSNs were successfully used in the photothermal treatment of AD. Under NIR laser illumination, a POM nanohybrid inhibited and disaggregated Aβ fibers, as well as crossed the blood–brain-barrier [411]. Co– and Ni-substituted

POMs showed greater inhibitory effects on amyloid Aβ aggregation than a WD POM substituted with Mn^{III}, Cu^{II}, Fe^{II} or a non-substituted WD, or other types of POMs such as Kegging or Anderson.

In addition to the anticancer properties of this type of POMs, it has been recently found that the hierarchical assembly of nMOFs incorporating WD POMs acts as a multifarious radio-enhancer for anticancer therapy [412]. The hierarchical assembly of nMOFs consists of Hf-based metalloxo clusters, an Ir-based bridging ligand, and a WD POM. It has been shown that this system acts as a radioelectric enhancer for the efficient generation of reactive oxygen species (ROSs), showing an excellent antitumor effect on colon cancer tumor models (MC38 and CT26 cell lines). The assembly facilitated synergy interactions among high-Z components, generating three types of ROSs: hydroxyl radicals (•OH) through the radiolysis of water, singlet oxygen ($^1O_2$) through the photosensitization of DBB-Ir, and superoxide formation through W_{18} (Fig. 43).

The biological application of WD POMs is often related to their inhibition activity toward PMCA Ca^{II} and SERCAATPase [414]. The inhibitory effect against *Ab*PPO4 has been tested on intact, mono-, tri- and *hexa*-lacunary forms of WD POMs. The monolacunary form, $[\alpha_2\text{-}P_2W_{17}O_{61}]^{10-}$, retains its structural integrity and exhibits the strongest inhibition of *Ab*PPO4 (Ki = 6.5 mM), while the trilacunary type rearranges to a more stable monolacunary form and shows the weakest inhibition [415].

A number of studies with WD POM types have proved their antiviral effect. A screening study of POMs for anti-HIV-1 and HIV-2 activity demonstrated that organic moieties enhanced the inhibitory potential [416–418].

Interestingly, WD structures were also used as additive agents in protein crystallization [404]. $K_6[P_2W_{18}O_{62}]$ bound RNA polymerase II during speciation chain elongation and was successfully used for phasing a large protein [419]. In the recent study Leyssens et al. also presented the use of the $K_{10}[\alpha_2\text{-}P_2W_{17}O_{61}]\cdot 20H_2O$ WD POM and the hafnium(IV)-substituted WD POM, $K_{16}[Hf(\alpha_2\text{-}P_2W_{17}O_{61})_2]\cdot 19H_2O$, as contrast-enhancing staining agents in X-ray microfocus computed tomography [420]. Imaging of rat, porcine and human blood vessels revealed microstructural differences between the type of blood vessels, which may be useful in computer modeling for future graft material design and for understanding the function of blood vessels and improving current disease treatments.

7. Conclusions and perspectives

Over the past two decades, we have seen dynamic development in the field of WD POMs which, when functionalized, lend themselves to easy post-functionalization with other organic or inorganic molecules, leading to advanced material design and an extensive range of applications. In this review, we have discussed the possibilities for the functionalization of the WD POM basic subunit and classified them according to modifications made in respective structural parts: templates/heteroatoms, addenda atoms (CAP modification: trilacunar and monolacunar, and belt modification) and non-conventional WD POM motifs (open and sandwich-type WD POMs). The review also presents an analysis of speciation in solution and includes ion distribution plots over a wide pH range for WD POMs, knowledge of which is essential for further modifications, as suboptimal selection of reaction conditions such as pH in the first place can prove detrimental to the WD POM subunit. In addition, the ionic interactions of negatively charged WD POM subunits with counter cations are also shown. As part of this review, we also discussed the path of further post-functionalization of the currently available hybrid WD POM platforms and classified them based on the available post-functionalization approaches into single and double linker modularities and the other different linker modularities, such as polymers with POMs. This review reveals how WD POM post-functionalization can generate materials with new and/or improved physicochemical properties with a significant impact on the development of their applications in the following scientific fields: energy-related applications, catalysis (photocatalysis, electrocatalysis), functional materials (sensors, optical materials, electrochromic materials, magnetic materials), biology/medicine (anticancer and antibacterial activity).

Additionally, to better illustrate the current trends and present less researched aspects of this field, we include below data from a *meta*-analysis of studies on WD POMs. Owing to the bibliometric data available in the Scopus database a network constructed on the basis of keywords can be generated, searching the latest scientific and technological developments regarding WD POMs. In the field of science and technology, the Scopus database was used, searching "Wells-Dawson" and "structure" (Fig. 44), "Wells-Dawson" and "properties" (Fig. 45) as combined keywords, in articles published until May 2024.

Duplicate papers found in more than one of the databases that did not focus on the selected keywords were excluded. VOSviewer software version 1.6.20 (https://www.vosviewer.com) was used to analyze the

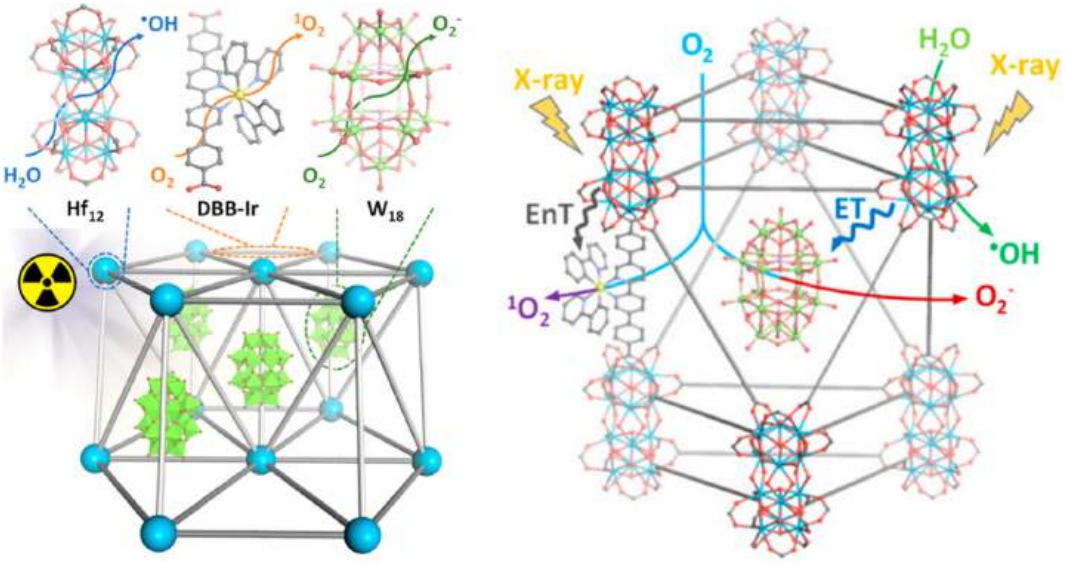

Fig. 43. The assembly of nMOF consisting of Hf-based metalloxo clusters (Hf_{12}), an Ir-based bridging ligand (DBB-Ir), and a WD POM (W_{18}) and mechanisms of ROS generation. EnT: energy; ET: electron transfer. Reproduced from [412] with permission of the copyright holders.

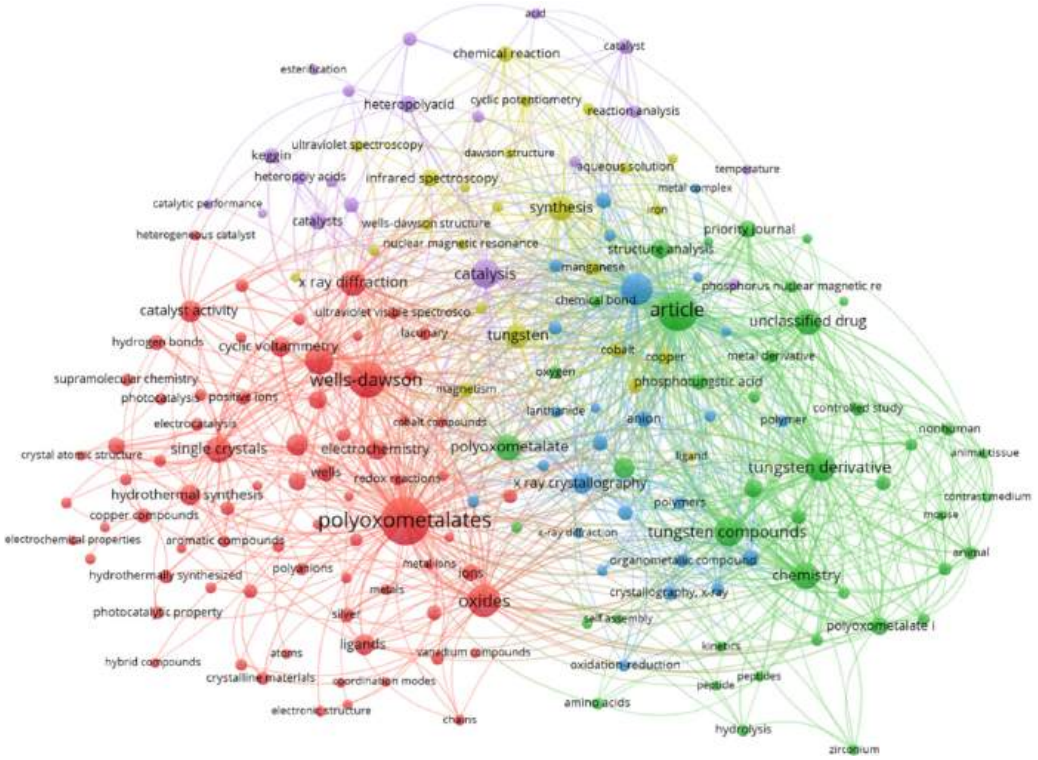

Fig. 44. A bibliometric map obtained with VOSviewer version 1.6.20 (https://www.vosviewer.com) [421] using "Wells-Dawson" and "structure"as keywords, recorded from the Scopus database.

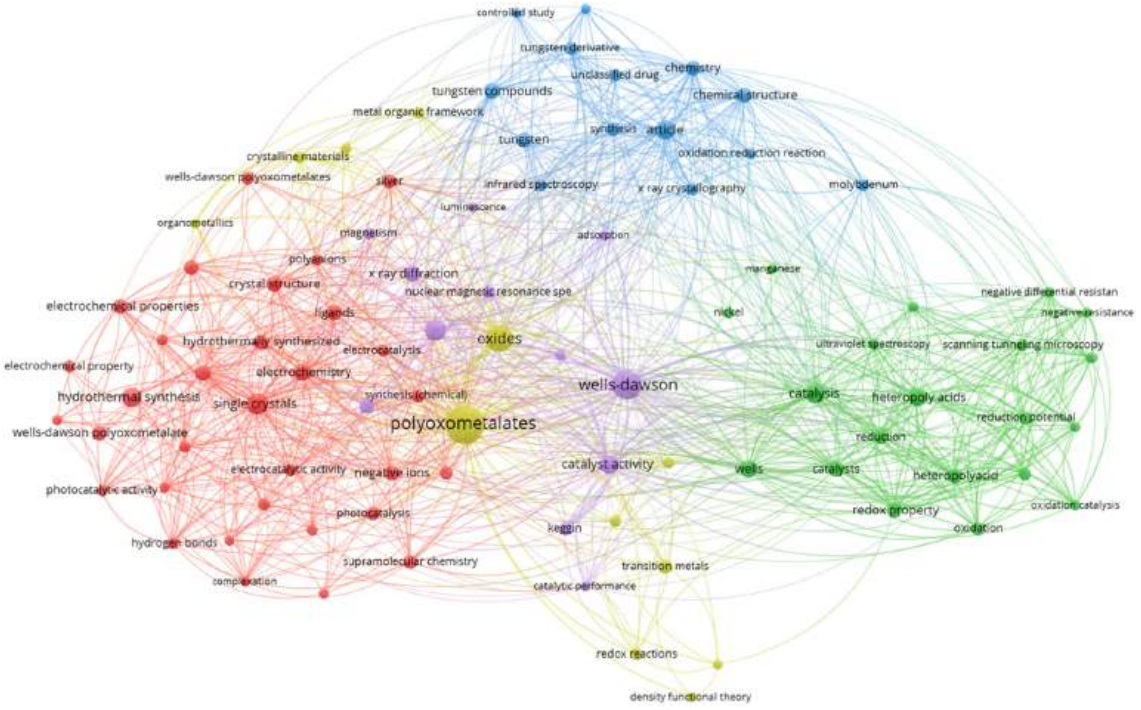

Fig. 45. A bibliometric map obtained with VOSviewer version 1.6.20 (https://www.vosviewer.com) [421] using "Wells-Dawson" and "properties" as keywords, recorded from the Scopus database.

data and generate the bibliometric maps [421]. Each keyword is represented by a circle and the lines show the frequency and relationships between them; the larger the circle, the more often the keyword appeared in publications. The keywords are assigned to a cluster, each cluster corresponding to a different research area and shown in a different color. The combined "Wells-Dawson" and "structure" search gave five main clusters (Fig. 44), focusing mainly on (i) single crystals, X ray diffraction (red, 75 items), (ii) tungsten derivatives, unclassified drug (green, 42 items), (iii) chemical structure, metal complexes (blue, 26 items), (iv) synthesis (yellow, 24 items) and (v) catalysis (purple, 19

items). For the second network, the combination of "Wells-Dawson" and "properties" search recorded five main clusters (Fig. 45), focusing mainly on (i) single crystals, electrochemical properties (red, 32 items), (ii) catalysis, heteropoly acids (green, 20 items), (iii) synthesis, tungsten compounds (blue, 14 items), (iv) oxides, transition metals (yellow, 12 items) and (v) catalyst activity (purple, 12 items). The above *meta*-analysis clearly shows that mainly the archetypical tungsten WD POMs were employed for majority of the studies, but the hybrid systems are gaining more attention. Efficient protocols for integration with *d-/f*-block metal ions, small molecules or even polymers was demonstrated, therefore means necessary for improvement of the desired properties are already known. The concepts of supramolecular chemistry seem to be the another promising option to explore in this manner. Integration of WD POMs with MOFs was demonstrated and should be expanded into other well-defined porous materials such as Covalent Organic Frameworks (COFs). Tunable redox properties and acid/base character confer to the most often explored catalytic applications, including photo- and electrocatalysis. Whereas WD POMs can improve the properties of lithium-ion batteries, their application in sodium/zinc/aluminum-based energy storage systems is yet to be demonstrated. Finally, significant amount of WD POM studies targeted their biological properties, as anticancer and antibacterial agents or for their interactions with proteins. The latter can be potentially used in tackling the neurodegenerative diseases, but it remains to be seen *in vivo*.

Based on the research conducted so far, we expect that in the coming years, advances in the functionalization and post-functionalization approaches to WD POM subunits will further improve their physicochemical properties and increase their importance in their downstream applications. However, for this to happen there are several challenges to overcome. One of the limitations associated with the synthesis is the presence of oxo groups on the WD POM surface, which can only bind to a limited number of organic groups to form hybrid materials for further post-functionalization. In addition, the WD POM subunit itself has poor chemical stability, and conducting a chemical reaction in which the reactant is based on the POM subunit is limited by the pH value. Therefore, the rational design and synthesis of new WD POM hybrids that can combine WD POM subunits containing oxide groups with organic or inorganic linkers that enable further functionalization is the key task in advanced engineering, carrying the prospect of obtaining materials with excellent and improved properties that could be used in many scientific fields. A great advantage of WD POM-based materials is their ability to modify their acid-base and redox properties by changing their chemical composition, and their ability to accept and release electrons. In addition, WD POM hybrids have unique properties such as well-defined structure or Brønsted acidity. These features as well as the ability to modify and introduce suitable linkers will be crucial to improve electrochemical properties manifested in improved energy storage and delivery capabilities, and will also make WD POM hybrids even better catalysts for many chemical reactions. In addition, the applications of WD POM hybrids in biology and medicine are largely due to their shape and negative surface charge, resulting in specific interactions with various biomolecules, and further optimization of the charge and shape of the subunits could minimize potential toxicity and improve *in vivo* stability.

The most important features of WD-POMs and how they transform into the desired properties that have been discussed in this review are summarized in Fig. 46.

The future may bring even more POM-based applications, given the available strategies and the rapid development and progress in designing novel functionalizations of the WD POM subunit, so that the potential of WD POMs in various domains of technology could be fully leveraged.

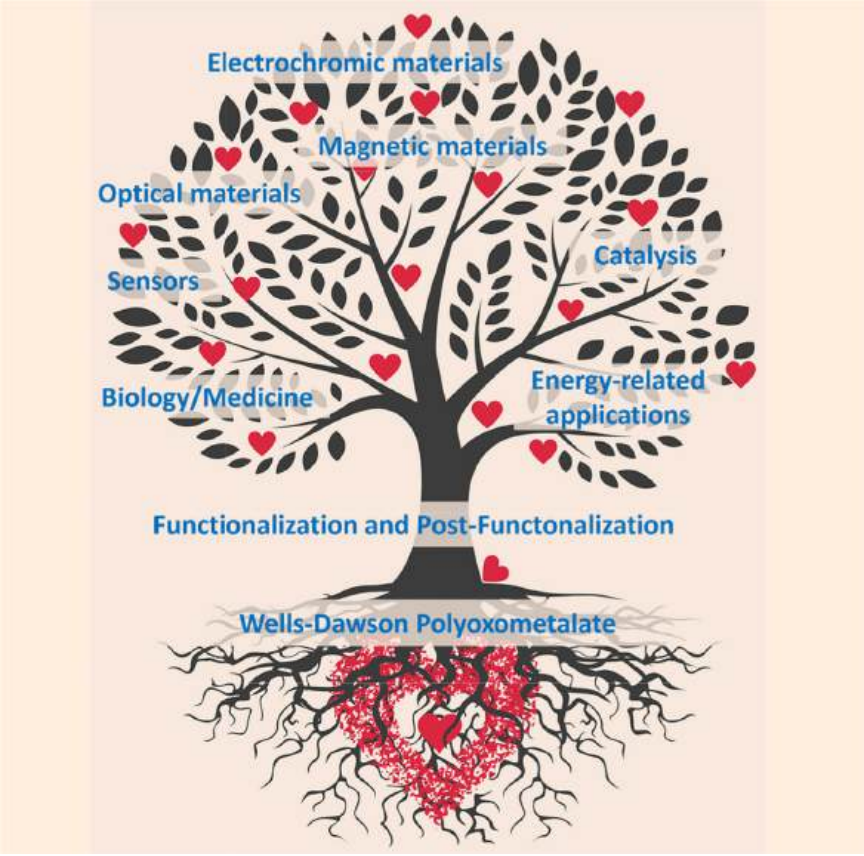

Fig. 46. Schematic visualization of a tree in which the roots of the WD POM expand into the tree trunk, and from there the respective closely related branches represent various applications.

Declaration of competing interest

The authors declare that they have no known competing financial interests or personal relationships that could have appeared to influence the work reported in this paper.

Data availability

Data will be made available on request.

Acknowledgements

This work was supported by the National Science Centre, Poland (grant numbers UMO-2022/45/N/ST4/00632 (D.N.), UMO-2020/39/D/ST4/01182 (A.G.), UMO-2022/44/C/ST4/00017 (E.W-S.), 2022/47/B/ST4/02310 (V.P.)). Daria Nowicka is a scholarship holder of the Adam Mickiewicz University in Poznan Foundation for the 2023/2024 academic year. Adam Gorczyński is a scholarship holder of the Polish Ministry of Education and Science for outstanding young scientists.

References

[1] N.I. Gumerova, A. Rompel, Nat. Rev. Chem. 2 (2018) 0112.
[2] A.V. Anyushin, A. Kondinski, T.N. Parac-Vogt, Chem. Soc. Rev. 49 (2020) 382–432.
[3] J.-X. Liu, X.-B. Zhang, Y.-L. Li, S.-L. Huang, G.-Y. Yang, Coord. Chem. Rev. 414 (2020) 213260.
[4] M. Hutin, M. Rosnes, D.-L. Long, L. Cronin, Comprehensive Inorganic Chemistry II (second edition): From Elements to Applications, 2 (2013) 241-269.
[5] M. Aureliano, N.I. Gumerova, G. Sciortino, E. Garribba, C.C. McLauchlan, A. Rompel, D.C. Crans, Coord. Chem. Rev. 454 (2022) 214344.
[6] R. Sheng, R. Sun, L. Chen, R. Lv, Y. Li, T. Du, Y. Zhang, Y. Qi, Crit. Rev. Anal. Chem. 54 (2024) 315–332.
[7] B. Yu, X. Zhao, J. Ni, F. Yang, Chem. Phys. Mater. 2 (2023) 20–29.
[8] N. Ogiwara, T. Iwano, T. Ito, S. Uchida, Coord. Chem. Rev. 462 (2022) 214524.
[9] J.M. Cameron, G. Guillemot, T. Galambos, S.S. Amin, E. Hampson, K. Mall Haidaraly, G.N. Newton, G. Izzet, Chem. Soc. Rev. 51 (2022) 293–328.
[10] C. Dey, J. Clust. Sci. 33 (2022) 1–18.
[11] M.J.W. Budych, K. Staszak, A. Bajek, F. Pniewski, R. Jastrząb, M. Staszak, B. Tylkowski, K. Wieszczycka, Coord. Chem. Rev. 493 (2023) 215306.
[12] Y. Zhang, Y. Li, H. Guo, Y. Guo, R. Song, Mater. Chem. Front. 8 (2024) 732–768.
[13] X.-K. Lian, H.-B. Chen, Y.-D. Lin, X.-X. Li, S.-T. Zheng, Coord. Chem. Rev. 497 (2023) 215440.
[14] F. Carvalho, M. Aureliano, Int. J. Mol. Sci. 24 (2023) 5043.
[15] Q. Liu, X. Wang, Angew. Chem. Int. Ed. 62 (2023) e202217764.
[16] C.M. Granadeiro, D. Julião, S.O. Ribeiro, L. Cunha-Silva, S.S. Balula, Coord. Chem. Rev. 476 (2023) 214914.
[17] J. Rieger, T. Antoun, S.-H. Lee, M. Chenal, G. Pembouong, J. Lesage de la Haye, I. Azcarate, B. Hasenknopf, E. Lacôte, Chem. – Eur. J. 18 (2012) 3355–3361.
[18] C.P. Pradeep, F.Y. Li, C. Lydon, H.N. Miras, D.L. Long, L. Xu, L. Cronin, Chemistry (Weinheim an der Bergstrasse, Germany) 17 (2011) 7472–7479.
[19] G. Izzet, B. Abécassis, D. Brouri, M. Piot, B. Matt, S.A. Serapian, C. Bo, A. Proust, J. Am. Chem. Soc. 138 (2016) 5093–5099.
[20] L. Vandebroek, Y. Mampaey, S. Antonyuk, L. Van Meervelt, T.N. Parac-Vogt, Eur. J. Inorg. Chem. 2019 (2019) 506–511.
[21] Y. Gao, M. Choudhari, G.K. Such, C. Ritchie, Chem. Sci. 13 (2022) 2510–2527.
[22] M.-T.-K. Ng, N.L. Bell, D.-L. Long, L. Cronin, J. Am. Chem. Soc. 143 (2021) 20059–20063.
[23] I. Lindqvist, Acta Crystallogr. 5 (1952) 667–670.
[24] J.F. Keggin, Nature 132 (1933) 351.
[25] B. Dawson, Acta Crystallogr. 6 (1953) 113–126.
[26] D.D. Dexter, J.V. Silverton, J. Am. Chem. Soc. 90 (1968) 3589–3590.
[27] J.A. Fernández, X. López, C. Bo, C. de Graaf, E.J. Baerends, J.M. Poblet, J. Am. Chem. Soc. 129 (2007) 12244–12253.
[28] H.T. Evans, J. Am. Chem. Soc. 70 (1948) 1291–1292.
[29] J.S. Anderson, Nature 140 (1937) 850.
[30] Y. Zhang, J. Liu, S.-L. Li, Z.-M. Su, Y.-Q. Lan, Energy Chem. 1 (2019) 100021.
[31] L.E. Briand, G.T. Baronetti, H.J. Thomas, Appl. Catal. A: Gen. 256 (2003) 37–50.
[32] S.-S. Wang, G.-Y. Yang, Chem. Rev. 115 (2015) 4893–4962.
[33] Q. Hu, K. Li, X. Chen, Y. Liu, G. Yang, Polyoxometalates 3 (2024) 9140048.
[34] Z. Wei, S. Ru, Q. Zhao, H. Yu, G. Zhang, Y. Wei, Green Chem. 21 (2019) 4069–4075.
[35] G. Dai, Q. Li, D. Zang, Y. Wei, Green Chem. 25 (2023) 6263–6269.
[36] H. Yu, Q. Zhao, Z. Wei, Z. Wu, Q. Li, S. Han, Y. Wei, Chem. Commun. 55 (2019) 7840–7843.
[37] Y.-F. Liu, C.-W. Hu, G.-P. Yang, Chin. Chem. Lett. 34 (2023) 108097.
[38] Y. Liu, G. Zeng, Y. Cheng, L. Chen, Y. Liu, Y. Wei, G. Yang, Chin. Chem. Lett. 35 (2024) 108480.
[39] X. Gao, R. Ma, Z. Liu, S. Wang, Y. Wu, G. Song, Appl. Catal. B: Environ. Energy 352 (2024) 124059.
[40] Q. Hu, H. Zhou, Y. Ding, T. Wågberg, X. Han, ACS Catal. 14 (2024) 5898–5910.
[41] A. Ebrahimi, L. Krivosudský, A. Cherevan, D. Eder, Coord. Chem. Rev. 508 (2024) 215764.
[42] Y.-F. Liu, X.-L. Lin, B.-M. Ming, Q.-L. Hu, H.-Q. Liu, X.-J. Chen, Y.-H. Liu, G.-P. Yang, Inorg. Chem. 63 (2024) 5681–5688.
[43] X. Wei, Y. Jiang, Y. Ma, H. Liao, S. Dai, P. An, Z.-Q. Wang, X.-Q. Gong, Z. Hou, ACS Catal. 14 (2024) 5344–5355.
[44] J.M. Cameron, S. Fujimoto, K. Kastner, R.-J. Wei, D. Robinson, V. Sans, G. N. Newton, H.H. Oshio, Chem. – Eur. J. 23 (2017) 47–50.
[45] N. Shi, Y. Ding, N. Li, F. Wen, D. Liu, J. Environ. Chem. Eng. 11 (2023) 110558.
[46] S. Li, N. Li, G. Li, Y. Ma, M. Huang, Q. Xia, Q. Zhao, X. Chen, Polyoxometalates 2 (2023) 9140024.
[47] C. Gu, C. Li, N. Minezawa, S. Okazaki, K. Yamaguchi, K. Suzuki, Nanoscale 16 (2024) 8013–8019.
[48] J.-Y. Zhang, Y. Song, J. Yang, W.-Y. Pei, J.-F. Ma, Inorg. Chem. Front. 11 (2024) 3011–3020.
[49] S. Fu, S. Ullah Khan, R. Yang, H. Pang, C.-M. Au, H. Ma, X. Wang, G. Yang, W. Sun, W.-Y. Yu, J. Colloid Interface Sci. 666 (2024) 496–504.
[50] K. Talbi, F. Penas-Hidalgo, A.L. Robinson, P. Gotico, W. Leibl, P. Mialane, M. Gomez-Mingot, M. Fontecave, A. Solé-Daura, C. Mellot-Draznieks, A. Dolbecq, Appl. Catal. B: Environ. Energy 345 (2024) 123681.
[51] Y. Yang, K. Guo, M. Zhu, A. Zhang, M. Xing, Y. Lu, X. Bai, X. Ji, Y. Hu, S. Liu, Inorg. Chem. 63 (2024) 7876–7885.
[52] M. Yamaguchi, K. Shioya, C. Li, K. Yonesato, K. Murata, K. Ishii, K. Yamaguchi, K. Suzuki, J. Am. Chem. Soc. 146 (2024) 4549–4556.
[53] J.M. Clemente-Juan, E. Coronado, A. Gaita-Ariño, Chem. Soc. Rev. 41 (2012) 7464–7478.
[54] Z.-X. Yang, F. Gong, D. Lin, Y. Huo, Coord. Chem. Rev. 492 (2023) 215205.
[55] L. Martinez, P. Alborés, Eur. J. Inorg. Chem. 27 (2024) e202300687.
[56] D.R.M. Clyde, D.L. Cortie, S. Granville, D.C. Ware, P.J. Brothers, J. Malmström, Nano Lett. 24 (2024) 2165–2174.
[57] M. Palacios-Corella, V. García-López, J.C. Waerenborgh, B.J.C. Vieira, G. Mínguez Espallargas, M. Clemente-León, E. Coronado, Chem. Sci. 14 (2023) 3048–3055.
[58] M.R. Horn, A. Singh, S. Alomari, S. Goberna-Ferrón, R. Benages-Vilau, N. Chodankar, N. Motta, K. Ostrikov, J. MacLeod, P. Sonar, P. Gomez-Romero, D. Dubal, Energy Environ. Sci. 14 (2021) 1652–1700.
[59] C. Mu, Z. Du, W. Li, Polyoxometalates 3 (2024) 9140062.
[60] Q. Liu, Y. Cui, L. Zhu, D. Cheng, C. Wang, S. Lu, B. Li, X. Chen, H.-Y. Zang, Polyoxometalates 2 (2023) 9140036.
[61] L. Ni, J. Gu, X. Jiang, H. Xu, Z. Wu, Y. Wu, Y. Liu, J. Xie, Y. Wei, G. Diao, Angew. Chem. Int. Ed. Engl. 62 (2023) e202306528.
[62] D. Pakulski, A. Gorczyński, D. Brykczyńska, V. Montes-García, W. Czepa, I. Janica, M. Bielejewski, M. Kubicki, V. Patroniak, P. Samorì, A. Ciesielski, Angew. Chem. Int. Ed. 62 (2023) e202305239.
[63] Á. Barros, B. Artetxe, U. Eletxigerra, E. Aranzabe, J.M. Gutiérrez-Zorrilla, Materials 16 (2023) 5054.
[64] D. Pakulski, A. Gorczyński, W. Czepa, Z. Liu, L. Ortolani, V. Morandi, V. Patroniak, A. Ciesielski, P. Samorì, Energy Storage Mater. 17 (2019) 186–193.
[65] C. Wang, B. Wang, H. Yang, Y. Wan, H. Fang, W. Bao, W. Wang, N. Wang, Y. Lu, Chem. Eng. J. 483 (2024) 149143.
[66] H. Hu, L. Lian, X. Ji, W.-L. Zhao, H. Li, W. Chen, H.N. Miras, Y.-F. Song, Coord. Chem. Rev. 503 (2024) 215640.
[67] S. Zhang, R. Liu, C. Streb, G. Zhang, Polyoxometalates 2 (2023) 9140037.
[68] A. Das, M. Mohapatra, S. Basu, Carbon 223 (2024) 119007.
[69] Á. Barros, E. Aranzabe, B. Artetxe, J.C. Duburg, L. Gubler, J.M. Gutiérrez-Zorrilla, U. Eletxigerra, ACS Appl. Energy Mater. 7 (2024) 3729–3739.
[70] E. Svensson Grape, J. Huang, D. Roychowdhury, T.T. Debela, H. Chang, A. Jenkins, A.M. Schimpf, C.H. Hendon, C.K. Brozek, ACS Appl. Energy Mater. (2024).
[71] A. Bijelic, M. Aureliano, A. Rompel, Angew. Chem. Int. Ed. 58 (2019) 2980–2999.
[72] S. Lentink, D.E. Salazar Marcano, M.A. Moussawi, T.N. Parac-Vogt, Angew. Chem. Int. Ed. 62 (2023) e202303817.
[73] A. Kondinski, Polyoxometalates 3 (2024) 9140058.
[74] L. Wang, P. Dai, H. Ma, T. Sun, J. Peng, Inorg. Chem. Front. 11 (2024) 1339–1365.
[75] M. Tahmasebi, M. Mirzaei, M. Darroudi, J.T. Mague, J. Mol. Struct. 1309 (2024) 138102.
[76] B. Li, X. Xu, Y. Lv, Z. Wu, L. He, Y.-F. Song, Small 20 (2024) 2305539.
[77] H. Soria-Carrera, E. Atrián-Blasco, R. Martín-Rapún, S.G. Mitchell, Chem. Sci. 14 (2023) 10–28.
[78] R. Khan, M. Tariq, K.H. Shah, S. Rani, N.A. Osman, H.M. Asif, S. Mehar, A. K. Alanazi, H.M. Abo-Dief, J. Photoch. Photobio. A 442 (2023) 114774.
[79] C. Zhang, R. Liu, X. Kong, H. Li, D. Yu, X. Fang, L. Wu, Y. Wu, Int. J. Mol. Sci. 24 (2023) 8858.
[80] D. Nowicka, D. Marcinkowski, N. Vadra, M. Szymańska, M. Kubicki, G. Consiglio, W. Drożdż, A.R. Stefankiewicz, V. Patroniak, M. Fik-Jaskółka, A. Gorczyński, Dalton Trans. 53 (2024) 11678–11688.
[81] M. Xu, C. Liu, Y. Wang, J. Wang, J. Feng, J. Sha, J. Clust. Sci. 32 (2021) 1–10.
[82] C.-G. Liu, W. Guan, L.-K. Yan, Z.-M. Su, P. Song, E.-B. Wang, J. Phys. Chem. C 113 (2009) 19672–19676.
[83] S. Liu, L. Xu, G.-G. Gao, B. Xu, Thin Solid Films 517 (2009) 4668–4672.
[84] F. Xiao, X. Meng, L. Wang, J. Hao, C. Lv, Y. Wei, Polyoxometalates 3 (2024) 9140055.

[85] H.-X. Sheng, B.-Y. Lin, C.-Q. Chen, J. Du, P. Yang, Polyoxometalates 3 (2024) 9140060.
[86] A. Bocian, W. Drożdż, M. Szymańska, J. Lewandowski, M. Fik-Jaskółka, A. Gorczyński, V. Patroniak, A.R. Stefankiewicz, Nanoscale 12 (2020) 4743–4750.
[87] G. Markiewicz, D. Pakulski, A. Galanti, V. Patroniak, A. Ciesielski, A. R. Stefankiewicz, P. Samorì, Chem. Commun. 53 (2017) 7278–7281.
[88] A. Blazevic, A. Rompel, Coord. Chem. Rev. 307 (2016) 42–64.
[89] D. Li, P. Ma, J. Niu, J. Wang, Coord. Chem. Rev. 392 (2019) 49–80.
[90] D.E. Salazar Marcano, M.A. Moussawi, A.V. Anyushin, S. Lentink, L. Van Meervelt, I. Ivanović-Burmazović, T.N. Parac-Vogt, Chem. Sci. 13 (2022) 2891–2899.
[91] P. Wang, Z. Wang, P. Wang, A.N. Chishti, H. Zhang, J. Shi, L. Ni, S. Jamil, Y. Wei, Polyoxometalates 3 (2024) 9140047.
[92] S.-R. Li, W.-D. Liu, L.-S. Long, L.-S. Zheng, X.-J. Kong, Polyoxometalates 2 (2023) 9140022.
[93] Q. Zhang, F. Li, L. Xu, Polyoxometalates 2 (2023) 9140018.
[94] H. Zhang, W.-L. Zhao, H. Li, Q. Zhuang, Z. Sun, D. Cui, X. Chen, A. Guo, X. Ji, S. An, W. Chen, Y.-F. Song, Polyoxometalates 1 (2022) 9140011.
[95] Z. Zeb, Y. Huang, L. Chen, W. Zhou, M. Liao, Y. Jiang, H. Li, L. Wang, L. Wang, H. Wang, T. Wei, D. Zang, Z. Fan, Y. Wei, Coord. Chem. Rev. 482 (2023) 215058.
[96] B. Li, L. Wu, Polyoxometalates 2 (2023) 9140016.
[97] C. Dey, Coord. Chem. Rev. 510 (2024) 215847.
[98] H.M. Asif, R.B. Bi, M. Tariq, N. Shaheen, M. Khalid, M. Nadeem, M. Ali Khan, T. M. Ansari, Russ. J. Inorg. Chem. 66 (2021) 340–347.
[99] L. Wang, W. Li, L. Wu, X. Dong, H. Hu, G. Xue, Inorg. Chem. Commun. 35 (2013) 122–125.
[100] S.-M. Wang, J. Hwang, E. Kim, J. Mater. Chem. C. 7 (2019) 7828–7850.
[101] S. Vanhaecht, G. Absillis, T.N. Parac-Vogt, Dalton Trans. 41 (2012) 10028–10034.
[102] S. Vanhaecht, T. Quanten, T.N. Parac-Vogt, Dalton Trans. 46 (2017) 10215–10219.
[103] S. Yoshitaka, Y. Shoko, H. Takeshi, M. Hideyuki, N. Kenji, B. Chem. Soc. Jpn. 80 (2007) 1965–1974.
[104] B. Yan, R. Liang, K. Zheng, R. Li, P. Ma, J. Wang, J. Niu, Inorg. Chem. 60 (2021) 8164–8172.
[105] M.-X. Li, Y. Zhang, Z.-M. Zhu, F. Su, L.-C. Zhang, X.-J. Sang, J. Coord. Chem. 73 (2020) 2437–2449.
[106] J. Guo, D. Zhang, L. Chen, Y. Song, D. Zhu, Y. Xu, Dalton Trans. 42 (2013) 8454–8459.
[107] G. Zhu, E.N. Glass, C. Zhao, H. Lv, J.W. Vickers, Y.V. Geletii, D.G. Musaev, J. Song, C.L. Hill, Dalton Trans. 41 (2012) 13043–13049.
[108] S. Nellutla, J. van Tol, N.S. Dalal, L.-H. Bi, U. Kortz, B. Keita, L. Nadjo, G. A. Khitrov, A.G. Marshall, Inorg. Chem. 44 (2005) 9795–9806.
[109] F.-Q. Zhang, J.-P. Gao, L.-K. Yan, W. Guan, R.-X. Yao, X.-M. Zhang, Dalton Trans. 46 (2017) 16145–16158.
[110] X. Xu, H.-L. Dong, R.-L. Sang, L. Xu, Chem. Commun. 48 (2012) 12177–12179.
[111] Q. Zheng, L. Vilà-Nadal, Z. Lang, J.-J. Chen, D.-L. Long, J.S. Mathieson, J. M. Poblet, L. Cronin, J. Am. Chem. Soc. 140 (2018) 2595–2601.
[112] H.N. Miras, D.L. Long, L. Cronin, Chapter one - exploring self-assembly and the self-organization of nanoscale inorganic polyoxometalate clusters, in: R. van Eldik, L. Cronin (Eds.), Adv. Inorg. Chem., Academic Press, 2017, pp. 1–28.
[113] I.M. Mbomekalle, B. Keita, L. Nadjo, P. Berthet, W.A. Neiwert, C.L. Hill, M. D. Ritorto, T.M. Anderson, Dalton Trans. (2003) 2646–2650.
[114] T. Ueda, M. Suzuki, T. Toya, J. Clust. Sci. 27 (2016) 501–511.
[115] T. Minato, K. Suzuki, K. Kamata, N. Mizuno, Chem. – Eur. J. 20 (2014) 5946–5952.
[116] C.J. Gomez-Garcia, J.J. Borras-Almenar, E. Coronado, L. Ouahab, Inorg. Chem. 33 (1994) 4016–4022.
[117] L.-H. Bi, E.-B. Wang, J. Peng, R.-D. Huang, L. Xu, C.-W. Hu, Inorg. Chem. 39 (2000) 671–679.
[118] J. Luo, G. Jin, F. Zhang, Y. Liu, L. Chen, S. Xie, J. Zhao, Eur. J. Inorg. Chem. 2018 (2018) 143–152.
[119] J. Xie, B.F. Abrahams, A.G. Wedd, Chem. Commun. (2008) 576–578.
[120] G. Cao, J. Xiong, Q. Xue, S. Min, H. Hu, G. Xue, Electrochim. Acta 106 (2013) 465–471.
[121] T. Rüther, V.M. Hultgren, B.P. Timko, A.M. Bond, W.R. Jackson, A.G. Wedd, J. Am. Chem. Soc. 125 (2003) 10133–10143.
[122] M.K. Seery, L. Guerin, R.J. Forster, E. Gicquel, V. Hultgren, A.M. Bond, A. G. Wedd, T.E. Keyes, J. Phys. Chem. A 108 (2004) 7399–7405.
[123] S.-S. Zhu, B. Yue, X.-Q. Shi, Y.-D. Gu, J. Liu, M.-Q. Chen, Y.-F. Huang, J. Chem. Soc., Dalton Trans. (1993) 3633–3634.
[124] D.-L. Long, H. Abbas, P. Kögerler, L. Cronin, Angew. Chem. Int. Ed. 44 (2005) 3415–3419.
[125] J. Yan, D.-L. Long, H.N. Miras, L. Cronin, Inorg. Chem. 49 (2010) 1819–1825.
[126] P. Lapham, L. Vilà-Nadal, L. Cronin, V.P. Georgiev, J. Phys. Chem. C 125 (2021) 3599–3610.
[127] Q. Zheng, M. Kupper, W. Xuan, H. Oki, R. Tsunashima, D.-L. Long, L. Cronin, J. Am. Chem. Soc. 141 (2019) 13479–13486.
[128] Q. Han, X. Sun, J. Li, P. Ma, J. Niu, Inorg. Chem. 53 (2014) 2006–2011.
[129] Z. Han, Q. Hao, Z. Wang, X. Zhai, J. Chem. Crystallogr. 43 (2013) 1–5.
[130] L. Shi, X.-M. Gao, T.-Y. Liu, X.-H. Huang, Z.-H. Gong, Y.-P. Chen, Y.-Q. Sun, Dalton Trans. 47 (2018) 1347–1354.
[131] S. He, Y. Xin, J. Li, Z. Zhu, P. Zhao, W. You, Acta Crystallogr. Sect. C 74 (2018) 1267–1273.
[132] J. Gao, J. Yan, S. Beeg, D.-L. Long, L. Cronin, Angew. Chem. Int. Ed. 51 (2012) 3373–3376.
[133] L. Liu, J. Jiang, L. Cui, J. Zhao, X. Cao, L. Chen, Inorg. Chem. 61 (2022) 1949–1960.
[134] C. Busche, L. Vilà-Nadal, J. Yan, H.N. Miras, D.L. Long, V.P. Georgiev, A. Asenov, R.H. Pedersen, N. Gadegaard, M.M. Mirza, D.J. Paul, J.M. Poblet, L. Cronin, Nature 515 (2014) 545–549.
[135] U. Kortz, M.T. Pope, Inorg. Chem. 33 (1994) 5643–5646.
[136] M. Bugnola, R.E. Schreiber, Y. Kaufman, G. Leitus, L.J.W. Shimon, R. Neumann, Eur. J. Inorg. Chem. 2019 (2019) 482–485.
[137] R.E. Schreiber, H. Cohen, G. Leitus, S.G. Wolf, A. Zhou, L. Que Jr., R. Neumann, J. Am. Chem. Soc. 137 (2015) 8738–8748.
[138] F. Chauveau, P. Doppelt, J. Lefebvre, Inorg. Chem. 19 (1980) 2803–2806.
[139] R. Ben-Daniel, A.M. Khenkin, R. Neumann, Chem. – Eur. J. 6 (2000) 3722–3728.
[140] D.-L. Long, P. Kögerler, A.D.C. Parenty, J. Fielden, L. Cronin, Angew. Chem. Int. Ed. 45 (2006) 4798–4803.
[141] J. Yan, D.L. Long, E.F. Wilson, L. Cronin, Angew. Chem. Int. Ed. 48 (2009) 4376–4380.
[142] L. Vilà-Nadal, S.G. Mitchell, D.-L. Long, A. Rodríguez-Fortea, X. López, J. M. Poblet, L. Cronin, Dalton Trans. 41 (2012) 2264–2271.
[143] D.-L. Long, Y.-F. Song, E.F. Wilson, P. Kögerler, S.-X. Guo, A.M. Bond, J.S. J. Hargreaves, L. Cronin, Angew. Chem. Int. Ed. 47 (2008) 4384–4387.
[144] Y.-Y. Zhang, S.-X. Liu, C.-J. Yu, Q. Tang, D.-D. Liang, C.-D. Zhang, F.-J. Ma, S.-J. Li, W. Zhang, R.-K. Tan, Inorg. Chem. Commun. 13 (2010) 1418–1420.
[145] L. Ni, F. Hussain, B. Spingler, S. Weyeneth, G.R. Patzke, Inorg. Chem. 50 (2011) 4944–4955.
[146] J. Wang, S. Li, Y. Shen, J. Niu, Cryst. Growth Des. 8 (2008) 372–374.
[147] M. Haouas, I.-M. Mbomekallé, N. Vila, P. de Oliveira, F. Taulelle, Inorg. Chem. 53 (2014) 5568–5574.
[148] H. Li, C. Lian, L. Chen, J. Zhao, G.-Y. Yang, Nanoscale 12 (2020) 16091–16101.
[149] Y. Zhang, B. Zeng, Y. Liu, P. Li, L. Chen, J. Zhao, Eur. J. Inorg. Chem. 2020 (2020) 3416–3425.
[150] N. Shen, F. Tian, J. Chang, K.-L. Huang, Z.-H. Zhang, X. Feng, J. Gu, S.-C. Chen, M.-Y. He, Q. Chen, Cryst. Eng. Comm. 22 (2020) 3656–3663.
[151] T.L. Jorris, M. Kozik, L.C.W. Baker, Inorg. Chem. 29 (1990) 4584–4586.
[152] T. Minato, D. Salley, N. Mizuno, K. Yamaguchi, L. Cronin, K. Suzuki, J. Am. Chem. Soc. 143 (2021) 12809–12816.
[153] S. Li, G. Li, P. Ji, J. Zhang, S. Liu, J. Zhang, X. Chen, ACS Appl. Mater. Interfaces. 11 (2019) 43287–43293.
[154] A. Müller, E. Krickemeyer, H. Bögge, M. Schmidtmann, F. Peters, Angew. Chem. Int. Ed. 37 (1998) 3359–3363.
[155] O. Oms, A. Dolbecq, P. Mialane, Chem. Soc. Rev. 41 (2012) 7497–7536.
[156] Y. Hayashi, Coord. Chem. Rev. 255 (2011) 2270–2280.
[157] M. Nyman, Dalton Trans. 40 (2011) 8049–8058.
[158] S.S. Amin, J.M. Cameron, M. Winslow, E.S. Davies, S.P. Argent, D. Robinson, G. N. Newton, Eur. J. Inorg. Chem. 2022 (2022) e202200019.
[159] R. Contant, R. Thouvenot, Inorg. Chim. Acta 212 (1993) 41–50.
[160] L. Vilà-Nadal, S. Romo, X. López, J. Poblet, Structural and Electronic Features of Wells-Dawson, Polyoxometalates (2012).
[161] E. Janusson, N. de Kler, L. Vilà-Nadal, D.-L. Long, L. Cronin, Chem. Commun. 55 (2019) 5797–5800.
[162] F.-Q. Zhang, W. Guan, L.-K. Yan, Y.-T. Zhang, M.-T. Xu, E. Hayfron-Benjamin, Z.-M. Su, Inorg. Chem. 50 (2011) 4967–4977.
[163] L. Yan, X. López, J.J. Carbó, R. Sniatynsky, D.C. Duncan, J.M. Poblet, J. Am. Chem. Soc. 130 (2008) 8223–8233.
[164] J. Zhang, A.M. Bond, P.J.S. Richardt, A.G. Wedd, Inorg. Chem. 43 (2004) 8263–8271.
[165] C.R. Graham, R.G. Finke, Inorg. Chem. 47 (2008) 3679–3686.
[166] I.-M. Mbomekalle, Y.W. Lu, B. Keita, L. Nadjo, Inorg. Chem. Commun. 7 (2004) 86–90.
[167] X. Ma, P. Wang, Z. Liu, C. Xin, S. Wang, J. Jia, P. Ma, J. Niu, J. Wang, Inorg. Chem. 59 (2020) 8690–8698.
[168] P. Huang, X.-J. Wang, J.-J. Qi, X.-L. Wang, M. Huang, H.-Y. Wu, C. Qin, Z.-M. Su, J. Mater. Chem. A. 5 (2017) 22970–22974.
[169] T. Zhang, L.-K. Yan, S. Cong, W. Guan, Z.-M. Su, Inorg. Chem. Front. 1 (2014) 65–70.
[170] W. Guo, H. Lv, J. Bacsa, Y. Gao, J.S. Lee, C.L. Hill, Inorg. Chem. 55 (2016) 461–466.
[171] C.P. Pradeep, M.F. Misdrahi, F.Y. Li, J. Zhang, L. Xu, D.L. Long, T. Liu, L. Cronin, Angew. Chem. Int. Ed. 48 (2009) 8309–8313.
[172] C.P. Pradeep, D.-L. Long, G.N. Newton, Y.-F. Song, L. Cronin, Angew. Chem. Int. Ed. 47 (2008) 4388–4391.
[173] P. Yin, C.P. Pradeep, B. Zhang, F.-Y. Li, C. Lydon, M.H. Rosnes, D. Li, E. Bitterlich, L. Xu, L. Cronin, T. Liu, Chem. – Eur. J. 18 (2012) 8157–8162.
[174] J. Oble, B. Riflade, A. Noël, M. Malacria, S. Thorimbert, B. Hasenknopf, E. Lacôte, Org. Lett. 13 (2011) 5990–5993.
[175] J. Li, I. Huth, L.-M. Chamoreau, B. Hasenknopf, E. Lacôte, S. Thorimbert, M. Malacria, Angew. Chem. Int. Ed. 48 (2009) 2035–2038.
[176] H. Dridi, A. Boulmier, P. Bolle, A. Dolbecq, J.-N. Rebilly, F. Banse, L. Ruhlmann, H. Serier-Brault, R. Dessapt, P. Mialane, O. Oms, J. Mater. Chem. C 8 (2020) 637–649.
[177] W. Chen, U. Tong, T. Zeng, C. Streb, Y.-F. Song, J. Mater. Chem. C 3 (2015) 4388–4393.
[178] B. Riflade, D. Lachkar, J. Oble, J. Li, S. Thorimbert, B. Hasenknopf, E. Lacôte, Org. Lett. 16 (2014) 3860–3863.
[179] I. Azcarate, I. Ahmed, R. Farha, M. Goldmann, X. Wang, H. Xu, B. Hasenknopf, E. Lacôte, L. Ruhlmann, Dalton Trans. 42 (2013) 12688–12698.

[180] M.-P. Santoni, A.K. Pal, G.S. Hanan, M.-C. Tang, A. Furtos, B. Hasenknopf, Dalton Trans. 43 (2014) 6990–6993.
[181] V. Kalyani, V.S.V. Satyanarayana, V. Singh, C.P. Pradeep, S. Ghosh, S.K. Sharma, K.E. Gonsalves, Chem. – Eur. J. 21 (2015) 2250–2258.
[182] S. Martín, Y. Takashima, C.-G. Lin, Y.-F. Song, H.N. Miras, L. Cronin, Inorg. Chem. 58 (2019) 4110–4116.
[183] R. Gupta, W. Huang, L.C. Francesconi, T. Polenova, Solid State Nucl. Magn. Reson. 84 (2017) 28–33.
[184] M. Abbessi, R. Contant, R. Thouvenot, G. Herve, Inorg. Chem. 30 (1991) 1695–1702.
[185] W.W. Laxson, S. Özkar, R.G. Finke, Inorg. Chem. 53 (2014) 2666–2676.
[186] W. Xiao, S. Li, Y. Zhao, Y. Ma, N. Li, J. Zhang, X. Chen, Dalton Trans. 50 (2021) 8690–8695.
[187] G. Zhang, E. Gadot, G. Gan-Or, M. Baranov, T. Tubul, A. Neyman, M. Li, A. Clotet, J.M. Poblet, P. Yin, I.A. Weinstock, J. Am. Chem. Soc. 142 (2020) 7295–7300.
[188] X. Fang, M. Speldrich, H. Schilder, R. Cao, K.P. O'Halloran, C.L. Hill, P. Kögerler, Chem. Commun. 46 (2010) 2760–2762.
[189] A.M. Khenkin, G. Leitus, L. Weiner, R. Neumann, J. Clust. Sci. 25 (2014) 687–693.
[190] X.-X. Li, W.-H. Fang, J.-W. Zhao, G.-Y. Yang, Chem. – Eur. J. 20 (2014) 17324–17332.
[191] Y.-C. Liu, C.-H. Fu, S.-T. Zheng, J.-W. Zhao, G.-Y. Yang, Dalton Trans. 42 (2013) 16676–16679.
[192] Y. Sakai, Y. Kitakoga, K. Hayashi, K. Yoza, K. Nomiya, Eur. J. Inorg. Chem. 2004 (2004) 4646–4652.
[193] C.P. Pradeep, D.-L. Long, P. Kögerler, L. Cronin, Chem. Commun. (2007) 4254–4256.
[194] S. Li, Y. Zhou, N. Ma, J. Zhang, Z. Zheng, C. Streb, X. Chen, Angew. Chem. Int. Ed. 59 (2020) 8537–8540.
[195] S. Li, Y. Zhao, S. Knoll, R. Liu, G. Li, Q. Peng, P. Qiu, D. He, C. Streb, X. Chen, Angew. Chem. Int. Ed. 60 (2021) 16953–16957.
[196] S. Li, Y. Zhao, H. Qi, Y. Zhou, S. Liu, X. Ma, J. Zhang, X. Chen, Chem. Commun. 55 (2019) 2525–2528.
[197] A.M. Khenkin, D. Kumar, S. Shaik, R. Neumann, J. Am. Chem. Soc. 128 (2006) 15451–15460.
[198] K. Stroobants, G. Absillis, P.S. Shestakova, R. Willem, T.N. Parac-Vogt, J. Clust. Sci. 25 (2014) 855–866.
[199] S. Vanhaecht, G. Absillis, T.N. Parac-Vogt, Dalton Trans. 42 (2013) 15437–15446.
[200] W. Wang, N.V. Izarova, J. van Leusen, P. Kögerler, Chem. Commun. 56 (2020) 14857–14860.
[201] A. Sap, L. Vandebroek, V. Goovaerts, E. Martens, P. Proost, T.N. Parac-Vogt, ACS Omega 2 (2017) 2026–2033.
[202] L. Vandebroek, E. De Zitter, H.G.T. Ly, D. Conić, T. Mihaylov, A. Sap, P. Proost, K. Pierloot, L. Van Meervelt, T.N. Parac-Vogt, Chem. – Eur. J. 24 (2018) 10099–10108.
[203] Q.-H. Luo, R.C. Howell, M. Dankova, J. Bartis, C.W. Williams, W.D. Horrocks, V. G. Young, A.L. Rheingold, L.C. Francesconi, M.R. Antonio, Inorg. Chem. 40 (2001) 1894–1901.
[204] A. Ostuni, R.E. Bachman, M.T. Pope, J. Clust. Sci. 14 (2003) 431–446.
[205] J. Iijima, H. Naruke, J. Mol. Struct. 1040 (2013) 33–38.
[206] W. Huang, M. Schopfer, C. Zhang, R.C. Howell, L. Todaro, B.A. Gee, L. C. Francesconi, T. Polenova, J. Am. Chem. Soc. 130 (2008) 481–490.
[207] G. Gao, L. Xu, W. Wang, W. An, Y. Qiu, J. Mater. Chem. 14 (2004) 2024–2029.
[208] R. Wan, P. Ma, M. Han, D. Zhang, C. Zhang, J. Niu, J. Wang, Dalton Trans. 46 (2017) 5398–5405.
[209] M. Sadakane, A. Ostuni, M.T. Pope, J. Chem. Soc., Dalton Trans. (2002) 63–67.
[210] Q. Luo, R.C. Howell, J. Bartis, M. Dankova, W.D. Horrocks, A.L. Rheingold, L. C. Francesconi, Inorg. Chem. 41 (2002) 6112–6117.
[211] C. Zhang, L. Bensaid, D. McGregor, X. Fang, R.C. Howell, B. Burton-Pye, Q. Luo, L. Todaro, L.C. Francesconi, J. Clust. Sci. 17 (2006) 389–425.
[212] C. Boglio, G. Lenoble, C. Duhayon, B. Hasenknopf, R. Thouvenot, C. Zhang, R. C. Howell, B.P. Burton-Pye, L.C. Francesconi, E. Lacôte, S. Thorimbert, M. Malacria, C. Afonso, J.-C. Tabet, Inorg. Chem. 45 (2006) 1389–1398.
[213] Y. Lu, Y. Xu, Y. Li, E. Wang, X. Xu, Y. Ma, Inorg. Chem. 45 (2006) 2055–2060.
[214] M. Sadakane, M.H. Dickman, M.T. Pope, Inorg. Chem. 40 (2001) 2715–2719.
[215] F. Hu, P. Ma, M. Han, R. Wan, J. Wang, J. Niu, Inorg. Chem. Commun. 67 (2016) 103–106.
[216] X. Wang, Y. Liu, M. Jin, Y. Wu, L. Chen, J.-W. Zhao, Cryst. Growth Des. 17 (2017) 5295–5308.
[217] M.A. AlDamen, M.O. Sinnokrot, S.B. Atta, R.A. Al Qawasmeh, C.J. Gómez-García, J. Struct. Chem. 61 (2020) 559–565.
[218] Y.-Q. Jiao, C. Qin, X.-L. Wang, F.-H. Liu, P. Huang, C.-G. Wang, K.-Z. Shao, Z.-M. Su, Chem. Commun. 50 (2014) 5961–5963.
[219] N.V. Izarova, L. Klaß, P. de Oliveira, I.M. Mbomekalle, V. Peters, F. Haarmann, P. Kögerler, Dalton Trans. 44 (2015) 19200–19206.
[220] S.S. Mal, M.H. Dickman, U. Kortz, A.M. Todea, A. Merca, H. Bögge, T. Glaser, A. Müller, S. Nellutla, N. Kaur, J. van Tol, N.S. Dalal, B. Keita, L. Nadjo, Chem. – Eur. J. 14 (2008) 1186–1195.
[221] S. Yao, Z. Zhang, Y. Li, E. Wang, Dalton Trans. 39 (2010) 3884–3889.
[222] X. Yi, N.V. Izarova, T. Iftikhar, J. van Leusen, P. Kögerler, Inorg. Chem. 58 (2019) 9378–9386.
[223] S. Yao, Z. Zhang, Y. Li, Y. Lu, E. Wang, Z. Su, Cryst. Growth Des. 10 (2010) 135–139.
[224] F. Hussain, U. Kortz, B. Keita, L. Nadjo, M.T. Pope, Inorg. Chem. 45 (2006) 761–766.
[225] C.-H. Zhan, Q. Zheng, D.-L. Long, L. Vilà-Nadal, L. Cronin, Angew. Chem. Int. Ed. 58 (2019) 17282–17286.
[226] S.S. Mal, M.H. Dickman, U. Kortz, Chem. - Eur. J. 14 (2008) 9851–9855.
[227] L.-H. Bi, U. Kortz, Inorg. Chem. 43 (2004) 7961–7962.
[228] N. Laronze, J. Marrot, G. Hervé, Chem. Commun. (2003) 2360–2361.
[229] J. Feng, G. Sun, F. Pei, M. Liu, J. Inorg. Biochem. 92 (2002) 193–199.
[230] S. Matsunaga, Y. Inoue, T. Otaki, H. Osada, K. Nomiya, Z. Anorg. Allg. Chem. 642 (2016) 539–545.
[231] K. Dong, P. Ma, H. Wu, Y. Wu, J. Niu, J. Wang, Inorg. Chem. 58 (2019) 6000–6007.
[232] I.M. Mbomekalle, B. Keita, L. Nadjo, W.A. Neiwert, L. Zhang, K.I. Hardcastle, C. L. Hill, T.M. Anderson, Eur. J. Inorg. Chem. 2003 (2003) 3924–3928.
[233] Z. Wang, X. Xin, M. Zhang, Z. Li, H. Lv, G.-Y. Yang, Sci. China Chem. 65 (2022) 1515–1525.
[234] I.F. Bamba, C. Falaise, J. Marrot, G.K. Gbassi, P. Atheba, R. Guillot, M. Haouas, E. Cadot, Inorg. Chem. 61 (2022) 8309–8319.
[235] L. Ruhlmann, D. Schaming, I. Ahmed, A. Courville, J. Canny, R. Thouvenot, Inorg. Chem. 51 (2012) 8202–8211.
[236] F. Doungmene, P.A. Aparicio, J. Ntienoue, C.S.A. Mezui, P. de Oliveira, X. López, I.M. Mbomekallé, Electrochim. Acta 125 (2014) 674–682.
[237] M.R. Farsani, F. Jalilian, B. Yadollahi, H.A. Rudbari, Polyhedron 76 (2014) 102–107.
[238] X. Fang, T.M. Anderson, C.L. Hill, Angew. Chem. Int. Ed. 44 (2005) 3540–3544.
[239] R.G. Finke, M.W. Droege, Inorg. Chem. 22 (1983) 1006–1008.
[240] M. Lebrini, I.M. Mbomekallé, A. Dolbecq, J. Marrot, P. Berthet, J. Ntienoue, F. Sécheresse, J. Vigneron, A. Etcheberry, Inorg. Chem. 50 (2011) 6437–6448.
[241] C. Costa-Coquelard, S. Sorgues, L. Ruhlmann, J. Phys. Chem. A 114 (2010) 6394–6400.
[242] D. Schaming, R. Farha, H. Xu, M. Goldmann, L. Ruhlmann, Langmuir 27 (2011) 132–143.
[243] D. Schaming, C. Costa-Coquelard, S. Sorgues, L. Ruhlmann, I. Lampre, Appl. Catal. A: Gen. 373 (2010) 160–167.
[244] N.I. Gumerova, A. Rompel, Chem. Soc. Rev. 49 (2020) 7568–7601.
[245] N.I. Gumerova, A. Rompel, Sci. Adv. 9 (2023) eadi0814.
[246] R. Contant, A. Teze, Inorg. Chem. 24 (1985) 4610–4614.
[247] L.-Y. Guo, M. Jagodič, S.-Y. Zeng, Z. Wang, Z.-Q. Shi, X.-P. Wang, C.-H. Tung, D. Sun, Dalton Trans. 45 (2016) 8404–8411.
[248] X. Fang, P. Kögerler, Chem. Commun. (2008) 3396–3398.
[249] L. Pettersson, I. Andersson, L.O. Oehman, Inorg. Chem. 25 (1986) 4726–4733.
[250] L. Pettersson, I. Andersson, L.-O. Öhman, I. Persson, F. Salvatore, Acta Chem. 39a (1985) 53–58.
[251] A. Misra, K. Kozma, C. Streb, M. Nyman, Angew. Chem. Int. Ed. 59 (2020) 596–612.
[252] D.E. Salazar Marcano, S. Lentink, M.A. Moussawi, T.N. Parac-Vogt, Inorg. Chem. 60 (2021) 10215–10226.
[253] A. Proust, B. Matt, R. Villanneau, G. Guillemot, P. Gouzerh, G. Izzet, Chem. Soc. Rev. 41 (2012) 7605–7622.
[254] S. Thorimbert, B. Hasenknopf, E. Lacôte, Isr. J. Chem. 51 (2011) 275–280.
[255] A.J. Kibler, G.N. Newton, Polyhedron 154 (2018) 1–20.
[256] J. Zhang, Y. Huang, G. Li, Y. Wei, Coord. Chem. Rev. 378 (2019) 395–414.
[257] H.M. Asif, Y. Zhou, L. Zhang, N. Shaheen, D. Yang, J. Li, Y. Long, A. Iqbal, Y. Li, Inorg. Chem. 56 (2017) 9436–9447.
[258] M.-P. Santoni, A.K. Pal, G.S. Hanan, A. Proust, B. Hasenknopf, Inorg. Chem. 50 (2011) 6737–6745.
[259] T. Auvray, M.-P. Santoni, B. Hasenknopf, G.S. Hanan, Dalton Trans. 46 (2017) 10029–10036.
[260] M. Glöβ, R. Pütt, M. Moors, E. Kentzinger, W. Pyckhout-Hintzen, K.Y. Monakhov, Nanoscale 11 (2019) 4267–4277.
[261] I. Azcarate, Z. Huo, R. Farha, M. Goldmann, H. Xu, B. Hasenknopf, E. Lacôte, L. Ruhlmann, Chem. – Eur. J. 21 (2015) 8271–8280.
[262] D. Lachkar, D. Vilona, E. Dumont, M. Lelli, E. Lacôte, Angew. Chem. Int. Ed. 55 (2016) 5961–5965.
[263] J. Lesage, A. Pontes da Costa, G. Pembouong, L. Ruhlmann, B. Hasenknopf, E. Lacôte, J. Rieger, Polymer 57 (2015) 173–182.
[264] J. Lesage de la Haye, P. Beaunier, L. Ruhlmann, B. Hasenknopf, E. Lacôte, J. Rieger, Chem. Plus. Chem. 79 (2014) 250–256.
[265] S. Bareyt, S. Piligkos, B. Hasenknopf, P. Gouzerh, E. Lacôte, S. Thorimbert, M. Malacria, J. Am. Chem. Soc. 127 (2005) 6788–6794.
[266] C. Boglio, K. Micoine, É. Derat, R. Thouvenot, B. Hasenknopf, S. Thorimbert, E. Lacôte, M. Malacria, J. Am. Chem. Soc. 130 (2008) 4553–4561.
[267] H.G.T. Ly, T. Mihaylov, G. Absillis, K. Pierloot, T.N. Parac-Vogt, Inorg. Chem. 54 (2015) 11477–11492.
[268] C.R. Mayer, C. Roch-Marchal, H. Lavanant, R. Thouvenot, N. Sellier, J.-C. Blais, F. Sécheresse, Chem. – Eur. J. 10 (2004) 5517–5523.
[269] F. Odobel, M. Séverac, Y. Pellegrin, E. Blart, C. Fosse, C. Cannizzo, C.R. Mayer, K. J. Elliott, A. Harriman, Chem. – Eur. J. 15 (2009) 3130–3138.
[270] B. Matt, S. Renaudineau, L.M. Chamoreau, C. Afonso, G. Izzet, A. Proust, J. Org. Chem. 76 (2011) 3107–3112.
[271] A.V. Anyushin, S. Vanhaecht, T.N. Parac-Vogt, Inorg. Chem. 59 (2020) 10146–10152.
[272] E. Hampson, J.M. Cameron, S. Amin, J. Kyo, J.A. Watts, H. Oshio, G.N. Newton, Angew. Chem. Int. Ed. 58 (2019) 18281–18285.
[273] E. Hampson, J.M. Cameron, J.A. Watts, G.N. Newton, Chem. Commun. 56 (2020) 8237–8240.
[274] K. Kastner, A.J. Kibler, E. Karjalainen, J.A. Fernandes, V. Sans, G.N. Newton, J. Mater. Chem. A 5 (2017) 11577–11581.
[275] M. Glöß, R. Pütt, M. Moors, E. Kentzinger, S. Karthäuser, K.Y. Monakhov, Adv. Mater. Interfaces 9 (2022) 2200461.

[276] Y. Hou, C.L. Hill, J. Am. Chem. Soc. 115 (1993) (1830) 11823.
[277] D. Vilona, M. Lelli, E. Dumont, E. Lacôte, Chem. – Eur. J. 27 (2021) 17761–17764.
[278] H. Zeng, G.R. Newkome, C.L. Hill, Angew. Chem. Int. Ed. 39 (2000) 1771–1774.
[279] P. Yin, T. Li, R.S. Forgan, C. Lydon, X. Zuo, Z.N. Zheng, B. Lee, D. Long, L. Cronin, T. Liu, J. Am. Chem. Soc. 135 (2013) 13425–13432.
[280] M. Piot, S. Hupin, H. Lavanant, C. Afonso, L. Bouteiller, A. Proust, G. Izzet, Inorg. Chem. 56 (2017) 8490–8496.
[281] B. Matt, X. Xiang, A.L. Kaledin, N. Han, J. Moussa, H. Amouri, S. Alves, C.L. Hill, T. Lian, D.G. Musaev, G. Izzet, A. Proust, Chem. Sci. 4 (2013) 1737–1745.
[282] F. Zonnevijlle, M.T. Pope, J. Am. Chem. Soc. 101 (1979) 2731–2732.
[283] M. Boujtita, J. Boixel, E. Blart, C.R. Mayer, F. Odobel, Polyhedron 27 (2008) 688–692.
[284] B. Matt, C. Coudret, C. Viala, D. Jouvenot, F. Loiseau, G. Izzet, A. Proust, Inorg. Chem. 50 (2011) 7761–7768.
[285] W.-K. Miao, Y.-K. Yan, X.-L. Wang, Y. Xiao, L.-J. Ren, P. Zheng, C.-H. Wang, L.-X. Ren, W. Wang, ACS Macro Lett. 3 (2014) 211–215.
[286] W.-K. Miao, A. Yi, Y.-K. Yan, L.-J. Ren, D. Chen, C.-H. Wang, W. Wang, Polym. Chem. 6 (2015) 7418–7426.
[287] Z. Huo, I. Azcarate, R. Farha, M. Goldmann, H. Xu, B. Hasenknopf, E. Lacôte, L. Ruhlmann, J. Solid State Electrochem. 19 (2015) 2611–2621.
[288] G. Wang, T. Chen, S. Li, H. Pang, H. Ma, Dalton Trans. 46 (2017) 13897–13902.
[289] F. Gomollón-Bel, Chem. Int. 41 (2019) 12–17.
[290] M. Kato, M. Kamigaito, M. Sawamoto, T. Higashimura, Macromol. 28 (1995) 1721–1723.
[291] J.-S. Wang, K. Matyjaszewski, J. Am. Chem. Soc. 117 (1995) 5614–5615.
[292] K. Matyjaszewski, N.V. Tsarevsky, J. Am. Chem. Soc. 136 (2014) 6513–6533.
[293] Y. Han, Y. Xiao, Z. Zhang, B. Liu, P. Zheng, S. He, W. Wang, Macromol. 42 (2009) 6543–6548.
[294] S.-J. Yu, Y.-K. Han, W. Wang, Polymer 162 (2019) 73–79.
[295] Y.-K. Han, Z.-J. Zhang, Y.-L. Wang, N. Xia, B. Liu, Y. Xiao, L.-X. Jin, P. Zheng, W. Wang, Macromol. Chem. Phys. 212 (2011) 81–87.
[296] J. Lesage de La Haye, J.-M. Guigner, E. Marceau, L. Ruhlmann, B. Hasenknopf, E. Lacôte, J. Rieger, Chem. – Eur. J. 21 (2015) 2948–2953.
[297] P. He, B. Xu, H. Liu, S. He, F. Saleem, X. Wang, Sci. Rep. 3 (2013) 1833.
[298] P. He, B. Xu, X. Xu, L. Song, X. Wang, Chem. Sci. 7 (2016) 1011–1015.
[299] M.A. Moussawi, N. Leclerc-Laronze, S. Floquet, P.A. Abramov, M.N. Sokolov, S. Cordier, A. Ponchel, E. Monflier, H. Bricout, D. Landy, M. Haouas, J. Marrot, E. Cadot, J. Am. Chem. Soc. 139 (2017) 12793–12803.
[300] M.-B. Hu, Z.-Y. Hou, W.-Q. Hao, Y. Xiao, W. Yu, C. Ma, L.-J. Ren, P. Zheng, W. Wang, Langmuir 29 (2013) 5714–5722.
[301] M. Piot, B. Abécassis, D. Brouri, C. Troufflard, A. Proust, G. Izzet, Proc. Natl. Acad. Sci. 115 (2018) 8895–8900.
[302] Q. Liu, P. He, H. Yu, L. Gu, B. Ni, D. Wang, X. Wang, Sci. Adv. 5 (2019) eaax1081.
[303] L.-L. Zhang, W.-K. Miao, L.-J. Ren, Y.-K. Yan, W. Wang, Chin. J. Polym. Sci. 39 (2021) 716–724.
[304] Q. Li, L. Zhang, J. Dai, H. Tang, Q. Li, H. Xue, H. Pang, J. Chem. Eng. 351 (2018) 441–461.
[305] F.M.B. Gusmão, D. Mladenović, K. Radinović, D.M.F. Santos, B. Šljukić, Energies 15 (2022) 9021.
[306] N.K. Sah, S.J. Phukan, D.N. Madhusudan, K. Sankaranarayanan, M. Roy, S. Garai, Polyoxometalate-Induced Nano-Engineered Composite Materials: Supercapacitor Applications, in: Nanomater. Sustainable Energy Appl., CRC Press, 2024, pp. 50–76.
[307] K. Li, T. Liu, J. Ying, A. Tian, X. Wang, J. Mater. Chem. A 12 (2024) 13576–13604.
[308] M. JE, P.R. Chandewar, D. Shee, S.S. Mal, RSC Adv. 13 (2023) 26744–26754.
[309] N.S. Mughal, D.A. Walsh, G.N. Newton, ACS Appl. Energy Mater. 3 (2020) 12308–12315.
[310] S.S. Amin, J.M. Cameron, R.B. Cousins, J. Wrigley, L. Liirò-Peluso, V. Sans, D. A. Walsh, G.N. Newton, Inorg. Chem. Front. 9 (2022) 1777–1784.
[311] C. Fleming, D.-L. Long, N. McMillan, J. Johnston, N. Bovet, V. Dhanak, N. Gadegaard, P. Kögerler, L. Cronin, M. Kadodwala, Nat. Nanotechnol. 3 (2008) 229–233.
[312] M. Vasilopoulou, A.M. Douvas, L.C. Palilis, S. Kennou, P. Argitis, J. Am. Chem. Soc. 137 (2015) 6844–6856.
[313] A.M. Douvas, D. Tsikritzis, C. Tselios, A. Haider, A.S. Mougharbel, U. Kortz, A. Hiskia, A.G. Coutsolelos, L.C. Palilis, M. Vasilopoulou, S. Kennou, P. Argitis, Phys. Chem. Chem. Phys. 21 (2019) 427–437.
[314] S.N.S., N. Basu, M. Cahay, S.M.N., S.S. Mal, P.P. Das, Physica Status Solidi (a) 217 (2020) 2000306.
[315] W. Sun, C. He, T. Liu, C. Duan, Chem. Commun. 55 (2019) 3805–3808.
[316] J.J. Walsh, C.T. Mallon, A.M. Bond, T.E. Keyes, R.J. Forster, Chem. Commun. 48 (2012) 3593–3595.
[317] I. Ahmed, R. Farha, M. Goldmann, L. Ruhlmann, Chem. Commun. 49 (2013) 496–498.
[318] J. Walsh, J. Zhu, A. Bond, R. Forster, T. Keyes, J. Electroanal. Chem. 706 (2013) 93–101.
[319] A. Harriman, K.J. Elliott, M.A.H. Alamiry, L.L. Pleux, M. Séverac, Y. Pellegrin, E. Blart, C. Fosse, C. Cannizzo, C.R. Mayer, F. Odobel, J. Phys. Chem. C 113 (2009) 5834–5842.
[320] H. Sun, L.-Y. Guo, J.-S. Li, J.-P. Bai, F. Su, L.-C. Zhang, X.-J. Sang, W.-S. You, Z.-M. Zhu, Chem. Sus. Chem. 9 (2016) 1125–1133.
[321] I. Ahmed, R. Farha, Z. Huo, C. Allain, X. Wang, H. Xu, M. Goldmann, B. Hasenknopf, L. Ruhlmann, Electrochim. Acta 110 (2013) 726–734.
[322] K.J. Elliott, A. Harriman, L. Le Pleux, Y. Pellegrin, E. Blart, C.R. Mayer, F. Odobel, Phys. Chem. Chem. Phys. 11 (2009) 8767–8773.
[323] H.M. Asif, H.F. Ashfaq, Y. Zhou, L. Zhang, A. Iqbal, X. Hu, F.K. Shehzad, Dalton Trans. 52 (2023) (1858) 11850–11851.
[324] B. Matt, J. Fize, J. Moussa, H. Amouri, A. Pereira, V. Artero, G. Izzet, A. Proust, Energy Environ. Sci. 6 (2013) 1504–1508.
[325] A. Panagiotopoulos, A.M. Douvas, 9 (2016) 3213-3219.
[326] Z.-M. Zhang, T. Zhang, C. Wang, Z. Lin, L.-S. Long, W. Lin, J. Am. Chem. Soc. 137 (2015) 3197–3200.
[327] H. Li, S. Yao, H.-L. Wu, J.-Y. Qu, Z.-M. Zhang, T.-B. Lu, W. Lin, E.-B. Wang, Appl. Catal. B: Environ. 224 (2018) 46–52.
[328] J. Tian, Z. Xu, D.-W. Zhang, H. Wang, S.-H. Xie, D.-W. Xu, Y.-H. Ren, H. Wang, Y. Liu, L. Zhanting, Nat. Commun. 7 (2016) 11580.
[329] L. Jiao, Y. Dong, X. Xin, L. Qin, H. Lv, Appl. Catal. B: Environ. 291 (2021) 120091.
[330] M. Alaaeddine, Q. Zhu, D. Fichou, G. Izzet, J.E. Rault, N. Barrett, A. Proust, L. Tortech, Inorg. Chem. Front. 1 (2014) 682–688.
[331] X.-W. Guo, X.-H. Li, Z.-J. Liu, W.-L. Chen, X.-T. Zheng, E.-B. Wang, Z.-M. Su, Inorg. Chem. Front. 4 (2017) 1187–1191.
[332] X.-Y. Yang, M.-T. Li, N. Sheng, J.-S. Li, G.-D. Liu, J.-Q. Sha, J. Jiang, Cryst. Growth Des. 18 (2018) 5564–5572.
[333] M. Li, L. Cong, J. Zhao, T. Zheng, R. Tian, J. Sha, Z. Su, X. Wang, J. Mater. Chem. A 5 (2017) 3371–3376.
[334] J. Hu, H. Diao, W. Luo, Y.-F. Song, Chem. - Eur. J. 23 (2017) 8729–8735.
[335] B.-W. Cong, Z.-H. Su, Z.-F. Zhao, B. Wang, CrystEngComm 19 (2017) 7154–7161.
[336] H. Zhang, Z. Ma, S. Duan, Y. Liu, X. Jiang, Q. Zhou, M. Chen, L. Ni, G. Diao, Electrochim. Acta 428 (2022) 140868.
[337] M. Wang, D. Yin, Y. Cao, X. Dong, G. Gao, X. Hu, C. Jin, L. Fan, J. Yu, H. Liu, Chin. Chem. Lett. 33 (2022) 4350–4356.
[338] H.D. Pratt Iii, T.M. Anderson, Dalton Trans. 42 (2013) 15650–15655.
[339] S. Chinnathambi, M. Ammam, J. Power Sources 284 (2015) 524–535.
[340] C. Mu, X. Wang, Z. Ma, X. Liu, W. Li, J. Mater. Chem. A. 10 (2022) 7207–7217.
[341] F.M. Mulder, B.M.H. Weninger, J. Middelkoop, F.G.B. Ooms, H. Schreuders, Energy Environ. Sci. 10 (2017) 756–764.
[342] J.-J. Chen, M.D. Symes, L. Cronin, Nat. Chem. 10 (2018) 1042–1047.
[343] N. Dupré, P. Rémy, K. Micoine, C. Boglio, S. Thorimbert, E. Lacôte, B. Hasenknopf, M. Malacria, Chem. – Eur. J. 16 (2010) 7256–7264.
[344] A. Rajan, A.S. Mougharbel, S. Bhattacharya, T. Nisar, V. Wagner, U. Kortz, Inorg. Chem. 59 (2020) 13042–13049.
[345] F. de Azambuja, T.N. Parac-Vogt, ACS Catal. 9 (2019) 10245–10252.
[346] G.-P. Yang, S.-X. Shang, B. Yu, C.-W. Hu, Inorg. Chem. Front. 5 (2018) 2472–2477.
[347] A. Modvig, C. Kumpidet, A. Riisager, J. Albert, Materials 12 (2019) 2175.
[348] S.E. Collins, S.R. Matkovic, A.L. Bonivardi, L.E. Briand, J. Phys. Chem. C 115 (2011) 700–709.
[349] S.L. Giles, J.G. Lundin, R.B. Balow, P.E. Pehrsson, J.H. Wynne, Appl. Catal. A: Gen. 542 (2017) 306–310.
[350] C. Streb, Dalton Trans. 41 (2012) 1651–1659.
[351] S.M. Mousavi, S.A. Hashemi, S. Bahrani, S. Mosleh, W.-H. Chiang, K. Yousefi, S. Ramakrishna, L.C. Wei, N. Omidifar, Environ. Sci. and Pollut. Res. 29 (2022) 56055–56067.
[352] G. Marcì, E.I. García-López, L. Palmisano, Eur. J. Inorg. Chem. 2014 (2014) 21–35.
[353] L. Li, Q.-Y. Wu, Y.-H. Guo, C.-W. Hu, Microporous Mesoporous Mater. 87 (2005) 1–9.
[354] S. Jiang, Y. Guo, C. Wang, X. Qu, L. Li, J. Colloid Interface Sci. 308 (2007) 208–215.
[355] J. Lü, J.-X. Lin, X.-L. Zhao, R. Cao, Chem. Commun. 48 (2012) 669–671.
[356] B. Keita, L. Nadjo, J. Mol. Catal. A: Chem. 262 (2007) 190–215.
[357] B. Keita, I.-M. Mbomekalle, L. Nadjo, P. de Oliveira, A. Ranjbari, R. Contant, C. R. Chim. 8 (2005) 1057–1066.
[358] B. Keita, R. Contant, P. Mialane, F. Sécheresse, P. de Oliveira, L. Nadjo, Electrochem. Commun. 8 (2006) 767–772.
[359] Y. Yang, S. Liu, C. Li, S. Li, G. Ren, F. Wei, T. Qun, Inorg. Chem. Commun. 17 (2012) 54–57.
[360] X. Zhao, D. Liang, S. Liu, C. Sun, R. Cao, C. Gao, Y. Ren, Z. Su, Inorg. Chem. 47 (2008) 7133–7138.
[361] L. Liu, B. Wang, J.H. Lv, K. Yu, L. Wang, H. Zhang, S. Wang, B.B. Zhou, Cryst. Eng. Comm. 19 (2017) 5653–5661.
[362] S. Imar, M. Yaqub, C. Maccato, C. Dickinson, F. Laffir, M. Vagin, T. McCormac, Electrochim. Acta 184 (2015) 323–330.
[363] N. Fay, E. Dempsey, T. McCormac, J. Electroanal. Chem. 574 (2005) 359–366.
[364] B. Keita, I. Mbomekallé, L. Nadjo, R. Contant, Electrochem. Commun. 3 (2001) 267–273.
[365] M. Zhou, L.P. Guo, F.Y. Lin, H.X. Liu, Anal. Chim. Acta 587 (2007) 124–131.
[366] D. Martel, A. Kuhn, Electrochim. Acta 45 (2000) 1829–1836.
[367] J.-J. Chen, L. Vilà-Nadal, A. Solé-Daura, G. Chisholm, T. Minato, C. Busche, T. Zhao, B. Kandasamy, A.Y. Ganin, R.M. Smith, I. Colliard, J.J. Carbó, J. M. Poblet, M. Nyman, L. Cronin, J. Am. Chem. Soc. 144 (2022) 8951–8960.
[368] M. Ammam, J. Mater. Chem. A 1 (2013) 6291–6312.
[369] N. Anwar, M. Vagin, F. Laffir, G. Armstrong, C. Dickinson, T. McCormac, Analyst 137 (2012) 624–630.
[370] C. Zhou, S. Li, W. Zhu, H. Pang, H. Ma, Electrochim. Acta 113 (2013) 454–463.
[371] F. Boussema, A.J. Gross, F. Hmida, B. Ayed, H. Majdoub, S. Cosnier, A. Maaref, M. Holzinger, Biosens. Bioelectron. 109 (2018) 20–26.
[372] P. He, B. Xu, P.P. Wang, H. Liu, X. Wang, Adv. Mater. 26 (2014) 4339–4344.

[373] G.-G. Gao, L. Xu, W. Wang, Z. Wang, Y. Qiu, E. Wang, J. Electrochem. Soc. 152 (2005) H102–H106.
[374] M. Rouhani, A. Soleymanpour, Mater. Sci. Eng. C Mater. Biol. Appl. 117 (2020) 111287.
[375] Q. Li, M. Xu, X. Li, S. Li, L. Hou, Y. Chen, J. Sha, Analyst 145 (2020) 4021–4030.
[376] X. Liu, Q. Zheng, D. Jia, W. Wang, H. Zhao, X. Tao, J. Sha, J. Clust. Sci. 34 (2023) 3095–3103.
[377] S. Muqaddas, H. Aslam, S. Ul Hassan, A. Raza Ashraf, M. Adeel Asghar, M. Ahmad, A. Nazir, R. Shoukat, M. Kaleli, S. Mostafa Ibrahim, S. Kyürekli, A. Haider, A. Ali, Mater. Sci. Eng. B. 293 (2023) 116446.
[378] I. Sakthinathan, N. Yamasaki, D. Barreca, C. Maccato, T. Ueda, T. McCormac, Electrochim. Acta 462 (2023) 142689.
[379] S.U. Hassan, Y. Zhou, L. Zhang, Z. Shi, D. Yang, H.M. Asif, N. Qu, J. Phys. Chem. C 120 (2016) 7757–7766.
[380] Y. Zhang, Y. Li, J. Pang, Y. Liu, P. Li, L. Chen, J. Zhao, Inorg. Chem. 58 (2019) 7078–7090.
[381] G. Gao, L. Xu, W. Wang, Z. Wang, Y. Qiu, E. Wang, Electrochim. Acta 50 (2005) 1101–1106.
[382] G. Gao, L. Xu, W. Wang, W. An, Y. Qiu, Z. Wang, E. Wang, J. Phys. Chem. B 109 (2005) 8948–8953.
[383] J. Zhang, X. Wang, G. Wang, Y. Feng, C. Zhang, T. Pang, G. Gao, L. Fan, H. Liu, Chin. Chem. Lett. 34 (2022) 107231.
[384] S.-M. Wang, L. Liu, W.-L. Chen, E.-B. Wang, Electrochim. Acta 113 (2013) 240–247.
[385] C. Boskovic, Acc. Chem. Res. 50 (2017) 2205–2214.
[386] X. Fang, P. Kögerler, M. Speldrich, H. Schilder, M. Luban, Chem. Commun. 48 (2012) 1218–1220.
[387] M. Ibrahim, Y. Xiang, B.S. Bassil, Y. Lan, A.K. Powell, P. de Oliveira, B. Keita, U. Kortz, Inorg. Chem. 52 (2013) 8399–8408.
[388] J. Goura, M. Choudhari, T. Nisar, T. Balster, J.K. Bindra, J. Kinyon, B. Ali, T. McCormac, N.S. Dalal, V. Wagner, U. Kortz, Inorg. Chem. 59 (2020) 13034–13041.
[389] M. Ibrahim, A. Baksi, Y. Peng, F.K. Al-Zeidaneen, I.M. Mbomekallé, P. de Oliveira, C.E. Anson, Molecules 25 (2020) 4229.
[390] J. Jia, P. Ma, P. Zhang, D. Zhang, C. Zhang, J. Niu, J. Wang, Dalton Trans. 47 (2018) 6288–6292.
[391] R. Pütt, P. Kozłowski, I. Werner, J. Griebel, S. Schmitz, J. Warneke, K. Y. Monakhov, Inorg. Chem. 60 (2021) 80–86.
[392] Y. Liu, S. Tian, S. Liu, E. Wang, Transit. Met. Chem. 30 (2005) 113–117.
[393] J. Hu, S.K. Tan, M.G.L. Lim, S.H. Chang, G. Cui, S. Liu, K. Narasimhan, S.Y. New, X. Wang, C. Chen, H. Chakravarty, P.R. Kolatkar, K.Y. Tam, Q. Lu, X. Su, R. Jauch, E. Cheung, Biochem. J. 475 (2018) 1965–1977.
[394] X.H. Wang, J.F. Liu, J. Coord. Chem. 51 (2000) 73–82.
[395] W. Xiao-Hong, H. Jiang-Hua, Z. Rong-Chang, L. Jing-Fu, Chin. J. Chem. 21 (2003) 415–418.
[396] L. Pérez-Álvarez, L. Ruiz-Rubio, B. Artetxe, M.d. Vivanco, J.M. Gutiérrez-Zorrilla, J.L. Vilas-Vilela, Carbohydr. Polym. 213 (2019) 159–167.
[397] Azizullah, M. Al-Rashida, A. Haider, U. Kortz, S.A. Joshi, J. Iqbal, Chem. Select 3 (2018) 1472–1479.
[398] R.N. Azizullah, A. Ur, U. Haider, S. Kortz, M. Afridi, S.A. Sohail, J.I. Joshi, Int. J. Pharm. 533 (2017) 125–137.
[399] F. Pu, E. Wang, H. Jiang, J. Ren, Mol. Biosyst. 9 (2013) 113–120.
[400] R. Prudent, V. Moucadel, B. Laudet, C. Barette, L. Lafanechère, B. Hasenknopf, J. Li, S. Bareyt, E. Lacôte, S. Thorimbert, M. Malacria, P. Gouzerh, C. Cochet, Chem. Biol. 15 (2008) 683–692.
[401] K. Narasimhan, S. Pillay, N.R. Bin Ahmad, Z. Bikadi, E. Hazai, L. Yan, P. R. Kolatkar, K. Pervushin, R. Jauch, ACS Chem. Biol. 6 (2011) 573–581.
[402] C. Pimpão, I.V. da Silva, A.F. Mósca, J.O. Pinho, M.M. Gaspar, N.I. Gumerova, A. Rompel, M. Aureliano, G. Soveral, Int. J. Mol. Sci. 21 (2020) 2467.
[403] Y. Liu, Y.-Y. Han, S. Lu, Y. Wu, J. Li, X. Sun, J. Yan, Biomater. Sci. 10 (2022) 1257–1266.
[404] A. Bijelic, M. Aureliano, A. Rompel, Chem. Commun. 54 (2018) 1153–1169.
[405] N. Fukuda, T. Yamase, Y. Tajima, Biol. Pharm. Bull. 22 (1999) 463–470.
[406] M. Inoue, T. Suzuki, Y. Fujita, M. Oda, N. Matsumoto, T. Yamase, J. Inorg. Biochem. 100 (2006) 1225–1233.
[407] J. Geng, M. Li, J. Ren, E. Wang, X. Qu, Angew. Chem. Int. Ed. 50 (2011) 4184–4188.
[408] N. Gao, H. Sun, K. Dong, J. Ren, T. Duan, C. Xu, X. Qu, Nat. Commun. 5 (2014) 3422.
[409] N. Gao, H. Sun, K. Dong, J. Ren, X. Qu, Chem. – Eur. J. 21 (2015) 829–835.
[410] Y. Guan, M. Li, K. Dong, N. Gao, J. Ren, Y. Zheng, X. Qu, Biomater. 98 (2016) 92–102.
[411] M. Ma, N. Gao, Y. Sun, X. Du, J. Ren, X. Qu, Adv. Healthc. Mater. 7 (2018) 1800320.
[412] G. Lan, K. Ni, S.S. Veroneau, T. Luo, E. You, W. Lin, J. Am. Chem. Soc. 141 (2019) 6859–6863.
[413] G. Geisberger, E.B. Gyenge, C. Maake, G.R. Patzke, Carbohydr. Polym. 91 (2013) 58–67.
[414] M. Aureliano, G. Fraqueza, M. Berrocal, J.J. Cordoba-Granados, N.I. Gumerova, A. Rompel, C. Gutierrez-Merino, A.M. Mata, J. Inorg. Biochem. 236 (2022) 111952.
[415] R. Lampl, J. Breibeck, N.I. Gumerova, M.S. Galanski, A. Rompel, Sci. Rep. 11 (2021) 19354.
[416] A. Flütsch, T. Schroeder, M.G. Grütter, G.R. Patzke, Bioorg. Med. Chem. Lett. 21 (2011) 1162–1166.
[417] M. Witvrouw, H. Weigold, C. Pannecouque, D. Schols, E. De Clercq, G. Holan, J. Med. Chem. 43 (2000) 778–783.
[418] R. Francese, A. Civra, M. Rittà, M. Donalisio, M. Argenziano, R. Cavalli, A. S. Mougharbel, U. Kortz, D. Lembo, Antiviral Res. 163 (2019) 29–33.
[419] J. Fu, A.L. Gnatt, D.A. Bushnell, G.J. Jensen, N.E. Thompson, R.R. Burgess, P. R. David, R.D. Kornberg, Cell 98 (1999) 799–810.
[420] L. Leyssens, T. Balcaen, M. Pétré, N. Béjar Ayllón, W. El Aazmani, A. de Pierpont, G. Pyka, V. Lacroix, G. Kerckhofs, Acta Biomater. 164 (2023) 303–316.
[421] N.J. van Eck, L. Waltman, Scientometrics 84 (2010) 523–538.

OŚWIADCZENIA WSPÓŁAUTORÓW

UNIWERSYTET IM. ADAMA MICKIEWICZA W POZNANIU
Wydział Chemii

Poznań, 02.02.2026 r.

Mgr Daria Nowicka
Uniwersytet im. Adama Mickiewicza w Poznaniu
Wydział Chemii
Zakład Syntezy Nanostruktur Funkcjonalnych

Oświadczenie doktoranta

W związku z ubieganiem się o stopień doktora nauk chemicznych oświadczam, że jestem współautorem publikacji:

1. **Daria Nowicka**, Karol Garbaczewski, Giuseppe Consiglio, Giuseppe Forte, Maciej Kubicki, Teresa Łuczak, Violetta Patroniak, Adam Gorczyński, *„Biomimetic O-demethylation at a copper(II) center with imine ligand: a structural and computational study"*, **New Journal of Chemistry,** 2026, DOI: 10.1039/D5NJ04478B.

Wkład doktorantki obejmował powtórzenie pierwszego etapu, przeprowadzenie drugiego etapu syntezy trzech nowych ligandów typu zasady Schiffa L1 [$C_{18}H_{20}N_4O_3$], L2 [$C_{16}H_{16}N_4O$] oraz L3 [$C_{18}H_{20}N_4O_2$], syntezę ich kompleksów z jonami metali: C1 [$Cu(L1)Cl_2$], C2 [$Cu((L1)\text{-}CH_3)Cl$], C3 [$Cu_2((L1)\text{-}CH_3)_2Cl(MeO)$], C4 [$Cu(L2)Cl_2$], C5 [$Cu(L3)Cl_2$] oraz C6 [$Cu(L3)_2Cl(ClO_4)$]MeOH, ich charakterystykę strukturalno-spektroskopową (HRMS ESI, FT-IR, ^{1}H NMR, ^{13}C NMR), w tym otrzymanie monokryształów odpowiednich do pomiarów rentgenostrukturalnych, wykonanie badań metodą spektroskopii UV-Vis, przeprowadzenie badań elektrochemicznych pod kierunkiem prof. UAM dr hab. Teresy Łuczak, przygotowanie części graficznej pracy, napisanie pierwszej wersji publikacji z wyłączeniem opisu struktur krystalicznych oraz obliczeń DFT, omówienie wyników w ujęciu całościowym, udział w edycji manuskryptu oraz naniesieniu poprawek edytorskich, w tym przygotowaniu odpowiedzi do recenzentów.

2. **Daria Nowicka**, Maciej Kubicki, Violetta Patroniak, Teresa Łuczak, Adam Gorczyński, *„Self-assembly of simple Schiff base ligand into unique saddle-type [4x4] tetranuclear architecture and its application as selective voltammetric dopamine sensor in aqueous conditions"*, **Electrochimica Acta**, 2024, 476, 143754.

Wkład doktorantki obejmował powtórzenie syntezy liganda typu zasady Schiffa HL [$C_{10}H_{11}N_5$], syntezę jego czterordzeniowego kompleksu z jonami Cu(II) Cu_4L_4 [$Cu_4(L\text{-}H)_4(BF_4)_2(MeOH)_2](BF_4)_2$, charakterystykę strukturalno-spektroskopową (ESI-MS, FT-IR), w tym otrzymanie monokryształu odpowiedniego do pomiarów rentgenostrukturalnych, modyfikacja powierzchni elektrody złotej, jej charakterystyka (SEM, EDAX, X-ray energy dispersion, ATR-IR) oraz przeprowadzenie badań elektrochemicznych pod kierunkiem prof. UAM dr hab. Teresy Łuczak z wykorzystaniem zmodyfikowanej elektrody wobec detekcji dopaminy, przygotowanie części graficznej pracy, wspólne napisanie publikacji, udział w edycji manuskryptu oraz naniesieniu poprawek edytorskich, w tym przygotowaniu odpowiedzi do recenzentów.

3. **Daria Nowicka**, Karol Garbaczewski, Teresa Łuczak, Giuseppe Forte, Giuseppe Consiglio, Maciej Kubicki, Violetta Patroniak, Adam Gorczyński, *„Application of a simple copper(II) complex compound as an epinephrine selective voltammetric sensor in the presence of uric acid under aqueous conditions"*, **Dalton Transactions**, 2025, 54, 1000 - 1012.

Wkład doktorantki obejmował powtórzenie syntezy liganda typu zasady Schiffa L [C10H11N5], syntezę jego kompleksu z jonem Cu(II) CuL_2 [$CuL_2](BF_4)_2$, charakterystykę strukturalno-spektroskopową (HRMS ESI, FT-IR), w tym otrzymanie monokryształu odpowiedniego do pomiarów rentgenostrukturalnych, modyfikacja powierzchni elektrody złotej poprzez utworzenie samoorganizującej się monowarstwy na powierzchni elektrody, jej charakterystyka (SEM, EDAX, X-ray energy dispersion, ATR-IR) oraz przeprowadzenie badań elektrochemicznych pod kierunkiem prof. UAM dr hab. Teresy Łuczak z wykorzystaniem zmodyfikowanej elektrody wobec detekcji epinefryny, przygotowanie części graficznej pracy, wspólne napisanie publikacji, udział w edycji manuskryptu oraz naniesieniu poprawek edytorskich, w tym przygotowaniu odpowiedzi do recenzentów.

4. **Daria Nowicka**, Dawid Marcinkowski, Nahir Vadra, Martyna Szymańska, Maciej Kubicki, Giuseppe Consiglio, Wojciech Drożdż, Artur R. Stefankiewicz, Violetta Patroniak, Marta Fik-Jaskółka, Adam Gorczyński, *„The effect of ionic versus covalent functionalization of polyoxometalate hybrid materials with coordinating subunits on their stability and interaction with DNA"*, **Dalton Transactions**, 2024, 53, 11678-11688.

Wkład doktorantki obejmował syntezę nowych materiałów hybrydowych: $H1^{cov}$ (POM + L^{tpy}) $[V_3POM+TRIZMA+L^{tpy}]TBA_6$; $H2^{cov}$ (POM+K1) $[Zn(V_3POM+TRIZMA+L^{tpy})Cl_2]TBA_6$; $H3^{cov}$ (POM+K2) $[Zn(V_3POM+TRIZMA+L^{tpy})_2(ClO_4)_2]TBA_{(12-x)}H_x$; x = 11.5; $H4^{cov}$ ($H1^{cov}$+$ZnCl_2$) $[Zn(V_3POM+TRIZMA+L^{tpy})Cl_2]H_2TBA_4$; $H5^{cov}$ ($H1^{cov}$+$Zn(ClO_4)_2$) $[Zn(V_3POM+TRIZMA+L^{tpy})_2(ClO_4)_2]H_{12}$; $H6^{cov}$ (POM+L^{tpy}+$ZnCl_2$) $[Zn(V_3POM+TRIZMA+L^{tpy})Cl_2]TBA_{(6-x)}H_x$; x = 5.75; $H7^{cov}$ (POM+L^{tpy}+$Zn(ClO_4)_2$) $[Zn(V_3POM+TRIZMA+L^{tpy})_2(ClO_4)_2]TBA_{(12-x)}H_x$; x = 11.5 oraz ich charakterystykę strukturalno-spektroskopową (ESI-MS, FT-IR, ^1H NMR, ^{31}P NMR), napisanie części publikacji dotyczącej syntezy oraz charakterystyki strukturalno-spektroskopowej, udział w przygotowaniu części graficznej pracy oraz wewnętrznej okładki czasopisma (*Inside Front Cover*), udział w edycji manuskryptu oraz naniesieniu poprawek edytorskich, w tym przygotowaniu odpowiedzi do recenzentów.

5. **Daria Nowicka**, Nahir Vadra, Ewelina Wieczorek-Szweda, Violetta Patroniak, Adam Gorczyński, *„Overview of Wells-Dawson Polyoxometalates: from structure and functionalization to application"*, **Coordination Chemistry Reviews,** 2024, 519, 216091.

Wkład doktorantki obejmował dogłębny przegląd literatury naukowej z zakresu polioksometalanów typu Wellsa-Dawsona, wyselekcjonowanie i zebranie pozycji literaturowych, podział artykułu na odpowiednie sekcje tematyczne, napisanie publikacji z wyłączeniem części aplikacyjnej, udział w przygotowaniu części graficznej pracy, zebranie copyright, udział w edycji manuskryptu oraz naniesieniu poprawek edytorskich, w tym przygotowaniu odpowiedzi do recenzentów.

Daria Nowicka

ul. Uniwersytetu Poznańskiego 8, 61-614 Poznań
tel. +48 61 829 15 61
depchem@amu.edu.pl
www.chemia.amu.edu.pl

UNIWERSYTET IM. ADAMA MICKIEWICZA W POZNANIU
Wydział Chemii

Poznań, 03.02.2026 r.

Prof. dr hab. Violetta Patroniak
Uniwersytet im. Adama Mickiewicza w Poznaniu
Wydział Chemii
Zakład Syntezy Nanostruktur Funkcjonalnych

Oświadczenie Promotora

Potwierdzam swój wkład w następujące publikacje:

1. **Daria Nowicka**, Karol Garbaczewski, Giuseppe Consiglio, Giuseppe Forte, Maciej Kubicki, Teresa Łuczak, Violetta Patroniak, Adam Gorczyński, *„Biomimetic O-demethylation at a copper(II) center with imine ligand: a structural and computational study"*, **New Journal of Chemistry,** 2026, DOI: 10.1039/D5NJ04478B.

2. **Daria Nowicka**, Maciej Kubicki, Violetta Patroniak, Teresa Łuczak, Adam Gorczyński, *„Self-assembly of simple Schiff base ligand into unique saddle-type [4x4] tetranuclear architecture and its application as selective voltammetric dopamine sensor in aqueous conditions"*, **Electrochimica Acta**, 2024, 476, 143754.

3. **Daria Nowicka**, Karol Garbaczewski, Teresa Łuczak, Giuseppe Forte, Giuseppe Consiglio, Maciej Kubicki, Violetta Patroniak, Adam Gorczyński, *„Application of a simple copper(II) complex compound as an epinephrine selective voltammetric sensor in the presence of uric acid under aqueous conditions"*, **Dalton Transactions**, 2025, 54, 1000 - 1012.

4. **Daria Nowicka**, Dawid Marcinkowski, Nahir Vadra, Martyna Szymańska, Maciej Kubicki, Giuseppe Consiglio, Wojciech Drożdż, Artur R. Stefankiewicz, Violetta Patroniak, Marta Fik-Jaskółka, Adam Gorczyński, *„The effect of ionic versus covalent functionalization of polyoxometalate hybrid materials with coordinating subunits on their stability and interaction with DNA"*, **Dalton Transactions**, 2024, 53, 11678-11688.

5. **Daria Nowicka**, Nahir Vadra, Ewelina Wieczorek-Szweda, Violetta Patroniak, Adam Gorczyński, *„Overview of Wells-Dawson Polyoxometalates: from structure and functionalization to application”*, **Coordination Chemistry Reviews,** 2024, 519, 216091.

Prowadziłam bezpośredni nadzór nad pracami doktorantki. Mój udział polegał na pomocy w opisach wyników badań oraz przygotowaniu odpowiedzi do recenzentów we wszystkich wymienionych wyżej publikacjach.

ul. Uniwersytetu Poznańskiego 8, 61-614 Poznań
tel. +48 61 829 15 61
depchem@amu.edu.pl
www.chemia.amu.edu.pl

UNIWERSYTET IM. ADAMA MICKIEWICZA W POZNANIU
Wydział Chemii

Poznań, 30.01.2026 r.

Dr Adam Gorczyński
Uniwersytet im. Adama Mickiewicza w Poznaniu
Wydział Chemii
Zakład Syntezy Nanostruktur Funkcjonalnych

Oświadczenie Promotora pomocniczego

Potwierdzam swój wkład w następujące publikacje:

1. **Daria Nowicka**, Karol Garbaczewski, Giuseppe Consiglio, Giuseppe Forte, Maciej Kubicki, Teresa Łuczak, Violetta Patroniak, Adam Gorczyński, *„Biomimetic O-demethylation at a copper(II) center with imine ligand: a structural and computational study"*, **New Journal of Chemistry,** 2026, DOI: 10.1039/D5NJ04478B.

2. **Daria Nowicka**, Maciej Kubicki, Violetta Patroniak, Teresa Łuczak, Adam Gorczyński, *„Self-assembly of simple Schiff base ligand into unique saddle-type [4x4] tetranuclear architecture and its application as selective voltammetric dopamine sensor in aqueous conditions"*, **Electrochimica Acta**, 2024, 476, 143754.

3. **Daria Nowicka**, Karol Garbaczewski, Teresa Łuczak, Giuseppe Forte, Giuseppe Consiglio, Maciej Kubicki, Violetta Patroniak, Adam Gorczyński, *„Application of a simple copper(II) complex compound as an epinephrine selective voltammetric sensor in the presence of uric acid under aqueous conditions"*, **Dalton Transactions**, 2025, 54, 1000 - 1012.

4. **Daria Nowicka**, Dawid Marcinkowski, Nahir Vadra, Martyna Szymańska, Maciej Kubicki, Giuseppe Consiglio, Wojciech Drożdż, Artur R. Stefankiewicz, Violetta Patroniak, Marta Fik-Jaskółka, Adam Gorczyński, *„The effect of ionic versus covalent functionalization of polyoxometalate hybrid materials with coordinating subunits on their stability and interaction with DNA"*, **Dalton Transactions**, 2024, 53, 11678-11688.

5. **Daria Nowicka**, Nahir Vadra, Ewelina Wieczorek-Szweda, Violetta Patroniak, Adam Gorczyński, *„Overview of Wells-Dawson Polyoxometalates: from structure and functionalization to application”*, **Coordination Chemistry Reviews,** 2024, 519, 216091.

Mój udział obejmował konceptualizację i koordynowanie prac badawczych oraz pomoc przy interpretacji wyników badań. Brałem również udział w przygotowywaniu ostatecznej wersji manuskryptu oraz dyskusji z recenzentami we wszystkich wymienionych wyżej publikacjach.

ul. Uniwersytetu Poznańskiego 8, 61-614 Poznań
tel. +48 61 829 15 61
depchem@amu.edu.pl
www.chemia.amu.edu.pl

UNIWERSYTET IM. ADAMA MICKIEWICZA W POZNANIU
Wydział Chemii

Poznań, 02.02.2026 r.

Prof. dr hab. Maciej Kubicki
Uniwersytet im. Adama Mickiewicza w Poznaniu
Wydział Chemii
Zakład Krystalografii

Oświadczenie o współautorstwie

Potwierdzam swój wkład w następujące publikacje:

1. **Daria Nowicka**, Karol Garbaczewski, Giuseppe Consiglio, Giuseppe Forte, Maciej Kubicki, Teresa Łuczak, Violetta Patroniak, Adam Gorczyński, *„Biomimetic O-demethylation at a copper(II) center with imine ligand: a structural and computational study"*, **New Journal of Chemistry,** 2026, DOI: 10.1039/D5NJ04478B.

2. **Daria Nowicka**, Maciej Kubicki, Violetta Patroniak, Teresa Łuczak, Adam Gorczyński, *„Self-assembly of simple Schiff base ligand into unique saddle-type [4x4] tetranuclear architecture and its application as selective voltammetric dopamine sensor in aqueous conditions"*, **Electrochimica Acta**, 2024, 476, 143754.

3. **Daria Nowicka**, Karol Garbaczewski, Teresa Łuczak, Giuseppe Forte, Giuseppe Consiglio, Maciej Kubicki, Violetta Patroniak, Adam Gorczyński, *„Application of a simple copper(II) complex compound as an epinephrine selective voltammetric sensor in the presence of uric acid under aqueous conditions"*, **Dalton Transactions**, 2025, 54, 1000 - 1012.

4. **Daria Nowicka**, Dawid Marcinkowski, Nahir Vadra, Martyna Szymańska, Maciej Kubicki, Giuseppe Consiglio, Wojciech Drożdż, Artur R. Stefankiewicz, Violetta Patroniak, Marta Fik-Jaskółka, Adam Gorczyński, *„The effect of ionic versus covalent functionalization of polyoxometalate hybrid materials with coordinating subunits on their stability and interaction with DNA"*, **Dalton Transactions**, 2024, 53, 11678-11688.

Mój udział w wyżej wymienionych publikacjach obejmuje pomiary dyfraktometryczne monokryształów, opis uzyskanych wyników oraz dyskusje z recenzentami.

ul. Uniwersytetu Poznańskiego 8, 61-614 Poznań
tel. +48 61 829 15 61
depchem@amu.edu.pl
www.chemia.amu.edu.pl

UNIWERSYTET IM. ADAMA MICKIEWICZA W POZNANIU
Wydział Chemii

Poznań, 02.02.2026 r.

Prof. UAM dr hab. Teresa Łuczak
Uniwersytet im. Adama Mickiewicza w Poznaniu
Wydział Chemii
Zakład Fizykochemii Środowiska

Oświadczenie o współautorstwie

Potwierdzam swój wkład w następujące publikacje:

1. **Daria Nowicka**, Karol Garbaczewski, Giuseppe Consiglio, Giuseppe Forte, Maciej Kubicki, Teresa Łuczak, Violetta Patroniak, Adam Gorczyński, *„Biomimetic O-demethylation at a copper(II) center with imine ligand: a structural and computational study”*, **New Journal of Chemistry,** 2026, DOI: 10.1039/D5NJ04478B.

2. **Daria Nowicka**, Maciej Kubicki, Violetta Patroniak, Teresa Łuczak, Adam Gorczyński, *„Self-assembly of simple Schiff base ligand into unique saddle-type [4x4] tetranuclear architecture and its application as selective voltammetric dopamine sensor in aqueous conditions”*, **Electrochimica Acta**, 2024, 476, 143754.

3. **Daria Nowicka**, Karol Garbaczewski, Teresa Łuczak, Giuseppe Forte, Giuseppe Consiglio, Maciej Kubicki, Violetta Patroniak, Adam Gorczyński, *„Application of a simple copper(II) complex compound as an epinephrine selective voltammetric sensor in the presence of uric acid under aqueous conditions”*, **Dalton Transactions**, 2025, 54, 1000 - 1012.

Mój udział w wyżej wymienionych publikacjach obejmuje koordynowanie prac badawczych związanych z określeniem właściwości elektrochemicznych (wykonanie pomiarów, interpretacja oraz opis wyników badań). Brałam także udział w przygotowywaniu manuskryptu, Supporting Information oraz odpowiedzi do recenzentów.

Teresa Łuczak

ul. Uniwersytetu Poznańskiego 8, 61-614 Poznań
tel. +48 61 829 15 61
depchem@amu.edu.pl
www.chemia.amu.edu.pl

Poznań, 21.07.2025 r.

Dr Nahir Vadra
Adam Mickiewicz University in Poznan
Faculty of Chemistry
Department of Synthesis of Functional Nanostructures

Statement of Co-authorship

I confirm my contribution to the publications:

1. **Daria Nowicka**, Dawid Marcinkowski, Nahir Vadra, Martyna Szymańska, Maciej Kubicki, Giuseppe Consiglio, Wojciech Drożdż, Artur R. Stefankiewicz, Violetta Patroniak, Marta Fik-Jaskółka, Adam Gorczyński, *„The effect of ionic versus covalent functionalization of polyoxometalate hybrid materials with coordinating subunits on their stability and interaction with DNA"*, **Dalton Transactions**, 2024, 53, 11678-11688.

My contribution consisted of taking part in writing the manuscript and preparing *Inside Front Cover*.

2. **Daria Nowicka**, Nahir Vadra, Ewelina Wieczorek-Szweda, Violetta Patroniak, Adam Gorczyński, *„Overview of Wells-Dawson Polyoxometalates: from structure and functionalization to application"*, **Coordination Chemistry Reviews,** 2024, 519, 216091.

My contribution consisted of writing selected sections from the application part of the publication and preparing figures. I also participated in the preparation of responses to the reviewers.

UNIWERSYTET IM. ADAMA MICKIEWICZA W POZNANIU
Wydział Chemii

Poznań, 21.07.2025 r.

Dr Dawid Marcinkowski
Uniwersytet im. Adama Mickiewicza w Poznaniu
Wydział Chemii
Zakład Syntezy Nanostruktur Funkcjonalnych

Oświadczenie o współautorstwie

Potwierdzam swój wkład w następującą publikację:

1. **Daria Nowicka**, Dawid Marcinkowski, Nahir Vadra, Martyna Szymańska, Maciej Kubicki, Giuseppe Consiglio, Wojciech Drożdż, Artur R. Stefankiewicz, Violetta Patroniak, Marta Fik-Jaskółka, Adam Gorczyński, *„The effect of ionic versus covalent functionalization of polyoxometalate hybrid materials with coordinating subunits on their stability and interaction with DNA"*, **Dalton Transactions**, 2024, 53, 11678-11688.

Mój wkład obejmuje syntezę oraz charakterystykę strukturalno-spektroskopową liganda, związków kompleksowych oraz prekursorów polioksometalanu typu Wellsa-Dawsona wraz z udziałem w przygotowywaniu manuskryptu.

Dawid Marcinkowski

UNIWERSYTET IM. ADAMA MICKIEWICZA W POZNANIU
Wydział Chemii

Poznań, 21.07.2025 r.

Dr Marta Fik-Jaskółka
Uniwersytet im. Adama Mickiewicza w Poznaniu
Wydział Chemii
Zakład Syntezy Nanostruktur Funkcjonalnych

Oświadczenie o współautorstwie

Potwierdzam swój wkład w następującą publikację:

1. **Daria Nowicka**, Dawid Marcinkowski, Nahir Vadra, Martyna Szymańska, Maciej Kubicki, Giuseppe Consiglio, Wojciech Drożdż, Artur R. Stefankiewicz, Violetta Patroniak, Marta Fik-Jaskółka, Adam Gorczyński, *„The effect of ionic versus covalent functionalization of polyoxometalate hybrid materials with coordinating subunits on their stability and interaction with DNA"*, **Dalton Transactions**, 2024, 53, 11678-11688.

Mój udział w wyżej wymienionej publikacji obejmuje badanie aktywności biologicznej, interpretację oraz opis uzyskanych wyników badań biologicznych. Brałam także udział w przygotowywaniu manuskryptu, „Electronic Supporting Information" oraz odpowiedzi do recenzentów.

Marta Fik-Jaskółka

ul. Uniwersytetu Poznańskiego 8, 61-614 Poznań
tel. +48 61 829 15 61
depchem@amu.edu.pl
www.chemia.amu.edu.pl

UNIWERSYTET IM. ADAMA MICKIEWICZA W POZNANIU
Wydział Chemii

Poznań, 21.07.2025 r.

Dr Ewelina Wieczorek-Szweda
Uniwersytet im. Adama Mickiewicza w Poznaniu
Wydział Chemii
Zakład Syntezy Nanostruktur Funkcjonalnych

Oświadczenie o współautorstwie

Potwierdzam swój wkład w następującą publikację:

1. **Daria Nowicka**, Nahir Vadra, Ewelina Wieczorek-Szweda, Violetta Patroniak, Adam Gorczyński, *„Overview of Wells-Dawson Polyoxometalates: from structure and functionalization to application”*, **Coordination Chemistry Reviews,** 2024, 519, 216091.

Mój udział w wyżej wymienionej publikacji obejmuje napisanie poszczególnych sekcji z części aplikacyjnej publikacji. Brałam także udział w przygotowywaniu odpowiedzi do recenzentów.

Ewelina Wieczorek-Szweda

ul. Uniwersytetu Poznańskiego 8, 61-614 Poznań
tel. +48 61 829 15 61
depchem@amu.edu.pl
www.chemia.amu.edu.pl